Université Clermont Auvergne
École de l'Observatoire de Physique du Globe de Clermont-Ferrand
École doctorale des Sciences Fondamentales

Numéro d'ordre : **561 bis**

Mémoire présenté en vue de l'obtention de l'habilitation à Diriger des Recherches

Spécialité : **Volcanologie**

par

Mathieu Gouhier

Physicien-Adjoint de l'UCA
Observatoire de Physique du Globe de Clermont-Ferrand
Laboratoire Magmas et Volcans

Sources and transport of volcanic eruptive products: Insight from remote sensing techniques

Date et lieu de soutenance : 16 Décembre 2020 - LMV/OPGC

Composition du jury :

Simon Carn	Professeur à l'Université du Michigan (MTU – USA)	Rapporteur
Edouard Kaminski	Professeur à l'université Paris/Diderot (IPGP)	Rapporteur
Simona Scollo	Professeure associée à INGV (Catane, Italie)	Rapporteur
Jean-François Lénat	Professeur émérite (UCA)	Référent
Franck Donnadieu	Physicien-Adjoint (UCA)	Examinateur

Contents

1. A short Introduction

My research interests resolve essentially around the study of the volcanic emissions' dynamics using remote sensing techniques. This ranges from the characterization of source mechanisms of eruptive products emissions (i.e., lava flows, ash and gas plumes) to the study of their transport processes toward distal locations.

The physical volcanology is a rapidly evolving discipline due to, in particular, the emergence of new technologies concerning on-board sensors (e.g., TIR hyperspectral) providing increasingly complex and voluminous datasets. However, this evolution is also the result of novel development within processing techniques (e.g., database interoperability, Parallel/GPU calculation, etc.), allowing refined modelling of physico-chemical mechanisms (e.g., radiative transfer, transport / sedimentation, etc.) and the integration of large monitoring datasets.

Consequently, and upstream to more fundamental work, this dependence on new technologies requires significant **methodological development** and **constitutes (*i*) the first axis of my current and future research activity**. In this specific part of the manuscript, I will present the main methodological developments carried out since my PhD in 2008, and related to the processing of both ground and space-based remote sensing data.

The use of remote sensing techniques is particularly suitable for measuring at safe distance parameters controlling the emplacement and transport of eruptive products; and each instrument has its own specificities and field of application. I have strived all these years to develop and improve quantitative retrieval methods (direct models and data inversions), using various remote sensing techniques, in order to bring new constraints on important scientific questions that I divide into two axes: **(*ii*) the understanding of eruptive source mechanisms** and **(*iii*) the characterization of eruptive transport processes.**

Finally, and in parallel to more fundamental research activities, **(*iv*) the development of operational routines** for the monitoring of active volcanoes constitutes the last major axis of my research activities. This comprises, the acquisition of long time series of referenced parameters (e.g., lava flow rates, ash concentration, etc.), as well as the real-time monitoring of eruptive products contributing to the operational volcanic crisis response.

In fact, the structuration presented here (methodology, fundamental research and operational monitoring) is directly related to my status (Physicien-Adjoint, CNAP), and constitutes a very coherent project around the study of active volcanoes.

2. Methodological development

The improvement of volcanic mechanisms understanding is often the result of new algorithm development handling large datasets, allowing faster calculations and more reliable processing. However, this computing work is not separable from physical models development describing the dynamics of volcanic mechanisms, such as early detection of volcanic lava hot spots or the precise quantification of ash cloud concentration. In this framework, I will often refer to "direct modelling", which correspond to the physical description of a given problem (ash diffusion, lava temperature radiation, SO_2 oxidation, etc.) using a set of appropriate equations that can be solved analytically or, in most cases, numerically. In essence, a model is a simplified view of the reality using assumptions, and the purpose of which is to provide key information on a specific question. The result of direct models gives you synthetic (i.e., modelled) values that can be further used for data inversion. Indeed, the use of direct models solely is not very useful, but combined with observation data (from any kind of sensors), allows you to bring more reliable information on acting mechanisms.

My research work published in 2008 on the study of Srombolian eruptions using ground-based Doppler radar measurements constitute a very good illustration of this methodological scheme (Gouhier & Donnadieu, 2008), and will be presented here as a key example. Also, I will present important developments carried out using space-based infrared measurements providing (i) improved detection routines of volcanic ah cloud (Guéhenneux et al., 2015) and (ii) allowing the operational quantification of volcanic ash cloud concentration and used in several publications (e.g.,. Bonadonna et al., 2011; Gouhier et al., 2012; Poret et al., 2018, Gouhier and Paris, 2019). Similarly, one other example will be presented, showing methodological development carried out for (i) operational detection of lava hot spots and (ii) for the quantification of lava volume flow rate.

2.1. Inversion of Doppler radar measurements

My published work on the study of Strombolian eruptions using Doppler radar methods (Gouhier & Donnadieu, 2008) is a good example of methodological research (see Fig. 1). This study allowed for the first time the quantification of the mass and the size of pyroclasts ejected at the source vent, from a ground-based instrument at Etna (Sicilia). This had been achieved through the development of a direct model of Mie scattering and the implementation of an appropriate inversion scheme. We will come back more extensively in chapter 3 and 4, on the volcanological purpose of such measurements. However, we must have in mind that today there is still no method to measure directly the eruptive mass flux of pyroclasts at the source (i.e., right above vent) hereafter referred to as the Mass Eruption Rate (MER). Yet, this parameter is essential to predict the ascent dynamics of the ash plume in the vertical column.

During my PhD, I had the opportunity to use VOLDORAD, which is a pulsed volcano Doppler radar developed by the Observatoire de Physique du Globe de Clermont-Ferrand (OPGC, France) specifically for the active remote sensing of volcanic eruption jets and plumes. The second version of the system is a medium-power (60 W) Doppler radar with a 9° beam width and a working wavelength (λ) of 23.5 cm. It is designed to monitor all types of explosive volcanic activity of variable magnitude. It operates at a medium distance range (0.4–12 km) under all weather conditions with a high sampling rate (10 Hz) that permits detailed analysis of early eruptive processes. Data from successive range gates are displayed as Doppler spectra (figure 1) representing the power spectral density versus radial velocity. From the processing of the series of Doppler spectra, two sets of parameters are directly retrieved for ascending (+) and descending (-) ejecta crossing the beam axis. (i) The velocity information (max and mean radial velocity) and (ii) the power information (P+, P-) resulting from the energy backscattered by particles moving away and toward the radar, respectively.

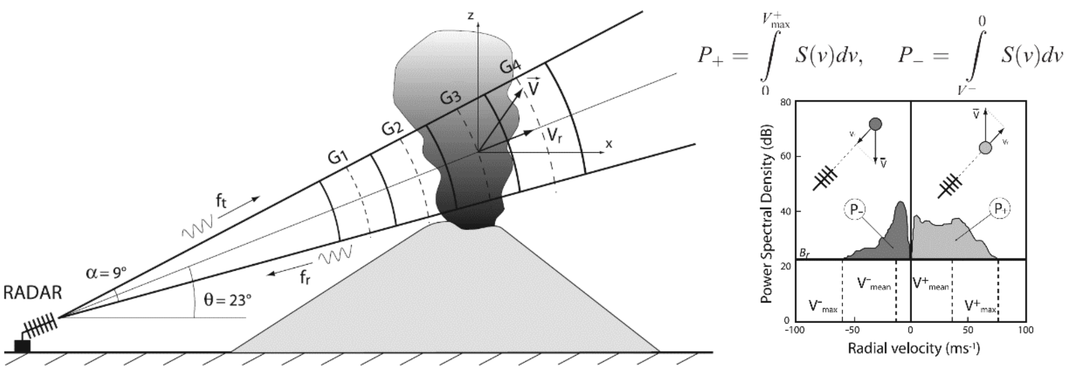

Figure 1. (*left*) Sketch of the radar sounding geometry used for the acquisition campaign on Mount Etna, on 4 July 2001. VOLDORAD was set up at an altitude of 3000 m, at a slanting distance of 930 m to the crater rim, 280 m below the summit of the SE crater, and with an antenna elevation angle of 23°. (*right*) Sketch of a typical Doppler spectrum obtained by VOLDORAD. The power spectral density is displayed as a function of the radial velocity in a given range. The horizontal line (Br) corresponds to the background noise level. Total echo power and maximum and mean velocities can be deduced from Doppler spectra. They are indexed (plus) and (minus) for ejecta with the radial component of their velocity vector moving away and toward the antenna, respectively.

The aim of that study was to estimate masses of volcanic ejecta from two Strombolian explosions by inversion of the Doppler radar measurements. For this purpose, a comparison between the total backscattered power measured by the radar (P_{mes}) and a synthetic (i.e., calculated) backscattered power (P_{synth}) is needed. The total backscattered power (i.e. through all range gates and for both ascending/descending trajectories) recorded by the radar is a measure of the amount (mass + size distribution) of pyroclasts at a given instant. The estimation of the synthetic backscattered power is not easy, and requires an electromagnetic scattering model. A good approximation for small particles is the Rayleigh scattering theory, the validity limit of which depends on the radar wavelength. In our case (λ= 23.5 cm), the Rayleigh theory could only be applied for particles of diameter smaller than λ/4, which corresponds to 5.9 cm. Thus, considering the wide range of particle diameters characterizing volcanic activity at the source, the complete scattering theory is required to account for the effects of larger particles. Mie

[1908] gave a general solution of electromagnetic (EM) wave scattering. This approach applies Maxwell's equations for plane waves scattered by compositionally homogeneous and spherical particles. Full development of the direct EM model of Mie can be found in Gouhier et al., (2008). In short, the power backscattered to the radar by a population of particles crossing the beam can be calculated from the so-called radar reflectivity (η). Thus, the synthetic power can then be defined as:

$$P_{synth} = \frac{C_r V_s \eta}{r^4}$$

where C_r is the radar constant, V_s the sampling volume, and r is the slant distance between the radar and the target. Then, the radar reflectivity (η) is simply the sum of the backscattering cross sections (σ_{bks}) of individual particles of given sizes and per unit volume, following:

$$\eta = \sum_{i=1}^{n} \frac{\sigma_{bks}}{V_s}$$

Scattering and attenuation by compositionally homogeneous spheres are significantly influenced by the complex refractive index (m) of the particle. VOLDORAD transmits power through a square array of four Yagi antennas, such that the incident electromagnetic wave is polarized parallel to the scattering plane. Being a monostatic radar (i.e., the same antenna is used for transmission and reception), we define a backscattering cross section (σ_{bks}) for horizontal linear polarization such as:

$$\sigma_{bks} = \frac{\lambda^4}{4\pi} \left| \sum_{n=1}^{\infty} (-1)^2 (2n+1)(a_n - b_n) \right|$$

where n is a positive integer, and a_n and b_n are the complex scattering coefficients (so-called Mie coefficients), derived from single complex amplitude function in the form of a convergent series. This part of the calculation can take significant computing time depending on the size distribution definition of particles. From the calculation of backscattering cross section, we can deduce the synthetic power emitted towards the radar to be further compared with the measured one. In figure 2, we show an example of Mie versus Rayleigh scattering patterns of an electromagnetic wave scattered by homogeneous spheres of four different sizes calculated for a signal at the wavelength used by VOLDORAD (λ = 23.5 cm) and with the complex dielectric factor of volcanic ash ($|K^2|$= 0.39).

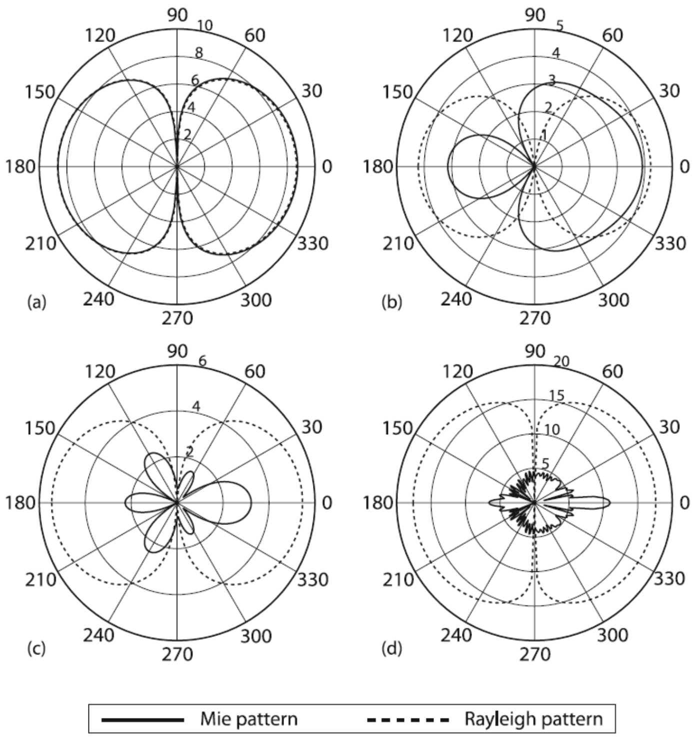

Figure 2. Mie versus Rayleigh scattering patterns of an electromagnetic wave, parallel polarized, scattered by a single homogeneous sphere with the complex dielectric factor of volcanic ash, $|K^2|=0.39$, and $\lambda = 23.5$ cm. The wave arrives from the left, and the particle is situated at the center of the pattern. Irradiance amplitude is normalized to that of Mie and expressed on a logarithmic scale. (a) Example of a small particle of diameter 2 cm. The Rayleigh and Mie scattering patterns are identical and symmetrical. Irradiance intensity is the same in front of and behind the particle. (b) Particle of diameter 14 cm. The Rayleigh and Mie scattering patterns are now significantly different. The Mie pattern still has two main lobes but is strongly asymmetric, as the backscattered intensity is lower than the forward scattered intensity. (c) Particle of diameter 20 cm. The Rayleigh pattern is still symmetrical, whereas the Mie pattern is divided into several lobes and shows much lower values of irradiance. (d) For a diameter of 2 m, the Mie (true) scattering pattern becomes very complex and shows always much lower values of irradiance than the Rayleigh approximation.

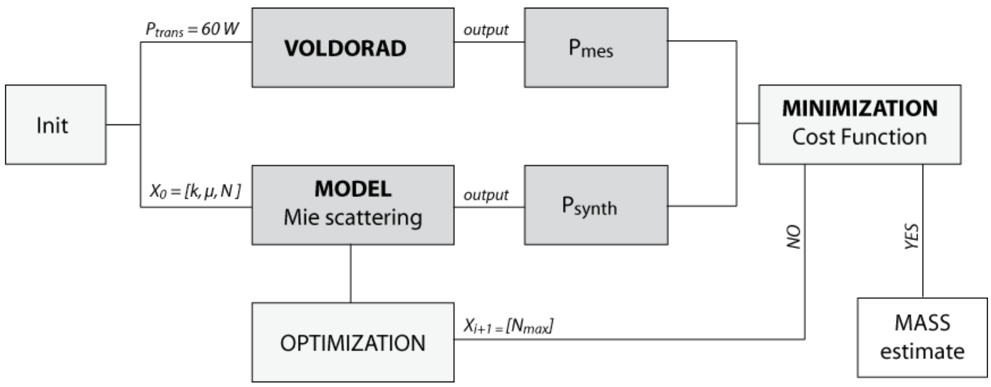

Figure 3. Inversion scheme of Doppler radar data using Mie scattering forward model.

Model inversions are frequently used in geophysics to recover initial parameters and boundary conditions from observed data of natural phenomena. In this case, the backscattered power (P_{mes}) is retrieved from radar measurements, while synthetic power (P_{synth}) is determined from the forward EM scattering model (figure 3). The inversion algorithm thus seeks the best correlation between P_{mes} and P_{synth}, by minimizing a cost function and eventually providing the input parameters sought. The model developed here takes into account two classes of parameters: (i) constant parameters describing the geometry of the system, the technical characteristics of the radar or material physical properties; and (ii) variable input parameters we are trying to estimate. In our case, what we are looking for is the (GSD) grain size distribution (i.e., number + size) of ejected pyroclasts. Physical parameters such as the ash plume mass and concentration can then deduced from the GSD. In the polydisperse model tested, the grain size distribution was characterized by a scaled Weibull function. The mode of the distribution is inferred from particle terminal velocities measured by Doppler radar for each explosion. A least squares estimation method is used on the basis of the minimization function S(X) characterized by the squared residual between radar measured data and synthetic data. The inversion procedure can be summarized in 5 different steps as follows:

Step 1: Attribution of initial values for estimation of the input parameters (GSD)

$$X_j = [X_1, X_2, \dots, X_n]$$

Step 2: Resolution of the forward model (Mie scattering)

$$X(\sigma_{bks}) \rightarrow \mathrm{P}_{synth}\,(X)$$

Step 3: Minimization of the cost function

$$S(X) = \sum \left[\mathrm{P}_{mes} - \mathrm{P}_{synth}\,(X)\right]^2$$

Step 4: Characterization of the iterative comparison criterion

$$\Delta P(X^i) = S(X^{i-1}) - S(X^i) =$$

Step 5: Testing of the fitness criterion:

$$\Delta P(X) < 0$$

2.2. Inversion thermal Infrared measurements

For over 25 years, thermal infrared data supplied by satellite-based sensors have been used to detect and characterize volcanic ash clouds using various methods. In this section, we distinguish two different objectives: (i) **early detection of volcanic ash cloud** and (ii) the **quantitative estimation of ash concentration**, and cloud altitude. For both objectives, **optical properties** need to be calculated to build a consistent forward EM model, allowing a better characterization of IR radiation interaction with ash particles. In the next section, we thus provide some necessary details on theoretical works.

2.2.1. Ash optical properties using Mie theory

We calculated optical properties for varying ash sizes and composition, but also for a variety of aerosols likely to coexist with ash particles. Therefore, we first achieve a detailed microphysics analysis for volcanic ash, water/ice, sulfuric acid, and mineral dust, using extinction efficiency (Q_{ext}), single scattering albedo (ϖ) and asymmetry parameter

(g) calculated by Mie theory as published in Guéhenneux et al., (2015). A good approximation for small particles is the Rayleigh scattering theory, the validity limit of which depends on the EM wavelength. In the case of thermal IR radiation emitted by the Earth surface (λ_{IR}= 8-14 µm) interacting with fine ash particles (1-100µm), the Rayleigh theory cannot be applied and the complete Mie scattering theory is required (figure 4). The relationship between the particle size and the EM wavelength is expressed in the form of a size parameter $x = kr$, where $k = 2\pi/\lambda$ is the wavenumber, r is the effective radius of the particle and λ is the wavelength of the incident light. For a typical ash particle radius of 10 µm the size parameter is $x \sim 6$.

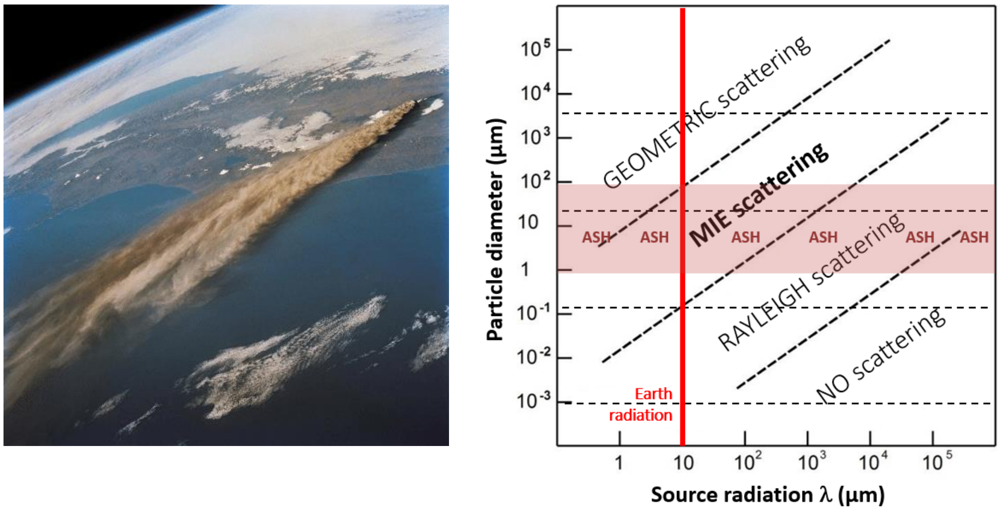

Figure 4. (*left*) Ash plume taken from the space shuttle Endeavour STS-68 of the Kliuchevskoi eruption in 1994. (*right*) Sketch of scattering regime as a function of particle sizes and source radiation wavelengths.

The total attenuation by the medium of incident light is commonly defined using the dimensionless extinction efficiency (Q_{ext}). It is the sum of absorption and scattering efficiencies ($Q_{ext} = Q_{abs} + Q_{sca}$) and usually defined as the ratio of the cross section coefficient (σ_{ext}) to the geometrical particle cross section (πr^2). The figure 5 (*left*) shows the interaction processes likely to exist between IR radiations and ash particles. The calculation of Mie cross sections are carried out using infinite series of the so-called Mie coefficients (a_n, b_n) and particle size parameters (x).

$$\sigma_{ext} = \frac{2}{x^2}\sum_{n=1}^{\infty}(2n+1)Re\{a_n - b_n\}$$

$$\sigma_{sca} = \frac{2}{x^2}\sum_{n=1}^{\infty}(2n+1)(|a_n|^2 + |b_n|^2)$$

Computation of the Mie coefficients (a_n and b_n), made from recursion relations for the spherical Bessel functions, also need complex refractive index ($m = n + ik$) of the particle. This is a critical point as it directly controls the relative importance of scattering (n) versus absorption (ik), although difficult to obtain. On figure 5 (*right*) we show typical extinction coefficients as a function of size parameters for three different particles having increasingly high absorption features. One striking property is that Q_{ext}

asymptotically approaches the limiting value 2 as the size parameter (x) increases. This means that brightness temperature difference will rapidly converges toward zero for radius > 20 µm (i.e., for a size parameter $x > 10$), hence preventing any retrieval of such ash particles. Low-amplitude high-frequency ripple waves are due to scattering processes and vanish as the absorption increases.

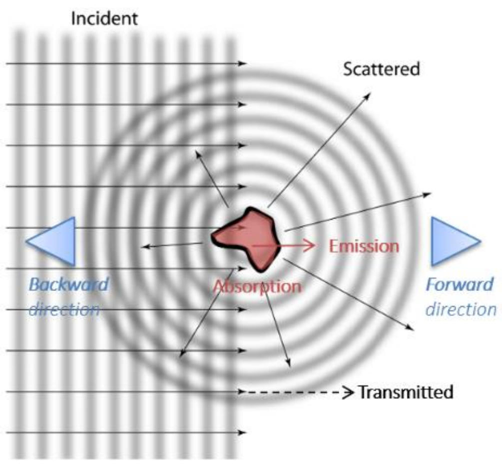

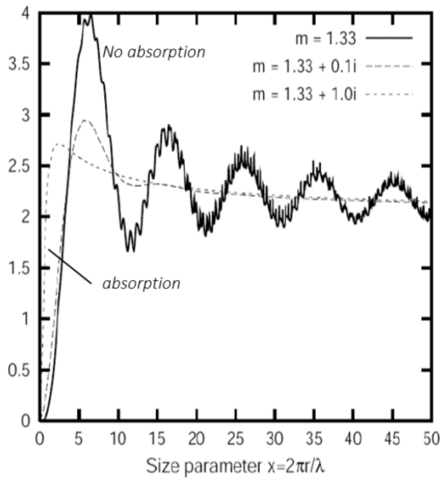

Figure 5. (left) Sketch of interaction processes likely to exist between IR radiations and ash particles. (right) typical extinction coefficients as a function of size parameters for three different particles having increasingly high absorption features.

However, the extinction efficiency alone is not enough to describe the actual attenuation, and we need to characterize the radial distribution of EM radiations scattered by ash particles. In the Mie regime, in particular, the direction of light scattered is strongly anisotropic. For this purpose, we calculated the ash scattering phase function $p(\mu,\mu')$ through the asymmetric factor (g). The phase function represents the fraction of incident light coming from the direction μ', to the scattered light in the direction μ. For spherical particles, the phase function only depends on the cosine of the angle (Θ) between the two directions (μ, μ'). The asymmetry factor (g) is the average cosine of the scattering angle (Θ), and characterizes the asymmetry of the scattering phase function. It is defined as the first moment of the phase function following:

$$P(\theta) = \frac{F(\theta)}{\int_0^\pi F(\theta) sin\theta d\theta}$$

$$g = \frac{1}{2}\int_{-1}^{1} P(cos\Theta) cos\Theta d(cos\Theta)$$

with $P(\theta)$ being the probability for a photon to be scattered in a given direction. The asymmetry factor may theoretically vary from $g = -1$ (pure backscattering: $\Theta = 180°$) to $g = +1$ (pure forward scattering: $\Theta = 0°$) and shows isotropic scattering for $g = 0$. Finally, g can be calculated from Mie coefficients using the following formulation:

$$g = \frac{4}{x^2 Q_{sca}}\left[\sum_n \frac{n(n+2)}{n+1} Re(a_n a_{n+1}^* + b_n b_{n+1}^*) + \frac{2n+1}{n(n+1)} Re(a_n b_n^*)\right]$$

In figure 6 (*left*) we show the phase function for various particle size parameters ranging from $x = 0.1$ hence having isotropic scattering phase function to $x = 30$ showing a strong forward peak (0°). Also (*right*) we computed the scattering phase function intensity for an andesitic ash particle of radius 10 µm ($x = 6$), already showing a strong forward peak. In this case the equivalent asymmetry factor is calculated to be $g = 0.81$. This is an important point to consider, as most of the scattered EM radiation will actually contribute to the at-sensor signal.

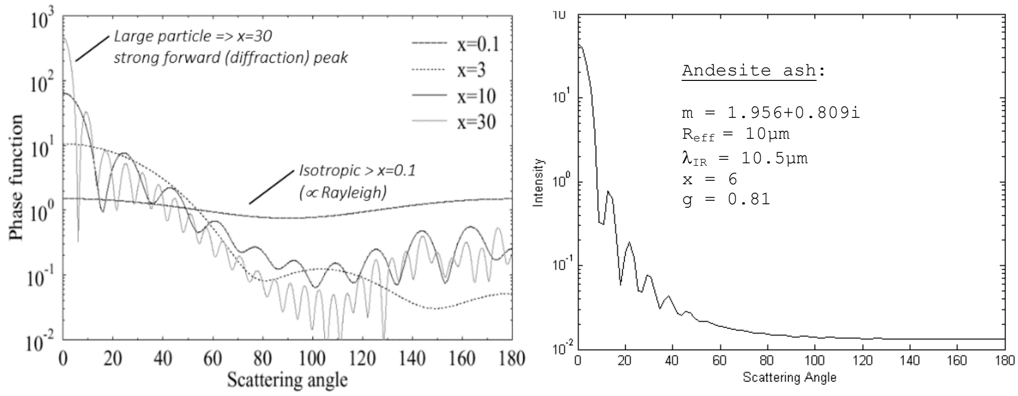

Figure 6. (left) plot of phase function for various particle size parameters, and (right) computed scattering phase function intensity for an andesitic ash particle of radius 10 µm ($x = 6$)

Finally, the single scattering albedo indicates how much a photon is scattered or absorbed by the particle using the ratio of the scattering efficiency over the extinction efficiency such as:

$$\varpi = \frac{Q_{sca}}{Q_{sca} + Q_{abs}}$$

The single scattering albedo varies from ϖ=0 (for purely absorbing particle) to ϖ=1 (for purely scattering particle). This information is also included in the complex refractive index but less directly. We are used to say that ash particles are strong absorbers in the infrared. This is true, compared to water droplets or ice crystals, but many variations in absorption efficiency exist within the IR range itself. This is an important point to consider because in optically thick media (optical depth $\tau>5$), where multiple scattering occurs, even a small absorption fraction will lead to a dramatic increase of the light extinction. In figure 7 (*top-left panel*), we provide a simple sketch showing this effect in a medium having 50% absorption and 50% scattering ($\varpi = 0.5$); the light cannot pass through the medium and is rapidly attenuated. By contrast (*top-right panel*), in a purely scattering medium photons succeed in crossing the medium, although undergoing a large number of collisions with particles. Similarly, the bottom panels show the path of light through two different media with (*left*) particles having an isotropic phase function ($g = 0$) and (*right*) particles having a strong forward diffraction peak ($g = 0.85$). In the first case, photons follow a browning motion such as a random walk, but hardly cross the cloud, while in the latter case photons are heading more directly towards the other side of the cloud. One must keep in mind that ash clouds usually behave as in top-left (for single scattering albedo) and bottom right panel (for asymmetry parameters)

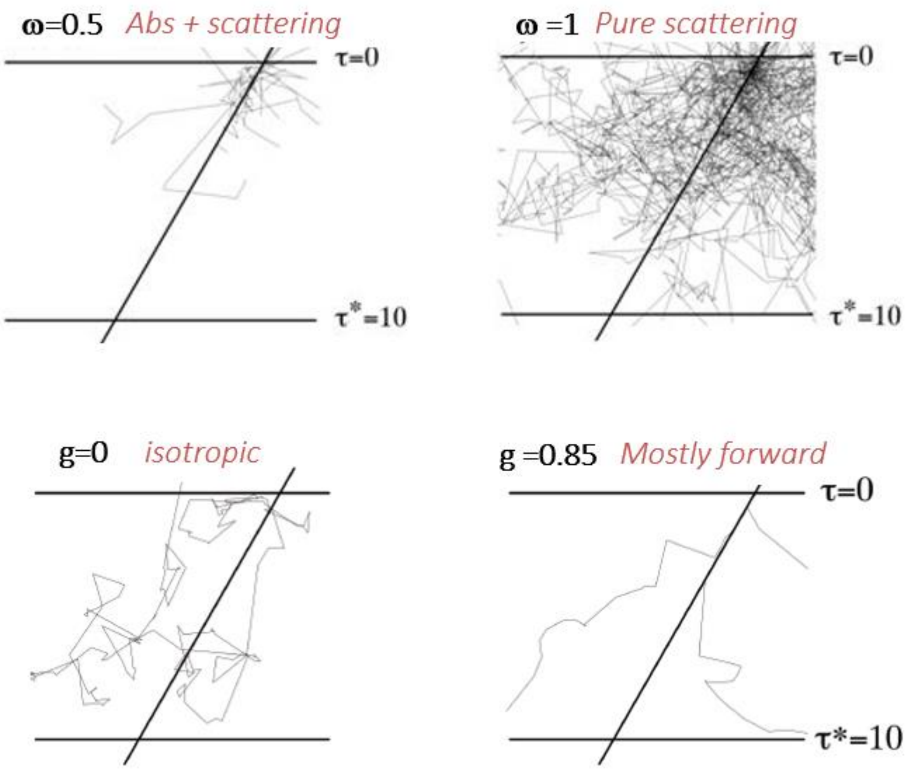

Figure 7. Sketch showing the effect on light propagation of two single scattering albedo ($\omega = 0.5$ and $\omega = 1$) and two different phase functions ($g = 0$ and $g = 0.85$).

Our ability to reliably detect and characterize ash particle in the atmosphere mostly depends on the accuracy of optical properties modelling. Indeed, in the reality and even at a given wavelength, optical properties remain highly variable, because they strongly depend on the particle size. In a volcanic cloud, the population of ash particles shows a large grain size distribution making more difficult the correct assessment for the forward model. For this purpose, we provide in figure 8 the asymmetry parameter; single scattering albedo and extinction efficiency for andesite ash particles ranging from 1-100µm at 8.7µm and 10.5µm wavelengths. In particular, we show (left panel) that the asymmetry factor is low (isotropic) for a ~1µm particle but strongly increases with radius until 10µm and then remains stable up to 100µm with values ranging from $0.8<g<0.9$ (forward scattering). Similarly, the single scattering albedo shows low values for small particle sizes then increases rapidly with radius reaching values ranging from $0.5<\varpi<0.6$ for particles greater than 10µm. This means that in the worst case, ash absorbs about 50% of incident wavelengths. Finally, one can observe that a great difference exists in the extinction efficiency for both wavelengths, showing a strong increase until 5µm and a regular decrease towards a value of two.

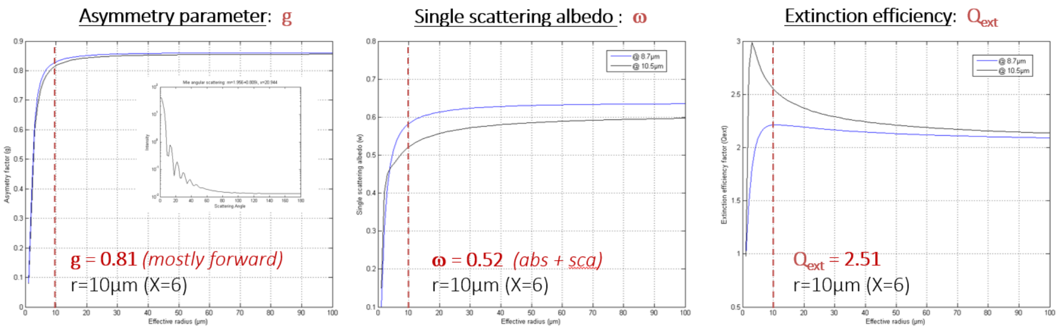

Figure 8. Plots of the asymmetry parameter; single scattering albedo and extinction efficiency for andesite ash particles ranging from 1-100 µm at 8.7 µm and 10.5 µm wavelengths.

2.2.2. Satellite-based volcanic ash cloud detection

Early detection of volcanic ash clouds has become an important objective for the volcanological community, as well as for civilian and military air space monitoring communities. The main purpose is to reduce to an absolute minimum the hazards posed by volcanic ash drifting into air routes. The aim of my published work (Guéhenneux et al., 2015) is precisely to provide an improved methodology allowing real-time monitoring of volcanic ash cloud drifting in the atmosphere.

The 2-Band method proposed by Prata (1989a, 1989b), has long been used to detect ash clouds during, for example, the April–May 2010 Eyjafjallajökull eruption (e.g., Bonadonna et al., 2011; Francis et al., 2012; Labazuy et al., 2012). This method is based on absorption and scattering of the upwelling ground radiance $I_0^+(\tau_i,\mu)$ by particles through their extinction cross section. From the calculation of the extinction efficiencies using Mie theory, Prata (1989b) has shown that $\sigma_{ext}(\lambda_{11})<\sigma_{ext}(\lambda_{12})$ for water and ice particles, while $\sigma_{ext}(\lambda_{11})>\sigma_{ext}(\lambda_{12})$ for ash particles. Therefore, Planck brightness temperature difference (BTD) between 11 µm and 12 µm channels is positive above a cloud of water/ice particles while it is negative above a cloud of ash particles. However, this method suffers well-documented limitations (e.g. Simpson et al., 2000; Prata et al., 2001; Pavolonis et al., 2006, Guéhenneux et al., 2015), and is ineffective for automated ash cloud detection as artifacts would lead to a large amount of false alarms. The list of main artifacts has been listed below:

Known issues and implications

- Moisture rich environments ⇨ ash underestimation
- Over ice-rich cold environment/clouds ⇨ ash underestimation
- Significant zenith angle ⇨ ash underestimation
- In the presence of mineral dust clouds ⇨ ash overestimation
- Over quartz-rich desert ⇨ ash overestimation
- Thermal relaxation in cloudless nighttime ⇨ ash overestimation
- Convective cloud overshoot the tropopause ⇨ ash overestimation

Therefore, alternative methods using IR satellite data have been developed to improve volcanic ash cloud detection, such as the Robust Satellite Technique (e.g., Tramutoli, 1998), the MIR band method (e.g. Ellrod and Connel, 1999), the atmospheric correction (Prata and Grant, 2001; Yu et al., 2002), the VIS–IR daytime method (Pavolonis et al., 2006) or more recently a 3-Band method (e.g., Pavolonis, 2010). **In this context, we**

developed two novel algorithms hereafter **named 3-band** (Guéhenneux et al., 2015) **and 5-band** (to be published) methods allowing an improved ash cloud detection from space. For this purpose, we explored additional spectral features as a complement to the existing 2-Band reverse absorption technique. The aim of these two methods is to allow fast and reliable detection of ash particles in a real-time fashion for a 24/7 monitoring of volcanic activity. Therefore, we need a routine simple enough to be performed within a couple of minutes (for operational response), but reliable enough to be performed in an automated way, and generating the least amount of false alarms possible. For both methods, **optical properties** need to be **calculated to build a consistent forward EM model**, allowing a better characterization of IR radiation interaction with ash particles, and which will ultimately help us **improving the ash cloud detection**.

i) 3-band method

The 3-Band algorithm uses two Boolean (true/false) tests based on brightness temperature differences (BTD) for three thermal infrared bands located at 8.7, 11 and 12 µm. The first test is the same as the 2-Band method of Prata (1989a), using the difference of brightness temperature between bands at 11µm and 12µm (BTD_{11-12}). The presence of ash-contaminated pixels (true statement) is usually given by a negative brightness temperature difference ($BTD_{11-12}<0$). However, some artifacts may lead ash-free pixels to be erroneously selected by this test. Therefore, we apply to this selection of pixels, a second test that uses the difference of brightness temperature between bands at 8.7 µm and 11 µm ($BTD_{8.7\ 11}$). The 8.7µm channel is mainly used for the SO_2 detection, but we demonstrated that it is also efficient to detect volcanic ash. Indeed, in Guéhenneux et al., (2015) we show that Q_{ext}(11-12) can only be used for ash particle sizes from 0.65-3.4µm and 7.5-10µm, while Q_{ext}(8.7-11) is effective for a much wider range ash particle sizes from 1.3-17µm. The presence of ash-contaminated pixels (true statement) is given by a positive brightness temperature difference (BTD8.7–11>0). Therefore, the combination of the two tests permits to eliminate a large majority of artifact pixels. In summary, in our method a pixel is considered as containing ash only if the two following conditions are met:

BT11µm – BT12µm < Tcutoff-1 (with Tcutoff ~ 0)
BT8.7µm – BT11µm > Tcutoff-2 (with Tcutoff ~ 0)

The figure 9 (*left*) perfectly illustrates problems related to thermal relaxation phenomena where land surfaces are considered as ash-contaminated whereas no eruption was actually occurring at this time on Mount Etna (Fig. 5b). By contrast, the figure 9 (*right*) shows that the 3-Band method is particularly efficient to remove artifact problems related to thermal relaxation phenomena

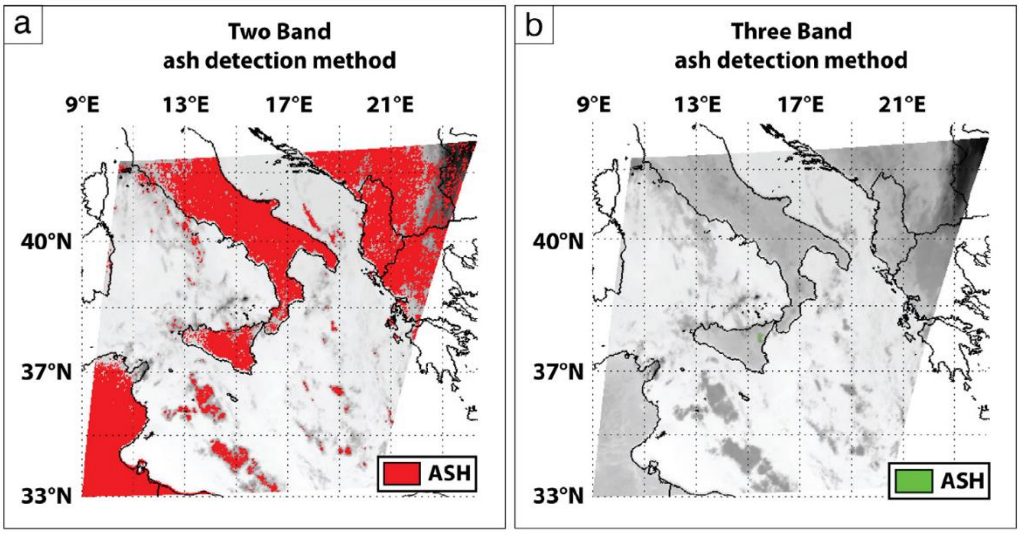

Figure 9. Comparison between the 2-Band and the 3-Band methods over the Mount Etna when no eruption occurs in cloudless night-time conditions using SEVIRI data in Mercator projection with Tcutoff-1 = +0.5 K and Tcutoff-2 = −1 K.

In the next example we show that the second test is also very efficient to remove other types of artifacts and preserve most of true ash-contaminated pixels. The 24 November 2006, an explosive eruption at Mount Etna began around 03:00 UTC and ended around 17:00 UTC on the same day. A mild cloud of ash was emitted towards SE causing ash fallouts on the international airport of Catania, which was closed to air traffic during the eruption. However, the 2-band method solely (fig. XX, left) did not allow reliable and automated detection of ash-bearing pixels. Indeed, large convective ice clouds overshooting the tropopause lead to false detection of ash, whereas the 3-band method (fig. XX, right) succeed in removing these artifacts while preserving the actual ash cloud mark.

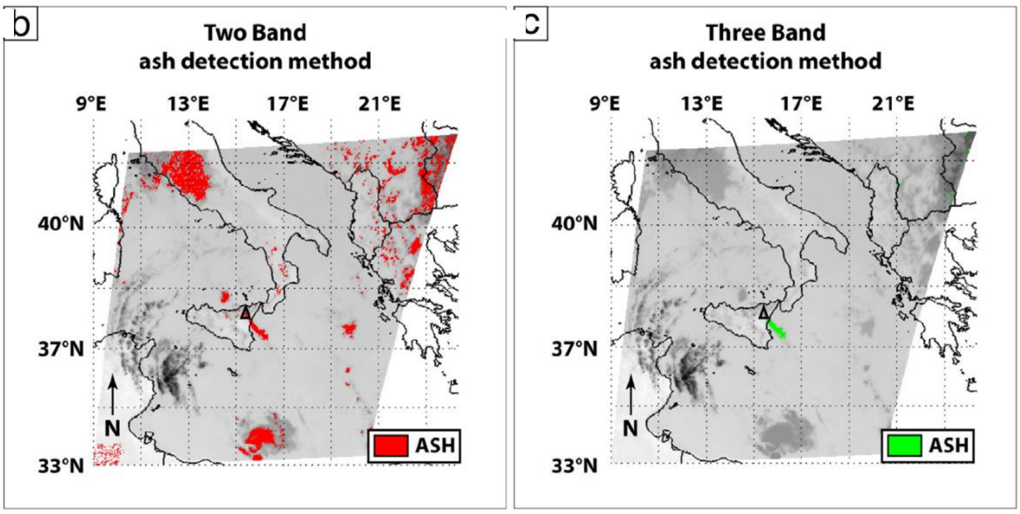

Figure 10. Comparison between the 2-Band and the 3-Band methods over the Mount Etna during eruption of 24 November 2006 at 12h00 UTC using SEVIRI data with Tcutoff-1 = +0.5 K and Tcutoff-2 = −1 K.

ii) 5-band method

The 5-band algorithm is a bit more complex as it uses several Boolean tests based on either brightness temperature differences (BTD) or spectral radiance for 5 different infrared bands located at 3.9, 8.7, 10.8, 12, and 13.4µm. The mid-wave infrared (3.9µm) allows us to better take into account the solar contribution within ash absorption and scattering using two different thresholds between night and day. Bands at 8.7, 10.8, and 12µm work as described above in the 3-band method while the 13.4-µm waveband shows good results for removing artefacts due to convective clouds, in particular. The algorithm can be divided into two main parts:

The first part uses a very restrictive detection scheme. The objective is to reduce to an absolute minimum the number of false ash detection, hence focusing on the core of the ash cloud.

Step 1: flagged pixels must fill both conditions simultaneously

- BT10.8 - BT 12.0 < -0.5K
- BT 8.7 - BT 10.8 > -0.5K

Step 2: flagged pixels that fill at least one condition are masked

- (Rad3.9 - Rad12)/(Rad3.9 + Rad12) < Threshold - (night: 0.042 - day: 0.055)
- (BT8.7 - BT 12.0)/(BT 10.8 - BT 13.4) > -0.05K
- [(BT 10.8 - BT 12.0)]/BT 13.4) * 100 > -0.35

The second part consists in a nearest neighbour search to identify closest pixels of the cloud core forming new clusters having a high probability to belong to the ash cloud. Once identified, new Boolean tests are carried out on those pixels and must fill the following two conditions simultaneously:

- BT10.8 - BT 12.0 < -0.25K
- BT 8.7 - BT 10.8 > -2K

Finally, pixels that fill the following condition are masked:

- (Rad3.9 - Rad12)/(Rad3.9 + Rad12) < Threshold - (nuit: 0.042 - jour: 0.055)

In figure 11 we provide one example showing differences between the 3 different algorithms used during the May 6, 2010 Eyjafjallajökull eruption. The 2-band method shows a good sensibility to ash detection but also produces a large number of false alarms. Those biases can sometimes be overcome from the supervision of a user, but prevent any automated warnings. The 3-band method succeeds in removing most of artefacts but one can observe that the ash detection sensibility has decreased significantly on the edge of the cloud. Finally, we show that the 5-band method allows removing all artefacts, while increasing the detection sensibility at the same time. This excellent result is due to an original multispectral combination associated with clustering routines. However, those methods remain complementary in some cases and we decided to keep them all three in the operational HOTVOLC observation system. (see section 5 for more details).

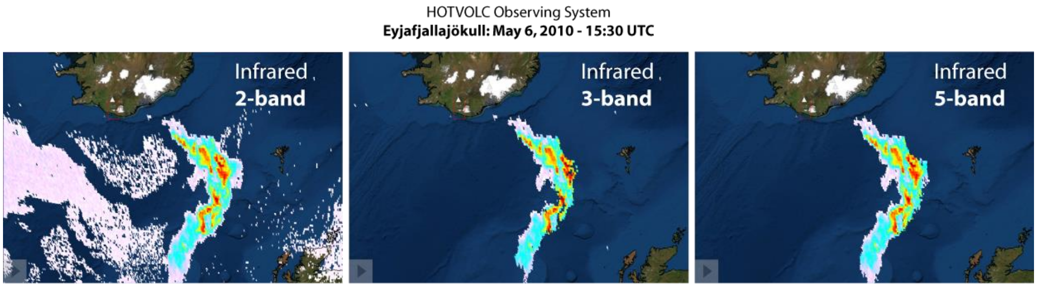

Figure 11. Maps of ash cloud detected during the May 6, 2010 Eyjafjallajökull eruption using the 2-band, 3-band, 5-band methods, respectively.

2.2.3. Ash cloud size and concentration

i) Forward and inverse Modelling

Thermal infrared (TIR) sensors have proven to be very useful for the operational characterization of volcanic ash cloud. They allow reliable 24/7 detection as demonstrated above from various techniques all using differential extinction properties of silicate particles. Since the 1990s, the **quantitative ash concentration and size retrieval was made possible from the inversion of satellite-based TIR data** (e.g., Prata et al., 1989a; Wen and Rose, 1994). I will now present some results based on methodological developments started during my postdoc at Michigan Technological University (USA), and built on early works from Wen and Rose (1994), in particular. Those results have been applied to a number of eruptions since 2010 and brought some interesting constraints on explosive eruption dynamics (see section 3 and 4 for more details). Those results have been published in several articles (e.g., Bonadonna et al., 2011; Labazuy et al., 2012; Poret et al., 2018, Gouhier et al., 2019, Gouhier and Paris, 2019).

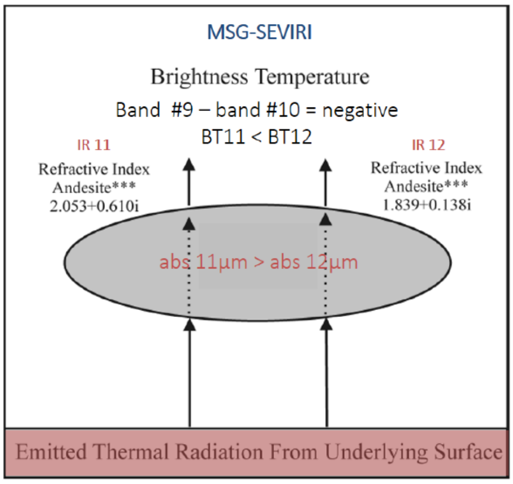

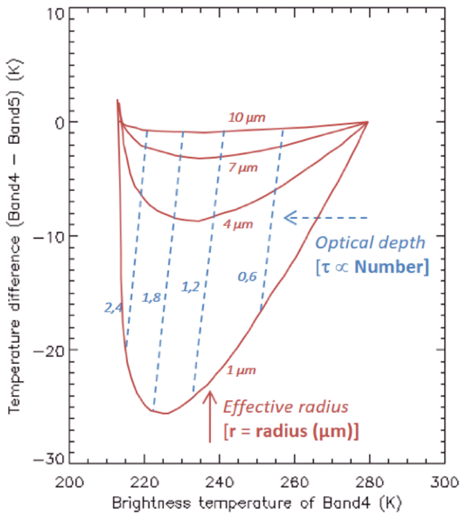

Figure 12. (left) Sketch showing the satellite-based configuration of acquisition for a plane-parallel ash cloud in the TIR. (right) LUT of BTD using effective radius and optical depth. Modified from Wen and rose (1994).

Inversion of satellite-based TIR data requires the development of a forward EM model that realistically accounts for the physics of the problem (i.e., source conditions, EM theory, geometrical setting, etc.). The figure 12 describes fairly well the geometrical setting and source conditions of ash cloud acquisition from space. The TIR radiation from

Earth is used as the source of energy (here after referred to as the spectral radiance) whose distribution is isotropic in the upper half-space and of constant intensity, at first order. In the presence of an ash cloud, a fraction of this energy is absorbed and scattered by silicate particles according to the Mie theory and does not reach the sensor. Wen and Rose (1994) developed a forward model describing the physics of ash cloud characterization from satellite-based IR sensors. They define a linear model of the at-sensor spectral radiance $L(\lambda)$ such as:

$$L(\lambda) = t_c \varepsilon_s B(\lambda, T_s) + \varepsilon_c B(\lambda, T_c)$$

- T_s the brightness temperature of the ground surface
- T_c the brightness temperature of the cloud top
- B the Planck function
- ε_s the emissivity of the ground surface
- ε_c the emissivity of the cloud
- L the at-sensor spectral radiance

To solve for the cloud emissivity, the cloud reflectivity (r_c) must be added (Watson et al., 2004) in the above equation so that we can rewrite the at-sensor radiance by a combination of the cloud transmissivity and reflectivity only:

$$L(\lambda) = (1 - r_c(r_e, \tau_c))\varepsilon_s B(\lambda, T_c) + t_c(r_e, \tau_c)\big(B(\lambda, T_s) - B(\lambda, T_c)\big)$$

Given a theoretical at-sensor radiance pair $L(\lambda_1)$ and $L(\lambda_2)$, computed by defining the effective radius (r_e) and the optical depth (τ_c), the corresponding brightness temperatures can be calculated using the Planck function.

$$r_e = \frac{\int r^3 n(r) dr}{\int r^2 n(r) dr}$$

$$\tau_c = \pi L \int_0^\infty r^2 Q_{ext}(r, \lambda)\, n(r) dr$$

This forward model allows a theoretical look-up table (LUT) to be generated for sets of variations of both r_e and τ_c as a function of brightness temperatures. The inverse procedure thus consists in retrieving, by best fit matching, the values of r_e and τ_c that correspond to recorded brightness temperature pair. Finally, the total mass of ash particle in a given pixel can be calculated from the integral of the grain size distribution (GSD) of effective radius retrieved. Usually, the GSD used for the LUT generation is polydisperse being either lognormal or modified-gamma distribution. In this case the total mass in a pixel is calculated following:

$$M = LS \frac{4\pi}{3} \rho \int_0^\infty r^3 n(r) dr$$

It can be very convenient to express the total mass as a function of the extinction efficiency as the cloud geometric thickness (L) collapses from the equation in favor of the optical depth (τ) such as:

$$M = S\frac{4}{3}\rho\, r_e\tau_c\frac{\int \pi r^2 n(r)dr}{\int Q_{ext}\pi r^2 n(r)dr}$$

Interestingly, for a uniform distribution n(r)=1 and the integrals collapse such that the total mass in a given pixel can simply be written as:

$$M = S\frac{4}{3Q_{ext}}\rho\, r_e\tau_c$$

It is important to understand that IR sensors provide plane-parallel (2D) image of the ash cloud, and the mass given in a pixel is the vertical integration of particles loading from the ground to the sensor and usually refereed to as vertical or slant column densities (VCD). As a result, we can only provide a surface concentration of the cloud, usually expressed in g/m^2, from the ratio of the total mass over the pixel surface *M/S*. In reality, the ash cloud has a limited vertical extent, and in cases where this geometric thickness is known, one can derive an average volume concentration *M/LS* and usually expressed in mg/m^3. Interestingly, the current threshold beyond which an airplane cannot fly is fixed at 4 mg/m^3 by EASA (European Aviation Safety Agency) and used since 2010 in the emergency plan EUR/NAT (EURopean and North Atlantic) as the so-called "high" level of contamination.

ii) Radiative Transfer Modelling

The calculation of the reflectivity and transmissivity of the medium can be very complex depending on assumption made and boundary conditions. In the case of ash cloud, I have chosen to adapt a two-stream method to solve the radiative transfer equation (RTE):

$$\mu\frac{dI}{d\tau} = I(\tau,\mu) - \frac{\omega}{2}\int_{-1}^{1} P(\mu,\mu')I(\tau,\mu')d\mu' + S(\tau,\mu)$$

where I is the diffuse radiance, µ the cosine of the zenith angle, P(µ,µ') is the axially-symmetric phase function defining the light incident at µ' which scattered in the direction µ. τ si the optical depth and ω is the single scattering albedo. The underlying idea is that for a thick plane parallel cloud of ash the angular distribution of the diffuse radiance does not change radically (i.e., ~isotropic). **The strategy is thus to introduce an effective angular-averaged intensity consisting of only two streams** (upward $I^{\uparrow}$ and downward $I^{\downarrow}$). The two-stream methods (such as Eddington approximation) provide analytical solutions to the single layer plane-parallel radiative transfer equation. There are many related two-stream methods that approximate the angular radiance field with two numbers (e.g., constant hemisphere [I^+, I^-], two point quadrature [$I(+\mu_1)$, $I(-\mu_1)$], Eddington 1st moment [$I(\mu) = I_0+I_1\mu$]). In these conditions, two-stream methods give very good results and ensure a fast computational speed. This is a critical point for providing quantitative estimates of the ash concentration in operational fashion. Many versions of two-stream methods exist, and for thick ash cloud (τ_c>8), the delta-Eddington approximation (Joseph et al., 1976), should be used for direct beam modelling. Assuming that the angular radiance field can be approximated by the two-term Legendre polynomial function, the Eddington approximation is written as follows:

$$I(\tau, \mu) = I_0(\tau) + I_1(\tau)\mu$$

In our specific case, the boundary conditions of the problem say that the medium is illuminated from below by a known source of **diffuse radiation** (i.e., TIR Earth radiation), such as:

$$I^{\downarrow}(0, -\mu, \varphi) = +F_0 \quad and \quad I^{\downarrow}(\tau^*, +\mu, \varphi) = 0$$

Then, for a single scattering albedo $\varpi < 1$, and whatever the cloud thickness (τ_c), we use the Eddington approximation version of Liou et al., (1982), where the reflectivity and transmissivity of the cloud can be written as:

$$R = \frac{(1 - U^2)(e^{k\tau} - e^{k\tau})}{(1 - U)^2 e^{-k\tau} - (1 + U)^2 e^{k\tau}}, \qquad T = \frac{4U}{(1 - U)^2 e^{-k\tau} - (1 + U)^2 e^{k\tau}}$$

with

$$U = \sqrt{\frac{4(1 - \omega)}{3(1 - \omega g)}}, \qquad k = \sqrt{(1 - \omega)(1 - \omega g)}$$

Of course, uncertainties associated with this methodology exist, linked in particular to the surface characteristics (temperature, emissivity), the geometry of the plume, the optical properties of ash, the presence of water vapor, and of course with the radiative transfer model itself. Overall, the error on ash concentrations and total mass is estimated to be around 30-40% (Stevenson et al., 2015). Infrared methods also allow the characterization of the cloud top altitude, which is critical information for aviation safety. For this we use the brightness temperature of the cloud surface at 11µm, obtained by satellite. This value is then compared to an atmospheric temperature-altitude profile (theoretical or measured from radio-sounding), thus allowing a first order estimation of the cloud altitude. This technique is known as the CTT method (i.e., Cloud Top Temperature). However, it is only applicable to tropospheric emissions because the atmospheric temperature profile above the tropopause is not monotonic. It is therefore impossible to obtain a single solution.

iii) Worked example

In summary thanks to the thermal infrared method, we are able to determine in near real-time the following quantities:

- Grain size distribution (effective radius, µm)
- Vertical column density (g/m2) and averaged concentration (mg/m3)
- Total mass of ash in the cloud (kt)
- Cloud top altitude (m, a.s.l)

In figure 13, I provide an example of IR data inversion allowing the quantitative characterization of the ash cloud emitted during the Eyjafjallajökull, 2010 eruption. This work has been published in Bonadonna et al., 2011. Thermal infrared data presented here have been acquired from the European geostationary satellite MSG-SEVIRI on May 6, at 19h30 UTC. Figure 13 (left) shows a map of the ash vertical column density (i.e. surface concentration in g/m2) in the cloud. These range from values >3.5g/m2 close to the vent, to values <0.5g/m2 far from the source. Figure 13 (right) shows the size distribution of ash in the cloud with effective radii varying from 1.5-3.5µm. Three different modes can be observed with the largest particles close to the source. Today, ash cloud concentration and altitude maps are provided automatically on the HOTVOLC observing system at a maximum rate of one image every 15 minutes. This type of data is essential for reducing the air traffic hazards posed by the emission of ash clouds in the atmosphere.

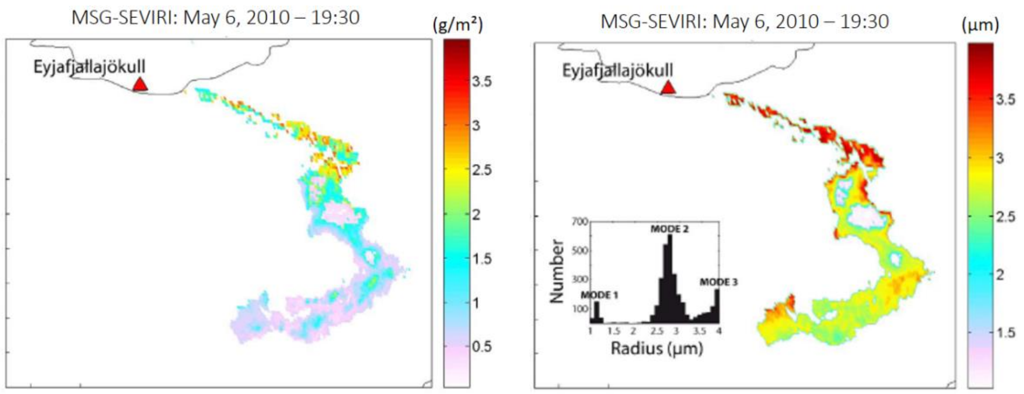

Figure 13. Detailed map of (left) ash effective radius with the corresponding particle-size distribution showing three main modes, (right) ash mass loading inside the Eyjafjallajökull ash plume on 6 May 2010 at 19:30 UT.

2.3. Monitoring of lava hotspots: developments

After my recruitment at LMV-OPGC in 2011, I have been involved in the "Service National d'Observation en Volcanologie" of the CNRS-INSU. Naturally, one of the priorities of the SNOV deals with the monitoring of French volcanic targets. Therefore, I have worked on Piton de la Fournaise, in particular, and I was led to develop new methodologies for the monitoring of lava flows. This includes (i) **improvement of detection techniques of lava hotspots** and (ii) the **development of new methods for real-time estimation of the lava volume flow rate.** Beyond fundamental issues on lava emplacement dynamics, the study of thermal anomalies on the ground is essential as lava flows represent a common hazard occurring during eruptions and can represent a major threat to the population living in the vicinity of volcanic areas

Since the 1980s, increasing efforts have been carried out to improve the use of satellite-based data to detect, quantify and track thermal radiance from high-temperature bodies such as lava flows and domes (e.g., Francis & Rothery 1987). Mid-to-thermal infrared sensors, in particular, are sensitive to electromagnetic emission from high-temperature bodies and are thus very useful in the detection of volcanic hot spots (e.g. Rothery et al. 1988). Therefore, since the 1990s much effort has been aimed at the development of near-real-time remote sensing systems that involve operational use of satellite data for hot spot tracking, as for example the work by the volcano remote sensing group at the University of Alaska Fairbanks (e.g. Dean et al. 1996).

2.3.1. Detection of lava hotspots

Satellite detection of hotspots has typically used sensor wavebands centred in the short, mid and thermal infrared. Peak spectral radiance emitted by a lava surface temperature, ranging from 100 to 1000°C, occurs in the mid-infrared (MIR: 3–5 mm), whereas the Earth's background surface temperature (~25°C) has a maximum emission in the thermal infrared (TIR: 8–12 mm). As a result, strong emission from a sub-pixel hotspot (i.e. a lava flow) in the MIR, will cause the pixel integrated temperature (PIT) in the MIR to be much higher than for the same pixel in the TIR. Defining a temperature difference threshold in the MIR, will thus indicate if a thermal anomaly exists. This principle has been developed and applied using three main classes of algorithms: fixed, contextual and temporal detection threshold, the case-type algorithms for each being: MODVOLC (Flynn et al. 2002; Wright et al. 2002), VAST (Harris et al. 1995) and RAT (Tramutoli 1998), respectively.

In this context I developed another detection procedure based on a contextual algorithm derived from Harris et al., (1995) that uses a modified Normalized Thermal Index (NTI*) which adapts the original NTI measure as developed by Flynn et al. (2002).

$$NTI^{*} = 1 - \left|\frac{L_{3.9} - L_{12}}{L_{3.9} + L_{12}}\right|$$

where $L_{3.9}$ and L_{12} are the spectral radiances (in $Wm^{-2}\ sr^{-1}\ \mu m^{-1}$) at 3.9 and 12 mm, respectively. This adjustment to the original formulation of the NTI means that it varies from 0 (for the lowest intensity) to 1 (for the highest intensity), making data reading more straightforward, and which is also more convenient for colourbar management when plotting thermal data. Our contextual algorithm uses a dynamic threshold which adapts to the spatial (each volcanic target) and temporal (night/day) variability of the NTI*. Our algorithm can thus be divided into four main steps:

<u>Step 1</u>: Subdivision of the image into two distinct zones
- Small 'volcanic zone' (10 × 10 pixels)
- Large 'non-volcanic zone' of variable size

<u>Step 2</u>: Calculation of NTI* indexes for the two zones
- NTI^*_{VOLC} and $NTI^*_{NON\text{-}VOLC}$
- $Mean\_NTI^*_{NON\text{-}VOLC}$ and $Std\_NTI^*_{NON\text{-}VOLC}$

<u>Step 3</u>: Calculation of the dynamic threshold,
- $NTI^*_{threshold} = Mean\_NTI^*_{NON\text{-}VOLC} + n \times Std\_NTI^*_{NON\text{-}VOLC}$

<u>Step 4</u>: Flag anomalous pixels
- $NTI^*_{VOLC} - NTI^*_{threshold} > 0$ thermal anomaly =true
- $NTI^*_{VOLC} - NTI^*_{threshold} < 0$ thermal anomaly =false

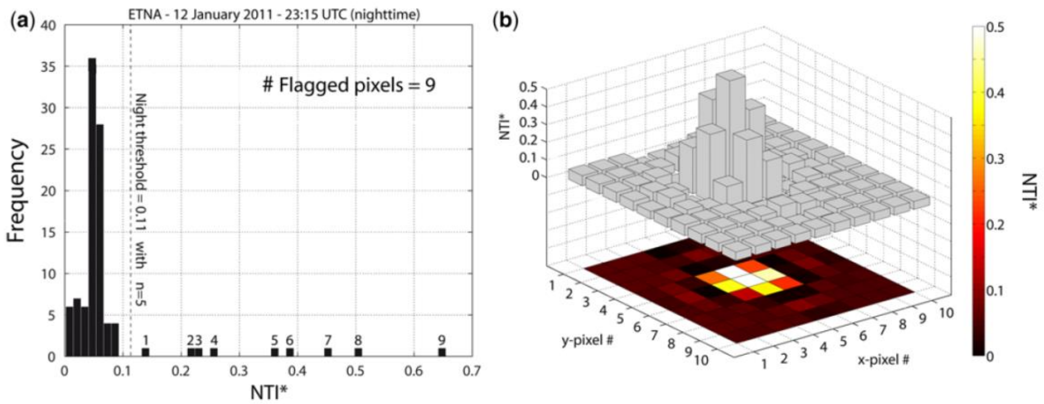

Figure 14. Plot of the NTI* during the 12–13 January 2011 eruption of Etna. (a) Histogram showing NTI* values recorded and flagged pixels from a 10 × 10 area during nighttime conditions (23:15 UTC), and (b) same information as a 3D plot with associated hot spot map.

2.3.2. Quantification of lava flow rate

The quantification of the lava flow rate is critical as it strongly controls the lava front speed and the area. If obtained quickly enough, the flow rate can be used as an input parameter for models used to forecast lava emplacement (e.g. Del Negro et al. 2008). The measurement of lava flow rates has evolved from field-based techniques (e.g. Pinkerton 1993) to methodologies using satellite and ground-based IR sensors (e.g. Harris et al. 1998). Infrared techniques are particularly relevant as effusion rates can be derived from a heat budget where the heat supplied to the active flow unit is lost from the flow surface (Pieri & Baloga, 1986). This method allows the calculation of Time-Averaged Discharge Rate (TADR) and is well adapted to low-earth orbiting platforms (i.e., weak temporal resolution) as one discharge rate value can be calculated from a single image. However, this method is designed for steady-state lava supply rate (Wright et al. 2001), and will not work properly while the flow is in its initial extension phase. Also, this method fails to actually distinguish between an active lava flow unit and one whose effusion has stopped but remains hot.

Therefore, I developed a new infrared methodology based on instantaneous lava volume estimation and using the equation of mass conservation. This method is particularly adapted to geostationary platforms as it uses a succession of images. The physical principle is as follows: the thermal anomaly measured at a given instant is the balance of contributions related to (1) hot lava material newly emplaced (at time *t*) and (2) the contribution of cooling lava material previously emplaced (at time *t-1*). This method allows the calculation of quasi-instantaneous lava flow rates (in m^3/s) and is referred to as the Volume Flow Rate (VFR) method (Gouhier, in prep)

VFR: Volume Flow Rate method

The first step is to calculate the active lava flow area from the pixel-integrated temperature (PIT) using MIR at-sensor radiance. This involves application of a simple two-component mixture model (Wright and Flynn, 2004) to estimate the active lava fraction (A_{lava}) within the pixel, and following:

$$A_{lava} = \frac{R_{MIR}(PIT) - L_{MIR}(T_a)}{L_{MIR}(T_h) - L_{MIR}(T_a)} A_{pix}$$

where $L_{MIR}(T_h)$ and $L_{MIR}(T_a)$ are the radiances for hot lava and ambient surface components of the pixel, respectively. A_{pix} is the pixel area of MSG-SEVIRI. $R_{MIR}(PIT)$ is the at-sensor radiance deriving from the pixel-integrated temperature, hence being a mixture between the surface lava and the ambient surface components. This calculation is made through all anomalous pixels on a given image. The instantaneous (i.e., on a given image) lava volume is then calculated from the product of the lava area (A_{lava}) and the lava flow thickness (h). Both lava surface temperature and flow thickness can be constrained from field measurements or assumed within a range of possible values.

$$V_{lava} = h \times A_{lava}$$

These calculations are then carried out at each time step (i.e., from images obtained by successive satellite overpasses), leading to a time series of apparent lava volumes. However, as mentioned above, the instantaneous lava volume detected at a given instant is the contribution of lava material previously emplaced but cooling with time. From this point of view, it is clear that the total lava volume emitted is not the sum of each individual volume estimate within the time series, as a significant overlap exists between two successive images. This problem can be addressed using the mass conservation equation following the differential equation:

$$\frac{dV(t)}{dt} = Q(t) - kV(t)$$

In this equation, V is the total volume of lava in a given image, Q is the lava volume flow rate (i.e., source term) and $-kV$ is the loss term with k being the cooling rate. Note that satellite observations provide discrete time series, so to obtain Q we solve analytically the above differential equation with Δt being the time interval between two consecutive images such that:

$$Q(t) = k\frac{V_i - V_{i-1}e^{-k\Delta t}}{1 - e^{-k\Delta t}}$$

The cooling rate k is a reaction rate constant (s^{-1}) expressed as $k=1/\tau$, where τ is the lava e-cooling time. This formulation is very convenient, because τ physically represents the time after which the temperature is divided by a factor 2.72 (i.e., e^{-1}). The cooling rate k is a spectrally dependent function and must be defined from calibrated MIR data. Indeed, the area detected at Visible, MIR or TIR wavelength for the same lava flow will show different values. Therefore, cooling rates have been calibrated from Gouhier et al., (2012) on Etna using satellite data on a fountain fed lava flow, and from Flynn and Mouginis-Mark (1992) using a ground-based spectro-radiometer on Hawaiian lava flow. Both data sets give very similar estimates of the lava flow surface e-cooling time ($\tau \sim 1.31$ hrs) for wavelengths located around the Mid-Wave InfraRed. Depending on the time interval (Δt) between two consecutive satellite acquisitions, ranging from 5 minutes for GEO satellite to a few days for LEO satellite, the method presented above possibly shows two end-member cases: (i) no cooling and (ii) complete cooling, between two consecutive images.

- *When Δt is small,* the case of "no cooling" applies. The analytical solution of the conservation equation simplifies as follows:

$$Q(1) = \frac{V_i - V_{i-1}}{\Delta t}$$

- *When Δt is large,* the case of "complete cooling" applies. The analytical solution of the conservation equation simplifies as follows:

$$Q(0) = \frac{V_i}{\Delta t}$$

Most of the time, both end-member cases are not realistic and if one use the "no cooling" equation this will underestimate the true flow rate estimate while the "complete cooling" will overestimate the true flow rate. In figure 15 we show an example of the Volume Flow Rate (VFR) calculated using equation XX for the eruption of September 11-18, 2016 at Piton de la Fournaise (Reunion). We used MSG-SEVIRI data acquired by the HOTVOLC system at a frame rate of 1 image / 15 min, hence representing 720 images (and flux values) on the period. The 3-point moving average (red curve) allows a smoother representation of the flow rate removing unwanted spikes inherent to this method. This method has now been implemented in operational mode in the HOTVOLC observing system for Etna and Piton de la Fournaise volcanoes.

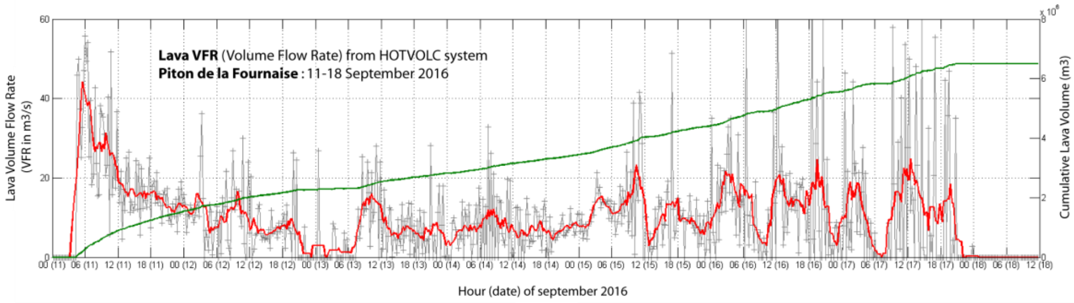

Figure 15: Time series of the lava volume flow rate (VFR) calculated from MSG-SEVIRI using Mid-Wave IR (MWIR) during the September 11-18, 2016 eruption at Piton de la Fournaise.

2.4. Ground-based Hyperspectral measurements of SO_2

Volatiles are important components of volcanic systems. The explosivity of an eruption in particular, depends mostly on the amount and composition of volatiles contained in the erupted magma. For that reason, measurements of volcanic degassing have been an integral part of monitoring networks at restless volcanoes for the past 40 years. Changes in degassing rates, and especially SO2, may reflect changes in magma supply rate and/or in the permeability of the system and help inform short-term forecast of ongoing or pending eruptions. Although it usually constitutes <5% of the total gases emitted (Oppenheimer et al., 2013) sulfur dioxide (SO2) is virtually absent from the background atmosphere, which makes it an ideal target gas to monitor volcanic emissions.

Molecular SO2 presents absorption features in various regions of the electromagnetic spectrum. Particularly strong absorptions appear in the ultraviolet (UV) and thermal infrared (TIR) range. Therefore, a large variety of spectroscopic methods have been developed to detect and quantify volcanic SO2 degassing in those spectral ranges. A number of instruments onboard satellite platforms and operating in the UV can be used to detect emissions from space, such as the Ozone Monitoring Instrument (OMI), and extensively used to quantify volcanic SO2 loading worldwide (e.g., Carn et al., 2003, 2008, 2016). Various ground-based instruments that exploit the same absorption features also exist such as COPSEC (Stoiber et al., 1983) and DOAS (Galle et al., 2003). In the last decade, UV imaging techniques have emerged, commonly referred to as SO2 cameras (Bluth et al., 2007). The SO2 absorption features in the UV are strong, and mainly associated with electronic transition. However, remote sensing measurements in the UV require the sun as a source of radiation, which limits their use to daytime only. For this reason, other techniques operating in the thermal infrared, allowing night and day monitoring, have been developed.

Indeed, the SO2 molecule presents two distinct absorption features in the TIR spectral region caused by vibrational transitions: a weak feature centred around 1150 cm^{-1} (v2 ~ 8.7μm) and a stronger feature centred around 1400 cm^{-1} (v3~7.3 μm). A very large number of sensors on-board satellite platforms operate at those wavelengths, and are used extensively to detect, track and quantify volcanic SO2 emissions worldwide (e.g., Carn et al., 2005; Corradini et al., 2009; Watson et al., 2004). In parallel, ground-based instruments operating in the TIR have been developed. While broadband infrared imaging has proved ineffective for SO2 detection, hyperspectral instruments such as Open-Path Fourier Transform Infrared (OPFTIR) produce high-resolution spectra over a narrow field of view (e.g., Allard et al., 2005; Burton et al., 2007). Multispectral imaging instruments, although offering a good compromise between spectral and spatial resolution at a relatively low cost, are relatively uncommon in the field of volcanology. One existing example is the Cyclops camera, an instrument developed by Prata and Bernardo (2014), that uses bandpass filters. Finally, a hyperspectral imager using an uncooled micro-bolometer array with the specific aim of measuring SO2 in volcanic plumes has recently been tested, and has already shown promising capabilities (Gabrieli et al., 2016).

Spectral range	850-1300 cm^{-1} (7.7-11.8 μm)
Spectral resolution	0.25-32 cm^{-1}
Frame rate	0.1-10 Hz
Sensor dimensions	320 x 256
Sensor technology	Cooled MCT (66 K)
Field of view	6.4° x 5.1° 24° x 20° (0.25x scope)
NESR	20 nW/cm^2 sr cm^{-1}
Radiometric accuracy	<1 K
Power consumption	180 W
Weight	31 kg
Operating temperature	-20 - 40°C
Data transfer	Camera Link

Figure 16: The Telops Hyper-Cam and its technical specifications. The instrument uses two blackbodies that can be rotated in the field of view for calibration and a visible camera. Not pictured is a computer for operation and data storage. Note that the NESR is an average over the entire spectral range and is based on tests made in laboratory settings with a blackbody target. Real NESR values may vary according to the combination of spectral, spatial and temporal resolution chosen, as well as the nature of the imaged target.

In this context, we used the Telops Hyper-Cam, a commercially available hyperspectral imager, for the observation of SO2 degassing during persistent volcanic activity at Stromboli volcano (Smekens and Gouhier, 2018). This LW hyperspectral imager operates in the thermal infrared (850–1300 cm^{-1} or 7.7–11.8 μm), following the principle of the Michelson interferometer and using a Mercury Cadmium Telluride (MCT) detector array. Each pixel of the detector array records the intensity of the radiation for each position of the moving mirror, producing data cubes. These data cubes are then processed using a Fourier Transform Infrared (FTIR) technique to produce a continuous radiance spectrum for each individual pixel. Figure 17 shows an illustration of such a data cube. The data cube can be divided into 2D images representing the radiation intensity for a given wavelength (top panel). Conversely, a continuous radiation spectrum can be extracted for any given pixel, which can then be converted to a brightness temperature spectrum following Planck's law. The instrument's field of view is 6.4 × 5.1°, projected on a 320 × 256 pixel sensor. The field of view can be adapted with various telescopes, either for target framing requirements or to increase temporal and/or spectral resolutions performance.

On October 3rd, 2015, we brought the instrument to the summit of Stromboli and acquired data from the Roccette viewpoint. Located on the edge of the detachment scarp at the top of the Sciara del Fuoco, Roccette is one of several shelters existing at the summit rim, and provides an unrestricted view on the NE craters, at a distance of 400 m and almost level with the vents (slight viewing angle of −2°). Several data sequences were acquired spanning durations of 5–45 min, with varying spectral configurations. We tested spectral resolutions ranging from 0.5 cm^{-1} to 32 cm^{-1}, corresponding to frequencies of acquisition ranging from 0.2 Hz (one data cube every 5 s) to 10 Hz (10 data cubes per second).

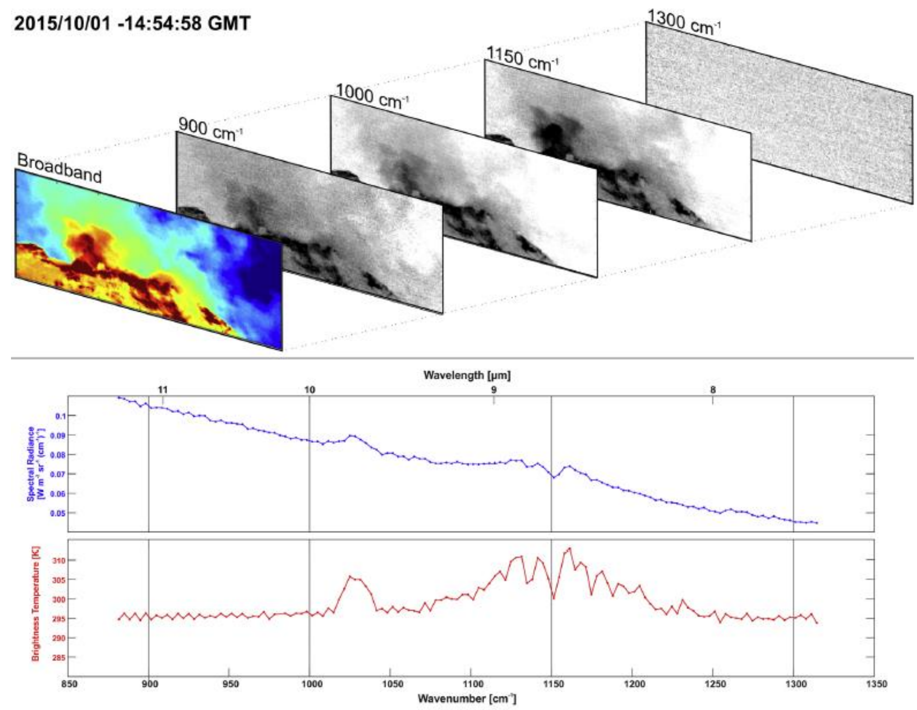

Figure 17. Illustration of a data cube produced by the Hyper-Caminstrument. Each data cube consists of a stack of 2-D images representing the intensity of the incoming radiance at a given wavelength (top panel). Conversely, each pixel can be plotted as a spectrumof radiance intensity for allwavelengths (blue curve) or converted into brightness temperatures (red curve).

In Gouhier and Smekens (2018), we focused on the detection procedure of SO2 using hyperspectral images, and we provide just one example here. Quantification of SO2 column densities are currently under development in collaboration with a PhD student at OPGC (C. Segonne). In light of the difficulties to adequately constrain the parameters for RT inversion, and in order to exploit the hyperspectral dataset to its full potential, we created a different type of indicator using a curve fitting method. Figure 18 illustrates the process by which we produce correlation factor maps for a given image. Each individual pixel extracted from the scene is compared to a laboratory spectrum of SO_2 whose resolution has been degraded to match that of the instrument. Their similarity is quantified over the spectral window of the distinctive feature (1100–1200 cm^{-1}) using a Pearson correlation factor (R):

$$R = \frac{1}{N-1}\sum_{i=1}^{N}\left(\frac{A_i-\mu_A}{\sigma_A}\right)\left(\frac{B_i-\mu_B}{\sigma_B}\right)$$

where N is the number of sampling points considered (15 over the spectral region of interest in the illustrated case), and μ and σ are the mean and standard deviation of each spectrum (A and B, respectively). The value of R ranges between −1 and 1, with 1 representing a direct positive correlation, which we interpret to represent a clear SO_2 signature. The process is repeated for every pixel in the image to produce a correlation factor map of the scene.

Figure 18 shows an image acquired on October 1st from the Roccette viewpoint, and illustrates our thresholding method. The scene considered in this example contains a gas burst from the NE crater, thermally distinguishable from the background in the broadband image. The bottom left panel of Fig. 7 presents the histogram of R values observed for all pixels contained within a rectangular ROI located right above the crater rim. It shows a bimodal distribution with the background pixels forming a large Gaussian distribution around a mean of ~0.1, and a second population of pixels forming an asymmetric Gaussian distribution with a peak around ~0.9. Based on these observations, we chose a threshold of R = 0.7 for positive identification as SO_2. The bottom right panel of Figure 18 shows the individual spectra of all pixels identified as SO_2 using this threshold (pale gray), their mean and the 1σ envelope (black). The mean spectrum of the population presents clear SO_2 features, confirming the efficacy of the index in isolating SO_2-bearing pixels.

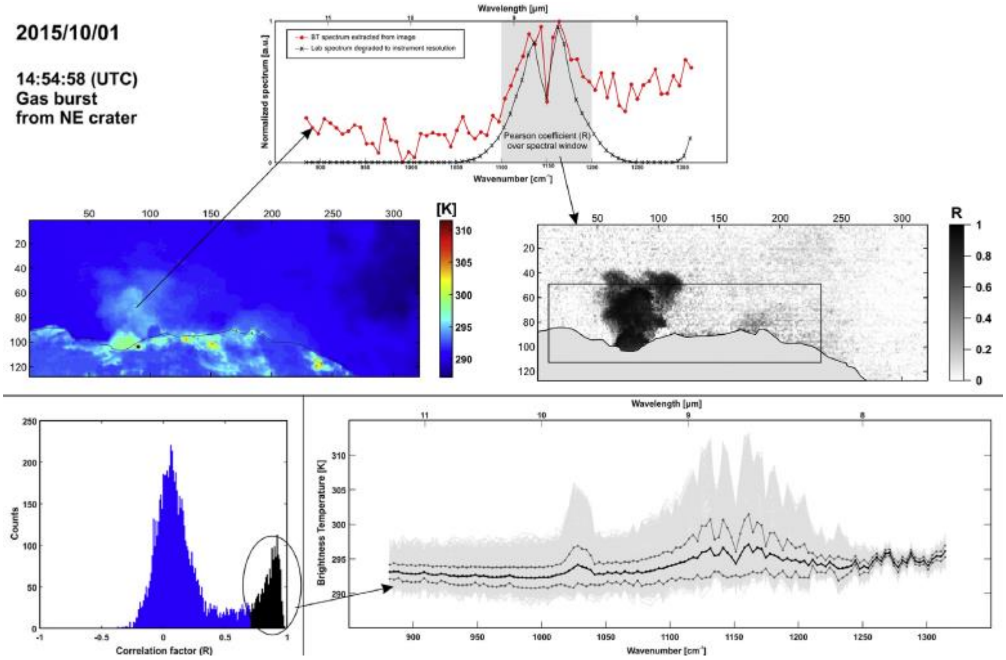

Figure 18. Illustration of the curve–fitting process on image acquired from the Osservatorio on October 1st, 2015. A full spectrum is extracted from each pixel and correlated with a laboratory spectrum of SO2 to produce a map of the resulting Pearson coefficients (R). Pixels classified as SO2-bearing constitute a separate population outside of the Gaussian distribution of background pixels. Spectra of all SO2 pixels.

3. Eruptive source mechanisms understanding

As for the methodological development chapter, all my research work cannot be detailed here. The idea is to provide key examples showing how remote sensing measurements can bring valuable information on eruptive source parameters (ESP), and help addressing scientific questions.

The nature of volcanic emissions (ash, gas and lava) as well as the dynamics of emission modes (plumes, fallout, flows), are directly associated with the **source eruptive mechanisms**. We call here source mechanisms, all physicochemical processes occurring from the shallow magmatic conduits to the eruptive vents. For instance, the mass eruption rate (MER) of tephra at the vent controls the plume ascent dynamics; the explosivity and grain size distribution (GSD) of an eruption depends mostly on the amount of volatiles contained in the erupted magma. However, direct measurements of source parameters are impossible most of the time. For this reason, we use either ground-based (camera, radar, geophysical sensors) or space (UV-VIS-IR, Radar) remote-sensing methods. These measurements provide us with indirect quantitative information (mass budget, flow rates, deformation, temperatures, grain size, etc.) allowing source eruptive mechanisms to be modeled. In fact, through this “fundamental research” axis, I am jointly carrying out works on the **quantification of eruptive observables from infrared remote-sensing**, and the **modeling of eruptive processes** resulting.

This chapter will be divided into two main parts: (i) in the first part, I will focus on the determination of the source MER of tephra from remote sensing techniques and examine the implications for the plume dynamics. (ii) In the second part, I will focus on shallow processes revealed by the examination of simultaneous SO2 and lava surface emission from remote sensing techniques.

3.1. Mass Eruption Rate

One-dimensional volcanic plume models have their origins in the mathematical description of turbulent Buoyant Plume Theory (BPT) by Morton et al., (1956). They describe the eruption column as a time-averaged Boussinesq plume, in which density differences are negligible. The characteristic timescale of the plume is considered to be longer than that of turbulent motion, removing the need to describe the turbulence in detail. Instead, Morton et al. (1956) described turbulent mixing as a horizontal inflow of ambient air into the plume, occurring at a rate proportional to the mean vertical velocity of the plume. Interestingly, in the description of the plume dynamics by Morton et al. (1956), one solution of transport equations shows that the plume height (H) varies approximately in proportion to the one-fourth power of the source flux (Q_0), here after referred to as the Mass Eruption Rate. This result shows how important is the **rapid assessment of the MER to predict the dynamics of the ash plume**. Conversely, the **measure of the plume height turns out to be very interesting to derive the source MER** and assess the amount of ash injected in the atmosphere during the eruption.

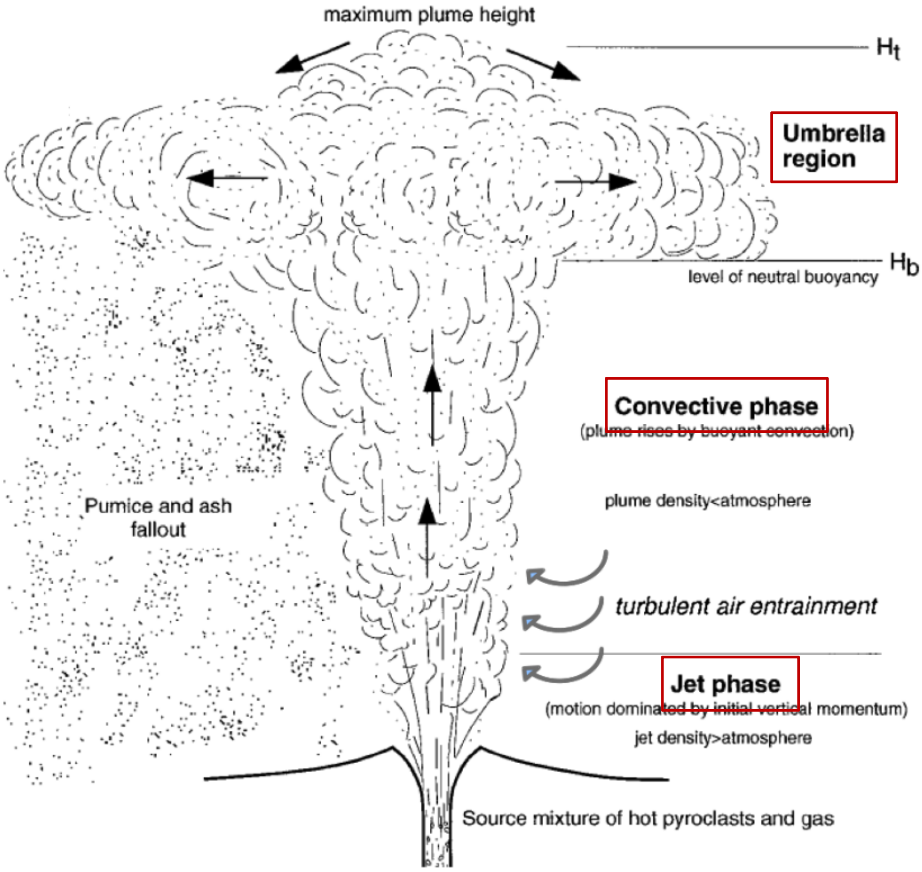

Figure 1. Sketch modified from A.C. Goglio (2014), and showing the three different regions of the volcanic plume ascent during explosive eruption.

Since about 20 years, one-dimensional integral models, based on different applications of the BPT by Morton et al. (1956) have been developed. We can cite, among others: Plumeria (Mastin, 2007), PlumeRise (Woodhouse et al. 2013), PPM (Girault et al., 2014), FPlume (Folch et al. 2015). Simpler 0^{th} order models also exist. These are empirical scaling relationships between plume height and mass eruption rate (MER) based on observed eruptions, some of which include a simplified description of the atmosphere (e.g., Mastin et al., 2009; Degruyter and Bonadonna 2012; Woodhouse et al. 2013; Carazzo et al. 2014)

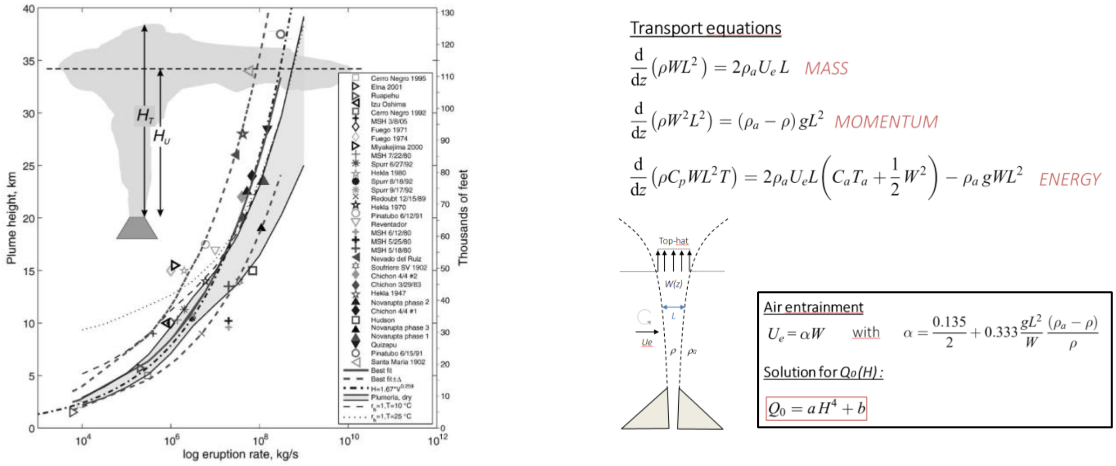

Figure 2. (left) 0th order empirical scaling relationships between plume height and mass eruption rate from Mastin et al., 2009. (right) Illustration of one-dimensional integral models characteristics, as described from the BPT by Morton et al. 1956.

In this context **my research work integrates at different levels**. To be very synthetic: (i) I developed in Gouhier & Donnadieu (2008) the only method capable of providing direct MER from inversion of Doppler radar measurements in the plume. (ii) I provided in Gouhier et al., (2019) the first statistically-derived model for predicting the MER from both the plume height (H) and the airborne fine ash mass flux (Q_a) with an unprecedentedly low level of uncertainty. (iii) More routinely, I have characterized eruptive source parameters (ESP) for a number of explosive eruptions, as in Gouhier & Paris, (2019), from satellite-based measurements.

(i) Direct MER from Doppler radar

Radar techniques are well adapted to derived quantitative information on ash plumes. Although difficult, we provide in Gouhier and Donnadieu (2008) an inversion method allowing mass loading and MER to be retrieved from backscattered power. Technical detailed can be found in chapter 2. Still today, active remote sensing techniques remain the only ones capable of direct soundings in a thick ash plume.

This study has been carried out using a volcano Doppler radar (VOLDORAD) during typical Strombolian activity from the southeast crater of Mount Etna on 4 July 2001. The inversion algorithm includes a Mie scattering forward model to generate synthetic backscattered power values. The mode of the distribution is inferred from particle terminal velocities directly measured by Doppler radar for each explosion. The combination of simultaneous velocities and backscattered power measurements make Doppler radar techniques even more relevant. **The inversion results give a lognormal GSD with a mode at 1.6 cm, and a MER value of 7.4×10^{4}kg/s**. Other parameters such as particle concentration, kinetic and thermal are also estimated.

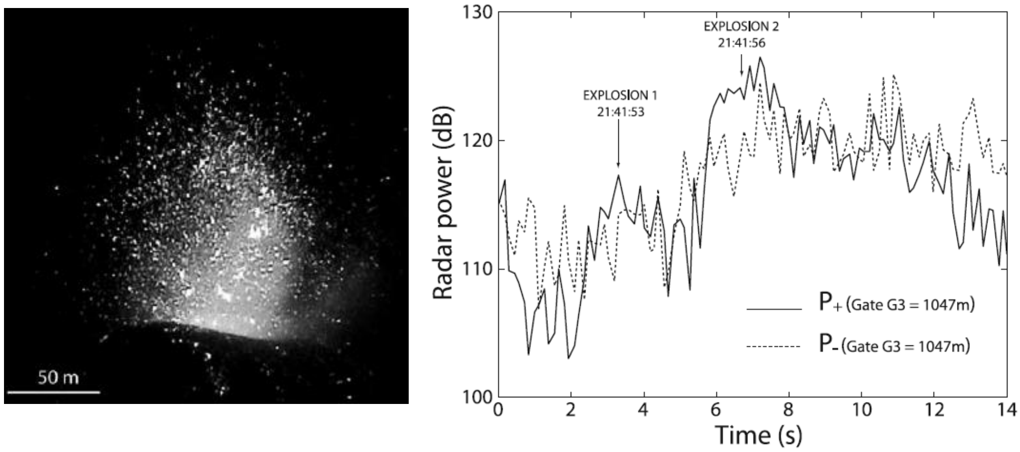

Figure 3. (left) Photography of a Strombolian explosion occurring at the southeast crater of Mount Etna on 4 July 2001. (right) Temporal evolution of radar echo power during the two explosions studied at Mount Etna on 4 July 2001, sampled at 10 Hz.

(ii) H/Q_a-derived MER statistical model

The idea published in Gouhier et al., (2019) was first to test if a relationship exists between the airborne ash mass flux and the eruption strength. For this purpose, we compiled a database of 22 eruptions of various magnitudes and intensities carefully selected from remarkably well documented case studies in the published records. They are characterized by distinct eruption styles describing the dynamics and phenomenology of the explosive activity. We distinguish sustained eruptions (9 Small/Moderate, 7 Subplinian and 4 Plinian styles) defined by quasi-steady discharge conditions (i.e., with a duration of tephra emission much longer than the time necessary to reach the neutral buoyancy level) from transient eruptions corresponding to unsteady impulsive explosions (i.e., 2 Vulcanian style). The database comprises satellite-based infrared measurements of airborne fine ash mass fluxes (Q_a) calculated by dividing the total airborne fine ash mass by the duration of active ash emission. The value of *MER* was calculated from the published mass of tephra deposited on the ground, divided by the duration of the explosive phase. Importantly, Q_a and *MER* refer to the same period of explosive activity and can thus be reliably compared. The temporal concordance required between these 2 parameters explains the relatively low number of eruptions finally selected.

The first results demonstrated that relationship actually exists between the MER, Q_a and eruption styles. This **interdependence thus leads us to develop statistical models for predicting MER using satellite measurements of Q_a** and additional controlling parameters. A reliable assessment of MER is essential for estimating plume dynamics close to the source, and hence for delineating zones impacted by tephra fallout, using tephra-deposition models for instance. However, direct measurements of *MER* remain difficult during the course of an eruption. Thus, as explained above for rapid assessment of *MER*, indirect methods have been developed using scaling laws based on relationships between measured plume height *H* and time-averaged *MER*; these are referred to as 0^{th} order empirical scaling laws (e.g. Sparks et al. 1997; Mastin et al. 2009). This methodology currently represents the standard for real-time determination of MER although associated with uncertainties as large as a factor of 54 at a 95% confidence interval.Data investigated here are small sized while the number of explanatory variables is relatively high. Therefore, we developed specifically a novel and robust statistical technique using a modified Akaike Information Criterion (AICc) allowing the selection of the best regression mixture model for the eruptions in our database (see Gouhier et al., 2019 for details). By combining Qs, Qa and H in three-dimensional space (figure 4), the best general model selected follows a power-law in the form:

$$MER = 30.22Q_a^{0.51}H^{2.25}$$

This relationship gives a low AICc with excellent p-values. The RMSE (Root Mean Square Error) yields an error factor of 12.8 at a 95% prediction interval. With an uncertainty four times lower than the empirical scaling law of Mastin et al., (2009), this new satellite-derived model improves significantly the estimation of *MER*. In particular, the error distribution is not uniform as shown in figure 4 from the projection of the 95% prediction interval envelope in the H-Q_a plane. This yields an error factor of ~2 only, close to the data centre of mass that encloses 12 of the 22 eruptions of our dataset.

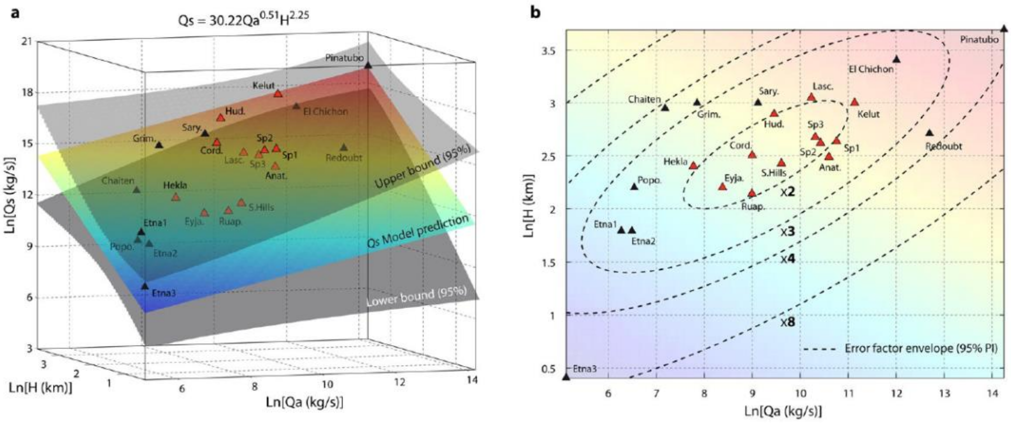

Figure 4. *MER* (referred to as Qs in the figure) prediction model using mixture model selection analysis. (**a**) Statistical relationship between *MER*, *Qa*, and H (above the vent), in a three-dimensional natural logarithm space. Error factor contour levels related to the MER estimation plotted on the two-dimensional plane *H* vs. *Qa* in natural logarithm, and showing the anisotropy of the error distribution

Then, we also collected 5 additional parameters (P1 to P5) related to magmatic system properties and external processes (referred to as modalities), likely to control the amount of very fine ash produced and injected in the plume. Each modality has been coded on a Boolean basis (0/1) so that they can be statistically analysed. We then proceeded to the selection steps to discriminate between all the possible models with 7 different variables (Q_a, H, $P1$ *to* $P5$), with modalities ($P1$, ..., $P5$) being class parameters for Q_a and H. The modalities include the SiO_2 (P1) and H2O (P2) contents of the magma, the open or closed character of the conduit (P3), the occurrence of phreatomagmatic activity (P4), and the formation of co-pyroclastic density current (co PDC) plumes (P5). Using our selection model analysis, these modalities allow clustering of the 22 data samples in the 3D space defined by *MER*, Q_a and H, and the identification of sub-models corresponding to different eruption scenarios. We found that P1 and P3 are the parameters that best improve the fitness criterion, with a low AICc value of 10.4. This leads to a new sub-model yielding an error factor of 9.3 at a 95% prediction interval based on four different equations (i.e., for four different eruptive scenarios) as follows:

$$MER = 25.95 Q_a^{0.72} H^{1.95} \qquad \text{low-SiO2 and closed-conduit}$$

$$MER = 25.95 Q_a^{0.72} H^{1.4} \qquad \text{low-SiO2 and closed-conduit}$$

$$MER = 25.95 Q_a^{0.62} H^{1.95} \qquad \text{high-SiO2 and closed-conduit}$$

$$MER = 25.95 Q_a^{0.62} H^{1.4} \qquad \text{high-SiO2 and open-conduit}$$

As a validation test, simulations are generated by the FALL3D tephra-transport deposition model with distinctive MER as input from the 23rd February 2013 Etna eruption (figure 5). The total erupted mass (TEM) according to these simulations yields values of 1.09×10^{10} and 6.58×10^{8} kg for simulation 1 and 2, respectively. The reference TEM value for this fallout deposit is 4.9×10^{9} kg, which means that the satellite-derived statistical model of Gouhier et al., (2019) overestimates the TEM by a factor of ~2.2, while the empirical scaling law of Mastin et al., (2009) underestimates the TEM by a factor ~7.4. This result shows the importance of accurate source MER estimate as it controls tephra fallouts, having a detrimental effect on water infrastructure, buildings or agriculture.

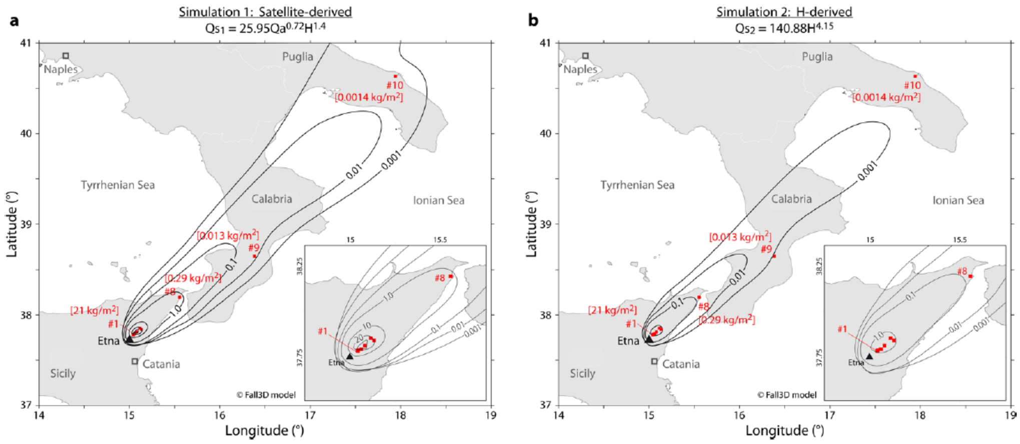

Figure 5. Simulations of the tephra fallout deposit from the 23rd February 2013 Etna eruption. The simulations are generated by the FALL3D tephra-transport deposition model with distinctive *Qs* as input.

(iii) Eruptive source parameters from Satellite: the Anak-krakatau

On December 22, 2018 at 13:50 UTC the south-western flank of Anak Krakatau volcano (Indonesia) collapsed to the sea and generated a tsunami in the Sunda Strait. Immediately after the collapse, Anak Krakatau experienced a long-lived eruption, from December 22, 2018 to January 06, 2019, of intense pheatomagmatic activity showing a series of strong volcanic explosions.

In this study, we focus on the mass budget of material emplaced during the post-collapse eruption. In particular, we provide estimations of airborne ash mass fluxes (Qa) and plume altitude (H) from IR satellite-based data. In this case, data from Himawari geostationary satellite have been processed. Both parameters are critical as they allow indirect assessment of the Mass Eruption Rates (MER) of tephra emitted at the source vent either empirical formulations (Sparks et al. 1997; Mastin et al. 2009) or statistical modelling as described in Gouhier et al. (2019). Also, Qa is essential in understanding the dynamics of particle transport and dispersion. As explained in chapter 2, we can distinguish silicate particles (e.g. volcanic ash) from other aerosols (e.g. ice crystals or H2SO4) using a two-channel difference model based upon the absorption feature between the 11- and 12 μm wavelengths. The differences between the at-sensor Planck brightness temperature (referred to as BTD) observed in these two channels are negative ($-\Delta T$) for ash and positive ($+\Delta T$) for ice. One can observe a plume of ash (blue colour) in figure 6A showing a minimum BTD of ~3.5K. In the case of optically thick cloud and tropospheric emission, the CTT (Cloud Top Temperature) method can be reliably used. In Figure 6B, we show as an example one image of the plume brightness temperature at 11,2 μm (H8 TIR waveband #02) that allows us to determine the plume top altitude between 14 and 15 km (a.s.l.) by comparing with local and synchronous atmospheric temperature profiles. For this study, temperature profiles were obtained using atmospheric sounding data of the station 96789 WIII-Jakarta

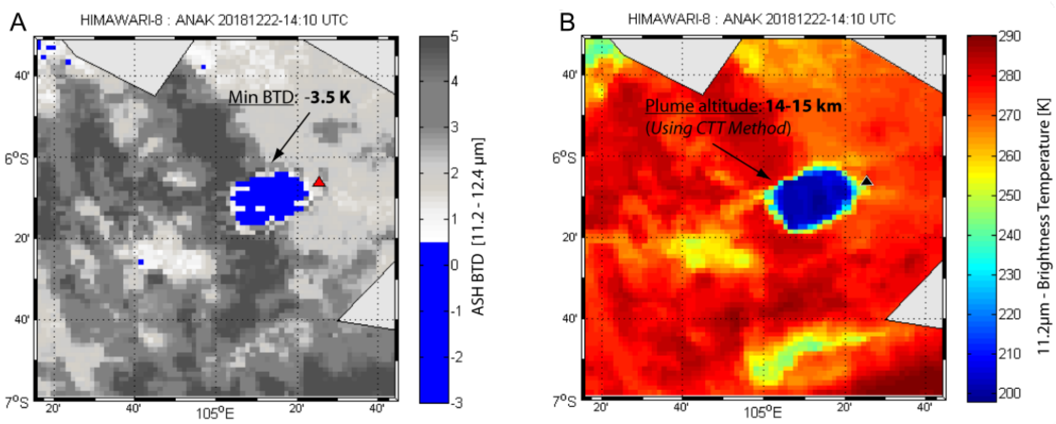

Figure 6. Ash plume characterization. [A] Brightness Temperature Difference (BTD) of band L02 (11:2 μm) and L03 (12:4 μm) from Himawari-8 satellite, showing the ash plume at 14:30 UTC on 22/12/2018. [B] Brightness Temperature (in Kelvin) at 11:2μm used for the plume height determination (see text for details).

The amount of airborne ash mass flux can also be estimated from a high-temporal series of TIR satellite-based images provided weather conditions are favourable. For this purpose, we used data from the geostationary platform Himawari-8 providing full-disc coverage at a 10-minutes time interval. From the improved split window technique using the 3-bands methods [Guéhenneux et al. 2015], we first selected ash-bearing pixels. Then, from inversion of TIR data using radiative transfer modelling (see chapter 2 for details) we give the ash cloud concentration (in g/m^2), and calculate the airborne ash mass flux Qa (in kg/s) from the image difference method. From figure 7, we observe that ash emissions can clearly be identified as early as 13:50 UTC, forming a transient high-altitude cloud of ash, coincident with the flank collapse. This first phase of effective ash emission only lasts about 40 minutes (13:50 to 14:30 UTC) and is directly related to the collapse itself. Thus, for the collapse-related plume we estimated a minimum airborne ash mass flux of $Q_a = 1\times10^4$ kg/s.

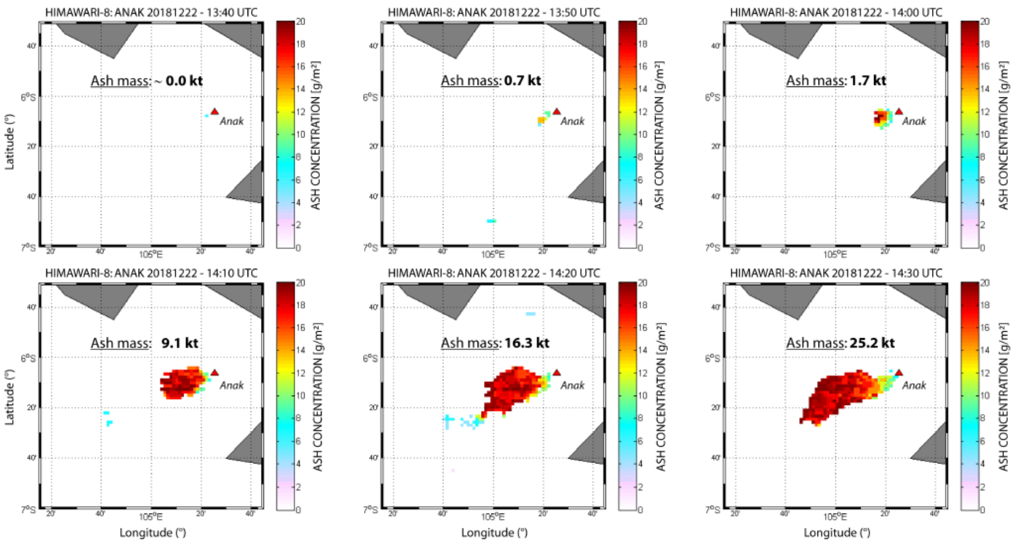

Figure 7. Airborne ash mass concentration (in g/m^2) retrieved from inversion of thermal infrared images using Himawari-8 data. These images show (i) the onset of the eruption at 13:50 UTC, i.e. synchronous with the collapse, (ii) the ash plume direction at a 10-minutes time resolution and (iii) the increase of the total ash mass loading.

In order to retrieve the source MER, one can use an empirical formulation including the plume top height solely (e.g. Sparks et al. 1997; Mastin et al. 2009). But the statistically-derived method we developed in Gouhier et al., (2019) using both the plume height and airborne ash mass fluxes gives much better results. In the present case, we have calculated both parameters, thus we can apply the following equation:

$$MER = 25.95 Q_a^{0.72} H^{1.4}$$

where Q_a is the airborne fine ash flux (in kg/s) and H is the top plume height (in *km* a.g.l.). Using this equation, we obtain a MER value of ~9×10^5 kg/s for the collapse-related plume. The eruption dynamics of both phases is quite different, but the first one only is described here. Indeed, the collapse-related plume resembles a Vulcanian eruption style. The reasons for that are (i) the short duration with impulsive emissions, (ii) and the high MER compared to a moderate plume altitude [Walker 1981; Clarke et al. 2002]. This study is a good example of source eruption characterization from IR satellite-based measurement. One should keep in mind that the collapse-related eruption occurred during the night, and no visual observation was made.

3.2. Shallow processes revealed by SO_2 and lava

In this second part, I will focus on the understanding of shallow processes revealed by the examination of simultaneous gas and lava surface emission from remote sensing techniques. In fact, volcanic gases released during open vent passive degassing or sustained eruptions represent a major source of information within the shallow system. The first 10 kilometres beneath the surface are the seat of intense interactions between the magma, gas and solid phases. Among major volatile species, CO2 is likely to degas first (~10 km) while SO2 degassing occurs at much shallow depth. Although SO2 usually constitutes <5% of the total gases emitted, it is virtually absent from the background atmosphere, which makes remote sensing measurement of sulphur dioxide fluxes much easier than that of more abundant gases (water vapour and carbon dioxide).

Interestingly, sulphur in volcanic emissions may have different origin: “primary” sulphur initially dissolved in the degassing magma, “secondary” sulfur released by the breakdown of S-bearing minerals (usually sulfides), and “external” sulphur present in a coexisting gas phase at depth (e.g., Scaillet et al., 2003), or stored in a shallow hydrothermal system. **All these processes may act as sinks or sources on the total magmatic sulphur budget**. Therefore, the idea is to compare the amount of SO_2 released at the surface with sulphur concentration in Melt Inclusions (MI), referred to as the petrologic method levels (e.g. Edmonds et al. 2003; Sigmarsson et al. 2013). If differences exist, in excess or deficit, one can invoke shallow sulphur sources or sinks as possible explanatory mechanisms. One common scheme for active volcanoes is that SO_2 realised at the surface, measured by remote sensing techniques, exceed by far those computed with the petrologic method. This is widely known as the so-called excess sulphur conundrum, recognized for several decades at arc volcanoes [e.g., Luhr et al., 1984] and extensively reviewed elsewhere [e.g., Scaillet et al., 2003; Wallace, 2005]. In contrast, during the sub-Plinian 2011 eruption at Grímsvötn volcano, Iceland, satellite measurements of SO_2 released at the surface gave order of magnitude lower SO_2 atmospheric mass loading than that of the petrologic method. That was explained by multiple inventories of sulphur and important role of sulfides as a sulphur sinks (Sigmarsson et al., 2013).

In this part, we present three different examples: (i) The study carried out on the April 2007 eruption at Piton de la Fournaise volcano (La réunion) in Gouhier and Coppola, (2011) is a good example for external sulphur sources, previously stored in a shallow hydrothermal system, and contributing to the SO_2 released at the surface after the collapse. By contrast, (ii) eruptions occurring at Holuhraun (Iceland) in 2014-2015 and Anak Krakatau (Indonesia) in 2018, show together no contribution neither as sources nor sinks of external sulphur.

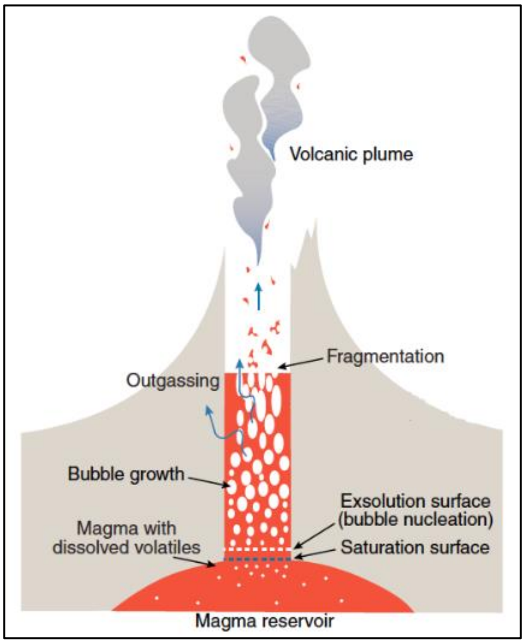

Figure 8. Sketch from A.C. Goglio (2014) showing the typical volatile exsolution sequence from the magma reservoir at depth to the surface. In this case, gas bubble exsolved are outgassed towards the surface. In processes invoked in this chapter, we show that many interactions actually occur between gas and the surroundings (wall-rock, hydrothermal fluids, etc.) acting either as sources or sinks of Sulphur, for instance.

(i) Hydrothermal system as a source of excess sulphur

Several studies have already suggested the existence of a shallow hydrothermal system beneath the summit craters at Piton de la Fournaise volcano (La Réunion), although there is still no clear evidence. Thus, in Gouhier and Coppola, (2011) we presented new arguments on the basis of joint assessment of lava and gas loading from satellite-based data acquired during April 2007 eruption suggesting the existence of a large hydrothermal system beneath the Dolomieu crater at Piton de la Fournaise.

The idea is to compare the actual amount of SO_2 actually outgassed during the collapse-related eruption, with SO_2 likely to be degassed if calculated from the volume of lava erupted, and hereafter referred to as "erupted SO2". The amount of SO_2 released in the atmosphere is estimated from the calculation of the mass flux using the Ozone Monitoring Instrument (OMI) on-board Aura platform, and following the method of Carn and Bluth (2003). The error margin of outgassed SO_2 is estimated at about 25% using TRL (low troposphere) SO_2 column algorithms. MODIS sensor data were used to derive the surface lava volumes at a rate of 4 images per day in average. This allows us to calculate a daily estimate of "erupted SO_2" following the petrologic method, and using a typical sulphur concentration in the magma of 1100 ppm (Collins et al., 2008).The error margin on erupted SO_2 is estimated at about 50%, taking into account the uncertainty on the mass flux rate, the magma density, and the variation of sulphur concentrations (Coppola et al., 2009). The SO_2 released during the collapse phase of the Dolomieu crater (~April 6–13) has been estimated at 935 ± 244 kilotons whereas "erupted SO_2" calculated from lava effusion rates was found to be clearly lower (179 ± 89 kilotons).

The whole SO_2 released during the April 2007 eruption cannot be explained by the lava effusion solely, and suggests a second source of SO_2 emission. The fact that on April 7 there was almost no SO_2 degassing from the vent suggests that this second source of SO_2 is likely located above the feeding dike and below the Dolomieu crater (see within the central column of the edifice). In addition the synchronization between the collapse and the net increase of the SO_2 released from the summit and measured by satellite are additional arguments for a non-magmatic origin. We suggested that the excess of SO_2 originated from a large hydrothermal system suddenly opened by the collapse.

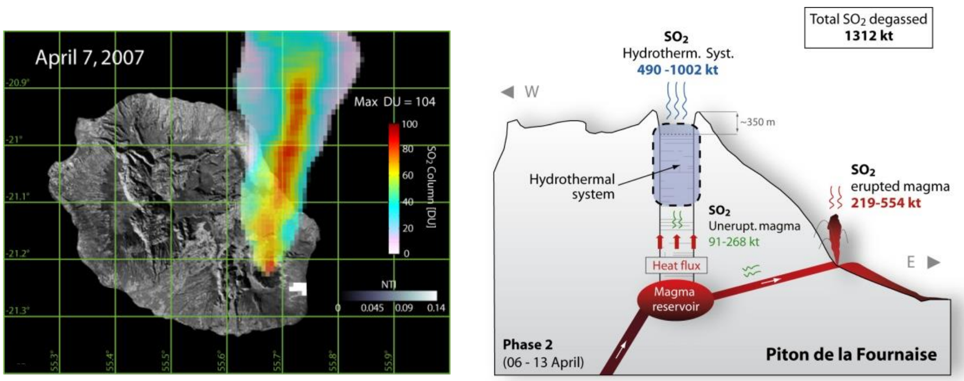

Figure 9. Location and quantification of volcanic SO2 and lava emissions emitted during the April 2007 eruption at Piton de la Fournaise from MODIS satellite sensor, and (right) model suggesting the existence of a hydrothermal system under the Dolomieu crater.

(ii) Sulphur sources and sinks from Anak krakatau

In this section, we applied a rather similar approach on eruption occurring at Anak Krakatau (Indonesia) in 2018. We had the opportunity to estimate the amount of SO_2 released in the atmosphere, and calculate the SO_2 likely to be degassed from erupted magma. However some fundamental differences exist in the eruptive dynamics and hence within the methodology used for the lava volume estimate. Here we processed data from the TROPOMI sensor on-board the Sentinel-5 platform. We used the Offline timeliness L2_SO2 data products from ESA-Copernicus Pre- Operation Data-Hub (https://scihub.copernicus.eu/). For estimating SO_2 emissions before the flank collapse, we used the middle troposphere elevation model (TRM, 5–10 km) as most emissions were injected to low/moderate altitudes. By contrast, for the 22/12/2018 eruption we used the 15-km elevation model (UTLS) from TROPOMI Slant Column Densities (SCD). We used the box method (Lopez et al. 2013) which allows mass fluxes to be determined from the estimation of SO_2 total columns divided by the duration of emission. In our case the travel time of the plume has been estimated from HYSPLIT trajectory model, and the loss term assessed by the application of an age dependent correction $e^{t/\tau}$ where τ is known as the SO_2 e-folding time, and found to be 30.4 hours. The total amount of SO_2 injected in the atmosphere is 173 ± 52kt.

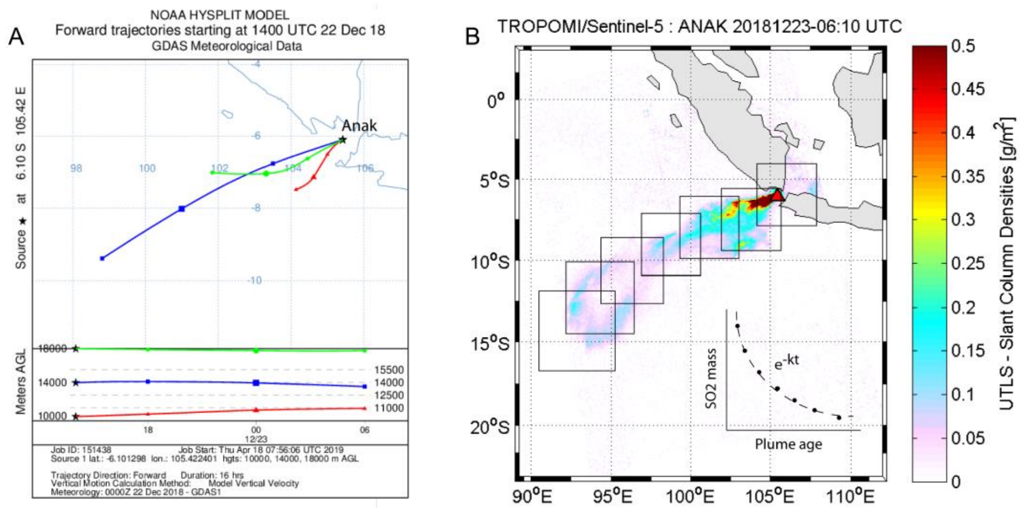

Figure 10. SO2 mass fluxes retrieval. [A] Run example of HYSPLIT forward trajectory on 22/12/2018 at 14:00UTC showing the best trajectory (blue line) drifting in the south westward direction at an altitude of 14 km AGL with an average velocity of 15m/s. [B] Tropomi/Sentinel-5 image on 23/12/2018 showing the SO2 plume slant column densities (g/m^2) at UTLS level (Upper Troposphere Lower Stratosphere). The boxes used for the assessment of e-folding time correction are represented.

Contrastingly to the study carried out at Piton de la Fournaise, here we calculated the magma involved (erupted or not), using the petrologic method, from SO_2 degassed and measured at the surface. For this purpose, we used the sulphur concentration of basaltic andesites reported for the 1883 Krakatau eruption [Mandeville et al. 1996; Fiege et al. 2014; Bani et al. 2015] as a reference. The average sulphur concentration in melt inclusions was found to be ~900 ppm (*SMI*) while the average dissolved sulphur concentration in matrix glass does not exceed 10 % (*SMG*): Calculating the concentration difference (S_{MI} -S_{MG}), yields an outgassed sulphur concentration of ~810 ppm. Then, from the outgassed sulphur concentration and the airborne SO_2 mass loading we can calculate the volume of parental magma, following:

$$Vol_m = \frac{M_{SO2} \times 100}{\alpha \rho_m (S_{MI} - S_{MI})}$$

where M_{SO2} is the total mass of sulphur dioxide measured by satellite (in kg), α is the molar mass ratio SO_2/S and ρ_m is the magma density taken as 2700 kg/m^3. Using a bulk porosity of ~40%, we obtain a bulk magma volume of 56.4×10^{6}m^3. By comparison, the minimum bulk volume of pyroclastic deposits emplaced after the collapse in the proximal field (on and around Anak Island) is around 45×10^{6}m^3. The 20% difference between the petrologic and the topographic methods can reasonably be explained by the significant amount of tephra fallouts and PDCs lost in the sea and not visible from the topographic analysis. We thus deduce that the existence of external sulphur sources and sinks are quite unlikely.

4. Eruptive products transport mechanisms

A large part of my research activities has been dedicated to the study of eruptive product transport mechanisms. These involve the advection/sedimentation of fine ash into the atmosphere, the oxidation of Sulphur dioxide into sulphuric acid droplets as well as lava effusion and cooling. Better understand the transport and dispersion mechanism is essential as it allows an improved assessment of the effects of these emissions on our environment, and bring important constraints on eruptive source parameters. As for previous chapter, here **I will provide key examples showing how remote sensing measurements can bring valuable information on parameters controlling transport of ash** material, in particular.

Volcanic tephra are produced during gas-rich explosive eruption from fragmentation processes in the conduit, and forming a buoyancy-driven vertical column above the vent. The total grain size distribution (TGSD) is very large, ranging from fine ash <100µm to metric blocs. Thus, associated transport mechanisms are very different, following ballistic trajectories for the coarser size fraction, to purely wind-advected routes for the finer size fraction. The latter forms volcanic ash clouds, which are distally transported in the atmosphere, up to distances ranging from a few hundreds to thousands of kilometres from the vent.

Tephra fall deposits are critical in determining the size and type of explosive eruptions. Current schemes for classifying eruption types (Walker 1973; Pyle 1989) rely on tephra layer features, such as dispersal, thinning rate, volume, etc. Interestingly, tephra fall deposits constitute very good witnesses to transport/sedimentation mechanisms of airborne ash. Compilations of many grain-size analyses of tephra have shown that most fallout deposit layers are characterized by fairly unimodal, log-normal distributions, with good sorting. Such ideal deposits suggest sedimentation processes controlled by the particle size and following an individual settling behaviour. **However, some key observations have revealed discrepancies to this common feature, and raised two main issues**: (i) Field observations of near-to-vent coarse-grained fall deposits may show mixing of ballistic and plume derived clasts, yielding polymodal grain-size distributions (Houghton et al. 2004). Similarly, Brazier et al. (1983) highlighted the influence of ash aggregation processes in volcanic plumes, and its multimodal grain-size distributions. Walker (1981a, b) reported the enrichment of fine particles in an ash deposit from the Taupo volcano (New Zealand) by early sedimentation prompted by rain-flushing. So, departures from simple, Gaussian-like distributions have thus been widely documented (e.g., Rose and Durant 2009) in fine-grained tephra fall deposits, although the controlling conditions for which such ash fallout deposits form remain unclear. (ii) Simultaneous ground and satellite observations have revealed major discrepancies within reconstruction of the fine ash fraction, also referred to as the "distal issue". TIR satellite-based measurements allow direct retrieval of the airborne fine ash fraction (mass and size distribution) which usually does not sediment within the ground sampling area: this fraction is lost from the tephra fallout layer. To address this issue, the tephra deposit mass (and distribution) is reconstructed by integrating the mass decay rate or the thinning rate of the fallout deposit (Pyle et al., 1989; Bonadonna and Houghton, 2005). These methods are sensitive to the quality and density of field data, to the mathematical function chosen (e.g., exponential, power-law, Weibull) to represent their spatial variations and to the distal extrapolation limit. Indeed, individual measurements of tephra thickness or mass are extrapolated at greater distances than the maximum sampling, allowing the finest ash fraction to be virtually accounted for.

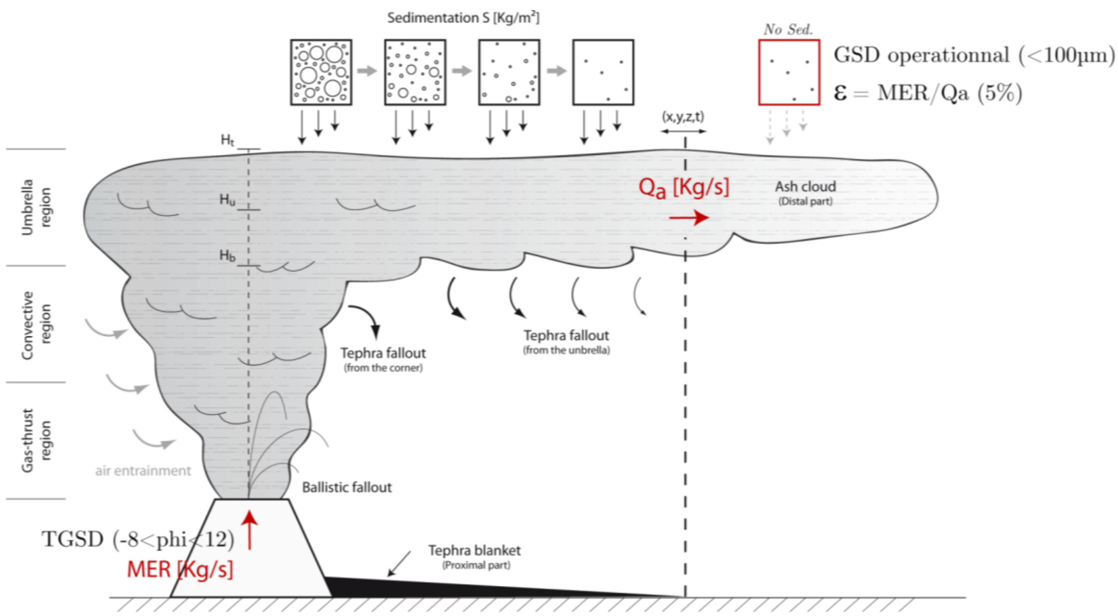

Figure 1. Sketch showing the main processes at work from the source vent (MER + TGSD + air entrainment) controlling the vertical ascent of the ash plume column, to distal locations with sequential sedimentation of tephra and forming a volcanic cloud of fine ash.

In this context, I have been using satellite-based IR techniques for more than 10 years for the **characterization of volcanic ash clouds** (mass, concentration, GSD, etc.) and to improve the **understanding of transport and sedimentation processes.** This chapter will be divided into three different parts: (i) In Gouhier et al., (2019) we present unexpected results showing early enhanced sedimentation of airborne fine ash. (ii) I provided in Poret et al., (2018) a detailed analysis of the ash cloud at Etna for an improved reconstruction of the source TGSD. (iii) In Bonadonna et al., (2011), we have carried out a multidisciplinary study on the Eyjafjallajökull 2010, eruption showing the importance of aggregation processes for the sedimentation of very fine ash.

i) Early enhanced sedimentation of fine ash

Volcanic ash clouds are composed of the finest fraction which survives proximal sedimentation, and referred to as fine ash (<100µm). Distal airborne fine ash represent only a fraction of the total amount of solid particles (referred to as tephra) injected into the volcanic plume column above the crater. In Gouhier et al., (2019), we examine this partitioning (ε; given in percentage) as the ratio between the fine ash flux transported in distal clouds (Q_a) estimated from satellite-based infrared measurements, and the flux of tephra emitted at the source (Q_s) inferred from ground studies of tephra fallout deposits. The latter is also referred to as the Mass Eruption Rate (MER). The ratio of Q_a/Q_s actually quantifies the volcanic ash removal efficiency in proximal areas: For a given MER, low values of ε indicate that a small amount of fine ash is effectively transported to distal area, and vice versa. This is a critical information for constraining ash sedimentation processes during the early stages of cloud dispersal, as well as for predicting the ash clouds properties as they are advected around the globe. We compiled a database of 22 eruptions of various MER and eruptive style from remarkably well documented case studies in the published records. The database comprises satellite-based infrared measurements of Qa inferred from the extinction properties of ash using the split-window method (see chapter 2 for details). The average value of Qs was calculated from the published mass of tephra deposited on the ground, divided by the duration of the explosive phase. Importantly, Qa and Qs refer to the same period of explosive activity and can thus be reliably compared.

We show that ε of sustained eruptions spans a wide range of values, from 0.1% (e.g., Plinian Kelut 2014 eruption) to 6.9% (Small/Moderate Ruapehu 1996 eruption). But remarkably, the variation of the partitioning coefficient is not arbitrary: ε decreases with increasing MER, with respect to eruption styles (figure 2). Indeed, fine ash removal from Plinian eruptions is about two orders of magnitude more efficient than that from Small/Moderate ones. The four Plinian eruptions selected have very large MER ($1.7\times10^7 < Qs < 1.8\times10^8$ kg/s), and produced copious amount of volcanic ash, as for the 1980 Mount St Helens, and the 1982 El Chichón eruptions, for which the mass fraction of ash smaller than 63 µm represents ~50% of the total mass of tephra emitted. Yet, they all exhibit a very small proportion of distal fine ash, as shown by the weak partitioning coefficient range ($0.1 < \varepsilon < 0.9\%$). To explain this observation, **we suggest that early enhanced fallout in proximal regions makes the actual proportion of very fine ash transported in distal clouds much lower than expected**. This highlights the critical role played by collective settling mechanisms, occurring preferentially in ash-rich plumes, which enhance the sedimentation rate of tephra regardless of grain size. Such mechanisms include aggregation (Van Eaton et al., 2015; Mueller et al., 2017), gravitational instabilities (Manzella et al., 2015), diffusive convection (Carazzo and Jellinek, 2013), particle-particle interactions (Del Bello et al., 2017), and wake-capture effects (Lovell and Rose, 1991). These are inferred to be key processes controlling the early depletion of ash-rich plumes, which cannot be explained by individual particle settling. Collective settling mechanisms, allow en masse sedimentation of particles of different sizes, which explains the significant amount of fine ash as well as the poor grain sorting sometimes observed in proximal tephra fallout deposits of large Plinian events. The fallout deposit from the 18 May 1980 eruption of Mount St. Helens (MSH80) for instance, shows both a poor grain sorting in proximal locations (Criswell, 1987; Eychenne et al., 2015) and an increase of mass and thickness at distances around 300 km demonstrating rapid removal of fine ash from the plume. The inverse relationship between ε and the MER shows that for very powerful eruptions, **the proximal sedimentation is mainly controlled by the concentration of fine ash**. This suggests that above a given threshold of the fine ash volume fraction, collective mechanisms dominate over individual particle settling, and conversely. Assessment of this threshold is very difficult as proximal measurements (i.e., in the first tens of kilometres from the source vent) of airborne volcanic ash concentration are scarce. But we believe that radar observations, in particular, must help obtaining crucial information on the dynamics of ash fallout in the umbrella corner region.

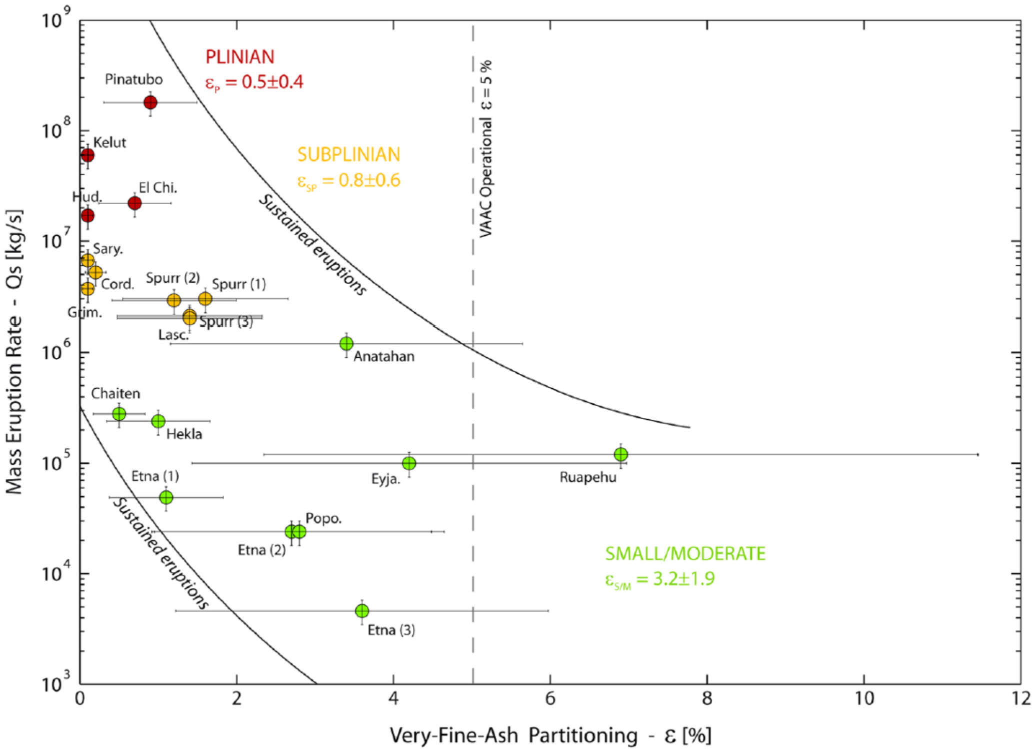

Figure 2. Style-derived volcanic ash partitioning of sustained eruptions. Mass erupting rate (Qs in kg/s) as a function of the partitioning coefficient ε (Qa/Qs in %) for the 20 sustained eruptions of our dataset. ε is the ratio between the very fine ash flux transported in distal clouds (Qa) and the flux of tephra in the plume (Qs) also referred to as MER. It quantifies the volcanic very fine ash removal efficiency. The sustained eruptions cluster following their eruption style (Plinian, Subplinian, Small/Moderate). This plot shows that ε of sustained eruptions scales with Qs, and spans about two orders of magnitude. The main trend shows that ε increases with decreasing MER. This indicates that very fine ash removal from ash-rich plumes (Plinian and Subplinian style) is more efficient than from plumes containing coarser tephra (Small/ Moderate style). Error bars are plotted from average bulk uncertainties given for fallout deposit and cloud masses. The vertical dashed line represents the current VAAC operational partitioning coefficient used by to forecast the atmospheric path of very fine ash clouds. The eruption dependant partitioning coefficients for each eruption style (ε_P, ε_{SP}, $\varepsilon_{S/M}$) have also been reported.

The partitioning parameter ε is crucial in operational volcanic risk mitigation, as it is required as input for ash-cloud-dispersal models used by several VAACs responsible for air traffic safety. They need rapid parameterization schemes to predict Q_a, and to provide frequent and reliable up-to-date forecast maps of atmospheric ash concentration during volcanic crises (Witham et al., 2007). With this aim, VAACs (such as London and Toulouse) have typically used a poorly constrained default ε value of 5% (Webster et al., 2012) to forecast the concentration of very fine ash composing distal ash clouds following $Q_a = \varepsilon \times Q_s$. However, as demonstrated before, the fraction of very fine ash that survives proximal settling varies by ~2 orders of magnitudes ($0.1\% > \varepsilon > 6.9\%$) with respect to the MER, and a constant partitioning value thus cannot be used. Therefore, in Gouhier et al., (2019) we propose a new operational eruption-style-dependant parameterization of ε using the mean values for Plinian ($\varepsilon_P = 0.5\%$), Subplinian ($\varepsilon_{SP} = 0.8\%$), and Small/Moderate ($\varepsilon_{S/M} = 3.2\%$) eruptions (figure 2). This parameterization is currently being tested in the MOCAGE-Accident model operated by Toulouse VAAC for operational use. For example, in figure 3, distal ash cloud dispersion maps were simulated using MOCAGE-Accident for a Plinian eruption scenario and showing the large difference of the no-fly-zone contours for both partitioning coefficients.

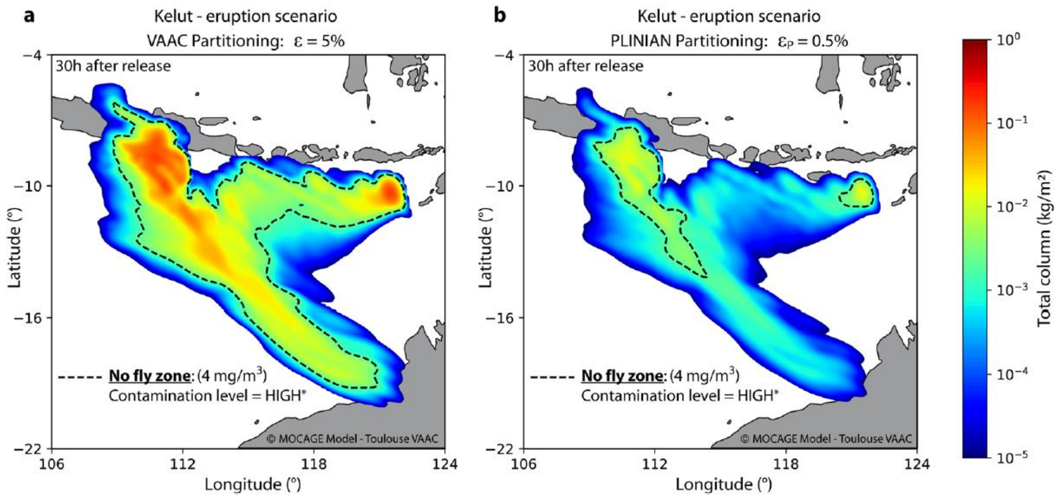

Figure 3. Ash cloud concentration simulations during Plinian eruptions. The two simulations are produced by the volcanic ash-cloud-dispersal model MOCAGE of the Toulouse VAAC based on the Plinian eruption of Kelut the 13 February, 2014 using different partitioning coefficients and present-day meteorological data. (**a**) Simulation of ash dispersion in the atmosphere at Kelut volcano 30 hours after the eruption, using the VAAC-default operational ε value of 5%. (**b**) Same simulation conditions and scenario, but using the Plinian ε value established in this study at 0.5%. The extent of the No-Fly zone (4 mg/m3 for an ash cloud 500-m thick*) is much larger for the VAAC-default ε, yielding a maximum concentration one order of magnitude higher. *The threshold at 4 mg/m^3 was first established by the European Commission after the Eyjafjallajökull 2010 eruption. It is now described by EASA (European Aviation Safety Agency) and used in the emergency plan EUR/NAT (EURopean and North ATlantic office) as the "High" contamination level.

ii) Fine-enriched TGSD reconstruction from satellite-based data

As mentioned above the reconstruction of the fine ash fraction from the analysis of tephra fallout deposit is not possible: Firstly, because the accumulation rate of this fraction is very low, making fine ash technically difficult to sample. Then, about 0.1-10% of the total mass of tephra (i.e., mostly the PM_{10}) is transported at much greater distances than the maximum possible sampling (Gouhier et al., 2019). However, the reconstruction of the TGSD is essential to calculate the total mass of tephra emitted during the eruption (e.g., Bonadonna et al., 2011). Characterization of the fine ash fraction, in particular, allows a better assessment of transport and sedimentation processes (Rose and Durant, 2009). The comprehensive retrieval of the TGSD is also interesting to better constrain the fragmentation occurring in the conduit. Indeed, ash population follows a power law distribution such that the number of fragments with radii larger than r, is given by $N \propto r^{-D}$ (Kaminski and Jaupart, 1998). Also, the TGSD is also important as it strongly affect the plume dynamics. Indeed, incorporation of a realistic TGSD in a 1D model has a first order impact on particle sedimentation, plume height and mass fluxes (Girault et al., 2014). Finally, the reliable assessment of the fine ash fraction is essential for air traffic safety (Casadevall, 1994).

Here I present the results published in Poret et al., (2018), where I provided a detailed analysis of the ash cloud, during the 23 February 2013 Etna eruption, for an improved reconstruction of the source TGSD. This study uses field measurements to estimate the field-based TGSD. Very fine ash distribution (particle matter below 10µm - PM_{10}) is explored parameterizing the field-TGSD through a bi-lognormal and bi-Weibull distribution. However, none of the two latter TGSDs allow simulating any far-traveling airborne ash up to distal areas. Accounting for the airborne ash retrieved from satellite (Spinning Enhanced Visible and Infrared Imager), we proposed an empirical modification of the field-based TGSD including very fine ash through a power law decay of the distribution The input eruption source parameters (ESP) are inverted by best-fit matching simulations against measurements. Simulations of the tephra dispersal and sedimentation are computed from FALL3D also using FPlume (Folch et al., 2016), which is a steady-state eruption column model based on the buoyant plume theory. Results suggest a column height of ~8.7 km a.s.l., a total erupted mass of ~4.9 × 10^9 kg, a PM_{10} content between 0.4-1.3 wt%, and an aggregate fraction of ~2 wt% of the fine ash.

For the retrieval of the fine ash airborne fraction, I processed the data from the Spinning Enhanced Visible and Infrared Imager (SEVIRI) sensor onboard Meteosat-10. It provides images every 15 min at a spatial resolution of ~3×3km at nadir. Satellite data were acquired from HOTVOLC (http://hotvolc.opgc.fr), a web-based satellite-data-driven monitoring system developed at the Observatoire de Physique du Globe de Clermont-Ferrand (France). Following the methodology described in chapter 2, I was able to provide the cloud top altitude, the airborne ash mass (kg) and the effective radius from 19:00 to 20:15 UTC.

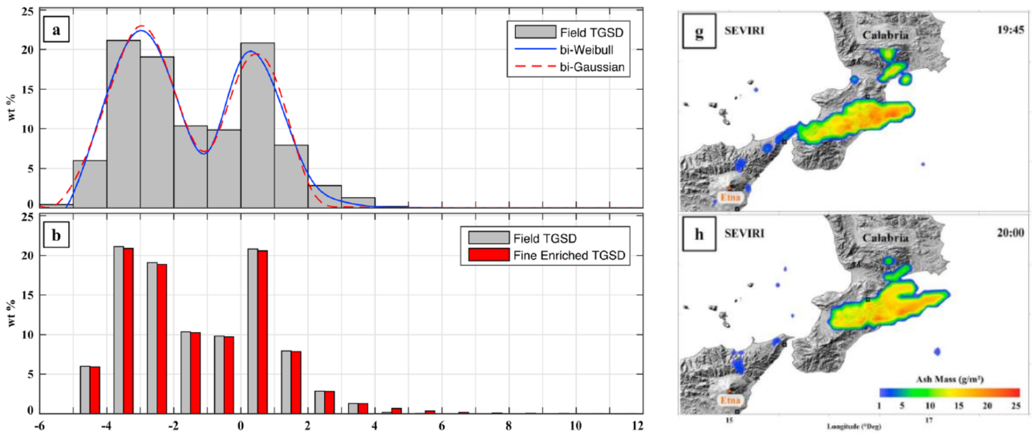

Figure 4. (left) Summary of the input total grain-size distributions (TGSDs) used within the simulations. (a) Field TGSD together with its best-fitting analytical curves (bi-Gaussian and bi-Weibull) (b) Fine-Enriched TGSD (red) obtained from the Field TGSD and accounting for the airborne fine ash retrieval from satellite. (right) Airborne ash mass retrieved from satellite (g–h) from 19:45 to 20:00 UTC.

iii) From source to cloud TGSD reconstruction

The 14 April to 21 May 2010, eruption of Eyjafjallajökull volcano (Iceland) was characterized by a nearly continuous injection of tephra into the atmosphere up to 10 km above sea level. Tephra were mainly dispersed toward the east and southeast, reaching as far as the southern parts of Europe, causing interruptions in global air traffic to an extent not seen since 11 September 2001 and the largest breakdown in European civil aviation since World War II. In Bonadonna et al., (2011), we provided a thorough analysis of the 6 May episode, in particular, using high-sampling-rate satellite data and ground-based techniques. It allows a detailed reconstruction of the source TGSD from the application of the Voronoi tessellation technique to the isomass map carried out from tephra fallout deposits sampling. The thorough analysis of sampled tephra using SEM images gives a refined characterization of aggregates sizes and types. The use of satellite-based data allows assessment of the unsedimented fine-rich ash fraction remaining in the cloud at distance up to hundreds of kilometers.

For the first time, we provided a total GSD (weighted average) representative of 30 min of eruption from the combination of simultaneous ground-based GSD and satellite-based fine-rich GSD (i.e., 7ϕ-9ϕ). The mass of the fine-rich GSD is retrieved from MSG-SEVIRI images at 11:00-11:30 and located between 100 and 1000 km from the vent (i.e., 3.3×10^6 kg, 4.5×10^6 kg and 2.1×10^6 kg for ϕ categories 7, 8, and 9, respectively). Between 11:00 and 11:30, the ash sedimentation flux is lower than the ash input flux. Thus, the excess mass between both images is mainly associated with ash emission during this time lapse (i.e., 30 min). Associated size fractions (100-1000 km from the vent) were averaged by weight with the size fraction collected on the ground between 2 and 56 km from the vent. The resulting grain-size distribution is comprehensive of the mass that fell up to the coastline (i.e., corresponding to the 0.05 kgm^{-2} isomass line; ~1×10^8 kg) and the mass that remained in the cloud up to 1000 km from the vent (i.e., ~1×10^7 kg). In figure 5c, **we provide the ground-based source TGSD (named "Voronoi ground", yellow bars), and the combination of "Ground + MSG-SEVIRI" source TGSD (red bars).** Associated Mdphi and sorting of the combined TGSD are of 2.1ϕ and 3.6, respectively. A secondary mode around 7ϕ is evident coming from the fine-rich airborne ash fraction retrieved from satellite-base measurements. The content of fine ash (<63 mm) is 26 wt% and 33 wt% for the ground-based and the combined data, respectively. SEM images of tephra show a wide range of aggregates types from clusters, coated particles and pellets, with sizes ranging from 100 to 400µm in average. This means that at a given moment and location in the cloud or plume, individual particles aggregate to form larger ones hence settling more rapidly. Of course, the clustering imprint has disappeared from the processing of the "Voronoi ground" TGSD due to sieving. Therefore, possible effects of particle aggregation on the actual grainsize range was investigated by aggregating all particles <63 mm in clusters between 1 mm and 63 mm (1ϕ - 4ϕ) based on our field and SEM observations. The amount of particles <63 mm in each aggregate-size category and the relative amount of aggregates in each size category could not be characterized in detail from our observations and therefore was equally distributed (white histograms in figure 5d). The portion observed in the volcanic cloud through the MSG-SEVIRI retrievals was left as individual particles (red histograms associated with the size categories 7, 8, and 9ϕ). **This grain-size distribution should be regarded as an airborne TGSD, and representative of aggregation processes** occurring at a specific moment and location in the cloud. Overall, about 5 to 9 wt % of the erupted mass remained in the cloud up to 1000 km from the vent, suggesting that nearly half of the ash $>7\phi$ settled as aggregates within the first 60 km.

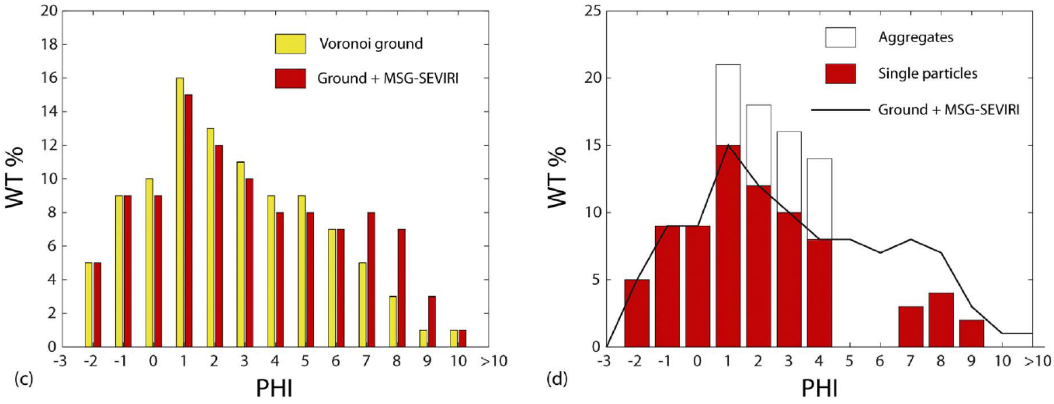

Figure 5. Comparison between ground-based total grain-size distribution (yellow histograms) and total grain-size distribution calculated from the combination of the mass deposited on the ground and the mass remaining in the cloud up to 1000 km from the vent (weighted on a 30 min period; red histograms). (d) Combination of the ground-based and satellite-based total grain-size distributions showing particle aggregation. The original grain-size distribution is indicated as a black solid line, whereas aggregates of various sizes and individual particles are indicated as white and red histograms, respectively.

5. Contributions for operational monitoring

As a "Physicien-Adjoint" from the CNAP (Conseil National des Astronomes et Physiciens), the operational monitoring associated with systematic observations is one of my statutory missions. I am in charge of the Observation Service (SO) HOTVOLC, which is based on real-time monitoring of volcanic eruptions from satellite-based infrared techniques. In fact, my observation activities are directly related to my research activities: HOTVOLC observation data feeds my research, and my research allows improvement of monitoring methods. It is therefore natural to present them here. Research works carried out so far, and methodological ones in particular, have enabled the development of operational algorithms for the detection and quantification of eruptive products. For the monitoring of ash plumes, for example, the theoretical study published in Guéhenneux et al., (2015) has enabled the implementation of a new, more reliable, operational algorithm for the monitoring of ash clouds. Similarly, my work published in Gouhier et al., (2012; 2016) has enabled the implementation of real-time automated detection and quantification procedures of lava flows. Today, the HOTVOLC web service is a comprehensive, user-friendly and scientifically mature interface. It is a multi-platform service, accessible from either PC workstation (http://hotvolc.opgc.fr), or from mobile devices (http://hotvolc.opgc.fr/m). The deliverables are validated and used, for instance, by French observatories (e.g., OVPF-IPGP for the lava monitoring at Piton de la Fournaise), and by Météo-France (for the monitoring of ash plumes)

- HOTVOLC system is labelled by the CSNO of CNRS-INSU (2012)
- HOTVOLC falls under the official function of the SMN (Météo-France, 2018)
- HOTVOLC is a certified product of EPOS (European Plate Observing System)

Figure 1. PC workstation + mobile HOTVOLC interfaces

With the democratization of satellite data access, several volcano observatories and research institutes have developed operational services for the monitoring of volcanic eruptions via web portals. Each of the platforms has its own specificities: types of sensors used, eruptive products observed, broadcasting interface for data visualization and dissemination, etc. Some of those services developed are not open-access and their use is therefore restricted to a small number of users. Others, on the contrary, are open-access and allow a wider dissemination. In table XX I succinctly described the main open-access platforms dedicated specifically to the operational monitoring of volcanic products.

Table 1 : Liste des capteur et services opérationnels disponibles principaux

Operational Portals	Products	Web URL	In-charge
HOTVOLC (CNRS-OPGC)	Cendres/Lave/SO2	hotvolc.opgc.fr	M. Gouhier
MODVOLC (NASA-HIGP)	Lave	modis.higp.hawaii.edu	R. Wright
MIROVA (UT/UF)	Lave	mirovaweb.it	D. Coppola
MOUNTS (GFZ-ESA)	SO2 / Lave	mounts-project.com	S. Valade
Global-SO2 (NASA-GSFC)	SO2	so2.gsfc.nasa.gov	S. Carn
Volcanic-Cloud (NOAA-CIMSS)	Cendres	volcano.ssec.wisc.edu	M. Pavolonis

Some web portals are "static" pages; they do not allow interactions with the user and provide images processed on a web page structured chronologically, in general. This is the case, for example, of the Global-SO2 service (NASA-GSFC) and Mounts project (GFZ-ESA) which provide quantitative images and graphical data of SO2 emissions on many volcanic targets. This type of web service is very effective for quick search and data mining; moreover, it allows easy automation of the data access from simple RSS feed, for instance, as each data (i.e., web-page) as its own URI. Other web portals are called "GIS", for Geographic Information System. They allow interaction with the user and cross-referencing of a huge amount of data through the use of a system of layers. They are very intuitive, allowing rapid extraction of the maximum of information, and in a short time, from complex geo-referenced data. The management of these operational services is however quite difficult and requires: (i) significant technical and IT resources, (ii) the use of interoperable databases, and (iii) high-performance servers. This is typically the case of the HOTVOLC observing system whose objective is to disseminate high value-added information on various volcanic products in real-time.

HOTVOLC uses data from the Meteosat Second Generation geostationary satellite (MSG) which uses the multispectral sensor SEVIRI (Spinning Enhanced Visible and Infrared Imager). It allows the tracking of about 50 volcanic targets at the frequency of 1 image / 15 minutes, with a pixel resolution of 3km × 3km at nadir. The spectral capabilities of the SEVIRI sensor allow volcanic ash, sulfur dioxide, and lava flows to be characterized. **To date, HOTVOLC is the only web-service allowing the real-time detection of simultaneous ash, SO_2, and lava emissions**. Information is provided in the form of geo-referenced tiled images (i.e., as geotiff) on an interactive map, and time-series (i.e., as CSV) managed using interactive data visualization technologies (® highchart). All numerical data can be freely downloaded from the user interface. **Many quantitative EO products can also be provided by HOTVOLC in real-time**, in particular: (i) ash cloud concentration, plume top altitude, and temperature; (ii) lava radiant flux (power) and lava volume flow rates. Many other auxiliary information, such as seismicity, is also accessible in real time through the web interface. I will not give more details here on the technical characteristics of the system. I will just mention that the whole chain of acquisition is installed at OPGC. It comprises the reception dish antenna ($\phi = 2$ m) using

HRIT dissemination protocol (10 Mbps) through a service level agreement with EUMETSAT (European Organisation for the Exploitation of Meteorological Satellites). Raw data are processed and archived using full mirroring SAN technologies, and high value-added data managed into interoperable databases and disseminated through a dedicated web-server. The HOTVOLC service has the support of the technical staff of OPGC. Finally, as part of the "Service National d'Observation en Volcanologie" (SNOV), the HOTVOLC system ensures real-time monitoring of lava eruptions at Piton de la Fournaise (Reunion), thus participating in the operational crisis management. Similarly, the HOTVOLC system provides quantitative data on ash cloud to the Toulouse VAAC (Volcanic Ash Advisory Centres) allowing a better risk assessment of air traffic. In this chapter **I will present one example for each type of eruptive product, and emphasize the operational applications** of the HOTVOLC system and discuss its usefulness for decision makers and other stakeholders.

i) Lava monitoring : Piton de la Fournaise (Reunion)

At Piton de la Fournaise (Reunion), before an eruption, the observatory is able to detect precursors: deformation of the ground, emission of volcanic gases on the surface, and earthquakes related to the ascent of the magma. In reality it is quite difficult to say whether the magma will finally reach the surface, or remain deep in the form of magmatic intrusion. However, experience shows that the onset of a continuous seismic tremor indicates, in most cases, the start of an eruption. But a visual confirmation is needed to validate the eruption beginning. In this context, the **HOTVOLC system (OPGC) provides early detection of thermal anomalies** and allows **real-time quantification of lava volume flow rate** at Piton de la Fournaise (Reunion). To date, it is the only open-access system to provide lava flow rates operationally.

On August 24, 2015, the onset of a continuous seismic tremor at 14:50 UTC marks the start of an eruption. Figure 2 shows that the HOTVOLC system records, at 15:00 UTC (i.e., 10 minutes after only), the presence of a high-intensity thermal anomaly due to the effusion of a lava flow on the surface. The "Lava hotspot" product selected from the HOTVOLC interface shows the pixels containing lava in red colour on the map. At this time, the activity level identified by the algorithm is at the highest and referred to as "activity level: HIGH" showing a TSR > 20 W/m²/sr/µm (i.e., Total Spectral Radiance), which gives a radiant flux of about 5GW. Likewise, the lava Volume Flow Rate (VFR) is calculated instantaneously and provided in real-time to the Observatory of Piton de la Fournaise (OVPF-IPGP) in the form of a time series that can also be visualized on the HOTVOLC Web-GIS interface (figure 2). During the first hour of eruption, the lava volume flow rates (VFR) calculated are very high, ranging between 90-120 m^3/s. As a comparison, most eruptions at Piton de la Fournaise usually range around 15-30m^3/s.

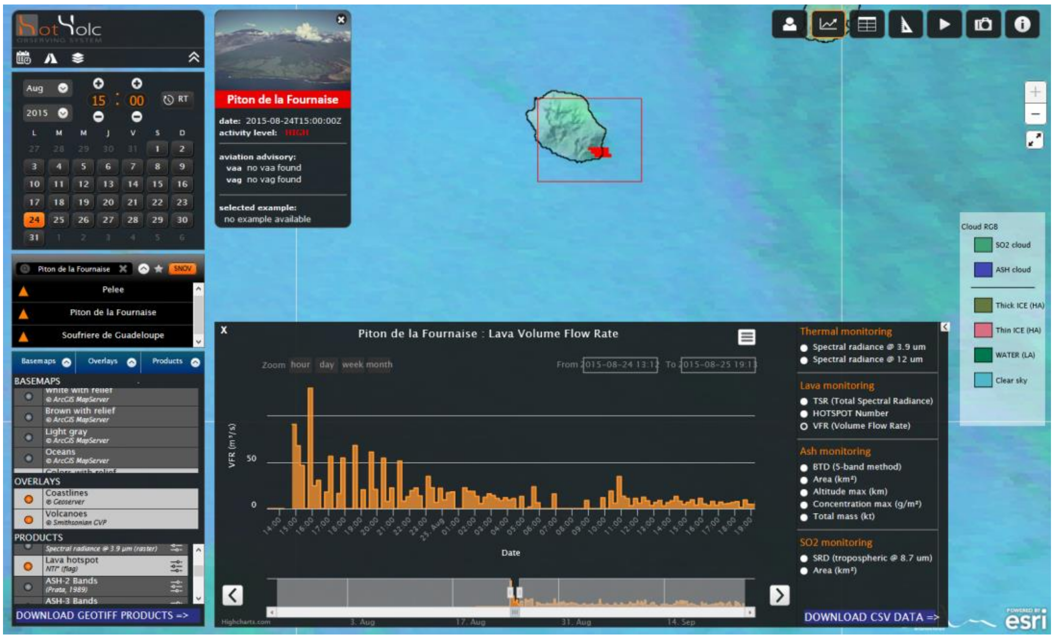

Figure 2. Snapshot of the HOTVOLC Web-GIS interface showing (i) the image of thermal anomalies detected (red pixels) due to the lava effusion at the surface, and (ii) the time series of lava volume flow rates associated with the August 24, 2015 eruption at Piton de la Fournaise.

ii) Ash monitoring : Mount Etna (Sicily)

The Etna (Sicily) eruption of December 24, 2018 was a flank eruption accompanied by significant lava flows and a plume of gas and ash. The plumes of ash from Etna are, in general, of low intensity and characteristic of the eruptive style known as "Violent Strombolian". As a result, these diluted ash plumes are difficult to detect and often masked by water vapour emissions and weather clouds. On December 24, 2018, the weather conditions were good, and despite the presence of water vapour from a magmatic origin, the HOTVOLC system perfectly detected the ash plume and allowed the quantification of ash concentration and cloud top altitude. The figure 3 is a snapshot of the HOTVOLC interface taken on December 24, 2018 at 12h15 UTC and clearly showing the ash cloud transported towards the southeast. Three different EO-products have been activated: (i) the “5-band” ash detection product (from Guéhenneux et al., 2015) and expressed as a Brightness Temperature Difference (BTD). This one allows to reliably detecting the presence of ash in the atmosphere, and makes possible the accurate assessment of the ash cloud location. This information is essential here, as the international airport of Catania is located about twenty kilometers south-east of Etna. In addition, the ash fallouts can seriously damage the building and jeopardize the population. (ii) The “cloud-top altitude” product using the CTT (Cloud Top Temperature) method. In the present case, the maximal value recorded lies around 7-8km a.s.l., just below the tropopause, and corresponding to flight altitude of many aircrafts. (iii) The “ash concentration” product is a surface concentration also known as a vertical column density (VCD) expressed in g/m^2. The maximal value recorded lies around $5g/m^2$, which is relatively high for an eruption at Etna. Under the assumption of a cloud thickness of 500-1000m, **we thus obtain an average volume concentration of 5-10g/m^3**. For information, the current threshold beyond which an aircraft cannot fly is fixed at

4mg/m^3 by EASA (European Aviation Safety Agency) and used since 2010 in the EUR/NAT emergency plan (EURopean and North Atlantic) as the so-called "high" level of contamination. The provision of this information in real-time constitutes a valuable support to decision makers for the reduction of air traffic risk. During this eruption, alert notifications in the form of VAA (Volcanic Ash Advisories) were issued by the VAAC of Toulouse (Météo-France), as well as forecast maps of the ash concentration in the form of VAG (Volcanic Ash Graphics) allowing aircrafts to be rerouted to other airports, thus avoiding ash encounters.

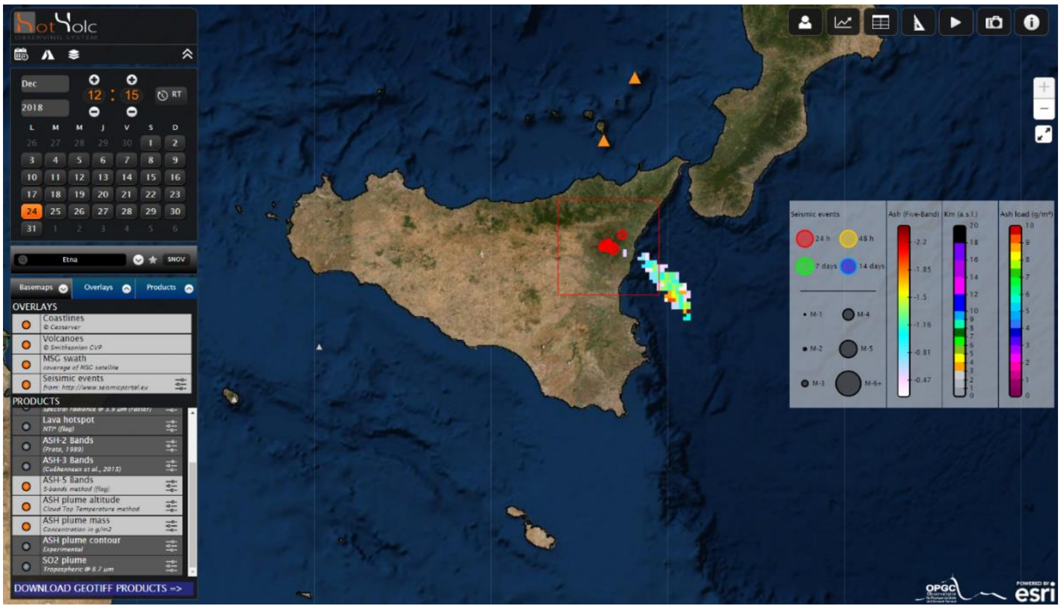

Figure 3. Snapshot of the HOTVOLC interface taken on December 24, 2018 at 12h15 UTC, and clearly showing the ash cloud transported towards the southeast, with associated seismic events (red circles)

iii) SO_2 monitoring : Fogo (Cape Verde)

In operational monitoring, early detection of SO_2 outgassing is essential. Indeed, the solubility of sulfur in magma is relatively high (compared to CO_2), and the degassing of SO_2 occurs at low pressure (close to the surface). Therefore, its detection can be used as a precursor of an eruption. MSG-SEVIRI has two main SO_2 absorption wavebands centered at ~7.3 µm (ν_1) and ~8.7 µm (ν_3), thus enabling the detection and quantification of volcanic SO_2 by satellite (Realmuto et al., 1994). The IR wavebands are less sensitive to SO_2 than the UV, but the sensors using this technology are much more efficient in terms of spatial and temporal resolution. The detection method is quite simple, the principle being to reveal the SO_2 anomaly by contrast with the atmospheric background level, called "clear sky", by using either the difference in brightness temperature between 2 spectral bands, one sensitive to SO_2 (ν_1 or ν_3) the other not (example: 7.3µm-13.4µm or 8.7µm-12µm), or by linear interpolation of the brightness temperature at 7.3 µm, calculated between wavebands at 6.3 µm and 10.8 µm. Note that for operational purpose, we favour the 8.7-µm waveband as it allows a reliable SO_2 detection whatever the altitude of emission. Thus, within the HOTVOLC system we used the BTD method following 8.7-12 µm. In these conditions of acquisition, early detection of SO_2 is possible, but with a detection threshold relatively high lying at ~12DU (i.e., 5 tons / km^2), which however do not allow the detection of inter-eruptive passive degassing.

At the start of an eruptive crisis, we first seek the location and altitude of the gas plume. But, rapidly, quantification of concentrations and fluxes of SO_2 become important because it informs us on the current dynamics and allows us to anticipate the future changes. Monitoring SO_2 is also very important for public health reasons: above 350 µg/m^3 the SO2 becomes harmful, as for example during the Icelandic eruption of Holuhraun in 2014-2015 (Gautier and al., 2016). Likewise, the oxidation of volcanic SO_2 in the atmosphere leads to the formation of sulfuric acid (H_2SO_4) droplets, also known as acid rain. They can have harmful effects on the environment (agriculture, water, etc.). In figure 4, we provide one example of a large plume of SO_2 emitted during the November 24, 2014 eruption at Fogo (Cape Verde). The RGB microphysics index used in HOTVOLC allows the detection of SO_2 from the light green colour. With a little experience it turns out to be quite sensitive and reliable. We have also selected the "SO2 plume" product from the Web-GIS interface, hence allowing the relative quantification of SO2 from the brightness temperature difference (BTD = 8.7-12µm). Interestingly one may observe that the RGB product remains much more sensitive "SO2 plume" one.

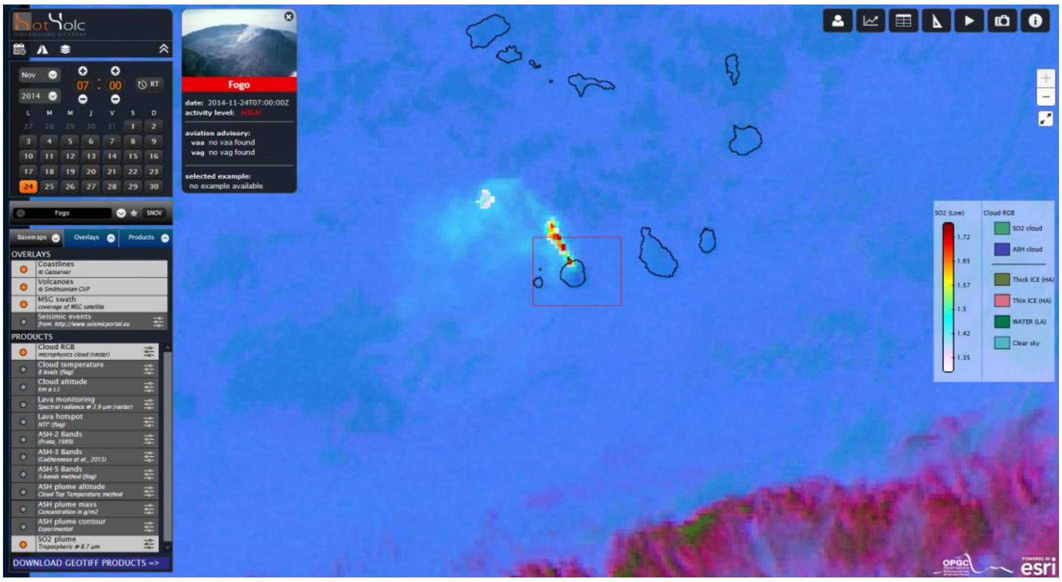

Figure 4: Snapshot of the HOTVOLC Web-GIS interface showing the plume of SO_2 emitted during the November 24, 2014 eruption at Fogo (Cape Verde).

6. Prospective and ongoing works

In this chapter, I will summarize the main ongoing and prospective works I want to carry out in the new few years at OPGC/LMV. As for past works, examples chosen here also reflects the different aspects of my research profile, comprising some methodological developments, fundamental research as well as some monitoring activities. In the first part, I will present a selection of three ongoing works I am leading, and carried out on collaboration with different colleagues. (i) The first one is related to the inversion of hyperspectral Thermal InfraRed (TIR) using the radiative transfer model ModTran for accurate SO2 detection and quantification. (ii) The second one deals with experimental ash plume retrieval from Bi-spectral TIR inversion. (iii) The third one is a study which combines satellite-based TIR measurements of airborne fine ash within distal clouds with the PPM 1D models.

6.1. Ongoing works

i) Hyperspectral TIR inversion using ModTran for SO2 monitoring

This study is related to the ongoing CNES PhD of Charlotte Segonne, which is currently working on the inversion of hyperspectral TIR data using MODTRAN radiative transfer model. We have a large set of hypercube data coming from Etna (June, 2015) and Stromboli (October, 2016) showing evident feature of passive and erupted SO_2, respectively. Contrarily to broadband instruments, the high spectral resolution (~0.5 cm^{-1} in average) allows SO_2 detection and quantification with unprecedented accuracy. However, inversion of such data is very complex and time-consuming. Therefore, we are developing strategies allowing fast, but reliable, algorithm to make the operational use of such instruments possible for SO_2 monitoring at unrest volcanoes.

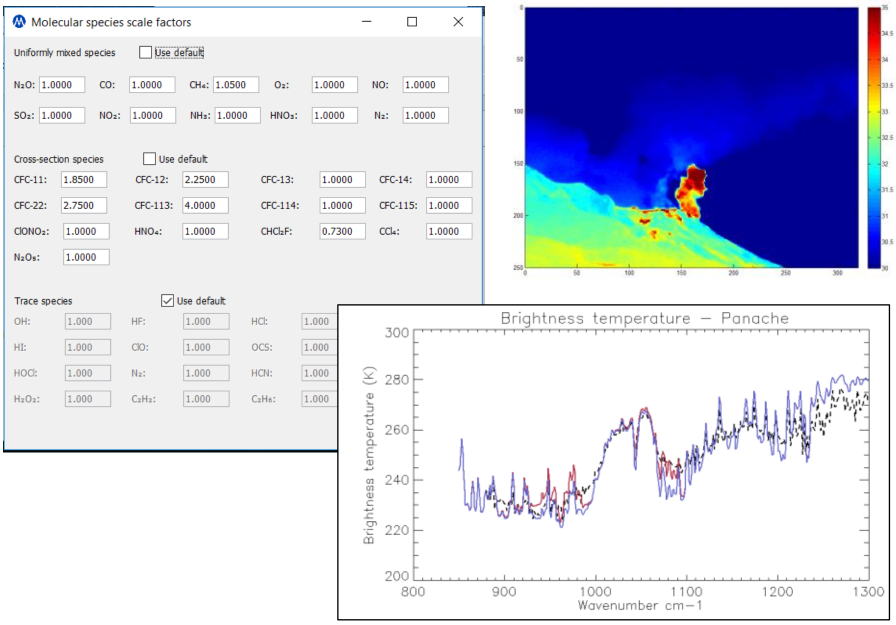

Figure 1. Multi-panel figure showing the ModTran RTM interface with observed (blue) and synthetic (red and black) spectra of the SO_2 plume shown in the coloured image, during the Stromboli October, 3 2015 field mission.

ii) Experimental ash plume retrieval from Bi-spectral TIR inversion

This study is related to the IRD Postdoctoral fellowship of Julia Eychenne, which is has just ended, and was working on the characterization of ash suspension from inversion of bi-spectral TIR data. The main objective is to improve the satellite-based TIR measurement of ash clouds using a controlled experimental setup, from a similar methodology. For this purpose, we developed a prototype device allowing the realisation of soda-lime glass particles aerial suspension using controlled GSD, mass and volume concentration. The main experimental challenge was to confine PM_{10} particles (i.e., with size <10µm) within the apparatus, while allowing IR measurements through the cellophane walls. Calibration and visual control were made using a high-speed camera.

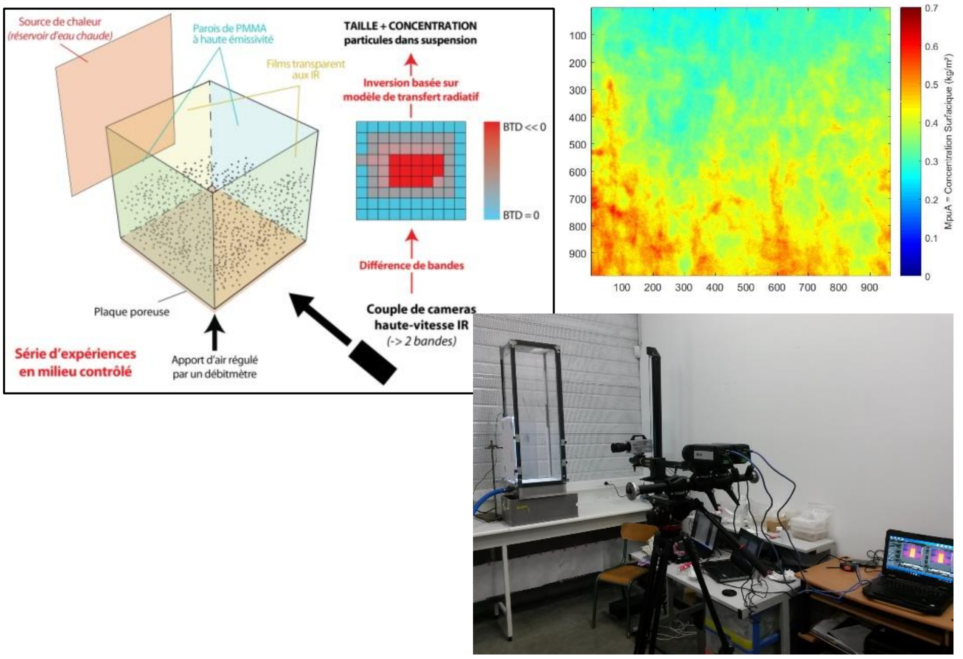

Figure 2. Multi-panel figure showing the acquisition setting of the TIR bi-spectral images on the soda-lime aerial suspension. The coloured image shows the surface concentration (VCD) retrieved from the inversion of TIR data.

iii) Combined satellite-based ash data with PPM 1D model

Volcanic ash clouds generated during explosive eruptions can be transported in the atmosphere up to distances ranging from a few hundreds to thousands of kilometres from the source vent. They are mainly composed of fine and very fine ash (i.e., <100µm) in varying proportion from one eruption to another. Ash clouds can have detrimental socio-economic impacts as demonstrated by air traffic disruption during Eyjafjallajökull (2010) and Cordón del Caulle (2011) eruptions. However, the **reliable assessment of distal ash concentration remains difficult**, and requires major improvement of (i) the source term estimation (MER and plume height), as well as (ii) the distal ash loading measurements, and (iii) description of sedimentation processes from the source to distal locations. In this aim **we proposed to combine** satellite-based measurements from the **HOTVOLC** operational system, **with PPM**, a fast-running 1D model of the eruption column (collab. G. Carazzo, IPGP). In one hand, satellite data give information on the airborne fine ash fraction within distal clouds, while in PPM, average characteristics of an explosive eruption column are calculated as a function of altitude hence allowing reliable estimates of the source term (MER and plume Height). Once the source parameters are known, direct calculations will provide the eruption cloud shape, total ash flux, load and GSD in the column.

We started in updating the fluid dynamics algorithm (PPM) now incorporating the key processes of turbulent mixing with the windy atmosphere and a robust particle sedimentation. It allows modelling the transition from the vertical column to the horizontal ash cloud using enhanced sedimentation rates within realistic atmospheric conditions. Many sensitivity tests have been carried out to assess the reliability of the new features. We then generated theoretical calibration curves with PPM (e.g., $Q^*_{N(D),Hb}$) to be compared with distal measurements of ash cloud flux rates ($Q_{a,sat}$) using HOTVOLC data. As an example, we provide in figure 3 the time series of ash flux rate ratios for varying cloud GSD (PM10, PM63, PM100) during the first 50 hours of cloud transportation. At time t_0, the ratios Q/Qs represents the fraction of a given GSD (i.e., Q63/Qs stands for <63µm) at the plume buoyancy height (H_b)

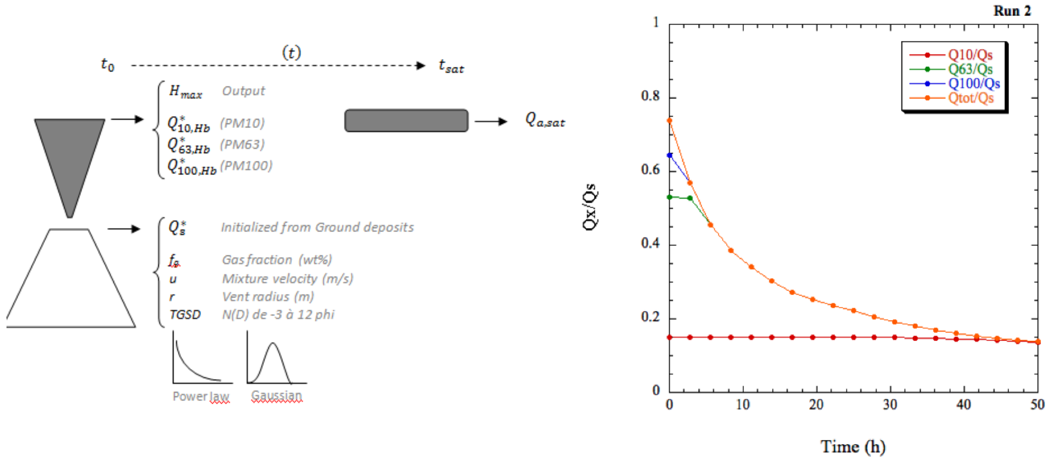

Figure 3. (left) Sketch illustrating the inputs and outputs of the updated PPM model and (right) time evolution of the ratios Q_{tot}/Q_s, Q_{100}/Q_s, Q_{63}/Q_s, and Q_{10}/Q_s in the atmosphere for a plume height of 11 km and a fine TGSD (μ=4) at the volcanic vent, run 2.

6.2. Prospective works

i) Statistical-to-physical insight of the early-enhanced ash sedimentation

In Gouhier et al., (2019), we provided a statistical model relating the source Mass Eruption Rates (MER) with both the column height (H) and the airborne fine ash flux (Q_a). If the buoyant plume theory (BPT) accounts relatively well to the relationship existing between H and MER, there is no evident physics accounting for both H and Q_a. I believe that, based on several works (e.g., Freret-Lorgeril et al., 2019; Lherm and Jellinnek, 2019; Cashman and Rust, 2019; Carazzo et al., 2020; Saxby et al., 2020), early-enhanced sedimentation takes its origin around the corner region; at the transition from the vertical column to the horizontal ash. The idea is to use actual values of MER, H and Qa to assess physical parameterizations (which differs from the statistical ones of Gouhier et al., 2019) of acting forces. For this purpose, a multidisciplinary approach (theoretical, experimental, radar + satellite data, etc.) is strongly encouraged. Figure 4 (left) is a good example showing that radar measurements are relevant for tracking coarse particles while VIS/IR wavelengths are more relevant for the assessment of the fine fraction. Most of all, this highlight the crucial need for using various technologies within the density-driven region in particular. In June 2020, Alessandro Tadini is starting a 2-years Postdoctoral fellowship (CLERVOLC LabEx fundings), to work on this subject using Plume-

Mom/Hysplit VATD model allowing both eruption column and long-range ash transport and dispersion modelling. The key point being the transition between both spatial domains. As a complement, A. Tadini will integrate Doppler radar (Voldorad) and IR satellite-based on key eruptions.

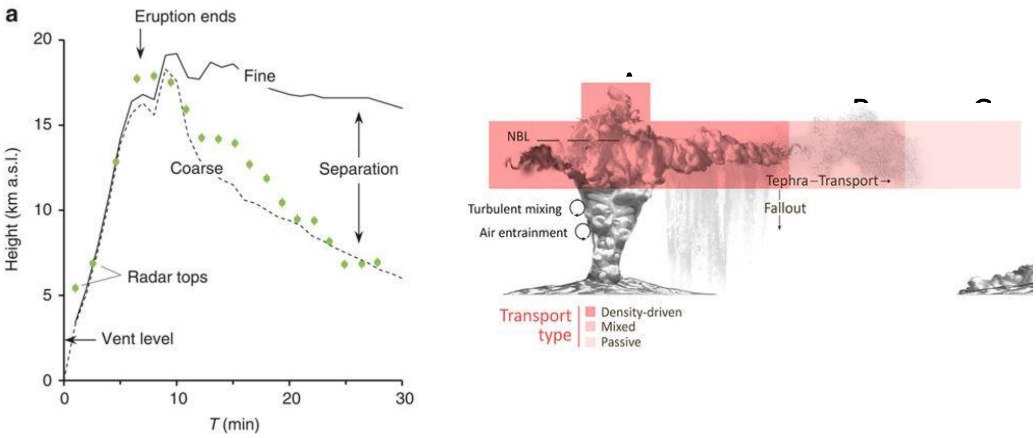

Figure 4. (left) plot showing radar measurements elevation tracking coarse particles in the first 30 minutes after the onset of the explosive eruption. (right) sketch of the different region of tephra transport and dispersion.

ii) SO_2 detection and quantification improvement from HOTVOLC

Quantification of SO_2 is now routinely been made using UV satellite data, as it is the case for OMI and TROPOMI sensors, and displayed within web-interfaces more or less operationally. As mentioned in chapter 5, the HOTVOLC interface uses IR satellite-based data and allows detection only of SO_2 from a simple BTD procedure. Here we present some monitoring perspectives for the improvement of SO_2 detection and quantification using HOTVOLC interface.
First of all, one may observe from RGB product (R = 10.8-12 µm; G = 10.8-8.7 µm; B = 10.8 µm) that SO_2 can be identified from simple colour inspection (light-green) at much lower threshold than from the" SO_2_BTD" product. Therefore, this means that it is possible to greatly improve our current algorithm from: (i) using a combination of BTD with carefully-selected threshold, (ii) including the highly-sensitive 7.3-µm waveband for high altitude SO_2 plumes, or (iii) using the linear interpolation method (see chapter 5 for details). Overall, the objective is to lower the detection threshold below 10DU, and allows early detection of SO_2 as being an important precursor to volcanic eruption.

Then, the second step is to provide quantitative information on SO_2 mass loading, in the form of Vertical Colum Densities (VCD), usually expressed in DU (Dobson Unit). As no sulphur dioxide calibration is available for the SEVIRI sensor, we have two main possibilities: (i) first, we can provide a parameterization of SO2 VCD by best fit matching between recorded SO2_BTD on key eruptions and synthetic SO2_BTD*. The latter being processed from direct models of the VCD and using radiative transfer calculations (such as ModTran). (ii) Secondly, we can provide a parameterization of the SO2 VCD by best fit matching between SO2 VCD derived from UV sensors and BTD derived from IR sensors.

Table 1: MTG-1 FCI characteristics (Flexible Combined Imager)

CHANNEL	CENTRE WAVELENGTH	SPECTRAL WIDTH	SPATIAL SAMPLING DISTANCE (SSD)
VIS 0.4	0.444 µm	0.060 µm	1.0 km
VIS 0.5	0.510 µm	0.040 µm	1.0 km
VIS 0.6	0.640 µm	0.050 µm	1.0 km; 0.5 km*
VIS 0.8	0.865 µm	0.050 µm	1.0 km
VIS 0.9	0.914 µm	0.020 µm	1.0 km
NIR 1.3	1.380 µm	0.030 µm	1.0 km
NIR 1.6	1.610 µm	0.050 µm	1.0 km
NIR 2.2	2.250 µm	0.050 µm	1.0 km; 0.5 km*
IR 3.8 (TIR)	3.800 µm	0.400 µm	2.0 km; 1.0 km*
WV 6.3	6.300 µm	1.000 µm	2.0 km
WV 7.3	7.350 µm	0.500 µm	2.0 km
IR 8.7 (TIR)	8.700 µm	0.400 µm	2.0 km
IR 9.7 (O_3)	9.660 µm	0.300 µm	2.0 km
IR 10.5 (TIR)	10.500 µm	0.700 µm	2.0 km; 1.0 km*
IR 12.3 (TIR)	12.300 µm	0.500 µm	2.0 km
IR 13.3 (CO_2)	13.300 µm	0.600 µm	2.0 km

The final point of this section deals with the future and possible use of the new generation of Meteosat. Indeed, since about two decades Meteosat Second Generation (MSG) has provided a huge amount of land and atmospheric data at a frame rate of 1 image / 15 minutes (full-disc). In 2021, the third generation of Meteosat will be launched, referred to as MTG-I (composed of 2 imaging satellites), comprising the FCI imagers, one providing a full-disc every 10 minutes (FDSS mode), and one covering Europe only at a frame rate of 1 image / 2.5 minutes (RSS mode). At this resolution, using stacking processing to increase the signal-to-noise ratio (SNR), we hope to be able to detect passive degassing from inter-eruptive periods, at Etna in particular. Note that the 3.8-µm wavebands will be given at the same spatial resolution than MODIS (1-km) allowing unprecedented capabilities for the detection of thermal anomaly.

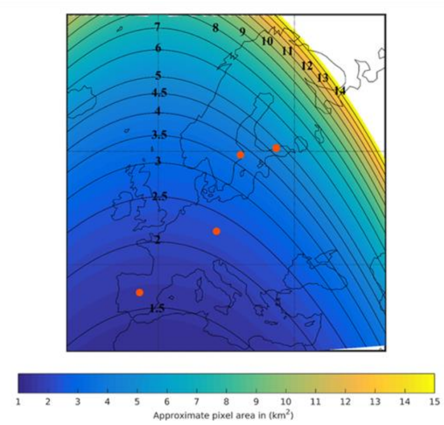

Figure 5. (left) Approximate pixel area over Europe for the Flexible Combined Imager (FCI, right image) onborad the future MTG-1, to be launched in 2021.

iii) Ground-based IR bi-spectral imager for SO_2/ash detection

Ground-based instruments using UV absorption features are common tools in volcanology for the monitoring of SO2, such as the Correlation Spectrometer (COPSEC) (Stoiber et al., 1983) and Differential Optical Absorption Spectroscopy methods (DOAS) (Galle et al., 2003) and are still extensively used (e.g., Mori et al., 2013; Menard et al., 2014). In the last decade, UV imaging techniques have emerged, commonly referred to as SO_2 cameras (Bluth et al., 2007; Mori and Burton, 2006). They allow quantification of the SO_2 column amount for every pixel in a 2D image, and are quickly becoming a common tool for gas monitoring (e.g., Aiuppa et al., 2015; Smekens et al., 2015). However, these UV-based techniques allow daytime measurements only, which prevent from 24/7 monitoring of SO2 emissions.

In parallel, many ground-based instruments operating in the TIR have been developed. There are two main advantages using these techniques: it allows night and day monitoring and makes possible the retrieval of both SO_2 and ash. However, the detection limit of SO_2 concentration is much higher than in the UV, and may limit their use during weak SO_2 emissions. While broadband infrared imaging has proved ineffective for SO_2 detection, hyperspectral sounders known as Open-Path Fourier Transform Infrared (OP-FTIR) instruments (medium-cost: ~100 K€) have shown very strong capabilities to study the composition of volcanic plumes (e.g., Allard et al., 2005). More recently, hyperspectral imagers have been tested (Gabrieli et al., 2016, Smekens and Gouhier, 2018; Huret et al., 2019) and show unprecedented capabilities for the quantitative assessment of both SO_2 and ash fluxes and total mass budget. However, commercial versions used in the literature have a prohibitive cost, lying around 600 K€, hence preventing from easy implementation at many volcano observatories. In this regard, multispectral imaging instruments, would offer a good compromise between spectral and spatial resolution at a relatively low cost. However, they are quite uncommon in the field of volcanology. One existing example is the Cyclops camera, an instrument developed by Prata and Bernardo (2014) that uses bandpass filters mounted on a wheel rotating ahead of a broadband TIR sensor (micro-bolometer array), providing near-simultaneous images of a scene at different wavelengths.

In near future I aim at developing a somewhat similar instrument but using two broadband high-speed TIR camera (250 Hz), each having a single spectral filter mounted between optics and the sensor, hence allowing simultaneous bi-spectral measurements. This limits its use to only one type of volcanic product at a time, but makes much easier, and cheaper, data acquisition and processing (low-cost: 20-30 K€). This instrument is currently being developed and first tests carried out in the lab during experimental works on ash particles are promising. The next step is to test this device at Vulcano (Eolian Island, Italy) using simultaneous UV measurements.

Short Curriculum Vitae

A/ Identification

Nom : **GOUHIER** Prénom : **Mathieu**
Date de naissance : 15/07/1980 mail : M.Gouhier@opgc.fr Tel : 04 73 40 55 88
Établissement d'affectation : Observatoire de Physique du Globe de Clermont-Ferrand (UCA)
Unité de recherche d'appartenance : UMR 6524 (LMV)
Section CNAP : Terre Interne
Section de CNU : 35
Statut et Grade : Physicien-Adjoint Classe Normale échelon 6

B/ Curriculum Vitae

Formation:

- **2020** – Soutenance HDR (*prévue le 27 Mars 2020*)
- **2008** – Doctorat de l'Université Blaise Pascal, Clermont-Ferrand - Volcanologie
- **2005** – École Normale Supérieure de Lyon (ENS-Lyon)

Expérience professionnelle:

- **2011-** Recrutement Physicien-Adjoint (OPGC/LMV)
- **2009-2011**: Post-Doctorat 2 – Laboratoire Magmas et Volcans (LMV)
  Télédétection spatiale des coulées de lave (directeur : P. Labazuy / JF. Lénat)
- **2008-2009**: Post-Doctorat 1 – Michigan Technological University (MTU)
  Télédétection spatiale des panaches volcaniques (directeur : W.I. Rose)

Activités statutaires:

1. Recherche – 33% : (LMV-UMR6524)
- Mon activité de recherche actuelle est centrée sur l'étude de la dynamique des émissions volcaniques (cendres, gaz et coulées de lave) par télédétection spatiale IR.

2. Observation – 33% : (OPGC-UMS833)
- Responsable du Service d'Observation HOTVOLC pour le suivi de l'activité éruptive des cibles prioritaires du SNOV, et labellisé par le CNRS en 2012.

3. Enseignement – 33% : (UCA)
- Mon service statutaire est de 66 heures eq./TD, que j'effectue en en Licence 3, en Master 1 & 2, essentiellement en télédétection, Mathématique et Géophysique.

Statistiques publications :

- ResearcherID (ISI): **D-48302017**
- h-index : **14**
- Nombre publications: **23** *(rang A)*
- Nombre total citations (ISI): **717**

Responsabilités collectives :

- **Co-directeur SNOV** (TS-ANO1)
- Membre élu du Conseil de l'OPGC
- Membre élu du Conseil Pédagogique de l'OPGC
- Membre invité du conseil Scientifique de l'OPGC
- Responsable des observations TS OPGC
- Membre du Copil Labex CLERVOLC

Extended Curriculum Vitae

IDENTIFICATION

Nom : GOUHIER Prénom : Mathieu

Date de naissance : 15/07/1980 mail : M.Gouhier@opgc.fr Tel : 04 73 40 55 88

Section CNAP : Terre Interne Section de CNU : 35

Établissement d'affectation : Observatoire de Physique du Globe de Clermont-Ferrand (UCA)

Unité de recherche d'appartenance : UMR 6524 (LMV)

Statut et Grade : Physicien-Adjoint Classe Normale - échelon 6

FORMATION

- 2020 Soutenance HDR (*prévue le 27 Mars 2020*) – (UCA)
  Sources and transport of volcanic eruptive products: Insight from remote sensing techniques
- 2008 Doctorat de l'Université Blaise Pascal, Clermont-Ferrand - Volcanologie (UBP)
  Application du radar Doppler aux éruptions Stromboliennes (sup. F. Donnadieu, T. Druitt)
- 2005 École Normale Supérieure de Lyon (ENS-Lyon)
  Mention : Sciences de la Terre et des Planète

EXPERIENCE

- 2011 Recrutement Physicien-Adjoint (OPGC/LMV)
- 2009-2011 Post-Doctorat 2 – Laboratoire Magmas et Volcans (LMV)
  Télédétection spatiale des coulées de lave (directeur : P. Labazuy, JF. Lénat)
- 2008-2009 Post-Doctorat 1 – Michigan Technological University (MTU)
  Télédétection spatiale des panaches volcaniques (directeur : W.I. Rose, S. Carn)

ACTIVITÉS DE RECHERCHE (33% statutaire)

Thématique :

- Processus de transport (agrégation, sédimentation) des cendres volcaniques dans l'atmosphère
- Dégazage de SO_2 volcanique (oxydation, transport, etc.)
- Dynamique de mise en place des coulées de lave (flux, modèles de refroidissement)
- Quantification des produits éruptifs (masse, flux, paramètres sources)

Outils :

- Télédétection spatiale IR multi-spectral, UV/VIS
- Télédétection sol IR hyperspectral, radar Doppler, acoustique
- Modélisation numérique (Électromagnétique, transfert radiatif)
- Modélisation analogique (écoulement/suspension particulaires – IR)

❖ **Projets scientifiques financés :**

- Responsable du Work-Package 2 de l'ANR STRAP – 2014/2018
- Responsable du Work-Package 4 EuroVolc (infraria – H2020)
- Porteur du projet CNES-TOSCA (HOTVOLC CAL/VAL) – 2012/2014
- Porteur du projet CNES-TOSCA (Dégazage-IASI) – 2014/2016
- Porteur du projet CNES-TOSCA (Stereo-Volc) – 2018
- Porteur du Projet LabEx CLERVOLC (Hypercam) – 2015
- Porteur du projet LabEx CLERVOLC (Panache) – 2020/2022
- Porteur projet INSU (dotation SNOV-HOTVOLC) – 2012/2016
- Porteur projet INSU (dotation SNOV-HOTVOLC) – 2017/2018
- Co-porteur du Projet IRD (IR SAT/SOL) – 2015/2017

- Co-porteur du pro TelluS (Math/Volc) – 2015 & 2017
- Co-Porteur du Projet I-site (challenge 4) – 2017/2019
- Participant projet européen EPOS phase1 (WP11, Task 11.5.3) – 2016/…
- Participant ANR CEDRE (Data OSU certification) – 2020/2022

❖ **<u>Responsabilités/diffusion scientifiques</u>** : (+missions d'intérêt général)

- Responsable de l'axe 1 (panaches volcaniques) du LabEx ClerVolc piloté par le Laboratoire Magmas et Volcans (2015-2020)
- Responsable du WP2 (Convective plumes: Fluxes, dynamics and modelling) de l'ANR STRAP sur l'étude des panaches volcaniques (2014-2018)
- Responsable du WP4 (Networking atmospheric observations/connecting the volcanological community with VAACs) du projet européen (H2020-infraria) EuroVolc (2018-2019)
- Participation au groupe de travail du WP11 (Volcano Observation) pour la partie « Satellite Product » (task 11.5.3) du programme EPOS (European Plate Observing System)
- Reviewer en tant que scientifique expert du projet Européen "Thematic services for geophysical risks - WP30200" dans le cadre du service GMES/SAFER (FP7 - Space Call Research)
- Reviewer en tant que scientifique expert pour des journaux scientifiques de rang A (e.g., JVGR, JGR, MDPI, etc.)
- Co-Investigator de la mission spatiale hyperspectrale <u>HYPXIM</u> CNES/ESA (Phase 0/A), définition besoins utilisateurs, spécifications instrumentales/orbitales (2013-2014)
- Co-Investigator de la mission spatiale IR haute résolution <u>THIRSTY</u> CNES/NASA (Phase 0/A) définition des besoins utilisateurs et spécifications instrumentales/orbitales (2014-2015)
- Co-Investigator de la mission spatiale <u>TRISHNA</u> CNES/ISRO (Phase A) définition des besoins utilisateurs et spécifications instrumentales/orbitales (2016-ongoing)
- Conseil Scientifique de l'OPGC - Membre invité permanent
- Participation aux groupes de travail sur la définition des enjeux scientifiques dans le domaine spatial aux journées de prospective du CNES (La rochelle - 2014)
- Convener de la session 2c «hot flows» à la 31st l'IUGG Conference on Mathematical Geophysics, Paris. Geo-Physics, from Mathematics to Experiments (2016)
- Membre du comité d'organisation du colloque CNFGG (Clermont-Ferrand - Octobre 2012)
- 6 Invited lecturer conferences : École d'été MEMOVOLC prog. ESF, (Sicile, 2012) + (Islande, 2016); Ash dispersal forecast and civil aviation - WMO (Geneva, 2010); ValGeo: Validation of Geo-information for Crisis Management at European Commission (Italie, 2011); Comité utilisateurs du pôle ICARE/CNES - (AERIS, 2012) ; VERTIGO (Chili, COV 8).
- Responsable de l'organisation des séminaires scientifiques du Laboratoire Magmas et Volcans (2014-2016)

ACTIVITÉS D'OBSERVATION (33% statutaire)

- **Co-directeur du Service National d'Observation en Volcanologie** (SNOV TS-ANO1)
- Responsable du Service d'Observation HOTVOLC labellisé par le CNRS depuis 2012. C'est un système d'observation et d'alerte en temps-réel de l'activité éruptive par télédétection spatiale infrarouge (http://hotvolc.opgc.fr)
- Responsable des activités d'observation Terre Solide de l'Observatoire de Physique du Globe de Clermont-Ferrand (OPGC, depuis 2019)

- HOTVOLC a obtenu un MS (Maturity Scorecard) de 100% suite aux IT survey du projet européen EPOS (European Plate Observing System) mettant en avant la qualité des données (validité et disponibilité) et la description des Métadonnées.

  - Maturity Scorecard HOTVOLC-DDSS (EPOS) ⇨ 100%
  - Classement HOTVOLC-DDSS (EPOS) ⇨ 3/71
  - Pourcentage du temps d'activité sur HOTVOLC ⇨ 33%
  - Coût de fonctionnement annuel moyen ⇨ 12K€/an

❖ **<u>Points forts de système HOTVOLC</u>:** (+missions d'intérêt général)

- SO HOTVOLC est labellisé par la CSNO du CNRS-INSU (2012)
- SO HOTVOLC relève de l'exercice de fonction officielle du SMN (Météo-France, 2018)

- Le système est opérationnel et temps-réel (récurrence données / 15 minutes)
- Délivrables validés et à forte valeur ajoutée directement utilisable pour les observatoires volcanologiques (ex « Volume Flow rate » = flux lavique en m^3/s) en temps-réel. HOTVOLC est le seul système dans le monde à fournir cette type de données.
- La présence d'une Interface utilisateur (UI) full Web-GIS conviviale et intuitive
- Le téléchargement de <u>toutes</u> les données est libre et gratuit sans restriction
- Les données HOTVOLC sont utilisées par l'OVPF/IPGP en cas d'éruption à la Fournaise dans les rapports à l'attention de la Préfecture et de la Protection Civile (Saint-Denis, La Réunion). http://www.ipgp.fr/fr/dernieres-actualites/344
- Suivi des panaches de cendres des volcans islandais (cf. communiqués INSU). Avec mise en place d'astreintes OPGC, mise en ligne (prévisions de trajectoires, mesures satellitaires, informations diverses), +18 communiqués avec la cellule de crise ministérielle du CMVOA.
- 4 communiqués INSU concernant le suivi des crises sur les autres cibles prioritaires : Etna (18/01/2011), Eyjafjallajökull (19/04/2010), Grismvötn (23/05/2011), Bardarbunga (01/09/2014), www.insu.cnrs.fr/terre-solide/catastrophes-et-risques/eruptions-volcaniques/
- Convention en cours entre OPGC/CNRS/Météo-France sur l'utilisation des données opérationnelles HOTVOLC pour l'aide à la gestion de crise liée au trafic aérien.

ACTIVITÉS D'ENSEIGNEMENT (33% statutaire)

❖ **<u>Service statutaire = 66 heures eq./TD</u> :**

Géophysique fondamentale	*(Resp. Module Licence 3 STPE) :*	*2012-ongoing*
Statistique & Géosciences	*(Resp. Module Master 1 STPE) :*	*2017- ongoing*
Imagerie et télédétection	*(Resp. Module Master 1 STPE) :*	*2012-2017*
Outils mathématiques	*(Licence 2 STPE)*	*2017-2018*
Méthodes numériques	(*Master 1 STPE*)	2011-2014
Volcanologie Physique	(*Master 2R MV*)	2011-2017
Géophysique générale	(CAPES/Agreg)	2011-2012
Phy/Chimie/environnement	(*Master 2R Physique)*	2015-2017

❖ **<u>Autres activités de diffusion des connaissances</u>** : (+missions d'intérêt général)

- Membre élu du conseil pédagogique de l'École de l'Observatoire (EOPGC 2018)
- Invited lecturer de l'école d'été MEMOVOLC (prog. ESF), Sicile (2012) + Islande (2016)
- Responsable et animateur des formations de la Maison Pour la Science en Auvergne (MPSA) dédiées aux enseignants du primaire et du secondaire en Sciences de la Terre (2012-2015)

- Coordination et intervention dans le film de l'agence "vanglabeke films" sur la formation universitaire en Volcanologie (diffusion dans le cadre de l'UNICEF, CIO)
- Intervention-Conférence pour l'Université Ouverte Clermont Auvergne (cycle : les grands volcans Européens) en Mai 2017.
- Représentant LMV-UCA aux journées de valorisation « concours défi-volcans » à Vulcania.
- Expert et création de sujet aux Olympiades de Géosciences académiques et nationales (2012)
- Tuteur stage élèves de 3ème (semaine complète) et intervention dans les collèges (2017-2018)
- Membre du jury permanent de Master 2 Recherche (2012-2013)

❖ <u>Encadrement scientifique</u>

- 1 Thèse (Y. Guéhenneux): direction 0% / encadrement 50% (2010/2013)
  Observation thermique de l'activité volcanique par traitement des données à très haute résolution temporelle du satellite météorologique Meteosat Second Generation
- 1 Thèse (C. Segonne): direction 33% / encadrement 25% (2018/2020)
  Traitement des données IR hyperspectral pour la quantification du SO2 volcanique à Stromboli/Etna via les modèles LARA et MODTRAN.
- 1 Postdoc (CNES) (J-F. Smekens): direction 100% / encadrement 100% (2015/2017)
  Étude du dégazage volcanique par couplage infrarouge hyperspectral sol-satellite (Hypercam-Telops/IASI-METOP)
- 1 Postdoc (IRD) (J. Eychenne): direction 50% / encadrement 80% (2016/2018)
  Validation et amélioration des méthodes satellites infrarouges et caractérisation des panaches volcaniques par l'étude couplée in-situ et en milieu contrôlé de cendres volcaniques
- 1 Postdoc (I-Site) (A. Tadini): direction 25% / encadrement 25% (2018/2020)
  Risques naturels catastrophiques et vulnérabilité socio-économique: Prédiction de la distribution des dépôts de retombées volcaniques par approche probabiliste.
- 1 Postdoc (Labex) (A. Tadini): direction 80% / encadrement 80% (2020/2022)
  Étude de la sédimentation des cendres fines dans l'atmosphère : approche couplée sol, satellite et modélisation numérique.

❖ <u>Encadrement Technique</u>

- 1 CDD-IE (CNES) (Y. Guéhenneux): direction 100% / encadrement 100% (2014/2015)
  Validation du service d'observation HOTVOLC pour la surveillance des volcans actifs par imagerie satellitale infrarouge (MSG-SEVIRI).
- 1 CDD-IE (CNES) (j. Decriem): direction 100%/encadrement 100% (2012/2013)
  Développement d'une interface Utilisateur Web-GIS pour le service d'Observation HOTVOLC
- 1 Stage-ISIMA (G. Raux): direction 100% /encadrement 100% (2016)
  Développement d'une interface Utilisateur Web-GIS pour le service d'Observation HOTVOLC
- 1 Stage-ISIMA (R. Huerta): direction 100% /encadrement 100% (2017)
  Développement d'une application mobile Web-GIS pour le service d'Observation HOTVOLC

❖ <u>Encadrement Licence/Master</u>

Master-1 Recherche à 100%	(M1: P. Condamine)	2011
Master-1 Recherche à 50%	(M1: E. Wavelet)	2017
Master-2 Recherche à 100%	(M2: N. Stewart)	2014
Master-2 Recherche à 100%	(M2: C. Biensan)	2020

- Co-encadrement d'un Travail d'Initiative Personnelle Encadré (TIPE) de trois étudiants de classe préparatoire BCPST (thème volcanologie) – 2011

List of Publications

For the sake of clarity, **we provide in the following part of the HDR manuscript the main publications only**, and highlighted in red font in the list of publications below.

LISTE DES PUBLICATIONS (Rang A)

1. Tadini, A., Roche, O., Samaniego, P., Guillin, A., Azzaoui, N., **Gouhier**, M., ... & Hidalgo, S. (2020). Quantifying the uncertainty of a coupled plume and tephra dispersal model: PLUME-MOM/HYSPLIT simulations applied to Andean volcanoes. *Journal of Geophysical Research: Solid Earth*, *125*(2), e2019JB018390.
2. Thivet, S., Gurioli, L., Di Muro, A., Derrien, A., Ferrazzini, V., **Gouhier**, M., ... & Arellano, S. Evidences of plug pressurization enhancing magma fragmentation during the September 2016 basaltic eruption at Piton de la Fournaise (La Réunion Island, France). *Geochemistry, Geophysics, Geosystems*, e2019GC008611.
3. **Gouhier**, M., Eychenne, J., Azzaoui, N., Guillin, A., Deslandes, M., Poret, M., ... & Husson, P. (2019). Low efficiency of large volcanic eruptions in transporting very fine ash into the atmosphere. *Scientific reports*, *9*(1), 1-12.
4. **Gouhier**, M., & Paris, R. (2019). SO2 and tephra emissions during the December 22, 2018 Anak Krakatau eruption. *Volcanica*, *2*(2), 91-103.
5. Poret, M., Finizola, A., Ricci, T., Ricciardi, G. P., Linde, N., Mauri, G., ... & **Gouhier**, M. (2019). The buried caldera boundary of the Vesuvius 1631 eruption revealed by present-day soil CO2 concentration. *Journal of Volcanology and Geothermal Research*, *375*, 43-56.
6. Sahyoun, M., Freney, E., Brito, J., Duplissy, J., **Gouhier**, M., Colomb, A., ... & Petäjä, T. (2019). Evidence of New Particle Formation Within Etna and Stromboli Volcanic Plumes and Its Parameterization From Airborne In Situ Measurements. *Journal of Geophysical Research: Atmospheres*, *124*(10), 5650-5668.
7. Poret, M., Costa, A., Andronico, D., Scollo, S., **Gouhier**, M., & Cristaldi, A. (2018). Modeling Eruption Source Parameters by Integrating Field, Ground-Based, and Satellite-Based Measurements: The Case of the 23 February 2013 Etna Paroxysm. *Journal of Geophysical Research: Solid Earth*, *123*(7), 5427-5450.
8. Smekens, J. F., & **Gouhier**, M. (2018), Observation of SO2 degassing at Stromboli volcano using a hyperspectral thermal infrared imager. *Journal of Volcanology and Geothermal Research*, doi.org/10.1016/j.jvolgeores.2018.02.018.
9. **Gouhier**, M., Y. Guéhenneux, P. Labazuy, P. Cacault, J. Decriem, and S. Rivet (2016), HOTVOLC: A web-based monitoring system for volcanic hot spots, in Detecting, Modelling and Responding to Effusive Eruptions, *Geol. Soc. London* Spec. Publ., vol. 426, edited by A. J. L. Harris et al., *doi: 10.1144/SP426.31*.
10. Gauthier, P.-J., Sigmarsson, O., **Gouhier**, M., Haddadi, B., and Moune, S. (2016), Elevated gas flux and trace metal degassing from the 2014–2015 fissure eruption at the Bárðarbunga volcanic system, Iceland, *J. Geophys. Res. Solid Earth*, 120, *doi:10.1002/2015JB012111.*
11. Guéhenneux, Y., **Gouhier**, M., & Labazuy, P. (2015), Improved space borne detection of volcanic ash for real-time monitoring using 3-Band method. *Journal of Volcanology and Geothermal Research*, 293, 25-45, *doi: 10.1016/j.jvolgeores.2015.01.005*
12. **Gouhier**, M., Harris, A., Calvari, S., Labazuy, P., Guéhenneux, Y., Donnadieu, F., Valade, S (2012), Lava discharge during Etna's 11-13 January 2011 fire fountain event tracked using MSG-SEVIRI, *Bull. Volcanol* 74: 787-793. *doi:10.1007/s00445-011-0572-y*
13. Chazette, P., Bocquet, M., Royer, P., Winiarek, V., Raut, J-C., Labazuy, P., **Gouhier**, M., Lardier, M., Cariou, J-P (2012), Eyjafjallajökull ash concentrations derived from both Lidar and modelling, *J. Geophys. Res* 117: D00U14. *doi:10.1029/2011JD015755*

14. Labazuy P., **Gouhier** M., Harris A., Guéhenneux Y., Hervo M., Bergès J-C., Cacault P., Rivet S., (2012) Near real-time monitoring of the April-May 2010 Eyjafjallajökull ash cloud: an example of a web-based, satellite data-driven, reporting system. *Int. J. of Environment and Pollution*, Vol.48, No.1/2/3/4, pp.262 - 272, *doi: 10.1504/IJEP.2012.049673*
15. Eychenne J., J-L. Le Pennec, L. Troncoso, **Gouhier** M., and J-M. Nedelec (2012), Causes and consequences of bimodal grain size distribution of tephra fall deposited in August 2006 eruption at Tungurahua volcano (Ecuador) *Bull. Volcanol* 74: 187-205. *doi:10.1007/s00445-011-0517-5*
16. Hervo, M., B. Quennehen, N. I. Kristiansen, J. Boulon, A. Stohl, P. Fréville, J. M. Pichon, D. Picard, P. Labazuy, M. **Gouhier**, A. Colomb, A. Schwarzenboeck, and K. Sellegri (2012), Physical and optical properties of 2010 Eyjafjallajökull volcanic eruption aerosol: ground-based, LIDAR and airborne measurements in France, *Atmos. Chem. Phys* 12 : 1721-1736. *doi:10.5194/acp-12-1721-2012*
17. Ganci, G., A. J. L. Harris, C. Del Negro, Y. Guehenneux, A. Cappello, P. Labazuy, S. Calvari, and M. **Gouhier** (2012), A year of lava fountaining at Etna: Volumes from SEVIRI, *Geophys. Res. Lett* 39 : L06305. *doi:10.1029/2012GL051026*
18. Bonadonna, C., Genco, R., **Gouhier**, M., Pistolesi, M., Alfano, F., Cioni, R., Hoskuldsson, A., Ripepe, M (2011), Tephra sedimentation during the 2010 Eyjafjallajökull eruption (Iceland) from deposit, radar and satellite observations, J. Geophys. Res 116: B12202. *doi:10.1029/2011JB008462*
19. **Gouhier**, M., and F. Donnadieu (2010), Physical properties of Strombolian explosions from Doppler radar measurements: Constraints on geometric features, Geophys. J. Int 183: 1376-1391. *doi:10.1111/j.1365-246X.2010.04829.x*
20. **Gouhier**, M. and F. Donnadieu (2011), Systematic retrieval of kinetic and loading parameters of Strombolian explosions using L-Band Doppler radar, Bull. Volcanol 73: 1139-1145. *doi:10.1007/s00445-011-0500-1*
21. Calvari. S., Salerno. G., Spampinato. L., **Gouhier**. M., Pecora. E., La Spina. A., Biale. E., Harris, A.J.L., Labazuy P., and Boschi E (2011), An unloading foam model to constrain Etna's 11-13 January 2011 lava fountaining episode, J. Geophys. Res 116: B11207. *doi:10.1029/2011JB008407*
22. **Gouhier**, M. and D. Coppola (2011), Satellite-based evidence for a large hydrothermal system at Piton de la Fournaise volcano (Reunion Island), Geophys. Res. Lett 38: L02302. *doi:10.1029/2010GL046183*
23. **Gouhier**, M., & Donnadieu, F. (2008). Mass estimations of ejecta from Strombolian explosions by inversion of Doppler radar measurements. *Journal of Geophysical Research: Solid Earth*, *113*(B10).

+ chapitres d'ouvrages & proceedings

- Azzaoui N., Guillin A., **Gouhier M.**, *Eychenne J., Valade S. (2014). Modélisation statistique pour la surveillance des éruptions volcaniques. *Revue d'Auvergne* 613, 153-170.
- **Gouhier M.**, *Guéhenneux Y., Cacault P., Labazuy P. (2017). Le Service d'Observation HOTVOLC dans "Des volcans aux nuages - l'Observatoire de Physique du Globe de Clermont-Ferrand". *Revue d'Auvergne* ISSN 035 1008.
- Miranda, V., Pina, P., Heleno, S., Gouhier, M., & Dumont, S. (2019, July). Reconstruction of the 2014-2015 FOGO Volcano (Cape Verde) Eruption Through Thermal Remotely Sensed Imagery. In *IGARSS 2019-2019 IEEE International Geoscience and Remote Sensing Symposium* (pp. 9306-9309). IEEE.
- Lagouarde, J. P., Bhattacharya, B. K., Crebassol, P., Gamet, P., Babu, S. S., Boulet, G., ... & Dedieu, G. (2018, July). The Indian-French Trishna Mission: Earth Observation in the Thermal Infrared with High Spatio-Temporal Resolution. In *IGARSS 2018-2018 IEEE International Geoscience and Remote Sensing Symposium* (pp. 4078-4081). IEEE.

SCIENTIFIC REPORTS

Corrected: Author Correction

OPEN

Low efficiency of large volcanic eruptions in transporting very fine ash into the atmosphere

Received: 13 July 2018
Accepted: 20 December 2018
Published online: 05 February 2019

Mathieu Gouhier[1], Julia Eychenne[1], Nourddine Azzaoui[2], Arnaud Guillin[2], Mathieu Deslandes[3], Matthieu Poret[4], Antonio Costa[4] & Philippe Husson[3]

Volcanic ash clouds are common, often unpredictable, phenomena generated during explosive eruptions. Mainly composed of very fine ash particles, they can be transported in the atmosphere at great distances from the source, having detrimental socio-economic impacts. However, proximal settling processes controlling the proportion (ε) of the very fine ash fraction distally transported in the atmosphere are still poorly understood. Yet, for the past two decades, some operational meteorological agencies have used a default value of ε = 5% as input for forecast models of atmospheric ash cloud concentration. Here we show from combined satellite and field data of sustained eruptions that ε actually varies by two orders of magnitude with respect to the mass eruption rate. Unexpectedly, we demonstrate that the most intense eruptions are in fact the least efficient (with ε = 0.1%) in transporting very fine ash through the atmosphere. This implies that the amount of very fine ash distally transported in the atmosphere is up to 50 times lower than previously anticipated. We explain this finding by the efficiency of collective particle settling in ash-rich clouds which enhance early and en masse fallout of very fine ash. This suggests that proximal sedimentation during powerful eruptions is more controlled by the concentration of ash than by the grain size. This has major consequences for decision-makers in charge of air traffic safety regulation, as well as for the understanding of proximal settling processes. Finally, we propose a new statistical model for predicting the source mass eruption rate with an unprecedentedly low level of uncertainty.

Volcanic ash clouds generated by explosive eruptions are distally transported in the atmosphere up to distances ranging from a few hundreds to thousands of kilometres from the vent. They are mainly composed of the finest ash fraction which survives proximal sedimentation, and referred to as very fine ash (<32 µm) following the physical volcanology-derived terminology of explosive eruptions[1]. However, in some cases coarser particles can reach distal location as recently demonstrated during moderate Icelandic eruptions[2]. Very fine ash can have damaging effects on aircraft, hence having detrimental impact on air traffic safety as demonstrated by air traffic disruption during Eyjafjallajökull[3] and Cordón del Caulle[4] eruptions. Distal airborne very fine ash represent only a fraction of the total amount of solid particles (referred to as tephra) injected into the volcanic plume column above the crater. Here we examine this partitioning (ε; given in percentage) as the ratio between the very fine ash flux transported in distal clouds (Q_a) estimated from satellite-based infrared measurements, and the total flux of tephra emitted at the source (Q_s) inferred from ground studies of tephra deposits. The latter is also referred to as the Mass Eruption Rate (MER). The ratio ε quantifies the volcanic ash removal efficiency in proximal areas, which is critical for constraining ash sedimentation processes during the early stages of cloud dispersal, as well as for predicting the ash clouds properties as they are advected around the globe.

We compiled a database of 22 eruptions of various magnitudes and intensities carefully selected from remarkably well documented case studies in the published records (Table 1). They are characterized by distinct eruption styles describing the dynamics and phenomenology of the explosive activity. Eruption styles can be defined from various classifications using different parameters[5,6]. In our case, we adopted the most recent one[6] for the following reasons: (i) it uses the MER (equivalent to Q_s) and the volcanic ash plume height (H) as input parameters; (ii) it allows individual eruption phases to be easily requalified; and (iii) permits a real-time first order classification

[1]Université Clermont Auvergne, CNRS, IRD, OPGC, Laboratoire Magmas et Volcans, F-63000, Clermont-Ferrand, France. [2]Laboratoire de Mathématiques Blaise Pascal, UMR 6620 CNRS & UCA, Aubière, France. [3]VAAC Toulouse, Météo France, Toulouse, France. [4]Istituto Nazionale di Geofisica e Vulcanologia, Sezione di Bologna, Bologna, Italy. Correspondence and requests for materials should be addressed to M.G. (email: M.Gouhier@opgc.fr)

Volcano	Explosive Phase selected	Duration (s)	Fallout deposit mass (Kg)	±Error (Kg)	Cloud mass (Kg)	±Error (Kg)	Plume Height (km)	Q_s (kg/s)	Q_a (kg/s)	ε (%)	±Error	Style
Pinatubo	Climactic phase on 15–16/06/1991	3.24E+04[1]	5.7E+12[2]	1.4E+12	5.0E+10[3]	2.5E+10	40[1]	1.8E+08	1.5E+06	0.9	0.6	Plinian[1,2]
Kelut	Full eruption 13/02/2014	1.08E+04[4]	6.5E+11[5]	1.6E+11	7.4E+08[4]	3.7E+08	20[4]	6.0E+07	6.9E+04	0.1	0.1	Plinian[5]
El Chichon	Phases B and C on 04/04/1982	3.96E+04[6]	8.7E+11[7]	2.2E+11	6.5E+09[8]	3.3E+09	30[8]	2.2E+07	1.6E+05	0.7	0.5	Plinian[6]
Hudson	Full eruption 12–15/08/1991	2.27E+05[9]	3.9E+12[10]	9.8E+11	2.9E+09[11]	1.5E+09	18[9,11]	1.7E+07	1.3E+04	0.1	0.0	Plinian[10]
Sarychev Peak	Subplinian events on 14–15/06/2009	5.94E+04[12]	4.0E+11[12]	1.0E+11	5.4E+08[12]	2.7E+08	20[12]	6.7E+06	9.1E+03	0.1	0.1	Subplinian*
Cordon Caulle	Climactic phase on 4–5/06/2011	8.64E+04[13]	4.5E+11[13]	1.1E+11	7.0E+08[14]	3.5E+08	12.2[14]	5.2E+06	8.1E+03	0.2	0.1	Subplinian[13]
Grimsvotn	Subplinian phase on 22/05/2011	1.91E+05[15]	7.0E+11[15,16]	1.8E+11	4.9E+08[17]	2.5E+08	20[17,18]	3.7E+06	2.6E+03	0.1	0.0	Subplinian[16]
Mt. Spurr	Full eruption 16/09/1992	1.30E+04[19]	3.9E+10[20]	9.8E+09	6.1E+08[21]	3.1E+08	13.9[21]	3.0E+06	4.7E+04	1.6	1.0	Subplinian[20]
Mt. Spurr	Full eruption 18/08/1992	1.25E+04[19]	3.6E+10[20]	9.0E+09	4.2E+08[21]	2.1E+08	13.7[21]	2.9E+06	3.4E+04	1.2	0.8	Subplinian[20]
Redoubt	Explosive events 1 to 5 on 22–23/03/2009	5.22E+03[22]	1.4E+10[22]	3.5E+09	1.7E+09[23]	8.5E+08	15[22]	2.7E+06	3.3E+05	12.1	8.0	Vulcanian[22]
Mt. Spurr	Full eruption 27/06/1992	1.46E+04[19]	3.1E+10[20]	7.8E+09	4.4E+08[21]	2.2E+08	14.5[21]	2.1E+06	3.0E+04	1.4	0.9	Subplinian[20]
Lascar	Full eruption 04/1993	1.73E+05[24]	3.5E+11[21,25]	8.6E+10	4.8E+09[21]	2.4E+09	21[24]	2.0E+06	2.8E+04	1.4	0.9	Subplinian*
Anatahan	Explosive phases on 10–11/05/2003	3.24E+04[26]	3.8E+10[27]	9.6E+09	1.3E+09[26]	6.5E+08	12[26]	1.2E+06	4.0E+04	3.4	2.2	Small/ Moderate[27]
Chaiten	Full eruption: 2–8/05/2008	6.05E+05[28]	1.7E+11[28]	4.3E+10	8.0E+08	4.0E+08	19[28]	2.8E+05	1.3E+03	0.5	0.3	Subplinian[28]
Hekla	Phase I + 8 hrs phase II on 26/02/2000	4.21E+04[29]	1.0E+10[30]	2.5E+09	1.0E+08[29]	5.0E+07	11[29]	2.4E+05	2.4E+03	1.0	0.7	Small/ Moderate*
Soufrière Hills	Full eruption: 26/09/1997	3.60E+03[31]	5.5E+08[32]	1.4E+08	5.4E+07[33]	2.7E+07	11.3[33]	1.5E+05	1.5E+04	9.8	6.4	Vulcanian[32]
Ruapehu	Full eruption: 17/06/1996	3.60E+04[34]	4.2E+09[35]	1.1E+09	2.9E+08[36]	1.5E+08	8.5[36]	1.2E+05	8.1E+03	6.9	4.6	Small/ Moderate*
Eyjafjallajökull	Phase I/III on 14–19/04 & 05–18/05/2010	1.90E+06[37]	2.0E+11[38]	4.9E+10	8.3E+09[39]	4.2E+09	9[38]	1.0E+05	4.4E+03	4.2	2.8	Small/ Moderate
Etna	Full eruption: 28/10/2002	2.16E+04[40]	1.1E+09[40]	2.6E+08	1.1E+07[41]	5.7E+06	6[42]	4.9E+04	5.3E+02	1.1	0.7	Small/ Moderate[40]
Popocatepetl	Climactic events on 10/03/1996	2.16E+04[43]	5.3E+08[44]	1.3E+08	1.5E+07[43]	7.5E+06	9[44]	2.4E+04	6.9E+02	2.8	1.9	Small/ Moderate*
Etna	Full eruption: 27/10/2002	3.60E+04[40]	8.7E+08[40]	2.2E+08	2.4E+07[42]	1.2E+07	6[42]	2.4E+04	6.6E+02	2.7	1.8	Small/ Moderate[40]
Etna	Full eruption: 24/11/2006	2.16E+04[45]	1.0E+08[46]	2.5E+07	3.6E+06[47]	1.8E+06	1.5[45]	4.6E+03	1.7E+02	3.6	2.4	Small/ Moderate[46]

Table 1. Eruptive parameters for the 22 eruptions of our dataset. The eruptions were selected in the dataset providing that quality published data existed in the literature on the mass of the fallout deposit (derived from field analyses) and the mass of the very fine ash cloud (derived from satellite-based measurements). The plume height above the vent comes from different types of observational data (remote-sensing, visual estimations, etc.). Q_s and Q_a are calculated as the fallout deposit mass and very fine ash cloud mass, respectively, divided by the duration of the eruption phase. ε is calculated as the ratio of Q_a over Q_s. Eruption styles have been determined using Q_s and the plume height[6] and are in agreement with related published records. *Eruption styles for explosive phases that have not been published and which may differ from existing classifications made for full eruption or a different phase.

of eruptive events, which is useful for operational applications. Therefore, we distinguish sustained eruptions (9 Small/Moderate, 7 Subplinian and 4 Plinian styles) defined by quasi-steady discharge conditions (i.e., with a duration of tephra emission much longer than the time necessary to reach the neutral buoyancy level) from transient eruptions corresponding to unsteady impulsive explosions (i.e., 2 Vulcanian style).

The database comprises satellite-based infrared measurements of Q_a inferred from the extinction properties of ash using the split-window method[7,8], except for the May, 2011 Grimsvötn and October 27, 2002 Etna eruptions, whose measurements were carried out using hyperspectral sounders. This technique provides vertical column densities as a mass per unit area, and allows total mass of very fine ash to be retrieved from integration of ash-bearing pixels over the whole cloud surface. Then, the average value of Q_a can be calculated by simply dividing the total mass by the duration of ash emission. Most of the data come from Low-Earth Orbiting (LEO) platforms, hence allowing image acquisition ∼10 hours on average after the start of the eruption. The large Instantaneous Field Of View (IFOV) of these sensors usually allows the observation of the whole cloud from a single or a few images. The extent of the cloud determines the ash emission duration and the timing of the image acquisition allows us to identify the explosive phase within the eruption chronology. The inversion of thermal infrared measurements is particularly relevant for the characterization of the very fine ash content of volcanic clouds because it allows the retrieval of particles in the size range 1–32 µm (at 2σ for a lognormal distribution[2]). However, some known uncertainties remain from (i) the split-window technique leading to false detection and missed ash-bearing pixels[9] as well as from (ii) the limits of the validity domain within the Mie scattering theory[2,8]. Overall uncertainty associated with satellite-based measurements was estimated to be in the range ±40–60%[2].

The average value of Q_s was calculated from the published mass of tephra deposited on the ground, divided by the duration of the explosive phase. Importantly, Q_a and Q_s refer to the same period of explosive activity and can thus be reliably compared. The temporal concordance required between these 2 parameters explains the relatively low number of eruptions finally selected. The deposit masses selected in this study (Table 1) were calculated by integrating the mass decay rate of the fallout deposit or integrating the thinning rate of the fallout deposit[10,11]. These methods are sensitive to the quality and density of field data, to the mathematical function chosen (e.g., exponential, power-law, Weibull) to represent their spatial variations and to the distal extrapolation limit. Indeed, individual measurements of tephra thickness or mass are extrapolated at greater distances than the maximum sampling, allowing the finest ash fraction to be accounted for, and the total mass of tephra estimated. Thus, Q_s represents the average MER of the total grain size distribution at the source vent and is given with an uncertainty of ±10–40%[12,13]. Note that uncertainties on each individual eruption for both satellite and ground deposits retrievals have not been systematically published or inferred, but we specifically selected eruptions for which the measurements errors should be low (e.g. no clouds in the atmosphere, no erosion of the deposit, sampling performed hours to days following the eruptions, etc.). The related error on ε has been calculated from the average bulk uncertainties of Q_a and Q_s and reported for each eruption in Table 1.

Results

Source-to-atmosphere very fine ash partitioning. We show that ε of sustained eruptions spans a wide range of values, from 0.1% (e.g., Plinian Kelut 2014 eruption) to 6.9% (Small/Moderate Ruapehu 1996 eruption; Table 1). Fine ash removal from Plinian eruptions is thus about two orders of magnitude more efficient than that from Small/Moderate ones. Remarkably, the variation of the partitioning coefficient is not arbitrary. From Fig. 1, ε decreases with increasing MER, with respect to eruption styles. The four Plinian eruptions selected have large MER ($1.7 \times 10^7 < Q_s < 1.8 \times 10^8$ kg/s). They all produced copious amount of volcanic ash, as for the 1980 Mount St Helens, and the 1982 El Chichón eruptions, for which the mass fraction of ash smaller than 63 µm represents ∼50% of the total mass of tephra emitted[14,15]. Such high fine ash contents are related to efficient magma fragmentation processes, occurrence of phreato-magmatic episodes, and contribution of ash elutriated from pyroclastic density currents (PDC) forming co-PDC plumes[16]. However, they all exhibit a very small proportion of distal very fine ash, as shown by the weak partitioning coefficient range ($0.1 < \varepsilon < 0.9\%$), and fall in a well delimited area in Fig. 1. To explain this observation, we suggest that early enhanced fallout in proximal regions makes the actual proportion of very fine ash transported in distal clouds much lower than expected. This highlights the critical role played by collective settling mechanisms, occurring preferentially in ash-rich plumes, which enhance the sedimentation rate of tephra regardless of grain size. Such mechanisms include aggregation[17,18], gravitational instabilities[19], diffusive convection[20], particle-particle interactions[21], and wake-capture effects[22]. These are inferred to be key processes controlling the early depletion of ash-rich plumes, which cannot be explained by individual particle settling. Aggregation efficiency, in particular, has been identified[23,24] to be proportional to a power greater than two of ash concentration. This means that the higher the fine ash concentration the more important the aggregation efficiency, which is in agreement with the observations made in our study.

Collective settling mechanisms, allow en masse sedimentation of particles of different sizes, which explains the significant amount of fine ash as well as the poor grain sorting sometimes observed in proximal tephra fallout deposits of large Plinian events. The fallout deposit from the 18 May 1980 eruption of Mount St. Helens (MSH80) for instance, shows both a poor grain sorting in proximal locations[25,26] and an increase of mass and thickness at distances >300 km[27] demonstrating rapid removal of fine ash from the plume. Different enhanced sedimentation processes have been invoked and successfully tested to explain these observations, including aggregation[28], and hydrometeor formation[14]. Subplinian eruptions, although less powerful than Plinian ones, remain very explosive and capable of efficient fragmentation, also leading to the formation of ash-rich plumes. For example, the August and September 1992 Mt. Spurr eruptions produced fallout deposits with fine ash contents reaching 30% and 40% of the total mass of tephra, respectively[29]. The origin of this fine ash is discussed, and could be related to heterogeneities in the source magma or secondary particle fragmentation in the volcanic conduit or eruption column[30]. They have MER in the range $0.28–6.7 \times 10^6$ kg/s and still exhibit low partitioning coefficient, although spanning a wider range of values ($0.1 < \varepsilon < 1.6\%$), hence implying collective settling mechanisms to be at work. The Mt Spurr fallout deposits also show an increase of mass and thickness at distances >150 km from the source, which can be explained by collective settling mechanisms including aggregation, topographic effects and gravitational instabilities[30]. Small/Moderate eruptions are drastically different from Plinian and Subplinian. The eruption explosivity and the MER are much weaker. The plume column height is generally lower and the fine ash fraction of the size distribution at the source vent is much smaller. Consequently, Small/Moderate eruptions do not produce ash-rich plumes, and enhanced sedimentation in proximal regions is limited, resulting in larger partitioning coefficients ($0.5 < \varepsilon < 6.9\%$). The wide range of ε values for Small/Moderate eruptions reflects the heterogeneity of grain size and concentration of the associated plumes. But, this can also be explained by the natural complexity of some

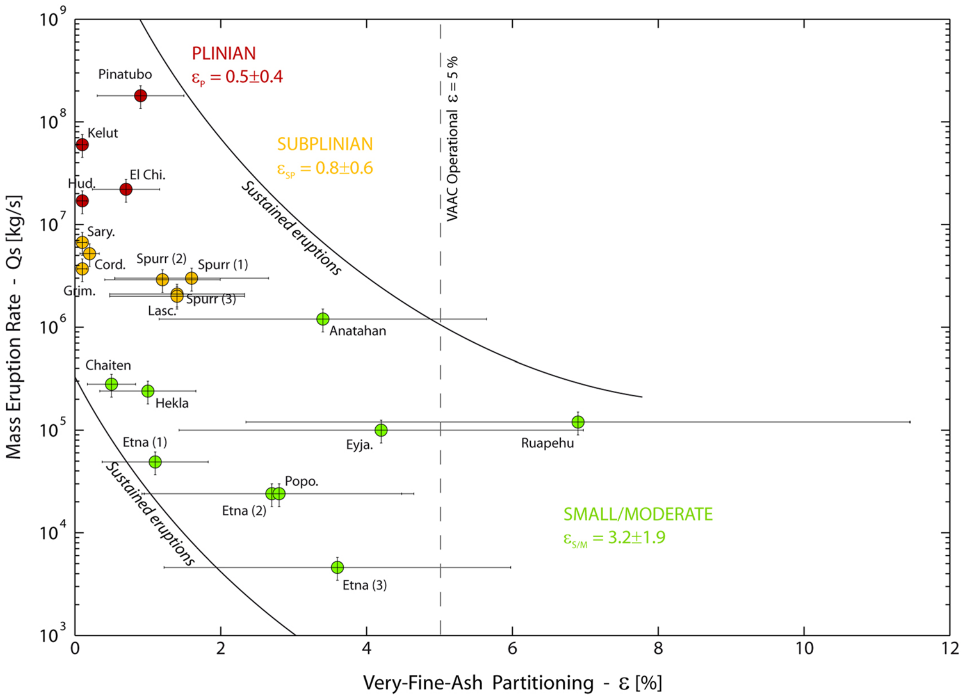

Figure 1. Style-derived volcanic ash partitioning of sustained eruptions. Mass erupting rate (Q_s in kg/s) as a function of the partitioning coefficient ε (Q_a/Q_s in %) for the 20 sustained eruptions of our dataset (see Table 1 for details about the eruptions). ε is the ratio between the very fine ash flux transported in distal clouds (Q_a) and the flux of tephra in the plume (Q_s) also referred to as MER. It quantifies the volcanic very fine ash removal efficiency. The sustained eruptions cluster following their eruption style (Plinian, Subplinian, Small/Moderate). This plot shows that ε of sustained eruptions scales with Q_s, and spans about two orders of magnitude. The main trend shows that ε increases with decreasing MER. This indicates that very fine ash removal from ash-rich plumes (Plinian and Subplinian style) is more efficient than from plumes containing coarser tephra (Small/Moderate style). Error bars are plotted from average bulk uncertainties given for fallout deposit and cloud masses (see Table 1 for detailed error values). The vertical dashed line represents the current VAAC operational partitioning coefficient used by to forecast the atmospheric path of very fine ash clouds. The eruption-dependant partitioning coefficients for each eruption style (ε_P, ε_{SP}, $\varepsilon_{S/M}$) have also been reported.

long-lasting eruptions. This is the case, in particular, for the Eyjafjallajökull 2010 eruption displaying multiple and discontinuous phases of explosive activity with varying intensity.

The inverse relationship between ε and the MER shows that for very powerful eruptions, the proximal sedimentation is mainly controlled by the concentration of fine ash. This suggests that above a given threshold of the fine ash volume fraction, collective mechanisms dominate over individual particle settling, and conversely. Assessment of this threshold is very difficult as proximal measurements (i.e., in the first tens of kilometres from the source vent) of airborne volcanic ash concentration are scarce. Indeed, satellite-based retrievals are usually impossible due to the opacity of the cloud. But, radar instruments operating at larger wavelengths are able to provide volcanic ash concentration within proximal cloud. The comparison of ash concentration at various distances, hence using various techniques, should bring precious information on early depletion processes and about sedimentation rate evolution. As an example, proximal measurements carried out in the first two hours after the MSH80 Plinian eruption by a 23-cm wavelength radar[31] give an ash cloud concentration of $\sim$8.5 g/m^3. In this region of the cloud we expect sedimentation rate to be high with a significant contribution of collective particle settling mechanisms. As a comparison, distal measurements carried out by satellite-based infrared sensors on the Kelut 2014 Plinian eruption[32] give an ash cloud concentration 3 orders of magnitude lower (maximum value $\sim$9 mg/m^3). In this region of the cloud, the sedimentation rate is very low and the individual particle settling is most likely to prevail.

Ash cloud hazards and operational response. The partitioning parameter ε is crucial in operational volcanic risk mitigation, as it is required as input for ash-cloud-dispersal models used by several VAACs responsible for global air traffic safety. Given that satellite images are not systematically available, the VAACs need rapid parameterization schemes to predict Q_a, and to provide frequent and reliable up-to-date forecast maps of atmospheric ash concentration during volcanic crises[33]. With this aim, VAACs (such as London and Toulouse) have typically used a poorly constrained default ε value of 5%[34] to forecast the concentration of very fine ash composing distal ash clouds following $Q_a = \varepsilon \times Q_s$. However, as demonstrated in Fig. 1, the fraction of very fine ash that survives proximal settling varies by $\sim$2 orders of magnitudes ($0.1\% > \varepsilon > 6.9\%$) with respect to the MER.

Therefore, a constant partitioning value cannot be used, even as first order estimate for operational purposes. Note that Q_s is needed, and usually obtained operationally from top plume height estimates following a power-law relationship[35] between the two parameters. The reliability of Q_s estimate from this method is discussed later in this work and compared with our satellite-based prediction model of Q_s (see next section). Here we propose a new operational eruption-style-dependant parameterization of ε using the mean values for Plinian ($\varepsilon_P = 0.5\%$), Subplinian ($\varepsilon_{SP} = 0.8\%$), and Small/Moderate ($\varepsilon_{S/M} = 3.2\%$) eruptions (Fig. 1). This parameterization is easily implementable in ash-cloud-dispersal models, allowing operational use by the VAACs. Also, the choice of the correct partitioning parameter to be used during the course of an eruption is not difficult. The phenomenology as well as the real-time assessment of Q_s will be particularly useful to discriminate the eruption style. In some cases, the eruptive history at each volcanic target can also be helpful. Our assessed values of ε significantly depart from the default 5% value used by the VAACs (Fig. 1), and the resulting differences will propagate into the modelled ash cloud concentrations.

Therefore, in order to test the sensitivity of concentration variations to partitioning values, distal ash cloud dispersion maps were simulated for 4 eruption scenarios (Supplementary Information Table S1) using MOCAGE-accident, the ash-cloud-dispersal model of VAAC Toulouse. This model is based upon the three-dimensional chemistry and transport model developed by Météo-France, and specifically adapted for the transport and diffusion of accidental release from the regional to the global scale. For this study, meteorological data were extracted from Météo-France operational database, including 20 pressure levels, from 1000 to 10 mb, with a time resolution of 1-hour and a horizontal resolution of 0.5°. MOCAGE-accident internal grid resolution is 0.5°. For each scenario, ash release was constant for the eruption phase duration and uniform along a vertical line rising from the vent to the maximum plume height. The particle size distribution in the distal cloud includes 6 grain size fractions between 0.1 and 100 µm, with 70 wt% of the particles smaller than 30 µm[36]. For modelling simplicity, we run the simulations using present-day meteorological data. For the Plinian case (see Supplementary Information Fig. S2 for Subplinian and Small/Moderate cases), we use an eruptive scenario based on the Kelut 2014 eruption (Supplementary Information, Table S1). We compare the ash cloud loading (i.e., integration of ash concentration along the vertical path; in kg/m^2) simulated using the VAAC-default ε value (5%) with the Plinian partitioning coefficient ($\varepsilon_P = 0.5\%$) derived from our model (Fig. 2). The ash cloud concentrations are drastically different, with maximum values of 1.7×10^{-1} and 1.6×10^{-2} kg/m^2 for the VAAC-default and our eruption-style-dependant coefficients, respectively (Fig. 2a,b). This means that for such Plinian eruptions, VAAC operational simulations could overestimate by a factor of ~10 the amount of very fine ash in the atmosphere. Consequently, this would overestimate the extent of the no-fly zone (delimited in Fig. 2 by the black dashed line) set by the European Commission beyond a threshold[37] of 4 mg/m^3 (Fig. 2). Patterns of the no-fly zones are drastically different, and the extent computed from the VAAC model is ~6.5 times larger than the other one, which could have serious implications for air traffic regulation during an eruption.

Volcanic ash particles can be responsible for the formation of indirect aerosols and/or droplets, the ones potentially having short term effect on the climate[38–40]. However, the systematic overestimation of the fine ash amount injected in the atmosphere during large sustained eruptions raises questions about the actual impact of volcanic ash on radiative forcing Conversely, when no calibration is available from ground deposits, the proximal sedimentation can be underestimated by such models (or other tephra-deposition models), as collective settling mechanisms are still not well constrained. This raises the question of the actual impact (buildings damage, agriculture and water pollution, health and respiratory problems, etc.) of tephra fallout in the vicinity of volcanic areas, likely to be larger than expected.

Satellite-based prediction model of Q_s. The interdependence of Q_a, Q_s and the eruption style leads us to develop statistical models for predicting Q_s using satellite measurements of Q_a with additional controlling parameters. A reliable assessment of Q_s is essential for estimating plume dynamics close to the source, and hence for delineating zones impacted by tephra fallout using tephra-deposition models[41]. However, direct measurements of Q_s remain impossible during the course of an eruption[42]. Thus, for rapid assessment of Q_s, indirect methods have been developed using scaling laws based on relationships between measured plume height H and time-averaged Q_s; these are referred to as empirical scaling laws[35,43]. This methodology currently represents the standard for real-time determination of Q_s, although associated with uncertainties as large as a factor of 54 at a 95% confidence interval[35]. Data investigated here are small sized while the number of explanatory variables is relatively high. Therefore, we developed specifically a novel and robust statistical technique using a modified Akaike Information Criterion (AICc; see Methods) allowing the selection of the best regression mixture model for the eruptions in our database (all statistical indicators are summarized in Table 2). By combining Q_s, Q_a and H in three-dimensional space (Fig. 3a), the best model selected follows a power-law in the form:

$$Q_s = 30.22 Q_a^{0.51} H^{2.25} \tag{1}$$

This relationship gives an AICc of 12.9 with excellent p-values (Table 2). The RMSE (Root Mean Square Error) yields an error factor of 12.8 at a 95% prediction interval. With an uncertainty four times lower than the empirical scaling laws[35], this new satellite-derived model improves significantly the estimation of Q_s (Table 2). In particular, the error distribution is not uniform as shown in Fig. 3b from the projection of the 95% prediction interval envelope in the H-Q_a plane. This yields an error factor of ~2, close to the data centre of mass that encloses 12 of the 22 eruptions of our dataset.

Then, we also collected 5 additional parameters (P_1 to P_5, Table 3) related to magmatic system properties and external processes (referred to as modalities), likely to control the amount of very fine ash produced and injected in the plume. Each modality has been coded on a Boolean basis (0/1) so that they can be statistically analysed. We then proceeded to the selection steps to discriminate between all the possible models with 7 different variables

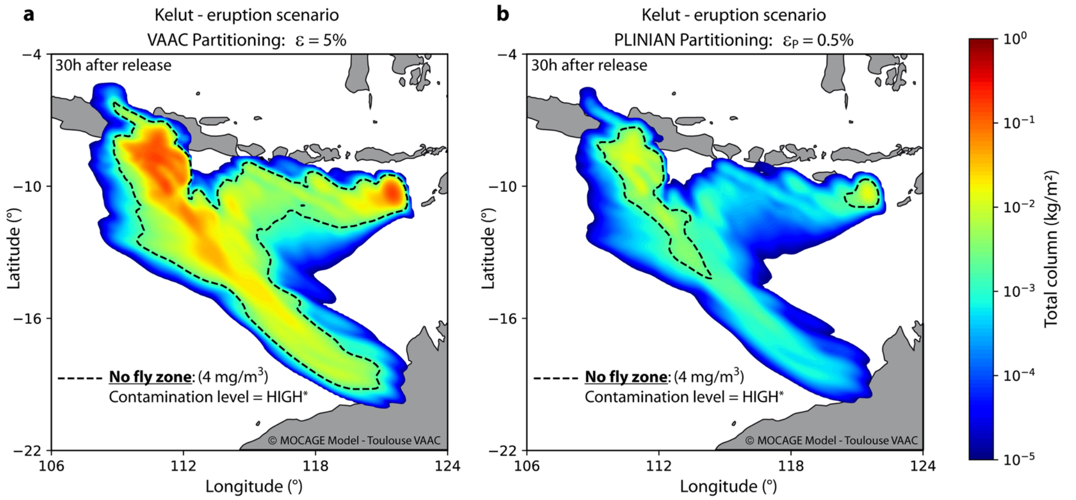

Figure 2. Ash cloud concentration simulations during Plinian eruptions. The two simulations are produced by the volcanic ash-cloud-dispersal model MOCAGE of the Toulouse VAAC based on the Plinian eruption of Kelut the 13 February, 2014 (Supplementary Information Table 1), using different partitioning coefficients and present-day meteorological data. (**a**) Simulation of ash dispersion in the atmosphere at Kelut volcano 30 hours after the eruption, using the VAAC-default operational ε value of 5%. (**b**) Same simulation conditions and scenario, but using the Plinian ε value established in this study at 0.5%. The extent of the No-Fly zone (4 mg/m^3 for an ash cloud 500-m thick*) is much larger for the VAAC-default ε, yielding a maximum concentration one order of magnitude higher. *The threshold at 4 mg/m^3 was first established by the European Commission after the Eyjafjallajökull 2010 eruption[23]. It is now described by EASA (European Aviation Safety Agency) and used in the emergency plan EUR/NAT (EURopean and North ATlantic office) as the "High" contamination level.

Models	Coefficients		p-value	AICc	RMSE (95%)	Error factor
$Qs = c_0Qa^{c1}$	c0	89.211	5.93E-03***	22.49	3.27	26.31
	c1	1.004	2.13E-06***			
$Qs = c_0Qa^{c1}H^{c2}$	c0	30.220	8.87E-03***	12.93	2.55	12.80
	c1	0.505	1.05E-02**			
	c2	2.249	1.31E-03***			
$Qs = c_0Qa^{c(P1)}H^{c(P3)}$	c0	25.946	2.16E-02**	10.43	2.23	9.29
	$c(P1_{(lo)})$	0.721	5.65E-03***			
	$c(P1_{(hi)})$	0.622	2.49E-03***			
	$c(P3_{(cl)})$	1.950	1.80E-03***			
	$c(P3_{(op)})$	1.396	3.17E-02**			

Table 2. Summary of statistic results using model selection analysis. p-values quality is illustrated using asterisk (***Excellent; **very good). The AICc stands for corrected Akaike Information Criterion, the RMSE is given as the natural logarithm of the Root Mean Square Error for a 95% prediction interval and the error factor is calculated as the exponential of the RMSE.

(Q_a, H, P_1 *to* P_5), with modalities (P_1, …, P_5) being class parameters for Q_a and H. The modalities include the SiO_2 (P_1) and H_2O (P_2) contents of the magma, the open or closed character of the conduit (P_3), the occurrence of phreatomagmatic activity (P_4), and the formation of co-pyroclastic density current (co-PDC) plumes (P_5). Using our selection model analysis, these modalities allow clustering of the 22 data samples in the 3D space defined by Q_s, Q_a and H, and the identification of sub-models corresponding to different eruption scenarios (see the Methods section for details). We found that P_1 and P_3 are the parameters that best improve the fitness criterion, with a low AICc value of 10.4. This leads to a new sub-model yielding an error factor of 9.3 at a 95% prediction interval based on four different equations as follows:

$$Q_S = 25.95Q_a^{0.72}H^{1.95} \quad \text{low-SiO}_2 \text{ and closed-conduit} \tag{2}$$

$$Q_S = 25.95Q_a^{0.72}H^{1.4} \quad \text{low-SiO}_2 \text{ and open-conduit} \tag{3}$$

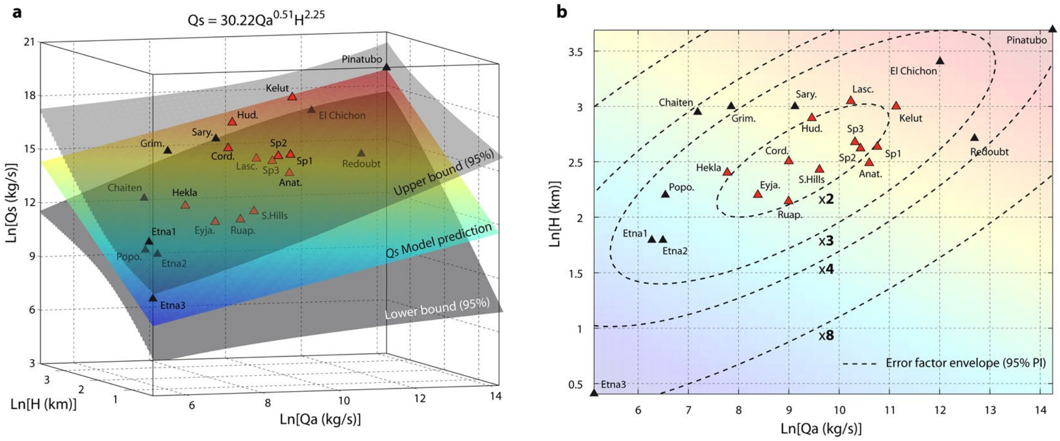

Figure 3. Q_s prediction model using model selection analysis. (**a**) Statistical relationship between Q_s derived from fallout deposits, Q_a derived from satellite-based measurements, and H (above the vent) derived from observations, in a three-dimensional natural logarithm space. The best Q_s prediction model is shown as the coloured plane and the related equation is given in natural scale following a power-law at the top of the plot. It was selected by the AICc (Corrected Akaike Information Criterion) which gives a robust evaluation of the goodness-of-the-fit for small datasets. The error factor and related RMSE are provided at a 95% prediction interval. See Supplementary Information Table 2 for all the goodness-of-the-fit evaluation criteria. (**b**) Error factor contour levels related to the MER estimation plotted on the two-dimensional plane H vs. Q_a in natural logarithm, and showing the anisotropy of the error distribution. Red triangles represent eruptions (12 over 22) for which the error factor value is ~2 or less. Practically, this means that estimations of MER for future eruptions falling in this range of Q_a (~1×10^3 to 1×10^5 kg/s) and H (~7 to 21 km) have a 95% probability to fall within an error factor of 2 only.

$$Q_S = 25.95 Q_a^{0.62} H^{1.95} \quad \text{high-SiO}_2 \text{ and closed-conduit} \tag{4}$$

$$Q_S = 25.95 Q_a^{0.62} H^{1.4} \quad \text{high-SiO}_2 \text{ and open-conduit} \tag{5}$$

The magma SiO_2 content (P_1), often associated with the magma viscosity is a critical parameter controlling the pressurization state of the shallow magmatic system provided sufficient gas is available. The parameter (P_3) related to the open/closed character of the conduit goes in the same direction. Indeed, closed systems usually designate volcanic conduits or vents sealed by cooled lava acting as an impermeable plug preventing from easy gas exhaust, and hence allowing a pressure increase in the shallow magmatic system. Exclusion of P_2 is unexpected, as the gas usually controls the MER at the source vent. This can be explained by the difficulty of comparing H_2O content measurements made with different techniques. Exclusion of P_4 is also interesting. Indeed, the phreatomagmatism is a mechanism involving external water and is frequently observed during recent subglacial Icelandic eruptions[44]. In one hand, magma-water interaction can enhance the explosivity hence the formation of very fine ash. On the other hand, water-rich eruptive column is likely to cause premature deposition of ash through wet aggregation and hydrometeor formation[14,29]. However, no significant influence of the phreatomagmatism could be demonstrated by the our statistical analysis. Significant amount of very fine ash can be produced by PDC as for MSH1980 Plinian eruption, therefore the contribution to airborne ash by co-PDC plumes needed to be tested. However, the variability of co-PDC plumes (P_5) dispersion mechanisms[45] associated with the difficulty to assess quantitatively their amplitude is likely to explain their exclusion. The power-law coefficients are related to the modalities (P_n) and show a strongly non-linear behaviour with power values of 0.72 and 0.62 on Q_a for low and high-SiO_2, respectively, and power values of 1.95 and 1.4 on H for closed and open-conduit respectively. The constant ($c_0 = 25.95$) is inherent to the general model structure and is not dependent on the explanatory variable Q_a and H, nor on the modalities P_1 and P_3.

Equations 2 to 5 offer a new tool for accurate, near-real-time estimation of Q_s during an eruption, provided that Q_a and H can be estimated. In order to validate our approach, we simulated the 23 February 2013 eruption of Mount Etna (Sicily) using two different Q_s inputs. The goal of this work is to test the ability of each parameterization (Q_{s1} and Q_{s2}) to reproduce the observed tephra fallout deposits. Simulations have been carried out using Fall3D; which is a tephra-transport and deposition model, and now represent a standard used at INGV (Italy), VAACs of Buenos Aires (Argentina) and Darwin (Australia). Thus, Fall3D is a perfect candidate for this analysis; a full description of its characteristics can be found in the litterature[41,46]. In one hand, Q_{s1} was estimated from our satellite-derived statistical model using the parameterization for low-SiO_2 content and open conduit (Eq. 3), and used as input parameter in simulation 1 (Fig. 4a). On the other hand, Q_{s2} was calculated from the standard empirical scaling law[35] (currently used operationally by the London and Toulouse VAAC), and used as input parameter in simulation 2 (Fig. 4b). Simulations were run between 00:00 (all times are in UTC) on the 23 and 24:00 on the 28 February 2013, within a 445 by 445 km grid domain using meteorological fields (from ECMWF data). They include 37 pressure levels with a time resolution of 6 hours and a horizontal resolution of 0.75°. The FALL3D

Volcano	Explosive Phase selected	P_1 SiO_2 content (wt%)	Coding	P_2 Inclusion Depth (km)	H_2O (wt%)	Coding	P_3 Open/Closed conduit	Coding	P_4 Phreato-magmatism	Coding	P_5 Co-PDC plumes	Coding
Pinatubo	Climactic phase on 15–16/06/1991	78[49]	1	8.5	6.5[49,50]	1	Closed[51]	0	No[52]	0	Yes[53]	1
Kelut	Full eruption 13/02/2014	56[5]	1	19	4.72[54]	0	Closed[55]	0	No[55]	0	Yes[56]	1
El Chichon (events B & C)	Phases B and C on 04/04/1982	55.9[57]	1	8	4[58]	1	Closed[59]	0	Yes[59]	1	Yes[59]	1
Hudson	Full eruption 12–15/08/1991	60–65[60]	1	4	3[60]	1	Closed[10]	0	Yes[61]	1	No[10]	0
Sarychev Peak	Subplinian events on 14–15/06/2009	54.4[12]	0	3.5	4[12]	1	Closed[12]	0	No[12]	0	Yes[12]	1
Cordón Caulle	Climactic phase on 4–5/06/2011	67–70[62]	1	3.75	2.7[PC]	1	Closed[63]	0	No[63]	0	Yes[64]	1
Grimsvotn	Subplinian phase on 22/05/2011	50[65,66]	0	15	0.7[66]	0	Closed[66]	0	Yes[67]	1	No[66]	0
Mt. Spurr (1)	Full eruption 16/09/1992	57[68]	1				Closed[69]	0	No[70]	0	No[71]	0
Mt. Spurr (2)	Full eruption 18/08/1992	57[68]	1				Closed[69]	0	No[70]	0	No[71]	0
Redoubt (events 1 to 5)	Explosive events 1 to 5 on 22–23/03/2009	57–62[72]	1	5	4.9[73]	1	Open[22]	1	No[22]	0	No[22]	0
Mt. Spurr (3)	Full eruption 27/06/1992	57[68]	1				Closed[69]	0	No[70]	0	No[71]	0
Lascar	Full eruption 04/1993	57–61[74]	1	4.5	5[75]	1	Open[74]	1	No[74]	0	Yes[76]	1
Anatahan	Explosive phases on 10–11/05/2003	60–61[77]	1	1	3.4[78]	1	Closed[78]	0	Yes[78]	1	No[79]	0
Chaiten	Full eruption: 2–8/05/2008	76[80]	1	5	2.3[80]	0	Closed[80]	0	No[80]	0	No[28]	0
Hekla	Phase I + 8 hrs phase II on 26/02/2000	55.5[81]	0	9	2.5[82]	0	Closed[81]	0	Yes[29]	1	Yes[81]	1
Soufrière Hills	Full eruption: 26/09/1997	57–61[83]	1	4.5	4.91[84]	1	Open[85]	1	No[85]	0	Yes[32]	1
Ruapehu	Full eruption: 17/06/1996	57.5–62[86]	1	1.5	1.9[86]	1	closed[87]	0	No[87]	0	No[87]	0
Eyjafjallajökull	Phase I/III on 14–19/04 & 05–18/05/2010	56.6–61.4[88]	1	5	1.8[89]	0	Closed[90]	0	Yes[91]	1	No[92]	0
Etna (1)	Full eruption: 28/10/2002	47[93]	0	4	3.4[93]	1	Open[94]	1	No[94]	0	No[94]	0
Popocatepetl	Climactic events on 10/03/1996	59.8–63.1[95]	1	10	3.2[96]	0	Open[44]	1	Yes[44]	1	No[44]	0
Etna (2)	Full eruption: 27/10/2002	47[93]	0	4	3.4[93]	1	Open[94]	1	No[94]	0	No[94]	0
Etna (3)	Full eruption: 24/11/2006	48[93]	0	4	3[93]	1	Open[94]	1	No[94]	0	No[94]	0

Table 3. Explicative variables used in the statistical analyses for the 22 eruptions. The five explicative variables considered here (SiO_2 (P_1) and H_20 (P_2) magma content, open or closed character of the conduit (P_3), occurrence of phreatomagmatism (P_4), and formation of co-PDC plumes (P_5)) are coded as Boolean data type (0/1) to be used in the model selection analysis. The threshold between low and high SiO_2 content is set at 56 wt% for P_1. The threshold between low and high water saturation for P_2 is set considering the inclusion entrapment depth. Missing data for P_2 are compensated by the model.

internal grid resolution was 4 by 4 km, obtained by interpolating linearly the meteorological data. The three main Eruption Source Parameters (ESP) required by FALL3D at the input of the model are the plume column height, the Total Grain-Size Distribution and Q_s. Then, the ability of each model to reproduce the observed tephra fallout deposits is assessed using field measurements[47] of tephra loading at 10 locations carried out after the 23 February 2013 eruption of Mount Etna (Fig. 4; Supplementary Information Table S2, Table S3 and Fig. S3). The two simulations are strikingly different. The first one (Fig. 4a) provides a faithful reconstruction of the deposits as shown by the 5 isomass contours (set at 10, 1, 0.1, 0.01, and 0.001 kg/m^2) correctly enclosing the sampling points #1 (21 kg/m^2), #8 (0.29 kg/m^2), #9 (0.013 kg/m^2), and #10 (0.0014 kg/m^2). On the contrary, the simulation 2 (Fig. 4b) using the empirical H-derived scaling law fails at reproducing the actual deposits and significantly underestimates the amount of tephra deposited on the ground. This is clearly shown by the restricted extent of the computed isomass contours, and is the direct consequence of the underestimation of Q_s. These results illustrate the robustness of our model and highlight the importance of including satellite-derived estimates of Q_a for reliable estimations of Q_s.

Conclusion

Volcanic very fine ash clouds can travel great distances and contaminate the atmosphere for long periods of time, disrupting air traffic as demonstrated during recent eruptions. However, the proportion of very fine ash distally transported in the atmosphere, and related proximal settling processes, are difficult to assess. Yet, for the past two decades, several operational meteorological agencies (VAACs) have used an unrealistic default value of $\varepsilon = 5\%$ as input for forecast models of atmospheric ash cloud concentration. Here, from the combination of field and satellite data, we provide first-time quantitative assessment of the source-to-atmosphere partitioning (ε) of very fine ash from 22 eruptions. We also developed a robust and novel statistical model for predicting the source mass eruption rate (Q_s) with an unprecedentedly low level of uncertainty. The main findings are summarized below:

i. The fraction of very fine ash (i.e., which survive proximal settling) varies by ~2 orders of magnitudes ($0.1 > \varepsilon > 6.9\%$) with respect to the MER. This partitioning is not arbitrary as ε decreases with increasing MER, with respect to eruption styles.
ii. Large plumes from Plinian eruptions are much less efficient (up to 50 times lower) at transporting very fine ash through the atmosphere than previously anticipated.

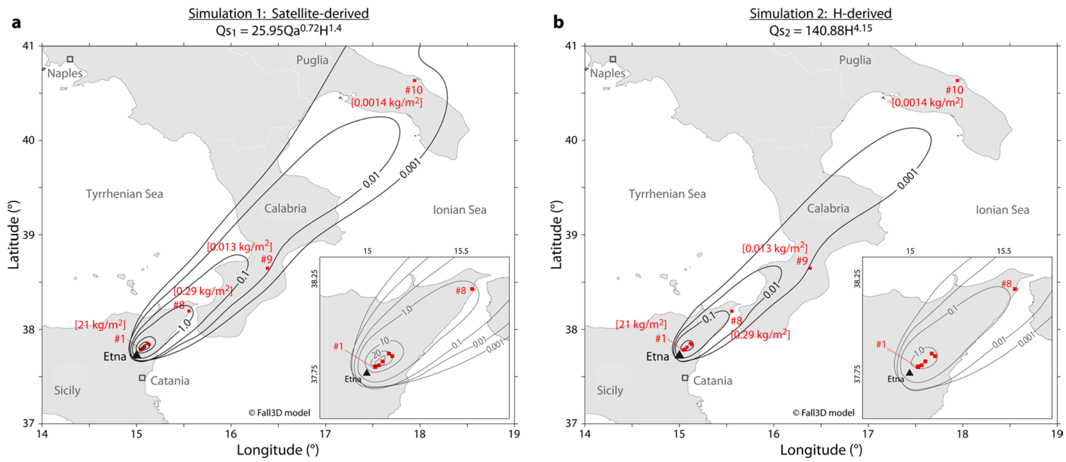

Figure 4. Simulations of the tephra fallout deposit from the 23rd February 2013 Etna eruption. The simulations are generated by the FALL3D tephra-transport deposition model with distinctive Q_s as input. The simulated tephra fallout deposits are displayed as isomass contour levels (black lines) that represent the "computed tephra load" on the ground in kg/m^2. The "measured tephra load" on the ground is indicated in red squares at individual locations of field sampling (red squares and numbers, see Supplementary Information Table 3 for details on sampling locations). (**a**) Simulation 1 uses an input Q_{s1} estimated with our satellite-derived statistical model (see equation at the top of the map for low SiO_2 content and open system). The simulated deposit is in very good agreement with the "measured tephra load" at locations #1, 8, 9 and 10 for instance. (**b**) Simulation 2 uses an input Q_{s2} estimated with the empirical scaling law[35] (see equation at the top of the map). The simulated deposit has a much smaller extent than in simulation 1, with "computed tephra loads" departing significantly from the "measured tephra loads". The total erupted mass (TEM) according to these simulations yields values of 1.09×10^{10} and 6.58×10^{8} kg for simulation 1 and 2, respectively. The reference TEM value[47] for this fallout deposit is 4.9×10^{9} kg which means that the Satellite-derived statistical model overestimates the TEM by a factor of ~2.2, while the empirical scaling law underestimates the TEM by a factor ~7.4.

iii. We explain this behaviour by the existence of collective particle settling mechanisms occurring in ash-rich plumes, which enhance early and en masse fallout of very fine ash.
iv. We suggest that proximal sedimentation during powerful eruptions is controlled by the concentration of fine ash regardless of the grain size.
v. We thus propose a style-derived parameterization of ε ($\varepsilon_P = 0.5\%$; $\varepsilon_{SP} = 0.8\%$; $\varepsilon_{S/M} = 3.2\%$) to be used into VAAC ash-cloud-dispersal models for operational applications.
vi. We provide a novel and robust statistical model for the estimation of the source Mass Eruption Rate (Q_s), with an unprecedented reduction of uncertainties from an error of a factor 54 (previous work used by some VAACs) to a factor 9.3 at a 95% prediction interval.

The fact that very fine ash from Plinian eruptions are not efficiently transported in the atmosphere and experience early sedimentation has major implications for risk management. On the ground, tephra fallouts can be more severe than predicted by current tephra-deposition models, having a detrimental effect on water infrastructure, buildings or agriculture. In the atmosphere, the concentration of far-travelled ash clouds can be much lower than predicted by current ash-cloud-dispersal models, hence having important impact for crisis management related to air traffic safety. We propose incorporating our eruption-style-dependant partitioning coefficients into VAAC ash-cloud-dispersal models, as well as the use of the equations (2–5) of our statistical model into tephra-deposition models. For this purpose, we provide (Supplementary Information, Table S4) operational parameters to be used in real-time for three standard eruptive scenarios (i.e., Plinian, Subplinian, and Small/Moderate). For each scenario, these parameters include the Total Grain Size Distribution[48] (TGSD), the total ash fraction with diameter <64 µm, the distal very fine ash fraction (ε_P, ε_{SP}, $\varepsilon_{S/M}$), and equations of Q_s for the estimation of the source mass eruption rate.

Methods

Statistical model. Data investigated here are small sized while the number of explanatory variables is relatively high. A classical solution consists in regularizing parameters estimation by introducing a penalty term into the maximum likelihood estimation problem. For instance, Ridge or Lasso regressions are based on this principle and have been introduced for variable grouping or to reduce the residuals variance[49,50]. However, each one is either specialized in the selection (grouping of variables) or in the reduction of quadratic errors[51–53]. Consequently, and in adequacy with our context, we propose to introduce a new penalty term that will allow: (i) grouping explanatory variables to determine the relevant number of predictors (ii) improving the estimation of the parameters assigned to each class and (iii) taking into account the small size of observed data. To avoid making any *a-priori*, the methodology has been at first, set in the general context of a Gaussian regression mixture models but it turned out by investigating the data set that only one Gaussian regression model is selected via our procedure. Therefore, we only present our methodology in this context, which moreover allows physical interpretations of the involved parameters. Indeed, consider $(y_1, \ldots, y_n)^t$ a sample observed from the interest variable Y (Mass Eruption Rate, Q_s) and let $(x^t, \ldots, x^t)^t$ be a matrix of explanatory variables X (Q_a, H, $P_1 \ldots$, P_5); x_i are vectors of $\Re^p$. The estimation problem reduces to maximize the following penalized log-likelihood function:

$$l(\beta, \sigma, Y, X) = \sum_{i=1}^{n} log\ f(y, x^t\beta, \sigma) - \boldsymbol{Pe}(\beta)$$

where $f(y, x^t\beta, \sigma)$ is a Gaussian probability density with mean $x^t\beta$ and variance σ^2. The penalty term **Pe** (.) is given by $Pe(\beta) = \alpha\sum_{j=1}^{p} |\beta| + (1-\alpha)\sum_{j=2}^{p}\sum_{l=1}^{j-1} \left|\beta_j - \beta_l\right|$. The quantity $0 < \alpha < 1$ is a tuning parameter whose optimal choice makes a balance between the error of the model and the numbers of predictors used in it. This procedure is confirmed and emphasized by using model's selection Criterion. The best known is the Akaike Information Criterion (AIC). It was designed as an asymptotically unbiased estimator of the Kullback divergence between the true model (that actually generated the data) and a statistical approximation of it. The measure of separation between the generating and a candidate model that we use is given by the Kullback's symmetric divergence[54]. If we denote $\Phi = (\beta, \sigma)$ and $\Phi_0 = (\beta_0, \sigma_0)$ this divergence is defined by:

$$J(\Phi_0, \Phi) = \{d(\Phi_0, \Phi) - d(\Phi_0, \Phi_0)\} + \{d(\Phi, \Phi_0) - d(\Phi, \Phi)\}$$

where $d(\Phi_0, \Phi) = E_{\Phi 0}\{-2\log f(Y|\Phi)\}$ is the Kullback-Leibler divergence and $E_{\Phi 0}$ denotes the expectation with respect to $f(Y|\Phi_0)$. Since $d(\Phi_0, \Phi_0)$ does not depend on Φ we use:

$$K(\Phi_0, \Phi) = d(\Phi_0, \Phi) + \{d(\Phi, \Phi_0) - d(\Phi, \Phi)\}$$

For large sample data and inspired by[55], one may prove that the criteria defined by:

$$AIC = nlog\ \hat{\sigma}^2 + 2(p+1)$$

is asymptotically unbiased estimator of $E_{\Phi 0}$ $(d(\Phi_0, \hat{\Phi}))$. In the case of small samples, we may prove that the criteria defined by:

$$AICc = nlog\ \hat{\sigma}^2 + 2\frac{n(p+1)}{n-p-2}$$

is unbiased estimator of $E_{\Phi 0}$ $(d(\Phi_0, \hat{\Phi}))$ and still satisfy the same asymptotic properties than the AIC. We say that a model is selected through the AIC_c if it has the lowest AIC_c in the family of chosen models.

Let us first observe that due to the range of the observations value, it is natural to consider $\log(y)$ as our new observations. The Gaussianity and independence of the observations will be asserted once the selection procedure is performed. Secondly, due to the very small number of observations, with respect to the number of covariables and using parameter estimations in a complete model, we then proceed to the selection steps to discriminate between all the possible models with 7 different variables (Q_a, H, P_1, …, P_5). To this end, let us remark that Q_a and H are physical parameters (directly related to Q_s), while other parameters (here named P_1 to P_5) are related to magmatic system properties and external processes likely to impact Q_s. We thus choose (P_1, …, P_5) to be class parameters for Q_a and H, which is natural from a physical interpretation of the different volcanoes and meteorological conditions. Namely, we test models depending on the modality of the parameters leading to the complete model with unknown parameters generically called β.

$$\log y^k = \beta_0 + \sum_{i=1}^{7}\beta_i P_i^k + \sum_{j=1}^{2}\sum_{i=3}^{7}\beta_{j,P_i^k}P_j^k + \sigma\xi^k$$

where (ξ^k) are independent standardized Gaussian variable. The selection via AIC_c criterion is then performed.

Data Availability

All data generated or analysed during this study are included in this published article (and its Supplementary Information files).

References

1. Rose, W. I. & Durant, A. J. Fine ash content of explosive eruptions. *Journal of Volcanology and Geothermal Research* **186**(1–2), 32–39 (2009).
2. Stevenson, J. A., Millington, S. C., Beckett, F. M., Swindles, G. T. & Thordarson, T. Big grains go far: reconciling tephrochronology with atmospheric measurements of volcanic ash. *Atmos. Meas. Tech. Discuss.* **8**, 65–120 (2015).
3. Budd, L., Griggs, S., Howarth, D. & Ison, S. A fiasco of volcanic proportions? Eyjafjallajökull and the closure of European airspace. *Mobilities* **6**, 31–40 (2011).
4. Wilson, T. M. *et al*. Impacts of the June 2011 Puyehue-Cordón Caulle volcanic complex eruption on urban infrastructure, agriculture and public health. *GNS Science Report* 2012/20 (2013).
5. Walker, G. Explosive volcanic eruptions — a new classification scheme. *Geologische Rundschau* **62**, 431–446 (1973).
6. Bonadonna, C. & Costa, A. Plume height, volume, and classification of explosive volcanic eruptions based on the Weibull function. *Bulletin of Volcanology* **75**, 1–19 (2013).
7. Prata, A. J. Infrared radiative transfer calculations for volcanic ash clouds. *Geophysical Research Letters* **16**, 1293–1296 (1989).
8. Wen, S. & Rose, W. I. Retrieval of sizes and total masses of particles in volcanic clouds using AVHRR bands 4 and 5. *Journal of Geophysical Research: Atmospheres* **99**, 5421–5431 (1994).

9. Guéhenneux, Y., Gouhier, M. & Labazuy, P. Improved space borne detection of volcanic ash for real-time monitoring using 3-Band method. *Journal of Volcanology and Geothermal Research* **293**, 25–45 (2015).
10. Pyle, D. M. The thickness, volume and grainsize of tephra fall deposits. *Bulletin of Volcanology* **51**, 1–15 (1989).
11. Bonadonna, C. & Houghton, B. F. Total grain-size distribution and volume of tephra-fall deposits. *Bulletin of Volcanology* **67**, 441–456 (2005).
12. Klawonn, M. *et al*. From field data to volumes: constraining uncertainties in pyroclastic eruption parameters. *Bulletin of Volcanology* **76**, 839 (2014).
13. Engwell, S. L., Aspinall, W. P. & Sparks, R. S. J. An objective method for the production of isopach maps and implications for the estimation of tephra deposit volumes and their uncertainties. *Bulletin of Volcanology* **77**, 1–18 (2015).
14. Durant, A. J., Rose, W. I., Sarna-Wojcicki, A. M., Carey, S. & Volentik, A. C. M. Hydrometeor-enhanced tephra sedimentation: Constraints from the 18 May 1980 eruption of Mount St. Helens. *Journal of Geophysical Research: Solid Earth*, ***114***(B3) (2009).
15. Rose, W. I. & Durant, A. J. El Chichón volcano, April 4, 1982: volcanic cloud history and fine ash fallout. *Natural hazards* **51**(2), 363 (2009).
16. Carey, S., Gardner, J. & Sigurdsson, H. The intensity and magnitude of Holocene plinian eruptions from Mount St. Helens volcano. *Journal of Volcanology and Geothermal Research* **66**(1–4), 185–202 (1995).
17. Van Eaton, A. R. *et al*. Hail formation triggers rapid ash aggregation in volcanic plumes. *Nat Commun* **6**, 7860, https://doi.org/10.1038/ncomms8860 (2015).
18. Mueller, S. B. *et al*. Stability of volcanic ash aggregates and break-up processes. *Scientific reports* **7**(1), 7440 (2017).
19. Manzella, I., Bonadonna, C., Phillips, J. C. & Monnard, H. The role of gravitational instabilities in deposition of volcanic ash. *Geology* **43**, 211–214 (2015).
20. Carazzo, G. & Jellinek, A. M. Particle sedimentation and diffusive convection in volcanic ash-clouds. *Journal of Geophysical Research: Solid Earth* **118**, 1420–1437 (2013).
21. Del Bello, E. *et al*. Effect of particle volume fraction on the settling velocity of volcanic ash particles: insights from joint experimental and numerical simulations. *Scientific Reports* **7**, 39620, https://doi.org/10.1038/srep39620 (2017).
22. Lovell, C. J. & Rose, C. W. Wake-Capture Effects Observed in a Comparison of Methods to Measure Particle Settling Velocity Beyond Stokes' Range. *Journal of Sedimentary Research* **61**, 575–582 (1991).
23. Costa, A., Folch, A. & Macedonio, G. A model for wet aggregation of ash particles in volcanic plumes and clouds: 1. Theoretical formulation. *J. Geophys. Res.* **115**, B09201, https://doi.org/10.1029/2009JB007175 (2010).
24. Folch, A., Costa, A. & Macedonio, G. FPLUME-1.0: An integral volcanic plume model accounting for ash aggregation. *Geosci. Model Dev.* **9**, 431–450, https://doi.org/10.5194/gmd-9-431 (2016).
25. Criswell, C. W. Chronology and pyroclastic stratigraphy of the May 18, 1980, eruption of Mount St. Helens, Washington. *J. Geophys. Res.* **92**(B10), 10,237–10,266 (1987).
26. Eychenne, J., Cashman, K., Rust, A. & Durant, A. Impact of the lateral blast on the spatial pattern and grain size characteristics of the 18 May 1980 Mount St. Helens fallout deposit. *J. Geophys. Res. Solid Earth* **120**, 6018–6038 (2015).
27. Sarna-Wojcicki, A., Shipley, S., Waitt, R. B., Dzurisin, D. & Wood S. Aerial Distribution, Thickness, Mass, Volume and Grain Size of Air-Fall Ash From the Six Major Eruptions of 1980. *U.S. Geol. Surv. Prof. Pap.* **1250**, 577–600 (1981).
28. Carey, S. N. & Sigurdsson, H. Influence of particle aggregation on deposition of distal tephra from the May 18, 1980, eruption of Mount St. Helens volcano. *Journal of Geophysical Research: Solid Earth* **87**(B8), 7061–7072 (1982).
29. Durant, A. J. & Rose, W. I. Sedimentological constraints on hydrometeor-enhanced particle deposition: 1992 Eruptions of Crater Peak, Alaska. *Journal of Volcanology and Geothermal Research* **186**(1–2), 40–59 (2009).
30. Eychenne, J., Rust, A. C., Cashman, K. & Wobrock, W. Distal enhanced sedimentation from volcanic plumes: Insights from the secondary mass maxima in the 1992 Mount Spurr fallout deposits. *Journal of Geophysical Research: Solid Earth*, **122** (2017).
31. Harris, D. M. *et al*. Radar observations of ash eruptions. *US Geological Survey professional paper* **1250**, 323–333 (1981).
32. Kristiansen, N. I., Prata, A. J., Stohl, A. & Carn, S. A. Stratospheric volcanic ash emissions from the 13 February 2014 Kelut eruption. *Geophysical Research Letters* **42**(2), 588–596 (2015).
33. Witham, C. S. *et al*. Comparison of VAAC atmospheric dispersion models using the 1 November 2004 Grimsvötn eruption. *Meteorological Applications* **14**, 27–38 (2007).
34. Webster, H. N. *et al*. Operational prediction of ash concentrations in the distal volcanic cloud from the 2010 Eyjafjallajökull eruption. *Journal of Geophysical Research: Atmospheres* **117**, D20, https://doi.org/10.1029/2011JD016790 (2012).
35. Mastin, L. G. *et al*. A multidisciplinary effort to assign realistic source parameters to models of volcanic ash-cloud transport and dispersion during eruptions. *Journal of Volcanology and Geothermal Research* **186**, 10–21 (2009).
36. Maryon, R. H., Ryall, D. B. & Malcolm, A. L. The NAME 4 Dispersion Model: *Science Documentation*. *UK Meteorological Office Report* (1999).
37. Stohl, A. *et al*. Determination of time- and height-resolved volcanic ash emissions and their use for quantitative ash dispersion modeling: the 2010 Eyjafjallajökull eruption. *Atmos. Chem. Phys.* **11**, 4333–4351 (2011).
38. Stenchikov, G. L. *et al*. Radiative forcing from the 1991 Mount Pinatubo volcanic eruption. *Journal of Geophysical Research: Atmospheres* **103**, 13837–13857 (1998).
39. Robock, A. Volcanic eruptions and climate. *Reviews of Geophysics* **38**, 191–219 (2000).
40. Oppenheimer, C. Climatic, environmental and human consequences of the largest known historic eruption: Tambora volcano (Indonesia) 1815. *Progress in Physical Geography* **27**, 230–259 (2003).
41. Costa, A., Macedonio, G. & Folch, A. A three-dimensional Eulerian model for transport and deposition of volcanic ashes. *Earth and Planetary Science Letters* **241**, 634–647 (2006).
42. Kaminski, E. *et al*. Estimation of ash injection in the atmosphere by basaltic volcanic plumes: The case of the Eyjafjallajökull 2010 eruption. *Journal of Geophysical Research: Solid Earth* **116**, B9, https://doi.org/10.1029/2011JB008297 (2011).
43. Sparks, R. S. J. *et al*. *Volcanic Plumes*. John Wiley & Sons, Chichester (1997).
44. Pálmadóttir, E. The 2010 Eyjafjallajökull summit eruption: Nature of the explosive activity in the initial phase (*Doctoral dissertation*) (2016).
45. Engwell, S. L. & Eychenne, J. In *Volcanic Ash: Hazard Observation* (eds Mackie, S. *et al.*) (Elsevier, 2016).
46. Folch, A., Costa, A. & Macedonio, G. FALL3D: A computational model for transport and deposition of volcanic ash. *Computers & Geosciences* **35**(6), 1334–1342 (2009).
47. Poret, M. *et al*. Modelling eruption source parameters by integrating field, ground-based and satellite-based measurements: The case of the 23rd February 2013 Etna paroxysm. *Journal of Geophysical Research: Solid Earth*, https://doi.org/10.1029/2017JB015163 (2018).
48. Costa, A., Pioli, L. & Bonadonna, C. Assessing tephra total grain-size distribution: Insights from field data analysis. *Earth and Planetary Science Letters* **443**, 90–107 (2016).
49. Tibshirani, R. Regression shrinkage and selection via the lasso. *Journal of the Royal Statistical Society* **Series B** (Methodological), 267–288 (1996).
50. Zou, H. & Hastie, T. ization and variable selection via the elastic net. *Journal of the Royal Statistical Society* **Series B** (Statistical Methodology), 301–320 (2005).
51. Friedman, J., Hastie, T. & Tibshirani, R. Regularization paths for generalized linear models via coordinate descent. *Journal of statistical software* **33**, 1 (2010).

52. Petry, S., Flexeder, C. & Tutz, G. Pairwise fused lasso. *University of Munich Technical Report* **102**, https://epub.ub.uni-muenchen.de/12164/1/petry_etal_TR102_2011.pdf (2011).
53. Städler, N. & Bühlmann, P. Missing values: sparse inverse covariance estimation and an extension to sparse regression. *Statistics and Computing* **22**, 219–235 (2012).
54. Kullback, S. Information Theory and Statistics *Dover Publications*, Mineola, N.Y (1968).
55. Cavanaugh, J. E. A large-sample model selection criterion based on Kullback symmetric divergence. *Statistics and Probability Letters* **42**, 333–343 (1999).

Acknowledgements
J.E. was funded by the Research Institute for Development (IRD). We are particularly grateful to Timothy H. Druitt for constructive scientific discussions. We warmly thank A. Folch and one anonymous reviewer for constructive comments.

Author Contributions
M.G. conceived the idea and defined the project strategy. M.G. and J.E. both compiled, analysed and interpreted the data, and co-wrote the manuscript. N.A. and A.G. designed and carried out the statistical analysis. M.D. and P.H. run the simulations of ash cloud dispersal using MOCAGE-accident model. M.P. and A.C. run the simulations of tephra deposition using FALL3D model.

Additional Information
Supplementary information accompanies this paper at https://doi.org/10.1038/s41598-019-38595-7.

Competing Interests: The authors declare no competing interests.

Publisher's note: Springer Nature remains neutral with regard to jurisdictional claims in published maps and institutional affiliations.

RESEARCH ARTICLE

VOLCANICA

SO_2 and tephra emissions during the December 22, 2018 Anak Krakatau flank-collapse eruption

Mathieu Gouhier*, Raphaël Paris

Université Clermont Auvergne, CNRS, IRD, OPGC, Laboratoire Magmas et Volcans, F-63000 Clermont-Ferrand, France.

Abstract

On December 22, 2018 the south-western flank of Anak Krakatau collapsed into the sea, removing 93.8×10^6 m^3 of subaerial lavas, and generated a tsunami. Synchronously with the collapse, a large volcanic plume of SO_2 and ash (14–15 km in height) has formed, marking the onset of a paroxysmal eruption lasting from December 22, 2018 to January 06, 2019. From remote sensing analysis, we show that the eruption can be divided into three main phases. Phase I and II show both tephra and gas emissions while phase III is mostly degassing. The total amount of SO_2 injected in the atmosphere is 173±52 kt, while the minimum bulk magma volume emplaced, estimated from a topographic reconstruction, is ~45×10^6 m^3. This value compares well with a petrologic-based estimate of 56.4×10^6 m^3, making the existence of external sulphur sources and sinks quite unlikely. The ice-rich ash plume formation shows that a strong sea-water/magma interaction was responsible for the phreatomagmatic activity throughout the eruption. However, we distinguish a first Vulcanian blast-derived eruption (lasting 40 min) just after the collapse having a Mass Eruption Rate (MER) of 9×10^5 kg s^{-1}, followed by a sustained lower-intensity eruption resulting in ash emissions over hours (MER = 5×10^5 kg s^{-1}). From December 23, daytime photos show typical Surtseyan activity.

Résumé

Le 22 décembre 2018, le flanc sud-ouest de l'Anak Krakatau s'est effondré dans la mer, arrachant 93.8×10^6 m^3 de roches volcaniques à l'édifice préexistant et provoquant ainsi un tsunami. Parallèlement à l'effondrement, un important panache volcanique de SO_2 et de cendres (14 à 15 km de haut) s'est formé, marquant le début d'une éruption paroxysmale qui s'est déroulée du 22 décembre 2018 au 06 janvier 2019. À partir de l'analyse des données de télédétection spatiale, on montre que l'éruption peut être divisée en trois phases principales. Les phases I et II présentent à la fois des émissions de téphra et de gaz, tandis que la phase III est essentiellement associée à du dégazage. La quantité totale de SO_2 injectée dans l'atmosphère est de 173±52 kt, tandis que le volume minimal de magma mis en place, estimé par reconstruction topographique, est de ~45×10^6 m^3. Cette valeur est comparable à l'estimation basée sur la méthode pétrologique ($56{,}4 \times 10^6$ m^3), ce qui écarte l'hypothèse de sources (ou de puits) additionnelles de soufre dans le budget global de SO_2 émis en surface. La formation d'un panache de cendres riche en glace démontre une forte interaction entre l'eau de mer et le magma. Ce mécanisme est responsable de l'activité phréatomagmatique tout au long de l'éruption. Dans le détail, nous identifions une première phase Vulcanienne initiée par une explosion latérale de courte durée (~40 min) juste après l'effondrement, avec un flux de masse éruptif (MER) de 9×10^5 kg s^{-1}. Juste après, l'éruption montre une colonne plus soutenue mais de faible intensité entraînant des émissions de cendres sur plusieurs heures (MER = 5×10^5 kg s^{-1}). À partir du 23 décembre, de nombreuses photos attestent d'une activité typiquement Surtseyenne.

Keywords: SO_2 degassing; Volcanic ash; Flank Collapse; Anak Krakatau;

1 Introduction

Anak Krakatau is a volcanic island located in the Sunda Strait (Indonesia), which emerged in 1927 on the rim of the submarine caldera that was formed during the 1883 eruption of Krakatau. On December 22, 2018 at 13:50 UTC the south-western flank of Anak Krakatau volcano (Indonesia) collapsed to the sea and generated a tsunami in the Sunda Strait [ESDM 2018]. Tsunami waves devastated the coasts of Java and Sumatra, killing 431 people and damaging thousands of houses and boats, as reported by BNPB (Badan Nasional Penanggulangan Bencana: https://bnpb.go.id). Although this scenario of collapse-generated tsunami had been predicted and simulated by Giachetti et al. [2012], the disaster could not be prevented and became one of the deadliest volcanic eruptions of the last decades. After 16 months of quiescence, Anak Krakatau's activity resumed in June 2018 in the form of both explosive and effusive eruptions. The collapse followed a period of 6 months of volcanic activity and rapid growth of the volcanic cone, as evidenced by satellite images captured in 2018 (MODIS, Sentinel constellation, PlanetScope, etc.), reports on seismic activity by PVMBG (Pusat Vulkanologi dan Mitigasi

*Corresponding author: Mathieu.Gouhier@opgc.fr

Bencana Geologi: https://magma.vsi.esdm.go.id) and photographs available on the web (e.g. http://www.oysteinlundandersen.com). Immediately after the collapse, Anak Krakatau experienced a long-lived eruption, from December 22, 2018 to January 06, 2019, of intense pheatomagmatic activity showing a series of strong volcanic explosions. The amount of SO_2 and tephra released as well as the dynamics of the eruption contrast with the moderate activity of the last 6 months.

In this study, we focus on the mass budget of material emplaced during the post-collapse eruption. In particular, we provide a time-averaged estimation of bulk magma volume emitted from topographic reconstruction techniques using remote sensing data. Then, from the processing of daily UV satellite-based data, we provide a detailed analysis of SO_2 emissions. Estimates of mass fluxes of outgassed SO_2 are particularly important as they provide information on the eruptive activity at the surface [e.g. Carn and Prata 2010], the shallow plumbing system [e.g. Gauthier et al. 2016], and the magma ascent dynamics [e.g. Allard 1997]. The combination of SO_2 released at the surface with sulphur concentration in Melt Inclusions (MI) can yield key information on possible external sulphur sources and sinks at shallow levels [e.g. Edmonds et al. 2003; Sigmarsson et al. 2013]. Finally, estimation of ash plume concentration and altitude are obtained from IR satellite-based data [Prata 1989a; Wen and Rose 1994]. These parameters are critical as they allow indirect assessment of the Mass Eruption Rates (MER) of tephra emitted at the source vent from empirical formulations [Sparks et al. 1997; Mastin et al. 2009] or statistical modelling [Gouhier et al. 2019]. Also, the evaluation of airborne ash mass fluxes (Q_a) is essential in understanding the dynamics of particle transport and dispersion, and better constraining sedimentation mechanisms [e.g. Carey and Sigurdsson 1982; Durant and Rose 2009; Carazzo and Jellinek 2013; Manzella et al. 2015].

2 Data and Methods

2.1 Pre- and post-collapse topography of the island

Pre-collapse topography of Anak Island was derived from the DEMNAS (national digital elevation model of Indonesia, spatial resolution of 0.27 arcsecond using the vertical datum EGM2008, provided by the Indonesian Geospatial Agency, and available at http://tides.big.go.id/DEMNAS/index.html). This DEM was built from InSAR, TerraSAR-X and ALOS-PALSAR data collected from 2000 to 2013. The original DEMNAS raster file was converted into a shapefile (contour lines) that was modified in order to include the latest growth of the edifice, as seen on photographs taken in August and November 2018 (http://www.oysteinlundandersen.com), and satellite images (e.g. Sentinel-2 image captured on 30 September 2018, and PlanetScope image captured on 17 December 2018: see Figure A1). Pre-collapse bathymetry is from Deplus et al. [1995].

The contour of the collapse scar was inferred from a Sentinel-1A image captured ~8:30 hours after the collapse (22/12/2018 at 22:33:44 UTC) and photographs taken by Susi Air flight crew the day after (23/12/2018). There is no data available on post-collapse bathymetry and the submarine extent of the collapse scar.

Intense phreatomagmatic activity rising from the sea surface inside the scar produced a significant volume of pyroclastic deposits, thus reshaping the island in a few days. Post-collapse evolution of the island's perimeter could be traced from different satellite images captured between 22 December 2018 and 31 March 2019 (Sentinel-1-A/B, Sentinel-2, TerraSAR-X, PlanetScope). The topography of the island on January 10, 2019 was reconstructed using drone photogrammetry (drone footage by James Reynolds, Earth Uncut TV: https:/www.earthuncut.tv). Images were processed using Agisoft Photoscan Pro (https:/www.agisoft.com). Using a Structure-from-Motion workflow, the software (1) detected matching points and aligned all images, (2) constructed a dense point cloud from depth information of each aligned image, (3) calculated a triangulated mesh, (4) and built a digital elevation model after 11 ground control points (GCP) were implemented (from a Sentinel 2 image captured on 13 January 2019). The resulting DEM has a resolution of 2 m per pixel, but its completeness is unequal from one flank to another due to the spatial distribution of the drone images. In order to locally complete the model, additional points were extrapolated from different aerial and ground photographs available on the web (e.g. BNPB survey of 13 January 2019). Although the method might be further optimised in the future by better parameterising the drone survey and implementing GNSS GCPs, it provides a rough estimate of the new topography of the island less than 20 days after the collapse.

2.2 Satellite-based SO_2 retrieval

Volcanic sulphur dioxide emissions (SO_2) have long been characterized from satellite-based UV sensors [e.g. Schneider et al. 1999; Carn et al. 2003; Yang et al. 2007]. A variety of sensors (IR/UV) and platforms (GEO/LEO) now exists and allows a detailed description and quantification of SO_2 mass loading during eruptive events. Firstly, in this study we used the combination of Aura/OMI data (~90 %) and Suomi-NPP/OMPS data (~10 %) in order to capture the long-term (195 days, between 10/06/2018 and 22/12/2018) SO_2 emission pattern before the Anak flank collapse. The combination of both sensors allowed us to avoid data gaps in the time series. Data were acquired from NASA's EarthData (https://search.earthdata.nasa.gov/)

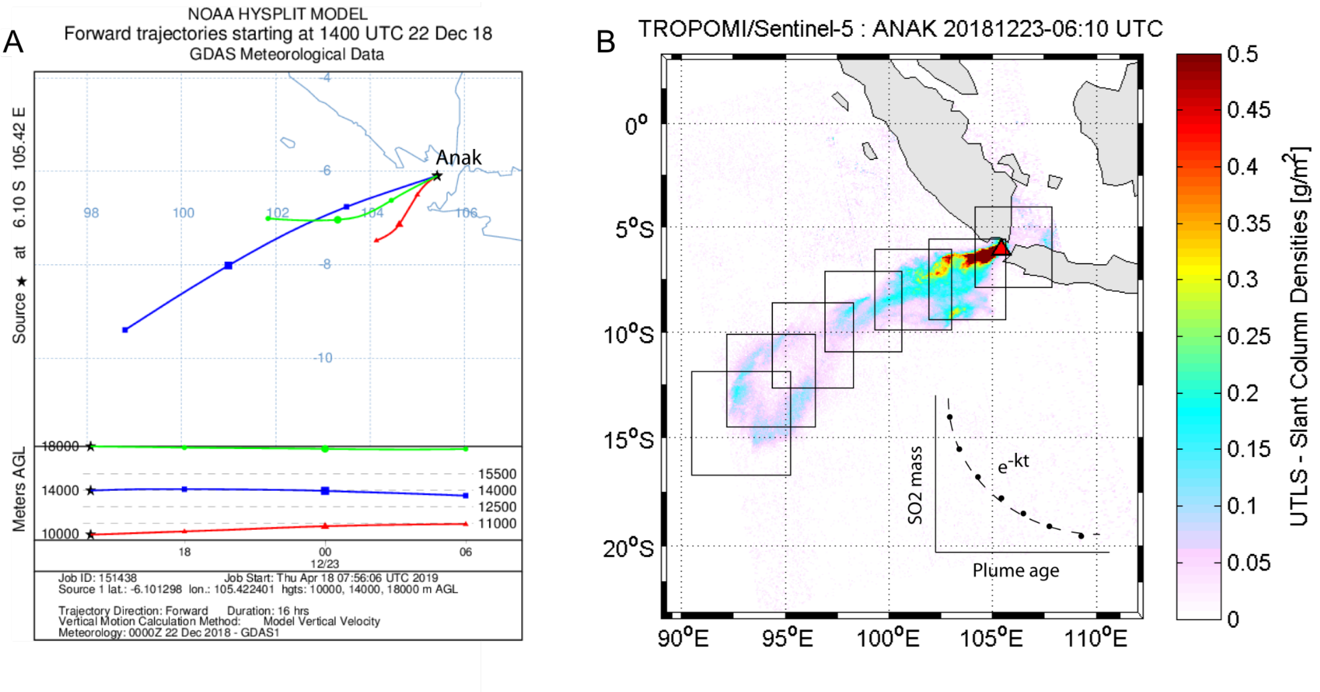

Figure 1: SO_2 mass fluxes retrieval. [A] Run example of HYSPLIT forward trajectory on 22/12/2018 at 14:00UTC showing the best trajectory (blue line) drifting in the south-westward direction at an altitude of 14 km AGL with an average velocity of 15m/s. [B] Tropomi/Sentinel-5 image on 23/12/2018 showing the SO_2 plume slant column densities (g/m^2) at UTLS level (Upper Troposphere Lower Stratosphere). Also, the boxes used for the assessment of e-folding time correction are represented.

using the "Total Column 1-orbit L2 Swath 13x24 km V003 (OMSO2)" product for OMI/Aura Sulphur Dioxide, and the "Total Column 1-Orbit L2 Swath 50x50 km" product for OMPS/NPP Sulphur Dioxide. Then, in order to better assess the eruption dynamics and provide a refined evaluation of SO_2 emissions, we processed data from the TROPOMI sensor onboard the Sentinel-5 platform. We used the Offline timeliness L2_SO2 data products from ESA-Copernicus Pre-Operation Data-Hub (https://scihub.copernicus.eu/). For estimating SO_2 emissions before the flank collapse, we used the middle troposphere elevation model (TRM, 5–10 km) as most emissions were injected to low/moderate altitudes. By contrast, for the 22/12/2018 eruption we used the 15-km elevation model (UTLS) from TROPOMI Slant Column Densities (SCD).

The calculation of the mass loadings or/and mass fluxes have already been widely described in the literature (see, e.g. Theys et al. [2013], for a review). A variety of methods associated with satellite-based data exists, such as the Traverse, Box, Delta-M or Inverse methods. They all have their specificity and domain of application. For our study we used the box method [Lopez et al. 2013] which allows mass fluxes to be determined from the estimation of SO_2 total columns divided by the duration of emission. In our case the travel time of the plume, which is directly related to the wind velocity, has been estimated from HYSPLIT trajectory model (Figure 1A). However, for large plumes extending over several hundreds of kilometres the SO_2 loss term, mainly due to the plume dilution and SO_2 oxidation into sulphuric acid, is not negligible. In the case of a significant interaction between the eruption column and the sea water, as it is most likely here, it is possible that a significant amount of SO_2 is rapidly lost to scrubbing. Finally, note that the cloud cover may have sometimes obscured and prevented SO_2 detection and quantification. This is true in particular during the pre-collapse, as weak emissions are typically of low altitude. We thus provide here a minimum estimate during this period. During the post-collapse paroxysm, a plume column altitude of ~14 km makes the SO_2 estimation much more reliable, as few or no water cloud obscuration should occur. Overall, the budget of SO_2 from a satellite image is thus a balance between SO_2 emissions and losses. This problem can be modelled from the solution of the mass conservation law:

$$\frac{\partial c}{\partial t} = -kc \quad (1)$$

where the loss term is simply assessed by the application of an age dependent correction $e^{t/\tau}$, where τ (i.e. $1/k$) is known as the SO_2 e-folding time. This parameter is difficult to assess and can be highly variable from one eruption to another [Rodrıguez et al. 2008; Krotkov et al. 2010; McCormick et al. 2014; Beirle et al. 2014]. Indeed it actually depends on weather and atmospheric conditions into which the eruption injects the gas. It will also greatly depend on plume altitude as higher atmospheric layers are much more dryer than lower ones, hence having longer lifetimes. Thus, we have calculated the SO_2 e-folding time for this eruption (Figure 1B) using a sequence of small boxes of variable sizes but enclosing the full width of the plume (i.e. crosswind). Under the simplifying, but mandatory, assumption that the flux is constant within the current plume formation, we calculate an e-folding time of τ ~30.4 hours.

2.3 Airborne ash retrieval from TIR

Satellite-based Thermal infrared (TIR) sensors are very useful for characterizing volcanic ash. In the TIR region (i.e. 7–14 µm), we can distinguish silicate particles (e.g. volcanic ash) from other aerosols (e.g. ice crystals or H_2SO_4) using a two-channel difference model based upon the absorption feature between the 11- and 12 µm) wavelengths [Prata 1989b; Wen and Rose 1994; Watson et al. 2004]. It was shown that the differences between the at-sensor "Planck" brightness temperature (referred to as BTD) observed in these two channels are negative ($-\Delta T$) for ash and positive ($+\Delta T$) for ice (Figure 2A). Building on earlier work [Prata 1989b], Wen and Rose [1994] developed a forward retrieval model that quantifies the effective radius (r_e) and optical depth (τ_c) from the extinction efficiency factor (Q_{ext}) calculated using Mie theory. This allows theoretical look-up-tables (LUT) to be generated for sets of variations of both r_e and τ_c as a function of the brightness temperature. Thus, from inverse procedures, one can retrieve a value of r_e and τ_c for any given brightness temperature pair (see Prata and Grant [2001] and Watson et al. [2004] for details), hence leading to the estimation of the vertically-integrated ash concentration ($g\,m^{-2}$) of a volcanic cloud. However, satellite retrievals are affected by several factors such as the surface characteristics (i.e. temperature and emissivity), plume geometry (i.e. altitude and thickness), ash optical properties and water vapour. These factors produce an uncertainty of ~40 % and ~30 % respectively associated with the total mass retrieval and the effective radius [Corradini et al. 2008]. Another source of uncertainty is related to the presence of large particles (typically for $r_{eff} > 6\,\mu m$), possibly existing in fine ash clouds, which cannot be retrieved using the Mie theory because Q_{ext} does not vary strongly for $r_{eff} > \lambda/2$[Guéhenneux et al. 2015; Stevenson et al. 2015]. Overall, effects related to both misdetection issues (i.e. BTD) and the presence of coarse ash particles in the cloud may lead to a mass underestimation of about 50 % [Stevenson et al. 2015]. Also, we can provide the ash cloud top altitude (Figure 2B) using a combination of the cloud surface brightness temperature at 11.2 µm (H8 TIR waveband #02) and temperature profiles from atmospheric soundings. This technique refers to the Cloud Top Temperature (CTT) method and is only possible in the troposphere, where the temperature profile is monotonic [e.g. Prata and Grant 2001]. Here we used TIR data from Himawari-8 (H8) geostationary satellite operated by the Japan Meteorological Agency (JMA) which provides images every 10 minutes at a spatial resolution of $\sim 2 \times 2$ km at nadir. Data were collected through the Centre for Environmental Remote Sensing (CEReS) using gridded data products from full-disc observation mode (http://www.cr.chiba-u.jp/english/database.html). The very high time resolution of TIR images used allows us to catch the dynamics of the ash plume at the initial stage, during and after the collapse (i.e. on 22/12/2018 at 13:50 UTC). In Figure 2B, we show as an example one image of the plume brightness temperature at 11.2 µm (H8 TIR waveband #02) that allows us to determine the plume top altitude between 14 and 15 km (a.s.l.) by comparing with local and synchronous atmospheric temperature profiles. For this study, temperature profiles were obtained using atmospheric sounding data of the station 96789 WIII-Jakarta (accessible from the Department of Atmospheric Science of the University of Wyoming: http://weather.uwyo.edu/upperair/sounding.html).

3 Results

3.1 Volume of post-collapse pyroclastic deposits

The flank collapse removed 93.8×10^6 m^3 (Figure 3) of subaerial lavas from the western flank of the volcano. This volume corresponds to a minimum value, as the submarine extent of the collapse remains unknown. However, the collapse scar was rapidly filled by post-collapse pyroclastic deposits (Figures 3 and A1). On early January imagery, the collapse headwalls are already buried by new pyroclastic deposits, and details of the pre-collapse topography such as 10 m-high coastal cliffs are no longer visible (e.g. south-eastern coast of the island). Vegetation on Panjang Island, located 2.5 km east of Anak Island, was severely damaged by ash fallout and surges, as evidenced by drone footage and Sentinel-2 images captured on January 8 and March 31, 2019 (Figure A2).

Reconstruction of post-collapse topography at two different time steps (22/12/2018: just after the collapse; and 10/01/2019: 19 days after the collapse) confirms that an important volume of juvenile tephra was deposited by ash fallouts and pyroclastic density currents after the collapse (Figure 3). On Anak Island, post-collapse pyroclastic deposits represent a volume of 29.4×10^6 m^3. There is no information available on the volume of submarine pyroclastic deposits. Analysis of shoreline evolution from 17 December 2018 to 31 March 2019 (Figure 4) shows a clear increase of the surface area of the island, with a shoreline progradation of up to 270 m on the eastern coast of the island. This progradation corresponds to a volume of 8.3×10^6 m^3

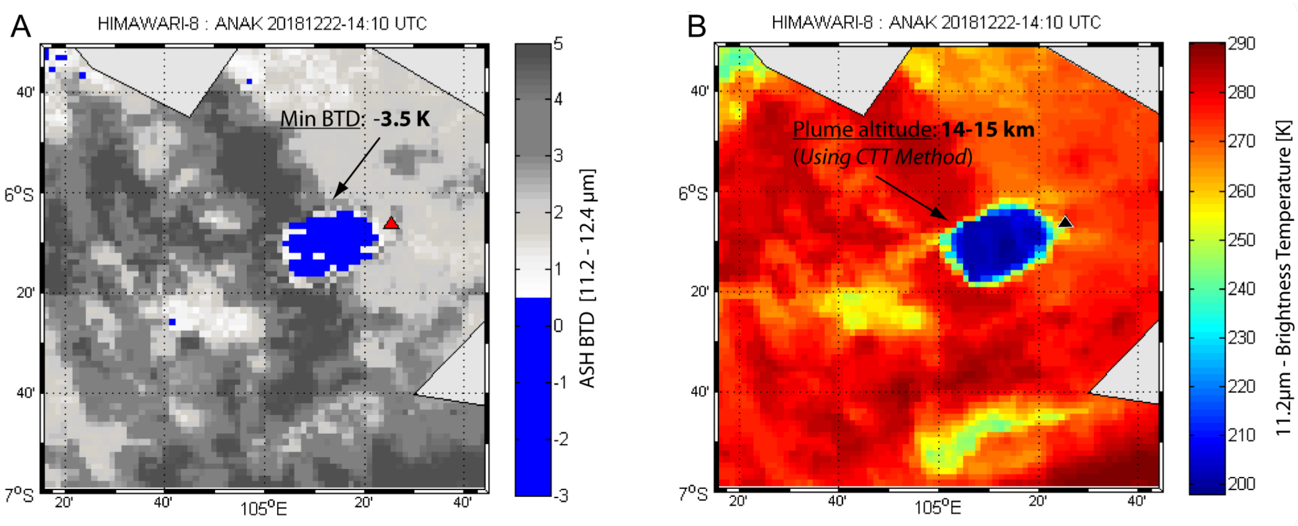

Figure 2: Ash plume characterization. [A] Brightness Temperature Difference (BTD) of band L02 (11.2 µm) and L03 (12.4 µm) from Himawari-8 satellite, showing the ash plume at 14:30 UTC on 22/12/2018. [B] Brightness Temperature (in Kelvin) at 11.2 µm used for the plume height determination (see text for details).

of submarine pyroclastic deposits, which is probably a minimum value compared to the total volume of pyroclastic deposits that were emplaced on the sea bottom. We thus estimate that the total volume of post-collapse pyroclastic deposits, both subaerial and submarine, is larger than $\sim 45 \times 10^6$ m^3 ($>27 \times 10^6$ m^3 DRE magma volume). Most of these deposits were produced in less than one week, as evidenced by satellite images captured from 23 to 29 December (Figure 4). The shoreline of the island just after the collapse (23/12/2018) is similar to the pre-collapse shoreline (17/12/2018), with the exception of the area of the collapse scar. Between 29 December 2018 and 31 March 2019, the shorelines of the island did not change significantly.

3.2 SO_2 mass loading and magma volume

In Figure 5, we processed a time series of volcanic SO_2 emitted by the Anak Krakatau in the period ranging from June 10, 2018 to January 15, 2019. These values represent the SO_2 daily mass loading (in kilotons). They have been estimated from the calculation of time-averaged mass fluxes (in kg s^{-1}, Figure 5) based on a time/distance window corresponding to the plume footprint for each image of the sequence, and referred to as the box method [Lopez et al. 2013]. It includes the e-folding time correction (τ) estimated at ~30.4 hours, and accounting for the SO_2 loss term (Figure 1). SO_2 emitted before the collapse (10/06/2018–22/12/2018) has been calculated using a combination of OMI/Aura and OMPS/Suomi satellite-based data in order to avoid data gaps. SO_2 emitted during the 22/12/2018 collapse and subsequent explosions has been calculated from TROPOMI/Sentinel-5 satellite-based data, hence allowing a refined determination of the SO_2 mass loading (see method section for details). Indeed, since early June, three main periods have been identified before the collapse. The first one spanning 30/06–04/08/2018 is associated with weak emissions of SO_2 yielding a total of 12.4 kt. A second one has been identified from 09/09 to 11/10/2018 with significantly higher SO_2 emission, and totalling 19.4 kt. Then, except a short pulse on 18–19/11/2018, no significant SO_2 emissions have been detected until the major flank collapse on 22/12/2018. The pre-collapse emissions were typically of moderate altitude (low-middle troposphere) and associated with weak to mild explosive activity (i.e. mainly Strombolian). Finally, post-collapse volcanic activity emitted 173±52 kt of SO_2 in 11 days (see inset in Figure 5). Errors on SO_2 retrieval are difficult to assess accurately, but they can be relatively large. Indeed, Lee et al. [2009] have estimated in a study dedicated to validation and error analysis that the total uncertainty in the retrieval of SO_2 columns from similar instruments is in the range of 20–40 %. The flank collapse occurred on 22/12/2018 around 13:50 UTC. This has been confirmed by thermal infrared data recorded by Himawari-8 geostationary satellite (Figure 6), allowing the full-disc image acquisition every 10 minutes. By contrast, the TROPOMI/Sentinel-5 platform provides one image/day with an acquisition time above this region lying between 06:00 and 07:00 UTC. Thus, the first peak reaching 32.3 kt of SO_2 is detected ~16 hours after the collapse (23/12/2018), hence corresponding to a time-averaged mass flux of 373.4 kg s^{-1} (Figure 5). The plume had already drifted south-westward ~1670 km away from the source vent. Processing of HYSPLIT trajectories (Figure 1) has allowed the determination of the SO_2 plume altitude at ~14 km a.s.l., which is in agreement with the ash plume altitude (14–15 km) determined from Himawari-8 TIR wavebands using the Cloud Temperature Method (CTT)

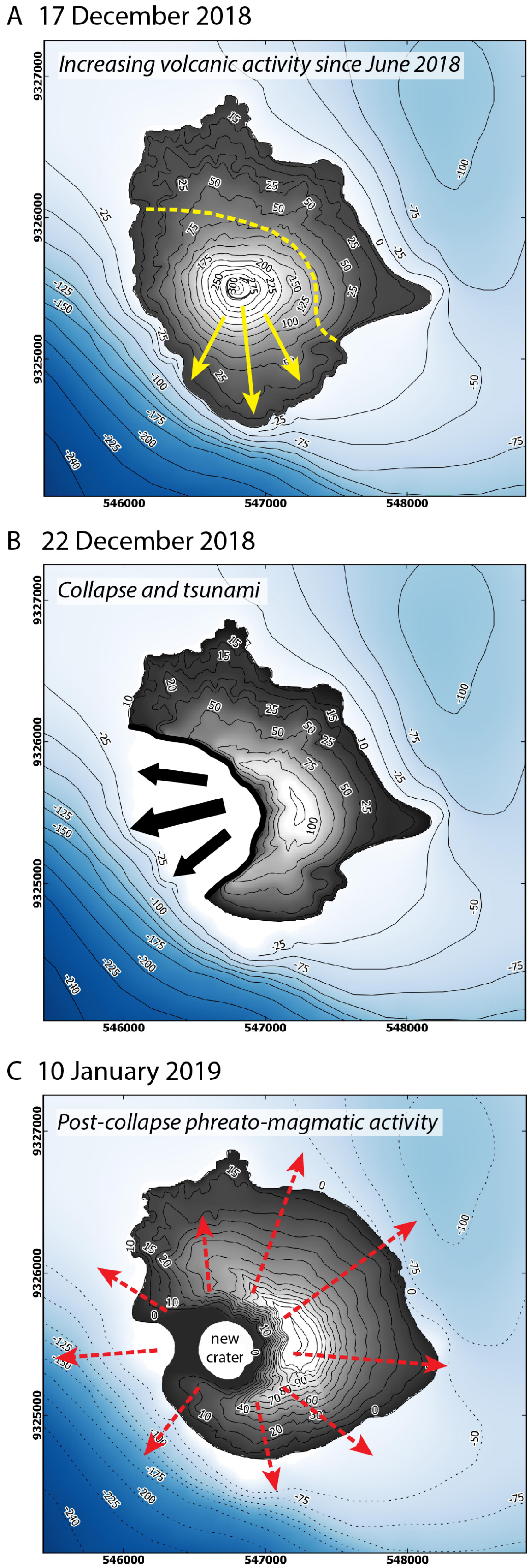

Figure 3: [Left] Evolution of the topography of Anak Krakatau volcano following the 22 December flank collapse. [A] 17 December 2018: lava flows emplaced since June 2018 (yellow arrows) are located on the south-western flank (southwest of the yellow dotted line). [B] 22 December 2018: the western flank of the active cone is truncated by a $> 93.8 \times 10^6$ m^3 collapse (black arrows). [C] 10 January 2019: rapid island growth, with $> 45 \times 10^6 m^3$ of new tephra deposited on land and offshore (mostly between 22 and 29 December 2018, see Figure 5) by ash fallout and pyroclastic density currents (red arrows). UTM coordinates (zone 48S).

From the SO_2 mass flux time series (Figure 5), we can discretize 3 different phases: the first one, including the initial flank collapse, starts on 22/12/2018 and spans 5 days of intense activity (Phase I: 22-27/12/2018), with emissions totalling 98 kt of SO_2. During the first phase, SO_2 mass fluxes gradually decrease from 373.4 to 27.5 $kg\,s^{-1}$ and resumed in a strong pulse of SO_2 recorded on 28/12 with fluxes peaking at 442 $kg\,s^{-1}$. This new pulse signals the onset of the second phase, lasting only 2 days (phase II: 28-29/12/2018), and totalling 50 kt of SO_2. Finally, after 4 days of pseudo-quiescence, the third phase begins on 3 January 2019 showing lower mass fluxes (phase III: 03-06/01/2019) and with emissions totalling 25 kt of SO_2. Since then, no new emissions occured, at least within the next 2 months. Phases 2 and 3 were clearly observed on live seismograms provided

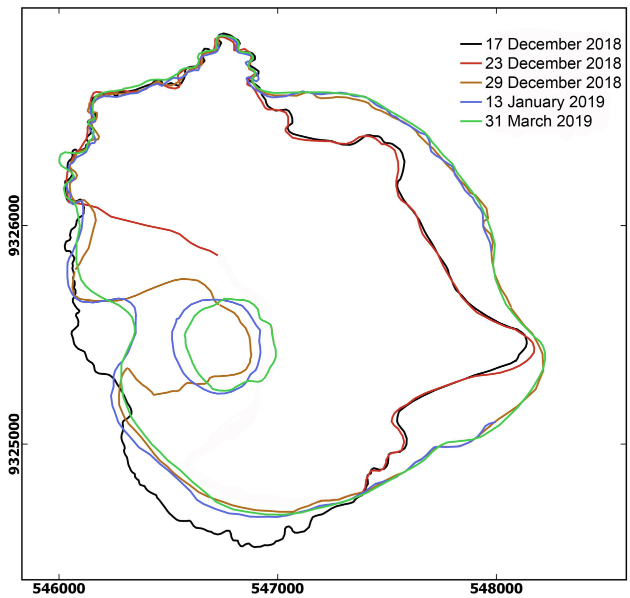

Figure 4: Shoreline evolution of Anak Island between December 2018 and March 2019 (23 December 2018 Sentinel-1A; 29 December 2018, 13 January 2019, and 31 March 2019 Sentinel-2; 17 December 2018 Planetscope data).

and atmospheric soundings (Figure 2). Such altitudes confirm a very explosive eruption, probably caused by the rapid and massive decompression of the shallow magma system due to the initial flank collapse.

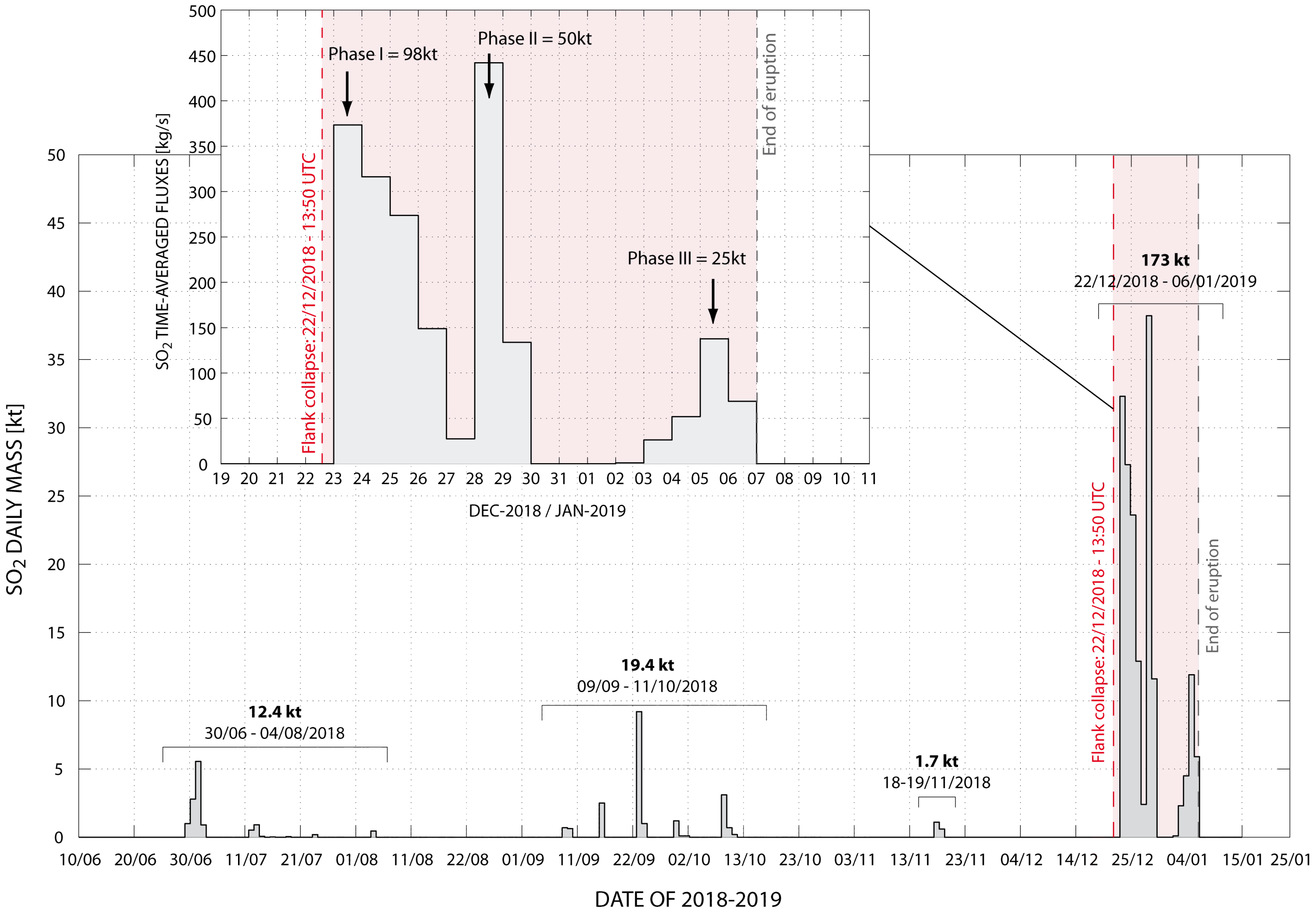

Figure 5: Daily mass of SO_2 calculated from a combination of OMI/Aura and Suomi-NPP/OMPS satellite before the collapse (10/06/2018–22/12/2018) and using Tropomi/Sentinel-5 satellite data after the collapse. Also, we provide SO_2 time-averaged mass fluxes (in kg s^{-1}) for the post-collapse eruption (top panel) clearly showing the 3 different phases of post-collapse degassing.

by PVMBG (https://magma.vsi.esdm.go.id). The three different phases following the collapse total together about 173 ±52 kt of SO_2 injected in the atmosphere.

From SO_2 degassed and measured at the surface, we can retrieve the amount of related magma involved (erupted or not) using petrologic methods [Devine et al. 1984]. For this purpose, we used the sulphur concentration of basaltic andesites reported for the 1883 Krakatau eruption [Mandeville et al. 1996; Fiege et al. 2014; Bani et al. 2015] as a reference. The average sulphur concentration in melt inclusions was found to be ~900 ppm (S_{MI}) while the average dissolved sulphur concentration in matrix glass does not exceed 10 % (S_{MG}): Calculating the concentration difference ($S_{MI} - S_{MG}$), yields an outgassed sulphur concentration of ~810 ppm. Then, from the outgassed sulphur concentration and the airborne SO_2 mass loading we can calculate the volume of parental magma, following:

$$Vol_m = \frac{M_{SO_2} \times 100}{\alpha \rho_m (S_{MI} - S_{MG})} \tag{2}$$

where M_{SO_2} is the total mass of sulphur dioxide measured by satellite (in kg), α is the molar mass ratio SO_2/S and ρ_m is the magma density taken as 2700 km^3 [Bani et al. 2015]. We have thus estimated a DRE parental magma volume of 39.5× 10^6 m^3. Using a bulk porosity of ~40 %, accounting for both erupted tephra and lava flows [Bani et al. 2015], we obtain a bulk magma volume of 65.9×10^6 m^3 (i.e. ~0.066 km^3).

By comparison, the minimum bulk volume of post-collapse pyroclastic deposits emplaced after the collapse in the proximal field (on and around Anak Island) is around ~ 45×10^6 m^3 (Figure 3). From Sentinel-2 data (Figure 4) we observe that the very large majority of this volume was already emplaced on 29 December 2018 (i.e. 7 days only after the collapse). Therefore, this bulk tephra volume can be compared with the sulphur-derived magma volume over phase I and II, solely. As a result, both volumes are quite consistent with values of 45×10^6 m^3 and 56.4×10^6 m^3 for the topographic and petrologic methods, respectively. The 20 % difference can reasonably be explained by the significant amount of tephra fallouts and PDCs lost in the sea and not visible from the topographic analysis. Also, uncertainties on input parameters used in the petrologic method combined with SO_2 retrieval errors may account for this difference. The agreement between both estimations indicates that the amount of magma extruded as tephra during phase I and II is in accordance with the amount of SO_2 emitted and measured in the atmosphere. This makes the existence of external sulphur sources and sinks (e.g. sulphide globules, hydrothermal system storage) quite unlikely, at least during the first two phases (i.e. 22–29/12). Indeed, during the third phase the emission of tephra is limited, as suggested by satellite data of Anak Krakatau island contours, which do not extend after the 29/12 (Figure 4). Although some limited ash plumes remain sporadically visible, e.g. on 05/01, they cannot explain the 25 kt of SO_2 injected (i.e. equivalent to 9.5×10^6 m^3 of bulk magma for 810 ppm of outgassed sulphur) during phase III. Therefore, the SO_2 emissions during Phase III are likely mostly associated with degassing of magma in the shallow system now exposed by the flank collapse.

As most of the erupted material was in the form of tephra, it is interesting to calculate a MER averaged over the entire eruption duration. For this purpose, we take the DRE magma volume estimated from the topographic reconstruction before and after the eruption (Figure 3), which gives a minimum estimate of removed material, and the duration of phase I + II (i.e. 7 days) representing the period of active tephra emissions. This yields a MER time-averaged value of 1.2×10^5 $kg\,s^{-1}$. This is comparable to the September 26, 1997 Soufrière Hills Vulcanian eruption ($\sim 1.5 \times 10^5$ $kg\,s^{-1}$) or to the June 17, 1996 small/moderate Ruapehu eruption ($\sim 1.2 \times 10^5$ $kg\,s^{-1}$) [Gouhier et al. 2019]. Note, however, that in our case the averaged value does not account for variability of the MER possibly occurring during the 7-day averaging period.

3.3 Airborne ash mass and MER

The amount of airborne ash emitted can also be estimated from satellite-based Thermal Infra-Red (TIR) imagery provided weather conditions are favourable. For this purpose, we used data from the geostationary platform Himawari-8 providing full-disc coverage at a 10-minutes time interval (see method section for details). From the improved split window technique using the 3-bands methods [Guéhenneux et al. 2015], we first detected ash-bearing pixels. Then, from inversion of TIR data using radiative transfer modelling we give the ash cloud concentration (in $g\,m^{-2}$), as displayed in Figure 6, and the airborne ash flux Q_a (in $kg\,s^{-1}$).

From Figure 6 we observe that ash emissions can clearly be identified as early as 13:50 UTC, forming a transient high-altitude cloud of ash, coincident with the flank collapse. This first phase of effective ash emission only lasts about 40 minutes (13:50 to 14:30 UTC) and is directly related to the collapse itself. The initial plume seems to have a strong horizontal component reaching 120 km in only one hour. This has been assessed by tracking the evolution of the front edge of the plume over a sequence of Himawari-8 images. This strong horizontal component can possibly be explained by the rapid lateral decompression generated by the flank collapse oriented westward, acting as a blast-generating event. However this mechanism is not likely to be responsible for plume transport on scales of over 100 km in horizontal direction. By contrast, the front edge of the plume will likely propagate downwind at a speed higher than the wind speed as the eruption cloud expands [Sparks et al. 1986], which may also explain the high displacement velocity of the plume captured by satellite.

Note that the volcanic plume has a strong water-rich component (BTD $\gg$0), which is corroborated by daytime observations on 23/12 from detailed optical images (e.g. Terra-MODIS), and possibly preventing an accurate estimate of the ash mass loading. Thus, for this collapse-related plume we estimated a minimum airborne ash flux of $Q_a \sim 1 \times 10^4$ $kg\,s^{-1}$ using the mass difference method. Surprisingly, the ash plume emission stopped between 14:40 and 15:30 UTC, and then resumed forming a sustained high-altitude, water-rich cloud of ash for at least 10 hours. After this point, the content of water/ice in the cloud is so large that ash-containing pixels cannot be detected. This effect is enhanced by the decrease of ash emissions with time. Thus, during the first 10 hours of the post-collapse plume, a much more vertically oriented eruption column developed, still drifting in southwest direction, but at a lower velocity. Indeed, it covered only 65 km in one hour. The airborne ash flux of $Q_a \sim 5 \times 10^3$ $kg\,s^{-1}$ estimated using the mass difference method is only half that obtained during the initial blast. However, airborne ash represents only a fraction of the total amount of tephra emitted at the source vent [e.g. Rose et al. 2000; Webster et al. 2012; Gouhier et al. 2019]. Thus, in order to retrieve the total MER, one can use an empirical formulation including the plume top height [e.g. Sparks et al. 1997; Mastin et al. 2009]. But another method using both the plume height and airborne ash fluxes gives much better results [Gouhier et al. 2019], following in our case:

$$\mathrm{MER} = 25.95 Q_a^{0.72} H^{1.4} \tag{3}$$

where Q_a is the airborne fine ash flux in $kg\,s^{-1}$ and H is the top plume height (a.g.l.) in km. Using this equation, we obtain a MER of 9×10^5 $kg\,s^{-1}$ and 5×10^5 $kg\,s^{-1}$ for the collapse-related plume and the post-collapse plume, respectively (Figure 7). The eruption dynamics of both phases are quite different: the first collapse-related plume resembles a Vulcanian eruption style. The reasons for that are (i) the short duration with impulsive emissions, (ii) and the high MER compared to a moderate plume altitude [Walker 1981; Clarke et al. 2002]. The second phase lasts much longer showing sustained ash emissions over hours (at least) with a strong inter-

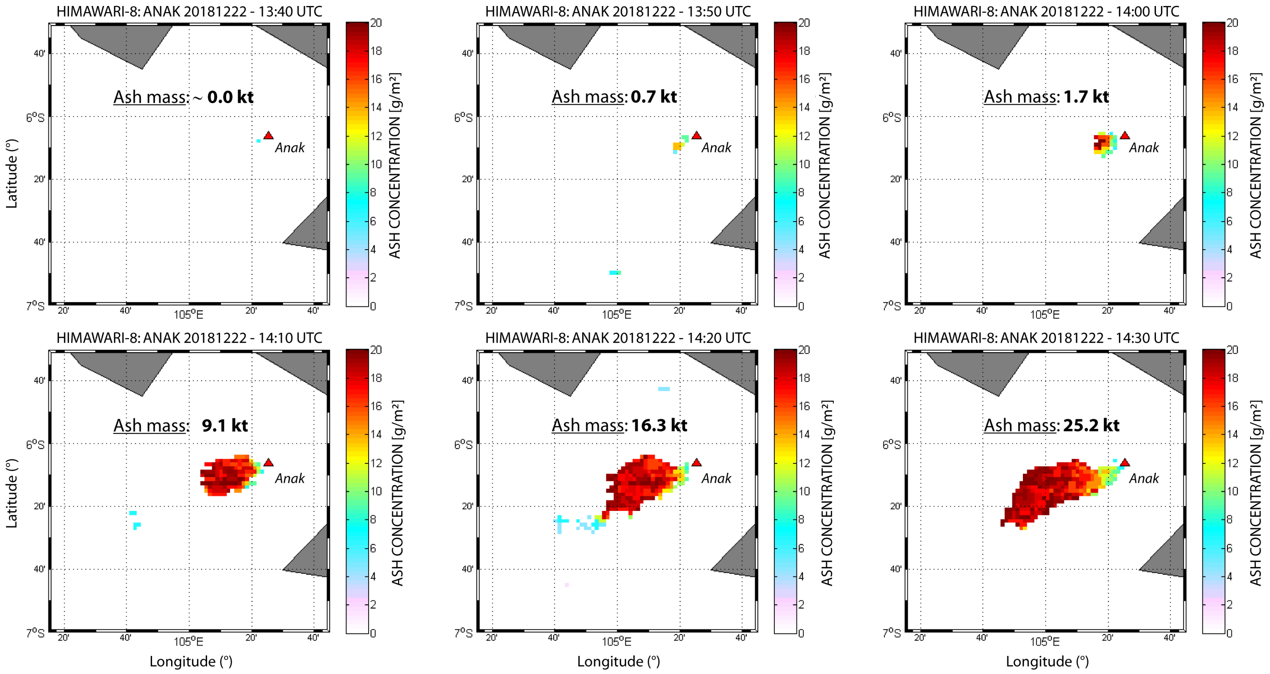

Figure 6: Airborne ash mass concentration (in $\mathrm{g\,m^{-2}}$) retrieved from inversion of thermal infrared images using Himawari-8 data. These images show (i) the onset of the eruption at 13:50 UTC, i.e. synchronous with the collapse, (ii) the ash plume direction at a 10-minutes time resolution and (iii) the increase of the total ash mass loading.

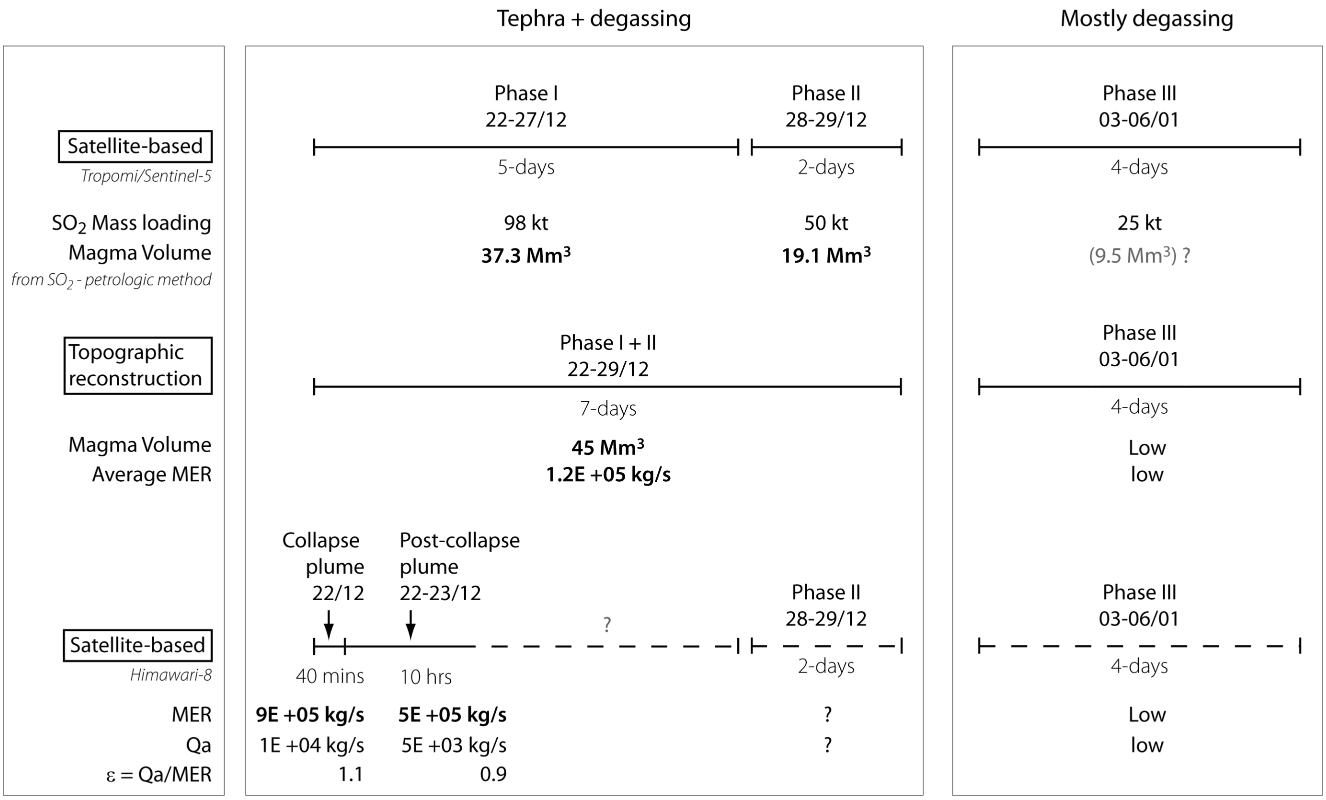

Figure 7: Main parameters for the December 2018–January 2019 eruption of Anak Krakatau summarizing the budget of material emplaced after the collapse from different techniques and spanning different time scales. "*kt*" stands for kilotons, "Mm^3" for millions of cubic meters, "MER" is Mass Eruption Rate, "Q_a" is the airborne fine ash flux, "ϵ" is the ratio between the airborne fine ash flux and the Mass Eruption Rate.

action with sea water. Daytime photos taken on 23 December, for instance, show typical Surtseyan activity (e.g. http://www.oysteinlundandersen.com). Finally, the time-averaged MER (7-days) calculated from the total volume of proximal tephra and estimated at 1.2×10^5 kg s^{-1} compares rather well with the above estimations of MER (Figure 7). Logically, the initial MER is the much higher ($\sim$ 10 times), although it is of short duration (40 min). Then the post-collapse MER, within the first 10 hours only, is still higher ($\sim$ 5 times). This leads us to believe that the MER during the last 6.5 days decreased drastically and that even periods of complete quiescence in ash emissions were perhaps possible.

4 Conclusions

The December 22, 2018 collapse-related eruption of Anak Krakatau occurred after a period of 6 months of enhanced volcanic activity and marks the climactic phase of a new eruptive cycle. Although Anak Krakatau is one of Indonesia's most active volcanoes very little information on gas emissions was available [Bani et al. 2015]. The results given in this study can be analysed in a broader perspective. Indeed, the volume of the subaerial volcanic cone of Anak Krakatau, built since 1927, has been estimated by Bani et al. [2015] during a field campaign in 2014 to be $\sim 320 \times 10^6$ m^3 (equivalent annual growth rate of 3.8×10^6 m^3 yr^{-1}). This means that the minimum estimates of the bulk volume of tephra emplaced during the 22–29/12/2018 period (45×10^6 m^3 during Phase I + II) represents the equivalent of $\sim$ 12 years of cone growth. Also, the total amount of SO_2 emitted for the whole eruption duration (173±52 kt) is significantly larger than the $\sim$70 kt yr^{-1} of SO_2 recorded at Anak Krakatau in 2014 by UV airborne spectrometer [Bani et al. 2015]. This means that the volcanic eruption produced the equivalent of 2.5 years of passive SO_2 emissions in only 11 days.

Finally, this study also shows the importance of long-term and continuous monitoring (deformation, degassing, etc.) of small volcanic islands. Collapse-related eruptions are difficult to predict, and rapid response to eruptive crises is essential for hazard mitigation. In this respect, the use of thermal infrared data onboard geostationary platforms is valuable, as it allows night and day acquisition at a time interval of 10 minutes. This is particularly important for air traffic as airborne ash may cause serious damage to aircraft potentially having dramatic consequences [Casadevall 1994].

Acknowledgements

The authors appreciated the relevant contribution of two anonymous reviewers. This is Laboratory of Excellence ClerVolc contribution no. 360. We also thank James Reynolds (Earth Uncut) for providing drone footage of Anak volcano.

Author contributions

MG processed and analyzed the Tropomi/Sentinel-5, Aura/OMI, Suomi-NPP/OMPS for SO2. MG processed `HYSPLIT` trajectory for the plume height and velocity determination. MG made the inversion of Infrared Himawari-8 satellite data from forward radiative transfer modelling. RP processed and analysed digital elevation models and satellite data (Sentinel-2 and PlanetScope). Both authors contributed to the preparation of the manuscript.

Data availability

Sentinel images are available on the Copernicus Open Access Hub (scihub.copernicus.eu). PlanetScope images (www.planet.com) were obtained by joining the Education and Research Program of the Planet Team (2017). Himawari-8 data, operated by the Japan Meteorological Agency (JMA), are available from the Centre for Environmental Remote Sensing (CEReS) using gridded data products.

References

Allard, P. (1997). "Endogenous magma degassing and storage at Mount Etna". *Geophysical Research Letters* 24.17, pp. 2219–2222. doi: 10.1029/97gl02101.

Bani, P., A. Normier, C. Bacri, P. Allard, H. Gunawan, M. Hendrasto, Surono, and V. Tsanev (2015). "First measurement of the volcanic gas output from Anak Krakatau, Indonesia". *Journal of Volcanology and Geothermal Research* 302, pp. 237–241. doi: 10.1016/j.jvolgeores.2015.07.008.

Beirle, S., C. Hörmann, M. P. de Vries, S. Dörner, C. Kern, and T. Wagner (2014). "Estimating the volcanic emission rate and atmospheric lifetime of SO&ltsub&gt2&lt/sub&gt from space: a case study for Kılauea volcano, Hawai'i". *Atmospheric Chemistry and Physics* 14.16, pp. 8309–8322. doi: 10.5194/acp-14-8309-2014.

Carazzo, G. and A. M. Jellinek (2013). "Particle sedimentation and diffusive convection in volcanic ash-clouds". *Journal of Geophysical Research: Solid Earth* 118.4, pp. 1420–1437. doi: 10.1002/jgrb.50155.

Carey, S. N. and H. Sigurdsson (1982). "Influence of particle aggregation on deposition of distal tephra from the May 18, 1980, eruption of Mount St. Helens volcano". *Journal of Geophysical Research: Solid Earth* 87.B8, pp. 7061–7072. doi: 10.1029/jb087ib08p07061.

Carn, S. A., A. J. Krueger, G. J. S. Bluth, S. J. Schaefer, N. A. Krotkov, I. M. Watson, and S. Datta (2003). "Volcanic eruption detection by the Total Ozone Mapping Spectrometer (TOMS) instruments: a 22-year record of sulphur dioxide and ash emissions". *Geological Society, London, Special Publications* 213.1, pp. 177–202. doi: 10.1144/gsl.sp.2003.213.01.11.

Carn, S. A. and F. J. Prata (2010). "Satellite-based constraints on explosive SO2release from Soufrière Hills Volcano, Montserrat". *Geophysical Research Letters* 37.19. doi: 10.1029/2010gl044971.

Casadevall, T. J. (1994). *Volcanic ash and aviation safety: proceedings of the First international symposium on Volcanic ash and aviation safety*. Tech. rep. doi: 10.3133/b2047.

Clarke, A. B., B. Voight, A. Neri, and G. Macedonio (2002). "Transient dynamics of vulcanian explosions and column collapse". *Nature* 415.6874, pp. 897–901. doi: 10.1038/415897a.

Corradini, S., C. Spinetti, E. Carboni, C. Tirelli, M. F. Buongiorno, S. Pugnaghi, and G. Gangale (2008). "Mt. Etna tropospheric ash retrieval and sensitivity analysis using Moderate Resolution Imaging Spectroradiometer measurements". *Journal of Applied Remote Sensing* 2.1, p. 023550. doi: 10.1117/1.3046674.

Deplus, C., S. Bonvalot, D. Dahrin, M. Diament, H. Harjono, and J. Dubois (1995). "Inner structure of the Krakatau volcanic complex (Indonesia) from gravity and bathymetry data". *Journal of Volcanology and Geothermal Research* 64.1-2, pp. 23–52. doi: 10.1016/0377-0273(94)00038-i.

Devine, J. D., H. Sigurdsson, A. N. Davis, and S. Self (1984). "Estimates of sulfur and chlorine yield to the atmosphere from volcanic eruptions and potential climatic effects". *Journal of Geophysical Research: Solid Earth* 89.B7, pp. 6309–6325. doi: 10.1029/jb089ib07p06309.

Durant, A. J. and W. I. Rose (2009). "Sedimentological constraints on hydrometeor-enhanced particle deposition: 1992 Eruptions of Crater Peak, Alaska". *Journal of Volcanology and Geothermal Research* 186.1-2, pp. 40–59. doi: 10.1016/j.jvolgeores.2009.02.004.

Edmonds, M., C. Oppenheimer, D. Pyle, R. Herd, and G. Thompson (2003). "SO2 emissions from Soufrière Hills Volcano and their relationship to conduit permeability, hydrothermal interaction and degassing regime". *Journal of Volcanology and Geothermal Research* 124.1-2, pp. 23–43. doi: 10.1016/s0377-0273(03)00041-6.

Fiege, A., F. Holtz, N. Shimizu, C. W. Mandeville, H. Behrens, and J. L. Knipping (2014). "Sulfur isotope fractionation between fluid and andesitic melt: An experimental study". *Geochimica et Cosmochimica Acta* 142, pp. 501–521. doi: 10.1016/j.gca.2014.07.015.

Gauthier, P.-J., O. Sigmarsson, M. Gouhier, B. Haddadi, and S. Moune (2016). "Elevated gas flux and trace metal degassing from the 2014-2015 fissure eruption at the Bárðarbunga volcanic system, Iceland". *Journal of Geophysical Research: Solid Earth* 121.3, pp. 1610–1630. doi: 10.1002/2015jb012111.

Giachetti, T., R. Paris, K. Kelfoun, and B. Ontowirjo (2012). "Tsunami hazard related to a flank collapse of Anak Krakatau Volcano, Sunda Strait, Indonesia". *Geological Society, London, Special Publications* 361.1, pp. 79–90. doi: 10.1144/sp361.7.

Gouhier, M., J. Eychenne, N. Azzaoui, A. Guillin, M. Deslandes, M. Poret, A. Costa, and P. Husson (2019). "Low efficiency of large volcanic eruptions in transporting very fine ash into the atmosphere". *Scientific Reports* 9.1. doi: 10.1038/s41598-019-38595-7.

Guéhenneux, Y., M. Gouhier, and P. Labazuy (2015). "Improved space borne detection of volcanic ash for real-time monitoring using 3-Band method". *Journal of Volcanology and Geothermal Research* 293, pp. 25–45. doi: 10.1016/j.jvolgeores.2015.01.005.

Kementerian Energi dan Sumber Daya Mineral [Ministry of Energy and Mineral Resources] (2018). *Surat Kaban Laporan Gunung Anak Krakatau – Report on the activity of Anak Krakatau volcano, 31 December 2018*. Tech. rep.

Krotkov, N. A., M. R. Schoeberl, G. A. Morris, S. Carn, and K. Yang (2010). "Dispersion and lifetime of the SO2cloud from the August 2008 Kasatochi eruption". *Journal of Geophysical Research* 115. doi: 10.1029/2010jd013984.

Lee, C., R. V. Martin, A. van Donkelaar, G. O'Byrne, N. Krotkov, A. Richter, L. G. Huey, and J. S. Holloway (2009). "Retrieval of vertical columns of sulfur dioxide from SCIAMACHY and OMI: Air mass factor algorithm development, validation, and error analysis". *Journal of Geophysical Research* 114.D22. doi: 10.1029/2009jd012123.

Lopez, T., S. Carn, C. Werner, D. Fee, P. Kelly, M. Doukas, M. Pfeffer, P. Webley, C. Cahill, and D. Schneider (2013). "Evaluation of Redoubt Volcano's sulfur dioxide emissions by the Ozone Monitoring Instrument". *Journal of Volcanology and Geothermal Research* 259, pp. 290–307. doi: 10.1016/j.jvolgeores.2012.03.002.

Mandeville, C. W., S. Carey, and H. Sigurdsson (1996). "Magma mixing, fractional crystallization and volatile degassing during the 1883 eruption of Krakatau volcano, Indonesia". *Journal of Volcanology and Geothermal Research* 74.3-4, pp. 243–274. doi: 10.1016/s0377-0273(96)00060-1.

Manzella, I., C. Bonadonna, J. C. Phillips, and H. Monnard (2015). "The role of gravitational instabilities in deposition of volcanic ash". *Geology* 43.3, pp. 211–214. DOI: 10.1130/g36252.1.

Mastin, L. et al. (2009). "A multidisciplinary effort to assign realistic source parameters to models of volcanic ash-cloud transport and dispersion during eruptions". *Journal of Volcanology and Geothermal Research* 186.1-2, pp. 10–21. DOI: 10.1016/j.jvolgeores.2009.01.008.

McCormick, B. T., M. Herzog, J. Yang, M. Edmonds, T. A. Mather, S. A. Carn, S. Hidalgo, and B. Langmann (2014). "A comparison of satellite- and ground-based measurements of SO2emissions from Tungurahua volcano, Ecuador". *Journal of Geophysical Research: Atmospheres* 119.7, pp. 4264–4285. DOI: 10.1002/2013jd019771.

Prata, A. J. (1989a). "Infrared radiative transfer calculations for volcanic ash clouds". *Geophysical Research Letters* 16.11, pp. 1293–1296. DOI: 10.1029/gl016i011p01293.

Prata, A. J. and I. F. Grant (2001). "Retrieval of microphysical and morphological properties of volcanic ash plumes from satellite data: Application to Mt Ruapehu, New Zealand". *Quarterly Journal of the Royal Meteorological Society* 127.576, pp. 2153–2179. DOI: 10.1002/qj.49712757615.

Prata, A. (1989b). "Observations of volcanic ash clouds in the 10-12 μm window using AVHRR/2 data". *International journal of Remote sensing* 10.4-5, pp. 751–761. DOI: 10.1080/01431168908903916.

Rodrıguez, L. A., I. M. Watson, M. Edmonds, G. Ryan, V. Hards, C. M. Oppenheimer, and G. J. Bluth (2008). "SO2 loss rates in the plume emitted by Soufrière Hills volcano, Montserrat". *Journal of Volcanology and Geothermal Research* 173.1-2, pp. 135–147. DOI: 10.1016/j.jvolgeores.2008.01.003.

Rose, W. I., G. J. S. Bluth, and G. G. J. Ernst (2000). "Integrating retrievals of volcanic cloud characteristics from satellite remote sensors: a summary". *Philosophical Transactions of the Royal Society of London. Series A: Mathematical, Physical and Engineering Sciences* 358.1770. Ed. by P. Francis, J. Neuberg, and R. S. J. Sparks, pp. 1585–1606. DOI: 10.1098/rsta.2000.0605.

Schneider, D. J., W. I. Rose, L. R. Coke, G. J. S. Bluth, I. E. Sprod, and A. J. Krueger (1999). "Early evolution of a stratospheric volcanic eruption cloud as observed with TOMS and AVHRR". *Journal of Geophysical Research: Atmospheres* 104.D4, pp. 4037–4050. DOI: 10.1029/1998jd200073.

Sigmarsson, O., B. Haddadi, S. Carn, S. Moune, J. Gudnason, K. Yang, and L. Clarisse (2013). "The sulfur budget of the 2011 Grımsvötn eruption, Iceland". *Geophysical Research Letters* 40.23, pp. 6095–6100. DOI: 10.1002/2013gl057760.

Sparks, R. J., J. G. Moore, and C. J. Rice (1986). "The initial giant umbrella cloud of the May 18th, 1980, explosive eruption of Mount St. Helens". *Journal of Volcanology and Geothermal Research* 28.3-4, pp. 257–274. DOI: 10.1016/0377-0273(86)90026-0.

Sparks, R. S. J., M. Bursik, S. Carey, J. Gilbert, L. Glaze, H. Sigurdsson, and A. Woods (1997). *Volcanic plumes*. Wiley.

Stevenson, J., S. Millington, F. Beckett, G. Swindles, and T. Thordarson (2015). "Big grains go far: understanding the discrepancy between tephrochronology and satellite infrared measurements of volcanic ash". *Atmospheric Measurement Techniques* 8.5, pp. 2069–2091. DOI: 10.5194/amt-8-2069-2015.

Theys, N. et al. (2013). "Volcanic SO2 fluxes derived from satellite data: a survey using OMI, GOME-2, IASI and MODIS". *Atmospheric Chemistry and Physics* 13.12, pp. 5945–5968. DOI: 10.5194/acp-13-5945-2013.

Walker, G. P. (1981). "Generation and dispersal of fine ash and dust by volcanic eruptions". *Journal of Volcanology and Geothermal Research* 11.1, pp. 81–92. DOI: 10.1016/0377-0273(81)90077-9.

Watson, I., V. Realmuto, W. Rose, A. Prata, G. Bluth, Y. Gu, C. Bader, and T. Yu (2004). "Thermal infrared remote sensing of volcanic emissions using the moderate resolution imaging spectroradiometer". *Journal of Volcanology and Geothermal Research* 135.1-2, pp. 75–89. DOI: 10.1016/j.jvolgeores.2003.12.017.

Webster, H. N. et al. (2012). "Operational prediction of ash concentrations in the distal volcanic cloud from the 2010 Eyjafjallajökull eruption". *Journal of Geophysical Research: Atmospheres* 117.D20. DOI: 10.1029/2011jd016790.

Wen, S. and W. I. Rose (1994). "Retrieval of sizes and total masses of particles in volcanic clouds using AVHRR bands 4 and 5". *Journal of Geophysical Research* 99.D3, p. 5421. DOI: 10.1029/93jd03340.

Yang, K., N. A. Krotkov, A. J. Krueger, S. A. Carn, P. K. Bhartia, and P. F. Levelt (2007). "Retrieval of large volcanic SO2 columns from the Aura Ozone Monitoring Instrument: Comparison and limitations". *Journal of Geophysical Research: Atmospheres* 112.D24. DOI: 10.1029/2007JD008825.

A Appendix 1

Supplementary figures (Figure A1 and Figure A2).

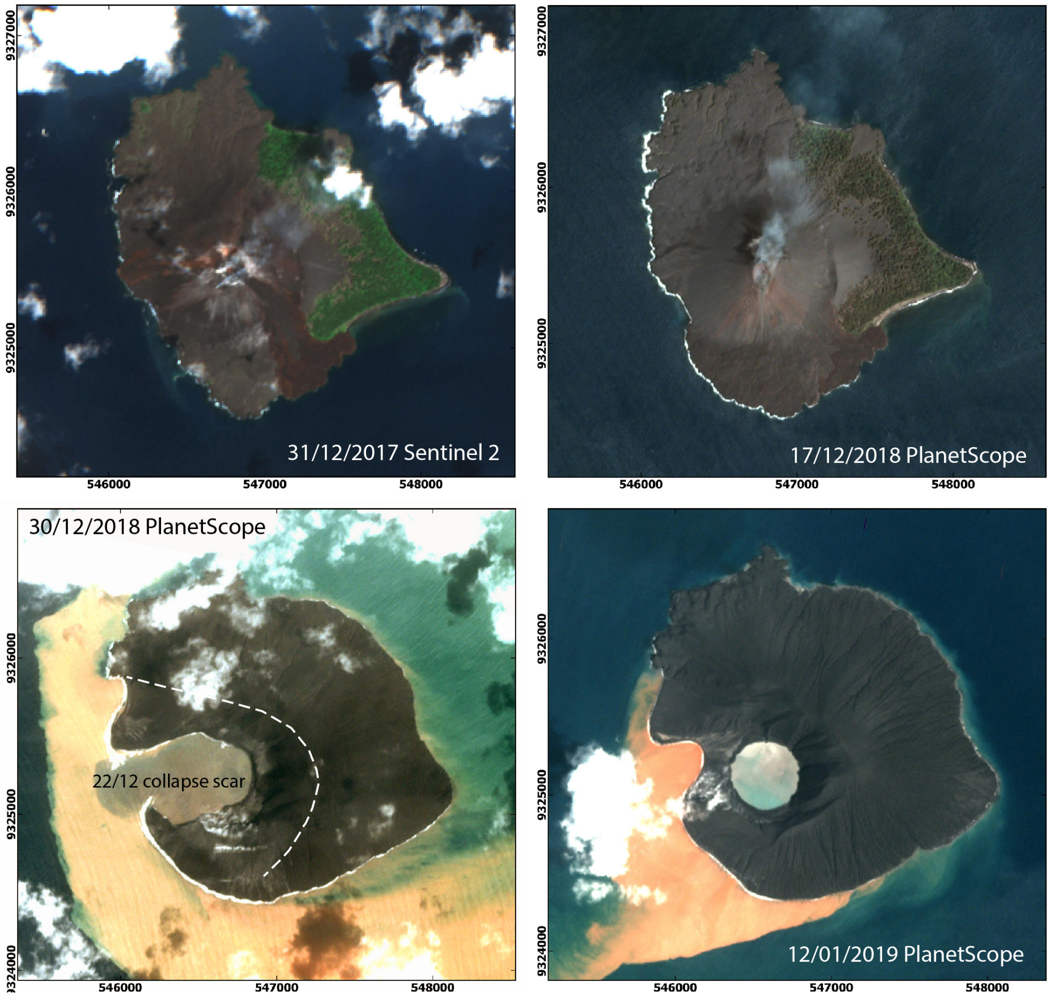

Figure A1: Evolution of the island of Anak Krakatau from December 2017 to January 2019, as seen from satellite imagery (Sentinel-2 and PlanetScope).

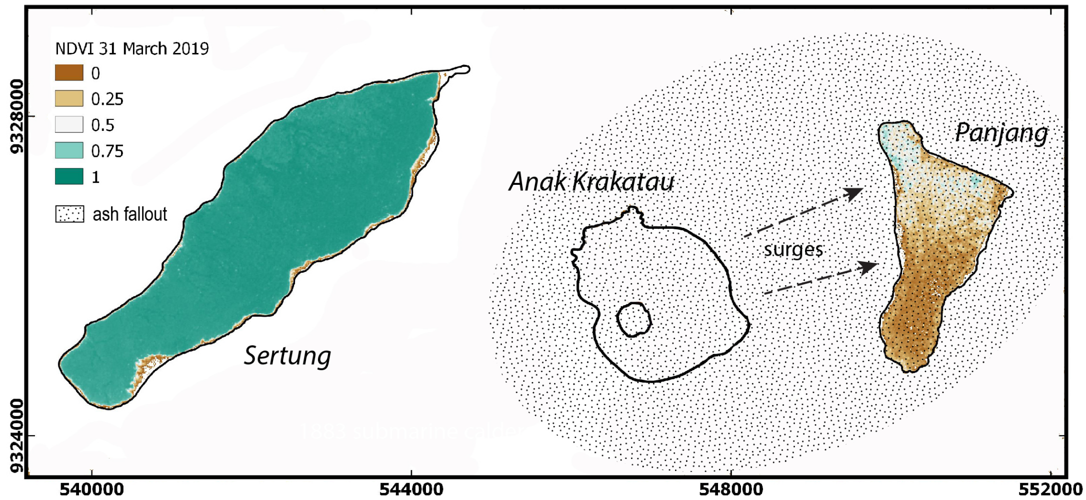

Figure A2: NDVI (Normalized Difference Vegetation Index) calculated from bands 4 (red) and 8 (NIR) of a Sentinel-2B image captured on 31 March 2019, showing loss of vitality of vegetation on Panjang Island due to successive ash plume fallouts and pyroclastic surges after the 22 December 2018 flank collapse (as shown on photographs captured on 23 December 2018).

Journal of Volcanology and Geothermal Research 356 (2018) 75–89

Contents lists available at ScienceDirect

Journal of Volcanology and Geothermal Research

journal homepage: www.elsevier.com/locate/jvolgeores

Observation of SO_2 degassing at Stromboli volcano using a hyperspectral thermal infrared imager

Jean-François Smekens [a,b,*], Mathieu Gouhier [a]

[a] Université Clermont Auvergne, CNRS, IRD, OPGC, Laboratoire Magmas et Volcans, F-63000 Clermont-Ferrand, France
[b] Northern Arizona University, Department of Physics and Astronomy, Flagstaff, AZ, USA

ARTICLE INFO

Article history:
Received 28 April 2017
Received in revised form 8 December 2017
Accepted 25 February 2018
Available online 27 February 2018

Keywords:
Remote sensing
Hyperspectral imager
Thermal infrared
Sulfur dioxide
Volcanic plumes
Stromboli

ABSTRACT

Thermal infrared (TIR) imaging is a common tool for the monitoring of volcanic activity. Broadband cameras with increasing sampling frequency give great insight into the physical processes taking place during effusive and explosive event, while Fourier transform infrared (FTIR) methods provide high resolution spectral information used to assess the composition of volcanic gases but are often limited to a single point of interest. Continuing developments in detector technology have given rise to a new class of hyperspectral imagers combining the advantages of both approaches. In this work, we present the results of our observations of volcanic activity at Stromboli volcano with a ground-based imager, the Telops Hyper-Cam LW, when used to detect emissions of sulfur dioxide (SO_2) produced at the vent, with data acquired at Stromboli volcano (Italy) in early October of 2015. We have developed an innovative technique based on a curve-fitting algorithm to quickly extract spectral information from high-resolution datasets, allowing fast and reliable identification of SO_2. We show in particular that weak SO_2 emissions, such as inter-eruptive gas puffing, can be easily detected using this technology, even with poor weather conditions during acquisition (e.g., high relative humidity, presence of fog and/or ash). Then, artificially reducing the spectral resolution of the instrument, we recreated a variety of commonly used multispectral configurations to examine the efficiency of four qualitative SO_2 indicators based on simple Brightness Temperature Difference (BTD). Our results show that quickly changing conditions at the vent – including but not limited to the presence of summit fog – render the establishment of meaningful thresholds for BTD indicators difficult. Building on those results, we propose recommendations on the use of multispectral imaging for SO_2 monitoring and routine measurements from ground-based instruments.

1. Introduction

Volatiles are a crucial component of volcanic systems. The explosivity of an eruption in particular, depends in large part on the amount and composition of volatiles contained in the erupted magma, and the relative ease with which they can be exsolved from the melt and released at the surface. For that reason, measurements of volcanic degassing have been an integral part of monitoring networks at restless volcanoes for the past 40 years. Changes in degassing rates may reflect changes in magma supply rate and/or in the permeability of the system and help inform short-term forecast of ongoing or pending eruptions (e.g., de Moor et al., 2015; Fischer et al., 1994; Watson et al., 2000). In addition, the composition of volcanic gases offers insight into physical processes occurring at depth (e.g., Burton et al., 2007; Vergniolle and Jaupart, 1990). Although it usually constitutes <5% of the total gases emitted (Oppenheimer et al., 2013) sulfur dioxide (SO_2) is virtually absent from the background atmosphere, which makes it an ideal target gas to monitor volcanic emissions. The shallow exsolution depth of SO_2, compared to carbon dioxide (CO_2) for instance, makes it a good indicator of the presence of a degassing magmatic body near the surface, and therefore provides a tool to forecast eruptions. Molecular SO_2 presents absorption features in various regions of the electromagnetic spectrum. Particularly strong absorptions appear in the ultraviolet (UV) and thermal infrared (TIR) range. Therefore, a large variety of spectroscopic methods have been developed to detect and quantify volcanic SO_2 degassing in those spectral ranges.

The SO_2 absorption features in the UV are strong, and mainly associated with electronic transition. However, remote sensing measurements in the UV require the sun as a source of radiation, which limits their use to daytime only. A number of instruments onboard satellite platforms and operating in the UV can be used to detect emissions from space. They are typically instruments that were originally developed for ozone monitoring (which presents absorption features at similar wavelengths) such as the Total Ozone Monitoring Satellite (TOMS), and more recently the Ozone Monitoring Instrument (OMI), for which specialized algorithms have been developed (e.g., Krotkov et al., 2006) and used to quantify volcanic SO_2 loading worldwide (e.g., Carn et al.,

* Corresponding author.
E-mail address: Jean-Francois.Smekens@nau.edu (J.-F. Smekens).

https://doi.org/10.1016/j.jvolgeores.2018.02.018

2003, 2008, 2016). Ground-based instruments that exploit the same absorption features also exist, such as the Correlation Spectrometer (COPSEC) (Stoiber et al., 1983) and Differential Optical Absorption Spectroscopy methods (DOAS) (Galle et al., 2003) and are still extensively used (e.g., Arellano et al., 2008; Barrancos et al., 2008; Menard et al., 2014; Mori et al., 2013). In the last decade, UV imaging techniques have emerged, commonly referred to as SO_2 cameras (Bluth et al., 2007; Mori and Burton, 2006). They allow quantification of the SO_2 column amount for every pixel in a 2D image, and are quickly becoming a common tool for gas monitoring (e.g., Aiuppa et al., 2015; Barnie et al., 2015; Moussallam et al., 2016; Nadeau et al., 2015; Pering et al., 2014; Smekens et al., 2015).

At the other end of the electromagnetic spectrum, infrared spectroscopy is an invaluable diagnostic tool to determine the composition of solid and gaseous materials, and has also been used extensively for volcano monitoring. At typical eruption temperatures (1000–1500 K), most magmas emit electromagnetic radiation with a peak located at a wavelength of 3–4 μm, otherwise designated as the Middle Wave Infrared (MWIR) spectral range. At lower terrestrial or atmospheric temperatures (200–350 K), the maximum emission is located in the Thermal Infrared (TIR) region of the spectrum (7–14 μm). Those natural IR emitters are used opportunistically as radiation sources for the detection and quantification of SO_2. Indeed, the SO_2 molecule presents two distinct absorption features in the TIR spectral region caused by vibrational transitions: a weak feature centred around 1150 cm^{-1} (v2 ~ 8.6 μm) and a stronger feature centred around 1400 cm^{-1} (v3 ~ 7.3 μm). A very large number of sensors on-board satellite platforms operate at those wavelengths, and are used extensively to detect, track and quantify volcanic SO_2 emissions worldwide (e.g., Carn et al., 2005; Corradini et al., 2009; Karagulian et al., 2010; Prata and Kerkmann, 2007; Watson et al., 2004). Spaceborne measurements in the TIR, where radiation is of relatively low energy, offer a range of capabilities due to variable sensor characteristics and orbital specifications. However, the waveband with the stronger absorption feature (v3) sits outside the atmospheric window and cannot be exploited at low altitude, and is mostly relevant in the upper troposphere and lower stratosphere (UTLS). Given that the summit of Stromboli, our target volcano, stands at 926 m, we will focus on the v2 feature only, which lies within an atmospheric window with a high transmissivity factor (i.e., water vapor essentially), allowing SO_2 detection in the planetary boundary layer (PBL). Both wavebands and their associated retrieval methods have been widely used on SO_2 plumes either in the UTLS (e.g., Doutriaux-Boucher and Dubuisson, 2009; Thomas et al., 2011; Urai, 2004; Watson et al., 2004), or in the PBL (e.g., Pugnaghi et al., 2006; Urai, 2004). In parallel, many ground-based instruments operating in the TIR have been developed. While broadband infrared imaging has proved ineffective for SO_2 detection, hyperspectral instruments have shown very strong capabilities in that regard. Indeed, detailed studies of the composition of volcanic plumes have been conducted with Open-Path Fourier Transform Infrared (OP-FTIR) instruments that produce high-resolution spectra over a narrow field of view (e.g., Allard et al., 2005; Burton et al., 2007; Duffell et al., 2001; La Spina et al., 2015). Multispectral imaging instruments, although offering a good compromise between spectral and spatial resolution at a relatively low cost, are relatively new and uncommon in the field of volcanology. One existing example is the Cyclops camera, an instrument developed by Prata and Bernardo (2014), that uses bandpass filters (see Fig. 1) mounted on a wheel rotating ahead of a broadband TIR sensor (micro-bolometer array), providing near-simultaneous images of a scene at different wavelengths. This instrument has been successfully tested at Etna volcano for the detection and quantification of SO_2 emissions, and was later deployed at Karymsky volcano for use in a multi-disciplinary study of volcanic activity (Lopez et al., 2013). Note that we are currently developing a novel instrument at the Observatoire de Physique du Globe de Clermont-Ferrand (OPGC) for laboratory experiments, that consists of a synchronized dual camera system, each of which is equipped with a narrow bandpass filter, allowing simultaneous acquisition of two images at different wavelengths. Finally, a hyperspectral imager using an uncooled micro-bolometer array with the specific aim of measuring SO_2 in volcanic plumes has recently been tested, and has already shown promising capabilities (Gabrieli et al., 2016).

In this paper, we present results from the observation of SO_2 degassing during persistent volcanic activity at Stromboli volcano with the Telops Hyper-Cam, a commercially available hyperspectral imager. Stromboli is a basaltic stratovolcano in the Aeolian island chain, located north of Sicily. Its activity encloses a range of behaviors, from continuous passive degassing (Allard et al., 1994) to occasional larger eruptions with effusive episodes and Vulcanian paroxysmal explosions (Calvari et al., 2006; Pistolesi et al., 2011). The volcano, however, is better known for a style of eruption which has been persistent at Stromboli since at least 1000 CE, and consisting of intermittent small explosions every few tens of minutes (Rosi et al., 2000, 2013). Produced by a mechanism of bubble coalescence starting in the magma chamber (Jaupart and Vergniolle, 1988), these explosions can manifest in a variety of ways at the surface, from short fountains of incandescent ballistics to weak ash plumes (Patrick et al., 2007). The summit area is host to several active vents, each characterized by a distinct type of activity. At the time of our measurements, the Northeast craters (NE1 and NE2)

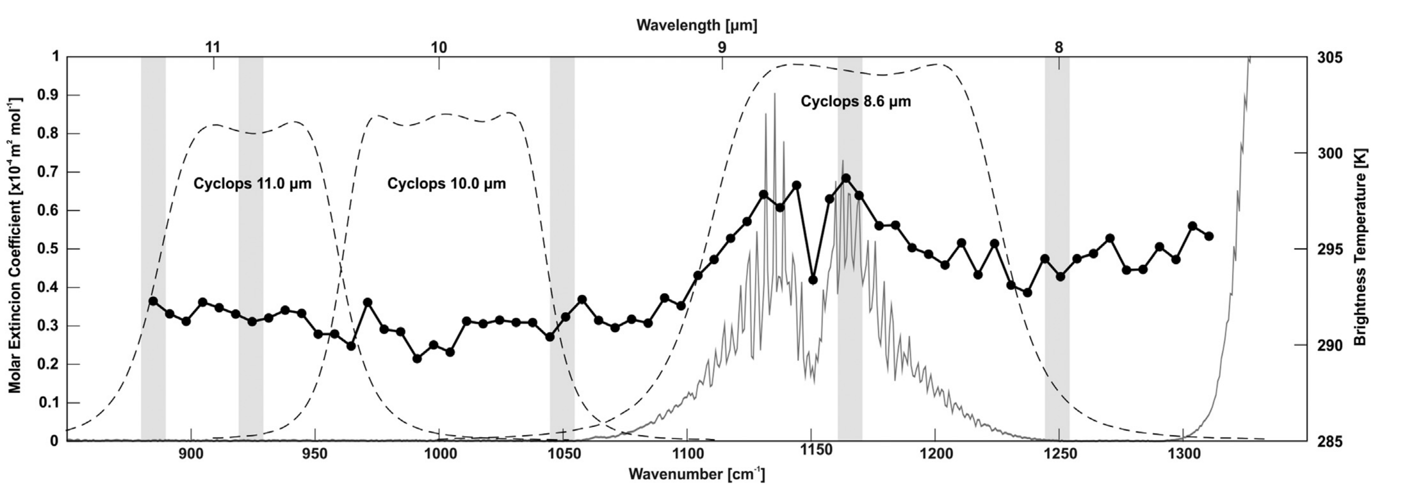

Fig. 1. SO_2 absorption spectrum and imaging instruments filter responses in the thermal infrared. Laboratory measurement of the molar absorption cross-section of SO_2 (Vandaele et al., 1994) (light gray, y-axis on the left) and brightness temperature spectrum of a typical SO_2-bearing pixel extracted from a Hyper-Cam data cube at moderate resolution (black circles, y-axis on the right). Also shown are the bandwidths of bandpass filters on the Cyclops ground-based camera operating at that wavelength range (dotted lines). Shaded areas represent the spectral bandwidths used for bi-spectral indices in this work.

exhibited the typical Strombolian activity, with small gas bursts accompanied by the ejection of ballistics every 5–10 min, while the Southwest crater (SW) produced less frequent ash-rich explosions. The central crater was passively degassing in a continuous manner. The TELOPS Hyper-Cam LW follows the principle of the Michelson interferometer and equipped of a cooled Mercury Cadmium Telluride (MCT) detector array. This instrument offers state-of-the-art temporal and spectral resolution, and allows us to explore ways in which spectral information can be extracted to inform algorithms of SO_2 detection with instruments of lower resolution.

2. Data acquisition

2.1. The instrument: Telops Hyper-Cam-LW

The data presented in this work was acquired with the Telops Hyper-Cam LW (Fig. 2). This hyperspectral imager operates in the thermal infrared (850–1300 cm^{-1} or 7.7–11.8 μm). Following the principle of the Michelson interferometer, incoming radiation is split into two beams using a beam splitter. One beam is sent towards a fixed mirror while the other is sent in a perpendicular direction towards a moving mirror. Each of those is then reflected back towards the beam splitter and onto a Mercury Cadmium Telluride (MCT) detector array. The movement of the mirror produces interferences when the two arms are recombined. Each pixel of the detector array records the intensity of the radiation for each position of the moving mirror, producing data cubes. These data cubes are then processed using a Fourier Transform Infrared (FTIR) technique to produce a continuous radiance spectrum for each individual pixel. Fig. 3 shows an illustration of such a data cube. The data cube can be divided into 2D images representing the radiation intensity for a given wavelength (top panel). Conversely, a continuous radiation spectrum can be extracted for any given pixel, which can then be converted to a brightness temperature spectrum following Planck's law. The instrument's field of view (without any entry optics) is $6.4 \times 5.1°$, projected on a 320×256 pixel sensor. The field of view can be adapted with various telescopes, either for target framing requirements or to increase temporal and/or spectral resolutions performance. The operating resolutions of the instrument are defined by the speed of the moving mirror, which can be adjusted. The intensity of the radiation reaching the sensor is measured at fixed intervals during the movement of the mirror. There is a tradeoff between spectral and temporal resolution when using a moving mirror to produce interferograms. Data cubes with higher spectral resolutions are acquired over a longer period of time.

2.2. Viewing geometry

We acquired data sets from two different vantage points on the island of Stromboli (see Fig. 4). The terrace of the restaurant l'Osservatorio, located at the southern end of the island and on the edge of the Sciara del Fuoco, offers a direct view at the NE craters, while the central and SW craters are not directly visible. The Osservatorio viewpoint is located ~1800 m from the NE crater (horizontal distance) and offers a line of sight with an almost straight N azimuth and a 23° viewing angle (slant distance = 1955 m). Datasets from this vantage point were acquired over two days (October 1st and 2nd, 2015). On October 3rd, 2015, we brought the instrument to the summit of Stromboli and acquired data from the Roccette viewpoint. Located on the edge of the detachment scarp at the top of the Sciara de Fuoco, Roccette is one of several shelters existing at the summit rim, and provides an unrestricted view on the NE craters, at a distance of 400 m and almost level with the vents (slight viewing angle of −2°). At both locations, several data sequences were acquired spanning durations of 5–45 min, with varying spectral configurations.

We tested spectral resolutions ranging from 0.5 cm^{-1} to 32 cm^{-1}, corresponding to frequencies of acquisition ranging from 0.2 Hz (one data cube every 5 s) to 10 Hz (10 data cubes per second). Hereafter we mostly present results with what we found to be the most useful configuration: full frame sensor, fitted with a wide angle 0.25× telescope to provide the most contextual information, and with a spectral resolution of ~6.6 cm^{-1}. When observing dynamic phenomena such as the rapid changes in gas emissions and frequent explosions at Stromboli, we decided to favor temporal resolution over spectral resolution. With the spectral resolution set at 6.6 cm^{-1}, which is far sufficient to detect SO_2, we were able to attain a sampling frequency of ~0.6 Hz (i.e., one data cube every ~1.66 s). Over the 3 days of acquisition, the weather conditions were quite similar with a mild cloud cover accompanied by transient but thick water vapor plumes, particularly during daytime, and rapidly condensing around the summit in large hazy clouds of water droplets. Acquisitions carried out during nighttime conditions usually show better weather conditions with a homogeneous and cold background, and are favorable to high-quality data acquisition. Note that simultaneous measurements were made with an SO_2-camera, with the goal of comparing the two datasets. However, UV methods failed to detect SO_2 for most of the observation periods, as the plume was masked by low-altitude clouds around the summit, and ultimately proved unreliable in the specific weather conditions encountered during our measurement campaign. This underlines another significant advantage of IR methods over UV, even during daytime observation.

Spectral range	850-1300 cm^{-1} (7.7-11.8 μm)
Spectral resolution	0.25-32 cm^{-1}
Frame rate	0.1-10 Hz
Sensor dimensions	320 x 256
Sensor technology	Cooled MCT (66 K)
Field of view	6.4° x 5.1° 24° x 20° (0.25x scope)
NESR	20 nW/cm^2 sr cm^{-1}
Radiometric accuracy	<1 K
Power consumption	180 W
Weight	31 kg
Operating temperature	-20 - 40°C
Data transfer	Camera Link

Fig. 2. The Telops Hyper-Cam and its technical specifications. The instrument uses two blackbodies that can be rotated in the field of view for calibration and a visible camera. Not pictured is a computer for operation and data storage. Note that the NESR is an average over the entire spectral range and is based on tests made in laboratory settings with a blackbody target. Real NESR values may vary according to the combination of spectral, spatial and temporal resolution chosen, as well as the nature of the imaged target.

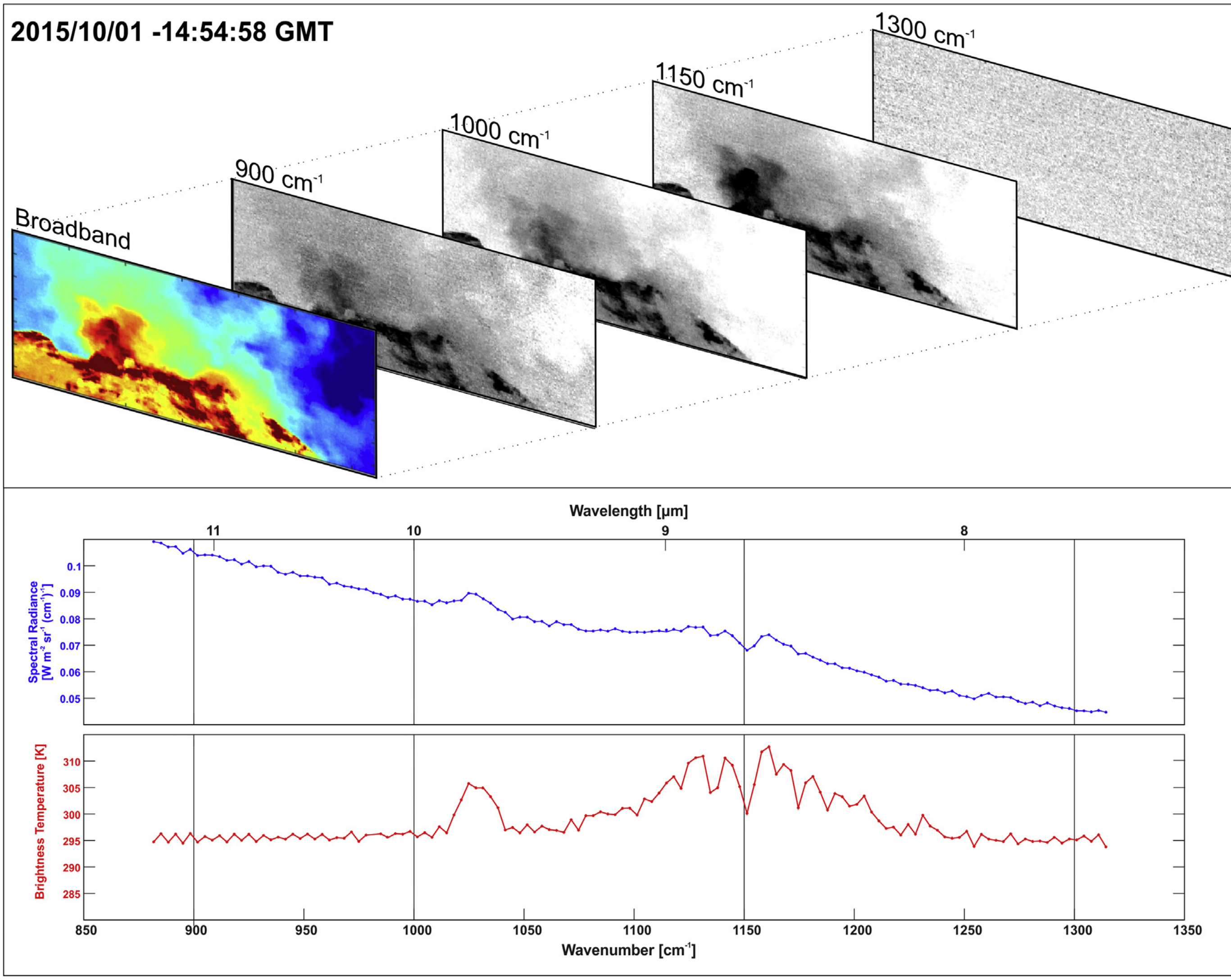

Fig. 3. Illustration of a data cube produced by the Hyper-Cam instrument. Each data cube consists of a stack of 2-D images representing the intensity of the incoming radiance at a given wavelength (top panel). Conversely, each pixel can be plotted as a spectrum of radiance intensity for all wavelengths (blue curve) or converted into brightness temperatures (red curve).

3. Spectral characterization of typical scenes

3.1. Osservatorio viewpoint

Fig. 5 shows an example of the data produced by the instrument at the "Osservatorio" location, and illustrates the complexity of spectral information contained in a single frame, as well as the temporal variability that can be found even in relatively short data sequences. This variability contributes to the difficulty in unravelling volcanic plume information from meteorological components (cloud, haze, water vapor, etc.). The top two panels are broadband images (integrated brightness temperature over the entire spectral range of the instrument). Individual spectra from selected pixels are extracted and plotted (items 1 to 8), showing the diversity of atmospheric objects commonly recorded/observed in the field of view.

3.1.1. Cold sky spectra (1 and 2)

Spectra 1 and 2 were extracted within cloud free windows at approximately the same elevation (~25°) in both images, and illustrate the typical spectral signature of a "cold sky" background. Both spectra look very similar mainly showing negative temperatures from 880 cm^{-1} to 1150 cm^{-1} with values as low as 245 K. They both have strong O_3 emission features between 1000 cm^{-1} and 1075 cm^{-1}. They show a large increase in brightness temperatures from 1150 cm^{-1} to 1300 cm^{-1} due to the emission of "hot" water vapor component directly ahead the camera and representing the first few hundreds of meters within the line of sight (LOS). Although similar, there is a systematic difference of ~10 K between the two spectra, which is the result of the difference in the observation angle. Indeed, spectrum from a more horizontal LOS will appear warmer, having a longer slant distance along with the water vapor rich boundary layer. This will result in a flatter spectrum, with smoothed spectral features mainly controlled by water vapor. Conversely, higher elevation angles will yield increasingly colder spectra with very discernible O_3 features. This last consideration is very important, as the background temperature is a key parameter for gas detection and quantification.

3.1.2. Water clouds spectra (3–5)

Spectra 3, 4 and 5 were extracted from regions of the field of view (FOV) with different types of water clouds. Items 3 and 4 are both hazy clouds, formed by the condensation of water vapor, and attached to the summit area. This semi-permanent cloud results from both volcanic degassing and weather conditions. In both images, it is fair to assume that the surface temperature of the condensing cloud should remain the

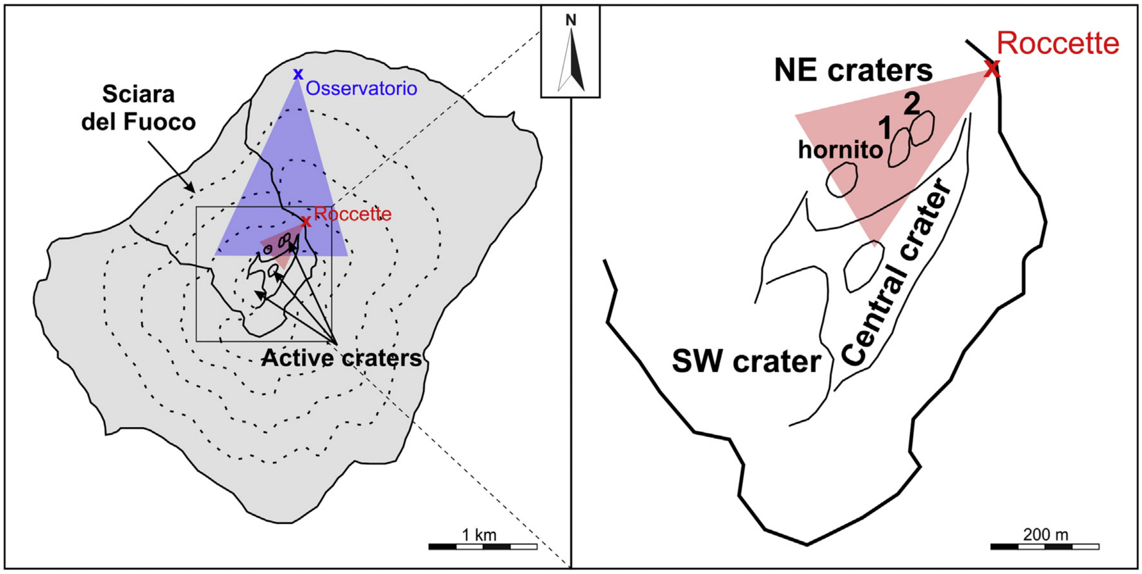

Fig. 4. Location of the observation stations with respect to the active craters on the island of Stromboli. *L'Osservatorio* is located ~1800 m from the NE crater, at an altitude of 120 m a.s.l. *Roccette* is located on the detachment scarp surrounding the Sciara de Fuoco, ~400 m from the NE crater and at level with it.

same. However, the brightness temperature of item 3 appears significantly colder than that of item 4. This can be explained by a difference in optical thickness. In the TIR, a thick and opaque cloud of water droplets (i.e., with no or low transmission) will yield brightness temperatures close to the cloud surface temperature because no emission from behind the plume contributes to the at-sensor radiance. In contrast, the brightness temperature of a thin cloud (i.e., high transmission) will include contributions from both the cold sky (i.e., the background) and the cloud itself. As a result, spectrum 3 can be identified as a warm but thin hazy cloud with colder brightness temperatures than spectrum 4, which can be qualified as a warm but opaque hazy cloud. Finally, spectrum 5 is an example extracted from a low-altitude (i.e., warm) and opaque meteorological cloud not connected with the volcano summit. Despite a high elevation angle (i.e., very cold background), the brightness temperature in spectrum 5 resembles the spectral signature of spectrum 4, as the observed signal comes solely from the cloud surface and no background radiation passes through the cloud.

3.1.3. Volcanic plume spectra (gas – 6,7 and ash 8)

Spectra 6, 7 and 8 are associated with volcanic emissions: gas bursts and/or small explosions comprising both SO_2 and ash. These volcanic products also appear in emission as long as the plumes remain warmer than the background. In the rescaled zoom panel at the bottom of Fig. 5, spectra 6 and 7 show the characteristic SO_2 emission at 1130 cm^{-1} and 1170 cm^{-1} (spectrum 7 in particular). Although less marked, the SO_2 signature remains discernible for item 6. Indeed, spectrum 6 appears somewhat flatter. This could be the result of one or both of the following factors: (i) the concentration of SO_2 in the plume is lower, and (ii) the temperature contrast between the plume and the background is smaller, which in turn could occur because the plume is emitted through or in front of a thick hazy cloud. Interestingly, we can also observe an emission feature around 1032 cm^{-1}, which most likely corresponds to the signature of SiF_4. This gas is frequently observed in our data set but only in gas bursts from the NE crater, and is never associated with ash explosions. Finally, spectrum 8 corresponds to a pixel located in an ash plume emitted from the SW crater. The ash-contaminated spectrum is warmer (>300 K) than that of the gas plume, and shows a flat profile with a small slope towards lower wavenumbers in the interval 880–950 cm^{-1}, characteristic of silicate particles (Prata, 1989). Ash plumes generally remain hot for longer because they are denser and have greater thermal inertia. Sometimes ash pixels are saturated (mostly in closer viewpoint Roccette). Ash plume spectrum shows similarity with spectra of the edifice itself, with slope towards the lower wavenumber. This is consistent with emission feature of silicate, which is a major component of ash particles and pyroclasts forming the edifice.

3.1.4. Water vapor

Note that at high wavenumber (1250–1300 cm^{-1}), all spectra converge towards 295 K. This is due to the strong absorption/emission features of warm water vapor component directly ahead the camera and representing the first few hundreds of meters in the LOS. Indeed, 1250 cm^{-1} marks the edge of the TIR atmospheric window. This is an important point to consider because whatever the elevation angle, and the type of cloud/plume observed (ash/SO_2/water; hot/cold; thin/thick), this range of the spectrum will never depart from 295 $\pm$ 1 K.

3.2. Roccette viewpoint

Fig. 6 shows some examples of the data collected from the Roccette viewpoint with a similar configuration: spectral resolution of 6.6 cm^{-1}, 0.25× telescope and a sensor window of 200 × 200 pixels. The first image illustrates a situation of passive degassing from the NE craters, while the second image shows a bubble burst event from NE1 crater. The geometry of observation is very different from the Osservatorio. The viewpoint at Roccette is approximately level with the craters (−2° elevation at the centre of the frame), and at a distance of only 400 m. As a result, the variability of spectra found in a single image is somewhat smaller. However, similar observations can be made:

3.2.1. Cold sky spectra (1 and 2)

Even at the top of the frame and with extremely clear conditions (no condensing cloud), the typical cold sky spectrum (1) shows brightness temperatures warmer than those observed at Osservatorio. This is expected, as the elevation angle at the top of the frame does not exceed 10°. Similarly to what we observed from Osservatorio, the typical spectral features of a “cold sky” background (water vapor bands and O_3 emission) are smoothed as the elevation angle decreases and the overall spectrum appears flatter and warmer (2).

3.2.2. Degassing plume spectrum (3)

Spectrum 3 is extracted from the degassing plume out of the NE crater 1. This is a warm water vapor cloud and shows almost no spectral features at a temperature of ~290 K, close to ambient temperature at the time of observation. It is the typical spectrum of the degassing

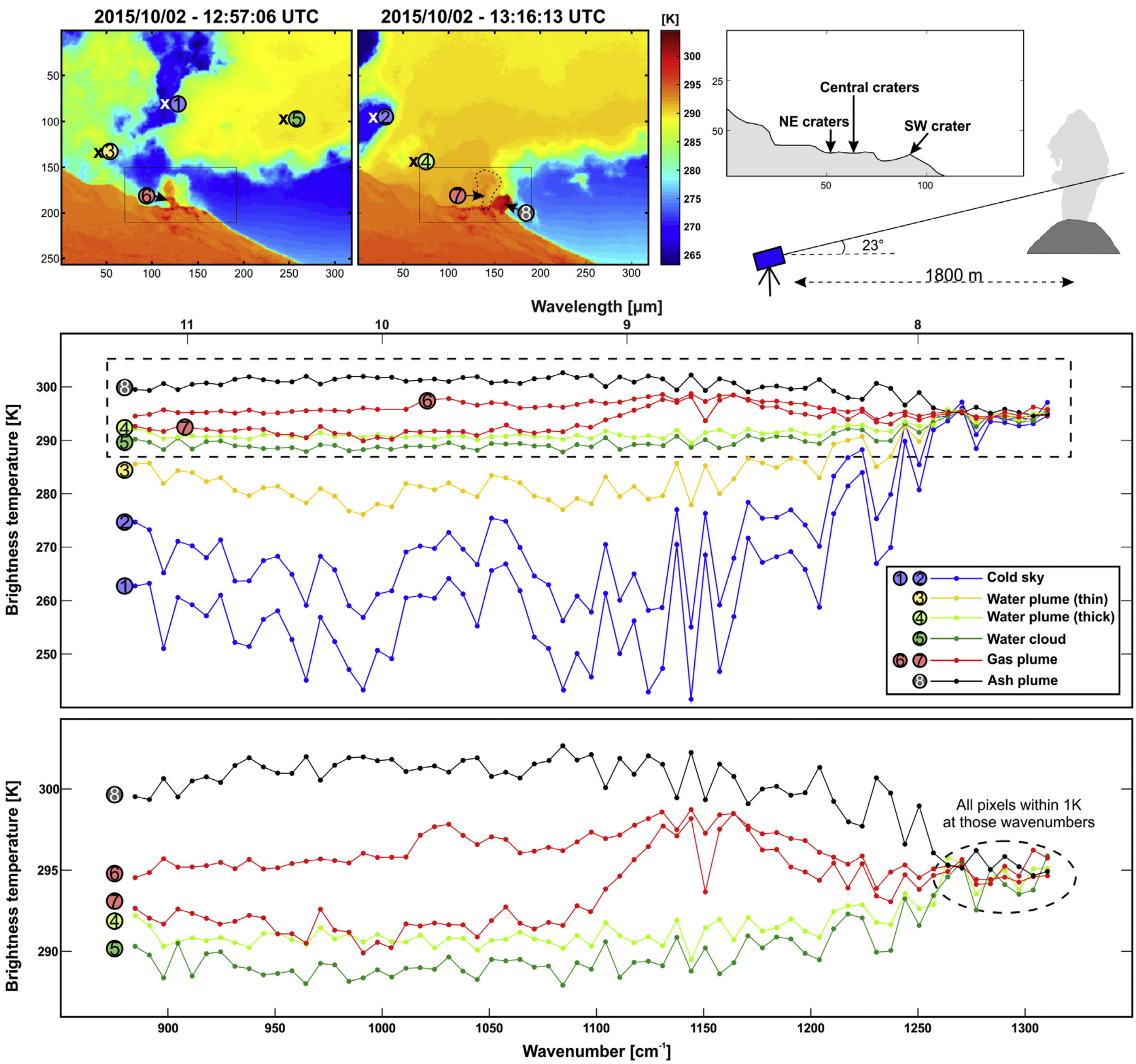

Fig. 5. Example of spectra extracted from individual pixels in a dataset collected from L'Osservatorio viewpoint (see Fig. 3) on October 2nd, 2015. The top two panels are broadband images (average brightness temperature over the entire range of the detector) showing the variability of weather conditions around the target area over short timescales. Individual pixels are extracted at the locations denoted by the circled numbers and shown in the middle panel. Note the continuum between clear sky spectra (in blue) and a very thick water plume or cloud (in green). The bottom panel shows examples of pixels extracted from volcanic plumes on a vertically exaggerated scale to emphasize the differences between a thick water plume (in green), an SO_2-bearing plume (in red) and an ash plume (in black).

plume in the absence of SO_2 and this type of degassing is regularly observed throughout all of our data sets at Roccette.

3.2.3. Volcanic plume spectrum (4 and 5)

Spectrum 4 shows a typical burst of gas emissions with SO_2 from the NE2 crater. The double peak of the emission feature at 1130 and 1170 cm^{-1} reveals the presence of SO_2 in this burst. These SO_2 bursts are often referred to as "gas puffing" (Ripepe et al., 2002) and are produced on a regular basis from both NE1 and NE2 craters. We can also discern the emission peak of SiF_4 at 1032 cm^{-1}, which is only observed in bursts out of the NE2 crater. Spectrum 5 shows a typical SO_2 signature during a bubble burst event from the NE1 crater. The very pronounced SO_2 emission feature indicates a hot and SO_2-rich gas plume (~40 K difference with background brightness temperature).

3.2.4. Ground spectra (6 and 7)

For reference, we also included two spectra extracted from pixels on the volcanic edifice itself. They exhibit brightness temperatures typically warmer than the ambient air temperature. Spectrum 6 is taken from the rim of the hornito. This vent is also continuously degassing and it is possible that the spectral signature of SO_2 is observed in absorption from a gas plume rising in front of the hot hornito. Spectrum 7 is taken from the ground near crater NE1.

The observations listed above are consistent with previous observations of volcanic plumes and illustrate the importance of a number of

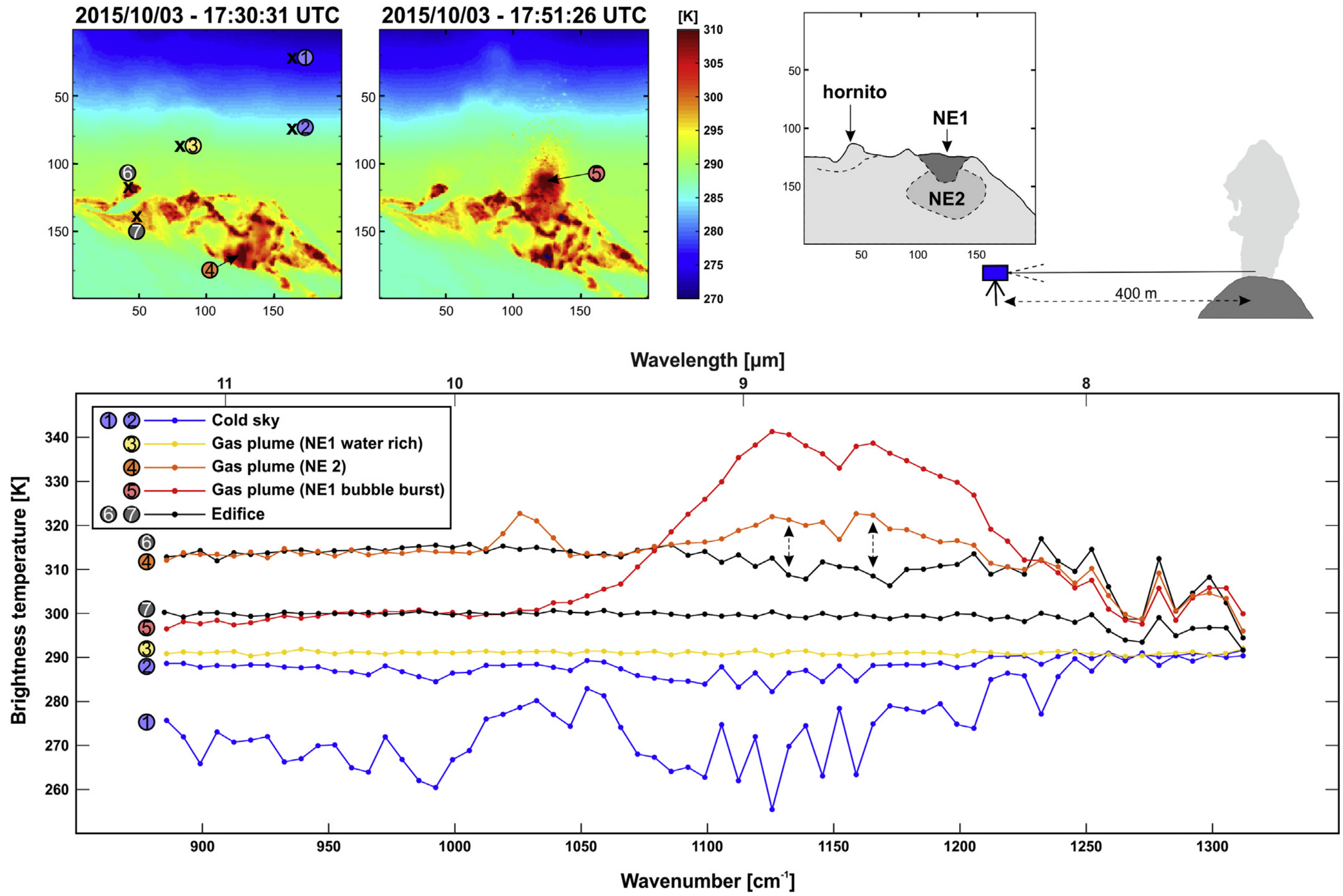

Fig. 6. Examples of spectra extracted from individual pixels in a dataset collected from Roccette viewpoint (see Fig. 3) on October 3rd, 2015. The top two panels are broadband images (average brightness temperature over the entire range of the detector) showing two events at the NE craters. Individual pixels are extracted at the locations denoted by the circled numbers and shown in the middle panel.

environmental factors on our ability to recognize and quantify SO_2 in a volcanic plume. The magnitude of the observed absorption or emission feature will depend on three factors: the plume SO_2 concentration and the thickness of the plume (together defining the path concentration), the temperature of the plume itself, and the thermal contrast with the background. A temperature contrast between the background (either cold sky or warmer water cloud) and the volcanic plume must exist in order to recognize the existence of an emitted plume, and to investigate its contents. The importance of this thermal contrast has been recognized in a number of studies conducted with space-based instruments, where the background surface is generally warmer than the plume (e.g., Pugnaghi et al., 2006; Realmuto et al., 1994; Urai, 2004), as well as in ground-based efforts with OP-FTIR instruments, where the plume was contrasted with a hot source of radiation such as lava (e.g., Allard et al., 2016; Burton et al., 2007; La Spina et al., 2015; Oppenheimer et al., 1998) or even the sun (Duffell et al., 2001). The latter ground-based configurations are extremely constraining in terms of viewing geometry, and recent efforts with imaging instruments have exploited a negative thermal contrast between a cold sky background and a warmer volcanic plume (Gabrieli et al., 2016; Prata and Bernardo, 2014). When observing a volcanic plume many kilometres away from its emission source, assumptions can be made that the plume is thermally uniform, and in thermal equilibrium with the surrounding atmosphere. In contrast, when observing plumes very close to their source, they cannot be assumed to be in equilibrium with their surroundings, and their temperature can vary, both temporally between measurements and spatially within a single scene. This greatly complicates the task of quantifying SO_2 column amounts using radiative transfer inversion algorithms. The elevation angle will also greatly influence the background emission, affecting not only the temperature contrast between plume and background, but also the depth of various spectral features, as the line-of-sight intersects various layers of the lower and upper atmosphere (Love et al., 1998; Swinbank, 1963). Our measurements support that observation, displaying a large variety of spectral features and average brightness temperature differences of >50 K between various parts of a scene. The presence of low-altitude clouds further complicates the problem, as they will introduce spatial and temporal variability in the background, that must be evaluated on a pixel-by-pixel basis. Finally, the emittance from the foreground (the atmosphere between the plume and the sensor) must also be known for any subsequent RT inversion.

In our configuration of acquisition (i.e., almost exclusively with an atmospheric background), the spectral characteristics of the species contained in the gas plume (SO_2, SiF4, and even ash) will appear as emission (crest in the spectrum) features. Note that in very exceptional condition, the cloud/plume may be hugging the ground and descending along the slope of the volcano. In that particular case, the background composed of the blocks and tephra fall deposits composing the border of the crater is then warmer than the over passing plume. Plumes will then mostly appear as absorption features (troughs in the spectrum), and gas plumes in particular will be easier to detect at close distances from the vent, before they have a chance to entrain ambient air and equilibrate with the surrounding atmosphere. Finally, note that the plume must be semi-transparent (not opaque) to allow for quantitative retrieval of gas, aerosols, or droplet concentration.

4. SO_2 detection from hyperspectral images

In light of the difficulties to adequately constrain the parameters for RT inversion, and in order to exploit the hyperspectral dataset to its full potential, we created a different type of indicator using a curve fitting method. Fig. 7 illustrates the process by which we produce correlation factor maps for a given image. Each individual pixel extracted from the scene is compared to a laboratory spectrum of SO_2 whose resolution has been degraded to match that of the instrument. Their similarity is quantified over the spectral window of the distinctive feature (1100–1200 cm^{-1}) using a Pearson correlation factor (R):

$$R = \frac{1}{N-1}\sum_{i=1}^{N}\left(\frac{A_i-\mu_A}{\sigma_A}\right)\left(\frac{B_i-\mu_B}{\sigma_B}\right) \quad (1)$$

where N is the number of sampling points considered (15 over the spectral region of interest in the illustrated case), and μ and σ are the mean and standard deviation of each spectrum (A and B, respectively). The value of R ranges between −1 and 1, with 1 representing a direct positive correlation, which we interpret to represent a clear SO_2 signature. The process is repeated for every pixel in the image to produce a correlation factor map of the scene. In order to reduce computing time, a mask is manually drawn by the user over the edifice and only the pixels with an atmospheric background are considered. Fig. 7 shows an image acquired on October 1st from the Roccette viewpoint, and illustrates our thresholding method. The scene considered in this example contains a gas burst from the NE crater, thermally distinguishable from the background in the broadband image. The bottom left panel of Fig. 7 presents the histogram of R values observed for all pixels contained within a rectangular ROI located right above the crater rim. It shows a bimodal distribution with the background pixels forming a large Gaussian distribution around a mean of ~0.1, and a second population of pixels forming an asymmetric Gaussian distribution with a peak around ~0.9. Based on these observations, we chose a threshold of $R = 0.7$ for positive identification as SO_2. The bottom right panel of Fig. 7 shows the individual spectra of all pixels identified as SO_2 using this threshold (pale gray), their mean and the 1σ envelope (black). The mean spectrum of the population presents clear SO_2 features, confirming the efficacy of the index in isolating SO_2-bearing pixels. The elevated BT at 1032 cm^{-1} is attributed to emission by the gas SiF_4.

Because background and summit conditions, as well as the temperature of the gas plume itself can change over the course of a single time series, similar levels of degassing (a given path concentration) can result in SO_2 emission features of varying magnitude, and which may be affected by a variety of additional spectral features. However, our qualitative indicator is not based on the magnitude, but rather the spectral shape of the SO_2 emission feature. Moreover, resampling the data at a resolution of 10 cm^{-1} or higher allows us to smooth the spectra to minimize the influence of narrow water vapor lines over the spectral window of interest. As a result, we observe similar distributions of the R value in a number of images at different times over the course of the time series, despite changes in scene background and ambient atmospheric conditions. Similar distributions were also observed in images extracted from data acquired at Roccette, again over the course of time series representing weather summit conditions. We therefore

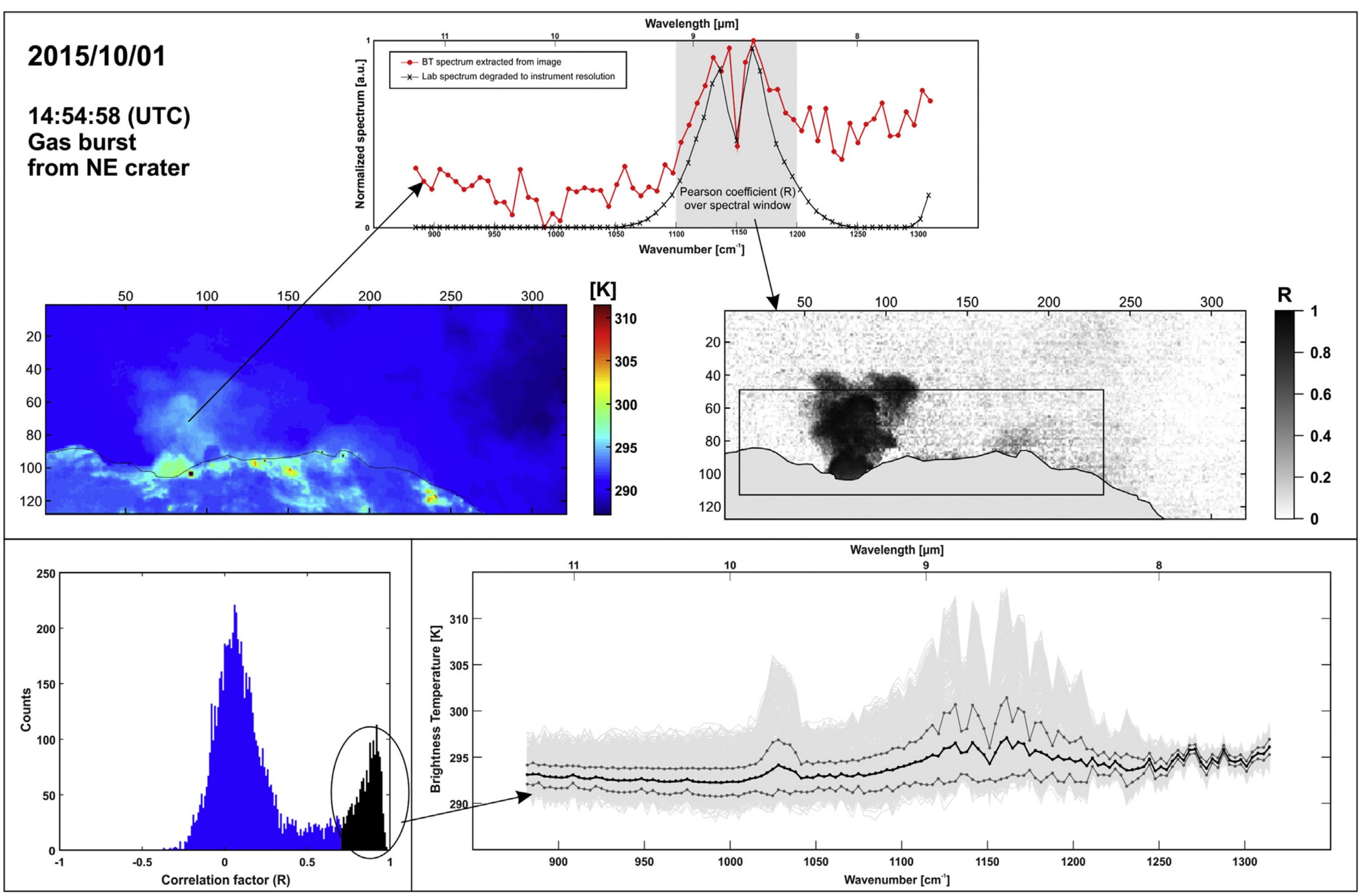

Fig. 7. Illustration of the curve–fitting process on an example image acquired at the Osservatorio viewpoint on October 1st, 2015. [top panel] A full spectrum is extracted from each pixel and correlated with a laboratory spectrum of SO_2 degraded to instrument resolution to produce a map of the resulting Pearson coefficients (R). [bottom left panel] Histogram of the R-values for the example image. Pixels classified as SO_2-bearing ($R > 0.7$ in black) constitute a separate population outside of the Gaussian distribution of background pixels. [bottom right] Spectra of all SO_2 pixels ($n = 1235$, with the mean and 1σ deviations represented by thick darker lines.

believe this distribution to be representative of a scene containing SO_2-bearing pixels, and chose to apply the same threshold ($R = 0.7$) to all time series.

In order to evaluate the efficacy of the correlation factor as an activity indicator, it is helpful to consider time series. Fig. 8 shows a time series of the total number of SO_2 pixels (as identified with the method described above) within a predefined ROI for a data sequence taken from the Osservatorio viewpoint on October 2nd, 2015. Essentially no pixels are identified as SO_2 during quiescent phase (passive degassing) and a number of explosive events stand out. Given the geometry of the viewpoint and the extent of the ROI, these events can be gas bursts and/or ash explosions, and emanate from any of the 3 main craters at Stromboli. Three events are illustrated with their *R*-value map: (A) a gas burst from the NE crater; (B) an ash explosion from the SW crater accompanied by a separate gas plume whose origin is difficult to attribute to a specific crater; and (C) an ash explosion from the SW crater. Event C was identified as a hot plume in the corresponding broadband image, and yet does not correspond to a peak in *R*-values. As well, the ash plume in event B does not correspond to high values on the *R*-value map, while the distinct gas plume is characterized by strong correlation factors. This demonstrates the reliability of the method to isolate SO_2-bearing pixels based on their spectral signature.

Similar results can be observed at the second viewpoint at Roccette. Fig. 9 shows the time series of the number of SO_2 pixels identified in a data sequence taken from the Roccette viewpoint on October 3rd, 2015. Roccette offers a much closer viewpoint and the field of view was restricted to the NE craters. As demonstrated in Section 2, the spectral characteristics of typical radiation sources (ash, gas, water vapor, ground, etc.) remain very similar between the two vantage points considered in this study. However, a key difference comes from the viewing angle (pitch). At Roccette, we observed emissions almost at a horizontal angle. This results in significantly warmer and flatter spectra for the areas of “cold” sky that constitute the background. Combined with the short distance to the target, which increases the spatial resolution and limits the dilution of the signal through the proximal atmosphere, this results in an increased ability to detect volcanic emissions. The three snapshots illustrated in Fig. 9 represent passive degassing from one or both vents (NE1 and NE2). Both passive degassing and explosive events are detectable from that viewpoint, and periodic patterns of passive degassing can be observed with a characteristic period of 15–20 s.

5. BTD indicators

Spectral indices like the correlation factor described here are powerful detection tools and relatively easy to implement. However, they require data acquired at sufficiently high spectral resolution. The instrument used for this study, though producing high-quality data, would represent a challenge if considered for day-to-day monitoring activity, mainly due to its cost and its power requirements. Significantly cheaper and more practical instruments exist that can image a scene in the thermal infrared at multiple wavelengths. Those instruments operate with bandpass filters and radiation can only be quantified for a limited number of channels (usually 2–4). As a result, qualitative indicators are reduced to simple Brightness Temperature Difference (BTD) indices. In the second part of this work, we use the hyperspectral data to evaluate bi-spectral BTD indices and the influence of various factors on their efficacy. We created four bi-spectral indices using the mean brightness temperature observed over a narrow spectral window around the peak of the SO_2 feature (on-peak channel: 1130 cm^{-1} and/or 1170 cm^{-1}) and the mean brightness temperature over a reference window outside of the SO_2 feature (off-peak channel). The choice of the off-peak channel was guided by previous efforts with ground-based and satellite instruments and reflect waveband centers commonly found on the filters from such instruments. Retrieval algorithms commonly used to detect and/or quantify volcanic emissions are often based on the use of BTD indicators employing spectral channels with centers at 11 and 12 μm (910 and 833 cm^{-1}, respectively) (e.g., Corradini et al., 2010; Prata, 1989; Realmuto et al., 1994; Wen and Rose, 1994). With regards to ground based instruments, the Cyclops instrument (Prata and Bernardo, 2009, 2014) also makes use of filters centered at 11 and 12 μm, and the retrieval algorithm used for SO_2 quantification in particular is based on BTD images using a reference channel centered at 11 μm. The reasoning behind this choice of channels is that the absorption of silicate particulates at those two wavelengths

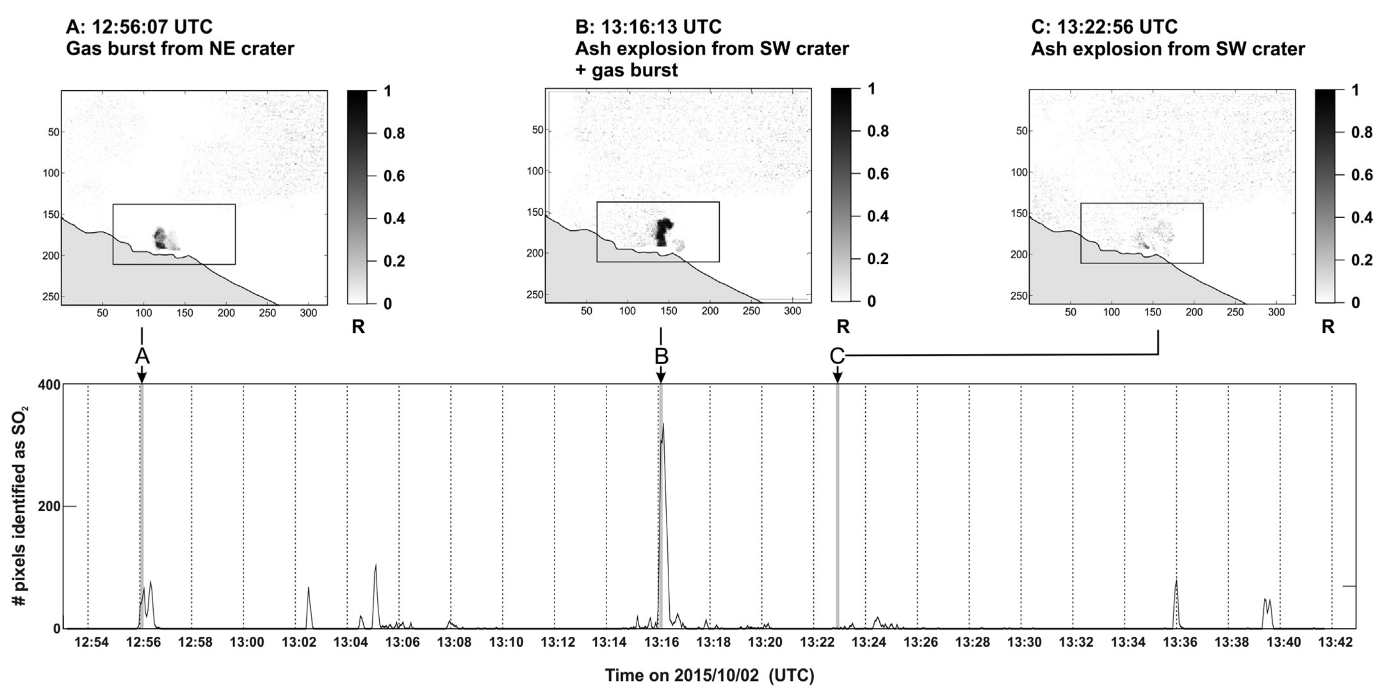

Fig. 8. Time series of the total number of pixels identified as SO_2 ($R > 0.7$) within each image for a data sequence acquired from the Osservatorio viewpoint on October 2nd, 2015. The three image inserts at the top show the *R*-map for three selected events: (A) A gas burst from the NE crater; (B) an ash explosion from the SW crater accompanied by a simultaneous gas burst from the NE crater; and (C) an ash explosion from the SW crater.

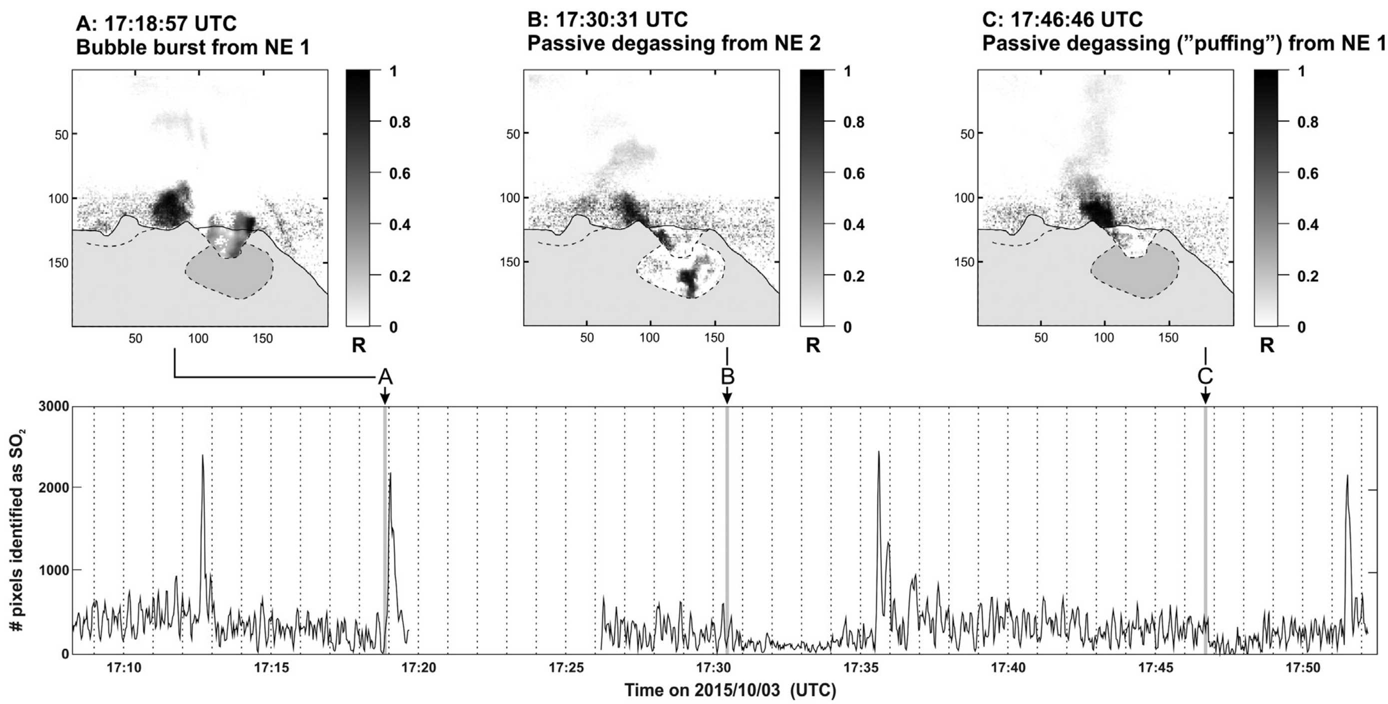

Fig. 9. Time series of total number of pixels identified as SO_2 (R^2 value > 0.7) within each image for two sequences acquired from the Roccette viewpoint on October 3rd, 2015. The three image inserts at the top show the R^2 map for selected events: (A) a gas burst from NE1 crater; (B) passive degassing from NE1 and NE2 craters; and (C) passive degassing from NE1 crater. Patterns of puffing with a period of ~30 s are discernable during the passive degassing, and gas burst/explosions occur every 5–10 min.

presents a negative slope between the two channels (decreasing between 11 and 12 μm) while other atmospheric constituents usually exhibit a positive slope, allowing for the detection of ash clouds. While the Hyper-Cam's spectral range does not extend to 12 μm, we have opted for two reference channels at the edge of the spectral range (925 and 880 cm^{-1}, or 10/8 and 11.4 μm, respectively) that may be able to capture this difference in absorption (and emission) and help us explore the potential interference of the presence of ash on SO_2 detection. We also opted for a reference channel at 1050 cm^{-1} (9.5 μm), centered at the location of a prominent O_3 absorption band. Finally, we chose a reference channel on the other side of the SO_2 absorption feature, centered at 1250 cm^{-1} (8 μm), where the incoming radiation is dominated by the absorption of water vapor in the proximal atmosphere regardless of the nature of the background, therefore providing a stable reference channel. Both on-peak and off-peak values are averaged over a 10 cm^{-1} wide window and the four indices are calculated as follows:

Index 1: $BT_{1170}–BT_{1250}$.
Index 2: $BT_{1170}–BT_{1050}$.
Index 3: $BT_{1170}–BT_{925}$.
Index 4: $BT_{1170}–BT_{880}$.

All four BTDs should produce positive values in the presence of SO_2, provided the plume is in positive thermal contrast with the background. Such a contrast should always be achieved when observing plumes in front of a sky background, because the background radiation is integrated over a line of sight going all the way out to space and including all layers of the atmosphere, yielding BT values much colder than the ambient temperature at the plume altitude. We briefly considered the use of various on-peak windows: peak at 1170 cm^{-1}, peak at 1130 cm^{-1}, a mean of both peaks, or a wide sampling of 50 cm^{-1} over both peaks. Results were virtually identical in all situations, but for decreased sensitivity when considering the wider sampling window (see discussion of spectral resolution below). In the following results, we decided to use the BT at 1170 cm^{-1} as our on-peak frequency. In addition to the presence of SO_2 in a hot plume, a number of alternative situations can also produce positive BTD values, and could be falsely interpreted as SO_2. We will refer to those as false positives. Conversely, in some situations, the presence of weak SO_2 emission can also be missed, either because the intensity of the emission peak is not strong enough to create a significant BT difference, or because the signal is lost in a high noise level.

Fig. 10 shows snapshots of the four BTD indices and the curve-fitting algorithm for three example scenes taken from the Osservatorio viewpoint: a gas burst from the NE crater (A); an ash explosion from the SW crater, which was preceded by a gas burst (B); and an ash explosion from the SW crater without a gas burst (C). All four indices produce positive BTD values for the gas burst event. The spatial distribution of the pixels showing positive BTD values is consistent between the indices, and overall the structures within the gas plumes can be identified in all indices. However, the spatial extent of the detected area and the intensity of individual pixel values vary from one index to the next, reflecting changes in sensitivity and reliability. Index 1 in particular, seems not to be sensitive to the rightmost part of the plume. In the second snapshot, the gas plume once again appears in a similar fashion between the indices. Ash emissions also produce positive BTD values in all four indices, and those values seem to be highest at the expanding front, where the plume may be more concentrated and/or warmer. This means that BTD indices are incapable of distinguishing between ash and SO_2 emissions. Finally, note the difference in the BTD value in areas of the background around the plumes. Index 1 consistently produces null or negative values for the background atmosphere, be it cold sky or a warmer water cloud. The other indices, however, can produce positive values when evaluating an atmospheric pixel in the absence of volcanic emissions. The curve fitting index, on the other hand, allows us to unequivocally identify SO_2 and more importantly, to distinguish it from ash emissions. The event depicted in panel B of Fig. 10 comprises two distinct plumes: an ash plume drifting towards the right of the image and a gas plume rising vertically at the center. Note that the curve-fitting index only shows high values of the correlation factor for the gas plume, while all BTD indices exhibit high values on both plumes.

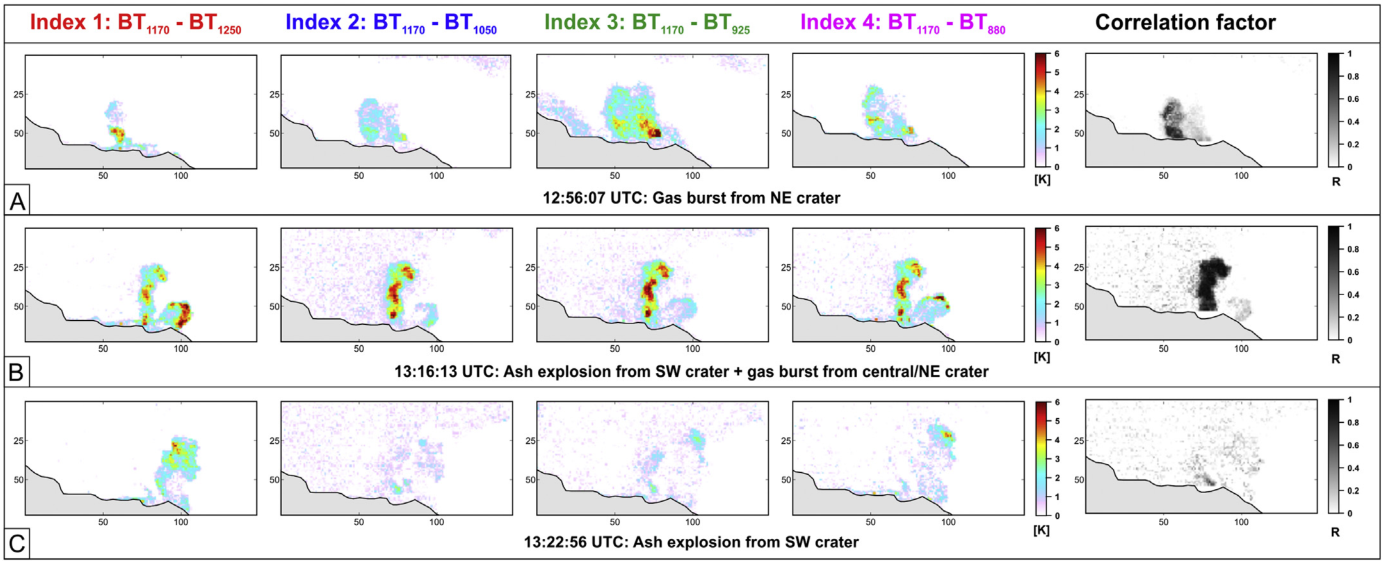

Fig. 10. Snapshots taken from a data sequence on October 2nd, 2015, illustrating the effectiveness of the 4 BTD indices compared to the curve-fitting index on three types of events: (A) A gas burst from the NE crater; (B) an ash explosion from the SW crater accompanied by a simultaneous gas burst from the NE crater; and (C) an ash explosion from the SW crater. The four hyperspectral indices are expressed as the difference between the brightness temperature measured at 1170 cm^{-1} and a reference brightness temperature at a wavenumber outside of the SO_2 absorption feature: 1) reference at 1250 cm^{-1} [in red]; 2) reference at 1050 cm^{-1} [in blue]; 3) reference at 925 cm^{-1} [in green]; and 4) reference at 880 cm^{-1} [in magenta]. The curve fitting images represent the value of the correlation coefficient (R^2) between the theoretical absorption spectrum of SO_2 between and the measured BT between 1050 and 1250 cm^{-1}. Both signals are normalized before comparison to emphasize pattern recognition.

Similarly to what we have presented for the *R* index, it is helpful to consider time series of the BTD indicators. Fig. 11 shows time series of the four BTD indicators described above (as well as the curve-fitting indicator for a data sequence taken from the Osservatorio viewpoint on October 2nd, 2015. For the BTD indices, the time series plots the sum of the BTD value for all pixels in a region of interest (ROI) above the craters (150 × 75 pixel zoom). The curve-fitting time series is also provided for reference.

Taking event B as an example, note that the peak shows quite similar values in all time series (~3000–4000 K of cumulative BTD). This indicates that for all indices, the number and BTD intensity of flagged pixels are comparable. Simultaneously, the peak of event B has been reliably identified as SO_2 by the curve-fitting index (last time series) demonstrating the "first order" consistency of all indices in detecting powerful SO_2 emissions. However, the cumulative value of BTDs outside of the peak remains significant for indices 2, 3 and 4 that corresponds to "false positives" BTD produced during non-volcanic periods. This cannot be attributed to permanent gas puffing as this signal does not appear in the time series of the curve-fitting index. The strength of the BTD index during degassing events compared to that observed in between the events is relatively small for indices 2 and 3 with BT values as high as 5000 K, preventing unambiguous detection of small SO_2 peaks (such as event A) as revealed by the curve fitting index. This relative difference is much higher for Index 3 and allows the detection of small peaks of

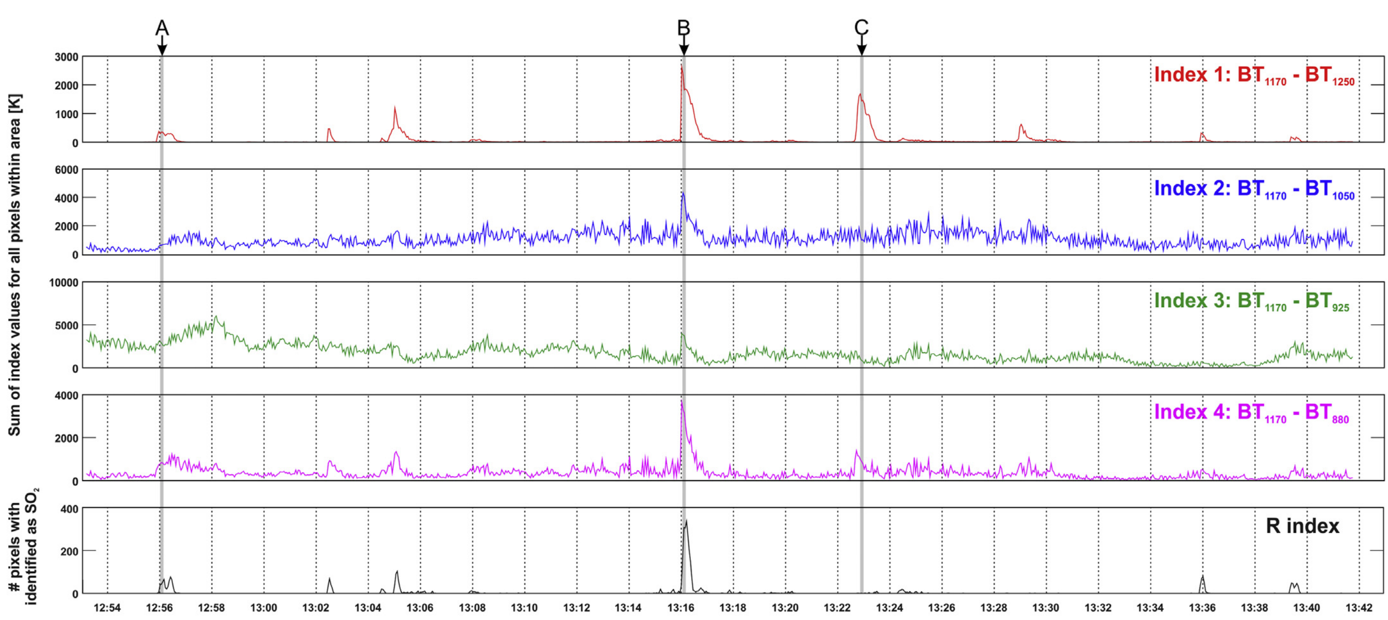

Fig. 11. Time series of 4 hyperspectral BTD indices and the curve-fitting index for a data sequence on Oct 2nd, 2015, from the Osservatorio viewpoint. The plots show the sum of the index value for all pixels over the area delimited by the rectangle in Fig. 10. For the curve fitting, the plot shows the number of pixels identified as SO_2 ($R > 0.7$).

SO_2. Interestingly, this occurs only for BTD with off-peaks values (BT_{1050}, BT_{925} and BT_{880}) at frequency lower than that of the on-peak value (BT_{1170}). Theoretically, this can be attributed to the natural slopes observed in this part of the spectrum due to characteristic spectral features of either clear sky or water-rich conditions. During clear sky conditions (see Fig. 5) the spectrum is uneven showing a BT crest around 1050 cm^{-1} due to O_3 with trough on either side (~950 cm^{-1} and ~1100 cm^{-1}), and a light BT increase towards the smallest frequency (880 cm^{-1}). In the same conditions, index 2 (BT_{1170}–BT_{1050}), with an off-peak located on the O_3 absorption line, will be weakly sensitive, potentially leading us to miss weak SO_2 plumes. On the other hand, index 3 (BT_{1170}–BT_{925}) with an off-peak frequency located near a trough will basically have the same BT value as the on-peak value during non-eruptive periods. In this case, the noise can be important, alternatively showing positive and negative values. Finally, index 4 (BT_{1170}–BT_{880}) with off-peak at the lower end of the spectrum offers a good balance between sensitivity and false positives. In the case of a water-rich environment (see Fig. 5) this part of the spectrum is expected to be warmer and much flatter. The impact will be the same for all indices: (i) the noise can be important hence regularly producing "false positive" BTD, and (ii) indices will be poorly sensitive to "cool" SO_2 emissions.

For index 1, the off-peak value (BT_{1250}) is located at a higher frequency than that of the on-peak value (BT_{1170}). At these wavelengths the water vapor absorption/emission features are important, leading to consistently elevated brightness temperatures (295 ± 1 K) depending on the temperature and relative humidity of the proximal atmosphere. Therefore, index 1 is poorly sensitive to SO_2, and will mostly yield negative BTD values, which will be automatically discarded. Nevertheless, we observe that even small SO_2 peaks can be detected using this BTD index.

Although not distinguishable in the time series for indices 2 and 3, event C - an ash explosion from the SW crater - appears as a strong peak on the time series for indices 1 and 4. The curve-fitting index however, reveals no SO_2 during this event. For index 1, this apparent detection is due to the presence of hot ash creating a slope (see Fig. 5) between the on-peak BT (1170) and the off-peak BT (1250), which is affected by strong water vapor absorption and consistently displays BT values around 298 K. This leads to positive BTD values even in the absence of SO_2. The presence of ash also introduces a slope at the lower end of the frequency spectrum (between 850 and 950 cm^{-1}), a characteristic that can be exploited to detect and quantify ash emissions with satellite instruments (Prata, 1989). As a result, index 4 will also produce positive values for pixels containing hot ash. The fact that event C is not visible in the time series for indices 2 and 3 is mostly due to the strong signal produced by false positives in the background areas, diluting smaller events in the surrounding "noise". Note that the curve-fitting index clearly discards event C, which further confirms its efficiency at detecting SO_2 only.

In summary, index 1 is the least sensitive, even if it shows very good results at detecting weak SO_2 emission. However, it gives important false positive BTD in presence of ash. Indices 2 and 3 produce a large number of false positives, especially when the background is a cold clear sky, and have proven difficult to use for routine measurements or as a monitoring tool for automated SO_2 detection. Index 4 shows a low level of noise and looks less affected by the presence of ash, while remaining extremely sensitive to SO_2. The curve fitting time series, using hyperspectral features, logically appears to be the most effective at detecting SO_2 without producing false positives. Only the events containing SO_2 appear on the time series. For future quantitative efforts, this curve-fitting index could invaluable in allowing us to flag SO_2-bearing pixels and limit radiative transfer modeling to a select group of pixels.

6. Sensitivity to spectral resolution

BTD indicators commonly used to detect SO_2 often utilize filters at frequencies similar to those we described for index 4 (e.g., Ackerman et al., 2008; Corradini et al., 2009; Theys et al., 2013; Watson et al., 2004). However, bandpass filters consider a much wider range of frequencies when evaluating the brightness temperature on- and off-peak. This spectral resolution is a key element when defining a TIR multispectral sensor as it controls the ability to distinguish between gas species and aerosols. We explore the influence of spectral resolution by artificially increasing the bandwidth over which the BT are averaged for the BTD indices, until achieving spectral resolution comparable to those commonly used filters. We then compare those results with simulated BTDs as would be observed with the specific Cyclops filters. In order to calculate the Cyclops BTD index, we determined the brightness temperature in each filter by computing a weighted mean of the observed BT from the Hyper-Cam spectrum using the transmission of the corresponding filter as the weighing function. The resulting BTs were then used to compute the BTD indices as follows:

Index Cyclops: $BT_{11.0}$–$BT_{8.6}$.

Fig. 12 shows 5 time series of the BTD index 4, computed with increasing bandwidths for the on-peak and off-peak BT windows. As the bandwidth increases, the "noise" in the time series increases as well, and volcanic events become more difficult to identify. For the very low-resolution indices, we even observe dips in the cumulative value of SO_2 within the box after large events. This occurs when hot material is present in the scene (ash and/or hot gas). The elevated temperature of the plume produces negative BTD values because the sampling region of the on-peak SO_2 band encroaches on the water vapor absorption area, artificially lowering the apparent on-peak BT. This results in negative BTD values, which are discarded, and the event appears as a sudden drop in the time series. When comparing the time series produced using a bandwidth of 200 cm^{-1}, and the simulated Cyclops filter results, we can see that individual degassing events are impossible to identify, hindering the use of those BTD indicators for monitoring. When considering individual snapshots from the time series (top panel on Fig. 12), it becomes apparent that a BTD index using such filters would create large areas of false positives, especially in background areas of clear sky.

At Roccette, in higher proximity to the source and with lower viewing angles, filter BTD indices remain adequate for the detection of SO_2 and produce more consistent results. However, it is worth noting that the same phenomena that produced false positives in background areas still affect the top of the images taken at Roccette (corresponding to higher viewing angles). Moreover, the presence of ash will also produce false positives and impede the detection of SO_2 even at low viewing angles.

7. Conclusion and perspectives

Our results demonstrate the utility of hyperspectral TIR imaging for the observation of volcanic degassing. The instrument offers a significant increase in the amount of context that can be gathered from a scene. High-resolution datasets revealed a great diversity of spectral areas within a scene. Radiative transfer inversion proves to be a challenge, as a simple geometry cannot be established and applied to an entire scene. Considerable variations exist in the viewing angle from the bottom of an image to the top, that will introduce variations not only in the overall apparent temperature of the background, but also in the prominence of certain spectral features such as the O_3 emission (high-elevation angle) and water vapor absorption lines (low-elevation angle). As well, the presence of low altitude clouds can create areas where the spectral characteristics of the background will be vastly different, and their position changes over the course of data acquisition. Finally, the presence of a heavily condensing plume at the summit also introduces temporal and spatial heterogeneity to the scene. All those factors complicate the interpretation of the measurements, and underline the importance of measuring the intensity of radiation at multiple wavelengths.

Even at relatively low spectral resolution, the instrument produces vast amounts of data, which can prove very challenging to process in a

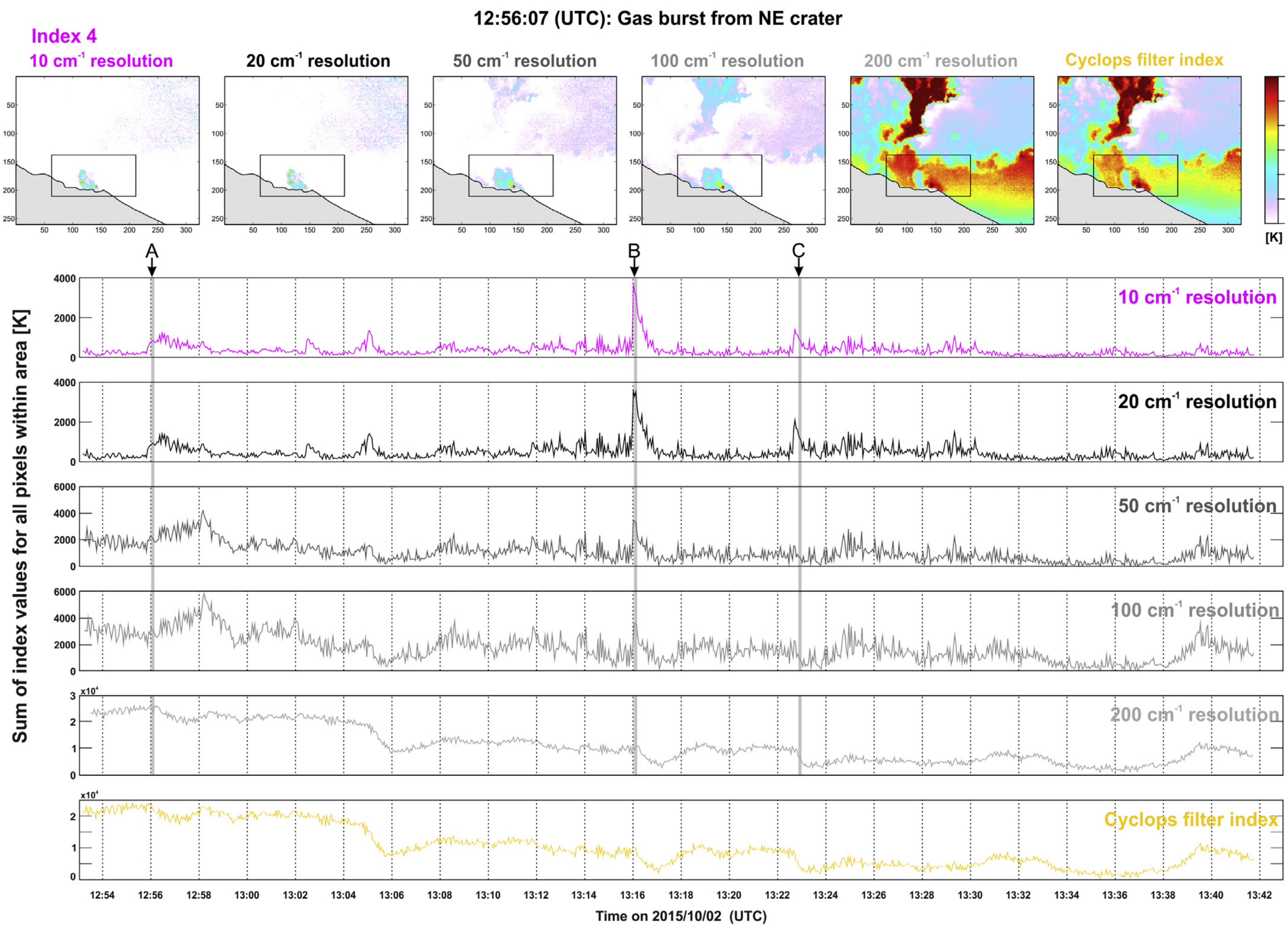

Fig. 12. Time series of the BTD 4 index for a data sequence on Oct 2nd, 2015, using spectral windows of increasing size. Each time series represents the cumulative value of BTD values for all pixels contained within the boxed area. The bottom time series represents a BTD index computed using the bandpass filters from the Cyclops ground-based instrument (Prata and Bernardo, 2014). The image inserts at the top are example BTD images for each of the resolutions at the time of a gas burst from the NE crater at 12:56:07 on October 2nd, 2015 (event A).

timely manner. For monitoring purposes, we show that a simple method can be implemented that is both fast in terms of computing time and unequivocal in its ability to detect the presence of SO_2 in a plume. We developed a curve-fitting algorithm which identifies SO_2-bearing pixels based on their spectral signature. With this simple method, we can detect the presence of SO_2 with accuracy for all areas of a scene, regardless of the viewing geometry and the nature of the background (clear sky, fog, ash, low altitude clouds, etc.). Although this particular indicator is not related to the magnitude of the SO_2 emission feature, the Pearson correlation factor offers a reliable method to quantify the confidence with which SO_2 has been identified. It should be noted that the *R* value is not indicative of the relative SO_2 path concentration in a plume, nor of the relative intensity of degassing. Instead, the characterization with the Pearson coefficient can be used to single out pixels of interest in a scene and segment the volcanic plume for further processing and quantification efforts for example (which are typically more demanding in terms of computing time).

We then set out to evaluate the reliability of simpler BTD indicators, which represent one of the most common ways to identify SO_2 in remote sensing data. The principle is to contrast the brightness temperature (BT) at two wavelengths: one at the location of the SO_2 absorption feature (on-peak) and the other at a reference wavelength outside of that absorption (off-peak). We tested four different BTD indicators and found that the choice of the reference wavelength has a significant impact on the ability of the indicator to reliably detect the presence of SO_2, even when considering narrow sampling wavebands (10 cm^{-1}). BTD index 1, with a reference channel located at 1250 cm^{-1}, surprisingly proved very effective at identifying major volcanic events. The high absorption of water vapor at 1250 cm^{-1} results in almost identical BT values for all pixels in a scene, making it a stable reference channel. However, this stability is also the reason for its failure to distinguish between ash explosions, SO_2 bursts and even warm water vapor bursts, since all of those will result in elevated BT in the on-peak channel and positive values of the BTD. The production of positive values that are not indicative of SO_2 is the measure by which these BTD indicators can be evaluated. BTD indices with reference channels at 1050 cm^{-1} and 925 cm^{-1} (indices 2 and 3) produce positive values of varying intensity, depending on the apparent temperature of the background sky. As a result, their intensity can vary within a single image and over time, reflecting changes in the viewing angle, the movement of low altitude clouds across the scene, or the amount of haze or fog around the vent. Choosing a reference channel at lower frequencies (index 4, 880 cm^{-1}) seems to reduce these variations, while allowing to discriminate between events that simply produce hot pixels (ash or water emissions) and those that actually contain SO_2.

Our observations in this work allow us to make several recommendations when considering the choice of appropriate filters on a multispectral instrument. For optimal use in monitoring tropospheric SO_2 emissions from the ground, we recommend the following: (i) the spectral width of the on-peak waveband (8.6 μm or 1150 cm^{-1}) should not be larger than 50 cm^{-1} at FWHM (ii) its central peak value should match one of the two SO_2 peaks, or both (at 1130 cm^{-1} and 1170 cm^{-1}); and (iii) avoid a spectral response of the filter envelope above 1200 cm^{-1}. Indeed, in this region, water vapor is much less transparent to IR wavelengths, which may significantly reduce the sensor ability to detect SO_2 plumes in the low troposphere.

Acknowledgments

This is Laboratory of Excellence CLERVOLC contribution no. 289. This work was supported by the TOSCA program of the Centre National d'Études Spatiales (CNES-France), through the Convention CNES/131425-BC-T21. The camera rental was made possible thanks to the CLERVOLC LabEx support. This work is part of the ANR STRAP project. We are grateful to TELOPS for the Hyper-Cam rental, and particularly to Marc-André Gagnon for the technical support in the field that made this mission a success. Special thanks to INGV and Sébastien Valade (UNIFI) for the valued logistical support and assistance in the field during the mission at Stromboli. Finally, we would also like to thank an anonymous reviewer for their insightful comments, which helped us greatly improve the final version of this manuscript

References

Ackerman, S.A., Schreiner, A.J., Schmit, T.J., Woolf, H.M., Li, J., Pavolonis, M., 2008. Using the GOES Sounder to monitor upper level SO_2 from volcanic eruptions. J. Geophys. Res. 113:D14S11. https://doi.org/10.1029/2007JD009622.

Aiuppa, A., Bani, P., Moussallam, Y., Di Napoli, R., Allard, P., Gunawan, H., Hendrasto, M., Tamburello, G., 2015. First determination of magma-derived gas emissions from Bromo volcano, eastern Java (Indonesia). J. Volcanol. Geotherm. Res. 304:206–213. https://doi.org/10.1016/j.jvolgeores.2015.09.008.

Allard, P., Burton, M., Muré, F., 2005. Spectroscopic evidence for a lava fountain driven by previously accumulated magmatic gas. Nature 433:407–410. https://doi.org/10.1038/nature03246.

Allard, P., Burton, M., Sawyer, G., Bani, P., 2016. Degassing dynamics of basaltic lava lake at a top-ranking volatile emitter: Ambrym volcano, Vanuatu arc. Earth Planet. Sci. Lett. 448. https://doi.org/10.1016/j.epsl.2016.05.014.

Allard, P., Carbonnelle, J., Metrich, N., Loyer, H., Zettwoog, P., 1994. Sulphur output and magma degassing budget of Stromboli volcano. Nature 368, 326–330.

Arellano, S.R., Hall, M., Samaniego, P., Le Pennec, J.L., Ruiz, A., Molina, I., Yepes, H., 2008. Degassing patterns of Tungurahua volcano (Ecuador) during the 1999–2006 eruptive period, inferred from remote spectroscopic measurements of SO_2 emissions. J. Volcanol. Geotherm. Res. 176:151–162. https://doi.org/10.1016/J.Jvolgeores.2008.07.007.

Barnie, T., Bombrun, M., Burton, M.R., Harris, A., Sawyer, G., 2015. Quantification of gas and solid emissions during Strombolian explosions using simultaneous sulphur dioxide and infrared camera observations. J. Volcanol. Geotherm. Res. 300:167–174. https://doi.org/10.1016/j.jvolgeores.2014.10.003.

Barrancos, J., Roselló, J., Calvo, D., Padrón, E., Melián, G., Hernández, P., Pérez, N., Millán, M., Galle, B., 2008. SO_2 emission from active volcanoes measured simultaneously by COSPEC and mini-DOAS. Pure Appl. Geophys. 165:115–133. https://doi.org/10.1007/s00024-007-0290-8.

Bluth, G.J.S., Shannon, J.M., Watson, I.M., Prata, A.J., Realmuto, V.J., 2007. Development of an ultra-violet digital camera for volcanic SO(2) imaging. J. Volcanol. Geotherm. Res. 161:47–56. https://doi.org/10.1016/J.Jvolgeores.2006.11.004.

Burton, M., Allard, P., Mure, F., La Spina, A., 2007. Magmatic gas composition reveals the source depth of slug-driven strombolian explosive activity. Science 317 (80): 227–230. https://doi.org/10.1126/science.1141900.

Calvari, S., Spampinato, L., Lodato, L., 2006. The 5 April 2003 vulcanian paroxysmal explosion at Stromboli volcano (Italy) from field observations and thermal data. J. Volcanol. Geotherm. Res. 149:160–175. https://doi.org/10.1016/j.jvolgeores.2005.06.006.

Carn, S.A., Clarisse, L., Prata, A.J., 2016. Multi-decadal satellite measurements of global volcanic degassing. J. Volcanol. Geotherm. Res. 311:99–134. https://doi.org/10.1016/j.jvolgeores.2016.01.002.

Carn, S.A., Krueger, A.J., Bluth, G.J.S., Schaefer, S.J., Krotkov, N.A., Watson, I.M., Datta, S., 2003. Volcanic eruption detection by the Total Ozone Mapping Spectrometer (TOMS) instruments: a 22-year record of sulphur dioxide and ash emissions. Geol. Soc. Lond. Spec. Publ. 213:177–202. https://doi.org/10.1144/GSL.SP.2003.213.01.11.

Carn, S.A., Strow, L.L., de Souza-Machado, S., Edmonds, Y., Hannon, S., 2005. Quantifying tropospheric volcanic emissions with AIRS: the 2002 eruption of Mt. Etna (Italy). Geophys. Res. Lett. 32, L02301. https://doi.org/10.1029/2004GL021034.

Carn, S.A.A., Krueger, A.J.J., Arellano, S., Krotkov, N.A.A., Yang, K., 2008. Daily monitoring of Ecuadorian volcanic degassing from space. J. Volcanol. Geotherm. Res. 176:141–150. https://doi.org/10.1016/J.Jvolgeores.2008.01.029.

Corradini, S., Merucci, L., Prata, A.J., 2009. Retrieval of SO_2 from thermal infrared satellite measurements: correction procedures for the effects of volcanic ash. Atmos. Meas. Tech. 2:177–191. https://doi.org/10.5194/amt-2-177-2009.

Corradini, S., Merucci, L., Prata, A.J., Piscini, A., 2010. Volcanic ash and SO_2 in the 2008 Kasatochi eruption: retrievals comparison from different IR satellite sensors. J. Geophys. Res. 115:D00L21. https://doi.org/10.1029/2009JD013634.

Doutriaux-Boucher, M., Dubuisson, P., 2009. Detection of volcanic SO_2 by spaceborne infrared radiometers. Atmos. Res. 92:69–79. https://doi.org/10.1016/j.atmosres.2008.08.009.

Duffell, H., Oppenheimer, C., Burton, M., 2001. Volcanic gas emission rates measured by solar occultation spectroscopy. Geophys. Res. Lett. 28:3131–3134. https://doi.org/10.1029/2000gl012425.

Fischer, T.P., Morrissey, M.M., Calvache, M.L., Gomez, D., Torres, R., Stix, J., Williams, S.N., 1994. Correlations between SO_2 flux and long-period seismicity at Galeras volcano. Nature 368, 135–137.

Gabrieli, A., Wright, R., Lucey, P.G., Porter, J.N., Garbeil, H., Pilger, E., Wood, M., 2016. Characterization and initial field test of an 8–14 μm thermal infrared hyperspectral imager for measuring SO_2 in volcanic plumes. Bull. Volcanol. 78, 73. https://doi.org/10.1007/s00445-016-1068-6.

Galle, B., Oppenheimer, C., Geyer, A., McGonigle, A.J.S., Edmonds, M., Horrocks, L., 2003. A miniaturised ultraviolet spectrometer for remote sensing of SO_2 fluxes: a new tool for volcano surveillance. J. Volcanol. Geotherm. Res. 119:241–254. https://doi.org/10.1016/S0377-0273(02)00356-6.

Jaupart, C., Vergniolle, S., 1988. Laboratory models of Hawaiian and Strombolian eruptions. Nature 331, 58–60.

Karagulian, F., Clarisse, L., Clerbaux, C., Prata, A.J., Hurtmans, D., Coheur, P.F., 2010. Detection of volcanic SO_2, ash, and H_2SO_4 using the Infrared Atmospheric Sounding Interferometer (IASI). J. Geophys. Res. 115:D00L02. https://doi.org/10.1029/2009JD012786.

Krotkov, N.A., Carn, S.A., Krueger, A.J., Bhartia, P.K., Yang, K., 2006. Band residual difference algorithm for retrieval of SO_2 from the Aura Ozone Monitoring Instrument (OMI). IEEE Trans. Geosci. Remote Sens. 44, 1259–1266.

La Spina, A., Burton, M., Allard, P., Alparone, S., Muré, F., 2015. Open-path FTIR spectroscopy of magma degassing processes during eight lava fountains on Mount Etna. Earth Planet. Sci. Lett. 413. https://doi.org/10.1016/j.epsl.2014.12.038.

Lopez, T., Fee, D., Prata, F., Dehn, J., 2013. Characterization and interpretation of volcanic activity at Karymsky volcano, Kamchatka, Russia, using observations of infrasound, volcanic emissions, and thermal imagery. Geochem. Geophys. Geosyst. 14, 5106–5127.

Love, S.P., Goff, F., Counce, D., Siebe, C., Delgado, H., 1998. Passive infrared spectroscopy of the eruption plume at Popocatépetl volcano, Mexico. Nature 396, 563.

Menard, G., Moune, S., Vlastélic, I., Aguilera, F., Valade, S., Bontemps, M., González, R., 2014. Gas and aerosol emissions from Lascar volcano (Northern Chile): insights into the origin of gases and their links with the volcanic activity. J. Volcanol. Geotherm. Res. 287:51–67. https://doi.org/10.1016/j.jvolgeores.2014.09.004.

de Moor, J.M., Aiuppa, A., Pacheco, J., Avard, G., Kern, C., Liuzzo, M., Martínez, M., Giudice, G., Fischer, T.P., 2015. Short-period volcanic gas precursors to phreatic eruptions: insights from Poás volcano, Costa Rica. Earth Planet. Sci. Lett. https://doi.org/10.1016/j.epsl.2016.02.056.

Mori, T., Burton, M., 2006. The SO_2 camera: a simple, fast and cheap method for ground-based imaging of SO_2 in volcanic plumes. Geophys. Res. Lett. 33, L24804.

Mori, T.T., Shinohara, H., Kazahaya, K., Hirabayashi, J., Matsushima, T., Mori, T.T., Ohwada, M., Odai, M., Iino, H., Miyashita, M., 2013. Time-averaged SO2 fluxes of subduction-zone volcanoes: example of a 32-year exhaustive survey for Japanese volcanoes. J. Geophys. Res. Atmos. 118:8662–8674. https://doi.org/10.1002/jgrd.50591.

Moussallam, Y., Bani, P., Curtis, A., Barnie, T., Moussallam, M., Peters, N., Schipper, C.I., Aiuppa, A., Giudice, G., Amigo, Álvaro, Velasquez, G., Cardona, C., Amigo, Á., Velasquez, G., Cardona, C., 2016. Sustaining persistent lava lakes: observations from high-resolution gas measurements at Villarrica volcano, Chile. Earth Planet. Sci. Lett. 454:237–247. https://doi.org/10.1016/j.epsl.2016.09.012.

Nadeau, P.A., Werner, C.A., Waite, G.P., Carn, S.A., Brewer, I.D., Elias, T., Sutton, A.J., Kern, C., 2015. Using SO_2 camera imagery and seismicity to examine degassing and gas accumulation at Kilauea volcano, May 2010. J. Volcanol. Geotherm. Res. 300:70–80. https://doi.org/10.1016/j.jvolgeores.2014.12.005.

Oppenheimer, C., Fischer, T.P., Scaillet, B., 2013. Volcanic degassing: process and impact. Treatise on Geochemistry, Second Edition:pp. 111–179 https://doi.org/10.1016/B978-0-08-095975-7.00304-1.

Oppenheimer, C., Francis, P., Burton, M., Maciejewski, A.J.H., Boardman, L., 1998. Remote measurement of volcanic gases by Fourier transform infrared spectroscopy. Appl. Phys. B Lasers Opt. 67:505–515. https://doi.org/10.1007/s003400050536.

Patrick, M.R., Harris, A.J.L., Ripepe, M., Dehn, J., Rothery, D.A., Calvari, S., 2007. Strombolian explosive styles and source conditions: insights from thermal (FLIR) video. Bull. Volcanol. 69:769–784. https://doi.org/10.1007/s00445-006-0107-0.

Pering, T.D., Tamburello, G., McGonigle, A.J.S., Aiuppa, A., James, M.R., Lane, S.J., Sciotto, M., Cannata, A., Patanè, D., 2014. Dynamics of mild strombolian activity on Mt. Etna. J. Volcanol. Geotherm. Res. 300:103–111. https://doi.org/10.1016/j.jvolgeores.2014.12.013.

Pistolesi, M., Delle Donne, D., Pioli, L., Rosi, M., Ripepe, M., 2011. The 15 March 2007 explosive crisis at Stromboli volcano, Italy: assessing physical parameters through a multidisciplinary approach. J. Geophys. Res. 116:B12206. https://doi.org/10.1029/2011JB008527.

Prata, A.J., 1989. Observations of volcanic ash clouds in the 10–12 μm window using AVHRR/2 data. Int. J. Remote Sens. 10:751–761. https://doi.org/10.1080/01431168908903916.

Prata, A.J., Bernardo, C., 2009. Retrieval of volcanic ash particle size, mass and optical depth from a ground-based thermal infrared camera. J. Volcanol. Geotherm. Res. 186:91–107. https://doi.org/10.1016/j.jvolgeores.2009.02.007.

Prata, A.J., Bernardo, C., 2014. Retrieval of sulfur dioxide from a ground-based thermal infrared imaging camera. Atmos. Meas. Tech. 7:2807–2828. https://doi.org/10.5194/amt-7-2807-2014.

Prata, A.J., Kerkmann, J., 2007. Simultaneous retrieval of volcanic ash and SO_2 using MSG-SEVIRI measurements. Geophys. Res. Lett. 34. https://doi.org/10.1029/2006GL028691.

Pugnaghi, S., Gangale, G., Corradini, S., Buongiorno, M.F., 2006. Mt. Etna sulfur dioxide flux monitoring using ASTER-TIR data and atmospheric observations. J. Volcanol. Geotherm. Res. 152:74–90. https://doi.org/10.1016/J.Jvolgeores.2005.10.004.

Realmuto, V.J., Abrams, M.J., Buongiorno, M.F., Pieri, D.C., 1994. The use of multispectral thermal infrared image data to estimate the sulfur-dioxide flux from volcanos - a case-study from Mount Etna, Sicily, July 29, 1986. J. Geophys. Res. Earth 99, 481–488.

Ripepe, M., Harris, A.J.L.L., Carniel, R., 2002. Thermal, seismic and infrasonic evidences of variable degassing rates at Stromboli volcano. J. Volcanol. Geotherm. Res. 118: 285–297. https://doi.org/10.1016/S0377-0273(02)00298-6.

Rosi, M., Bertagnini, A., Landi, P., 2000. Onset of the persistent activity at Stromboli Volcano (Italy). Bull. Volcanol. 62:294–300. https://doi.org/10.1007/s004450000098.

Rosi, M., Pistolesi, M., Bertagnini, A., Landi, P., Pompilio, M., Di Roberto, A., 2013. Chapter 14 Stromboli volcano, Aeolian Islands (Italy): present eruptive activity and hazards. Geol. Soc. Lond. Mem. 37:473–490. https://doi.org/10.1144/M37.14.

Smekens, J.-F., Clarke, A.B., Burton, M.R., Harijoko, A., Wibowo, H.E., 2015. SO_2 emissions at Semeru volcano, Indonesia: characterization and quantification of persistent and periodic explosive activity. J. Volcanol. Geotherm. Res. 300:121–128. https://doi.org/10.1016/j.jvolgeores.2015.01.006.

Stoiber, R.E., Malinconico, L.L., Williams, S.N., 1983. Use of the Correlation Spectrometer at Volcanoes. Forecast. Volcan. Events. Elsevier, Amsterdam, pp. 425–444.

Swinbank, W.C., 1963. Long-wave radiation from clear skies. Q. J. R. Meteorol. Soc. 89: 339–348. https://doi.org/10.1002/qj.49708938105.

Theys, N., Campion, R., Clarisse, L., Brenot, H., van Gent, J., Dils, B., Corradini, S., Merucci, L., Coheur, P.-F., Van Roozendael, M., Hurtmans, D., Clerbaux, C., Tait, S., Ferrucci, F., 2013. Volcanic SO_2 fluxes derived from satellite data: a survey using OMI, GOME-2, IASI and MODIS. Atmos. Chem. Phys. 13:5945–5968. https://doi.org/10.5194/acp-13-5945-2013.

Thomas, H.E., Watson, I.M., Carn, S.A., Prata, A.J., Realmuto, V.J., 2011. A comparison of AIRS, MODIS and OMI sulphur dioxide retrievals in volcanic clouds. Geomat. Nat. Haz. Risk 2:217–232. https://doi.org/10.1080/19475705.2011.564212.

Urai, M., 2004. Sulfur dioxide flux estimation from volcanoes using advanced spaceborne thermal emission and reflection radiometer - a case study of Miyakejima volcano, Japan. J. Volcanol. Geotherm. Res. 134:1–13. https://doi.org/10.1016/J.Jvolgeores.2003.11.008.

Vandaele, A.C., Simon, P.C., Guilmot, J.M., Carleer, M., Colin, R., 1994. SO_2 absorption cross section measurement in the UV using a Fourier transform spectrometer. J. Geophys. Res. Ser. 99, 25.

Vergniolle, S., Jaupart, C., 1990. Dynamics of degassing at Kilauea volcano, Hawaii. J. Geophys. Res. Solid Earth 95:2793–2809. https://doi.org/10.1029/JB095iB03p02793.

Watson, I..M., Realmuto, V..J., Rose, W..I., Prata, A..J., Bluth, G.J..J.S., Gu, Y., Bader, C..E., Yu, T., 2004. Thermal infrared remote sensing of volcanic emissions using the moderate resolution imaging spectroradiometer. J. Volcanol. Geotherm. Res. 135:75–89. https://doi.org/10.1016/J.Jvolgeores.2003.12.017.

Watson, I.M., Oppenheimer, C., Voight, B., Francis, P., Clarke, A., Stix, J., Miller, A., Pyle, D.M., Burton, M.R., Young, S.R., Norton, G., Loughlin, S., Darroux, B., Staff, M.V.O., 2000. The relationship between degassing and ground deformation at Soufriere Hills volcano, Montserrat. J. Volcanol. Geotherm. Res. 98, 117–126.

Wen, S., Rose, W.I., 1994. Retrieval of sizes and total masses of particles in volcanic clouds using AVHRR bands 4 and 5. J. Geophys. Res. 99:5421. https://doi.org/10.1029/93JD03340.

Journal Code J G R B | Article ID 52879 | Dispatch: 22.06.18 | CE: JAQA | No. of Pages: 23 | ME:

AGU100 ADVANCING EARTH AND SPACE SCIENCE

JGR

Journal of Geophysical Research: Solid Earth

RESEARCH ARTICLE

10.1029/2017JB015163

Modeling Eruption Source Parameters by Integrating Field, Ground-Based, and Satellite-Based Measurements: The Case of the 23 February 2013 Etna Paroxysm

M. Poret[1,2], A. Costa[1], D. Andronico[3], S. Scollo[3], M. Gouhier[4], and A. Cristaldi[3] Q2 Q3

[1]Sezione di Bologna, Istituto Nazionale di Geofisica e Vulcanologia, Bologna, Italy, [2]Geophysics Department, University of Bologna, Bologna, Italy, [3]Osservatorio Etneo, Sezione di Catania, Istituto Nazionale di Geofisica e Vulcanologia, Catania, Italy, [4]Laboratoire Magmas et Volcans, Université Blaise Pascal, Clermont-Ferrand, France Q4

Key Points:
- The 23 February 2013 Etna eruption features were reconstructed integrating tephra, satellite, and aerosol optical depth measurements
- Synergetic use of field and satellite data to assess the total grain-size distribution from coarse lapilli to very fine ash
- Simultaneous numerical simulations of the tephra loading and airborne ash dispersal

Supporting Information:
- Supporting Information S1
- Figure S1
- Figure S2
- Figure S3

Correspondence to:
M. Poret,
matthieu.poret@gmail.com

Citation:
Poret, M., Costa, A., Andronico, D., Scollo, S., Gouhier, M., & Cristaldi, A. (2018). Modeling eruption source parameters by integrating field, ground-based, and satellite-based measurements: The case of the 23 February 2013 Etna paroxysm. *Journal of Geophysical Research: Solid Earth*, *123*. https://doi.org/10.1029/2017JB015163

Received 27 OCT 2017
Accepted 2 JUN 2018
Accepted article online 9 JUN 2018

Abstract Volcanic plumes from Etna volcano (Italy) are governed by easterly winds driving ash over the Ionian Sea. The limited land tephra deposit makes total grain-size distribution (TGSD) assessment and its fine ash fraction highly uncertain. On 23 February 2013, a lava fountain produced a ~9-km-high column above sea level (a.s.l.). The atypical north-easterly wind direction dispersed the tephra from Etna to the Puglia region (southern Italy) allowing sampling up to very distal areas. This study uses field measurements to estimate the field-based TGSD. Very fine ash distribution (particle matter below 10 μm—PM_{10}) is explored parameterizing the field-TGSD through a bi-lognormal and bi-Weibull distribution. However, none of the two latter TGSDs allow simulating any far-traveling airborne ash up to distal areas. Accounting for the airborne ash retrieved from satellite (Spinning Enhanced Visible and Infrared Imager), we proposed an empirical modification of the field-based TGSD including very fine ash through a power law decay of the distribution. The input source parameters are inverted by comparing simulations against measurements. Results suggest a column height of ~8.7 km a.s.l., a total erupted mass of ~4.9 × 10^9 kg, a PM_{10} content between 0.4 and 1.3 wt%, and an aggregate fraction of ~2 wt% of the fine ash. Aerosol optical depth measurements from the AErosol RObotic NETwork are also used to corroborate the results at ~1,700 km from the source. Integrating numerical models with field, ground-based, and satellite-based data aims at providing a better TGSD estimation including very fine ash, crucial for air traffic safety.

Plain Language Summary On 23 February 2013, an intense lava fountain at Etna volcano, Italy, produced a ~9-km-high volcanic plume. The effect of a south-westerly winds dispersed the erupted material (tephra) from Etna to the Puglia region (~410 km from the source; southern Italy). These conditions permitted tephra sampling from the volcano up to Puglia. Field data are used to assess the total grain-size distribution (TGSD) to feed the FALL3D tephra dispersal model to reconstruct the tephra loading and airborne ash dispersal. To account for satellite data, we modified the TGSD adding the missing very fine ash content. Best simulations were selected by comparing computed and observed measurements in terms of tephra loadings and airborne ash mass. Results give an eruptive column height of ~8.7 km a.s.l., a total erupted mass of ~4.9 × 10^9 kg, a very fine ash content between 0.4 and 1.3 wt%, and an aggregated ash fraction of ~2 wt% of the fine ash. Results are also compared with aerosol measurements. Integrating numerical models with field and satellite-based data aims at providing a better TGSD estimation including the very fine ash fraction (below 0.01 mm), crucial for air traffic safety.

1. Introduction

One of the main goals of modern volcanology is a better understanding and quantification of eruption source parameters (ESP) governing tephra dispersal during a volcanic crisis. This is done using field (e.g., Andronico, Cristaldi, et al., 2008; Andronico, Scollo, et al., 2008; Andronico, Scollo, Lo Castro, et al., 2014), remote-sensing retrievals (e.g., Corradini et al., 2008, 2016; Gouhier et al., 2016; Scollo et al., 2012, 2014), laboratory experiments (e.g., Bagheri & Bonadonna, 2016; Cigala et al., 2017; Mueller, Ayris, et al., 2017; Mueller, Kueppers, et al., 2017), and numerical models (e.g., Bonadonna & Costa, 2012; Folch et al., 2016; Scollo et al., 2008). ESP assessment (e.g., Folch, 2012; Mastin et al., 2009) involves the estimation, among others, of the mass eruption rate (MER), which combined with the eruption duration provides the total erupted mass (TEM). The field-derived TEM is obtained by integrating the isomass maps (e.g., Bonadonna & Costa, 2013), which requires tephra deposits to be sampled at several locations (Bonadonna et al., 2015). In addition to the

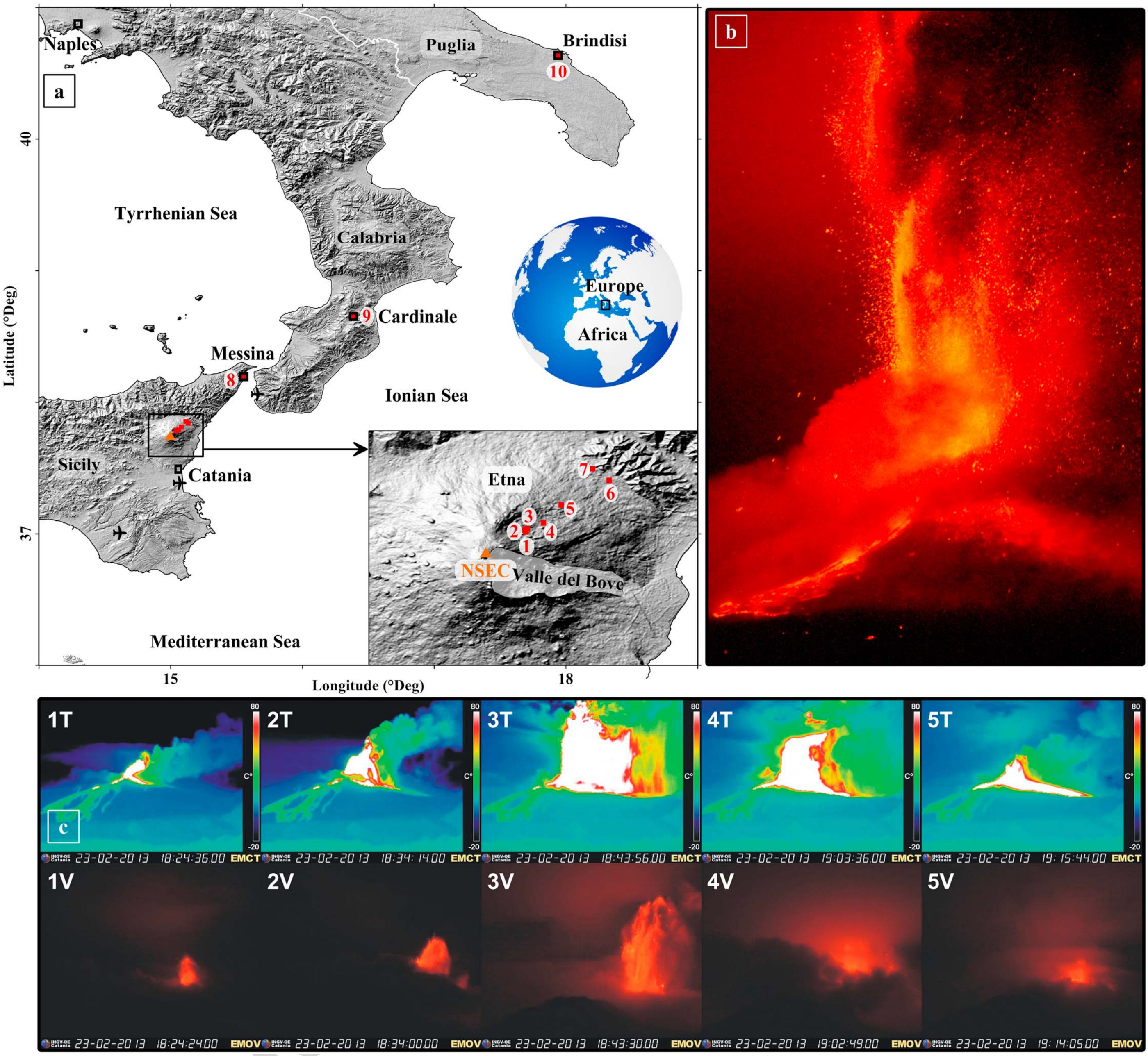

Figure 1. (a) The Italian regions (i.e., Sicily, Calabria and Puglia) affected by tephra fallout of the 23 February 2013 Etna paroxysm. NSEC stands for New Southeast Crater from which the eruption occurred. Red numbers refer to the sample sites, whereas the aircraft symbols localize the Fontanarossa (Catania), the Pio La Torre (Sicily), and the Tito Minniti (Calabria) airports. The inset zooms on Etna indicate the proximal samples (details in Table 1). (b) Photograph of the eruption. Courtesy of Marco Neri. (c) Time series pictures of the eruption in thermal (1–5 T) and visible (1–5 V) spectrum. Source: INGV-OE.

TEM, field data give geolocalized grain-size distributions (GSD) permitting the total grain-size distribution (TGSD) to be estimated by integrating local GSD (Bonadonna et al., 2015; Bonadonna & Houghton, 2005). Tephra is classified depending on the size (e.g., Folch, 2012), as bombs or blocks (i.e., diameter—$d \geq 64$ mm), lapilli ($2 \leq d < 64$ mm), and ash ($d < 2$ mm). Within ash, we further distinguish fine ash ($d < 1$ mm), very fine ash ($d < 30$ μm; Rose & Durant, 2009), and ultra-fine ash ($d < 5$ μm). Hereinafter, we define the very fine ash as particle matter below 10 μm (hereinafter PM_{10}). Nonetheless, the TGSD strongly depends on the sampling distance from the source (Costa, Pioli, et al., 2016), the number of available

Table 1
List of the Collected Samples With Their Numerical Results for Each Input Total Grain-Size Distribution (TGSD)

	Field observations					Computed loading (kg/m^2)			
Sample	Location	Longitude	Latitude	Mode (Φ)	Loading (kg/m^2)	Field TGSD	Bi-Gaussian TGSD	Bi-Weibull TGSD	Fine Enriched TGSD
1	Baracca	15.042	37.782	−3.5	2.1×10^1	4.5×10^0	7.6×10^0	6.5×10^0	4.5×10^0
2	Casetta	15.041	37.784	−4.0	5.9×10^0	4.5×10^0	7.7×10^0	6.6×10^0	4.6×10^0
3	Bivio-007	15.044	37.786	−4.0	5.5×10^0	4.7×10^0	7.9×10^0	6.8×10^0	4.7×10^0
4	Forestale	15.061	37.792	−3.5	2.2×10^1	5.1×10^0	8.5×10^0	7.3×10^0	5.1×10^0
5	Chalet	15.081	37.813	−2.5	3.2×10^1	6.1×10^0	9.6×10^0	8.4×10^0	6.1×10^0
6	Castiglione	15.114	37.854	−1.5	5.2×10^0	8.0×10^0	1.1×10^1	9.5×10^0	8.1×10^0
7	Linguaglossa Out	15.133	37.840	−3.0	1.2×10^0	8.4×10^0	1.1×10^1	1.0×10^1	8.5×10^0
8	Messina	15.554	38.195	1.0	2.9×10^{-1}	1.2×10^0	1.1×10^0	9.4×10^{-1}	1.3×10^0
9	Cardinale	16.384	38.650	2.0	1.3×10^{-2}	3.9×10^{-2}	2.0×10^{-2}	2.2×10^{-2}	4.0×10^{-2}
10	Brindisi	17.941	40.634	3.0	1.4×10^{-3}	1.8×10^{-3}	1.5×10^{-4}	5.4×10^{-4}	1.8×10^{-3}

Note. Sampling includes locations, tephra loadings, and modes. The computed loadings result from the use of the Field, bi-Gaussian, bi-Weibull, and Fine Enriched TGSDs (Figure 4).

samples (Bonadonna et al., 2015; Bonadonna & Houghton, 2005), and the spatial distribution (Bonadonna et al., 2015; Spanu et al., 2016). Moreover, the fine ash fraction within the TGSD is likely underestimated due to the long atmospheric residence time ranging from hours to days (Rose & Durant, 2009), preventing very fine ash from sampling at reasonable distance (Costa, Pioli, et al., 2016). For these reasons, TGSD assessment is highly uncertain, especially for the fine ash fraction (Bonadonna et al., 2011; Costa, Pioli, et al., 2016), which depends on the eruption type (Rose & Durant, 2009). Indeed, a basaltic volcano commonly produces a fine ash fraction of a few percent of the erupted material, whereas the fraction from silicic eruption contains between 30% and 50% (Rose & Durant, 2009).

The statements described above highlight the need for an integrated approach that encompasses the grain-size spectrum down to the very fine ash. Recent eruptions reveal how an accurate estimation of such fraction is crucial for air traffic safety (e.g., Bonadonna et al., 2011; Casadevall, 1994; Folch et al., 2012). As an example, Bonadonna et al. (2011) integrated field and satellite information to better characterize the TGSD of the May 2010 Eyjafjallajökull eruption, which had a relatively large very fine ash population (Costa, Pioli, et al., 2016). Motivated by their results, we aim at reconstructing the entire TGSD (including PM_{10}), integrating field measurements and satellite-based observations of the 23 February 2013 Etna paroxysm.

At Etna, more than 200 lava fountains occurred from the New Southeast Crater (NSEC) between 1995 and 2014 (Andronico, Scollo, Lo Castro, et al., 2014; De Beni et al., 2015; Corsaro et al., 2017). Most eruption columns reached several kilometers high releasing ash into the atmosphere. The prevailing easterly winds over the Etnean region (Barsotti et al., 2010; Scollo et al., 2013) dispersed the tephra downwind over the Ionian Sea. Consequently, the narrow land surface (i.e., 5–20 km eastward from source) affects the sampling area and, therefore, the field-derived TGSD. Andronico, Scollo, Cristaldi, et al. (2014) demonstrated how an incomplete field data set for Etna (e.g., location and spatial distribution) influences the TGSD estimation and the TEM retrieval. In addition, Azzopardi et al. (2013) showed that an incorrect ESP assessment may also impact the forecast of the plume transport over neighboring countries, such as the Maltese Islands.

On 23 February 2013, the eruption dispersed tephra fallout north-eastward permitting sampling from the proximal volcanic slopes to Brindisi (Puglia region) about 410 km from the source (Figure 1 and Table 1). In F1T1 the literature, only a few studies on Etna eruptions used similar distal field observations (Dellino & Kyriakopoulos, 2003), but the paucity of data prevented using within the TGSD calculation. Here, starting from the field-derived TGSD for the 23 February 2013 paroxysm, we inverted the PM_{10} fraction required within the TGSD for numerically reconstructing simultaneously the tephra loading and far-traveling airborne ash mass. Simulations were run coupling FPlume (Folch et al., 2016) with the FALL3D tephra dispersal model (Costa et al., 2006; Folch et al., 2009). Simulation input parameters (ESP) were inverted by best-reproducing field and satellite retrievals.

Worldwide high time-resolution satellite coverage allows most eruptive processes to be recorded (Gouhier et al., 2016). Geostationary platforms, such as meteosat second generation, are particularly suited to rapidly evolving volcanic plume observations (Prata & Kerkmann, 2007) with an acquisition frequency of up to one image every 5 min with the rapid scan service. In addition to satellite data, the ground-based AErosol RObotic NETwork (AERONET) is used to validate the satellite retrievals and simulations of ultra-fine particles (i.e., few micrometers; Folch et al., 2012). Although combining data from different instruments is challenging due to their own operative window, this work aims to show that an integrated multidisciplinary approach is necessary for better assessing the TGSD, which is pivotal for air traffic safety (e.g., Beckett et al., 2015; Folch et al., 2012). Indeed, improving ash plume characterization in terms of ash concentration and dispersion is highly relevant for the volcanic ash advisory centers (VAACs) and the pilots to prevent ash encounters. As testified by several cases worldwide in the last 30 years (Casadevall, 1994; Casadevall et al., 1999; Grindle & Burchamn, 2003; Guffanti et al., 2005; Prata, 1989a), the data can be used for delimiting the no-fly zones, helping the decision makers, such as those working in the VAACs. Considering that there is no operational single method capable of describing fully the volcanic eruption processes, tracking the plume, and assessing the ESPs, their estimation can only be obtained through a synergetic integrated approach.

To provide alerts of volcanic activity in support of air traffic safety, the nine VAACs use operational volcanic ash transport and dispersion models, such as (1) the Numerical Atmospheric-dispersion Modeling Environment (NAME; Beckett et al., 2014; Witham et al., 2007) for the London VAAC, (2) the "MOdèle de Chimie Atmosphérique à Grande Echelle" (MOCAGE-accident; Sič et al., 2015) for the Toulouse VAAC, and (3) the FALL3D for the Buenos Aires and Darwin VAACs. However, their initializations commonly use simplified TGSD. For example, NAME assumes a standard grain-size distribution from a preexisting eruption (Maryon et al., 1999), arbitrarily considering 5% in weight of the TEM for the fine ash content.

Besides the aviation hazard, volcanic ash also affects populations living near active volcanoes (e.g., Sulpizio et al., 2012). In particular, PM_{10} has respiratory health effects even for eruptions produced by Etna (e.g., Andronico & Del Carlo, 2016; Horwell, 2007; Horwell et al., 2013, 2017; Rose & Durant, 2009; Tomašek et al., 2016).

The paper describes, first, the 23 February 2013 eruption features. Then, the modeling approach is followed by the methodology used to reconstruct the TGSD and assess the best ESPs. We report the different data set used (i.e., field, satellite, and ground based) prior to presenting and discussing the results.

2. Chronology of the 23 February 2013 Eruption

On 23 February 2013, an intense lava fountain took place at the NSEC (Figure 1b), which is the youngest and most active of Etna's craters (Andronico et al., 2015; Behncke et al., 2014). The eruptive activity initiated with Strombolian explosions, which increased around 18:15 UTC turning into lava fountaining (Figure 1c). The paroxysmal phase lasted 1 hr and 6 min. Despite bad weather conditions (i.e., cloudy, windy, and night) during the paroxysmal activity, images from the "Istituto Nazionale di Geofisica e Vulcanologia—Osservatorio Etneo" (INGV-OE) showed the growth of incandescent lava jets higher than 500 m above the crater (Figures 1b and 1c), from which a buoyant plume developed up to ~9 km above sea level (a.s.l.) forming the umbrella region. Figure 2 shows the main meteorological profiles (e.g., temperature, air moisture, wind speed, and direction) obtained from the European Center for Medium-range Weather Forecasts (ERA-Interim-Reanalysis). Considering the time for the ash to be transported from NSEC to Brindisi (i.e., ~5 h), the two profiles refer to 18:30 UTC and 23:30 UTC, respectively. This study benefitted from atypical meteorological conditions in wind speed and direction during the eruption and the following hours, with similar patterns over NSEC and Brindisi. Indeed, the wind speed at 18:30 UTC and 8.5 km a.s.l. is ~49.6 and ~32.6 m/s over NSEC and Brindisi, respectively, whereas at 23:30 UTC, it is ~50.6 and ~36.3 m/s. Such a context made sampling possible from Etna's slopes (5–16 km from the source) to Messina (~70 km) up to Calabria and Puglia regions (~160 and ~410 km, respectively). Field location and data are available in Figure 1 and Table 1, respectively.

In the deposit, we found lapilli up to 5–6 km from the vent (samples 1–7), coarse ash (i.e., 2–0.125 mm) in Messina (sample 8), fine ash with mode at 0.25 mm in Cardinale (sample 9), and the finest ash deposit in Brindisi (sample 10) with mode around 0.125 mm (details in Table 1). Geochemical analysis on several samples indicate a CaO/Al_2O_3 ratio in glass (Corsaro & Miraglia, 2013a), suggesting slightly different compositions

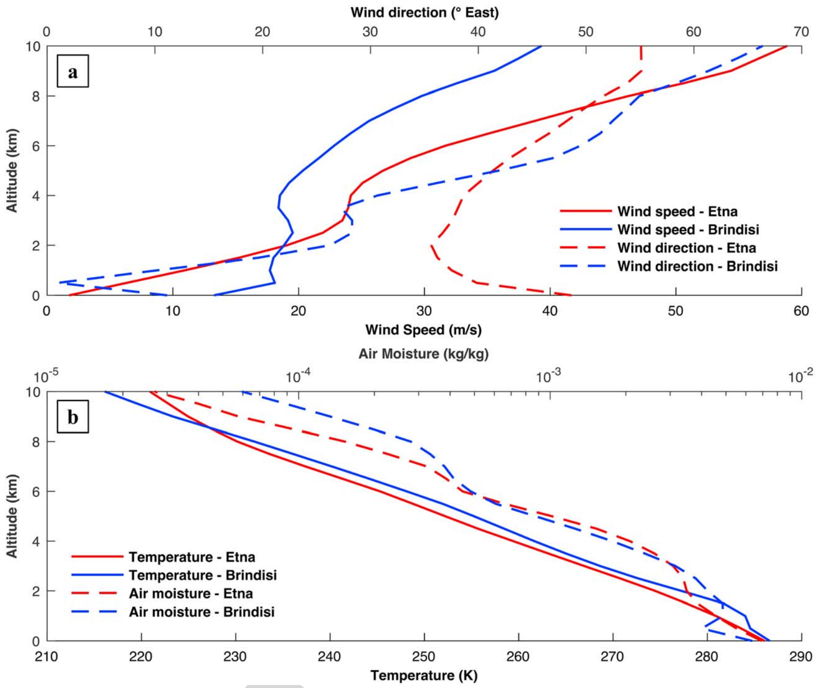

Figure 2. (a) Wind direction and speed profiles above the New Southeast Crater and Brindisi at 18:30 UTC and 23:30 UTC, respectively. (b) Associated air moisture and temperature profiles. Data refer to the 23 February 2013, which are provided by the European Center for Medium-range Weather Forecasts platform (ERA-Interim-Reanalysis).

from those measured during the 2011–2012 sequence (Behncke et al., 2014). They also show more evolved magma than on the 23 November 2013 (Andronico et al., 2015; Corsaro & Miraglia, 2013b).

3. Modeling Approach: FPlume and FALL3D Models

Tephra dispersal models are widely used in volcanology to quantify either the tephra loading (e.g., TEPHRA, Connor et al., 2001; HAZMAP, Macedonio et al., 2005; FALL3D, Costa et al., 2006; Folch et al., 2009) or the airborne volcanic ash (e.g., VOL-CALPUFF, Barsotti et al., 2008; FALL3D). All tephra dispersal models need input parameterizations of the source term (e.g., eruptive column, MER, TGSD). An overview of such models is available in Folch (2012) and Costa, Suzuki, et al. (2016).

This study uses FALL3D to compute the tephra dispersal and sedimentation by means of FPlume (Folch et al., 2016), which is a steady-state eruption column model based on the buoyant plume theory (Morton et al., 1956). FPlume solves for one-dimensional cross-section-averaged equations for mass, momentum, and energy conservations, accounting for the effects of wind coupling, air moisture, particle re-entrainment, and ash aggregation under wet conditions. Within FALL3D, FPlume uses the TGSD together with the initial magma temperature and water content to provide the vertical particle distribution inside the column. Etna is a basaltic volcano producing magmas typically at 1,300 K with ~2.5 wt% of magmatic water (Allard et al., 2005; Carbone et al., 2015; Metrich et al., 2004; Metrich & Rutherford, 1998; Spilliaert et al., 2006). FPlume estimates the MER for a column height and a given wind profile by using two turbulent air entrainment coefficients (i.e., radial (α) and cross-flow (β) coefficients; Bursik, 2001; Suzuki & Koyaguchi, 2015). α is internally calculated (details in Kaminski et al., 2005; Folch et al., 2016), whereas β is poorly constrained (Costa, Suzuki, et al., 2016), being calibrated based on best-fitting the field measurements. Characterizing the source term through FPlume implies uncertainties associated with the input parameters (see Macedonio et al., 2016).

The three-dimensional time-dependent Eulerian FALL3D model solves a set of advection-diffusion-sedimentation equations over a structured terrain-following grid using a finite difference method (Costa et al., 2006; Folch et al., 2009). Besides the ESPs, FALL3D requires the time-dependent meteorological fields across the computational domain (Figure 1). For the simulated period (i.e., from 00:00 UTC on 23 February

10.1029/2017JB015163

Table 2
List of the Input Parameters for FPlume and FALL3D Modeling With Their Ranges

Parameter	Explored range	
Column height (km a.v.)	3	10
Mass Eruption Rate (kg/s)	10^3	10^8
Exit velocity (m/s)	150	300
Exit water fraction (%)	0.5	3.2
Cross-flow entrainment coefficient (β)	0.3	1.0
Aggregate diameter (Φ_{Agg})	1	2.5
Density aggregates (kg/m^3)	200	1,200

Note. Other options and models are described in Appendix A.

up to 00:00 UTC on 29 February 2013), European Center for Medium-range Weather Forecasts meteorological data were obtained every 6 h for 37 pressure levels (i.e., from 1,000 to 1 mb) at 0.75° horizontal resolution. It is worth noting that the resolution is too low for capturing the orographic effects, which can be very important at local scale (e.g., around Etna's slopes), affecting the tephra loading (Watt et al., 2015). FALL3D uses an internal meteorological grid interpolated here at 4-km resolution (the grid mesh is displayed in Figure S1 in the supporting information). Although gravity currents in the umbrella region are not significant for such a small eruption (Costa et al., 2013), the simulations accounted for these effects. Ash aggregation, assumed negligible in terms of mass, was also investigated following a scheme based on a simplified solution of the Smoluchowski equation (Smoluchowski, 1917) proposed by Costa et al. (2010). Aggregation scheme uses a fractal relationship of the number of primary particles within an aggregate together with the effects of both magmatic water and air moisture (Folch et al., 2010, 2016). Further description of the models and the parameterizations used for ash aggregation are available in Poret et al. (2017).

4. Observational Data and Methodology

The methodology proposed here brings together field and satellite data to reconstruct the initial grain-size distribution in the plume before sedimentation (i.e., input TGSD). A summary of the input parameters is available in Table 2. As first step, we used the field samples to retrieve the TGSD. Then, the TGSD was parameterized using lognormal and Weibull distributions (Costa, Pioli, et al., 2016, 2017). ESPs were inverted by capturing the measurements. Finally, the field-based TGSD was extrapolated for implementing the very fine ash distribution through an analytical parameterization. Satellite retrievals were used to invert the PM_{10} fraction by best-fitting the simulated distal airborne ash mass. We also validated the results by analyzing the ultra-fine ash dispersal with the AERONET data.

4.1. Field Data Analysis

In volcanology, the particle-size spectrum is typically expressed in Φ-units through the relationship $d = 2^{-\Phi}$, with the diameter d in millimeters (Krumbein, 1934). Few hours after the eruption, tephra was sampled at 10 different locations (Figure 1). Prior to analysis, loading per unit area was measured, and samples were oven-dried at 110 °C for 12 hr at the sedimentology laboratory of the INGV-OE. Then, GSD was retrieved from −5 to 5 Φ (at 0.5 Φ interval) by sieving (via a Retsch vibratory sieve shaker AS 200 Basic). The farthest sample (i.e., no. 10 in Figure 1) contains only small fine ash (i.e., $d \geq 2$ Φ), preventing sieve analysis. The GSD was given by the CAMSIZER (Retsch) instrument, which has the same range size limit as the sieve (Lo Castro & Andronico, 2008). Andronico, Scollo, Cristaldi, et al. (2014) validated their alternative use showing the good match between the two methods above for grain-size analysis purpose. The field GSDs indicate a clear decay in size from proximal to distal areas and an increase in tephra sorting with distance (Figure 3). They also show unimodal behavior, peaking at −4 Φ for medial locations and 3 Φ for the distal ones (Table 1).

Beside GSD, we used the field data to estimate the total mass of the deposit using the method of Bonadonna and Costa (2012, 2013), which is based on the Weibull distribution of the deposit thinning. The resulting field-derived TEM estimate yields ~$2.0 \pm 0.5 \times 10^9$ kg.

4.2. Satellite Data (Spinning Enhanced Visible and Infrared Imager)

Satellite-based thermal infrared sensors are very useful for characterizing volcanic ash (Gouhier et al., 2016; Guéhenneux et al., 2015). In the thermal infrared region (i.e., 7–14 μm), we can distinguish silicate particles (e.g., volcanic ash) from other aerosols (e.g., ice crystals, SO_2, or H_2SO_4) using a two-channel difference model based on the absorption feature between the 11- and 12-μm wavelengths (Prata, 1989b; Watson et al., 2004; Wen & Rose, 1994). It was shown that the difference between the at-sensor "Planck" brightness temperature (referred to as BTD) observed in these two channels is negative ($-\Delta T$) for ash and positive ($+\Delta T$) for ice. Wen and Rose (1994), built on early work (Prata, 1989b), developed a forward retrieval model that quantifies the effective radius (r_e) and optical depth (τ_c) from the extinction efficiency factor (Q_{ext}) calculated using the

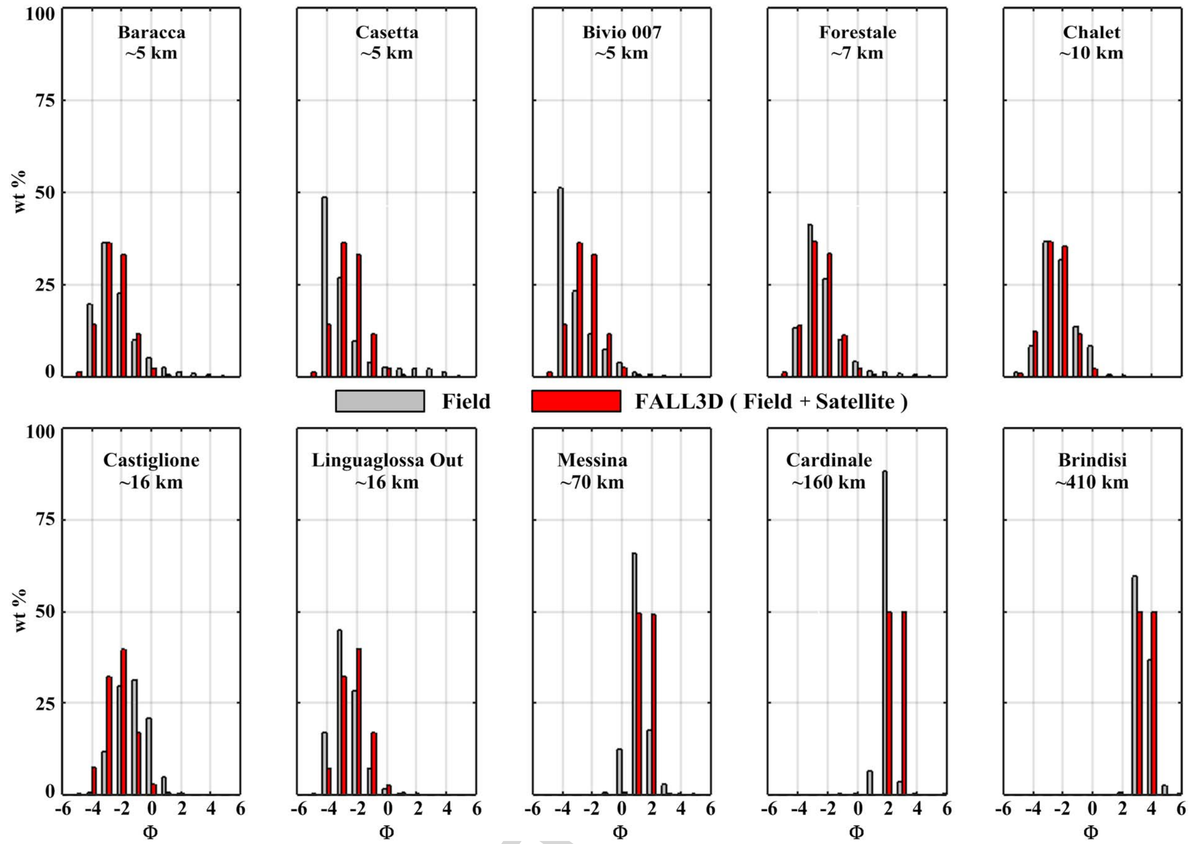

Figure 3. Individual field grain-size distribution of the 10 samples together with the ones computed by considering both field and satellite observations (i.e., Fine Enriched total grain-size distribution).

Mie theory. This allows a theoretical lookup table to be produced for sets of variations of both r_e and τ_c as a function of the brightness temperature. From the inverse procedure, r_e and τ_c (and hence the mass of the volcanic ash cloud) can be retrieved for any given brightness temperature pair (details in Prata & Grant, 2001; Watson et al., 2004). However, satellite retrievals are affected by several factors such as the surface characteristics (i.e., temperature and emissivity), plume geometry (i.e., altitude and thickness), ash optical properties, and water vapor. These factors produce an uncertainty of ~40% and ~30% respectively associated with the total mass retrieval and effective radius (Corradini et al., 2008). Another source of uncertainty is related to the presence of relatively large particles (typically for $r_e > 6$ μm), possibly within the fine ash clouds, which cannot be retrieved using the Mie theory as Q_{ext} does not vary significantly for $r_e > \lambda/2$ (Guéhenneux et al., 2015; Stevenson et al., 2015). Overall, the effects related to both misdetection issues (i.e., BTD) and the presence of coarse ash particles in the cloud lead to a mass underestimation of 50% (Stevenson et al., 2015).

We used data from the Spinning Enhanced Visible and Infrared Imager (SEVIRI) sensor onboard Meteosat-10, which provides images every 15 min at a spatial resolution of ~3 × 3 km at nadir. Satellite data were acquired from HOTVOLC (http://hotvolc. opgc.fr), a web-based satellite-data-driven monitoring system developed at the Observatoire de Physique du Globe de Clermont-Ferrand (France). The system is designed for real-time monitoring of active volcanoes (Gouhier et al., 2016). During the 23 February 2013 Etna eruption, the volcanic cloud was tracked in the SEVIRI data in terms of airborne ash mass (hereinafter AAM; in kilograms) over hundreds of kilometers. SEVIRI level 1.5 data recorded by the HOTVOLC system were initially converted into calibrated spectral radiance (in W $m^{-2}sr^{-1}$ μm^{-1}). Then, following the methodology described above (Guéhenneux et al., 2015; Wen & Rose, 1994), we provide the cloud top temperature (°C), altitude (m a.s.l.), AAM (kg), and r_e (μm) from 19:00 to 20:15 UTC.

4.3. AERONET Data

The AERONET is a ground-based remote sensing network (Holben et al., 1998) supervised by the National Aeronautics and Space Administration (NASA) and the Photométrie pour le Traitement Opérationnel de Normalisation Satellitaire. AERONET aims at retrieving in real time a global database from solar spectral irradiance to assess aerosol optical properties, for example, volume size distribution, particle sphericity (estimated here as the ratio between the backscattered and the depolarization signals), and aerosol optical depth (AOD) to validate satellite observations (Dubovik et al., 2006). The columnar AOD is measured from solar radiance (Holben et al., 2006) at diverse spectral channels (e.g., 500 nm) through three data quality levels (Dubovik et al., 2006). In addition, direct-sun-derived AOD processing (O'Neill et al., 2003; Watson & Oppenheimer, 2001) integrates signal (in voltage) from the sensor to the top of the atmosphere, given by the sun-photometer measurement at the Mauna Loa Observatory of Hawaii. The proportionality between the spectral irradiance at the sensor and the acquired signal is used to convert into AOD. However, wavelength-dependent gas (e.g., H_2O, O_3, NO_2, CO_2, and CH_4) may scatter light and must be subtracted when calculating the AOD. During the inversion procedure, the error is assumed to be distributed lognormally and uncorrelated giving a standard deviation of 5% associated with the sky radiance measurement (Dubovik, 2004; Dubovik et al., 2000; Dubovik & King, 2000). AOD at 500-nm wavelength is used as standard to compute the fine mode fraction of the total AOD (e.g., Folch et al., 2012). It is worth noting that the assumption of a lognormal distribution, made for both AERONET and satellite retrievals, is not fully consistent with the empirical distribution we adopt in this work and has to be considered as an approximation of it.

The 23 February 2013 Etna paroxysm released very fine ash toward south-eastern Europe. Among the AERONET sites, the station located at Çamlıbel, Turkey (station labeled IMS-METU ERDEMLI, ~1,700 km from Etna) detected particles from 24–26 February 2013. Unfortunately, the eruptive period overlapped with a substantial resuspension of Saharan dust from 20 to 23 February 2013. Even though the dust storm was in a final stage, the presence of airborne mineral dust affected the AOD retrieved over the station. To assess the volcanic ash AOD, we subtracted the dust contribution estimated from the Goddard Earth observing system (GEOS-chem) model (Bey et al., 2001; Chan & Chan, 2017; Fairlie et al., 2007; Park et al., 2004). Although such approach introduces a large uncertainty in the retrieval, we bear in mind that data were used to validate the satellite observations only by verifying if the input TGSD permits the reproduction of the ultrafine ash dispersal at ~1,700 km from the source. Indeed, we compared the computed volcanic ash AOD (FALL3D) with the AERONET measurements.

4.4. TGSD Estimation

Making use of the 10 field GSDs, the field-derived TGSD (hereinafter Field TGSD; Figure 4) is estimated **F4** through the Voronoi tessellation method (Bonadonna & Houghton, 2005). Regarding the spatial distribution of the samples, the Field TGSD suffers from the lack of field data, especially at medial and distal locations. Consequently, it cannot fully represent the initial magma fragmentation but only an estimation with, for the first time on Etna, medial and distal measurements. Figure 4a shows the bimodality of the Field TGSD with a first mode (i.e., the coarse sub-population) around $-3\ \Phi$ and a second mode (i.e., the fine sub-population) around 0.5 Φ. To reproduce the Field TGSD in a simple parametric way and extrapolate to the very fine ash fraction, we describe the TGSD as the sum of two lognormal distributions (bi-Gaussian in Φ, hereinafter bi-Gaussian distribution), and two Weibull distributions (hereinafter bi-Weibull distribution). The bi-Gaussian distribution was constructed following the equation (Costa, Pioli, et al., 2016):

$$f_{\text{bi-Gaussian}}(\Phi) = p\frac{1}{\sigma_1\sqrt{2\pi}}e^{-\frac{(\Phi-\mu_1)^2}{2\sigma_1^2}} + (1-p)\frac{1}{\sigma_2\sqrt{2\pi}}e^{-\frac{(\Phi-\mu_2)^2}{2\sigma_2^2}} \quad (1)$$

where Φ is the particle diameter in logarithmic scale, p and $(1-p)$ are the fractions of each subpopulation, and μ_1, μ_2, σ_1, and σ_2 (Table 3) are the mean and standard deviations of the two Gaussian distributions in Φ- **T3** units, respectively (Figure 4a). The cases well characterized in terms of fine ash fraction indicate that a lognormal distribution tends to underestimate the fine ash distribution (Costa, Pioli, et al., 2016). This becomes significant for TGSD produced by Etna eruptions, as most of the fine ash is typically not sampled. In the latter

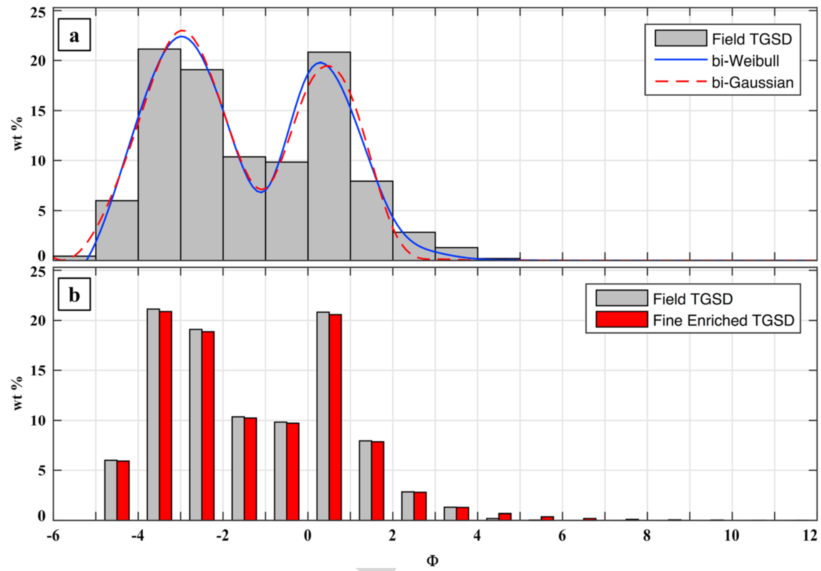

Figure 4. Summary of the input total grain-size distributions (TGSDs) used within the simulations. (a) Field TGSD together with its best-fitting analytical curves (bi-Gaussian and bi-Weibull distributions; details in Table 3). (b) Fine Enriched TGSD obtained from the Field TGSD by modifying empirically the fine ash distribution.

case, Costa, Pioli, et al. (2016, 2017) demonstrated that a better quantification of the fine ash fraction is given by the bi-Weibull distribution as follows:

$$f_{\text{bi-Weibull}}(d) = q\frac{1}{n_1^{\frac{1}{n_1}}\Gamma\left(1+\frac{1}{n_1}\right)}\frac{1}{\lambda_1}\left[\frac{d}{\lambda_1}\right]^{n_1} e^{-\frac{1}{n_1}\left(\frac{d}{\lambda_1}\right)^{n_1}} + (1-q)\frac{1}{n_2^{\frac{1}{n_2}}\Gamma\left(1+\frac{1}{n_2}\right)}\frac{1}{\lambda_2}\left[\frac{d}{\lambda_2}\right]^{n_2} e^{-\frac{1}{n_2}\left(\frac{d}{\lambda_2}\right)^{n_2}} \quad (2)$$

where q and $(1-q)$ are the fractions of each subpopulation and λ_1, λ_2, n_1, and n_2 (Table 3) represent the scale and shape parameters of the two distributions, respectively (Figure 4a).

Neither the Field TGSD, the bi-Gaussian, nor the bi-Weibull distributions (Figure 4) permit to capture numerically the satellite retrievals. We assume that this is due to the missing information relative to the very fine ash (PM_{10}, i.e., $\Phi \geq 6$) or the lognormal shape given to the partial GSD into the satellite data. Indeed, the long atmospheric residence time of the PM_{10}, for negligible ash aggregation, prevents a rapid deposition (Rose & Durant, 2009). To account for PM_{10} within the TGSD, without accurate satellite-derived GSD, we opted for an empirical modification of the Field TGSD to enrich in fines the corresponding classes (i.e., $\Phi \geq 5$; Figure 4b). Indeed, we assume that for a limited range within the TGSD (i.e., PM_{10}), the lognormal distribution can approximate the empirical distribution we used for characterizing the PM_{10}. For the sake of simplicity, we used an empirical power law dependence of the fraction with Φ according to the following relationship:

$$X(\Phi_i) = X(\Phi_4) \times \gamma^{(\Phi_i - \Phi_4)}, \Phi \geq 5 \quad (3)$$

where $X(\Phi_i)$ is the fraction (in weight %) allocated to the ith bin, $X(\Phi_4)$ is the fraction obtained for $\Phi = 4$, and γ is the empirical factor ($\gamma < 1$). Although PM_{10} refers to $\Phi \geq 6$, the Field TGSD does not permit calculating from $\Phi = 5$ implying to start at $\Phi = 4$ (see Figure 4b). The PM_{10} fraction required into the TGSD was inverted exploring γ between 0.5 and 0.7, which corresponds to a PM_{10} fraction of 0.3–1.3%. This empirical procedure aims at proposing the input TGSD (hereinafter Fine Enriched TGSD; Figure 4b)

Table 3
Parameterization of the Analytical Distributions Obtained in Best Fit of the Field Total Grain-Size Distribution

Bi-Gaussian distribution		Bi-Weibull distribution	
μ_1	−2.96 ± 0.07	λ_1	−3.28 ± 2.84
σ_1	1.03 ± 0.07	n_1	1.68 ± 0.24
μ_2	0.49 ± 0.07	λ_2	−1.25 ± 1.07
σ_2	0.79 ± 0.06	n_2	0.77 ± 0.16
p	0.59 ± 0.03	q	0.39 ± 0.06

Note. Values are expressed in Φ-units. The lognormal distribution is described through the coarse subpopulation fraction (p), the means of the of coarse- and fine-grained subpopulations (μ_1 and μ_2, respectively), and their standard deviations (σ_1 and σ_2, respectively). The Weibull distribution is constructed with the coarse subpopulation fraction (q), the scale parameters of the means of the coarse- and fine-grained subpopulations (λ_1 and λ_2, respectively), and the shape parameters of the means of the coarse- and fine-grained subpopulations (n_1 and n_2, respectively).

Table 4
Best Input Eruption Source Parameters and the Corresponding Statistical Analysis for the Tested Total Grain-Size Distributions (TGSDs)

Input parameter	Field TGSD	Bi-Gaussian TGSD	Bi-Weibull TGSD	Fine Enriched TGSD	
Column height (km a.v.)	5.5	5.5	5.5	5.5	5.5
Mass Eruption Rate (kg/s)	1.2×10^6	1.4×10^6	1.3×10^6	1.3×10^6	1.3×10^6
Exit velocity (m/s)	250	250	250	250	250
Exit temperature (K)	1,300	1,300	1,300	1,300	1,300
Exit water fraction (%)	2.5	2.5	2.5	2.5	2.5
Cross-flow entrainment coefficient (β)	0.53	0.55	0.53	0.54	0.54
Diameter (Φ_{Agg})	—	—	—	—	2
Density aggregates (kg/m^3)	—	—	—	—	1,000
Statistical metric					
$RMSE_1$	0.80	0.70	0.73	0.80	0.80
$RMSE_2$	2.28	2.84	2.46	2.31	2.31
K	1.00	1.01	0.99	0.99	0.99
k	3.36	3.58	2.96	3.37	3.37
Bias	0.0	0.0	0.0	0.0	0.0
Correlation	0.9	0.9	0.9	0.9	0.9
t test	1.0	1.0	1.0	1.0	1.0

Note. Ash aggregation is investigated through the Fine Enriched TGSD using the scheme introduced in Costa et al. (2010).

capable to account for both field and satellite data. γ is estimated by best-fitting the simulated AAM with the satellite retrievals.

4.5. Inverse Problem-Solving Methodology

The inverse problem presented above is solved carrying out hundreds of simulations to explore the input parameter ranges (Table 2 and Appendix A for further parameterizations). Although more sophisticated Bayesian approaches can be used to deal with atmospheric observations (e.g., Rodgers, 2000; Twomey, 1996), the quantity and quality of the available data in terms of tephra loading and airborne ash mass motivated the inversion by means of simple statistical metrics as in similar studies (e.g., Costa et al., 2012, 2014; Folch et al., 2010; Martí et al., 2016; Poret et al., 2017). By means of the following analyses, we aim at suggesting a simple method for integrating the data and assessing the reflecting ESP. However, when the data make it possible, more sophisticated comparison can be used (e.g., Wilkins et al., 2016).

We initiated the inversion procedure by optimizing the simulations best-fitting the observed tephra loadings. For this purpose, we used a goodness-of-fit criterion evaluated through different statistical metrics (Poret et al., 2017). One was the normalized root mean square error (i.e., *RMSE*) calculated on the basis of two different weighting factors for the computed tephra loadings (i.e., $RMSE_1$ and $RMSE_2$; equations and explanation in Appendix B). Besides *RMSE*, we measured the goodness-of-fit and uncertainty of the simulated tephra loadings through the statistical indexes *K* (i.e., geometric average of the distribution) and *k* (i.e., geometric standard deviation of the distribution) introduced by Aida (1978):

$$K = \exp\left[\frac{1}{N}\sum_i^N \log\left(\frac{Obs_i}{Sim_i}\right)\right] \quad k = \exp\left[\sqrt{\frac{1}{N}\sum_i^N \log\left(\frac{Obs_i}{Sim_i}\right)^2 - \left(\frac{1}{N}\sum_i^N \log\left(\frac{Obs_i}{Sim_i}\right)\right)^2}\right]$$

Making use of such criteria, the simulations are considered reliable when *K* lies between 0.95 and 1.05 (i.e., ±5% of the best theoretical mass estimation based on the sampled tephra loadings). In other words, a value of $K = 0.95$ indicates a 5% overestimation of the TEM for a given set of ESPs, whereas $K = 1.05$ gives an underestimation of 5%. The best simulations are selected when *k* is minimized. Additionally, we calculated also the bias (to be minimized), the correlation (to be maximized), and the Student *t* test (Folch et al., 2010).

To reproduce the tephra loading, we ran a set of simulations varying the parameters at constant steps within their ranges (Table 2). Then, we refined by means of a finer step around the best cases to optimize the goodness of fit. We started with the column height by changing the values from 6 to 13 km a.s.l. using the relationship between the column height and the MER (Folch et al., 2016). The latter was investigated iteratively between 10^3 and 10^8 kg/s. Then, the exit velocity and the magma water content were explored from 150 to 300 m/s and 0.5 to 3.2%, respectively. Regarding the FPlume inputs to compute the air entrainment, β was sampled from 0.3 to 1.0. The aggregation parameterization was explored by considering the aggregate diameter (Φ_{Agg}) and density from 1 to 2.5 Φ and 200 to 1,200 kg/m^3, respectively.

The methodology described above gives similar tephra loadings through diverse input combinations, which indicates non-uniqueness of the solution (Anderson & Segall, 2013; Bonasia et al., 2010; Connor & Connor, 2005; Scollo et al., 2008).

Regarding the satellite retrievals, the PM_{10} fraction was inverted by quantitatively comparing the retrieved whole ash mass contained within the volcanic cloud (SEVIRI) with the simulated total AAM (in kg). We applied the same statistical method to the observed airborne PM_{10} masses (section 4.4) than for field measurements.

5. Results

The following section describes the best-fit results of tephra loading and airborne ash dispersal. First, we summarize the results of the Fine Enriched TGSD. Then, we report the ESPs retrieved for the explored input TGSDs. The last sections refer to the validation of the reconstruction of the main eruption features by means of field, satellite, and AERONET observations, respectively.

5.1. ESP Estimation Solving the Inverse Problem

Regarding the tephra loading, Table 4 reports the results of the statistical analysis for the input parameter ranges (Table 2) with the different TGSDs. They indicate a minimum value of k = 2.96 associated with the bi-Weibull distribution, whereas the Field, bi-Gaussian, and Fine Enriched TGSDs yield k = 3.36, k = 3.37, and k = 3.37, respectively. Additionally, the $RMSE_1$ and $RMSE_2$ show similar values with a slight better performance for the bi-Weibull distribution. In other words, without considering other observations than the tephra loadings, the goodness-of-fit method presents the bi-Weibull distribution as best input TGSD for the simulations. The statistical values (Table 4) indicate an uncertainty on the TEM estimation of about a factor 2–3, similar to other classical methods (Bonadonna et al., 2015; Bonadonna & Costa, 2012, 2013).

The absence of PM_{10} within the Field, bi-Gaussian, and bi-Weibull TGSDs (Figure 4) motivated to empirically modifying the Fine Enriched TGSD (section 4.4 and Figure 4). The comparative results for the PM_{10} fractions (i.e., 0.3–1.3%) are reported in Table 5. They revealed a systematic AAM overestimation compared to the satellite retrievals (Table 6) for fractions higher than 0.5%. The statistical analysis (section 4.5 and Appendix B) indicates a best TGSD with 0.4% of PM_{10} (i.e., γ = 0.53) to reproduce the AAM. Indeed, Table 5 shows for γ = 0.53 a K index close to 1 and a minimum k around 1.3 (the *RMSE*s are also near the minimum). It follows that we selected the Fine Enriched TGSD modified with γ = 0.53 (i.e., PM_{10} = 0.4%). However, such a fraction does not permit the numerical reproduction of the maxima AAM per unit area, which is captured with a PM_{10} fraction of 1.3% (i.e., γ = 0.70; Figure S2 in the supporting information).

Regardless of the TGSD used, the simulations return a column height of ~8.7 km a.s.l., which is consistent with the in situ observations (i.e., ~9 km a.s.l.) from INGV-OE (Figure 1c). The relationship between the column height and the MER gives very similar values of MER: 1.2×10^6, 1.4×10^6, 1.3×10^6, and 1.3×10^6 kg/s for the Field, bi-Gaussian, bi-Weibull, and Fine Enriched TGSDs, respectively. The inverted exit velocity is obtained at 250 m/s, being similar to the value observed by Donnadieu et al. (2016). The β entrainment coefficient is calibrated by comparing both TEM released during the eruption (i.e., K optimization) and mean MER estimated from the column height by using FPlume. The resulting β values range from 0.53 to 0.55, which are similar to the value estimated by Devenish et al. (2010).

5.2. Tephra Loading Validation Against Field Observations

Figure 5 compares the 10 tephra loadings measured at the sampled sites with the simulated values obtained for the Field, bi-Gaussian, bi-Weibull, and Fine Enriched TGSDs. The sensitivity to the input TGSD can be seen from both Table 1 and Figure 5. Regardless of the TGSD, the 10 simulated values lie within a factor of 10 the measurements. In particular, 8 of the 10 loadings are between 1/5- and 5-times the observed values. The computed values of the proximal samples (labels 1–7) range between ~11 and ~4.5 kg/m^2, showing a narrower span than the field samples (~32 to ~1.2 kg/m^2). Medial samples (labels 8 and 9 in Figure 5) are slightly overestimated. The farthest sample (label 10 in Figure 5) is either overestimated or underestimated tephra

10.1029/2017JB015163

Table 5
Computed Airborne Ash Mass Time Series for Different γ Together With the Statistical Analysis

	Fine Enriched TGSD with					
	$\gamma = 0.50$ ($PM_{10} = 0.3\%$)	$\gamma = 0.53$ ($PM_{10} = 0.4\%$)	$\gamma = 0.55$ ($PM_{10} = 0.5\%$)	$\gamma = 0.60$ ($PM_{10} = 0.7\%$)	$\gamma = 0.65$ ($PM_{10} = 0.9\%$)	$\gamma = 0.70$ ($PM_{10} = 1.3\%$)
Time (UTC)	AAM (in kg; Computed AAM/Observed AAM)					
19:00	1.0×10^7	1.3×10^7	1.6×10^7	2.3×10^7	3.3×10^7	4.7×10^7
	(2.62)	*(3.43)*	*(4.16)*	*(5.84)*	*(8.49)*	*(12.16)*
19:15	1.4×10^7	1.8×10^7	2.1×10^7	3.1×10^7	4.4×10^7	6.3×10^7
	(0.98)	*(1.30)*	*(1.48)*	*(2.24)*	*(3.11)*	*(4.47)*
19:30	1.3×10^7	1.7×10^7	2.0×10^7	2.8×10^7	4.1×10^7	5.6×10^7
	(0.60)	*(0.79)*	*(0.95)*	*(1.34)*	*(1.96)*	*(2.69)*
19:45	1.2×10^7	1.6×10^7	1.9×10^7	2.8×10^7	3.9×10^7	5.4×10^7
	(0.62)	*(0.84)*	*(1.01)*	*(1.46)*	*(2.07)*	*(2.84)*
20:00	1.1×10^7	1.5×10^7	1.8×10^7	2.7×10^7	3.8×10^7	5.4×10^7
	(1.00)	*(1.39)*	*(1.62)*	*(2.49)*	*(3.44)*	*(4.93)*
20:15	1.1×10^7	1.5×10^7	1.8×10^7	2.6×10^7	3.7×10^7	5.1×10^7
	(2.21)	*(3.08)*	*(3.64)*	*(5.31)*	*(7.80)*	*(10.65)*
Statistical metric						
$RMSE_1$	0.33	0.24	0.29	0.79	1.47	2.45
$RMSE_2$	0.28	0.28	0.39	1.01	1.77	2.90
K	1.28	0.96	0.81	0.55	0.39	0.28
k	1.28	1.29	1.26	1.30	1.28	1.31
Bias	0.0	0.0	0.0	0.0	0.1	0.1
Correlation	0.3	0.1	0.5	−0.1	0.3	−0.1
t test	0.2	0.8	0.2	0.0	0.0	0.0

Note. Airborne ash masses (AAMs) are computed for different γ values used to produce the Fine Enriched total grain-size distribution (TGSD). Values inside parentheses refer to the ratio between computed and measured ash masses.

Table 6
Time Series of the Main Satellite Retrievals

Time (UTC)	19:00	19:15	19:30	19:45	20:00	20:15
Cloud top temperature (°C)	−54.2	−53.5	−53.5	−53.8	−49.9	−48.6
Cloud top altitude (m a.s.l.)	9,321	9,167	9,167	9,167	8839	8,678
Airborne ash mass (kg)	3.9×10^6	1.4×10^7	2.1×10^7	1.9×10^7	1.1×10^7	4.8×10^6
Effective radius (μm)	4.33	4.13	4.24	4.21	4.58	4.71

Note. Retrievals derived from SEVIRI data and come from 15-min internal observation.

loading, depending on the input TGSD. Proximal samples show a slight enrichment in coarse material for the bi-Gaussian distribution than the other TGSDs (Figure 4), explaining the larger tephra loading estimates. In contrast, the lack of fine particle results on underestimating in load the farthest sample of about a factor 10.

Figure 6 displays the tephra loading maps obtained with the four input TGSDs. It shows that the bi-Gaussian and bi-Weibull distributions fail to reproduce the tephra loading up to distal areas, whereas the maps associated with the Field and Fine Enriched TGSDs capture reasonably well all sites (Table 1). The corresponding time evolution of the tephra loading for the Fine Enriched TGSD is available as supporting information (Animation A1).

Considering an eruption duration of 1 hr and 6 min through a constant eruptive phase (i.e., a unique column height), FPlume estimated the MER, which is used to assess the TEM. The optimal simulations selected for the different input TGSDs yield a TEM of 4.8×10^9, 5.3×10^9, 4.8×10^9, and 4.9×10^9 kg for the Field, bi-Gaussian, bi-Weibull, and Fine Enriched TGSDs, respectively. The numerical TEM estimations are of the same order of magnitude than the field-derived TEM (i.e., $\sim 2.0 \pm 0.5 \times 10^9$ kg; section 4.1).

5.3. PM_{10} Validation Against Satellite Observations

Among the explored input distributions, only the Fine Enriched TGSD has enough PM_{10} (here 0.4% in weight) to inject enough particles to reproduce the far-traveling airborne ash mass retrieved from satellite data (Table 6). The airborne ash dispersion is shown in Figure 7, where the FALL3D results (a–d) are compared with the SEVIRI retrievals (e–h). The first-time window (in Figures 7a and 7e; 19:15 UTC) refers to 1 hr after the paroxysm started. It shows the PM_{10} fraction injected into the atmosphere spreading toward the Calabrian region. The volcanic cloud elevation estimated from the SEVIRI data indicates that it already reached its maximum altitude at ~9.3 km a.s.l. (Table 5). Hereinafter, we report the difference in terms of (1) total AAM and (2) maximum ash mass per unit area (all the values are reported in Table 4). At 19:15 UTC, the total AAM retrieved from SEVIRI returns 1.4×10^7 kg, whereas FALL3D estimates 1.8×10^7 kg (i.e., ~30% higher). The maximum ash mass per unit area measured from SEVIRI is ~22 g/m^2, while the computed value is ~12 g/m^2. The second-time window (19:30 UTC) illustrates the dispersal over the Calabria 15 min later. The total AAM estimated from SEVIRI is 2.1×10^7 kg while the simulated value is 1.7×10^7 kg (i.e., underestimation by ~21%). In this case, the maximum ash mass per unit area from SEVIRI (~20 g/m^2) is about three times the simulated value (~6 g/m^2). On the third-time window (19:45 UTC), satellite retrieval returns a total AAM of 1.9×10^7 kg, whereas FALL3D gives 1.6×10^7 kg (i.e., underestimation by ~16%). The simulation of the maximum ash mass per unit area is about four times lower than the retrieved one (~5 versus ~22 g/m^2, respectively). The last time window (in Figures 7d and 7h; 20:00 UTC) shows the volcanic ash cloud over the Ionian Sea at a slightly lower altitude (Table 5). The total AAM are 1.1×10^7 kg and 1.5×10^7 kg (i.e., overestimation by ~39%) from SEVIRI and FALL3D, respectively. Again, the simulation of the maximum ash mass per unit area is about five times lower than the retrieved one (~4 versus ~21 g/m^2, respectively). The full time-series of the airborne ash simulation is available as supporting information (Animation A2).

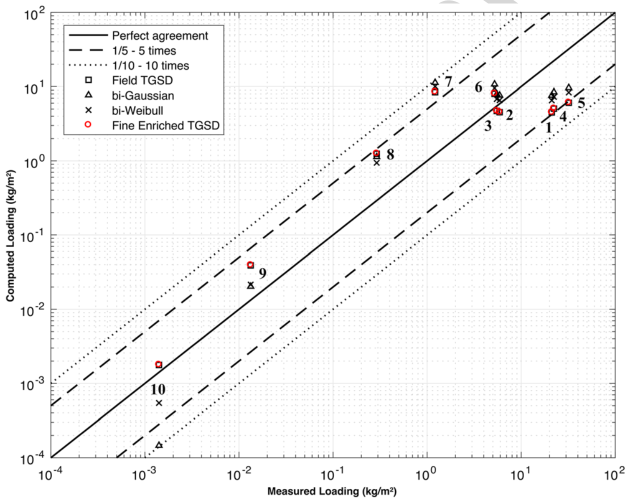

Figure 5. Observed tephra loadings versus computed data at 10 observation sites for the different input total grain-size distributions (TGSDs) used within the modeling simulations (details in Table 1). The typical errors are assumed of ~5–20% as described in Bonadonna et al. (2015).

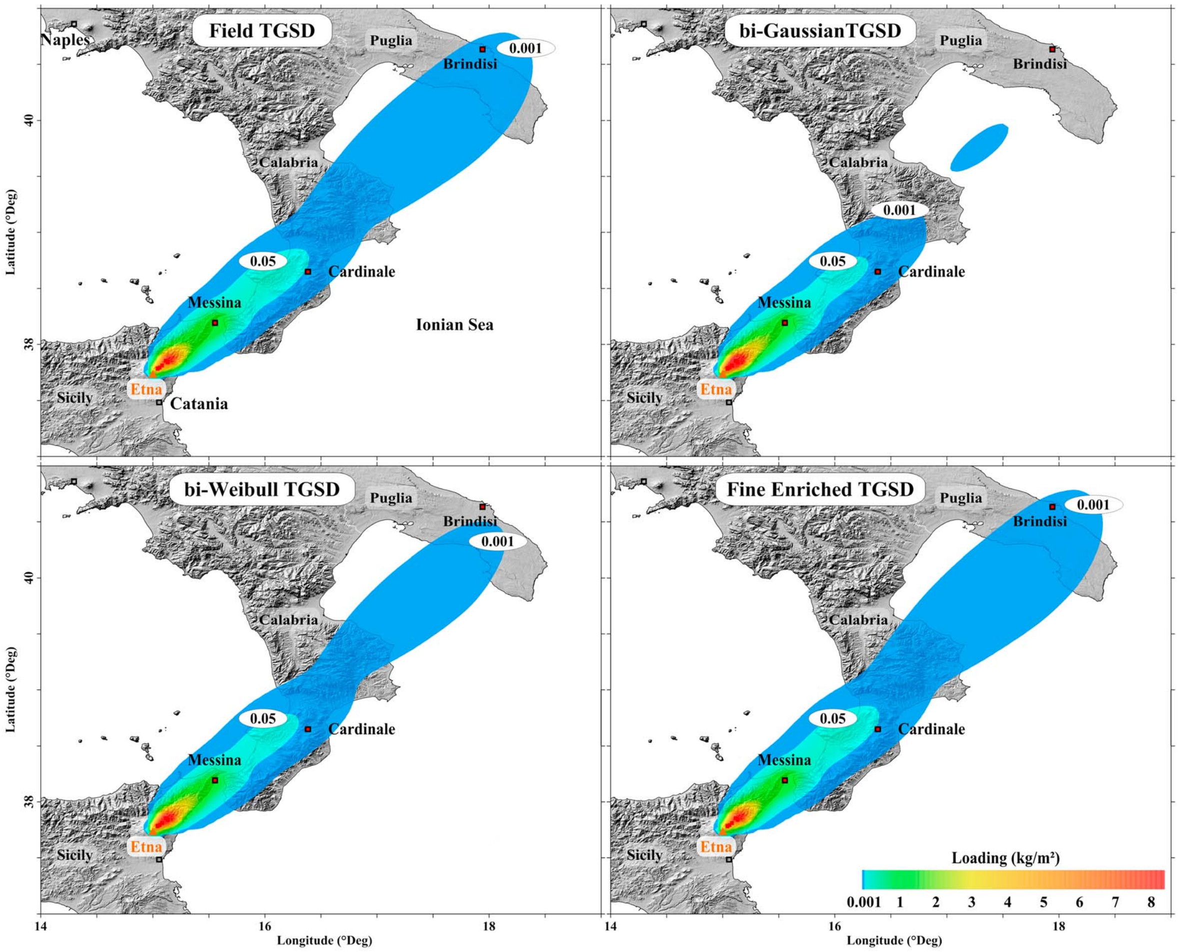

Figure 6. Tephra loading maps obtained for the different input total grain-size distributions (TGSDs; time series for the Fine Enriched TGSD is available as supporting information, Animation A1).

These results show that the simulation obtained using the Fine Enriched TGSD (section 4.4) reproduces AAM correctly but do not capture the local maxima. In general, the computed ash mass within the volcanic cloud (in Figures 7a–7d) appears to be much more diluted than the satellite retrievals (Figures 7e–7h). From a computational point of view, to reproduce the correct local maxima, the input TGSD needs a PM_{10} fraction about three times higher (i.e., 1.3 wt%). However, this implies an overestimation of the total AAM by a factor 6 in average (see Figure S2 in the supporting information).

5.4. AOD Validation Against AERONET Observations

As an independent validation of the simulation results described above, we use the AOD measurements obtained from the AERONET (Holben et al., 1998). On 24 February 2013, an AERONET station (Figure 8a) detected particles over the Çamlıbel village (Turkey; ~1,700 km from Etna) from 06:58 to 11:58 UTC. To compare the retrieved AODs with the computed values associated with the presence of volcanic ash at such distal areas, we considered the data relative to nonspherical particles only, as described in section 4.3. From 06:58–10:58 UTC, the average particle sphericity is retrieved by AERONET between 0.3 and 3.9, whereas at 11:58 UTC the value is 46.9 (hereinafter excluded). The corresponding AOD ranged between ~0.28 and 0.30 (hereinafter $AOD_{AERONET}$). As mentioned in section 4.3, we subtracted the Saharan dust contribution (i.e., ~0.23; GEOS-chem) from the $AOD_{AERONET}$ to assess the AOD associated with the volcanic ash over the Turkish station (hereinafter AOD_{ash}). The resulting AOD_{ash} ranges from ~0.05 to 0.07 (Figure 8b).

We compared AOD_{ash} with the numerical AOD (hereinafter AOD_{FALL3D}) computed by FALL3D for the Fine Enriched TGSD. Figure 8a shows we extended the domain including the southern Europe with a 10-km grid

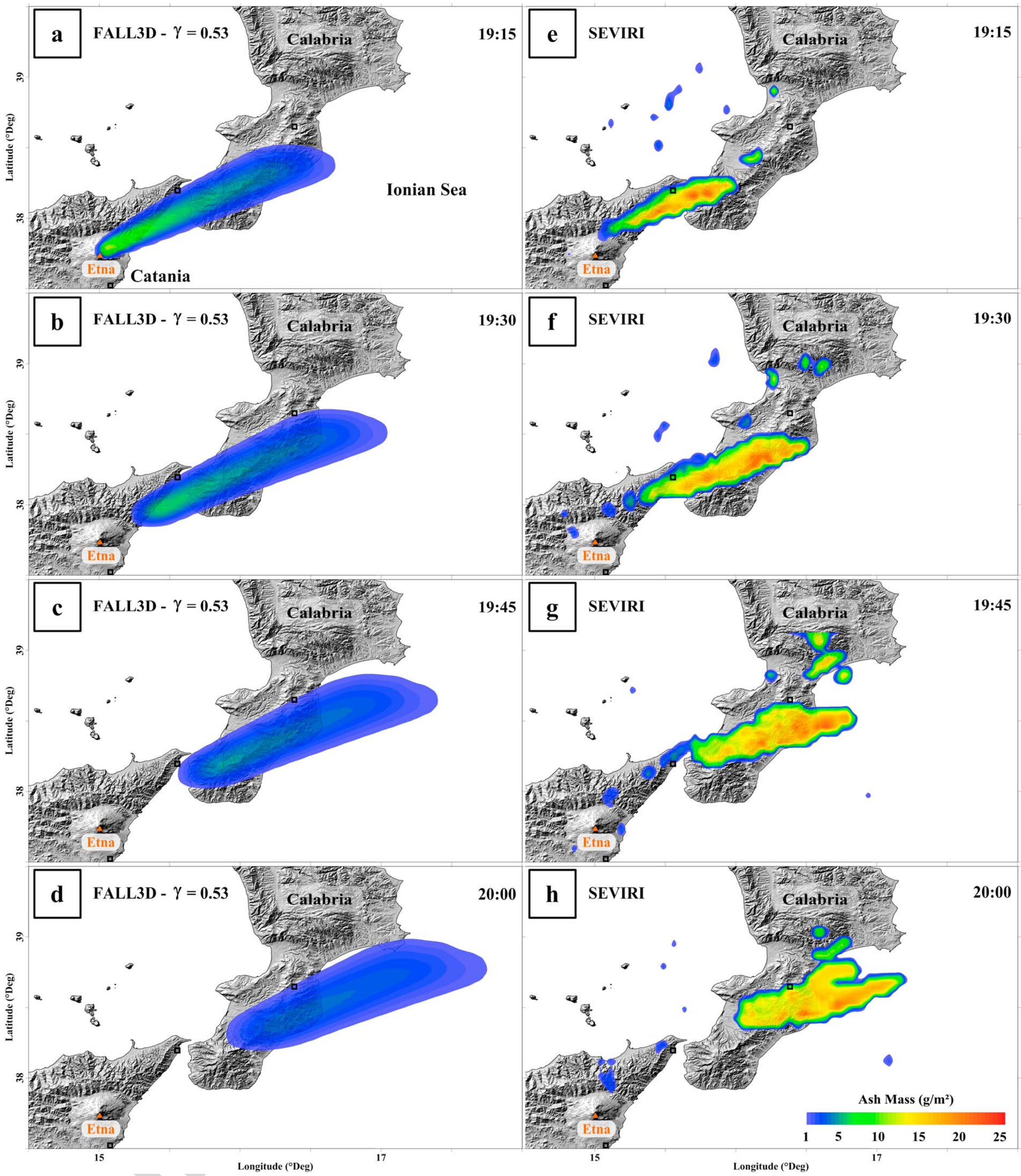

Figure 7. Airborne ash mass computed by FALL3D (a–d) and observed from satellite (e–h) from 19:15 to 20:00 UTC. Simulations correspond to the Fine Enriched total grain-size distribution obtained for $\gamma = 0.53$. The time-series animation is available as supporting information (Animation A2). SEVIRI = Spinning Enhanced Visible and Infrared Imager.

resolution. The time series of AOD_{FALL3D} shows a spreading over Albania, Greece, Macedonia, Serbia, Turkey, Bulgaria, Romania, Moldova, and Ukraine up to the Black Sea and the Russian borders (see Animation A3 in the supporting information). The comparative study (Figure 8b) indicates that AOD_{FALL3D} reproduces two orders of magnitude smaller than AOD_{ash} (i.e., 4.3×10^{-4}). Such a discrepancy is likely attributed mostly to the spatial-temporal shift of the meteorological fields due to the coarse resolution of the raw database (Dacre et al., 2011; Folch et al., 2012) used for the simulation (e.g., Poret et al., 2017). In fact, comparing

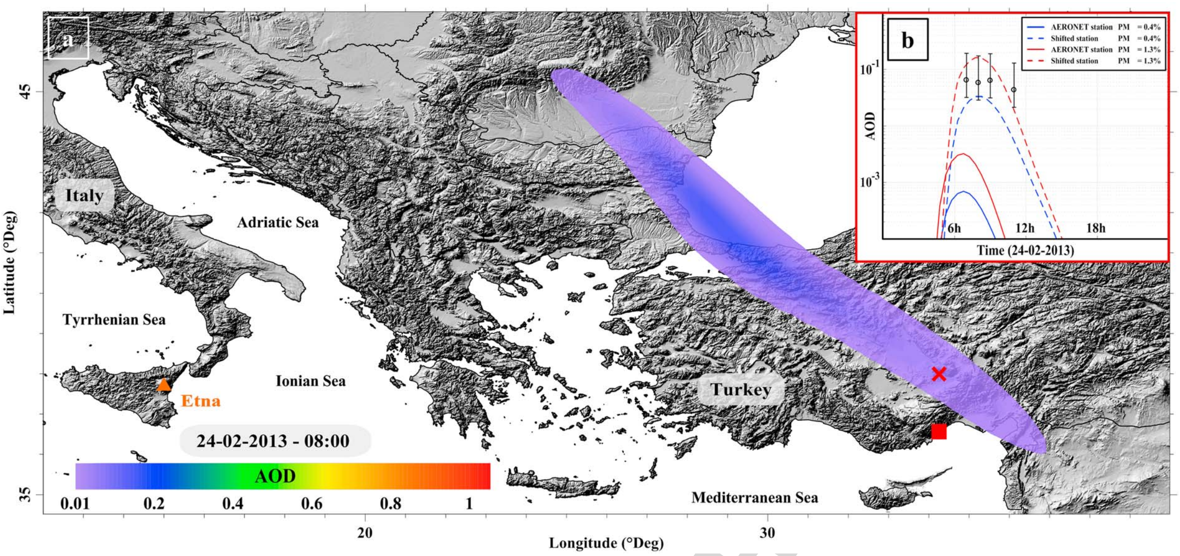

Figure 8. (a) Simulated aerosol optical depth (AOD) of the 23 February 2013 eruption for a computational domain extending over Turkey at 08:00 UTC (24 February 2013). The time series animation is available as supporting information (Animation A3). The red square refers to the AErosol RObotic NETwork (AERONET) station (labeled IMS-METU ERDEMLI), whereas the red cross is the virtual point located two grid-nodes northward. (b) AOD comparison between the AERONET measurements (circles) and the numerical results over both the AERONET station and the shifted station for PM_{10} fractions of 0.4% and 1.3%, respectively. The measurement uncertainty is estimated accordingly to Marenco et al. (2011).

with AOD_{FALL3D} computed two grid-nodes northward (~150 km from the station), AOD_{FALL3D} improved substantially being similar to the AOD_{ash} with ~0.02 (Figure 8a). It is worth noting that AOD_{FALL3D} is obtained with PM_{10} = 0.4% for the Fine Enriched TGSD, which is selected on the basis of the total AAM analysis. However, considering PM_{10} = 1.3% (section 5.3), AOD_{ash} became 8.6×10^{-4} and ~0.10 over the Çamlıbel and the two grid-nodes shifted sites, respectively. Although this comparative study has a large uncertainty for both AOD estimations and spatiotemporal delay of meteorological model, we bear in mind that we used AOD observations for simulation results validation only, without constraining the model inputs. Besides these limitations, we note the that Fine Enriched TGSD seems able to capture the concentration of ultrafine ash up to very distal areas (~1,700 km from source).

6. Discussion

This study proposes integrating field and satellite data of the 23 February 2013 Etna eruption to constrain the numerical reconstruction of the tephra loading and airborne ash mass. However, the input parameter interdependency implies the non-uniqueness solution through diverse ESP combinations (Anderson & Segall, 2013; Bonasia et al., 2010; Connor & Connor, 2005; Scollo et al., 2008). Although all the simulations capture reasonably the main features associated with the tephra loading, the Field, bi-Gaussian, and bi-Weibull TGSDs fail to best-fit simultaneously field and satellite data. In particular, only the Fine Enriched TGSD succeeds in reproducing both the tephra loading and airborne ash mass. This argues the need for developing an integrated method for assessing the initial grain-size distribution covering the entire size spectrum.

Considering GSD at the sampled sites, we compared each measurement with the numerical one (Figure 3) for the Fine Enriched TGSD. Overall, FALL3D captures 7 of the 10 GSDs by peaking at the same modes. However, two of the three most proximal samples (i.e., Casetta and Bivio 007 in Figure 3) are shifted by 1 Φ, which indicates coarser tephra deposits than the computed ones. In contrast, the Castiglione site (Figure 3) shows a finer field deposit than the computed one. These discrepancies can be attributed not only to the sample positions from the main plume axis but also to the sampling distance from the source (Spanu et al., 2016). In fact, the coarser material ($-4 \geq \Phi \geq -2$) deposits within a narrow area from the vent, highlighting the difficulty to correctly capture the coarse tail distribution through the Voronoi tessellation method when the deposit is not adequately sampled (Andronico, Scollo, Cristaldi, et al., 2014).

Regarding the comparative study of the tephra loadings (Figure 5), the proximal measurements range from 32 to 1.2 kg/m^2, whereas the computed are between 11 to 4.5 kg/m^2. These results are assumed acceptable as they are within the same order of magnitude (e.g., Costa et al., 2014; Folch et al., 2010; Scollo et al., 2008). Although the tephra loadings are not perfectly reproduced, the resulting values indicate a consistency with the field measurements by lying within the 1/5–5 times limits for five of the seven proximal samples, whereas the two others are within the 1/10–10 times limits. The difference between the computed and measured proximal tephra loadings can be partially attributed, among others, to the low meteorological resolution. Indeed, for simulating several hundred kilometers domain, we used a 4 × 4-km meteorological resolution (Figure S1 in the supporting information), which means only five grid nodes are representing the proximal samples (located between ~5 and ~16 km from the source).

Satellite retrievals were integrated into field data by inverting the PM_{10} fraction to use within the input TGSD. However, focusing on reproducing the AAM per unit area suggests a PM_{10} content of 0.4%, whereas capturing the local maxima requires a larger fraction (~1.3%). As most of Eulerian models, FALL3D has a numerical diffusion effect, which can partially explain the PM_{10} fraction discrepancy (Folch, 2012; Folch et al., 2012). Meanwhile, satellite retrievals have well-known ash discrimination issues associated with the BTD method. Indeed, spectral features in the thermal infrared may not allow a perfect discrimination of ash (see Guéhenneux et al., 2015, for a review). Additionally, atmospheric effects, such as convective clouds (Potts & Ebert, 1996) or mineral dust (Watkin, 2003), may produce negative BTD leading to false ash pixels detection. In contrast, moisture rich environment confounds BTD retrievals by adding a positive component (Pavolonis et al., 2006). These biases can affect the determination of the area containing airborne ash overestimating its extension.

Other complications can be attributed to the effect of ash aggregation, although for explosive basaltic eruptions (e.g., those ones from Etna) should not be significant (Rose & Durant, 2009). Indeed, the best simulations accounting for ash aggregation under the scheme developed in Costa et al. (2010) returns a contribution of only ~2 wt% over the fine ash. Such results are obtained for an effective aggregate diameter Φ_{Agg} of 2 and a density of 1,000 kg/m^3. As expected, ash aggregation appears negligible compared to the TEM.

The use of the Fine Enriched TGSD permitted capturing the observed tephra loading and airborne ash mass, providing a more realistic estimation of the initial magma fragmentation down to the very fine ash distribution compared to the field-derived TGSD. However, such a characterization still needs further work in terms of (1) parameterization of the partial GSD for satellite retrievals or (2) integration of field and remote-sensing tephra measurements, also for other eruptions benefiting from large data set. At this stage, we opted for a purely empirical approach, but a more theoretical study is the object of ongoing research. It is worth noting that the used inversion of the very fine ash distribution is done comparing with satellite retrievals, which assume a lognormal distribution. This comparison can introduce a bias in the results without considering for the satellite-derived GSD. However, this study aims at dealing specifically with the reconstruction of the ESP leading to simultaneously capturing the tephra loading and airborne ash dispersal using information relative to coarse and very fine tephra. Also, the results we reported aim at encouraging future work that integrates data from field, ground-based instruments (e.g., visible and infrared images, weather and Doppler radars, light detection and ranging systems, and AERONET network), and satellite sensors (e.g., SEVIRI) to converge toward a full reconstruction of the tephra dispersal and deposition.

The findings of this study have implications for volcanic hazards and the evaluation of the related impacts. In fact, assessing accurately the initial magma fragmentation contributes to a more realistic description of both tephra deposition and airborne ash dispersal. On one hand, the tephra can affect the populations in the vicinity of the volcano (e.g., fallout and tephra accumulation hazards; Andronico et al., 2015). On the other hand, fine ash has high impact both near the source with the effects of PM_{10} on public health (Horwell, 2007; Horwell et al., 2013, 2017; Andronico & Del Carlo, 2016; Tomašek et al., 2016) and far away from the volcano with threat on air traffic (Casadevall, 1994; Casadevall et al., 1999; Guffanti et al., 2005). Quantifying airborne ash (i.e., PM_{10}) released during the 23 February 2013 lava fountain, PM_{10} dispersed in the atmosphere remaining above 2 g/m^2 for 6 hr after the paroxysm up to several hundreds of kilometers from the source (see section 5.3 and Figures 7 and S2). Such a situation may pose hazards to air traffic safety highlighting again the necessity for assessing accurately the TGSD. As example, on December 2015, the Voragine crater of Etna produced four intense lava fountains within 3 days (Corsaro et al., 2017; Pompilio et al., 2017; Vulpiani et al., 2016). These similar episodes had sustained columns (i.e., high MERs) up to 15 km a.s.l. producing significant fine ash dispersed to distal regions. Although fine ash fraction during basaltic explosive eruptions represents a small fraction of the TEM, neglecting it within the TGSD can lead to a substantial underestimation of the far-traveling airborne ash mass, with implications for aviation safety. We showed that a better PM_{10} characterization is possible by adopting an integrated approach, which use models and all the available observations. We also encourage developing similar integrated approaches to other volcanoes for real-time forecast of tephra dispersal.

7. Concluding Remarks

On 23 February 2013, Etna volcano, Sicily, produced an intense lava fountain under strong north-easterly wind direction. The erupted tephra was deposited downwind from the volcano to the Puglia region, located ~410 km from the source. These untypical meteorological conditions gave a rare opportunity to collect field samples from proximal to distal locations. This study aims at numerically reconstructing tephra loading and airborne ash mass by means of field, satellite (SEVIRI), and ground-based (AERONET) retrievals. Among the input eruption source parameters required by FALL3D, a better estimation of the TGSD accounting for both field and satellite measurements was demonstrated and evaluated. In fact, the long residence time of very fine ash into the atmosphere prevents deposition at reasonable distances. To better characterize the very fines, we parameterized the field-based TGSD through a bi-lognormal and bi-Weibull distribution. None of the two latter TGSDs can provide a very fine ash fraction allowing the computation of any far-traveling airborne ash up to distal areas. For this reason, we suggested here the empirical modification of the field-based TGSD to include the very fine ash by assuming a power law decay of the tail of the distribution. The Fine Enriched TGSD is similar to other Etna eruptions with a more marked bimodal distribution peaking at -3 Φ and 0.5 Φ for the coarse- and fine-grained subpopulations, respectively. Eruption source parameters are inverted by means of a goodness-of-fit method best-reproducing simultaneously the tephra loading measurements and airborne ash mass retrieved by satellite. Results indicate a column height of 8.7 km a.s.l., a TEM of ~4.9×10^9 kg, a MER of ~1.3×10^6 kg/s for a paroxysmal phase of 1 hr and 6 min, a PM_{10} fraction of ~0.4–1.3 wt% with respect to the TEM, and an aggregate fraction of ~2 wt% of the fine ash. These encouraging results highlight the need for integrating further airborne/airspace multisensors with field measurements to better characterize the parameters controlling plume transport in the atmosphere and tephra sedimentation, with emphasis on the very fine ash distribution (PM_{10}) responsible for public health and air traffic safety issues.

Appendix A

Appendix A completes Tables 2 and 4 by reporting the other parameters and models used to run the simulations.

Parameterization	Description
Eruption duration (min)	66
Vent elevation (m a.s.l.)	3200
Vent longitude (°)	15.002012
Vent latitude (°)	37.746548
Time step meteo data (min)	30
Longitude nodes	100
Latitude nodes	111
Altitude layers(from 0 m a.s.l., 500-m step)	10,000
Eruption column model	FPlume[a]
Terminal velocity model	Ganser[b]
Vertical turbulence model	Similarity[c]
Horizontal turbulence model	CMAQ[d]
Gravity current	Yes[e]

Note. The computational domain extension starts at 9.75 and 34.5 (longitude/latitude in degrees) and ends at 40.5 and 52.5 (longitude/latitude in degrees).
[a]The eruption column model uses the buoyant plume theory (Folch et al., 2016). [b]The terminal settling velocity is calculated with the Ganser (1993) model. [c]The vertical component of the eddy diffusivity tensor (K_z) is estimated using the similarity option (Costa et al., 2006; Ulke, 2000). [d]The horizontal component of the eddy diffusivity tensor (K_h) is evaluated as in Byun and Schere (2006) by the CMAQ option. [e]The gravity current effects in the umbrella region, although negligible, were considered in the simulations (Costa et al., 2013; Suzuki & Koyaguchi, 2009).

Appendix B

The input parameters are inverted by means of the normalized root mean square error (*RMSE*) as defined by the following:

$$RMSE_j = \sqrt{\sum_i^N w_j (Sim_i - Obs_i)^2}$$

$$w_{j=1} = \frac{1}{\sum_i^N Obs_i^2}$$

$$w_{j=2} = \frac{1}{N \times Obs_i^2}$$

where w_j refers to the weighting factor used within the *RMSE* calculation, *i* corresponds to the *i*th sample over a set of *N*. Obs_i and Sim_i are the observed and simulated tephra loadings, respectively. The weights correspond to different assumptions on the error distribution (Aitken, 1935; Costa et al., 2009). The $RMSE_1$ is calculated with w_1 referring to a constant absolute error, whereas the $RMSE_2$ considers a constant relative error by implying the proportional weighting factor w_2 (Bonasia et al., 2012; Folch et al., 2010; Poret et al., 2017).

Notation

AAM	Airborne Ash Mass (in kg)
AERONET	AErosol RObotic NETwork
AOD	Aerosol Optical Depth (dimensionless)
BTD	Brightness Temperature Difference
ECMWF	European Center for Medium-range Weather Forecasts
ESP	Eruption Source Parameters
INGV-OE	Istituto Nazionale di Geofisica e Vulcanologia—Osservatorio Etneo
GSD	Grain-Size Distribution
MER	Mass Eruption Rate (in kg/m^2)
MOCAGE	MOdèle de Chimie Atmosphérique à Grande Echelle
NAME	Numerical Atmospheric-dispersion Modeling Environment
NASA	National Aeronautics and Space Administration
NSEC	New Southeast Crater
OPGC	Observatoire de Physique du Globe de Clermont-Ferrand
PHOTONS	PHotométrie pour le Traitement Opérationnel de Normalisation Satellitaire
PM_{10}	Particle Matter Below 10 μm
RMSE	Root Mean Square Error
SEVIRI	Spinning Enhanced Visible and Infrared Imager
TEM	Total Erupted Mass (in kg)
TGSD	Total Grain-Size Distribution
TIR	Thermal InfraRed
VAAC	Volcanic Ash Advisory Center

Acknowledgments
Figures S1 and S2 and Animations A1, A2, and A3 serves for illustrating the results and are available in the supporting information. This work is supported by the FP 7 Marie Curie Actions Framework (FP7-PEOPLE-2013-ITN), volcanic ash: field, experimental, and numerical investigations of processes during its lifecycles (VERTIGO project; grant agreement number 607905). A.C., D.A., and S.S. acknowledge the European project EUROVOLC (grant agreement number 731070) and the MIUR project Premiale Ash-RESILIENCE. We are grateful to M.G. and S. Costa for the rare ash sample collected in Cardinale and to ARPA Puglia for the Brindisi sample. Meteorological data were provided by the European Center for Medium-range Weather Forecasts. Data about dust contribution were provided by the GEOS-Chem model from the National Aeronautics and Space Administration Goddard Modeling and Assimilation Office (GMAO). We are grateful to Marco Neri and Boris Behncke for the fruitful discussions and the photo of the lava fountain. We also warmly acknowledge Ka Lok Chan for his help regarding the AOD comparison. We are deeply grateful to A. Martí, L. Mastin, I.M. Watson, anonymous reviewers, and Associate Editors for the criticism and constructive revision aimed to improve the quality and clarity of the manuscript.

References

Aida, I. (1978). Reliability of a tsunami source model derived from fault parameters. *Journal of Physics of the Earth*, *26*(1), 57–73. https://doi.org/10.4294/jpe1952.26.57

Aitken, A. C. (1935). On least squares and linear combinations of observations. *Proceedings of the Royal Society of Edinburgh*, *55*, 42–48.

Allard, P., Burton, M., & Murè, F. (2005). Spectroscopic evidence for a lava fountain driven by previously accumulated magmatic gas. *Nature*, *433*(7024), 407–410. https://doi.org/10.1038/nature03246

Anderson, K., & Segall, P. (2013). Bayesian inversion of data from effusive volcanic eruptions using physics-based models: Application to Mount St. Helens 2004–2008. *Journal of Geophysical Research - Solid Earth*, *118*, 2017–2037. https://doi.org/10.1002/jgrb.50169

Andronico, D., Cristaldi, A., & Scollo, S. (2008). The 4–5 September 2007 lava fountain at South-East Crater of Mt. Etna, Italy. *Journal of Volcanology and Geothermal Research*, *173*(3-4), 325–328. https://doi.org/10.1016/j.jvolgeores.2008.02.004

Andronico, D., & Del Carlo, P. (2016). PM_{10} measurements in urban settlements after lava fountain episodes at Mt. Etna, Italy: Pilot test to assess volcanic ash hazard on human health. *Natural Hazards and Earth System Sciences*, *16*(1), 29–40. https://doi.org/10.5194/nhess-16-29-2016

Andronico, D., Scollo, S., & Cristaldi, A. (2015). Unexpected hazards from tephra fallouts at Mt. Etna: The 23 November 2013 lava fountain. *Journal of Volcanology and Geothermal Research*, *304*, 118–125. https://doi.org/10.1016/j.jvolgeores.2015.08.007

Andronico, D., Scollo, S., Cristaldi, A., & Caruso, S. (2008). The 2002–03 Etna explosive activity: Tephra dispersal and features of the deposit. *Journal of Geophysical Research*, *113*, B04209. https://doi.org/10.1029/2007JB005126

Andronico, D., Scollo, S., Cristaldi, A., & Lo Castro, M. D. (2014). Representivity of incompletely sampled fall deposits in estimating eruption source parameters: A test using the 12–13 January 2011 lava fountain deposit from Mt. Etna volcano, Italy. *Bulletin of Volcanology*, *76*(10). https://doi.org/10.1007/s00445-014-0861-3

Andronico, D., Scollo, S., Lo Castro, M. D., Cristaldi, A., Lodato, L., & Taddeucci, J. (2014). Eruption dynamics and tephra dispersal from the 24 November 2006 paroxysm at south-east crater, Mt. Etna, Italy. *Journal of Volcanology and Geothermal Research 274*, 78–91. https://doi.org/10.1016/j.jvolgeores.2014.01.009

Azzopardi, F., Ellul, R., Prestifilippo, M., Scollo, S., & Coltelli, M. (2013). The effect on Etna volcanic ash clouds on the Maltese Islands. *Journal of Volcanology and Geothermal Research*, *260*, 13–26. https://doi.org/10.1016/j.jvolgeores.2013.04.019

Bagheri, G., & Bonadonna, C. (2016). On the drag of freely falling non-spherical particles. *Powder Technology*, *301*, 526–544. https://doi.org/10.1016/j.powtec.2016.06.015

Barsotti, S., Andronico, D., Neri, A., Del Carlo, P., Baxter, P. J., Aspinall, W. P., & Hincks, T. (2010). Quantitative assessment of volcanic ash hazards for health and infrastructure at Mt. Etna (Italy) by numerical simulation. *Journal of Volcanology and Geothermal Research*, *192*(1-2), 85–96. https://doi.org/10.1016/j.jvolgeores.2010.02.011

Barsotti, S., Neri, A., & Scire, J. (2008). The VOL-CALPUFF model for atmospheric ash dispersal. I. Approach and physical formulation. *Journal of Geophysical Research*, *113*, B03208. https://doi.org/10.1029/2006JB004623

Beckett, F. M., Witham, C. S., Hort, M. C., Stevenson, J. A., Bonadonna, C., & Millington, S. C. (2014). The sensitivity of NAME forecasts of the transport of volcanic ash clouds to the physical characteristics assigned to the particles. Met Office, *Forecasting Research*, Technical report n°592.

Beckett, F. M., Witham, C. S., Hort, M. C., Stevenson, J. A., Bonadonna, C., & Millington, S. C. (2015). Sensitivity of dispersion model forecasts of volcanic ash clouds to the physical characteristics of the particles. *J. Geophys. Res. – Atmos.*, *120*, 11,636–11,652. https://doi.org/10.1002/2015JD023609

Behncke, B., Branca, S., Corsaro, R. A., De Beni, E., Miraglia, L., & Proietti, P. (2014). The 2011–2012 summit activity of Mount Etna: Birth, growth and products of the new SE crater. *Journal of Volcanology and Geothermal Research*, *270*, 10–21. https://doi.org/10.1016/j.jvolgeores.2013.11.012

Bey, I., Jacob, D. J., Yantosca, R. M., Logan, J. A., Field, B. D., Fiore, A. M., et al. (2001). Global modeling of tropospheric chemistry with assimilated meteorology: Model description and evaluation. *Journal of Geophysical Research*, *106*(D19), 23073–23095. https://doi.org/10.1029/2001JD000807

Bonadonna, C., Biass, S., & Costa, A. (2015). Physical characterization of explosive volcanic eruptions based on tephra deposits: Propagation of uncertainties and sensitivity analysis. *Journal of Volcanology and Geothermal Research*, *296*, 80–100. https://doi.org/10.1016/j.jvolgeores.2015.03.009

Bonadonna, C., & Costa, A. (2012). Estimating the volume of tephra deposits: A new simple strategy. *Geology*, *40*(5), 415–418. https://doi.org/10.1130/G32769.1

Bonadonna, C., & Costa, A. (2013). Plume height, volume, and classification of explosive volcanic eruptions based on the Weibull function. *Bulletin of Volcanology*, *75*(8), 742. https://doi.org/10.1007/s00445-013-0742-1

Bonadonna, C., Genco, R., Gouhier, M., Pistolesi, M., Cioni, R., Alfano, F., et al. (2011). Tephra sedimentation during the 2010 Eyjafjallajokull eruption (Iceland) from deposit, radar, and satellite observations. *Journal of Geophysical Research*, *116*, B12202. https://doi.org/10.1029/2011JB008462

Bonadonna, C., & Houghton, B. F. (2005). Total grain-size distribution and volume of tephra-fall deposits. *Bulletin of Volcanology*, *67*(5), 441–456. https://doi.org/10.1007/s00445-004-0386-2

Bonasia, R., Costa, A., Folch, A., Macedonio, G., & Capra, L. (2012). Numerical simulation of tephra transport and deposition of the 1982 El Chichón eruption and implications for hazard assessment. *Journal of Volcanology and Geothermal Research*, *231–232*, 39–49. https://doi.org/10.1016/j.jvolgeores.2012.04.006

Bonasia, R., Macedonio, G., Costa, A., Mele, D., & Sulpizio, R. (2010). Numerical inversion and analysis of tephra fallout deposits from the 472 AD sub-Plinian eruption at Vesuvius (Italy) through a new best-fit procedure. *Journal of Volcanology and Geothermal Research*, *189*(3-4), 238–246. https://doi.org/10.1016/j.jvolgeores.2009.11.009

Bursik, M. (2001). Effect of wind on the rise height of volcanic plumes. *Geophysical Research Letters*, *28*(18), 3621–3624. https://doi.org/10.1029/2001GL013393

Byun, D., & Schere, K. L. (2006). Review of the governing equations, computational algorithms, and other components of the Models-3 Community Multiscale Air Quality (CMAQ) modeling system. *Applied Mechanics Reviews*, *59*(2), 51–77. https://doi.org/10.1115/1.2128636

Carbone, D., Zuccarello, L., Messina, A., Scollo, S., & Rymer, H. (2015). Balancing bulk gas accumulation and gas output before and during lava fountaining episodes at Mt. Etna. *Scientific Reports*, *5*(1), 18049. https://doi.org/10.1038/srep18049

Casadevall, T. J. (1994). Volcanic ash and aviation safety. Proceedings of the First International Symposium on Volcanic Ash and Aviation Safety. USGS Bull. 2047, p. 450

Casadevall, T. J., Thompson, T. B., & Fox, T. (1999). World map of volcanoes and principal aeronautical features. *USGS Map* I-2700, scale 1:34,268,000, reprinted 2001

Chan, K. L., & Chan, K. L. (2017). Aerosol optical depths and their contributing sources in Taiwan. *Journal of Atmospheric Environment*, *148*, 364–375. https://doi.org/10.1016/j.atmosenv.2016.11.011

Cigala, V., Kueppers, U., Peña Fernández, J. J., Taddeucci, J., Sesterhenn, J., & Dingwell, D. B. (2017). The dynamics of volcanic jets: Temporal evolution of particles exit velocity from shock-tube experiments. *Journal of Geophysical Research - Solid Earth*, *122*, 6031–6045. https://doi.org/10.1002/2017JB014149

Connor, C., Hill, B., Winfrey, B., Franklin, M., & La Femina, P. (2001). Estimation of volcanic hazards from tephra fallout. *Natural Hazards Review*, *2*(1), 33–42. https://doi.org/10.1061/(ASCE)1527-6988(2001)2:1(33)

Connor, L. J., & Connor, C. B. (2005). Inversion is the key to dispersion: Understanding eruption dynamics by inverting tephra fallout. In *Statistics in volcanology*, (pp. 231–242). London: Geological Society.
Corradini, S., Montopoli, M., Guerrieri, L., Ricci, M., Scollo, S., Merucci, L., et al. (2016). A multi-sensor approach for the volcanic ash cloud retrievals and eruption characterization. *Remote Sensing, Special Issue on Volcano Remote Sensing*, *8*(1), 58. https://doi.org/10.3390/rs8010058
Corradini, S., Spinetti, C., Carboni, E., Tirelli, C., Buongiorno, M. F., Pugnaghi, S., & Gangale, G. (2008). Mt. Etna tropospheric ash retrieval and sensitivity analysis using Moderate Resolution Imaging Spectroradiometer measurements. *Journal of Applied Remote Sensing*, *2*(1), 023550. https://doi.org/10.1117/1.3046674
Corsaro, R. A., Andronico, D., Behncke, B., Branca, S., De Beni, E., Caltabiano, T., et al. (2017). Monitoring the December 2015 summit eruptions of Mt. Etna (Italy): Implications on eruptive dynamics. *Journal of Volcanology and Geothermal Research*, *341*, 53–69. https://doi.org/10.1016/j.jvolgeores.2017.04.018
Corsaro, R. A., & Miraglia, L. (2013a). Composizione dei vetri dei prodotti emessi dal Nuovo Cratere di Sud-Est durante le fontane di lava del 23 e 28 febbraio 2013, INGV Report, at http://www.ct.ingv.it/it/rapporti/vulcanologia.html?view=docman
Corsaro, R. A., & Miraglia, L. (2013b). Composizione dei vetri dei prodotti emessi dal Nuovo Cratere di Sud-Est durante la fontana di lava del 23 novembre 2013, INGV Report, at http://www.ct.ingv.it/it/rapporti/vulcanologia.html?view=docman
Costa, A., Dell'Erba, F., Di Vito, M. A., Isaia, R., Macedonio, G., Orsi, G., & Pfeiffer, T. (2009). Tephra fallout hazard assessment at the Campi Flegrei caldera (Italy). *Bulletin of Volcanology*, *71*(3), 259–273. https://doi.org/10.1007/s00445-008-0220-3
Costa, A., Folch, A., & Macedonio, G. (2010). A model for wet aggregation of ash particles in volcanic plumes and clouds: 1. Theoretical formulation. *Journal of Geophysical Research*, *115*, B09201. https://doi.org/10.1029/2009JB007175
Costa, A., Folch, A., & Macedonio, G. (2013). Density-driven transport in the umbrella region of volcanic clouds: Implications for tephra dispersion models. *Geophysical Research Letters*, *40*, 4823–4827. https://doi.org/10.1002/grl.50942
Costa, A., Folch, A., Macedonio, G., Giaccio, B., Isaia, R., & Smith, V. C. (2012). Quantifying volcanic ash dispersal and impact from Campanian Ignimbrite super-eruption. *Geophysical Research Letters*, *39*, L10310. https://doi.org/10.1029/2012GL051605
Costa, A., Macedonio, G., & Folch, A. (2006). A three-dimensional Eulerian model for transport and deposition of volcanic ashes. *Earth and Planetary Science Letters*, *241*(3-4), 634–647. https://doi.org/10.1016/j.epsl.2005.11.019
Costa, A., Pioli, L., & Bonadonna, C. (2016). Assessing tephra total grain-size distribution: Insights from field data analysis. *Earth and Planetary Science Letters*, *443*, 90–107. https://doi.org/10.1016/j.epsl.2016.02.040
Costa, A., Pioli, L., & Bonadonna, C. (2017). Corrigendum to "Assessing tephra total grain-size distribution: Insights from field data analysis". (Earth and Planetary Science Letters 443, 90–107, 2016). *Earth and Planetary Science Letters*. https://doi.org/10.1016/j.epsl.2017.03.003
Costa, A., Smith, V. C., Macedonio, G., & Matthews, N. E. (2014). The magnitude and impact of the Youngest Toba Tuff super-eruption. *Frontiers in Earth Science*, *2*, 16. https://doi.org/10.3389/feart.2014.00016
Costa, A., Suzuki, Y. J., Cerminara, M., Devenish, B., Esposti Ongaro, T., Herzog, M., et al. (2016). Results of the eruption column model inter-comparison study. *Journal of Volcanology and Geothermal Research*, *326*. https://doi.org/10.1016/j.jvolgeores.2016.01.017
Dacre, H. F., Grant, A. L. M., Hogan, R. J., Belcher, S. E., Thomson, D. J., Devenish, B. J., et al. (2011). Evaluating the structure and magnitude of the ash plume during the initial phase of the 2010 Eyjafjallajökull eruption using lidar observations and NAME simulations. *Journal of Geophysical Research*, *116*, D00U03. https://doi.org/10.1029/2011JD015608
De Beni, E., Behncke, B., Branca, S., Nicolosi, I., Carluccio, R., D'Ajello Caracciolo, F., & Chiappini, M. (2015). The continuing story of Etna's New Southeast Crater (2012-2014): Evolution and volume calculations based on field surveys and aerophotogrammetry. *Journal of Volcanology and Geothermal Research*, *303*, 175–186. https://doi.org/10.1016/j.jvolgeores.2015.07.021
Dellino, P., & Kyriakopoulos, K. (2003). Phreatomagmatic ash from the ongoing eruption of Etna reaching the Greek island of Cefalonia. *Journal of Volcanology and Geothermal Research*, *126*(3–4), 341–345. https://doi.org/10.1016/S0377-0273(03)00154-9
Devenish, B. J., Rooney, G. G., Webster, H. N., & Thomson, D. J. (2010). The entrainment rate for buoyant plumes in a cross-flow. *Boundary-Layer Meteorology*, *134*(3), 411–439. https://doi.org/10.1007/s10546-009-9464-5
Donnadieu, F., Freville, P., Hervier, C., Coltelli, M., Scollo, S., Prestifilippo, M., et al. (2016). Near-source Doppler radar monitoring of tephra plumes at Etna. *Journal of Volcanology and Geothermal Research*, *312*, 26–39. https://doi.org/10.1016/j.jvolgeores.2016.01.009
Dubovik, O. (2004). Optimization of numerical inversion in photopolarimetric remote sensing. In G. Videen, Y. Yatskiv, & M. Mish-chenko (Eds.), *Photopolarimetry in remote sensing*, (pp. 65–106). Dordrecht, Netherlands: Kluwer Academic Publishers.
Dubovik, O., & King, M. D. (2000). A flexible inversion algorithm for retrieval of aerosol optical properties from Sun and sky radiance measurements. *Journal of Geophysical Research*, *105*(20), 673–696.
Dubovik, O., Sinyuk, A., Lapyonok, T., Holben, B. N., Mishchenko, M., Yang, P., et al. (2006). Application of spheroid models to account for aerosol particle nonsphericity in remote sensing of desert dust. *Journal of Geophysical Research*, *111*, D11208. https://doi.org/10.1029/2005JD006619
Dubovik, O., Smirnov, A., Holben, B. N., King, M. D., Kaufman, Y. J., Eck, T. F., & Slutsker, I. (2000). Accuracy assessment of aerosol optical properties retrieval from AERONET sun and sky radiance measurements. *Journal of Geophysical Research*, *105*(D8), 9791–9806. https://doi.org/10.1029/2000JD900040
Fairlie, T. D., Jacob, D. J., & Park, R. J. (2007). The impact of transpacific transport of mineral dust in the United States. *Journal of Atmospheric Environment*, *41*(6), 1251–1266. https://doi.org/10.1016/j.atmosenv.2006.09.048
Folch, A. (2012). A review of tephra transport and dispersal models: Evolution, current status, and future perspectives. *Journal of Volcanology and Geothermal Research*, *235–236*, 96–115. https://doi.org/10.1016/j.jvolgeores.2012.05.020
Folch, A., Costa, A., & Basart, S. (2012). Validation of the FALL3D ash dispersion model using observations of the 2010 Eyjafjallajökull volcanic ash clouds. *Atmospheric Environment*, *48*, 165–183. https://doi.org/10.1016/j.atmosenv.2011.06.072
Folch, A., Costa, A., Durant, A., & Macedonio, G. (2010). A model for wet aggregation of ash particles in volcanic plumes and clouds: 2. Model application. *Journal of Geophysical Research*, *115*, B09202. https://doi.org/10.1029/2009JB007176
Folch, A., Costa, A., & Macedonio, G. (2009). FALL3D: A computational model for transport and deposition of volcanic ash. *Computers and Geosciences*, *35*(6), 1334–1342. https://doi.org/10.1016/j.cageo.2008.08.008
Folch, A., Costa, A., & Macedonio, G. (2016). FPLUME-1.0: An integral volcanic plume model accounting for ash aggregation. *Geoscientific Model Development*, *9*(1), 431–450. https://doi.org/10.5194/gmd-9-431-2016
Ganser, G. H. (1993). A rational approach to drag prediction of spherical and non-spherical particles. *Powder Technology*, *77*(2), 143–152. https://doi.org/10.1016/0032-5910(93)80051-B
Gouhier, M., Guéhenneux, Y., Labazuy, P., Cacault, P., Decriem, J., & Rivet, S. (2016). HOTVOLC: A web-based monitoring system for volcanic hot spots. *Geological Society, London, Special Publications*, *426*, SP426–SP431.

Grindle, T. J., & Burchamn, F. W. (2003). Engine damage to a NASA DC-8-72 airplane from a high-altitude encounter with a diffuse volcanic ash cloud. National Aeronautics and Space Administration, Dryden Flight Research Center, Edwards, California, Report NASA/TM-2003-212030

Guéhenneux, Y., Gouhier, M., & Labazuy, P. (2015). Improved space borne detection of volcanic ash for real-time monitoring using 3-band method. *Journal of Volcanology and Geothermal Research*, *293*, 25–45. https://doi.org/10.1016/j.jvolgeores.2015.01.005

Guffanti, M., Ewert, J. W., Gallina, G. M., Bluth, G. J. S., & Swanson, G. L. (2005). Volcanic-ash hazard to aviation during the 2003–2004 eruption activity of Anatahan volcano Commonwealth of the Northern Mariana Islands. *Journal of Volcanology and Geothermal Research*, *146*(1-3), 241–255. https://doi.org/10.1016/j.volgeores.2004.12.011

Holben, B. N., Eck, T. F., Slutsker, I., Smirnov, A., Sinyuk, A., Schafer, J., et al. (2006). Aeronet's version 2.0 quality assurance criteria. *Proceedings of SPIE 6408, Remote Sensing of the Atmosphere and Clouds*, 64080Q. https://doi.org/10.1117/12.706524

Holben, B. N., Eck, T. F., Slutsker, I., Tanré, D., Buis, J. P., Setzer, A., et al. (1998). AERONET—A federated instrument network and data archive for aerosol characterization. *Remote Sensing of Environment*, *66*(1), 1–16. https://doi.org/10.1016/S0034-4257(98)00031-5

Horwell, C. J. (2007). Grain size analysis of volcanic ash for the rapid assessment of respiratory health hazard. *Journal of Environmental Monitoring*, *9*(10), 1107–1115. https://doi.org/10.1039/b710583p

Horwell, C. J., Baxter, P. J., Hillman, S. E., Calkins, J. A., Damby, D. E., Delmelle, P., et al. (2013). Physicochemical and toxicological profiling of ash from the 2010 and 2011 eruptions of Eyjafjallajökull and Grímsvötn volcanoes, Iceland using a rapid respiratory hazard assessment protocol. *Environmental Research*, *127*, 63–73. https://doi.org/10.1016/j.envres.2013.08.011

Horwell, C. J., Sargent, P., Andronico, D., Lo Castro, M. D., Tomatis, M., Hillman, S. E., et al. (2017). The iron-catalysed surface reactivity and health-pertinent physical characteristics of explosive volcanic ash from Mt. Etna, Italy. *Journal of Applied Volcanology*, *6*(1). https://doi.org/10.1186/s13617-017-0063-8

Kaminski, E., Tait, S., & Carazzo, G. (2005). Turbulent entrainment in jets with arbitrary buoyancy. *Journal of Fluid Mechanics*, *526*, 361–376. https://doi.org/10.1017/S0022112004003209

Krumbein, W. C. (1934). Size frequency distributions of sediments. *Journal of Sedimentary Research*, *4*, 65–67.

Lo Castro, M. D., & Andronico, D. (2008). Operazioni di base per la misura della distribuzione granulometrica di particelle vulcaniche tramite il CAMSIZER. *Rapporti Tecnici INGV*, *79*, 1–35.

Macedonio, G., Costa, A., & Longo, A. (2005). A computer model for volcanic ash fallout and assessment of subsequent hazard. *Computational Geosciences*, *31*(7), 837–845. https://doi.org/10.1016/j.cageo.2005.01.013

Macedonio, G., Costa, A., Scollo, S., & Neri, A. (2016). Effects of eruption source parameter variation and meteorological dataset on tephra fallout hazard assessment: Example from Vesuvius (Italy). *Journal of Applied Volcanology*, *5*(1), 5. https://doi.org/10.1186/s13617-016-0045-2

Marenco, F., Johnson, B., Turnbull, K., Newman, S., Haywood, J., Webster, H., & Ricketts, H. (2011). Airborne lidar observations of the 2010 Eyjafjallajökull volcanic ash plume. *Journal of Geophysical Research*, *116*, D00U05. https://doi.org/10.1029/2011JD016396

Martí, A., Folch, A., Costa, A., & Engwell, S. (2016). Reconstructing the Plinian and co-ignimbrite sources of large volcanic eruptions: A novel approach for the Campanian Ignimbrite. *Nature Communication – Science Report*, *6*(1), 21220. https://doi.org/10.1038/srep21220

Maryon, R. H., Ryall, D. B., & Malcolm, A. L. (1999) The NAME 4 dispersion model: Science documentation, turbulence and diffusion note no 262, Met Office

Mastin, L. G., Guffanti, M., Servranckx, R., Webley, P., Barsotti, S., Dean, K., et al. (2009). A multidisciplinary effort to assign realistic source parameters to models of volcanic ash-cloud transport and dispersion during eruptions. *Journal of Volcanology and Geothermal Research*, *186*(1-2), 10–21. https://doi.org/10.1016/j.jvolgeores.2009.01.008

Metrich, N., Allard, P., Spilliaert, N., Andronico, D., & Burton, M. (2004). 2001 flank eruption of the alkali- and volatile-rich primitive basalt responsible for Mount Etna's evolution in the last three decades. *Earth and Planetary Science Letters*, *228*(1-2), 1–17. https://doi.org/10.1016/j.epsl.2004.09.036

Metrich, N., & Rutherford, M. J. (1998). Low pressure crystallization paths of H_2O-saturated basaltic-hawaiitic melts from Mt. Etna: Implications for open-system degassing volcanoes. *Geochimica et Cosmochimica Acta*, *62*(7), 1195–1205. https://doi.org/10.1016/S0016-7037(98)00048-9

Morton, B. R., Taylor, G. I., & Turner, J. S. (1956). Turbulent gravitational convection from maintained and instantaneous source. *Philosophical Transactions of the Royal Society of London: London, A*, *234*(1196), 1–23. https://doi.org/10.1098/rspa.1956.0011

Mueller, S. B., Ayris, P. M., Wadsworth, F. B., Kueppers, U., Casas, A. S., Delmelle, P., et al. (2017). Ash aggregation enhanced by deposition and redistribution of salt on the surface of volcanic ash in eruption plumes. *Nature Communication - Science Report*, *7*, 45762. https://doi.org/10.1038/srep45762

Mueller, S. B., Kueppers, U., Ametsbichler, J., Cimarelli, C., Merrison, J. P., Poret, M., et al. (2017). Stability of volcanic ash aggregates and break-up processes. *Nature Communication - Science Report*, *7*, 7440. https://doi.org/10.1038/s41598-017-07927-w

O'Neill, N. T., Eck, T. F., Smirnov, A., Holben, B. N., & Thulasiraman, S. (2003). Spectral discrimination of coarse and fine mode optical depth. *Journal of Geophysical Research*, *108*(D17), 4559. https://doi.org/10.1029/2002JD002975

Park, R. J., Jacob, D. J., Field, B. D., Yantosca, R. M., & Chin, M. (2004). Natural and transboundary pollution influences on sulfate-nitrate-ammonium aerosols in the United States: Implications for policy. *Journal of Geophysical Research*, *109*, D15204. https://doi.org/10.1029/2003JD004473

Pavolonis, M. J., Feltz, W. F., Heidinger, A. K., & Gallina, G. M. (2006). A daytime complement to the reverse absorption technique for improved automated detection of volcanic ash. *Journal of Atmospheric and Oceanic Technology*, *23*(11), 1422–1444. https://doi.org/10.1175/JTECH1926.1

Pompilio, M., Bertagnini, A., Del Carlo, P., & Di Roberto, A. (2017). Magma dynamics within a basaltic conduit revealed by textural and compositional features of erupted ash: The December 2015 Mt. Etna paroxysms. *Scientific Reports*, *7*(1), 4805. https://doi.org/10.1038/s41598-017-05065-x

Poret, M., Costa, A., Folch, A., & Martì, A. (2017). Modeling tephra dispersal and ash aggregation: The 26th April 1979 eruption, La Soufrière St. Vincent. *Journal of Volcanology and Geothermal Research*, *347*, 207–220. https://doi.org/10.1016/j.jvolgeores.2017.09.012

Potts, R. J., & Ebert, E. E. (1996). On the detection of volcanic ash in NOAA AVHRR infrared satellite imagery. Paper Presented at 8th Australian Remote Sens. Conf. Canberra, 25–29

Prata, A. J. (1989a). Observations of volcanic ash clouds in the 10–12 μm window using AVHRR/2 data. *International Journal of Remote Sensing*, *10*, 4–5. 751–761

Prata, A. J. (1989b). Radiative transfer calculations for volcanic ash clouds. *Geophysical Research Letters*, *16*(11), 1293–1296. https://doi.org/10.1029/GL016i011p01293

Prata, A. J., & Grant, I. F. (2001). Retrieval of microphysical and morphological properties of volcanic ash plumes from satellite data: Application to Mt Ruapehu, New Zealand. *Quarterly Journal of the Royal Meteorological Society*, *127*(576), 2153–2179. https://doi.org/10.1002/qj.49712757615

Prata, A. J., & Kerkmann, J. (2007). Simultaneous retrieval of volcanic ash and SO_2 using MSGSEVIRI measurements. *Geophysical Research Letters*, *34*, L05813. https://doi.org/10.1029/2006GL0228691

Rodgers, C. D. (2000). *Inverse methods for atmospheric sounding: Theory and practice*. Singapore: World Scientific Pub Co Inc.

Rose, W. I., & Durant, A. J. (2009). Fine ash content of explosive eruptions. *Journal of Volcanology and Geothermal Research*, *186*(1-2), 32–39. https://doi.org/10.1016/j.jvolgeores.2009.01.010

Scollo, S., Boselli, A., Coltelli, M., Leto, G., Pisani, G., Spinelli, N., & Wang, X. (2012). Monitoring Etna volcanic plumes using a scanning LiDAR. *Bulletin of Volcanology*, *74*(10), 2383–2395. https://doi.org/10.1007/s00445-012-0669-y

Scollo, S., Coltelli, M., Bonadonna, C., & Del Carlo, P. (2013). Tephra hazard assessment at Mt. Etna (Italy). *Natural Hazards and Earth System Sciences Discussions*, *1*(3), 2945–2981. https://doi.org/10.5194/nhessd-1-2945-2013

Scollo, S., Folch, A., & Costa, A. (2008). A parametric and comparative study of different tephra fallout models. *Journal of Volcanology and Geothermal Research*, *176*(2), 199–211. https://doi.org/10.1016/j.volgeores.2008.04.002

Scollo, S., Prestifilippo, M., Pecora, E., Corradini, S., Merucci, L., Spata, G., & Coltelli, M. (2014). Eruption column height estimation of the 2011–2013 Etna lava fountains. *Annals of Geophysics*, *57*(2), S0214. https://doi.org/10.4401/ag-6396

Sič, B., El Amraoui, L., Marécal, V., Josse, B., Arteta, J., Guth, J., et al. (2015). Modeling of primary aerosols in the chemical transport model MOCAGE: Development and evaluation of aerosol physical parameterizations. *Geoscientific Model Development*, *8*(2), 381–408. https://doi.org/10.5194/gmd-8-381-2015

Smoluchowski, M. (1917). Veruch einer mathematischen Theorie der Koagulationkinetic kolloider Lösungen. *Zeitschrift für Physikalische Chemie*, *92*, 128–168.

Spanu, A., dé Vitturi, M. M., & Barsotti, S. (2016). Reconstructing eruptive source parameters from tephra deposit: A numerical study of medium-sized explosive eruptions at Etna volcano. *Bulletin of Volcanology*, *78*(9), 59. https://doi.org/10.1007/s00445-016-1051-2

Spilliaert, N., Allard, P., Me trich, N., & Sobolev, A. V. (2006). Melt inclusion record of the conditions of ascent, degassing, and extrusion of volatile-rich alkali basalt during the powerful 2002 flank eruption of Mount Etna (Italy). *Journal of Geophysical Research*, *111*, B04203. https://doi.org/10.1029/2005JB003934

Stevenson, J. A., Millington, S. C., Beckett, F. M., Swindles, G. T., & Thordarson, T. (2015). Big grains go far: Understanding the discrepancy between tephrochronology and satellite infrared measurements of volcanic ash. *Atmospheric Measurement Techniques*, *8*(5), 2069–2091. https://doi.org/10.5194/amt-8-2069-2015

Sulpizio, R., Folch, A., Costa, A., Scaini, C., & Dellino, P. (2012). Hazard assessment of far-range volcanic ash dispersal from a violent Strombolian eruption at Somma-Vesuvius volcano, Naples, Italy: Implications on civil aviation. *Bulletin of Volcanology*, *74*(9), 2205–2218. https://doi.org/10.1007/s00445-012-0656-3

Suzuki, Y. J., & Koyaguchi, T. (2009). A three-dimensional numerical simulation of spreading umbrella clouds. *Journal of Geophysical Research*, *114*, B03209. https://doi.org/10.1029/2007JB005369

Suzuki, Y. J., & Koyaguchi, T. (2015). Effects of wind on entrainment efficiency in volcanic plumes. *Journal of Geophysical Research - Solid Earth*, *120*, 6122–6140. https://doi.org/10.1002/2015JB012208

Tomašek, I., Horwell, C. J., Damby, D. E., Barošová, H., Geers, C., Petri-Fink, A., et al. (2016). Combined exposure of diesel exhaust particles and respirable Soufrière Hills volcanic ash causes a (pro-)inflammatory response in an in vitro multicellular epithelial tissue barrier model. *Particle and Fibre Toxicology*, *13*(1), 67. https://doi.org/10.1186/s12989-016-0178-9

Twomey, S. (1996). *Introduction to the mathematics of inversion in remote sensing and indirect measurements*. New York: Dover Publications.

Ulke, A. G. (2000). New turbulent parameterization for a dispersion model in atmospheric boundary layer. *Atmospheric Environment*, *34*(7), 1029–1042. https://doi.org/10.1016/S1352-2310(99)00378-7

Vulpiani, G., Ripepe, M., & Valade, S. (2016). Mass discharge rate retrieval combining weather radar and thermal camera observations. *Journal of Geophysical Research - Solid Earth*, *121*, 5679–5695. https://doi.org/10.1002/2016JB013191

Watkin, S. C. (2003). The application of AVHRR data for the detection of volcanic ash in a volcanic ash advisory centre. *Meteorological Applications*, *10*(4), 301–311. https://doi.org/10.1017/S1350482703001063

Watson, I. M., & Oppenheimer, C. (2001). Photometric observations of Mt. Etna's different aerosol plumes. *Atmospheric Environment*, *35*(21), 3561–3572. https://doi.org/10.1016/S1352-2310(01)00075-9

Watson, I. M., Realmuto, V. J., Rose, W. I., Prata, A. J., Bluth, G. J. S., Gu, Y., et al. (2004). Thermal infrared remote sensing of volcanic emissions using the moderate resolution imaging spectroradiometer. *Journal of Volcanology and Geothermal Research*, *135*(1-2), 75–89. https://doi.org/10.1016/j.jvolgeores.2003.12.017

Watt, S. F. L., Gilbert, J. S., Folch, A., & Phillips, J. C. (2015). An example of enhanced tephra deposition driven by topographic induced atmospheric turbulence. *Bulletin of Volcanology*, *77*(5), 35. https://doi.org/10.1007/s00445-015-0927-x

Wen, S., & Rose, W. I. (1994). Retrieval of sizes and total masses of particles in volcanic clouds using AVHRR bands 4 and 5. *Journal of Geophysical Research*, *99*(D3), 5421–5431. https://doi.org/10.1029/93JD03340

Wilkins, K. L., Watson, I. M., Kristiansen, N. I., Webster, H. N., Thomson, D. J., Dacre, H. F., & Prata, A. J. (2016). Using data insertion with the NAME model to simulate the 8 May 2010 Eyjafjallajökull volcanic ash cloud. *Journal of Geophysical Research – Atmospheres*, *121*, 306–323. https://doi.org/10.1002/2015JD023895

Witham, C. S., Hort, M. C., Potts, R., Servranckx, R., Husson, P., & Bonnardot, F. (2007). Comparison of VAAC atmospheric dispersion models using the 1 November 2004 Grimsvötn eruption. *Meteorological Applications*, *14*(1), 27–38. https://doi.org/10.1002/met.3

HOTVOLC: a web-based monitoring system for volcanic hot spots

M. GOUHIER*, Y. GUÉHENNEUX, P. LABAZUY, P. CACAULT, J. DECRIEM & S. RIVET

Laboratoire Magmas et Volcans, Université Blaise Pascal, CNRS, IRD, Observatoire de Physique du Globe de Clermont-Ferrand, 5 rue Kessler, 63038 Clermont Ferrand, France

**Corresponding author (e-mail: M.Gouhier@opgc.univ-bpclermont.fr)*

Abstract: Infrared (IR) satellite-based sensors allow the detection and quantification of volcanic hot spots. Sensors flown on geostationary satellites are particularly helpful in the early warning and continuous tracking of effusive activity. Development of operational monitoring and dissemination systems is essential to achieve the real-time ingestion and processing of IR data for a timely response during volcanic crises. HOTVOLC is a web-based satellite-data-driven monitoring system developed at the Observatoire de Physique du Globe de Clermont-Ferrand (Clermont-Ferrand), designed to achieve near-real-time monitoring of volcanic activity using on-site ingestion of geostationary satellite data (e.g. MSG-SEVIRI, MTSAT, GOES-Imager). Here we present the characteristics of the HOTVOLC system for the monitoring of effusive activity. The system comprises two acquisition stations and secure databases (i.e. mirrored archives). The detection of volcanic hot spots uses a contextual algorithm that is based on a modified form of the Normalized Thermal Index (NTI*) and VAST. Raster images and numerical data are available to open-access on a Web-GIS interface. Tests are carried out and presented here, particularly for the 12–13 January 2011 eruption of Mount Etna, to show the capability of the system to provide quantitative information such as lava volume and time-averaged discharge rate. Examples of operational application reveal the ability of the HOTVOLC system to provide timely thermal information about volcanic hot spot activity.

Thermal anomalies on the ground induced by lava emission, hereafter termed 'hot spots,' are common hazards occurring during eruptions and can represent a threat to the population living in the vicinity of volcanic areas (Tilling 1989; Herault *et al*. 2009; Vicari *et al*. 2011). The development of ground-based thermal remote sensing tools such as those aimed at studying fumarolic, open vent degassing and lava flow field evolution are now part of routine monitoring operations as implemented, for example, at Mount Etna (Italy) by the Istituto Nazionale di Geofisica e Vulcanologia (e.g. Bonaccorso *et al.* 2002; Andronico *et al.* 2005; Burton *et al.* 2005; Scollo *et al.* 2009). However, for volcanoes located in developing countries and remote areas, satellite-based techniques are more beneficial as satellite remote sensing systems can provide a rapid assessment of volcanic hot spot activity and can potentially be used to derive crucial information for decision makers. Since the 1980s, increasing efforts have been carried out to improve the use of satellite-based data to detect, quantify and track thermal radiance from high-temperature bodies such as lava flows and domes (Francis & Rothery 1987; Rothery *et al.* 1988; Oppenheimer 1991; Wooster & Rothery 1997). A thorough review of the IR remote sensing of such volcanic hot spots can be found in Harris (2013). Mid-to-thermal infrared sensors, in particular, are sensitive to electromagnetic emission from high-temperature bodies and are thus very useful in the detection of volcanic hot spots (e.g. Rothery *et al.* 1988; Oppenheimer 1991). Therefore, since the 1990s much effort has been aimed at the development of near-real-time remote sensing systems that involve operational use of satellite data for hot spot tracking, as for example the work by the volcano remote sensing group at the University of Alaska Fairbanks (e.g. Dean *et al.* 1996). Subsequently, many systems based on various infrared sensors (e.g. MODIS, SEVIRI) onboard various satellite platforms (Terra/Aqua, Meteosat) and using different techniques, have been developed, such as MODVOLC (Flynn *et al.* 2002; Wright *et al.* 2002), HOTSAT (Ganci *et al.* 2011, 2012*a*, *b*) and MIROVA (Coppola *et al.* 2012).

The HOTVOLC monitoring system that we present here, developed at the Observatoire de Physique du Globe de Clermont-Ferrand (OPGC, Clermont-Ferrand, France), falls within this framework. HOTVOLC has been developed since 2009, and has been designed for near-real-time monitoring of active volcanoes for ash, SO_2 and lava emissions using on-site ingestion of six geostationary satellites. OPGC is one of the French Observatories that comprise the Science of the Universe of the National Scientific Research Centre. It comprises

From: Harris, A. J. L., De Groeve, T., Garel, F. & Carn, S. A. (eds) *Detecting, Modelling and Responding to Effusive Eruptions*. Geological Society, London, Special Publications, **426**, http://doi.org/10.1144/SP426.31

one laboratory dedicated to volcanology (Laboratoire Magmas et Volcans) and one laboratory devoted to atmospheric sciences (Laboratoire de Météorologie Physique). The OPGC thus has a capability for tracking volcanic activity, drawing on both the volcanology and atmospheric science skills. The remote sensing group of the Laboratoire Magmas et Volcans now has a long expertise in satellite and ground-based measurements including radar interferometry (Froger *et al.* 2001) and infrared satellite-based applications, as well as ground-based Doppler radar (e.g. Dubosclard *et al.* 1999; Gouhier *et al.* 2012; Labazuy *et al.* 2012).

After a brief review of infrared satellite measurements of volcanic hot spots and current operational systems, we present the HOTVOLC monitoring system along with its main technical characteristics (on-site acquisition, raw data processing, archiving and dissemination). Next, we present the deliverables of HOTVOLC, including a review of the algorithms used for the detection and quantification of volcanic hot spots. This is followed by a worked example from Etna's 12–13 January 2011 eruption. We finish by describing miscellaneous hot spot monitoring examples, and then present two operational applications of the HOTVOLC system during eruptive crises at Piton de la Fournaise (La Réunion, France) and Kelut (Indonesia).

Infrared satellite measurements of volcanic hot spots

Satellite detection of hot spots has typically used sensor wavebands centred in the short, mid and thermal infrared. Peak spectral radiance emitted by a lava surface temperature, typically ranging from 100 to 1000°C (Harris 2013), occurs in the mid-infrared (MIR: 3–5 μm), whereas the Earth's background surface temperature (typically *c.* 25°C) has a maximum emission in the thermal infrared (TIR: 8–12 μm). This relationship is described by the Planck function (Planck 1901) that quantifies how spectral radiant exitance of a blackbody varies with temperature and wavelength. As a result, strong emission from a sub-pixel hot spot (i.e. a lava flow) in the MIR, will cause the pixel integrated temperature (PIT) in the MIR to be much higher than for the same pixel in the TIR (Dozier 1981; Rothery *et al.* 1988; Wright *et al.* 2004). Defining a temperature difference (DT) threshold in the MIR, as first described in fire-detection algorithms (e.g. Flannigan & Vonder Haar 1986; see also Miller & Harris, 2016) which magnitude depends on the size and temperature of the sub-pixel heat source, will thus indicate if a thermal anomaly exists (e.g. Kennedy *et al.* 1994; Harris *et al.* 1995, 1997*a*).

This principle has been developed and applied using three main classes of algorithms (see Steffke & Harris (2011) for a review): fixed, contextual and temporal detection threshold, the case-type algorithms for each being: MODVOLC (Flynn *et al.* 2002; Wright *et al.* 2002), VAST (Harris *et al.* 1995) and RAT (Tramutoli 1998), respectively. Algorithms based on fixed radiance thresholds use spectral features of the surface derived from MIR and/or TIR channels, on a pixel-by-pixel basis, to determine if a thermal anomaly exists (Harris 2013). Algorithms based on contextual thresholds use the temperature (or radiance) difference between a target pixel and its neighbourhood to determine whether or not it contains a hot spot. Finally, algorithms based on temporal thresholds use the temperature difference between the current pixel value and values obtained from past records for the same pixel, so as to take into account seasonal and atmospheric variation effects. The development of these algorithms has allowed observation systems to be set up for automated detection of volcanic hot spots (Steffke & Harris 2011; Harris 2013; Ramsey & Harris 2013).

Although much less easy, quantification of the lava discharge rate is critical as it strongly controls the lava flow progression speed and the area (see Harris & Rowland 2009, for review). If obtained quickly enough, the discharge rate can be used as an input parameter for models used to forecast lava flow emplacement (e.g. Del Negro *et al.* 2008; Wright *et al.* 2008; Vicari *et al.* 2011). The measurement of lava discharge rates has evolved from field-based techniques (e.g. Pinkerton 1993; Harris *et al.* 2007*a*, *b*) to methodologies using satellite and ground-based IR sensors (e.g. Harris *et al.* 1998, 2005; Calvari *et al.* 2005). Here, infrared methodologies are particularly relevant because lava discharge rates may be derived empirically, under steady-state conditions (Wright *et al.* 2001; Garel *et al.* 2012), from a heat budget where the heat supplied to the active flow unit is lost from the flow surface (Pieri & Baloga 1986; Crisp & Baloga 1990). This method was first applied to satellite thermal data by Harris *et al.* (1997*a*, *b*) to estimate time-averaged discharge rates (TADR) during the 1991–93 eruption of Mt. Etna (Italy), and has since used a variety of low Earth orbiting (LEO) sensor data (e.g. Harris *et al.* 2001; Calvari *et al.* 2005; Coppola *et al.* 2009) and geostationary (GEO) sensors (e.g. Ganci *et al.* 2012*b*; Gouhier *et al.* 2012).

Thermal IR sensors onboard LEO satellites such as MODIS and ASTER, nominally provide four images per day and one image every 16 days, respectively. Both are sensitive to the amount of hot material emplaced over the period prior to the satellite overpass. Therefore, LEO satellite measurements give a TADR. In contrast, sensors onboard GEO satellites such as SEVIRI provide up to 1 image every 5 minutes (i.e. 288 images/day), such as MSG-RSS over the north hemisphere (i.e. suitable for Etna). Note that new geostationary sensors such as Himawari-8 can provide imagery at even higher temporal resolution. This allows monitoring of lava flow emplacement dynamics through time, and permits the calculation of a lava discharge rate based on a much shorter time interval (Vicari *et al*. 2011).

As reviewed and collected in this volume, several hot spot monitoring systems are now operational and use data from GEO/LEO sensors such as ASTER, EO-1, AVHRR, MODIS, ASTER, GOES, MTSAT and/or SEVIRI. Distinctions can be made between these systems, based on (i) the type of algorithm used (fixed, contextual, temporal), (ii) type of satellite platform (GEO/LEO) used, (iii) accessibility to the data products (open/restricted), (iv) the dissemination environment (static web or interactive Web-GIS) and/or (v) whether systems focus on a single volcanic target or region (e.g. HOTSAT system) and those allowing global monitoring of volcanoes (e.g. MODVOLC). HOTSAT, for example, is a monitoring system operated by INGV-OE (Ganci *et al.* 2011, 2012*a*, *b*) that uses both SEVIRI and MODIS data to achieve near-real-time monitoring of thermal activity at Mt. Etna (Italy). It provides detection and quantification products on a password-protected GIS-like web interface. Other systems focusing on a larger number of targets have been developed, such as AVHotRR that uses AVHRR data (Lombardo *et al.* 2011) or MIROVA (Coppola *et al.* 2012) that uses MODIS data, and the RST technique (formerly RAT) that uses multiple sensors for multiple targets (Pergola *et al.* 2001). Other systems dedicated to the monitoring of wider volcanically-active regions have been operational since the 1990s, as at the AVO (Alaska Volcano Observatory) whose monitoring system is based on the OKMOK algorithm of Dehn *et al.* (2000). This system uses AVHRR, MODIS and GOES data, and allows the monitoring of all the volcanoes of the Aleutian arc and Kamchatka (Dean *et al.* 1996: Dean & Dehn 2015), and is not available in open access. Other examples of systems that target regional volcanic areas are the automated system of the Universidad de Colima (México) based on the use of AVHRR data for Mexican volcanoes (Galindo & Dominguez 2002, 2003), and the monitoring system of East Asian volcanoes developed at the University of Tokyo (Japan), which uses MTSAT-2 data (Kaneko *et al.* 2010). Finally, the MODVOLC system (Flynn *et al.* 2002; Wright *et al.* 2002) uses the fixed threshold algorithm, and has been operational since 2000. It allows the near-real-time detection of volcanic thermal activity using the NTI (Normalized Thermal Index) applied to MODIS data. It provides global coverage and there is open access to all current and archived data via the MODVOLC website. MODVOLC uses a GIS-like web interface where hot flagged pixels are displayed in a range of colours depending on the NTI (Wright 2015). The NTI values for each detected anomaly are catalogued, and can be downloaded as text files. MODVOLC is not designed to provide images of the volcanic activity, but instead locational and radiance information for detected hot spots (Wright *et al.* 2004). Other systems using geostationary data have now been in place for almost 20 years, such as the system developed at the Hawaii Institute of Geophysics and Planetology (Harris *et al.* 1997*c*, 2001), which was first used to propose an alert system applied to the full-disc coverage of GOES-East and GOES-West in 1997. In this broader historical context, we now present the HOTVOLC system.

The HOTVOLC monitoring system

HOTVOLC is a web-based satellite-data-driven monitoring system developed at the OPGC (Clermont-Ferrand, France), designed for near-real-time monitoring of active volcanoes in terms of ash, SO_2 and lava emissions, using on-site ingestion of geostationary satellite data. The HOTVOLC idea was launched in 2009 following the installation of the first recieving station at OPGC. In 2014, we duplicated (as a mirror site) the first station by installing a second dish antenna (diameter 2 m) allowing an excellent signal-to-noise ratio and using a second-generation transmission standard (DVB-S2) thus allowing satellite data acquisition of *c.* 30 Gb/day of data at a download rate of up to 10 Mb s^{-1}. We also set up a second processing system running on a 64 bit DELL PowerEdge server with 16 cores (Intel Xeon) using a Linux (red hat) operating system. The two acquisition stations are positioned at geographically distant locations. Therefore, in the event of the first station failing, acquisition and processing by the mirror site can still function so that HOTVOLC system can guarantee a 24/7 information feed. Likewise, the HOTVOLC data archive is secured through backup of all data at a distant mirror site using Storage Area Network technology. The archive comprises data from MSG-0 (Meteosat Second Generation; longitude position = 0°; acquisition rate = 1 image every 15 minutes) collected since 2004, and which is currently assured through operation of Meteosat-10. Since 2009 the archive has included data from MSG-RSS (Rapid Scan Service; longitude position = 9.5° E; rate = 1 image every 5 minutes), which is currently Meteosat-9, as well as Meteosat-7 (longitude position = 57° E; acquisition rate = 1 image every 30 minutes) and MTSAT-2 (Multi-functional Transport Satellites; longitude position = 145° E; rate = 1 image every 60 minutes). Since 2010 we have also been acquiring whole disc data from GOES-East and GOES-West (longitude positions = 75 and 135° W; rate = 1 image every 60 minutes). The two satellites currently in these orbital locations are GOES 13 and 15, respectively. In total, this represents about 10 Tb a^{-1}. Between 2011 and 2014 an open-access static web interface was used to display the data products in the form of small geo-referenced images. However, since early 2014 a new offline interactive Web-GIS version (Fig. 1) has been used in-house. This allows visualization and downloading of multiple data products. Figure 1 shows the current in-house HOTVOLC interface, which has a large Web-GIS map at the centre, and which is used to display the raster image plus other ancillary information. The left-hand panel is used to select the volcanic target, the date of enquiry, and to navigate temporally in 15 to 60 minutes time steps. The right-hand panel is used to display different EO (Earth observation) products using slider buttons, and to download image and numerical data in various formats. In this version of HOTVOLC, the operational implementation is designed for real-time processing of MSG-0 and MTSAT-2, hence allowing Earth coverage from *c.* 70° W (including the Lesser Antilles at the edge of the MSG-0 full-disc) to *c.* 145° W (including Hawaii and the Aleutian arc at the edge of the MTSAT-2 full-disc). The specific strengths of HOTVOLC for monitoring effusive activity can be summed up as follows:

- early warning of volcanic activity through near-real-time detection of thermal anomalies up to a rate of 1 image every 15 min using MSG-SEVIRI;
- 24/7 monitoring and tracking of volcanic hot spots through both the generation of time series (e.g. total spectral radiance and time-averaged discharge rate) and raster image dissemination of spectral radiance and NTI;
- global GEO satellite data archive from 2010 and download capabilities;
- numerous volcanic targets are currently operationally monitored using both MSG-0 and MTSAT-2 satellites;
- full web–GIS user interface with open access to a large number of EO products.

Deliverables of the HOTVOLC system

The HOTVOLC operational system currently uses on-site ingestion of MSG-0 and MTSAT-2 geostationary satellite data from the EUMETSAT primary dissemination protocol using the Digital Video Broadcasting – Satellite 2 (DVB-S2) service. This leads to acquisition of High Rate Information Transmission (HRIT) level 1.5 data format (following the Eumetsat description, http://www.eumetsat.int/website/home/Data/TechnicalDocuments/index.html) and corresponding to image data that have been corrected for unwanted radiometric and geometric effects. Images are geolocated using a standardized geostationary projection, calibrated and radiance linearized. HRIT digital numbers are then converted into spectral radiance (in $W\,m^{-2}\,sr^{-1}\,\mu m^{-1}$) following the EUMETSAT Level 1.5 data format description document. From these data, HOTVOLC provides a variety of EO products related to volcanic ash and gas emissions, as well as volcanic hot spots. In this paper we focus only on products related to volcanic thermal features (lava flows, lakes, domes, etc.). Our products can be divided into two categories: first, EO products related to the detection of volcanic hot spots (e.g. hot spot location NTI*, total spectral radiance) and disseminated in near real-time every 15–60 minutes; and second, EO products related to the quantification of volcanic hot spots (e.g. discharge rates, total lava volume, etc.) as calculated and provided on-demand.

Detection of volcanic hot spots

The detection procedure presented here is based on a contextual algorithm derived from Harris *et al.* (1995) that uses a modified Normalized Thermal Index (NTI*) which adapts the original NTI measure as developed by Flynn *et al.* (2002) and Wright *et al.* (2002):

$$\mathrm{NTI}^* = 1 - \left|\frac{L_{3.9} - L_{12}}{L_{3.9} + L_{12}}\right| \tag{1}$$

where $L_{3.9}$ and L_{12} are the spectral radiances (in $W\,m^{-2}\,sr^{-1}\,\mu m^{-1}$) at 3.9 and 12 μm, respectively. This slight adjustment to the original formulation of the NTI means that it varies from 0 (for the lowest intensity) to 1 (for the highest intensity), making data reading more straightforward, and which is also more convenient for colourbar management when plotting thermal data. The fixed threshold proposed by Wright *et al.* (2002) was abandoned in favour of a dynamic threshold which adapts to the spatial and temporal variability of NTI*, inspired by the VAST algorithm of Harris *et al.* (1995) and Higgins & Harris (1997); and as applied by Kervyn *et al.* (2008). Our algorithm can thus be divided into four main steps:

- **Step 1:** subdivision of the image into two distinct zones,
  - small 'volcanic zone' (10 × 10 pixels);
  - large 'non-volcanic zone' of variable size.

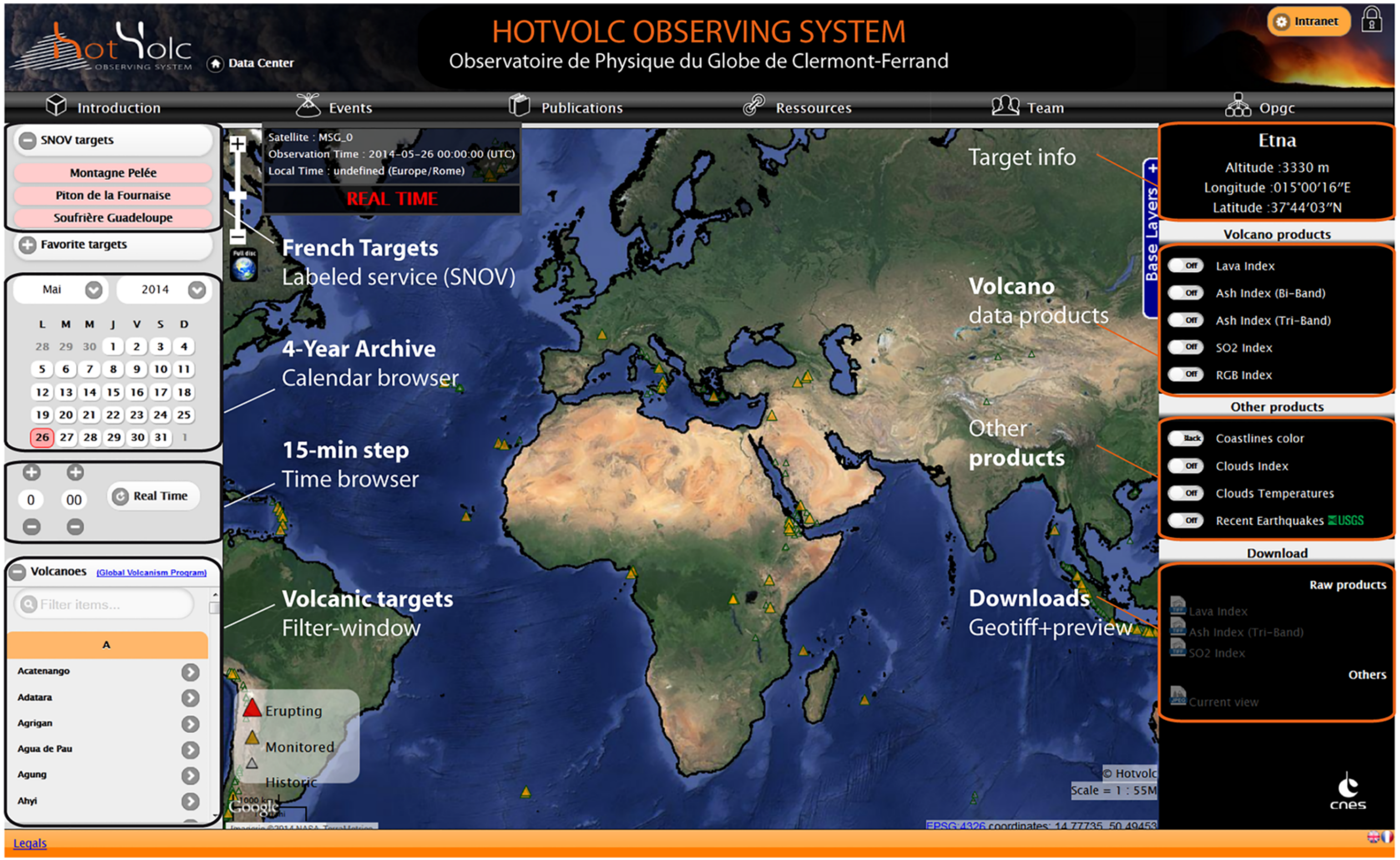

Fig. 1. Snapshot of the HotVolc Observing System Web–GIS Interface developed and maintained by the Observatoire de Physique du Globe de Clermont-Ferrand (France). It principally allows the visualization of raster images (Geotiffs) of various EO products (i.e. hot spots, ash clouds and SO_2 plumes).

- **Step 2:** calculation of NTI* indexes for the two zones,
  - NTI^*_{VOLC} and $NTI^*_{NON\text{-}VOLC}$;
  - $Mean\_NTI^*_{NON\text{-}VOLC}$ and $Std\_NTI^*_{NON\text{-}VOLC}$.
- **Step 3:** calculation of the dynamic threshold,
  - $NTI^*_{threshold} = Mean\_NTI^*_{NON\text{-}VOLC} + n \times Std\_NTI^*_{NON\text{-}VOLC}$.
- **Step 4:** flag anomalous pixels,
  - $NTI^*_{VOLC} - NTI^*_{threshold} > 0$ thermal anomaly = true;
  - $NTI^*_{VOLC} - NTI^*_{threshold} < 0$ thermal anomaly = false.

Note that the pixel area of the 'volcanic zone' depends on the location of the volcanic target as MSG-SEVIRI pixel size increases with latitude and longitude away from the nadir point. NTI^*_{VOLC} and $NTI^*_{NON\text{-}VOLC}$ are the normalized thermal indexes calculated for each pixel in the volcanic and the non-volcanic zones respectively. Then a threshold is calculated for the non-volcanic zone using $Mean\_NTI^*_{NON\text{-}VOLC}$ and $Std\_NTI^*_{NON\text{-}VOLC}$ (using one standard deviation) with a multiplication coefficient '*n*', which ranges from 5 to 15 depending on the solar zenith angle (which varies between day/night, latitude and season). This coefficient has been determined empirically from many tests carried out using MSG-SEVIRI on different volcanic targets (Guéhenneux 2013). Finally, a pixel is flagged as a 'hot spot' if the difference between NTI^*_{VOLC} and $NTI^*_{threshold}$ is positive. This flagging test needs to be performed on each pixel ($i = 1{:}n$) within the volcanic zone and for each image ($j = 1{:}k$) in the eruptive sequence. Figure 2 provides a schematic presentation of the HOTVOLC algorithm used for this hot spot detection. We also calculate a cloud cover index that combines (a) the fraction of the volcanic zone area contaminated by meteorological clouds, and (b) the cloud transparency using the 11 μm waveband. These measures are ultimately used as a quality flag to assess the likelihood of cloud contamination (low, medium, high) in the EO products. Assessment of cloud cover and data quality is very important as optically thick water/ice clouds (i.e. with optical thickness $\tau \gg 1$) will partially or even totally mask the thermal anomaly, hence leading to an inability to detect the volcanic hot spot. This will also result in the underestimation of TADR.

Quantification of volcanic hot spots

We are currently testing two different algorithms to assess their operational capabilities for near-real-time implementation in the HOTVOLC system. Which algorithm is used depends on eruption

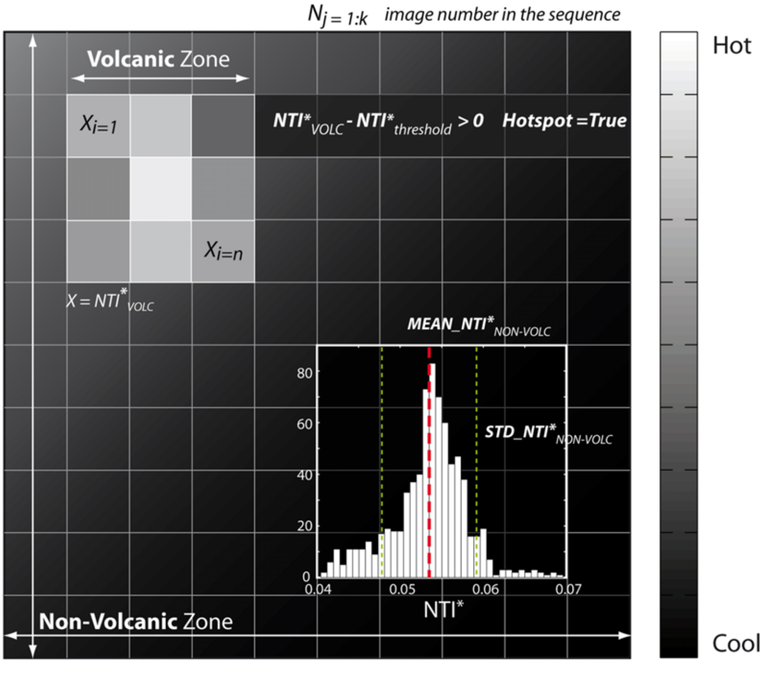

Fig. 2. Sketch to illustrate the detection algorithm used by HOTVOLC. It is a contextual algorithm that uses a dynamic threshold which adapts to the spatial (each volcanic target) and temporal (night/day) variability of the NTI*.

characteristics, such as duration of eruption, presence of signal interruption during the syn-eruptive phase, pulsed or steady supply rate and the availability of model input parameters.

First method: 'heat budget'. The first method is based on the heat budget approach of Pieri & Baloga (1986) following the adaption of Harris *et al.* (1997*a*), which allows the calculation of a TADR as follows:

$$\text{TADR} = A\frac{Q_{\text{rad}} + Q_{\text{conv}}}{\rho(C_{\text{p}}\Delta T + L\Delta\phi)} \qquad (2)$$

where ΔT is the difference between the eruption temperature and the temperature at which forward motion ceases, and $\Delta\phi$ is the fraction of crystals grown in cooling through the ΔT range (Pieri & Baloga 1986). C_{p} and L are the lava specific heat capacity and the latent heat of crystallization, repectively, with ρ being the bulk lava density. Q_{rad} and Q_{conv} are the total radiant heat flux and convective heat flux, respectively. A is the area of the active lava flow. The active lava area can be obtained from the PIT using one band of MIR and/or TIR data. This involves application of a simple two-component mixture model to estimate the active lava area (A_i) within the pixel i. This can be achieved using the dual-band (TIR and MIR) method (Dozier 1981) or by the single-band method in the TIR (Harris *et al.* 1997*a*) or in the MIR (Wright & Flynn 2004) where the surface temperature (T_{s}) is assumed so as to estimate the portion of the pixel occupied by active lava from Harris (2013):

$$A_i = \frac{R_{\text{MIR}}(\text{PIT}) - L_{\text{MIR}}(T_{\text{a}})}{L_{\text{MIR}}(T_{\text{s}}) - L_{\text{MIR}}(T_{\text{a}})} A_{\text{pix}} \qquad (3)$$

In which $L_{\text{MIR}}(T_{\text{s}})$ and $L_{\text{MIR}}(T_{\text{a}})$ are the MIR spectral radiances for the active lava surface component radiating at temperature T_{s}, and for the ambient

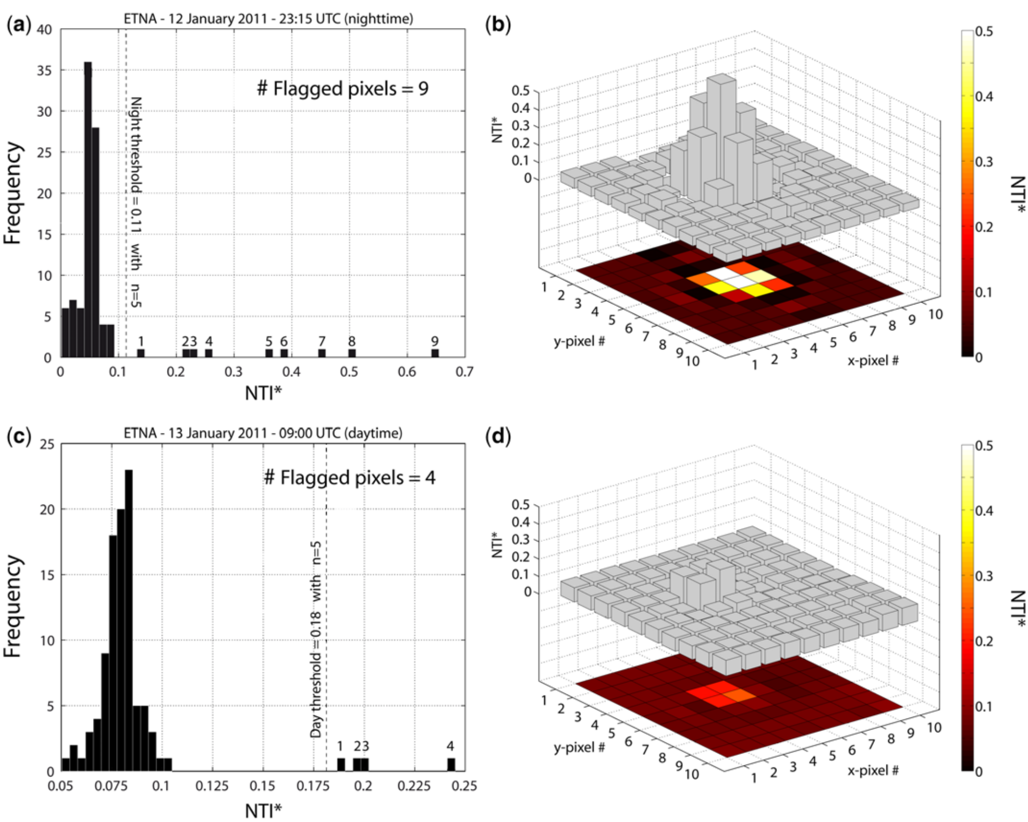

Fig. 3. Plot of the NTI* during the 12–13 January 2011 eruption of Etna. (**a**) Histogram showing NTI* values recorded and flagged pixels from a 10 × 10 area during night-time conditions (23:15 UTC), and (**b**) same information as a 3D plot with associated hot spot map. (**c**, **d**) Same plots as (a, b), but during day-time conditions (09:00 UTC) and thus having a higher NTI* threshold.

surface component surrounding the active lava flow and radiating at temperature T_a. R_{MIR}(PIT) is the at-sensor spectral radiance derived from the PIT and A_{pix} is the pixel area. At-sensor pixel-integrated radiances (L_m) need to be corrected for atmospheric effects. In the MIR, this involves removing the contributions owing to upwelling atmospheric path thermal radiance (L_u) and the surface-reflected downwelling and scattered radiance (L_d) from the measured at-sensor radiance (L_m). This leads to the actual surface radiance (L_s) following French *et al.* (2003):

$$L_{s,\lambda} = \frac{L_{m,\lambda} - L_{u,\lambda}}{\tau_\lambda} - (1 - \varepsilon_{s,\lambda})L_{d,\lambda} \qquad (4)$$

where τ_λ is the atmospheric transmissivity, $\varepsilon_{s,\lambda}$ is the surface emissivity at wavelength λ. This correction can be made using parameters stored in look-up-tables and previously generated using the MODerate resolution atmospheric TRANsmission (MODTRAN) model, for standard atmospheric conditions. Note that atmospheric corrections can also be made on the fly using the Matlab Class Wrapper, hence allowing direct calculation using MODTRAN. The first method, (hereafter termed 'heat-budget' TADR) reduces to an empirical relation, whereby (Wright *et al.* 2001)

$$\mathrm{TADR} = \frac{mA}{c} \qquad (5)$$

where m and c are coefficients defining a linear empirical relation between TADR and the active lava area (A). Note that these coefficients have to be set on a case-by-case basis (Harris & Baloga 2009). Also, the solution is given for a range of coefficients, including the lava surface temperature that needs to be assumed for a range of values (Harris *et al.* 2007*b*, 2010) or constrained from ground observations. The total lava volume can then be estimated through the integration of TADR values during the whole eruptive episode.

Second method: 'cooling curve'. The second method, known as the 'cooling curve' method as applied to satellite data by various authors (e.g. Wooster & Rothery 1997; Rowland *et al.* 2003; Ganci *et al.* 2012*a*, *b*; Gouhier *et al.* 2012), is designed to estimate the total lava volume using the post-eruptive radiant heat flux (Q_{out}). This is

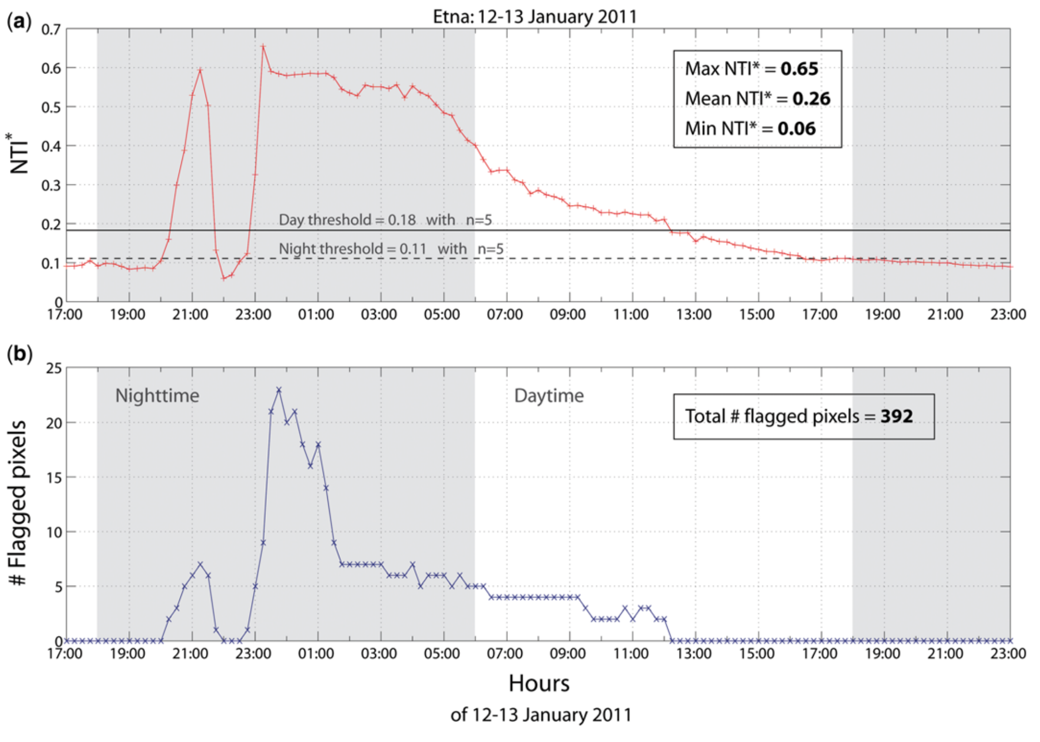

Fig. 4. (**a**) Time series of maximum NTI* values during the whole Etna eruption from 12–13 January 2011. (**b**) Time series of pixels flagged as hot spots by the HOTVOLC algorithm using the corresponding night-time and day-time thresholds.

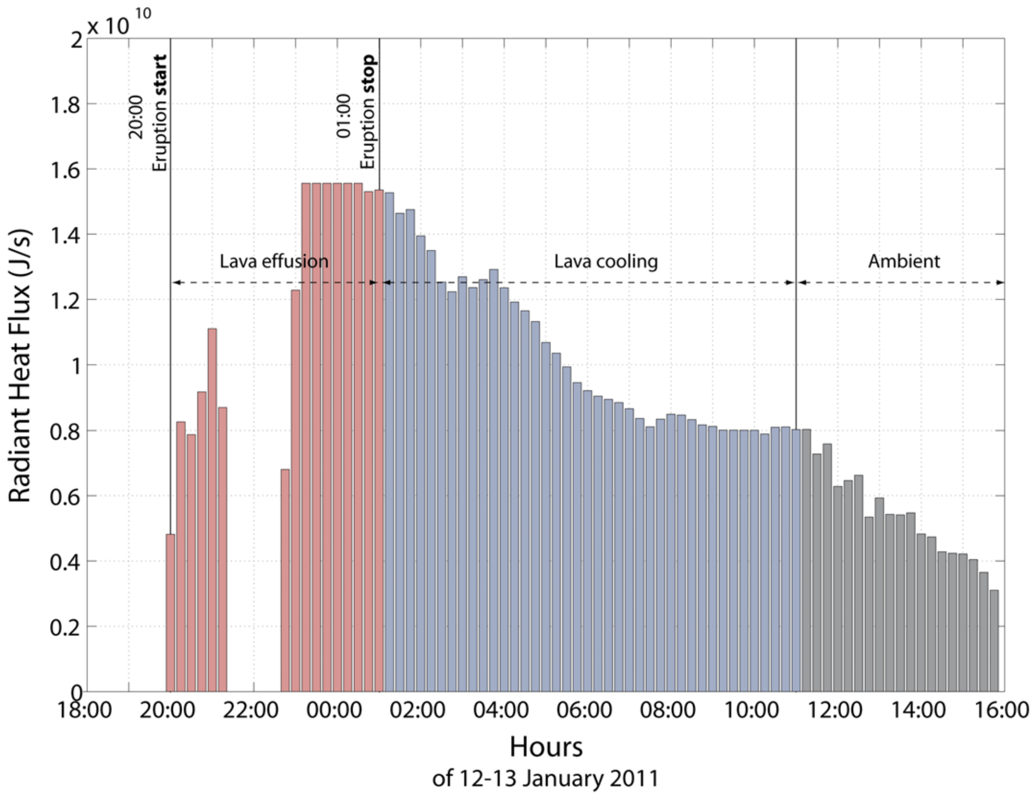

Fig. 5. Time series of the radiant heat flux (expressed in J s^{-1}) retrieved by MSG-SEVIRI during the whole Etna eruption from 12–13 January 2011.

integrated through time during the cooling phase (i.e. after the eruption) to estimate the total thermal energy (E_{th}, expressed in J) released:

$$E_{th} = \sum_i Q_{out} \Delta t. \tag{6}$$

Here Δt is the time interval between two images (i), and Q_{out} is the radiant heat flux lost from the surface of the lava flow unit. Finally, the total lava volume (V_{tot}) that needs to be cooled to generate this energy can be calculated using:

$$V_{tot} = \frac{E_{th}}{\rho(C_p \Delta T + L\Delta\phi)} \tag{7}$$

where E_{th} is the total thermal energy, and ΔT the cooling interval. This method uses post-eruptive data, and hence requires that the eruption is over and the lava fully cooled, which is not appropriate for monitoring or rapid response applications. The cooling curve method gives a Mean Output Rate (MOR), and cannot provide TADR during the eruption phase.

Worked example: Etna 12–13 January 2011 eruption

Detection of hot spots at Etna

The Etna 12–13 January 2011 eruption gave us one of the first satellite-based datasets for fountain-fed flows (e.g. Calvari *et al.* 2011; Ganci *et al.* 2012*a*, *b*; Gouhier *et al.* 2012), and which allowed us to test the HOTVOLC detection algorithm. Figure 3 plots the NTI* during day-time and night-time conditions for the Etna 12–13 January 2011 eruption. Emplacement of the resulting lava flow field was tracked by the HOTVOLC system using MSG-SEVIRI data. In Figure 3a, b we give the histogram frequency of NTI* from a 10 × 10 pixel area centred on the hot spot in the image acquired at 23:15 UTC on 12 January (i.e. night-time conditions). This was just before the climax of the

Table 1. *Total DRE lava volume and associated mean output rate*

Method	Total lava volume (DRE, m^3)	Mean output rate (DRE, $m^3\ s^{-1}$)	References
First – heat-budget	0.2×10^6	11	Gouhier *et al.* (2012)
Second – cooling curve	1.2×10^6	70	Gouhier *et al.* (2012)
Field measurements	$0.8–1.7 \times 10^6$	45–94	Calvari *et al.* (2011)

eruption, and while most 'background' pixels have NTI* < 0.1, nine pixels with NTI* values higher than the night-time threshold (i.e. 0.11) can be detected and flagged as hot spots. In this case, $\mathrm{NTI}^*_{\mathrm{threshold}}$ is calculated using $n = 5$. The NTI* map and associated 3D plot (Fig. 3b) highlight the nine illuminated pixels. Similarly, in Figure 3c, d we present the histogram frequency of NTI* from a 10 × 10 pixel area imaged at 09:00 UTC on 13 January (i.e. day-time conditions). By this time the lava flows were no longer being fed (Calvari *et al.* 2011) and the anomalies thus represent the cooling phase of the previously emplaced lava (Ganci *et al.* 2012*a*; Gouhier *et al.* 2012). However, we succeeded in detecting and flagging the four anomalous pixels, all of which had NTI* values that were higher than the day-time threshold (i.e. 0.18). In this case, mean NTI* of background pixels (i.e. sub-Gaussian distribution) is shifted toward higher values owing to the contribution of reflected

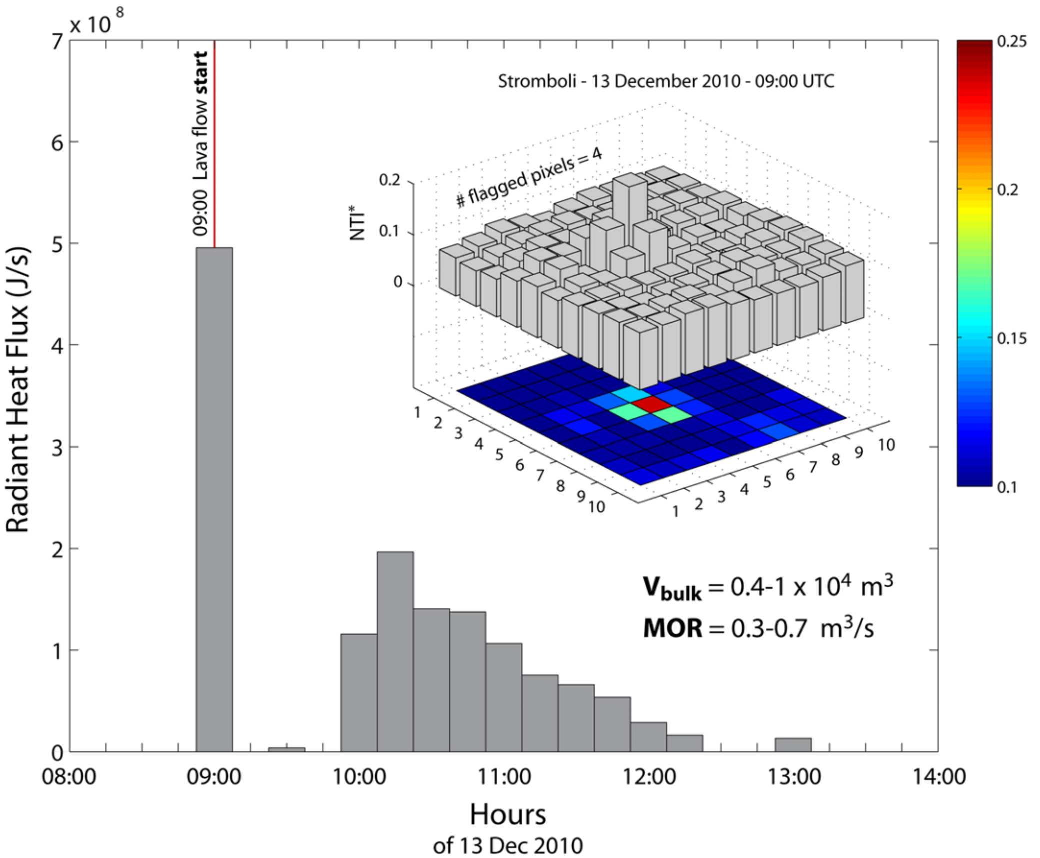

Fig. 6. Time series of the radiant heat flux retrieved by MSG-SEVIRI during the short-lived lava flow that occurred at Stromboli Volcano on 13 December 2010. The inset is an NTI* map and associated 3D plot of the first detected anomaly at 09:00 UTC.

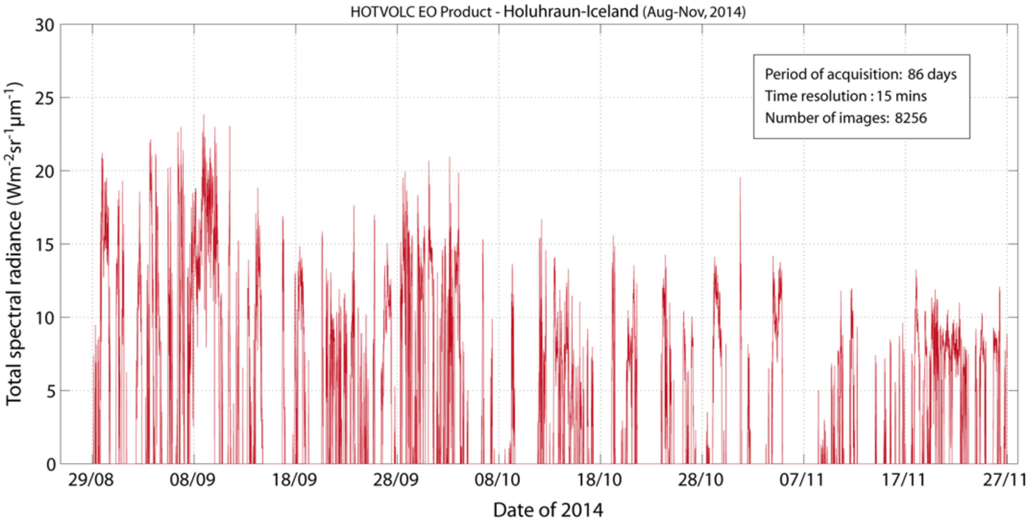

Fig. 7. Time series of total spectral radiance retrieved from MSG-SEVIRI data during the first 86 days of the Holuhraun eruption (Iceland).

solar radiance during day-time conditions in the MIR. Although they have a lower intensity than during the syn-eruptive period (Fig. 3b), these anomalous pixels are still clearly revealed by the NTI* map and associated 3D projection (Fig. 3d).

Finally, we provide a time series of maximum NTI* (Fig. 4a) and of the number of flagged pixels (Fig. 4b) during the whole eruptive episode. The first hot spot was detected at 20:15 UTC on 12 January (NTI* = 0.3), indicating the eruption start, with a maximum of 23 flagged pixels occurring at 23:45 UTC, when the maximum NTI* of *c.* 0.65 was also attained. NTI* then rapidly decreased, allowing the detection of hot spot pixels until 12:15 UTC on 13 January. Note that the end of the eruption occurs earlier, around 01:00 UTC (Calvari *et al*. 2011). From this point onward, thermal anomalies thus represent the remaining heat flux that originates from the lava flow field now cooling. No anomaly could be detected between 22:00 and 22:30 as a thick ash plume obscured the satellite view, hence preventing any reliable NTI* measurements. This period represents the lowest values of the whole time series, with NTI* = 0.06.

Quantification of hot spots at Etna

Here we present the results of the two quantitative algorithms applied for TADR extraction as applied to the same Etna 12–13 January 2011 eruption. Figure 5 plots the radiant heat flux during the eruption revealing the three different phases. The lava effusion phase lasted about 5–6 h (Calvari *et al.* 2011) beginning at 20:00 and ending at 01:00 UTC. After this time, lava flows were no longer supplied, and the lava cooling phase began as the flow stagnated and cooled over a period of about 10 h, between 01:00 and 11:00 UTC, until it became undistinguishable from the ambient signal (Gouhier *et al.* 2012).

The radiant heat flux was used to calculate the total lava volume (V_{tot}) from the first (heat budget) and the second (cooling curve) method, respectively. Given that TADR cannot be calculated using the cooling curve method, we provide a MOR for both methods so as to compare the results. We obtain a dense rock equivalent (DRE – using *c.* 22% vesicles; Calvari *et al.* 2011) total lava volume (V_{DRE}) of 0.2×10^6 m^3 and 1.2×10^6 m^3 for the heat budget and the cooling curve methods, respectively (Gouhier *et al.* 2012). Given a duration of the effusive event of 5 h, these two volumes convert to mean output rates of 11 and 70 m^3 s^{-1}, respectively. The discrepancy is mostly due to the obscuration of the lava flow field by a thick ash cloud, hence preventing any radiant heat flux measurement during this period. Moreover, saturation of the MIR channels during the climax of the eruption caps the radiant heat flux values. Therefore, in this case, the 'heat budget' method underestimates the total amount of lava erupted. Note that if the user/computer of the automated monitoring system has no information regarding the end time of the eruption, the 'heat budget' method will erroneously consider the whole lava cooling curve as being newly emplaced lava (false TADR), leading to the overestimation of the total lava volume; unless methods are applied to detect eruption cessation (e.g. Aries *et al.* 2001). Therefore, we do not recommend

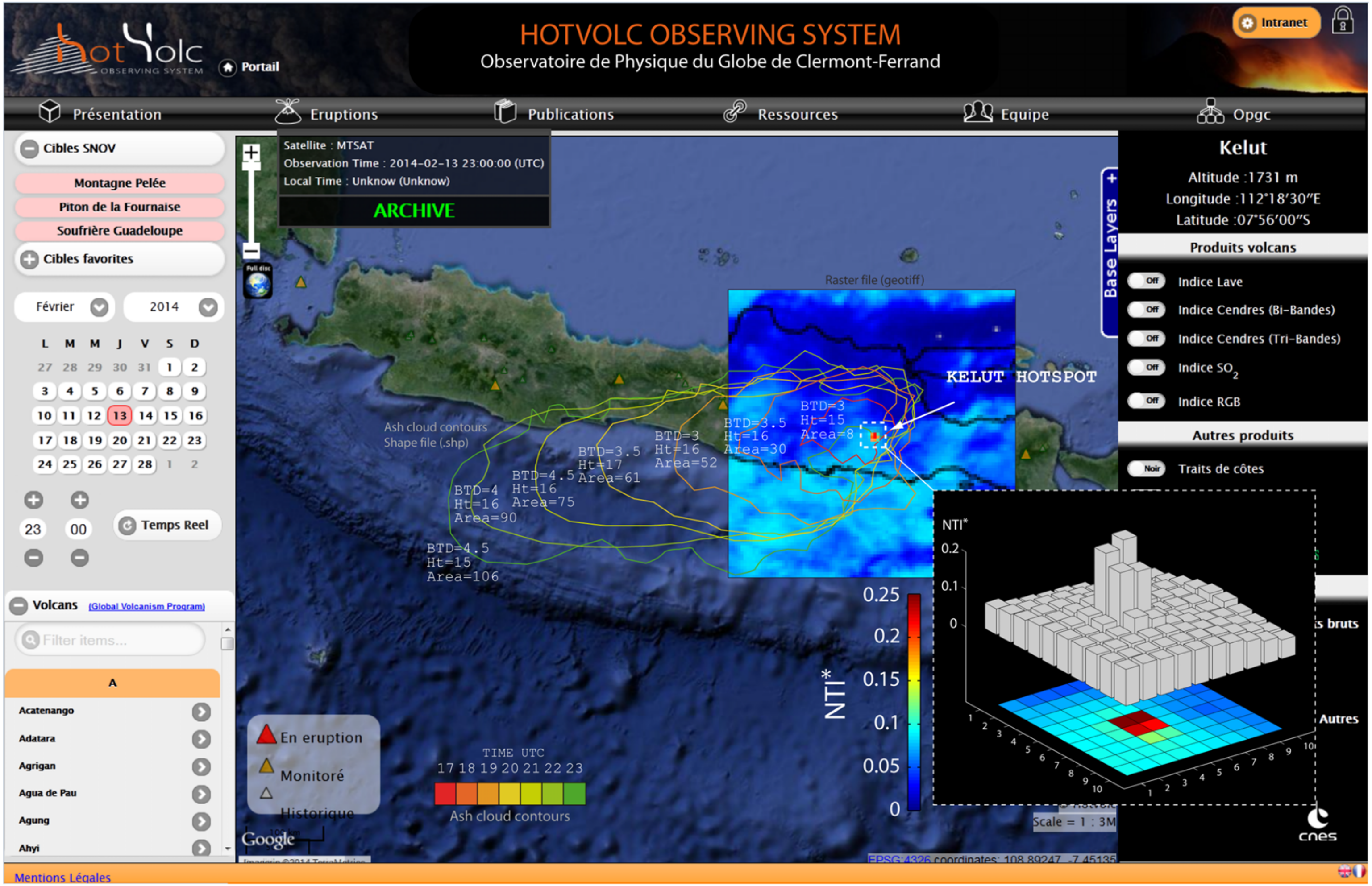

Fig. 8. Modified snapshot of the HOTVOLC Web–GIS interface showing NTI* map and ash cloud contours from 16:00 UTC to 23:00 UTC on 13 February 2014 during the Kelut eruption (Indonesia). Ash index (|BTD|, K), ash-cloud height (km) and cloud area ($\times 10^3$ km^2) are also given for each contour.

Table 2. *Summary of data processed during Piton de la Fournaise 2015 eruptions*

Eruption no.	Start date (yyyy/mm/dd)	End date (yyyy/mm/dd)	Duration (days)	Number of images processed (MSG-SEVIRI)
1	2015/02/04	2015/02/15	11	1100
2	**2015/05/17**	**2015/05/30**	**13**	**1220**
3	2015/07/31	2015/08/02	2	198
4	2015/08/24	2015/10/31	68	6528

using the 'heat budget' method for near-real-time quantitative assessment of lava volumes.

For this case, the 'cooling curve' method provides a good alternative for lava volume Estimation from the post-eruptive signal which is not affected by ash obscuration or saturation problems. However, this method, applicable only after the end of the eruption, may not be appropriate for continuous or pulsed effusive activity, as the cooling curve would be interrupted and masked by the heat flux signal of the next effusive event. This method is thus not appropriate for near-real-time implementation within operational and automated monitoring systems. We recommend using this method for single effusive events only. Results summarized in Table 1 indicate that the 'cooling curve' method is within the range of field measurement values, while the 'heat flux' method results in a significant discrepancy between measured and derived volumes. Thus, for this case, while the 'cooling curve' method can provide reliable volume estimates, but no syn-eruptive TADR information; the 'heat budget' has the potential to provide syn-eruptive TADR; but is less reliable for volume estimates (see Harris *et al.* 2001 for full test and discussion).

Miscellaneous examples of hot spot monitoring

In this section we focus on two contrasting examples of effusive activity to illustrate the capability of the HOTVOLC system for hot spot tracking using geostationary satellites for (a) early detection of weak and short-lived effusive activity (using Stromboli, Eolian Islands – 2010) and (b) intense and long-lived effusive activity (using Holuhraun, Iceland – 2014).

Stromboli (Eolian Islands, Italy: 2010)

Stromboli Volcano is well-known for its persistent explosive activity, consisting of small 'strombolian' explosions, and occasionally displaying more explosive events producing ash plumes and ejecting large blocks (Ripepe *et al.* 2005; Patrick *et al.* 2007; Métrich *et al.* 2010). Sometimes, Stromboli exhibits short-lived effusive activity that can possibly be detected from sensors onboard LEO satellites if the image acquisition is simultaneous of the eruption (Gaonac'h *et al.* 1994; Harris & Stevenson 1997; Ripepe *et al.* 2005; Coppola *et al.* 2012). In this case, we show that GEO satellites may be particularly useful for the detection and tracking of such events. By way of example, we plot in Figure 6 the detection using MSG-SEVIRI data of a short-lived lava flow which was active on Stromboli on 13–14 December 2010. The first hot spot was detected at 09:00 UTC, with a maximum NTI* of 0.24 (compared with the daytime threshold of 0.14). Four pixels were flagged as being anomalous on this image. The lava effusion was tracked over four hours during which time a total bulk lava volume of 0.4×10^4 m^3 was estimated as being erupted using the 'heat budget' method. This yields a MOR of 0.3 m^3 s^{-1}. This example illustrates that, in spite of low-level effusive activity, GEO satellites can be used for early warnings and tracking, and may be considered as an operational tool for most observatories.

Holuhraun (Iceland: 2014)

In contrast, during effusive events such as that of the 2014 Holuhraun eruption in the Bárdarbunga Volcanic System (Iceland), lava effusion can be very voluminous and last several months to years (e.g. Thordarson *et al.* 2003; Thordarson & Larsen 2007; Schmidt *et al.* 2015). However, the monitoring of effusion rates at a high time resolution is essential as it provides information about the dynamics of the eruption, and possibly reflects modifications in the deeper mechanisms where the eruption originates. Here we show how GEO satellite-based sensors such as GOES-Imager or MSG-SEVIRI may be used to produce long time series at a high acquisition rate (Mouginis-Mark *et al.* 2000; Harris *et al.* 2001; Gauthier *et al.* 2016). During the 2014 eruption of Holuhraun we processed 86 days of data from 1 September to 25 November 2014, at a temporal resolution of one image every 15 minutes, which totals 8256 images. Figure 7 is the plot of total spectral radiance for the first 86 days of the eruption, in which a series of strong peaks are apparent,

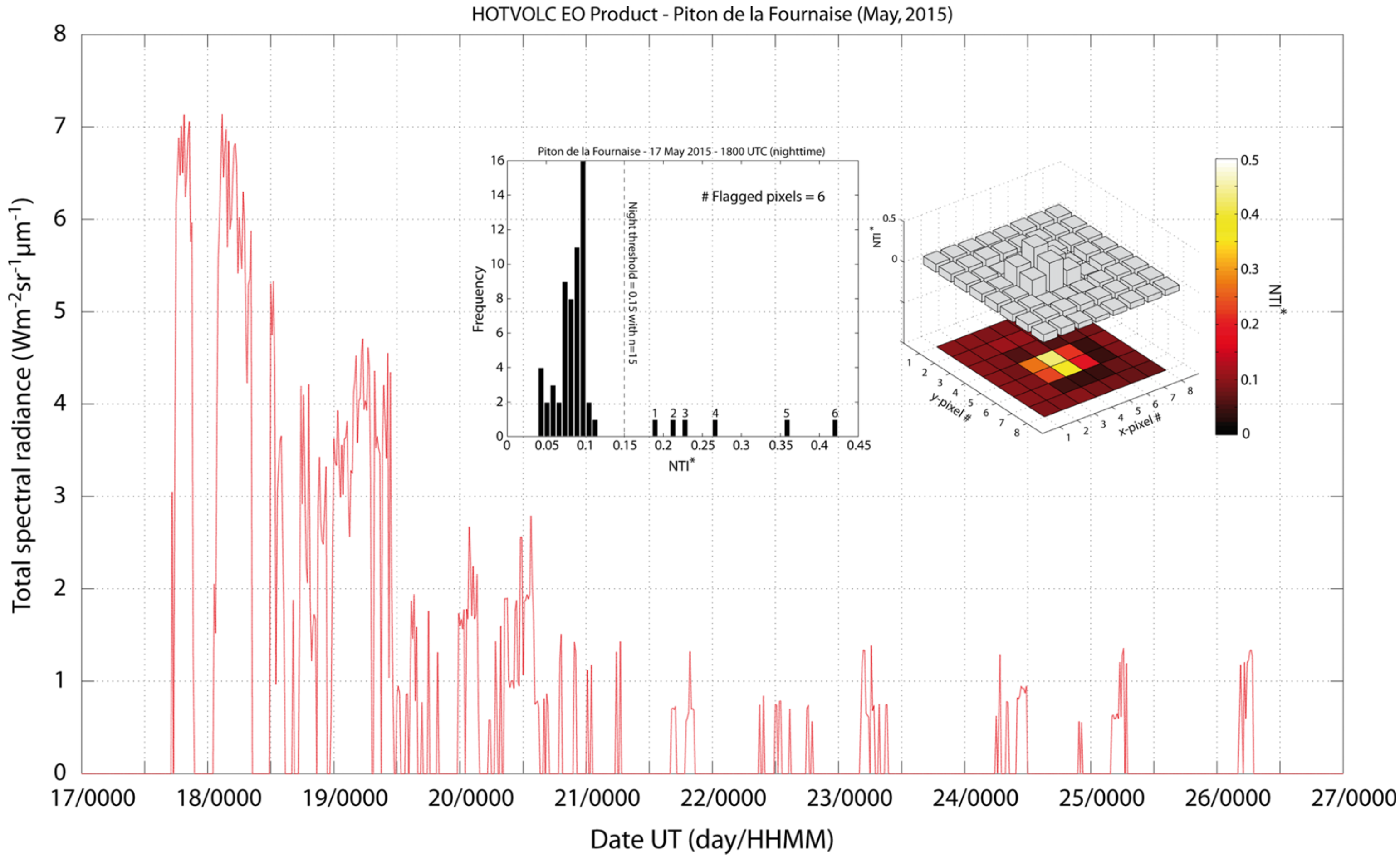

Fig. 9. Time series of the total spectral radiance during the 17–30 May 2015 Piton de la Fournaise eruption. Insert of a histogram showing NTI* values recorded and flagged pixels from a 8 × 8 area during night-time conditions (18:00 UTC) and illustrated on a 3D plot with associated map.

superimposed on longer wavelength oscillations. There is also an almost linear decrease in spectral radiance over the whole time series that most likely reflects the progressive weakening of the feeding system. Apparent spectral radiance troughs within the time series are due to cloud cover over Holuhraun, which prevented hot spot detection. However, the troughs arising at the end of October, for instance, are not related to cloud cover, and thus indicate transient weakening of the effusive activity.

Operational applications

Products from the HOTVOLC system have been requested several times by national or local authorities to provide an operational response during ash and SO_2 plume activity, as during the 2010 Eyjafjallajökull (Iceland) eruption and the 2011 Grimsvötn (Iceland) eruption as well as for the 2014 Kelut (Indonesia) eruption. The HOTVOLC system has also regularly been requested by the OVPF (Observatoire Volcanologique du Piton de la Fournaise) to aid on monitoring of the lava flow activity at Piton de la Fournaise Volcano (La Réunion). Here we present two examples related to hot spot monitoring. The first example is from Kelut (Indonesia) where both hot spots and ash clouds were visible, and the second is from Piton de la Fournaise (La Réunion) where thermal anomalies related to lava flow activity were tracked.

Kelut (Java, Indonesia: 2014)

HOTVOLC has been involved in the response to the Kelut eruption which occurred on February 13–14, 2014 on Java Island (Indonesia). For this target, we used infrared data from the geostationary satellite MTSAT-2, automatically received and processed by the HOTVOLC system every hour. This eruption began with effusive activity associated with the presence of a dome emplaced in the volcano's caldera during the previous eruption in 2007. A ground thermal anomaly was detected by HOTVOLC on 13 February 2014 at 16:00 UTC (just a few minutes after the dome collapse). The anomaly was composed of four pixels and had a maximum NTI* of 0.28 (compared with the day-time threshold of 0.11 set for this case). One hour later (17:00 UTC), we detected a large plume of ash rising vertically above Kelut, which totally masked the thermal anomaly for the rest of the eruption. From this point onwards we were connected with the CVGHM (Center for Volcanology and Geological Hazard Mitigation) via an email request to provide information regarding ash cloud content, altitude and location, in the form of maps, on an hourly basis until 14 February at 11:00 UTC. The ash cloud was particularly concentrated and extensive, and a few hours after the onset of the eruption the ash could be detected hundreds of kilometres to the west of Java Island. Consequently, the eruption prompted several tens of thousands of people to be evacuated, five airports to be closed and many flights to be cancelled. In the context of lava dome growth, the Kelut eruption nicely illustrates that early detection of effusive activity made by GEO satellites can be decisive for risk mitigation associated with explosive activity which may follow the opening effusive phase. The information provided to CVGHM is summarized in a snapshot of the HOTVOLC interface at work during the eruptive crisis as given in Figure 8.

Piton de la Fournaise (La Réunion: 2015)

Piton de la Fournaise Volcano is one of the most active effusive centres in the world, regularly displaying low-level explosive activity and lava flow events, with four effusive eruptions occurring in February, May, July and August of 2015. As part of the Service National d'Observation Volcanologique, the HOTVOLC system is routinely requested to contribute to thermal monitoring of Piton de la Fournaise by OVPF (Observatoire Volcanologique du Piton de la Fournaise). Basic information relating to the timing of the four eruptions monitored by HOTVOLC in 2015 is summarized in Table 2.

For these eruptions, maps of hot spot spectral radiance were provided on an hourly basis through the HOTVOLC website interface. Also, following an email request from the OVPF director, TADR and cumulative lava volume were provided. As an example, Figure 9 plots the total spectral radiance (TSR) for the May 2015 eruption which began at 14 h 00 UTC on 17 May. The TSR reached a value of 7 W m^{-2} sr^{-1} μm^{-1} on the first day and abruptly decreased on 18 May around midday to 4.5 W m^{-2} sr^{-1} μm^{-1} and decreased again on 19 May just before midday to 2 W m^{-2} sr^{-1} μm^{-1}. From 20 May the TSR declined through the termination of the eruption on 31 May. During the whole eruption the HOTVOLC system flagged 682 anomalous pixels in 864 images. The eruption analysis reveals a maximum NTI* of 0.46 with a maximum spectral radiance of 7.1 W m^{-2} sr^{-1} μm^{-1} with the total spectral radiance summed over the whole eruption being 670 W m^{-2} $sr^{-1}$$\mu m^{-1}$.

Conclusion

The HOTVOLC system has evolved since it was launched in 2009. Today, it operates in a near-real-time fashion using a secured acquisition station with a mirror site at a geographically distant location. It uses on-site ingestion of data from six geostationary satellites allowing worldwide coverage at high time-resolution, ranging from 5 min (MSG-RSS) to 1 hour (MTSAT-2). Note that currently only MSG-SEVIRI and MTSAT-2 are used in operational mode allowing near-real-time monitoring of *c.* 100 volcanic targets. Both geo-referenced images and time series are displayed and can be downloaded via a web-GIS interface. The worked example shown for the 12–13 January 2011 Etna eruption is a good means to present the capability of automated detection procedures and to compare different quantitative algorithms to be implemented as future routine EO products within the HOTVOLC system. Also, specific examples presented in the miscellaneous section such as the weak and short-lived eruption of Stromboli (2010/12/13) as well as the long-lived 2014–15 eruption of Bardarbunga, illustrate the HOTVOLC system product for two contrasting effusive events. The operational applications presented show the ability of the HOTVOLC system to provide meaningful information in a timely manner. Maps of the spectral radiance, in particular, allow a visual assessment of hot spots intensity and extent. Also, time series of TADR values at a high time resolution (15 min) are of great value for the rapid evaluation of the lava flow dynamics.

This work was supported by the TOSCA program of the Centre National d'Etudes Spatiales (France) through the convention CNES/92532-BC-T39. SEVIRI data were provided by the HOTVOLC reception platform (OPGC) through agreement with EUMETSAT and Météo-France. We also thank two anonymous reviewers and Andrew Harris for thoughtful comments as well as the corresponding editors, Simon Carn and Fanny Garel, for handling the manuscript and Fran van Wyk de Vries for rapid turn around of final edits.

References

Andronico, D., Branca, S. *et al.* 2005. A multidisciplinary study of the 2002–03 Etna eruption: insights for a complex plumbing system. *Bulletin of Volcanology*, **67**, 314–330, http://doi.org/10.1007/s00445-004-0372-8

Aries, S.E., Harris, A.J.L. & Rothery, D.A. 2001. Remote infrared detection of the cessation of volcanic eruptions. *Geophysics Research Letters*, **28**, 1803–1806.

Bonaccorso, A., Aloisi, M. & Mattia, M. 2002. Dike emplacement forerunning the Etna July 2001 eruption modeled through continuous tilt and GPS data. *Geophysics Research Letters*, **29**, http://doi.org/10.1029/2001GL014397

Burton, M.R., Neri, M., *et al.* 2005. Etna 2004–2005: an archetype for geodynamically-controlled effusive eruptions. *Geophysics Research Letters*, **32**, L09303, http://doi.org/10.1029/2005GL022527

Calvari, S., Spampinato, L. *et al.* 2005. Chronology and complex volcanic processes during the 2002–2003 flank eruption at Stromboli volcano (Italy) reconstructed from direct observations and surveys with a handheld thermal camera. *Journal of Geophysical Research*, **110**, B02201, http://doi.org/10.1029/2004JB003129

Calvari, S., Salerno, G. *et al.* 2011. An unloading foam model to constrain Etna's 11-13 January 2011 lava fountaining episode. *Journal of Geophysical Research*, **116**, B11207. http://doi.org/10.1029/2011JB008407

Coppola, D., Piscopo, D., Staudacher, T. & Cigolinia, C. 2009. Lava discharge rate and effusive pattern at Piton de la Fournaise from MODIS data. *Journal of Volcanology and Geothermal Research*, **184**, 174–192.

Coppola, D., Piscopo, D., Laiolo, M., Cigolini, C., Delle Donne, D. & Ripepe, M. 2012. Radiative heat power at Stromboli volcano during 2000–2011: twelve years of MODIS observations. *Journal of Volcanology and Geothermal Research*, **215–216**, 48–60, http://doi.org/10.1016/j.jvolgeores.2011.12.001

Crisp, J. & Baloga, S.M. 1990. A model for lava flows with two thermal components. *Journal of Geophysical Research*, **95**, 1255–1270, http://doi.org/10.1029/JB095iB02p01255

Dean, K.G. & Dehn, J. (eds) 2015. *Monitoring Volcanoes in the North Pacific*. Springer Praxis Books, http://doi.org/10.1007/978-3-540-68750-4-5

Dean, K., Searcy, C., Wyatt, C., George, S. & Engle, K. 1996. Monitoring volcanoes in the North Pacific Ocean region using satellite imagery, modeling and meteorological data. *In*: *Proceedings of the Pan Pacific Hazards Conference*, 27 July to 4 August, 1996, Vancouver (Canada), 1–29.

Dehn, J., Dean, K. & Engle, K. 2000. Thermal monitoring of North Pacific volcanoes from space. *Geology*, **28**, 755–758.

Del Negro, C., Fortuna, L., Herault, A. & Vicari, A. 2008. Simulations of the 2004 lava flow at Etna 388 volcano by the MAGFLOW cellular automata model. *Bulletin of Volcanology*, **70**, 805–812.

Dozier, J. 1981. A method for satellite identification of surface temperature fields of subpixel resolution. *Remote Sensing of Environment*, **11**, 221–229, http://doi.org/10.1016/0034-4257(81)90021-3

Dubosclard, G., Cordesses, R., Allard, P., Hervier, C., Coltelli, M. & Kornprobst, J. 1999. First testing of a volcano Doppler radar (Voldorard) at Mt. Etna. *Geophysics Research Letters*, **26**, 3389–3392, http://doi.org/10.1029/1999GL008371

Flannigan, M.D. & Vonder Haar, T.H. 1986. Forest fire monitoring using NOAA satellite AVHRR. *Canadian Journal of Forest Research*, **16**, 975–982.

Flynn, L., Wright, R., Garbeil, H., Harris, A.J.L. & Pilger, E. 2002. A global thermal alert system using MODIS: initial results from 2000 to 2001. *Advances in Environmental Monitoring and Modeling*, **1**, 37–69.

Francis, P.W. & Rothery, D.A. 1987. Using the Landsat Thematic Mapper to detect and monitor active volcanoes: an example from Lascar volcano, northern Chile. *Geology*, **15**, 614–617, http://doi.org/10.1130/0091-7613(1987)

French, A.N., Norman, J.M. & Anderson, M.C. 2003. A simple and fast atmospheric correction for spaceborne remote sensing of surface temperature. *Remote Sensing of Environment*, **87**, 326–333. http://doi.org/10.1016/j.rse.2003.08.001

Froger, J.L., Merle, O. & Briole, P. 2001. Active spreading and regional extension at Mount Etna imaged by SAR interferometry. *Earth and Planetary Science Letters*, **187**, 245–258.

Galindo, I. & Dominguez, T. 2002. Real-time AVHRR multispectral thermal monitoring and ash emission detection into the atmosphere: the case of Colima Volcano (México). *AGU Geophysical Monograph Series*, **139**, 133–149, http://doi.org/10.1029/139GM08

Galindo, I. & Dominguez, T. 2003. Near real-time satellite monitoring during 1997–2000 activity of Volcan de Colima (México) and its relationship with seismic monitoring. *Journal of Volcanology and Geothermal Research*, **117**, 91–104, http://doi.org/10.1016/S0377-0273(02)00238-X

Gaonac'h, H., Vandemeulebrouck, J., Stix, J. & Halbwachs, M. 1994. Thermal infrared satellite measurements of volcanic activity at Stromboli and Vulcano. *Journal of Geophysical Research: Solid Earth*, **99**(B5), 9477–9485.

Ganci, G., Vicari, A., Fortuna, L. & Del Negro, C. 2011. The HOTSAT volcano monitoring system based on combined use of SEVIRI and MODIS multispectral data. *Annals of Geophysics*, **54**, 544–550, http://doi.org/10.4401/ag-5338

Ganci, G., Vicari, A., Cappello, A. & Del Negro, C. 2012*a*. An emergent strategy for volcano hazard assessment: from thermal satellite monitoring to lava flow modeling. *Remote Sensing of Environment*, **119**, 197–207, http://doi.org/10.1016/j.rse.2011.12.021

Ganci, G., Harris, A.J.L. *et al.* 2012*b*. A year of lava fountaining at Etna: volumes from SEVIRI. *Geophysics Research Letters*, **39**, L06305. http://doi.org/10.1029/2012GL051026

Garel, F., Kaminski, E., Tait, S. & Limare, A. 2012. An experimental study of the surface thermal signature of hot subaerial isoviscous gravity currents: implications for thermal monitoring of lava flows and domes. *Journal of Geophysical Research*, **117**, B02205, http://doi.org/10.1029/2011JB008698

Gauthier, P.-J., Sigmarsson, O., Gouhier, M., Haddadi, B. & Moune, S. 2016. Elevated gas flux and trace metal degassing from the 2014–2015 fissure eruption at the Bárðarbunga volcanic system, Iceland. *Journal of Geophysical Research*, **120**, http://doi.org/10.1002/2015JB012111.

Gouhier, M., Harris, A.J.L. *et al.* 2012. Lava discharge during Etna's January 2011 fire fountain tracked using MSG-SEVIRI. *Bulletin of Volcanology*, **74**, 787–793, http://doi.org/10.1007/s00445-011-0572-y

Guéhenneux, Y. 2013. *Analyse thermique de l'activité volcanique par traitement des données à très haute resolution temporelle du satellite météorologique METEOSAT SECOND GENERATION*. PhD thesis, Université Clermont-Ferrand II Blaise Pascal: Laboratoire Magmas et Volcans.

Harris, A. 2013. *Thermal Remote Sensing of Active Volcanoes*. Cambridge University Press, New York.

Harris, A.J.L. & Baloga, S.M. 2009. Lava discharge rates from satellite-measured heat flux. *Geophysical Research Letters*, **36**, L19302, http://doi.org/10.1029/2009GL039717

Harris, A.J.L. & Rowland, S.K. 2009. Effusion rate controls on lava flow length and the role of heat loss: a review. *In*: Thordarson, T., Self, S. *et al.* (eds) *Studies in Volcanology: The Legacy of George Walker*. Special Publication of the International Association of the Volcanology and Chemistry of the Earth' s Interior. Geological Society, London, **2**, 33–51.

Harris, A.J. & Stevenson, D.S. 1997. Thermal observations of degassing open conduits and fumaroles at Stromboli and Vulcano using remotely sensed data. *Journal of Volcanology and Geothermal Research*, **76**, 175–198.

Harris, A.J.L., Swabey, S.E.J. & Higgins, J. 1995. Automated thresholding of active lavas using AVHRR data. *International Journal of Remote Sensing*, **16**, 3681–3686, http://doi.org/10.1080/01431169508954654

Harris, A.J.L., Blake, S., Rothery, D.A. & Stevens, N.F. 1997*a*. A chronology of the 1991 to 1993 Etna eruption using AVHRR data: implications for real time thermal volcano monitoring. *Journal of Geophysical Research*, **102**, 7985–8003, http://doi.org/10.1029/96JB03388

Harris, A.J.L., Keszthelyi, L. *et al.* 1997*b*. Chronology of the Episode 54 eruption at Kilauea Volcano, Hawaii, from GOES-9 satellite data. *Geophysical Research Letters*, **24**, 3281–3284, http://doi.org/10.1029/97GL03165

Harris, A.J.L., Butterworth, A.L., Carlton, R.W., Downey, I., Miller, P., Navarro, P. & Rothery, D.A. 1997*c*. Low-cost volcano surveillance from space: case studies from Etna, Krafla, Cerro Negro, Fogo, Lascar and Erebus. *Bulletin of Volcanology*, **59**, 49–64.

Harris, A.J.L., Flynn, L.P., Keszthelyi, L., Mouginis-Mark, P.J., Rowland, S.K. & Resing, J.A. 1998. Calculation of lava effusion rates from Landsat TM data. *Bulletin of Volcanology*, **60**, 52–71.

Harris, A.J.L., Pilger, E. *et al.* 2001. Automated, high temporal resolution, thermal analysis of Kilauea volcano, Hawaii, using GOES-9 satellite data. *International Journal of Remote Sensing*, **22**, 945–967, http://doi.org/10.1080/014311601300074487

Harris, A.J.L., Dehn, J. *et al.* 2005. Lava effusion rates from hand-held thermal infrared imagery: an example from the June 2003 effusive activity at Stromboli. *Bulletin of Volcanology*, **68**, 107–117.

Harris, A.J.L., Dehn, J. *et al.* 2007*a*. Pahoehoe cooling, discharge and coverage rates from thermal image chronometry. *Geophysical Research Letters*, **34**, L19303, http://doi.org/10.1029/2007GL030791

Harris, A.J.L., Dehn, J. & Calvari, S. 2007*b*. Lava effusion rate definition and measurement: a review. *Bulletin of Volcanology*, **70**, 1–22.

Harris, A.J.L., Favalli, M., Steffke, A., Fornaciai, A. & Boschi, E. 2010. A relation between lava discharge rate, thermal insulation, and flow area set using lidar data. *Geophysical Research. Letters*, **37**, L20308, http://doi.org/10.1029/2010GL044683

Herault, A., Vicari, A., Ciraudo, A. & Del Negro, C. 2009. Forecasting lava flow hazards during the 2006 Etna eruption: using the MAGFLOW cellular automata model. *Computers and Geosciences*, **35**, 1050–1060.

Higgins, J. & Harris, A.J.L. 1997. VAST: a program to locate and analyse volcanic thermal anomalies automatically from remotely sensed data. *Computers and Geosciences*, **23**, 627–645.

Kaneko, T., Yasuda, A., Aoki, Y., Kajiwara, K. & Kitagawa, S. 2010. Realtime monitoring of active volcanoes in east asia using MODIS and MTSAT data and its advancement by GCOM-C1 SGLI. *International Archives of the Photogrammetry, Remote Sensing and Spacial Information Science*, **38**, 209–212.

Kennedy, P.J., Belward, A.S. & Grégoire, J.M. 1994. An improved approach to fire monitoring in West Africa using AVHRR data. *International Journal of Remote Sensing*, **15**, 2235–2255, http://doi.org/10.1080/01431169408954240

Kervyn, M., Ernst, G.G.J., Harris, A., Mbede, E., Belton, F. & Jacobs, P. 2008. Thermal remote sensing of the low-intensity carbonatite volcanism of Oldoinyo Lengai, Tanzania. *International Journal of Remote Sensing*, **29**, 6467–6499.

Labazuy, P., Gouhier, M. *et al.* 2012. Near real-time monitoring of the April-May 2010 Eyjafjallajökull ash cloud: an example of a web-based, satellite-data-driven, reporting system. *International Journal of Environment and Pollution*, **48**, 262–272, http://doi.org/10.1504/IJEP.2012.049673

Lombardo, V., Silvestri, M. & Spinetti, C. 2011. Near real-time routine for volcano monitoring using infrared satellite data. *Annals of Geophysics*, **54**, 522–534, http://doi.org/10.4401/ag-5336

Métrich, N., Bertagnini, A. & Di Muro, A. 2010. Conditions of magma storage, degassing and ascent at Stromboli: new insights into the volcano plumbing system with interferences on the eruptive dynamics. *Journal of Petrology*, **51**, 603–626, http://doi.org/10.1093/petrology/egp083

Miller, P.I. & Harris, A.J. 2016. Near-real-time service provision during effusive crises at Etna and Stromboli: basis and implementation of satellite-based IR operations. *In*: Harris, A.J.L., De Groeve, T., Garel, F., Carn, S.A. (eds) *Detecting, Modelling and Responding to Effusive Eruptions*. Geological Society, London, Special Publications, **426**. First published online January 20, 2016, http://doi.org/10.1144/SP426.26

Mouginis-Mark, P.J., Snell, H. & Ellisor, R. 2000. GOES satellite and field observations of the 1998 eruption of Volcan Cerro Azul, Galapagos Islands. *Bulletin of Volcanology*, **62**, 188–198.

Oppenheimer, C. 1991. Lava flow cooling estimated from Landsat Thematic Mapper infrared data: the Lonquimay eruption (Chile, 1989). *Journal of Geophysical Research*, **96**, 21 865–21 878.

Patrick, M.R., Harris, A., Ripepe, M., Dehn, J., Rothery, D.A. & Calvari, S. 2007. Strombolian explosive styles and source conditions: insights from thermal (FLIR) video. *Bulletin of Volcanology*, **69**, 769–784.

Pergola, N., Pietrapertosa, C., Lacava, T. & Tramutoli, V. 2001. Robust satellite techniques for monitoring volcanic eruptions. *Annals of Geophysics*, **44**, 167–177, http://doi.org/10.4401/ag-3590

Pieri, D.C. & Baloga, S.M. 1986. Eruption rate area, and length relationships for some Hawaiian lava flows. *Journal of Volcanology and Geothermal Research*, **30**, 29–45, http://doi.org/10.1016/0377-0273(86)90066-1

Pinkerton, H. 1993. Measuring the properties of flowing lavas. *In*: Kilburn, C.R.J. & Luongo, G. (eds) *Active Lavas*. UCL Press, London, 175–191.

Planck, M. 1901. 'Über das Gesetz der Energieverteilung im Normalspektrum'. *Annalen der Physik*, **4**, 553, http://doi.org/10.1002/andp.19013090310

Ramsey, M.S. & Harris, A.J.L. 2013. Volcanology 2020: how will thermal remote sensing of volcanic surface activity evolve over the next decade? *Journal of Volcanology and Geothermal Research*, **249**, 217–233, http://doi.org/10.1016/j.jvolgeores.2012.05.011

Ripepe, M., Marchetti, E. *et al.* 2005. Effusive to explosive transition during the 2003 eruption of Stromboli volcano. *Geology*, **33**, 341–344, http://doi.org/10.1130/G21173.1

Rothery, D.A., Francis, P.W. & Wood, C.A. 1988. Volcano monitoring using short wavelength infrared data from satellites. *Journal of Geophysical Research*, **93**, 7993–8008, http://doi.org/10.1029/JB093iB07p07993

Rowland, S.K., Harris, A.J.L., Wooster, M.J., Amelung, F., Garbeil, H., Wilson, L. & Mouginis-Mark, P.J. 2003. Volumetric characteristics of lava flows from interferometric radar and multispectral satellite data. *Bulletin of Volcanology*, **65**, 311–330.

Schmidt, A., Leadbetter, S. *et al.* 2015. Satellite detection, long-range transport, and air quality impacts of volcanic sulfur dioxide from the 2014–2015 flood lava eruption at Bárðarbunga (Iceland). *Journal of Geophysical Research: Atmospheres*, **120**, 9739–9757.

Scollo, S., Prestifilippo, M., Spata, G., D'Agostino, M. & Coltelli, M. 2009. Monitoring and forecasting Etna volcanic plumes. *Natural Hazards and Earth Systems Science*, **9**, 1573–1585, http://doi.org/10.5194/nhess-9-1573-2009

Steffke, A.M. & Harris, A.J.L. 2011. A review of algorithms for detecting volcanic hot spots in satellite infrared data. *Bulletin of Volcanology*, **73**, 1109–1137, http://doi.org/10.1007/s00445-011-0487-7

Thordarson, T. & Larsen, G. 2007. Volcanism in Iceland in historical time: volcano types, eruption styles and eruptive history. *Journal of Geodynamics*, **43**, 118–152.

Thordarson, T., Self, S., Miller, D.J., Larsen, G. & Vilmundardóttir, E.G. 2003. Sulphur release from flood lava eruptions in the Veidivötn, Grímsvötn and Katla volcanic systems, Iceland. *In*: Oppenheimer, C., Pyle, D.M. & Barclay, J. (eds) *Volcanic Degassing*. Geological Society, London, Special Publications, **213**, 103–121.

Tilling, R.I. 1989. Volcanic hazards and their mitigation: progress and problems. *Reviews of Geophysics*, **27**, 237–269.

Tramutoli, V. 1998. Robust AVHRR Techniques (RAT) for environmental monitoring: theory and applications. *Proceedings of SPIE*, **3496**, 101–113, http://doi.org/10.1117/12.332714

Vicari, A., Ganci, G., Behncke, B., Cappello, A., Neri, M. & Del Negro, C. 2011. Near-real-time forecasting of lava flow hazards during the 12–13 January 2011 Etna eruption. *Geophysics Research Letters*, **38**, L13317, http://doi.org/10.1029/2011GL047545

Wooster, M.J. & Rothery, D.A. 1997. Thermal monitoring of Lascar Volcano, Chile, using infrared data from the along-track scanning radiometer: a 1992–1995 time series. *Bulletin of Volcanology*, **58**, 566–579, http://doi.org/10.1007/s004450050163

Wright, R. 2015. MODVOLC: 14 years of autonomous observations of effusive volcanism from space. *In*: Harris, A.J.L., De Groeve, T., Garel, F., Carn, S.A. (eds) *Detecting, Modelling and Responding to Effusive Eruptions*. Geological Society, London, Special Publications, **426**. First published online August 27, 2015, http://doi.org/10.1144/SP426.12

Wright, R., Garbeil, H. & Harris, A.J. 2008. Using infrared satellite data to drive a thermo-rheological/stochastic lava flow emplacement model: a method for near-real-time volcanic hazard assessment. *Geophysical Research Letters*, **35**, L19307, http://doi.org/10.1029/2008GL035228

Wright, R. & Flynn, L.P. 2004. Space-based estimate of the volcanic heat flux into the atmosphere during 2001 and 2002. *Geology*, **32**, 189–192, http://doi.org/10.1130/G20239.1

Wright, R., Blake, S., Harris, A. & Rothery, D. 2001. Asimple explanation for the space-based calculation of lava eruptions rates. *Earth and Planetary Science Letters*, **192**, 223–233.

Wright, R., Flynn, L., Garbeil, H., Harris, A.J.L. & Pilger, E. 2002. Automated volcanic eruption detection using MODIS. *Remote Sensing of Environment*, **82**, 135–155, http://doi.org/10.1016/S0034-4257(02)00030-5

Wright, R., Flynn, L.P., Garbeil, H., Harris, A.J.L. & Pilger, E. 2004. MODVOLC: Near-real-time thermal monitoring of global volcanism. *Journal of Volcanology and Geothermal Research*, **135**, 29–49.

Journal of Volcanology and Geothermal Research 293 (2015) 25–45

Contents lists available at ScienceDirect

Journal of Volcanology and Geothermal Research

journal homepage: www.elsevier.com/locate/jvolgeores

Improved space borne detection of volcanic ash for real-time monitoring using 3-Band method

Y. Guéhenneux *, M. Gouhier, P. Labazuy

Laboratoire Magmas et Volcans, Université Blaise Pascal-CNRS-IRD, OPGC, 5 rue Kessler, 63038 Clermont Ferrand, France

ARTICLE INFO

Article history:
Received 9 June 2014
Accepted 27 January 2015
Available online 7 February 2015

Keywords:
Volcanic ash clouds
MSG-SEVIRI
Infrared data
Real-time monitoring
3-Band method
Optical properties

ABSTRACT

For over 25 years, thermal infrared data supplied by satellite-based sensors are used to detect and characterize volcanic ash clouds using a commonly accepted method: the 2-Band reverse absorption technique. This method is based on a two-channel difference model using the opposite extinction features of water-ice and ash particles at 11 and 12 μm wavelengths. Although quite efficient with the supervision of a user, this method shows however some limitations for reliable automated detection of volcanic ash in a real-time fashion. Here we explore a method dedicated to the operational monitoring of volcanic ash that combines the 11–12 μm brightness temperature difference (BTD_{11-12}) with a second brightness temperature difference between channels 8.7 μm and 11 μm, ($BTD_{8.7-11}$). We first achieve a detailed microphysics analysis of different atmospheric aerosols (volcanic ash, water/ice, sulfuric acid, mineral dust) using optical properties (e.g., extinction efficiency, single scattering albedo and asymmetry parameter) calculated by Mie theory, and showing that $BTD_{8.7-11}$ can be particularly efficient to remove most of artifacts. Then, we tested this method for eight different eruptions between 2005 and 2011 from six different volcanoes (Mount Etna, Piton de la Fournaise, Karthala, Soufriere Hills, Eyjafjallajökull, and Grimsvötn) using data from the Spinning Enhanced Visible and Infrared Imager (SEVIRI) on board Meteosat Second Generation (MSG) geostationary satellite. We show that between 95.6% and 99.9% of ash-contaminated pixels erroneously identified by the BTD_{11-12} method (i.e., artifacts) were detected and removed by the 3-Band method. For all eruptions, the 3-Band method shows a high and constant reliability having a false alarm rate in the range 0.002–0.08%, hence allowing operational implementation for automated detection in case of a volcanic crisis.

1. Introduction

Early detection of volcanic ash clouds has become an important objective for the volcanological community, as well as for civilian and military air space monitoring communities. The main purpose is to reduce to an absolute minimum the hazards posed by volcanic ash drifting into air routes (e.g. Casadevall et al., 1999; Guffanti et al., 2005). Due to the increase of air traffic levels, volcanic ash clouds were predicted to be a major source of risk to aviation (Casadevall, 1994a, 1994b; Casadevall et al., 1996; Miller and Casadevall, 1999; Prata, 2009; Prata and Tupper, 2009). Indeed, the major disruption of air traffic operations associated with the loss of billions of Euros caused by the April–May 2010 eruption of Eyjafjallajökull volcano (Iceland), has first highlighted the importance to establish consistent ash concentration threshold and define safe levels of aircraft engine exposure to ash (IVATF, 2010; Schultz, 2012). Also, this eruptive crisis stressed the need for data and methods allowing early and reliable detection, as well as real-time tracking of ash clouds. These are key parameters for volcanic ash transport and dispersion models (VATD) (e.g., Devenish et al., 2012; Millington et al., 2012; Prata and Prata, 2012).

The aim of this paper is precisely to provide an improved methodology allowing real-time monitoring of volcanic ash cloud drifting in the atmosphere. For this purpose we need to address two main requirements. First, ash particle must be reliably distinguished from other atmospheric aerosols (e.g. water droplet, ice crystals, dust) and ground-based artifacts (e.g. thermal relaxation). Then, ash cloud monitoring must be carried out with a time resolution high enough to allow early detection and dynamic tracking. The 2-Band technique used to detect and characterize volcanic ash (Prata, 1989a, 1989b) is based on a two-channel difference model using the opposite extinction features of water/ice and ash particles at 11 and 12 μm wavelengths. This results on a negative brightness temperature difference for ash particles ($BTD_{11-12} < 0$), while water/ice particles exhibit a positive brightness temperature difference ($BTD_{11-12} > 0$). However some issues related to this method may limit its use for automated detection of volcanic ash in a real-time fashion.

Sensors onboard Low-Earth-Orbit (LEO) satellites such as the Advanced Very High Resolution Radiometer (AVHRR) or Moderate-

* Corresponding author at: Laboratoire Magmas et Volcans, 5 rue Kessler, 63038 Clermont-Ferrand cedex, France. Tel.: +33 633 548 785 (mobile).
E-mail address: y.guehenneux@opgc.univ-bpclermont.fr (Y. Guéhenneux).

http://dx.doi.org/10.1016/j.jvolgeores.2015.01.005
0377-0273/

Resolution Imaging Spectroradiometer (MODIS) have widely been used for detecting and mapping volcanic ash particles through their characteristic signal in the thermal infrared, with a high spatial resolution (e.g., Rose et al., 2001; Dean et al., 2003; Tupper et al., 2004). On the contrary, sensors onboard geostationary (GEO) satellites such as MSG-SEVIRI allow volcanic clouds dynamics to be tracked, and their ash content quantified within a typical time resolution of one image every 15 min (e.g., Prata and Kerkmann, 2007; Francis et al., 2012; Labazuy et al., 2012). This makes the use of geostationary satellites mandatory for real-time monitoring purposes, as compared to the low time resolution (2 images a day) of typical LEO satellites. In addition, this has increased our ability to provide accurate inputs for model based simulations and hazard assessment (e.g., Peuch et al., 1999; Kaminski et al., 2011; Folch, 2012).

We present here a method for ash clouds detection based on the 2-Band method (Prata, 1989a, 1989b), and previous work of Pavolonis (2010), Pavolonis and Sieglaff (2010) and Francis et al. (2012) using an additional brightness temperature difference test between channels 8.7 μm and 11 μm, ($BTD_{8.7-11}$). We tested here this methodology for eight different eruptions between 2005 and 2011 from six different volcanoes (Mount Etna, Piton de la Fournaise, Karthala, Soufriere Hills, Eyjafjallajökull and Grimsvötn) using data from MSG-SEVIRI. This sensor provides full-disc images every 15 min, with a 3 × 3 km pixel size at nadir, spanning visible to thermal infrared wavelengths through 12 channels. These characteristics make SEVIRI sensor totally appropriate for the real-time monitoring of ash clouds. For the purpose of our study, we will use specifically the spectral bands centered at 8.7, 11 and 12 μm.

2. Fundamental of volcanic ash detection

2.1. The reverse absorption technique

The 2-Band method proposed by Prata (1989a, 1989b), has long been used to detect ash clouds during, for example, the 1992 eruption of Crater Peak, Mt. Spurr Volcano, Alaska (Rose et al., 2001), the 2001 eruption of Mt. Cleveland, Alaska (Dean et al., 2003), the 24 November 2006 eruption of Mt. Etna, Sicily (Andronico et al., 2009), and during the April–May 2010 Eyjafjallajökull eruption (e.g., Bonadonna et al., 2011; Francis et al., 2012; Labazuy et al., 2012; Prata and Prata, 2012) This method is based on absorption and scattering of the upwelling ground radiance I_0^+ (τ_i,μ) by particles though their extinction cross section, which mainly varies with composition (complex refractive index), size, shape, incident wavelength, and surface roughness of particles. For a partially transparent plane-parallel ash cloud layer, and ignoring multiple scattering, the irradiance of light is exponentially attenuated from I_0 to I_t following:

$$\frac{I_t}{I_0} \approx \exp(-N_v \sigma_{\text{ext}}(x, m) \Delta Z)$$

where I_t is proportional to the at-sensor radiance, N_v is the number of particles per unit volume, and ΔZ is the vertical ash cloud thickness. The extinction cross section (σ_{ext}) represents the capacity of a given particle of radius (r) at a given wavelength (λ), through its size parameter ($x = 2\pi r/\lambda$), to attenuate the incident light in the direction of propagation (i.e. 0°). This attenuation is strongly related to the composition of a particle through its complex refractive index ($m = n + \chi i$): The real part (n) corresponds to scattering of light (i.e., sidetrack of the wavefront direction) and the imaginary part (χ) stands for the absorption of light (dissipation of the incident energy). Several studies (e.g. Spitzer and Kleinman, 1961; Hale and Querry, 1973; Pollack et al., 1973; Schaaf and Williams, 1973; Volz, 1973; Palmer and Williams, 1975; Wen and Rose, 1994) have pointed out significant differences between silicate, water/ice, and sulfuric acid as well as mineral dust refractive indexes in the infrared domain (Table 1), hence making possible the discrimination of volcanic ash.

2.2. The 2-Band method

Indeed, from the calculation of the extinction cross sections using Mie theory, Prata (1989b) has shown that σ_{ext} (λ_{11}) < σ_{ext} (λ_{12}) for water and ice particles, while σ_{ext} (λ_{11}) > σ_{ext} (λ_{12}) for ash particles. Therefore, Planck brightness temperature difference (BTD) between channel 11 and 12 μm, defined as T(λ_{11})–T(λ_{12}), is positive above a cloud of water and/or ice particles while it is negative above a cloud of ash particles. This means that, a simple BTD_{11-12} threshold set at 0 K may theoretically be applied to distinguish ash clouds from water and ice clouds. Several issues regarding ash detection using this method have already been highlighted in the literature and summed up in the next section (Section 2.3). Hereafter (Section 3) we give a detailed microphysics analysis of different aerosols using optical properties calculations, and showing why and how some of these issues can be overcome by using the 3-Band technique.

2.3. Known issues

The 2-Band method suffers well documented limitations (e.g. Simpson et al., 2000; Prata et al., 2001; Yu et al., 2002; Watkin, 2003; Pergola et al., 2004; Pavolonis et al., 2006). We can distinguish between two major types of limitations: [1] those leading to an underestimation of the ash cloud size (missed negative BTD_{11-12} signal) and [2] those which generate an overestimation of the ash cloud size (false negative BTD_{11-12} signal).

Underestimation of ash cloud size may occur:

(1) In moisture rich environments which act to mask the negative BTD_{11-12} (Pavolonis et al., 2006). The water may come directly from the magma, from groundwater beneath the crater, or/and more generally from the humid air training during the growth of the ash cloud (Rose et al., 2001). The wet atmospheric column

Table 1
Optical constants of the complex refractive index ($m = n + \chi i$) for 3 different ash compositions, water, ice, sulfuric acid (75% and 95%), and mineral dust (clay and quartz rich) particles at 8.7,11 and 12 μm wavelengths, with the corresponding source authors.

Aerosol type	λ = 8.7 μm		λ = 11 μm		λ = 12 μm		Authors
	Real (n)	Imaginary (χ)	Real (n)	Imaginary (χ)	Real (n)	Imaginary (χ)	
Ash (basalt: 53% SiO_2)	0.81	0.55	2.22	0.39	1.9	0.14	Pollack et al. (1973)
Ash (andesite: 54% SiO_2)	0.78	0.48	2.16	0.42	1.83	0.13	Pollack et al. (1973)
Ash (rhyolite: 73% SiO_2)	0.78	0.77	1.94	0.22	1.74	0.18	Pollack et al. (1973)
Water	1.27	0.038	1.15	0.097	1.11	0.2	Hale and Querry (1973)
Ice	1.28	0.04	1.09	0.2	1.26	0.41	Schaaf and Williams (1973)
H_2SO_4 (75%)	1.51	0.44	1.47	0.28	1.59	0.23	Palmer and Williams (1975)
H_2SO_4 (95%)	1.55	0.55	1.84	0.46	1.81	0.11	Palmer and Williams (1975)
Mineral dust (clay-rich)	1.19	0.29	1.83	0.2	1.78	0.43	Volz (1973)
Mineral dust (quartz-rich)	0.41	1.83	2.03	0.016	1.46	0.16	Spitzer and Kleinman (1961)

above and below the ash cloud is responsible for a shift of BTD_{11-12} signal towards positives values. Rose and Prata (1997) have shown at Montserrat that the BTD_{11-12} shift can reach $+3$ K.

(2) Over cold environment and in cold (less than 220 K) volcanic clouds in which large amounts of ice form (Prata et al., 2001). Ash particles act like condensation nuclei for ice, hence leading to a positive BTD_{11-12} signal typical of semi-transparent ice clouds. Rose et al. (1995) have shown during Rabaul eruption (September, 1994), that BTD_{11-12} signal of ash-ice mixed particles was in the range $+3$ to $+12$ K.

(3) In the case of images acquired with a significant zenith angle, the length of the atmospheric column and the absorption by water vapor may cause a positive BTD_{11-12} signal.

Overestimation of ash cloud may occur:

(1) In the presence of mineral dust clouds (Ackermann, 1997; Watkin, 2003). Mineral dust from erosion of non-vegetated surfaces mostly contains clay and silicate particles hence having optical properties similar to volcanic ash. Mineral dust clouds hence have negative BTD_{11-12} signal and are classified as ash clouds by the 2-Band inverse absorption method. A trajectory model can help to determine if the area of negative BTD_{11-12} signal has a volcanic origin, or if it comes from a mineral dust source (Simpson et al., 2000).

(2) Under desert conditions if the ground soil is rich in quartz (Barton and Takashima, 1986). Under dry and pristine atmospheric conditions, radiance measured by the sensor in the Thermal Infra-Red (TIR) region mostly depends on the soil characteristics. In these conditions quartz-rich surfaces have an emissivity that leads to negative BTD_{11-12} signal.

(3) During cloudless nighttime conditions when the ground releases heat accumulated during the day, the thermal relaxation will cause an atmospheric layer inversion above the ground which leads to a negative BTD_{11-12} signal (Platt and Prata, 1993).

(4) When meteorological convective cloud tops overshoot the tropopause: the stratospheric temperature inversion will lead to a negative BTD_{11-12} signal (Potts and Ebert, 1996).

(5) Misalignment between the bands at 11 and 12 μm to the sensor (particularly with AVHRR) may cause negative BTD_{11-12} inhomogeneities (Watkin, 2003). Also, rapid changes in the field radiance intensity may introduce parasitic effects possibly resulting into negative or positive BTD_{11-12} signal (Prata et al., 2001).

2.4. Alternative methods

Even if the 2-Band method is very powerful under the supervision of a user, this method is ineffective for automated ash cloud detection as artifacts would lead to a large amount of false alarms. As a result, other techniques using satellite data to detect volcanic ash clouds have been developed such as the Robust Satellite Technique (Tramutoli, 1998; Pergola et al., 2001, 2004), the MIR band method (e.g. Ellrod and Connel, 1999; Mosher, 1999; Ellrod et al., 2003), the atmospheric correction (Prata and Grant, 2001; Yu et al., 2002), the VIS–IR daytime method (Pavolonis et al., 2006) or more recently the 3-Band method (Pavolonis, 2010; Pavolonis and Sieglaff, 2010; Francis et al., 2012).

(1) The Robust Satellite Technique for Ash Detection (Pergola et al., 2001, 2004) is an adaptation of the Robust AVHRR Technique for the hotspot detection proposed by Tramutoli (1998). The basic precept is that the signal acquired by the satellite is the composite of several different contributions which are variable in time and space. The RST technique is a multi-temporal approach which considers each anomaly in the spatio-temporal domain as a deviation from an undisturbed state. With this method a pixel is considered as ash contaminated if the measured signal deviates from a reference value determined locally in space and time. This technique requires a consistent database, specifically geolocated and over a long period of time (Pergola and Tramutoli, 2003) and thus cannot be used ad-hoc on relatively small datasets or one-off (single image) acquisitions. After offline processing of multi-year satellite records to generate reference values, this method can easily be used to identify and monitor ash clouds in near real-time thanks to short processing times (Marchese et al., 2014). This method was compared to the 2-Band method (Marchese et al., 2007; Piscini et al., 2011) and have shown improved efficiency to detect and monitor volcanic ash cloud.

(2) The technique for improved detection of volcanic ash proposed by Ellrod and Connel (1999) uses brightness temperature difference between three infrared bands centered at 3.9, 11, and 12 μm wavelengths. The "experimental volcanic product" defined by this method can be described as the sum of BTD_{12-11} and $BTD_{3.9-11}$. It is used to enhance the contrast between volcanic ash cloud and other clouds, or surrounding environment, in GOES scenes. However, the automated detection using fixed thresholds is not easy, due to the complexity and variability of radiative processes at 3.9 μm, and makes the discrimination of volcanic ash difficult. By contrast, dynamic thresholds set in conjunction with radiative properties evolution of the surrounding give better results. Indeed, evaluation of the product (Ellrod et al., 2003) shows improved ash detection in most cases, with the best results occurring during daytime, when there is a strong solar reflectance in the 3.9 μm band, and at night over the ocean.

(3) The atmospheric correction proposed by Prata and Grant (2001) and Yu et al. (2002) is an improvement of the reverse absorption technique. It is based on the observation that, in a moisture rich environment, the BTD temperatures are pulled towards positive values. As a consequence, only the dense core part of the ash cloud can be detected (Mayberry et al., 2002). Prata and Grant (2001) and Yu et al. (2002) have shown a strong linear correlation between the BTD_{11-12} and the precipitable water content in the atmospheric column. This correlation allows the estimation of the BTD_{11-12} positive shift, due to the water vapor content, and commonly reaching 1 or 2°.

(4) The VIS–IR daytime method proposed by Pavolonis et al. (2006) is based on the analysis of the single scattering albedo of ash, water and ice and uses four spectral bands located at 0.65 μm, 3.75 μm 11 μm and 12 μm. The ash detection is performed by various tests: on the BTD_{11-12}, the reflectance ratio of 3.75 μm to 0.65 μm, the reflectance at 3.75 μm and the brightness temperature at 11 μm. This method has shown good results, and helps to solve problems of underestimation of the ash cloud size in moisture rich environment, but also problems of overestimation related to the core of large convective cloud, thermal relaxation phenomena and desert surface. However the use of spectral channels located at 0.65 μm and 3.75 μm sensitive to solar variation makes this technique unusable during nighttime which is detrimental for the 24/7 operational detection of volcanic ash.

(5) Pavolonis (2010) and Pavolonis and Sieglaff (2010) proposed an ash cloud detection method based on the use of three spectral bands centered at 8.5, 11, and 12 μm. The principle of this method is to calculate effective absorption optical depth ratios known as β-ratios (Pavolonis, 2010). Pavolonis and Sieglaff (2010) have shown that simultaneous estimates of $\beta(8.7, 11)$ and $\beta(12, 11)$ yield quantitative information on whether individual pixels are affected by volcanic ash. Finally, based on the "Dust RGB" product from EUMETSAT (European Organisation for the Exploitation of Meteorological Satellites), Francis et al. (2012) developed a 3-Band method defined by five different tests using brightness

temperature differences (BTD_{11-12} and $BTD_{11-8.7}$), measured and simulated radiances, and the "β-ratios" introduced by (Pavolonis, 2010; Pavolonis and Sieglaff, 2010).

3. Optical properties of aerosols

3.1. Calculation of optical properties

Optical properties calculation presented here are made using Mie scattering theory. Mie formulation is the direct application of Maxwell's equations giving a solution for light scattering from an isotropic, homogeneous, dielectric sphere. The size range of application for "Mie regime" is defined from the size parameter (x) following:

$$x = kr, \qquad 0.1 < x < 100$$

where $k = 2\pi/\lambda$ is the wavenumber, r being the effective radius of the particle and λ being the wavelength of the incident light. The total attenuation of incident light by the medium is commonly defined using the dimensionless extinction efficiency (Q_{ext}), being the sum of absorption and scattering efficiencies:

$$Q_{ext} = Q_{abs} + Q_{sca}$$

and defined as ratios of respective cross section coefficients (σ_{ext}) to the geometrical particle cross section (πr^2) such that $Q_{ext} = \sigma_{ext}/\pi r^2$. The detailed analysis of ash and aerosols microphysics presented hereafter aims to estimate the impact of particles optical properties on BTDs, evaluate the limits of the proposed algorithm and, finally, and to valid the use of the 3-Bands method for discriminating volcanic particles from others.

3.2. Optical properties of volcanic ash

Volcanic ash composition may be complex, and shows significantly different silicate compositions. So we first needed to test how much ash composition affects the optical properties. Here we compare (Fig. 1) optical properties for 3 different ash compositions likely to exist during explosive eruptions: basaltic (53% SiO_2), andesitic (54% SiO_2), and rhyolite (73% SiO_2). Optical properties are presented in the form of extinction efficiency difference between the 11 μm and 12 μm wavelengths hereafter called $\Delta Q_{ext}(11–12)$, and the extinction efficiency difference between the 8.7 μm and 11 μm wavelengths hereafter called $\Delta Q_{ext}(8.7–11)$. The ΔQ_{ext} are plotted as a function of the particle radius, ranging from 0 to 50 μm.

At first order, we show (Fig. 1a) that all ash particles roughly display a similar $\Delta Q_{ext}(11–12)$ pattern, having a $\Delta Q_{ext}(11–12) > 0$ for small size particles only (~0–5 μm), and a $\Delta Q_{ext}(11–12) < 0$ for intermediate size particles (~5–10 μm). One may observe some slight amplitude variations and a limited shift toward larger particles for rhyolite composition. Then, $\Delta Q_{ext}(11–12)$ rapidly converges toward zero for radius >20 μm (i.e., for a size parameter x > 10). This is due to the so-called extinction paradox, where Q_{ext} asymptotically approaches the limiting value 2 as the size parameter (x) increases. Also, we show in Fig. 1b that all ash particles roughly display a similar $\Delta Q_{ext}(8.7–11)$ pattern, having a $\Delta Q_{ext}(8.7–11) > 0$ for very fine ash (<3 μm) and a $\Delta Q_{ext}(8.7–11) < 0$ for a wide range of particle radius ranging from ~3 μm up to 50 μm. Here again, the rhyolite pattern displays a slightly higher amplitude and a positive shift towards larger particles.

3.3. Optical properties at 11–12 μm: ash vs. aerosols

In this section, we present the results of optical properties for a variety of aerosols likely to coexist with ash particles, and originating from magmatic activity or from external sources. Ash optical properties

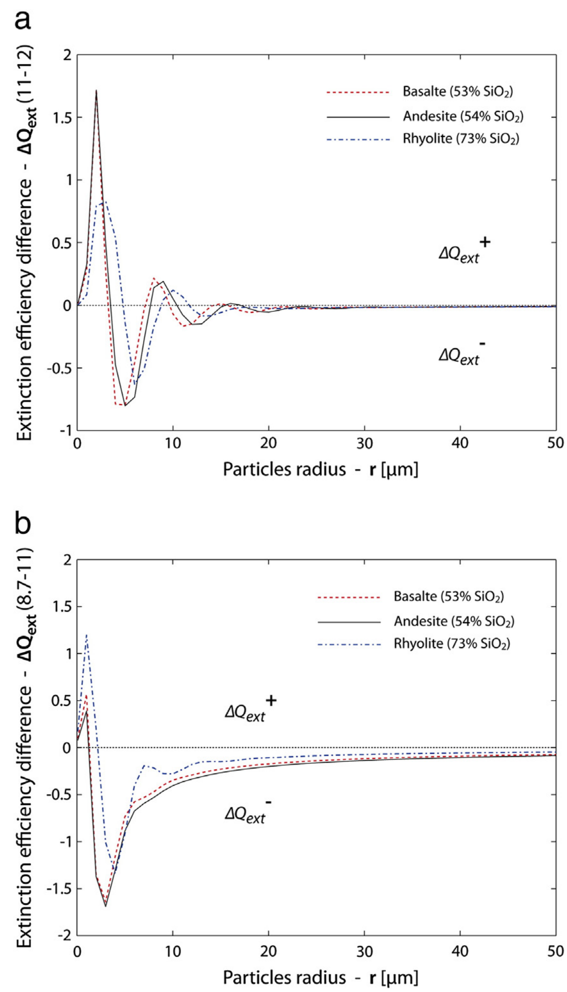

Fig. 1. Extinction efficiency differences between (a) 11–12 μm and (b) 8.7–11 μm for 3 different compositions of ash (basalt, andesite and rhyolite) for particle radius in the range 0–50 μm.

used for comparison with others aerosols are calculated for andesitic composition having 54% of SiO_2. Aerosols studied are listed below:

(1) Water droplets
(2) Ice crystals
(3) Sulfuric acid droplets
(4) Clay-rich mineral dust
(5) Quartz-rich mineral dust

3.3.1. Water/ice vs. ash

We show Fig. 2a that $\Delta Q_{ext}(11–12) < 0$ for water droplets between 0 and 10 μm, while $\Delta Q_{ext}(11–12) > 0$ for ash particles between 0.65–3.5 μm and 7.5–10 μm (true detection). This means that the 2-Band method can be reliably applied for very fine ash essentially. Indeed, from 3.5 to 7.5 μm, $\Delta Q_{ext}(11–12) < 0$ for both water and ash, which means that ash have also positive BTD_{11-12}. Ash-contaminated pixels with average radii falling in this size range will be discarded by the 0-Kelvin BTD cutoff, and will result in a total ash loading underestimation. Finally, from 10 up to 50 μm, $\Delta Q_{ext}(11–12) > 0$ for water droplets, while $\Delta Q_{ext}(11–12) \approx 0$ for ash particles. In this case, ash-contaminated pixels may not be detected, and water droplets may erroneously be considered as ash particles (false detection). This would result into a total ash loading overestimation. By contrast, we show in Fig. 2b that $\Delta Q_{ext}(11–12)$ of ice is always negative making the discrimination between ash and ice particles in the

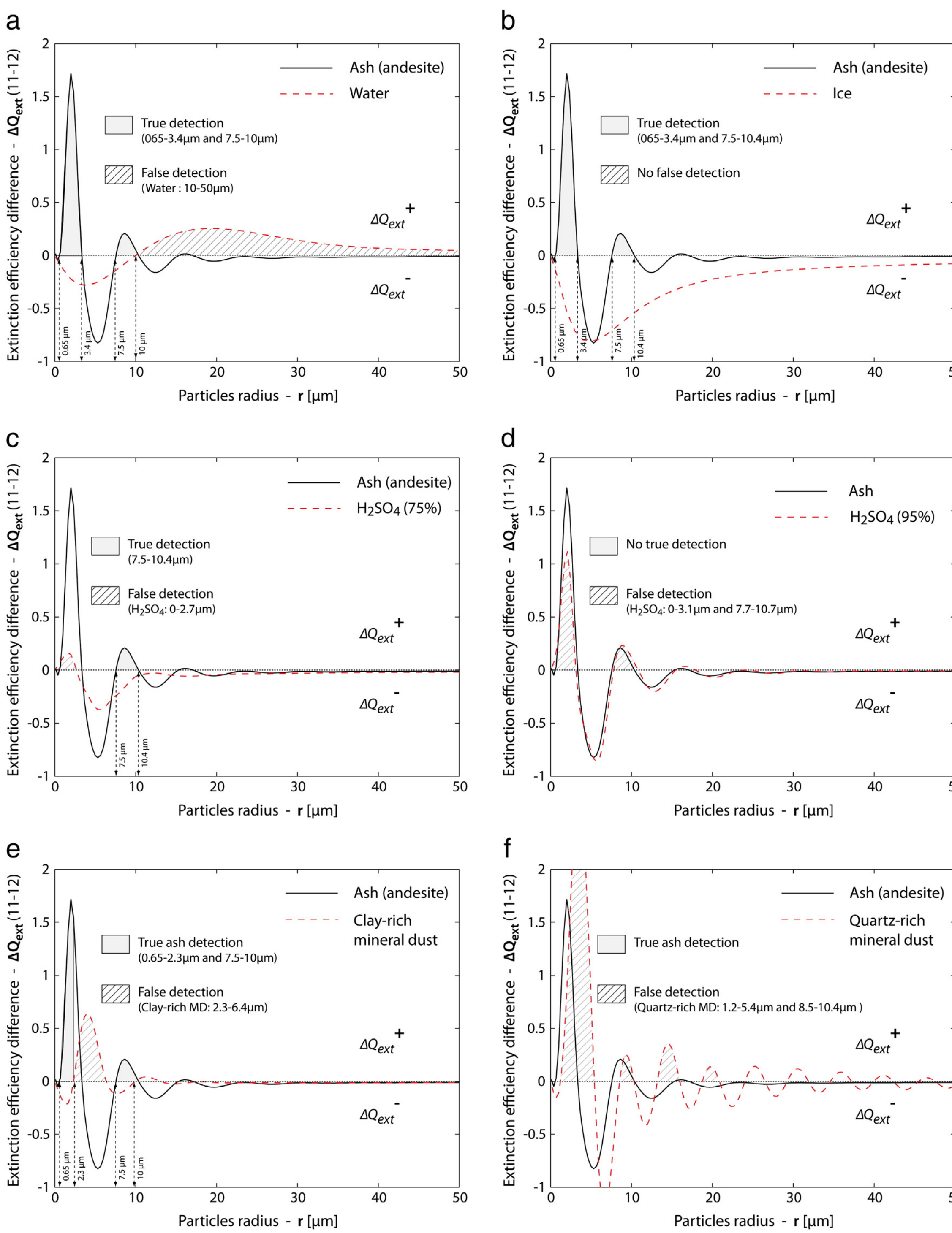

Fig. 2. Extinction efficiency differences between 11 and 12 μm wavelengths as a function of particles radius in the range 0–50 μm for ash (andesite) and a variety of aerosols showing true ash detection (unambiguous) and false detection related to non ash particles.

size range 0.65–3.5 μm and 7.5–10.4 μm theoretically easy. Also, no false detection is to be expected from pure ice content. However, extinction efficiencies have been calculated using spherical particles. If this assumption turns out to be acceptable for water droplets, the actual extinction efficiency of ice crystals may significantly differ from those values.

3.3.2. Sulfuric acid vs. ash

During volcanic eruptions, large amounts of SO_2 may be released in the atmosphere and subsequently converted into sulfuric acid particles. We present in Fig. 2c and d the $\Delta Q_{ext}(11–12)$ for droplets composed of 75% and 95% of sulfuric acid respectively. In the first case (75% of H_2SO_4), we show that the $\Delta Q_{ext}(11–12)$ amplitude is weak, although roughly showing a similar trend to the one of andesitic ash. Thus, small size (<2.7 μm) sulfuric acid droplets will have a negative BTD_{11-12}, and will be erroneously considered as ash. True detection of ash is made possible around 7.5–10.4 μm only. In the second case (95% of H_2SO_4), we show that the $\Delta Q_{ext}(11–12)$ trend is very similar to the one of andesitic ash, hence making impossible their discrimination, and possibly leading to a large overestimation of the total ash loading. This is a major issue as H_2SO_4-rich droplets may be quite common during eruptions, especially for old volcanic clouds, where most ash have been removed from atmosphere (Wen and Rose, 1994).

3.3.3. Mineral dust vs. ash

We present in Fig. 2e and f the $\Delta Q_{ext}(11\text{–}12)$ for mineral dust mainly composed of clay and quartz respectively. In the first case, the $\Delta Q_{ext}(11\text{–}12)$ of Clay-rich mineral dust looks fairly in opposition of phase with andesitic ash, hence allowing true detection of very fine ash (0.65–2.3 μm) as well as coarser ash particles (7.5–10 μm). However, a large positive peak of Clay-rich mineral dust exists in the range 2.3–6.4 μm hence leading to a negative BTD_{11-12} and resulting into a large overestimation of the total ash loading. In the second case, the $\Delta Q_{ext}(11\text{–}12)$ of Quartz-rich mineral dust looks much more in phase with the one of andesitic ash hence preventing from any easy true ash detection. The strong peak of quartz-rich mineral dust in the range 1.2–5.4 μm will lead to an increase of false alarms as well as the overestimation of ash loading.

3.4. Optical properties at 8.7–11 μm: ash vs. aerosols

In this section (Fig. 3) we provide the extinction efficiency difference between channels at 8.7 μm and 11 μm as a function of the particle radius. The $\Delta Q_{ext}(8.7\text{–}11)$ have been calculated for water and sulfuric acid (75%) droplets, as well as for clay-rich and quartz-rich mineral dust particles; and compared to andesitic ash. Note that as ice shows no false detection between 11 μm and 12 μm wavelengths, we did not plot its extinction efficiency difference.

3.4.1. Water vs. ash

We point out from Fig. 3a that $\Delta Q_{ext}(8.7\text{–}11)$ is in opposition of phase for ash and water particles in the range 1.3–17 μm. $\Delta Q_{ext}(8.7\text{–}11) < 0$ for ash particles, while $\Delta Q_{ext}(8.7\text{–}11) > 0$ for water particles, hence leading to a positive $BTD_{8.7-11}$ for ash particles and a negative $BTD_{8.7-11}$ for water droplets. Thus, $BTD_{8.7-11}$ will permit to rule out false detections related to water droplets in the range 10–17 μm, erroneously considered as ash, when using BTD_{11-12} solely. The relevance of this second test ($BTD_{8.7-11}$) might be very important as we know that mean water droplets size composing meteorological clouds typically ranges from 10 to 15 μm (e.g., Houze, 1993).

3.4.2. Sulfuric acid vs. ash

We show in Fig. 3b that $\Delta Q_{ext}(8.7\text{–}11)$ is also in opposition of phase for sulfuric acid droplets (75%) and ash particles, specifically in the range 1.2–5.3 μm. $\Delta Q_{ext}(8.7\text{–}11) < 0$ for ash particles, while $\Delta Q_{ext}(8.7\text{–}11) > 0$ for sulfuric acid droplets, hence leading to a positive $BTD_{8.7-11}$ for ash particles and a negative $BTD_{8.7-11}$ for sulfuric acid droplets. Therefore, the $BTD_{8.7-11}$ allows every false detections related to sulfuric acid droplets (0–2.7 μm) to be removed.

3.4.3. Mineral dust vs. ash

In Fig. 3c, the $\Delta Q_{ext}(8.7\text{–}11)$ patterns of clay-rich mineral dust and ash particles look very similar, making the discrimination of ash using the $BTD_{8.7-11}$ test not possible. By contrast, the $\Delta Q_{ext}(8.7\text{–}11)$ patterns of quartz-rich mineral dust and ash particles (Fig. 3d) are mainly in opposition of phase, having a $\Delta Q_{ext}(8.7\text{–}11) < 0$ for ash and a $\Delta Q_{ext}(8.7\text{–}11) > 0$ for quartz-rich mineral dust over the whole particle size range. Thus, $BTD_{8.7-11}$ test can be used for the discrimination of

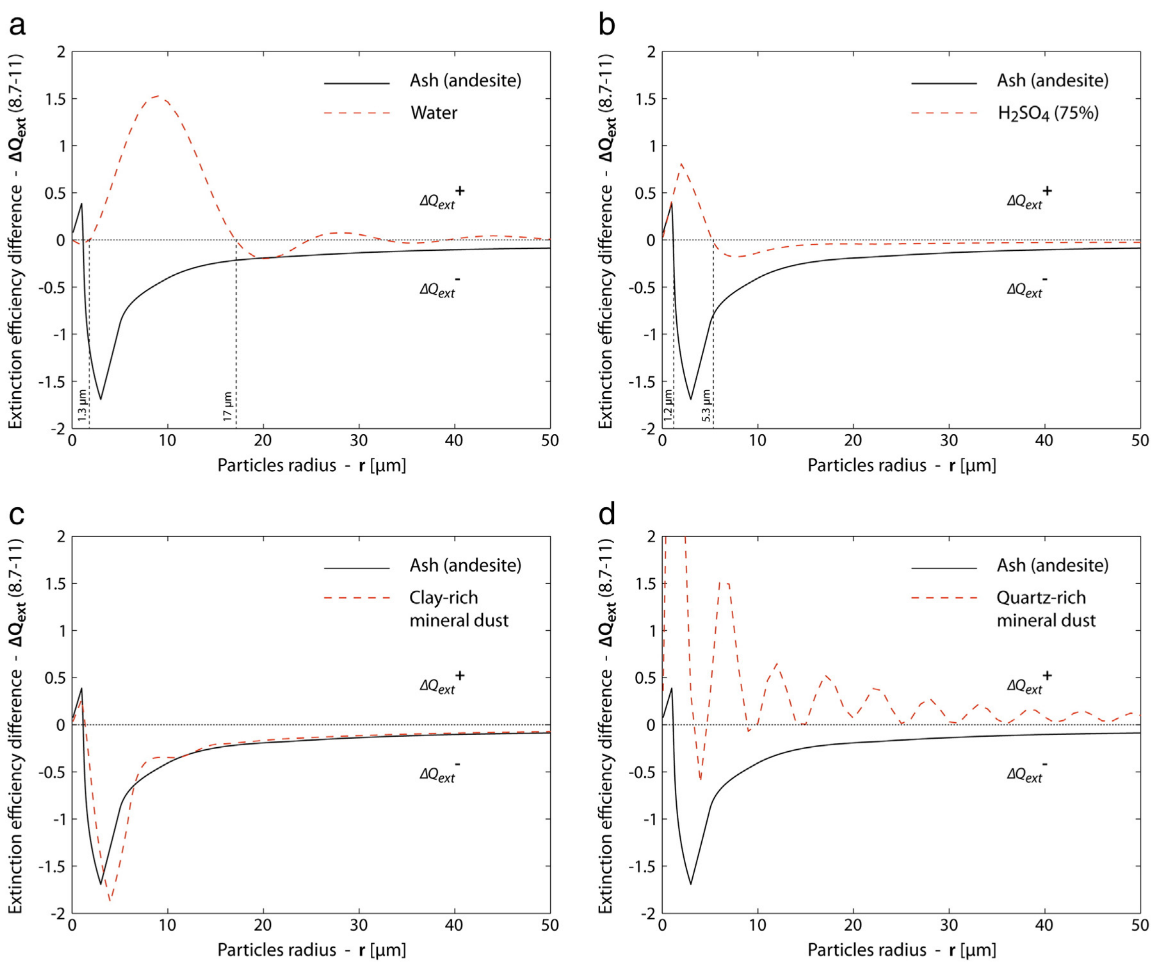

Fig. 3. Extinction efficiency differences between 8.7 and 11 μm wavelengths as a function of particles radius in the range 0–50 μm for ash (andesite) and a variety of aerosols.

ash from quartz-rich mineral dust, as well as to remove false detections related to quartz-rich mineral dust, erroneously considered as ash, when using BTD_{11-12} solely.

3.5. Ash scattering efficiency and anisotropy

The capability of the so-called reverse "absorption" method to distinguish ash from other particles is mainly due to absorption features in the TIR, as commonly highlighted in the literature. We have shown (Fig. 2) that $\Delta Q_{ext}(11\text{–}12)$ for andesitic ash becomes negative in the range 3.4–7.5 μm, hence making their detection from the 0-Kelvin BTD_{11-12} cutoff not possible.

Here we show that the evolution of the extinction efficiency (Q_{ext}) along with particles sizes is due to the increase of the scattering efficiency (Q_{sca}). For a 1-μm ash particle (Fig. 4a), the single scattering albedo, given by $\varpi = Q_{sca}/(Q_{sca} + Q_{abs})$, around TIR wavelengths is low ($\varpi \approx 0.25$), showing the predominance of the absorption efficiency. By contrast, for a 5-μm ash particle (Fig. 4b), ϖ increases up to 0.75 showing the predominance of the scattering efficiency. In Fig. 4c, we show separately each efficiency factor for a 5-μm ash particle. Reminding that $Q_{ext} = Q_{abs} + Q_{sca}$, we illustrate that the negative $\Delta Q_{ext}(11\text{–}12)$ is controlled by the scattering efficiency as its slope between 11 μm and 12 μm strongly increases. Additionally, we provide in Fig. 4a,b information about the ash scattering phase function $p_v(\mu, \mu')$ through the asymmetric factor (g). The phase function represents the fraction of incident light coming from the direction u', to the scattered light in the direction u. For spherical particles, the phase function only depends on the cosine of the angle (Θ) between the two directions (μ, μ'). The asymmetry factor (g) is the average cosine of the scattering angle (Θ), and characterizes the asymmetry of the scattering phase function. It is defined as the first moment of the phase function following:

$$g = \int_{4\pi} p_{v,11}(\Theta) \cos\Theta d\Omega$$

and can be calculated using Mie coefficient following Bohren and Huffman (1983) formulation (Eq. (A.5)). The asymmetry factor may theoretically varies from $g = -1$ (pure backscattering: $\Theta = 180°$) to $g = 1$ (pure forward scattering: $\Theta = 0°$) and shows isotropic scattering for $g = 0$. The asymmetry factor significantly increases with particles radius (Fig. 4a,b), having values in the TIR of about $g = 0.1$ for 1-μm ash particles hence showing an isotropic phase function, and $g = 0.7$ for 5-μm ash particles, showing a predominance of the forward scattering. For small viewing zenith angle in the former case, most scattered photons are attenuated (i.e., not seen by the sensor), while in the latter case, the majority of scattered photons propagate toward the sensor ($+\mu$, upward direction) and only a small fraction of them are "attenuated" (i.e., not seen by the sensor). Understanding of scattering effects is very important especially as particle size distribution of ash in distal clouds typically lies around 5 μm. Indeed, ash clouds in the size range 3.4–7.5 μm thus have to be considered as a scattering medium more than an absorbing one. The parameters Q_{ext}, ϖ, and g used to characterize the scattering properties of ash particles are summarized in Table 2.

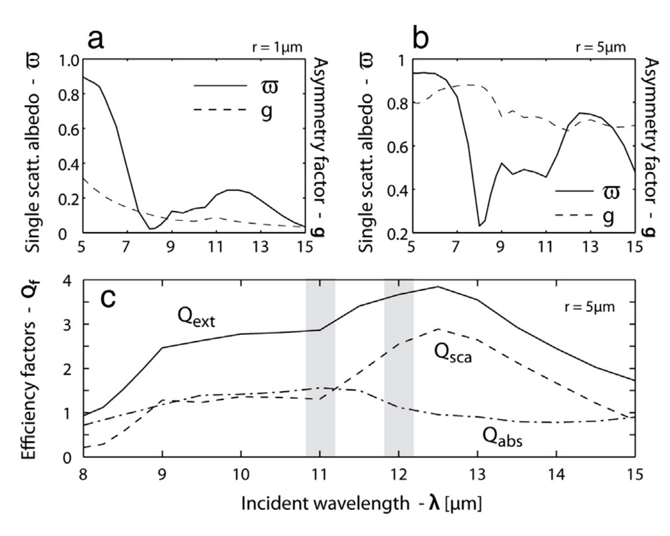

Fig. 4. (a,b) Single scattering albedo (ϖ) and asymmetry factor (g) for ash particles with radii of 1 and 5 μm respectively. (c) Efficiency factors: extinction, absorption, and scattering of ash particle of radius 5 μm, as a function of the incident wavelength defined in the TIR range.

4. The 3-Band method

4.1. Methodology

We present here a simple and fast detection algorithm based on the previous works of Pavolonis (2010), Pavolonis and Siegla ff (2010) and Francis et al. (2012), and where we explore additional spectral features as a complement to the existing 2-Band reverse absorption technique as defined by Prata (1989a). The aim of this method is to allow fast and reliable detection of ash particles in a real-time fashion for a 24/7 monitoring of volcanic activity. First we need a routine simple enough to be performed within a couple of minutes so as to fit with the very high acquisition frequency of geostationary satellites. Then, we need a routine reliable enough to be performed in an automated way, and generating the least amount of false alarms possible.

Our 3-Band algorithm uses two Boolean (true/false) tests based on brightness temperature difference (BTD) and using three thermal infrared bands located at 8.7, 11 and 12 μm. The first test is the same as the 2-Band method of Prata (1989a), using the difference of brightness temperature between bands at 11 μm and 12 μm (BTD_{11-12}). The presence of ash-contaminated pixels (true statement) is usually given by a negative brightness temperature difference ($BTD_{11-12} < 0$). However, some artifacts (see Section 2.3) may lead ash-free pixels to be erroneously selected by this test. The Fig. 5a perfectly illustrates these problems with almost all land surfaces considered as ash contaminated whereas no eruption was actually occurring at this time on Mount Etna (Fig. 5b). Indeed, Fig. 5b shows that this 3-Band method is particularly efficient to overcome artifact problems related to thermal relaxation phenomena. We demonstrate in the next section from a series of fully detailed examples, that the second test is also very efficient to remove other types of artifacts and preserve most of true ash-contaminated pixels. As a consequence we apply to this selection of pixels, a second test that uses the difference of brightness temperature between bands at 8.7 μm and 11 μm ($BTD_{8.7-11}$). The 8.7 μm channel is mainly used for the SO_2 detection due to its absorption feature, but Corradini et al. (2009, 2010) have shown that the SO_2 abundance quantification from data at 8.7 μm, have to be corrected from the effect of volcanic ash clouds. In their methodology they used the 2-Band method to identify ash contaminated pixels, but the 8.7 μm channel can be used itself in the ash detection process (Pavolonis, 2010; Pavolonis and Siegla ff, 2010; Francis et al., 2012). We show hereafter that the presence of ash-contaminated pixels (true statement) is given by a positive brightness temperature difference ($BTD_{8.7-11} > 0$). So the combination of the two tests permits to eliminate a large majority of artifact pixels, as demonstrated on examples of Section 3.2. To sum up, in our method, a pixel is regarded as containing ash only if the two following conditions are met:

$$\text{(test 1) } BT_{11\mu m} - BT_{12\mu m} < T_{cutoff\text{-}1} \qquad (\text{with } T_{cutoff\text{-}1} \approx 0)$$
$$\text{(test 2) } BT_{8.7\mu m} - BT_{11\mu m} > T_{cutoff\text{-}2} \qquad (\text{with } T_{cutoff\text{-}2} \approx 0)$$

$BT_{11\mu m}$, $BT_{12\mu m}$, and $BT_{8.7\mu m}$ are the brightness temperatures at 11 μm, 12 μm and 8.7 μm, with $T_{cutoff\text{-}1}$ and $T_{cutoff\text{-}2}$ being the threshold for

Table 2
Scattering parameters for ash particles (andesitic sphere) of sizes ranging from 0.1 to 100 μm, with Q_{ext} being the extinction efficiency, ϖ being the single scattering albedo, and g being the asymmetry factor calculated using Mie theory.

Ash radius	$\lambda = 8.7$ μm			$\lambda = 10.8$ μm			$\lambda = 12$ μm		
(μm)	*Qext*	ϖ	*g*	*Qext*	ϖ	*g*	*Qext*	ϖ	*g*
0.1	0.1037	0.0001	0.0007	0.0275	0.0004	0.0009	0.0105	0.0004	0.0006
1	0.8833	0.0779	0.0824	0.4994	0.2251	0.0919	0.1719	0.2453	0.063
2	1.3615	0.2544	0.3808	2.738	0.4939	0.4135	1.0215	0.6113	0.2829
3	1.6657	0.3557	0.6394	3.3615	0.5302	0.5782	2.8915	0.7026	0.569
4	1.8558	0.4195	0.7428	3.1622	0.4912	0.656	3.6375	0.708	0.6505
5	1.9747	0.4612	0.7918	2.8653	0.455	0.724	3.6687	0.6949	0.6701
10	2.1554	0.5419	0.8624	2.5606	0.51	0.8246	2.5082	0.4714	0.813
15	2.1712	0.5663	0.8783	2.4373	0.5329	0.845	2.4514	0.5055	0.8701
20	2.166	0.5781	0.8851	2.3659	0.5462	0.8533	2.4202	0.5199	0.8928
25	2.1572	0.5851	0.8887	2.3186	0.5549	0.8577	2.3371	0.5224	0.8985
50	2.1206	0.5986	0.8947	2.2065	0.5749	0.8651	2.2167	0.5451	0.908
100	2.0855	0.6043	0.8965	2.133	0.5866	0.8674	2.1381	0.5584	0.9113

BTD_{11-12} and $BTD_{8.7-11}$ respectively. Theoretically $T_{cutoff\text{-}1}$ and $T_{cutoff\text{-}2}$ have to be set at 0 K but due to water vapor, mixed pixel, scattering effect and viewing geometry, values can be in the range -2 to $+2$ K (Prata and Grant, 2001; Watkin, 2003). For all the figures presented in this paper, thresholds were used at $+0.5$ K and -1 K for $T_{cutoff\text{-}1}$ and $T_{cutoff\text{-}2}$ respectively. The selection of thresholds $T_{cutoff\text{-}1}$ and $T_{cutoff\text{-}2}$ values is discussed in detail in Section 5.

4.2. Results

In order to illustrate the efficiency of the 3-Band method we compared the results obtained with the 2-Band method of Prata (1989a, 1989b) with those of the 3-Band method. The comparison was completed for eight eruptions at six different volcanoes between 2005 and 2011 (Karthala 2005, Mount Etna 2006, Piton de la Fournaise 2007, Soufriere Hills 2010, Eyjafjallajökull 2010 and Grimsvötn 2011); all of which were captured by MSG-SEVIRI. For each eruption, we provide a time series of the number of pixels considered as ash (# flagged ash pixels) by the 2-Band (gray) and the 3-Band method (blue) for the whole duration of the eruption. Attached to this plot, we also provide ash maps showing the amount of flagged pixel for both methods at a given instant. Finally, the results are summarized in Table 3 showing (i) the percentage of artifacts (i.e., ash-contaminated pixels erroneously identified by the 2-Band method) removed by the 3-Band method, and (ii) the False Alarm Rate (FAR) for both methods and calculated as follow:

$$FAR = \frac{f-t}{p}$$

where f is the number of flagged ash pixels (# Flagged ash pixels), t is the number of true ash pixels (# True ash pixels) and p is the total number of pixels (total # Pixels) analyzed in the sequence of images. This index is particularly interesting as it is independent of the existence of an ash cloud in the sense that $(f-t)$ is a measure of the number of artifact pixels contained in a given image whether or not there is a cloud of ash. Indeed, if $t=0$ (i.e., no ash cloud), such as for Fig. 5, one may observe that numerous artifact pixels may, nonetheless, exist (particularly for the 2-Band method, Fig. 5a), hence leading to a large number of false alarms, and preventing from any reliable automated ash detection.

4.2.1. The 25 November 2005 Karthala eruption

The eruption began on 24 November 2005 around 18:00 UTC with an initial phreatic phase, and entered into a magmatic phase during the afternoon of 25 November (Smithsonian Institution, 2005, 2006). As reported by the Meteorological Department of the international airport of Karthala, the ash fall led to the cancellation of some international flights and several local flights during 26–27 November (Prata and

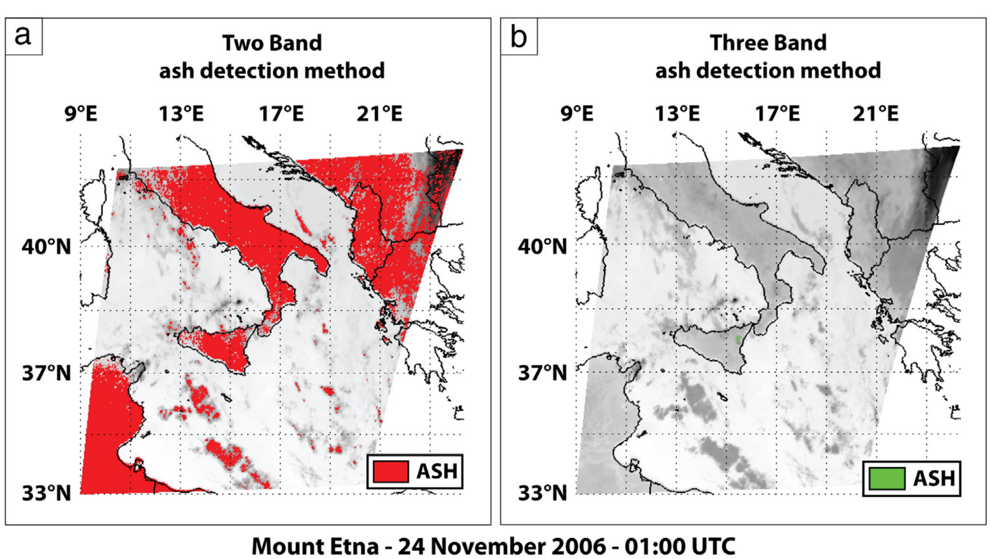

Fig. 5. Comparison between the 2-Band and the 3-Band methods over the Mount Etna when no eruption occurs in cloudless night-time conditions using SEVIRI data in Mercator projection with $T_{cutoff\text{-}1} = +0.5$ K and $T_{cutoff\text{-}2} = -1$ K.

Table 3
Summary of the comparison between the 2-Band method and the double split-window method. Column 3 is the number of SEVIRI images in each dataset. Column 4 is the number of pixels which have been checked. Column 5 is the cutoff used for the BTD_{11-12}. Column 6 is the cutoff used for the $BTD_{8.7-11}$. Column 7 is the number of pixels considered as ash by the 2-Band method. Column 8 is the number of pixels considered as ash by the 3-Band method. Column 9 is the percentage of pixels considered as ash by the 2-Band method which have been excluded and considered as artifacts by the 3-Band method. Column 10 is the percentage of pixels highlighted as ash by the 2-Band method, but which are also considered as ash by the 3-Band method. Column 11 is the main sources of artifacts indentified where CC means convective clouds, MRE: moisture rich environment, TR: thermal relaxation phenomena, DG: desert ground, and CE: cold environment.

Volcano	Date	Total # images	Total # pixels	$T_{cutoff-1}$	$T_{cutoff-2}$	# flagged ash pixels		# true ash pixels	False Alarm rate (%)		% artifacts removed	Sources of artifacts
						2-Band method	3-Band method	Supervised control	2-Band method	3-Band method		
Karthala	23–25/11/2005	288	24,128,928	+0.5 K	−1 K	264,553	50,130	40,237	0.9	0.040	95.6	CC + MRE
Mount Etna	24/11/2006	96	8,388,864	+0.5 K	−1 K	1,577,869	2,496	1,866	18.8	0.008	99.9	CC + TR + DG
Fournaise (Piton)	05–07/04/2007	144	1,368,000	+0.5 K	−1 K	133,488	6,889	5,798	9.3	0.080	99.1	CC + MRE
Soufriere Hills 1	08–10/01/2010	345	15,680,595	+0.5 K	−1 K	2,340,821	4,217	3,652	14.9	0.004	99.9	CC + MRE
Soufriere Hills 2	11–12/02/2010	128	6,556,160	+0.5 K	−1 K	365,033	79,199	79,094	4.4	0.002	99.9	CC + MRE
Eyjafjallajökull 1	14–20/04/2010	672	259,695,072	+0.5 K	−1 K	77,271,756	124,449	74,587	29.7	0.020	99.9	CC + TR + CE
Eyjafjallajökull 2	05–14/05/2010	912	352,443,312	+0.5 K	−1 K	88,882,104	1,871,084	1,805,529	24.7	0.019	99.9	CC + TR + CE
Grimsvötn	22–25/05/2011	360	113,201,640	+0.5 K	−1 K	2,384,760	405,681	380,889	1.8	0.022	98.8	CC + TR + CE

Kerkmann, 2007). We show a large difference (Fig. 6a,b,c) of the number of flagged ash pixels between the two methods, especially during the first two days. In total, 95.6% of artifacts have been removed by the 3-Band method. This leads to a False Alarm Rate (FAR) of 0.9% and 0.04% for the 2-Band and 3-Band methods respectively. Identified artifacts are due to the top of meteorological convective cloud (CC) in the northern part of Madagascar Island, and to moisture rich environment (MRE) (Table 3). Note that some artifacts are already visible in Fig. 6a before the beginning of the eruption.

4.2.2. The 24 November 2006 Mount Etna eruption

The 24 November 2006 explosive eruption at Mount Etna began around 03:00 UTC and ended around 17:00 UTC on the same day. At the onset of activity, the wind blew towards the SE causing ash fallouts on the international airport of Catania, which was closed to air traffic during the eruption (Andronico et al., 2009). We show a huge difference (Fig. 7a,b,c) of the number of flagged ash pixels particularly during the night, and leading to a FAR of 18.8% and 0.008% for the 2-Band and 3-Band methods respectively. In total, 99.9% of artifacts have been removed by the 3-Band method. In this case, artifacts originate from thermal relaxation (TR) phenomena during night-time (see Fig. 5), as well as from convective clouds (CC) and desert ground (DG) conditions (see Table 3). Two animated gif which present the results obtained with the 2-Band method and the 3-Band method on the entire dataset are available as auxiliary material.

4.2.3. The 06 April 2007 Piton de la Fournaise eruption

Piton de la Fournaise's April 2007 eruption was the largest eruption at Réunion Island for at least one century. The eruption began at 06:00 UTC on 2 April along a 1-km fissure. On 5 April at 20:48 UTC, a magnitude 3.2 earthquake coincided with the onset of the caldera collapse (Michon et al., 2007). Associated with caldera collapse, a large SO_2 cloud (Gouhier and Coppola, 2011) and a small ash cloud began to drift Northeastward (Tulet and Villeneuve, 2011). Interestingly, the time series presented in Fig. 8a shows the increase of flagged ash pixels with time, due in fact to a tropical storm being more and more apparent in the satellite field of view. In total, 99.1% of artifacts have been removed by the 3-Band method, and the FAR is of 9.3% and 0.08% for the 2-Band and 3-Band methods respectively (Table 3). Fig. 8b and c illustrates the capability of the 3-Band method to remove those artifacts due to the misclassification of meteorological convective clouds (CC) and the moisture rich environment (MRE).

4.2.4. The 08 January 2010 Soufriere Hills

Between the 08 and 11 January 2010, three explosions were recorded at Soufriere Hills at 19:49 UTC on 08 January, and then at 06:28 UTC and 01:27 UTC on 10 January (MVO, 2010a). All of these explosions were accompanied by seismic signals that lasted 11, 7 and 4 min, respectively, and generated pyroclastic flows with ash clouds that reached altitudes of 7.6 km, 6.7 km and 5.4 km, respectively (MVO, 2010a). For these eruptions (Fig. 9a), the FAR calculated is of 14.9% and 0.004% for the 2-Band and 3-Band methods respectively, and 99.9% of artifacts have been removed by the 3-Band method (Table 3). Fig. 9b and c also clearly illustrates the ability of the 3-Band method to avoid misclassification due to the moisture rich environment (MRE) and large meteorological convective clouds (CC).

4.2.5. The 11 February 2010 Soufriere Hills eruption

A dome collapse event at Soufriere Hills began at 17:35 UTC on 11 February 2010 and lasted 55 min. It was associated with pyroclastic flows, mainly moving to the northeast (MVO, 2010b). The resulting ash cloud reached 15 km (from pilot reports) and finally drifted Southeastward. Ash fallouts occurred in northeastern Montserrat, and were reported in southwest Antigua, Guadeloupe and Dominica (MVO, 2010b). The time series presented in Fig. 10a shows a net increase of flagged ash pixels from the start of the eruption. However, the difference between the two methods remains important as the FAR is of 4.4% and 0.002% for the 2-Band and 3-Band methods respectively. Also, 99.9% of artifacts have been removed by the 3-Band method. This difference is due essentially to the influx of a large meteorological convective cloud (CC) over Haiti and Dominican Republic (Fig. 10b, c), traveling Southeastward (Table 3). Two animated gif of the ash cloud, using the 2-Band and the 3-Band methods, on the entire dataset are available as auxiliary material.

4.2.6. The April–May 2010 Eyjafjallajökull eruption

This eruption has been characterized by two main explosive phases. The first one occurred between 14–20 April, and the second one around 05–14 May 2010. The first explosive phase started early in the morning on 14 April, when an eruptive fissure opened in the glacier, and triggered an ash plume rising at about 8 km (Gudmundsson et al., 2010, 2012). This phase was characterized by phreatomagmatic activity leading to explosive events, producing very fine ash (Davies et al., 2010), and large emissions of water vapor, rapidly converted into droplets and ice crystals (Labazuy et al., 2012). During this period, the 2-Band method appears particularly ineffective to reliably detect ash particles (Fig. 11a) giving a FAR of 29.7% against 0.02% only for the 3-Band method. In total, 99.9% of artifacts have been removed by the 3-Band method. The huge number of artifacts, using the 2-Band method only, is mostly attributed to the existence of large and cold meteorological clouds (Fig. 11b, c), as well as some thermal relaxation phenomena during cloudless nighttime. One may observe the day/night variations on the 2-Band time series (Fig. 11a).

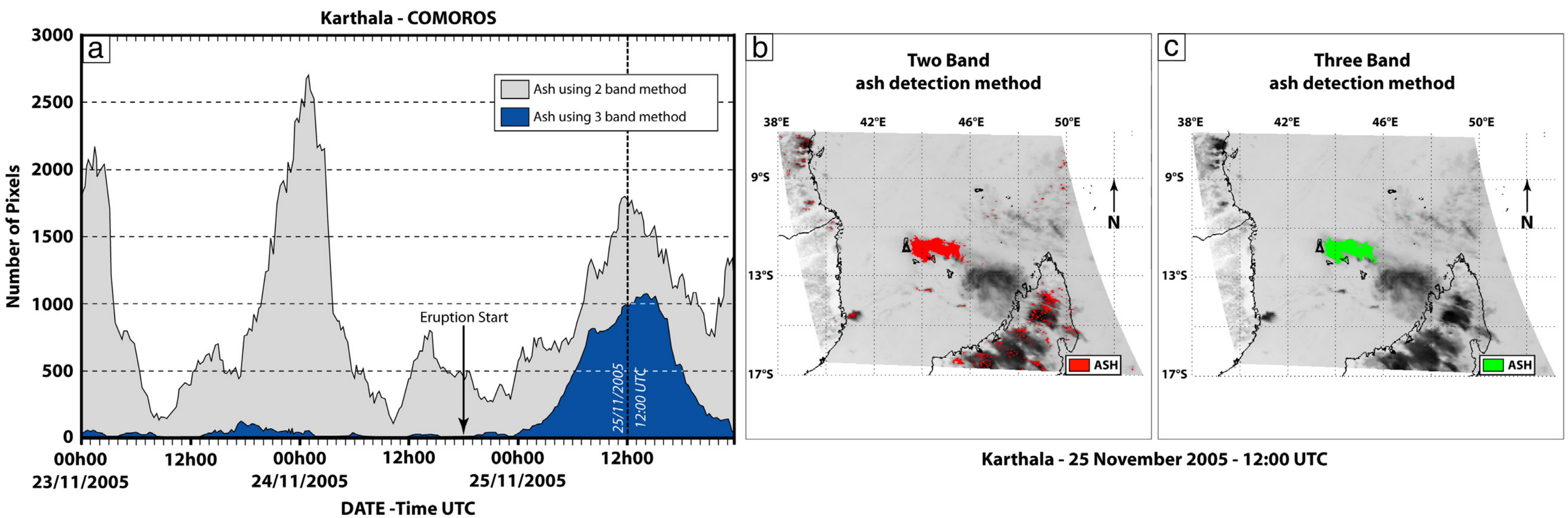

Fig. 6. Comparison between the 2-Band method and the 3-Band method for Karthala between 23 and 25 November 2005. Part ‘a’ is a time series of the number of pixels considered as ash by the 2-Band method (gray) and the 3-Band method (blue) where the start of the eruption is signaled by the arrow and the dashed line indicates when the two SEVIRI scenes on the right take place in the time sequence. Parts ‘b’ and ‘c’ are examples of the SEVIRI images in Mercator projection used to make the time series with $T_{cutoff\text{-}1}$ and $T_{cutoff\text{-}2}$ set at respectively + 0.5 K and − 1 K. They respectively represent the results obtain with the 2-Band method (pixels in red are ash) and with the 3-Band method (pixels in green are ash). The position of the volcano is indicated by a triangle, and a black arrow indicates the North. (For interpretation of the references to color in this figure legend, the reader is referred to the web version of this article.)

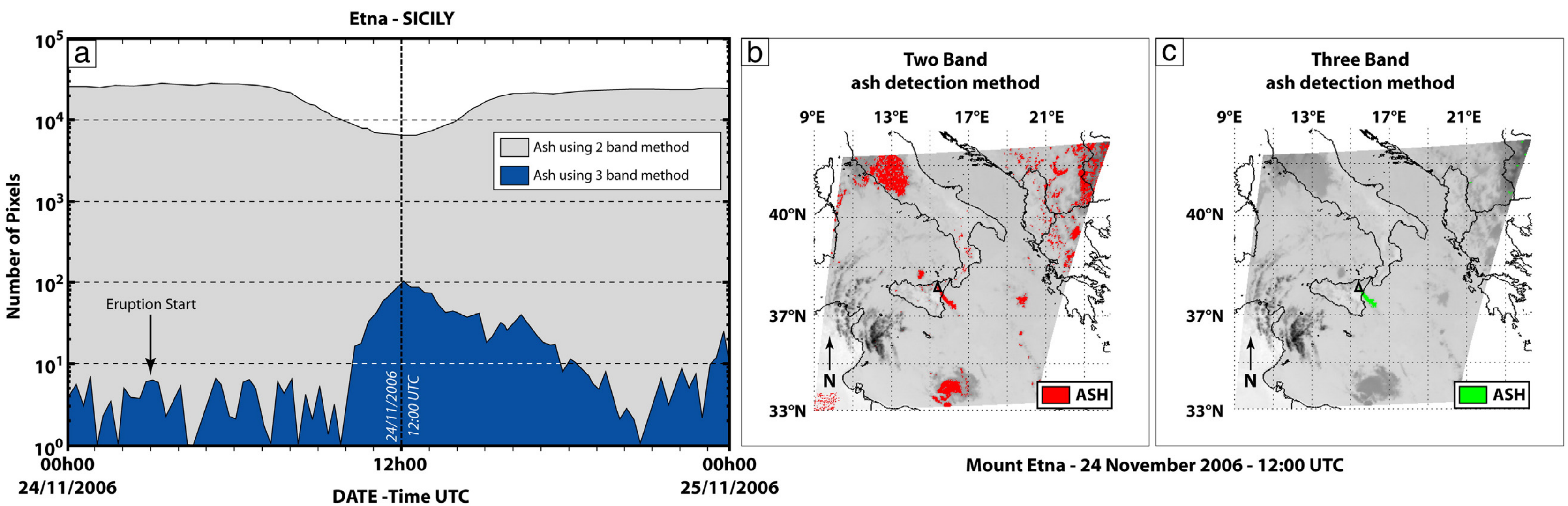

Fig. 7. Comparison between the 2-Band method and the 3-Band method for the Mount Etna eruption of 24 November 2006. For explanation see Fig. 6.

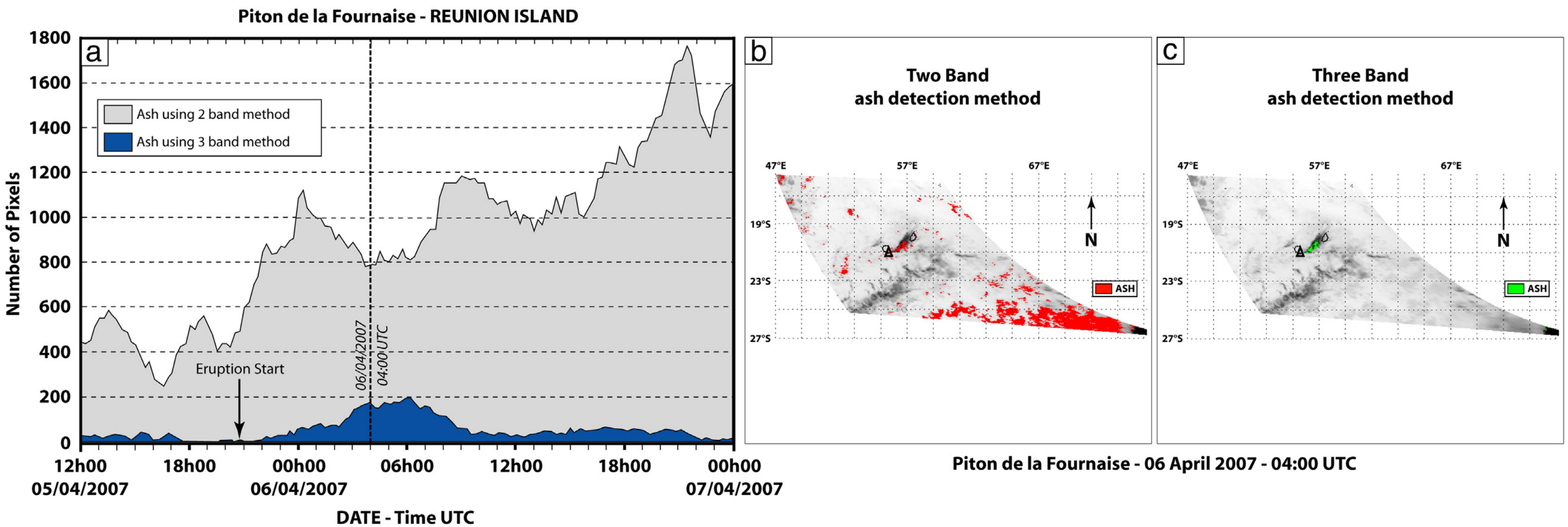

Fig. 8. Comparison between the 2-Band method and the 3-Band method for the Piton de la Fournaise eruption of 05 to 07 April 2007. For explanation see Fig. 6.

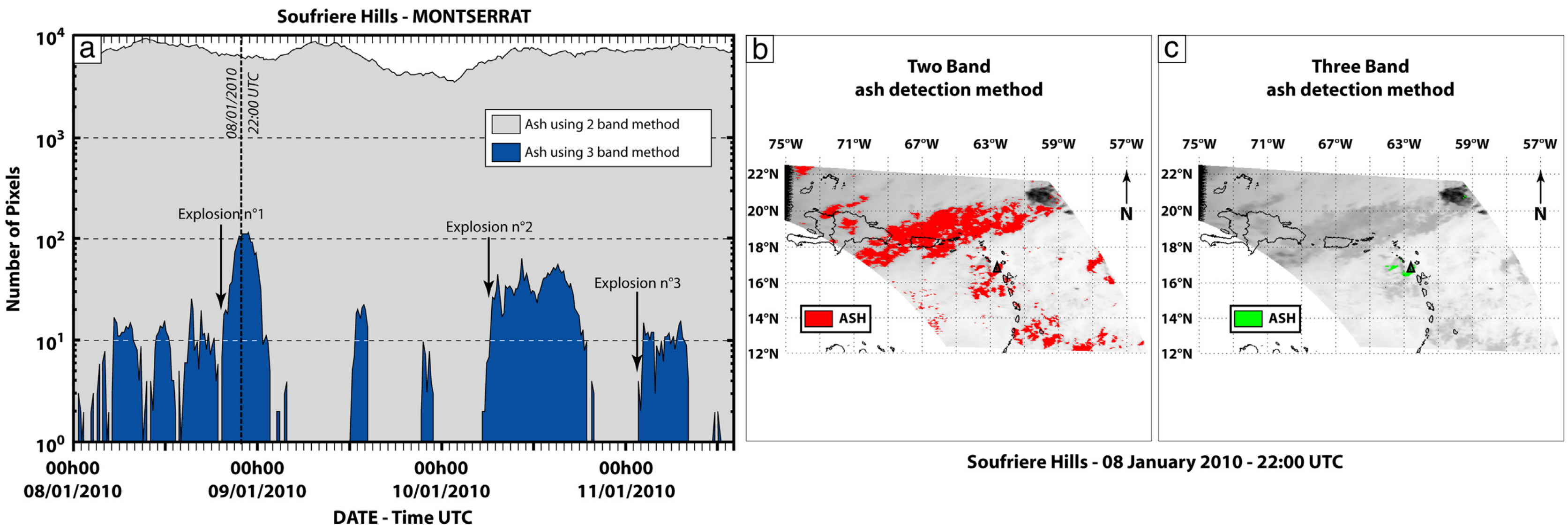

Fig. 9. Comparison between the 2-Band method and the 3-Band method for the Soufriere Hills eruptions of 08 to 11 January 2010. For explanation see Fig. 6.

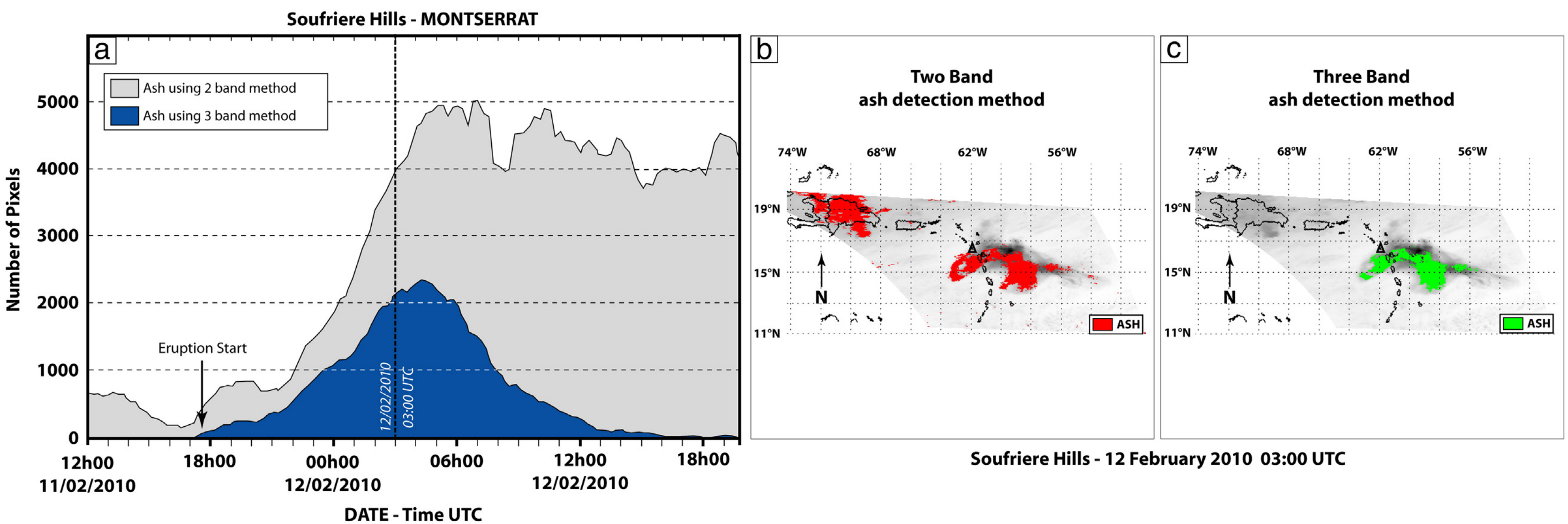

Fig. 10. Comparison between the 2-Band method and the 3-Band method for the Soufriere Hills eruption of 11 to 12 February 2010. For explanation see Fig. 6.

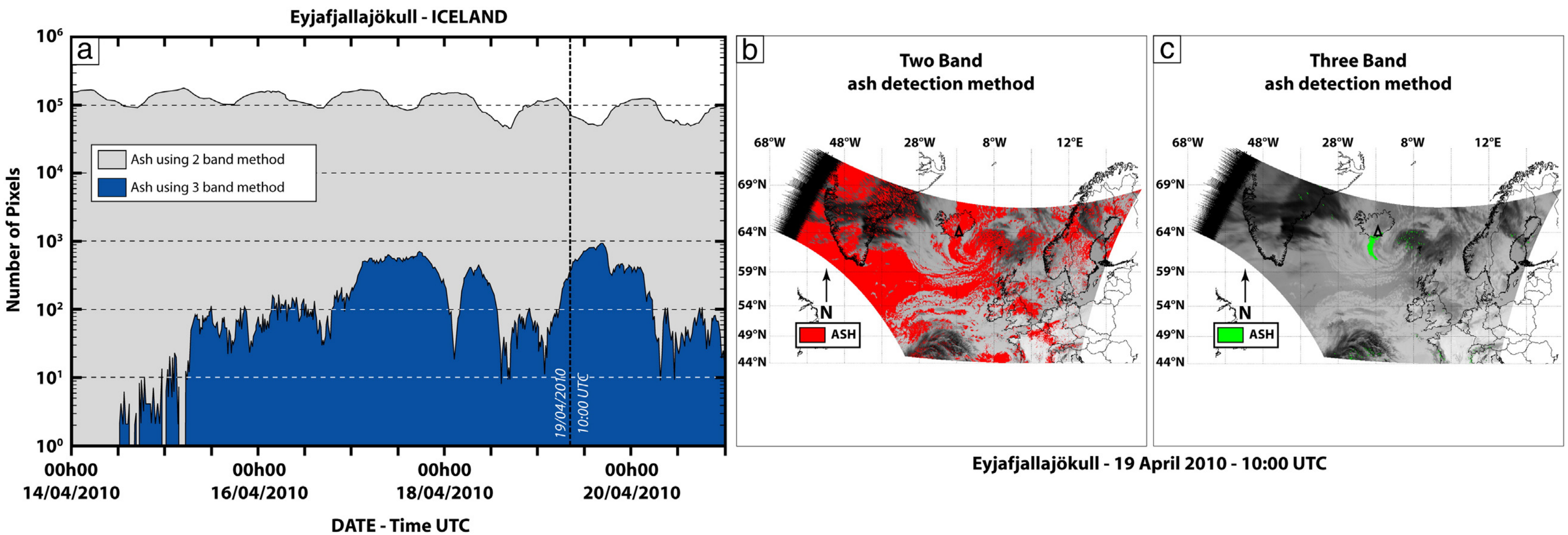

Fig. 11. Comparison between the 2-Band method and the 3-Band method for the first phase of the April–May Eyjafjallajökull eruption. For explanation see Fig. 6.

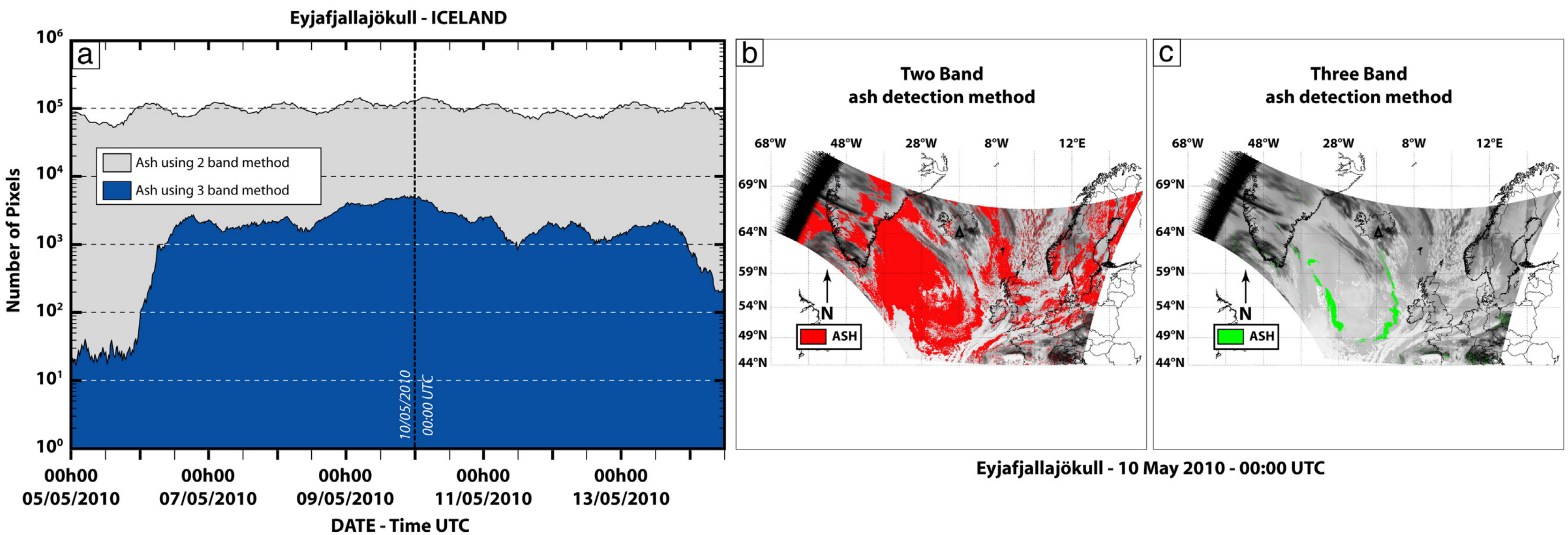

Fig. 12. Comparison between the 2-Band method and the 3-Band method for the second phase of the April–May Eyjafjallajökull eruption. For explanation see Fig. 6.

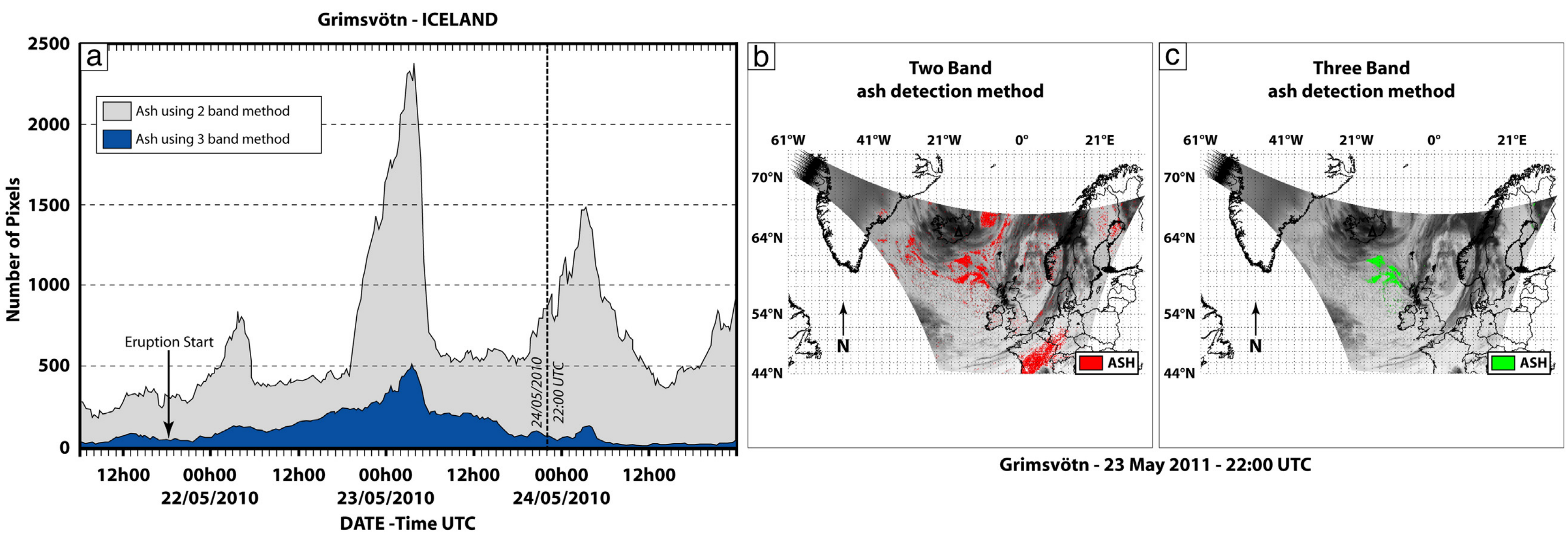

Fig. 13. Comparison between the 2-Band method and the 3-Band method for the Grimsvötn eruption of 22 to 24 May 2011. For explanation see Fig. 6.

Between 21 April and 2 May, explosivity had significantly decreased (Gudmundsson et al., 2010). The second explosive phase started on 5 May, and was marked by an abrupt renewal of the explosive activity that coincides with a sudden change in the magma composition (Gudmundsson et al., 2010, 2012). Again, the 2-Band method is marked by a large number of artifacts (Fig. 12a, b, c) showing a FAR of 24.7% against 0.019% only for the 3-Band method, mainly due to cold meteorological clouds, and nighttime thermal relaxation. In total, 99.9% of artifacts have been removed by the 3-Band method.

4.2.7. The May 2011 Grimsvötn eruption

On 21 May 2011, Grimsvötn erupted producing an ash cloud that quickly reached an altitude of 20 km as noted by the Icelandic Meteorological Office (IMO, 2011). During 22 and 23 May, the activity decreased, such that on 24 May the cloud height reached 3–7.5 km (Icelandic Met. Office, 2011). Although brief, this eruption resulted in the closure, for several hours, of airspace across Iceland, Greenland, Scotland and Northern Ireland, and the cancellation of more than 900 flights (EUROCONTROL, 2011). Here we show a significant difference between the two methods (Fig. 13a), leading to a FAR of 1.8% and 0.022% for the 2-Band and 3-Band methods respectively. In total, 98.8% of artifacts have been removed by the 3-Band method. Fig. 13b and c illustrates that the capability of the 3-Band method to remove artifacts both related to thermal relaxation phenomena (over France area particularly), and meteorological cloud in a cold environment (CE).

5. Conclusion and discussion

The results presented in this work and summarized in Table 3 demonstrate the ability of the 3-Band method to remove a very large number of artifact pixels, ranging from 95.6% to 99.9%, and previously flagged by the 2-Band method as containing ash. The False Alarm Rate (FAR) over the total number of pixels analyzed is in the range 0.9–29.7% and 0.002–0.08% for the 2-Band and the 3-Band methods respectively. This means that up to ~1/3 of a given image could be flagged as ash by the 2-Band method, even when no eruption occurs. Those calculations were carried out using a large image area (~400 × 400 pixels), around the volcanic target, which guarantees full coverage of ash clouds by the monitoring system. Through the analysis of eight different eruptions between 2005 and 2011 from six different volcanoes (Mount Etna, Piton de la Fournaise, Karthala, Soufriere Hills, Eyjafjallajökull, and Grimsvötn), we show that the 3-Band method provides very good and constant results whatever the environment. Indeed, the variety of volcanic targets location allows us to test our method in moisture rich environments (Karthala, Piton de la Fournaise, Soufriere Hills), over frozen land surface (Eyjafjallajökull, Grimsvötn), or during the night in presence of strong thermal relaxation phenomena (Etna).

Additionally, the easy implementation and reliability of the detection scheme proposed here makes appropriate the 3-Band method for operational use in the context of a volcanic crisis. Indeed, the dynamics of ash clouds is driven by complex (e.g., transport, sedimentation, aggregation) and fast-acting processes that make necessary the rapid

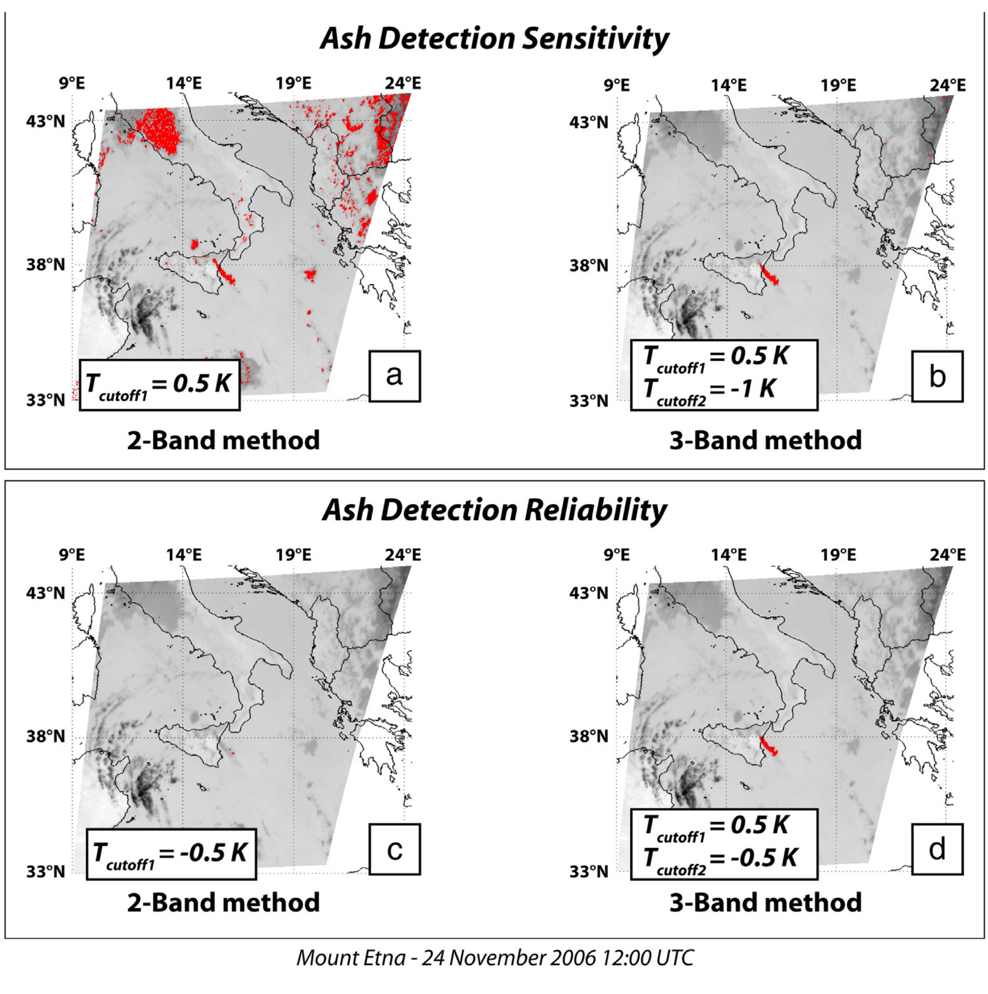

Fig. 14. Impact of $T_{cutoff-1}$ and $T_{cutoff-2}$ on the sensitivity and the reliability between the 2-Band and 3-Band method. On (a) and (b) cutoffs are set in order to increase the sensitivity of ash detection (no missed pixel), while on (c) and (d) cutoffs are set in order to increase the reliability of ash detection (no false alarm).

response of operational monitoring system. Another important idea to consider in operational mode is the balance between sensitivity and reliability. The sensitivity is the ability to detect low concentration ash content so as to avoid "missed pixels", whereas the reliability is the capacity to detect true ash pixels while discarding ash-free ones. The False Alarm Rate (FAR) is thus an indicator of the method reliability. They are both related to the sensor detection limit (spectral and spatial resolutions, instrument noise, etc.) as well as the method applied. Indeed, the choice of the BTD cutoffs, for instance, may greatly influence the balance between detection threshold (i.e., sensitivity), and reliability. $T_{cutoff\text{-}1}$, in particular, may widely vary and possibly ranging from −2 K to +2 K (e.g., Prata and Grant, 2001), depending especially on the existence of water vapor, mixed pixels, coated particles or scattering effects. Note that in this work the different tests have been carried out using fixed cutoffs, set at +0.5 K for $T_{cutoff\text{-}1}$ and −1 K for $T_{cutoff\text{-}2}$, in order to make possible and relevant the comparison between both methods at different volcanoes. These parameters provide, overall, the best balance between sensitivity (i.e., ash cloud well detected), and reliability (i.e., small number of false alarm).

However, in order to test the sensitivity and reliability of the 2 methods, we tested different cutoffs (Fig. 14) during the 24 November 2006 Etna eruption. Indeed, in Fig. 14a (2-Band method) we show that for a $T_{cutoff\text{-}1}$ value at +0.5 K the sensitivity (i.e., amount of true ash-contaminated pixels detected) is good, but the reliability (i.e., number of false alarm) is weak as many water/ice clouds are erroneously flagged as ash. It is not appropriate for automated detection of ash in a real-time fashion. In Fig. 14c (2-Band method), we show that for a $T_{cutoff\text{-}1}$ lowered at −0.5 K the reliability apparently increases as no false alarm remain. However, the sensitivity decreases a lot, as almost no ash can be detected. In this case, ash emissions can clearly be missed by the monitoring system. By contrast, in Fig. 14b and d (3-Band method), we use a fixed $T_{cutoff\text{-}1}$ value at +0.5 K, and we vary the $T_{cutoff\text{-}2}$ value from −1 K to −0.5 K. In the first case (Fig. 14b) we observe a maximum sensitivity of ash detection with a very small number of false alarms already. In the second case (Fig. 14d), we set the $T_{cutoff\text{-}2}$ at −0.5 K, which allows to remove every false alarms (i.e., increased reliability), but at the same time, the number of true ash-contaminated pixels remains almost unchanged (i.e., constant sensitivity). In conclusion to Fig. 14, we do not recommend to adjust the $T_{cutoff\text{-}1}$ value in order to improve ash detection. In detail, additional work would be necessary to determine the best couple $T_{cutoff\text{-}1}$ and $T_{cutoff\text{-}2}$ for each volcanic target.

Other methods have already been tested to decrease the number of false alarm, such as Pavolonis and Sieglaff (2010) using a noise filter to eliminate random and incoherent false alarms. Furthermore, the 3-Band method is fully compatible with the atmospheric correction method (Prata and Grant, 2001; Yu et al., 2002) which allows to overcome problems of ash cloud size underestimation in a moisture rich environment, and increasing the sensitivity of the reverse absorption technique.

In the context of operational response to a volcanic crisis, previous studies have shown that an automated notice, such as an email, based on the 2-Band method only would lead to a huge number of false alarms, hence preventing from any relevant use of the monitoring system (e.g. Simpson et al., 2000; Prata et al., 2001; Yu et al., 2002; Pavolonis et al., 2006). That is why some alternative methods were developed such as those briefly presented in Section 2.4: the technique for improved detection of volcanic ash (Ellrod and Connel, 1999; Ellrod et al., 2003), the VIS/IR daytime method (Pavolonis et al., 2006) or the Robust Satellite Technique (Pergola et al., 2001, 2004; Pergola and Tramutoli, 2003; Marchese et al., 2007, 2014; Piscini et al., 2011) with which the occurrence of false alarms is low enough to allow an effective automatic notice to the operator in presence of airborne ash.

The work presented here shows that the 3-Band method when used with an appropriate couple of $T_{cutoff\text{-}1}$ and $T_{cutoff\text{-}2}$, combines reliability and sensitivity of more sophisticated methods. It allows daytime and nighttime detection, hence allowing a 24/7 monitoring of volcanic ash eruptions. The short processing time required allows the monitoring over a large number of volcanic targets at the same time, with a time resolution of up to 5 min when using Meteosat-RSS (Rapid Scan Service). Finally, such a method requires spectral channels located at 8.7 μm, 11 μm and 12 μm wavelengths, which are available on most sensors.

The 3-Band method is currently used as part of an operational monitoring system named HOTVOLC, run at the Observatoire de Physique du Globe de Clermont-Ferrand, France (OPGC). It uses data from various geostationary satellite, such as MSG-SEVIRI, GOES, or MTSAT, whose acquisition and processing are made in real-time, on site.

Acknowledgments

This work was supported by the TOSCA program of the Centre National d'Etudes Spatiales (CNES, France) through the convention CNES/92532 - BC - T39. SEVIRI data were provided by the HOTVOLC reception platform (OPGC) through agreement with EUMETSAT and Météo-France. We also thank anonymous reviewers for thoughtful comments that have greatly improved the manuscript.

Appendix A. Calculations of optical properties

The Mie code we used to calculate optical properties derived from Bohren and Huffman (1983) formulation and follows the subsequent steps.

1. Computation of the so-called Mie coefficients (a_n and b_n) from size parameter (x) and complex refractive index ($m = n + \chi i$) using the recursion relations for the spherical Bessel functions:

$$a_n = \frac{m\psi_n(mx)\Psi'_n(x) - \psi_n(x)\psi'_n(mx)}{m\psi_n(mx)\xi'_n(x) - \xi_n(x)\psi'_n(mx)} \tag{A.1}$$

$$b_n = \frac{\psi_n(mx)\psi'_n(x) - m\psi_n(x)\psi'_n(mx)}{\psi_n(mx)\xi'_n(x) - m\xi_n(x)\psi'_n} \tag{A.2}$$

where m is the complex refractive index, x is the size parameter, and ψ_n and ξ_n are the Riccati–Bessel functions. See Bohren and Huffman (1983) for more details on Mie coefficients.

2. Computation of extinction (Q_{ext}) and scattering (Q_{sca}) efficiency factors as well as the asymmetry parameter (g) from a_n and b_n following:

$$Q_{ext} = \frac{2}{x^2}\sum_{n=1}^{\infty}(2n+1)Re\{a_n + b_n\} \tag{A.3}$$

$$Q_{sca} = \frac{2}{x^2}\sum_{n=1}^{\infty}(2n+1)\left(|a_n|^2 + |b_n|^2\right) \tag{A.4}$$

$$g = \frac{4}{x^2 Q_{sca}}\left[\sum_n \frac{n(n+2)}{n+1}Re\left(a_n a^*_{n+1} + b_n b^*_{n+1}\right) + \frac{2n+1}{n(n+1)}Re\left(a_n b^*_n\right)\right]. \qquad [A.5]$$

3. Calculation of absorption efficiency and single scattering albedo using the following relation:

$$Q_{abs} = Q_{ext} - Q_{sca} \tag{A.6}$$

and

$$\omega = \frac{Q_{sca}}{Q_{ext}}. \tag{A.7}$$

Appendix B. Supplementary data

Supplementary data to this article can be found online at http://dx.doi.org/10.1016/j.jvolgeores.2015.01.005.

References

Ackermann, S.A., 1997. Remote sensing aerosols using satellite infrared observations. J. Geophys. Res. 102 (14), 17069–17079. http://dx.doi.org/10.1029/96JD03066.

Andronico, D., Spinetti, C., Cristaldi, A., Buongiomo, M.F., 2009. Observations of Mt Etna volcanic ash clouds in 2006: an integrated approach from ground-base and polar satellite NOAA–AVHRR monitoring system. J. Volcanol. Geotherm. Res. 180, 135–147. http://dx.doi.org/10.1016/j.jvolgeores.2008.11.013.

Barton, I.J., Takashima, T., 1986. An AVHRR investigation of surface emissivity near Lake Eyre Australia. Remote Sens. Environ. 20, 153–163. http://dx.doi.org/10.1016/0034-4257(86)90020-9.

Bohren, C.F., Huffman, D.R., 1983. Absorption and Scattering of Light by Small Particles. John Wiley and Sons, New York. http://dx.doi.org/10.1002/9783527618156.

Bonadonna, C., Genco, R., Gouhier, M., Pistolesi, M., Cioni, R., Alfano, F., Hoskuldsson, A., Ripepe, M., 2011. Tephra sedimentation during the 2010 Eyjafjallajökull eruption (Iceland) from deposit, radar, and satellite observations. J. Geophys. Res. 116, B12202. http://dx.doi.org/10.1029/2011JB008462.

Casadevall, T.J., 1994a. The 1989/1990 eruption of Redoubt volcano Alaska: impacts on aircraft operations. J. Volcanol. Geotherm. Res. 62 (30), 301–316. http://dx.doi.org/10.1016/0377-0273(94)90038-8.

Casadevall, T.J., 1994b. Volcanic ash and aviation safety. Proceedings of the First International Symposium on Volcanic Ash and Aviation Safety. USGS Bull 2047, p. 450.

Casadevall, T.J., Delos Reyes, P.J., Schneider, D.J., 1996. The 1991 Pinatubo Eruptions and Their Effects on Aircraft Operations, in Fire and Mud: Eruptions and Lahars of Mount Pinatubo, Philippines. In: Newhall, C.G., Punongbayan, R.S. (Eds.), Univsersity of Washington Press, Seattle, pp. 625–636.

Casadevall, T.J., T.B. Thompson, and T. Fox (1999), World Map of Volcanoes and Principal Aeronautical Features. USGS Map I-2700, scale 1:34,268,000, reprinted 2001.

Corradini, S., Merucci, L., Prata, A.J.L., 2009. Retrieval SO_2 from thermal infrared satellite measurements: correction procedures for the effects of volcanic ash. Atmos. Meas. Tech. 2, 177–191. http://dx.doi.org/10.5194/amt-2-177-2009.

Corradini, S., Merucci, L., Prata, A.J.L., Piscini, A., 2010. Volcanic Ash and SO_2 in the 2008 Kasatochi eruption: Retrievals comparison from different IR satellite sensors. J. Geophys. Res. 115, D00L21. http://dx.doi.org/10.1029/2009JD013634.

Davies, S.M., Larsen, G., Wastegård, S., Turney, C.S.M., Hall, V.A., Coyle, L., Thordarson, T., 2010. Widespread dispersal of Icelandic tephra: how does the Eyjafjöll eruption of 2010 compare to pas Icelandic events? J. Quaternary Sci. 25, 605–611. http://dx.doi.org/10.1002/jqs.1421.

Dean, K.G., Dehn, J., Papp, K., Smith, S., Izbekov, P., Peterson, R., Kearney, C., Steffke, A., 2003. Integrated satellite observations of the 2001 eruption of Mt Cleveland Alaska. J. Volcanol. Geotherm. Res. 135, 51–73. http://dx.doi.org/10.1016/j.jvolgeores.2003.12.013.

Devenish, B.J., Francis, P.N., Johnson, B.T., Sparks, R.S.J., Thomson, D.J., 2012. Sensitivity analysis of dispersion modeling of volcanic ash from Eyjafjallajökull in May 2010. J. Geophys. Res. 117, D00U21. http://dx.doi.org/10.1029/2011JD016782.

Ellrod, G.P., Connel, B.H., 1999. Improvements in volcanic ash detection using GOES multispectral image data, Preprint volume 8th Conference on Aviation Range an Aerospace Meteorology. Am. Meteorol. Soc. 326–329.

Ellrod, G.P., Connell, B.H., Hillger, D.W., 2003. Improved detection of airborne volcanic ash using multispectral infrared satellite data. J. Geophys. Res. 108 (D12), 4356. http://dx.doi.org/10.1029/2002JD002802.

EUROCONTROL, 2011. http://wwweurocontrolint/news/update-european-air-traffic-situation-following-grimsvoetn-eruption-1000-cet-1.

Folch, A., 2012. A review of tephra transport and dispersal models: evolution, current status, and future perspectives. J. Volcanol. Geotherm. Res. 235–236, 96–115. http://dx.doi.org/10.1016/j.jvolgeores.2012.05.020.

Francis, P.N., Cooke, M.C., Saunders, R.W., 2012. Retrieval of physical properties of volcanic ash using Meteosat: a case study from 2010 Eyjafjallajökull eruption. J. Geophys. Res. 117, D00U09. http://dx.doi.org/10.1029/2011JD016788.

Gouhier, M., Coppola, D., 2011. Satellite-based evidence for a large hydrothermal system at Piton de la Fournaise volcano (Reunion Island). Geophys. Res. Lett. 38, L02302. http://dx.doi.org/10.1029/2010GL046183.

Gudmundsson, M.T., Pedersen, R., Vogfjörd, K., Thorbjarnardóttir, B., Jakobsdóttir, S., Roberts, M.J., 2010. Eruptions of Eyjafjallajökull volcano, Iceland. Eos. Trans. AGU 91 (21), 190–191. http://dx.doi.org/10.1029/2010EO210002.

Gudmundsson, M.T., Thordarson, T., Höskuldsson, A., Larsen, G., Björnsson, H., Prata, F.J., Oddsson, B., Magnusson, E., Hognadóttir, T., Petersen, G.N., Hayward, C.L., Stevenson, J.A., Jonsdóttir, I., 2012. Ash generation and distribution from the April–May 2010 eruption of Eyjafjallajökull, Iceland. Nature 2 (572). http://dx.doi.org/10.1038/srep00572.

Guffanti, M., Ewert, J.W., Gallina, G.M., Bluth, G.J.S., Swanson, G.L., 2005. Volcanic-ash hazard to aviation during the 2003–2004 eruption activity of Anatahan volcano Commonwealth of the Northern Mariana Islands. J. Volcanol. Geotherm. Res. 146, 241–255. http://dx.doi.org/10.1016/j.jvolgeores.2004.12.011.

Hale, G.M., Querry, M.R., 1973. Optical Constants of Water in the 200-nm to 200-μm Wavelength Region. Appl. Opt. 12 (3), 555–563. http://dx.doi.org/10.1364/AO.12.000555.

Houze, R., 1993. Cloud Dynamics. Academic Press, San Diego 0123568803.

Icelandic Meteorological Office, 2011. http://enveduris/earthquakes-and-volcanism/articles/nr/2180.

International Volcanic Ash Task Force (IVATF), 2010. Perspective on aircraft airworthiness when operating in airspace containing volcanic ash. Working Paper — First Meeting Montréal, 27 to 30 July 2010.

Kaminski, E., Tait, S., Ferrucci, F., Martet, M., Hirn, B., Husson, P., 2011. Estimation of ash injection in the atmosphere by basaltic volcanic plumes: THE case of the Eyjafjallajökull 2010 eruption. J. Geophys. Res. 116, B00C02. http://dx.doi.org/10.1029/2011JB008297.

Labazuy, P., Gouhier, M., Harris, A.J.L., Guéhenneux, Y., Hervo, M., Bergès, J.-C., Fréville, P., Cacault, P., Rivet, S., 2012. Near real-time monitoring of the April–May 2012 Eyjafjallajökull ash cloud: an example of a web-based satellite data-driven reporting system. Int. J. Environ. Pollut. 48, 262–272. http://dx.doi.org/10.1504/IJEP.2012.049673.

Marchese, F.A., Malvasen, G., Ciampa, M., Filizzola, C., Pergola, N., Tramutoli, V., 2007. A robust multitemporal satellite technique for volcanic activity monitoring: possible impacts on volcanic hazard mitigation. International Workshop on the Analysis of Multi-Temporal Remote Sensing Images, 18–20 July 2007 http://dx.doi.org/10.1109/MULTITEMP.2007.4293056.

Marchese, F., Flaconieri, A., Pergola, N., Tramutoli, V., 2014. A retrospective analysis of the Shinmoedake (Japan) eruption of 26–27 January 2011 by means of Japanese geostationary satellite data. J. Volcanol. Geotherm. Res. 269, 1–13. http://dx.doi.org/10.1016/j.jvolgeosres.2013.10.011.

Mayberry, G.C., Rose, W.I., Bluth, G.J.S., 2002. Dynamics of the volcanic and meteorological clouds produced by December 26, 1997 eruption of Soufrière Hills, Montserrat, W.I. In: Duitt, T., Kokelaar, P. (Eds.), The eruption of the Soufrière Hills, Montserrat 1995-99. Mem. Geol. Soc. London, 21, pp. 539–555. http://dx.doi.org/10.1144/GSL.MEM.2002.021.01.24.

Michon, L., Staudacher, T., Ferrazzini, V., Bachelery, P., Marti, J., 2007. April 2007 collapse of Piton de la Fournaise: a new example of caldera formation. Geophys. Res. Lett. 31, l21301. http://dx.doi.org/10.1029/2007GL031248.

Miller, T.P., Casadevall, T.J., 1999. Volcanic ash hazards to aviation. In: Sigurdsson, H., et al. (Eds.), Encyclopedia of Volcanoes. Academic Press, San Diego, pp. 915–930.

Millington, S.C., Saunders, R.W., Francis, P.N., Webster, H.N., 2012. Simulated volcanic ash imagery: a method to compare NAME ash concentration forecasts with SEVIRI imagery for the Eyjafjallajökull eruption in 2010. J. Geophys. Res. 117, D00U17. http://dx.doi.org/10.1029/2011JD016770.

Montserrat Observatory Volcano (MVO), 2010a. 08 to 15 January Weekly Report. http://wwwmvoms/whats-new/last-activity-a-weekly-reports/weekly-reports-archive/1248-8-to-15-january-2010.

Montserrat Observatory Volcano (MVO), 2010b. 05 to 12 February Weekly Report. http://wwwmvoms/whats-new/last-activity-a-weekly-reports/weekly-reports-archive/1254-5-to-12-february-2010.

Mosher, F.R., 1999. Four Channel Volcanic Ash Detection Algorithm. Aviation Weather Center Staff Publication.

Palmer, K.F., Williams, D., 1975. Optical constants of sulfuric acid; application to the clouds of Venus? Appl. Opt. 14 (1), 208–219. http://dx.doi.org/10.1365/AO.14.000208.

Pavolonis, M.J., 2010. Advances in extracting cloud composition information from spaceborne infrared radiance — a robust alternative to brightness temperature, PART I: THEORY. J. Appl. Meteorol. Climatol. 49, 1992–2012. http://dx.doi.org/10.1175/2010JAMC2433.1.

Pavolonis, M.J., Sieglaff, J., 2010. GOES-R advanced baseline imager (ABI) algorithm theoretical basis document for volcanic ash: detection and height, version 2.0, report. NOAA Silver Spring (72 pp., available at: http://www.goes-r.gov/products/ATBDs/baselined/Aviation_VolAsh_v2.0_no_color.pdf).

Pavolonis, M.J., Feltz, W.F., Heidinger, A.K., Gallina, G.M., 2006. A daytime complement to the reverse absorption technique for improved automated detection of volcanic ash. J. Atmos. Ocean. Technol. 23 (11), 1422. http://dx.doi.org/10.1175/JTECH1926.1.

Pergola, N., Pietrapertosa, C., Lacava, T., Tramutoli, V., 2001. Robust satellite technique for volcanic eruptions monitoring. Ann. Geophys. 44 (2), 167–177. http://dx.doi.org/10.4401/ag-3590.

Pergola, N., Tramutoli, V., Marchese, F., Scaffidi, I., Lacava, T., 2004. Improving volcanic ash cloud detection by a robust satellite technique. Remote Sens. Environ. 90, 1–22. http://dx.doi.org/10.1016/j.rse.2003.11.014.

Pergola, N., Tramutoli, V., 2003. Two years of operational use of Subpixel Automatic Navigation of AVHRR scheme: accuracy assessment and validation. Remote Sens. Environ. 85, 190–203. http://dx.doi.org/10.1016/S0034-4257(02)00205-5.

Peuch, V.H., Amodei, M., Barthet, T., Cathala, M.L., Josse, B., Michou, M., Simon, P., 1999. MOCAGE, MOdéle de Chimie Atmosphèrique à Grande Echelle. Proceedings of Météo France Workshop on Atmospheric Modelling, pp. 33–36.

Piscini, A., Corradini, S., Marchese, F., Merucci, L., Pergola, N., Tramutoli, V., 2011. Volcanic ash cloud detection from space: a comparison between RSTASH technique and water vapour corrected BTD procedure. Geomatics Nat. Hazards Risk 2 (3), 263–277. http://dx.doi.org/10.1080/19475705.2011.568069.

Platt, C.M.R., Prata, A.J., 1993. Nocturnal effects in the retrieval of land surface temperatures from satellite measurements. Remote Sens. Environ. 45, 127–136. http://dx.doi.org/10.1016/0034-4257(93)90037-X.

Pollack, J.B., Toon, O.B., Khare, B.N., 1973. Optical properties of some terrestrial rocks and glasses. Icarus 19 (3), 372–389. http://dx.doi.org/10.1016/0019-1035(73)90115-2.

Potts, R.J., Ebert, E.E., 1996. On the detection of volcanic ash in NOAA AVHRR infrared satellite imagery. Paper Presented at 8th Australian Remote Sens. Conf., Canberra, 25–29 March 1996.

Prata, A.J., 1989a. Observations of volcanic ash clouds using AVHRR-2 radiances. Int. J. Remote Sens. 10 (4–5), 751–761. http://dx.doi.org/10.1080/01431168908903916.

Prata, A.J., 1989b. Radiative transfer calculations for volcanic ash clouds. Geophys. Res. Lett. 16 (11), 1293–1296. http://dx.doi.org/10.1029/GL016i011p01293.

Prata, A.J., 2009. Satellite detection of hazardous volcanic clouds and the risk to global air traffic. Nat. Hazards 51 (2), 303–324. http://dx.doi.org/10.1007/s11069-008-9273-z.

Prata, A.J., Grant, I.F., 2001. Retrieval of microphysical and morphological properties of volcanic ash clouds from satellite data: application to Mt Ruapehu New Zealand. Q. J. R. Meteorol. Soc. 127 (576B), 2153–2179. http://dx.doi.org/10.1002/qj.49712757615.

Prata, A.J., Kerkmann, J., 2007. Simultaneous retrieval of volcanic ash and SO_2 using MSG-SEVIRI measurements. Geophys. Res. Lett. 34, L05813. http://dx.doi.org/10.1029/2006GL0228691.

Prata, A.J., Prata, A.T., 2012. Eyjafajallajökull volcanic ash concentrations determined using spin enhanced visible and infrared imager measurements. J. Geophys. Res. 117, D00U23. http://dx.doi.org/10.1029/2011JD016800.

Prata, A.J., Tupper, A., 2009. Aviation hazards from volcanoes: the state of the science. Nat. Hazards 51 (2), 239–244. http://dx.doi.org/10.1007/s11069-009-9415-y.

Prata, A.J., Bluth, G.J.S., Rose, W.I., Schneider, D.J., Tupper, A.C., 2001. Comments on failures in detecting volcanic ash from satellite-based technique. Remote Sens. Environ. 78, 341–346. http://dx.doi.org/10.1016/S0034-4257(01)00231-0.

Rose, W.I., Prata, A.J., 1997. Atmospheric corrections for two band infrared volcanic cloud discriminations and retrievals. EOS trans. AGU, Fall Meeting Supplement, p. F818.

Rose, W.I., Delene, D.J., Bluth, G.J.S., Kruger, A.J., Sprod, I., McKee, C., Davies, H.L., Ernst, G.J., 1995. Ice in the 1994 Rabaul eruption: implications for volcanic hazard and atmospheric effects. Nature 375, 477–479. http://dx.doi.org/10.1038/375477a0.

Rose, W.I., Bluth, G.J.S., Schneider, D.J., Ernst, G.G.J., Riley, C.M., Henderson, L.J., McGimsey, R.G., 2001. Observations of Volcanic clouds in their first few days of atmospheric residence: the 1992 eruptions of Crater Peak Mount Spurr volcano Alaska. J. Geol. 109 (6), 677–694. http://dx.doi.org/10.1086/323189.

Schaaf, J.W., Williams, D., 1973. Optical constants of ice in the infrared. J. Opt. Soc. Am. 63, 726–732. http://dx.doi.org/10.1364/JOSA.63.000726.

Schultz, C., 2012. Fine aspherical ash source of Eyjafjallajökull's influence. Eos Trans. AGU 93 (10), 116. http://dx.doi.org/10.1029/2012EO100016.

Simpson, J.J., Hufford, G., Pieri, D., Berg, J., 2000. Failures in detecting volcanic ash from satellite-based technique. Remote Sens. Environ. 72, 191–217. http://dx.doi.org/10.1016/S0034-4257(99)00103-0.

Smithsonian Institution, 2005. Karthala. Bull. Glob. Volcanism Netw. 30 (11), 2–4.

Smithsonian Institution, 2006. Karthala. Bull. Glob. Volcanism Netw. 31 (11), 2–4.

Spitzer, W.G., Kleinman, D.A., 1961. Infrared lattice bands of quartz. Phys. Rev. 121, 1324–1325. http://dx.doi.org/10.1103/PhysRev.121.1324.

Tramutoli, V., 1998. Robust AVHRR Techniques (RAT) for environmental monitoring: theory and applications. II Proceedings SPIE. Earth Surf. Remote Sens 3496, pp. 101–113. http://dx.doi.org/10.1117/12.332714.

Tulet, P., Villeneuve, N., 2011. Large scale modeling of the transport chemical transformation and mass budget of the sulfur emitted during the April 2007 eruption of Piton de la Fournaise. Atmos. Chem. Phys. 11, 4533–4546. http://dx.doi.org/10.5194/acp-11-4533-2011.

Tupper, A., Carn, S., Davey, J., Kamada, Y., Potts, R., Prata, F., Tokuno, M., 2004. An evaluation of volcanic cloud detection techniques during recent significant eruptions in the western 'Ring of Fire'. Remote Sens. Environ. 91, 27–46. http://dx.doi.org/10.1016/j.rse.2004.02.004.

Volz, F.E., 1973. Infrared optical constants of ammonium sulphate, Saharan dust, volcanic pumice, and flyash. Appl. Opt. 12, 564–568. http://dx.doi.org/10.1364/AO.12.000564.

Watkin, S.C., 2003. The application of AVHRR data for the detection of volcanic ash in a Volcanic Ash Advisory Centre. Meteorol. Appl. 10, 301–311. http://dx.doi.org/10.1017/S1350482703001063 (in this issue).

Wen, S., Rose, W.I., 1994. Retrieval of sizes and total masses of particles in volcanic clouds using AVHRR bands 4 and 5. J. Geophys. Res. 99 (D3), 5421–5431. http://dx.doi.org/10.1029/93JD03340.

Yu, T., Rose, W.I., Prata, A.J., 2002. Atmospheric correction for satellite-based volcanic ash mapping and retrievals using "split window" IR data from GOES and AVHRR. J. Geophys. Res. 107 (D16), 10,1029. http://dx.doi.org/10.1029/2001JD000706.

Tephra sedimentation during the 2010 Eyjafjallajökull eruption (Iceland) from deposit, radar, and satellite observations

C. Bonadonna,[1] R. Genco,[2] M. Gouhier,[3] M. Pistolesi,[4] R. Cioni,[5,6] F. Alfano,[1] A. Hoskuldsson,[7] and M. Ripepe[2]

Received 22 April 2011; revised 5 October 2011; accepted 6 October 2011; published 16 December 2011.

[1] The April–May 2010 eruption of the Eyjafjallajökull volcano (Iceland) was characterized by a nearly continuous injection of tephra into the atmosphere that affected various economic sectors in Iceland and caused a global interruption of air traffic. Eruptive activity during 4–8 May 2010 was characterized based on short-duration physical parameters in order to capture transient eruptive behavior of a long-lasting eruption (i.e., total grain-size distribution, erupted mass, and mass eruption rate averaged over 30 min activity). The resulting 30 min total grain-size distribution based on both ground and Meteosat Second Generation-Spinning Enhanced Visible and Infrared Imager (MSG-SEVIRI) satellite measurements is characterized by Mdphi of about 2 ϕ and a fine-ash content of about 30 wt %. The accumulation rate varied by 2 orders of magnitude with an exponential decay away from the vent, whereas Mdphi shows a linear increase until about 18 km from the vent, reaching a plateau of about 4.5 ϕ between 20 and 56 km. The associated mass eruption rate is between 0.6 and 1.2×10^5 kg s^{-1}. In situ sampling showed how fine ash mainly fell as aggregates of various typologies. About 5 to 9 wt % of the erupted mass remained in the cloud up to 1000 km from the vent, suggesting that nearly half of the ash >7ϕ settled as aggregates within the first 60 km. Particle sphericity and shape factor varied between 0.4 and 1 with no clear correlation to the size and distance from vent. Our experiments also demonstrate how satellite retrievals and Doppler radar grain-size detection can provide a real-time description of the source term but for a limited particle-size range.

Citation: Bonadonna, C., R. Genco, M. Gouhier, M. Pistolesi, R. Cioni, F. Alfano, A. Hoskuldsson, and M. Ripepe (2011), Tephra sedimentation during the 2010 Eyjafjallajökull eruption (Iceland) from deposit, radar, and satellite observations, *J. Geophys. Res.*, *116*, B12202, doi:10.1029/2011JB008462.

1. Introduction

[2] Volcanic eruptions typically result in the generation of silicate particles of various sizes, shapes, densities, and composition (tephra) that, depending on terminal velocity, are carried up within a convective plume, advected by the surrounding wind field, and then sediment on the ground, forming tephra deposits. The transport of volcanic particles within the plume and associated sedimentation are complicated by plume and atmospheric turbulence, by particle-particle interaction, and by atmospheric conditions (e.g., humidity, temperature). In particular, fine ash (<63 μm) typically aggregates within the vertical plume and the horizontally spreading umbrella cloud, forming particle clusters and accretionary pellets of various sizes and types, mainly depending on the presence of solid and liquid water and on their residence time within the turbulent currents [*Brown et al.*, 2011; *Costa et al.*, 2010; *Gilbert and Lane*, 1994].

[3] The 14 April to 21 May 2010 eruption of Eyjafjallajökull volcano (Iceland) was characterized by a nearly continuous injection of tephra into the atmosphere up to 10 km above sea level (Figure 1a) that was mainly dispersed toward the east and southeast, reaching as far as the southern parts of Europe, causing interruptions in global air traffic to an extent not seen since 11 September 2001 and the largest breakdown in European civil aviation since World War II. The eruption started as clearly phreatomagmatic because of

[1]Section of Earth and Environmental Sciences, University of Geneva, Geneva, Switzerland.
[2]Department of Earth Sciences, University of Florence, Florence, Italy.
[3]Laboratoire Magmas et Volcans, Université Blaise Pascal, Clermont-Ferrand, France.
[4]Department of Earth Sciences, University of Pisa, Pisa, Italy.
[5]Department of Earth Sciences, University of Cagliari, Cagliari, Italy.
[6]Also at Istituto Nazionale di Geofisica e Vulcanologia, Sezione di Pisa, Pisa, Italy.
[7]Institute of Earth Sciences, University of Iceland, Reykjavik, Iceland.

0148-0227/11/2011JB008462

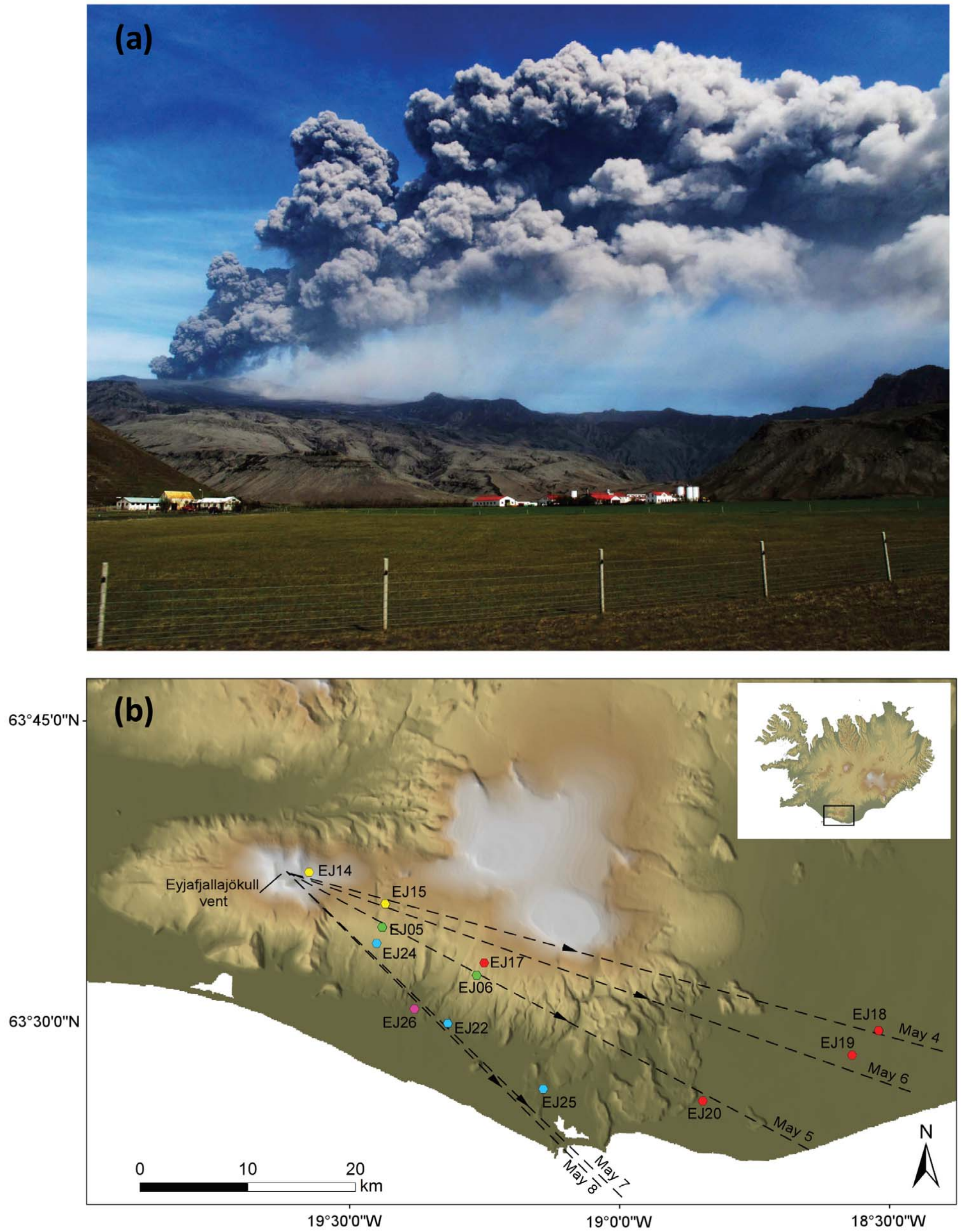

Figure 1. (a) Eyjafjallajökull plume spreading toward the southeast of Iceland on 4 May 2010. (b) Map showing sampling locations and main wind direction for the different sampling days averaged below the maximum plume height provided by the IMO radar for those time periods (i.e., 5.5 km for 4 May, 8.1 km for 5 May, 5.9 km for 6 May, 5.5 km for 7 May, and 5.4 km for 8 May). Locations are indicated with circles of different colors according to the date (i.e., green, 4 May; yellow, 5 May; red, 6 May; blue, 7 May; pink, 8 May).

the interaction with the overlying glacier and then evolved into more magmatic and dry explosions [*Hoskuldsson et al.*, 2011]. During 4–8 May 2010 various experiments were carried out in order to investigate particle sedimentation. In particular, at specific locations (Figure 1b) we have (1) collected tephra in dedicated trays to determine particle grain size and accumulation rate, (2) collected volcanic particles and aggregates while they were falling in order to characterize their size, shape, and surface features, (3) carried out Doppler radar measurements of settling velocities. Ash retrievals from satellite images of 6 May are also presented and discussed for a better understanding of ash transport and sedimentation.

2. Methods and Conditions During Sampling

2.1. Particle Collection

[4] Direct tephra sampling was carried out during the activity between 4 and 8 May 2010 in containers of various sizes (0.1–0.4 m^2) between 2 and 56 km from the vent in the

Table 1. Summary of Collection and Deposit Characteristics of All Samples Analyzed[a]

Locality	Distance From Vent (km)	Collection Date	Collection Time (UT)	Deposit Density (kg/m^3)	TOT Mass/ Area (kg/m^2)	Acc. Rate ($kg/m^2/s$)	30 Min Mass/ Area (kg/m^2)	Mdphi	Sorting
EJ05	10.1	4 May	18:30–19:30	–	0.02	4.64E-06	0.01	1.4	0.7
EJ06	20.0	4 May	21:45–22:15	1243	0.36	2.02E-04	0.36	3.9	2.1
EJ14	2.0	5 May	17:39–17:49	1096	0.42	6.98E-04	1.26	−0.9	1.2
EJ15 tot	9.6	5 May	19:00–20:36	1377	0.68	1.19E-04	0.21	0.7	0.8
EJ15 (1)	9.6	5 May	19:00–19:15	1240	0.10	1.13E-04	–	0.9	0.8
EJ15 (2)	9.6	5 May	19:20–19:35	1332	0.12	1.37E-04	–	0.8	0.8
EJ15 (3)	9.6	5 May	19:37–19:52	1383	0.22	2.45E-04	–	0.8	2.8
EJ15 (4)	9.6	5 May	19:56–20:11	1315	0.19	2.12E-04	–	0.6	0.8
EJ15 (5)	9.6	5 May	20:11–20:36	1228	0.06	6.66E-05	–	0.8	0.9
EJ17	20.1	6 May	14:55–15:45	-	0.02	8.17E-06	0.01	4.4	2.0
EJ18	56.0	6 May	18:17–18:47	1147	0.04	1.96E-05	0.04	4.5	1.8
EJ19	55.0	6 May	19:11–19:31	1207	0.05	4.14E-05	0.07	4.5	1.7
EJ20	44.1	6 May	20:07–20:43	1134	0.11	5.28E-05	0.09	4.4	2.0
EJ25	31.2	6–7 May	23:13 (6 May) to 01:30 (7 May)	1279	0.18	2.01E-05	0.04	2.5	0.8
EJ22	20.6	7 May	12:17 12:50	1321	0.21	1.05E-04	0.19	4.2	2.6
EJ24	10.7	7 May	15:35–16:20	1192	0.29	1.07E-04	0.19	1.3	1.0
EJ26	17.3	8 May	12:16–12:42	1264	0.19	1.25E-04	0.22	1.0	0.8

[a]Sample locations are indicated in Figure 1. Samples EJ14–EJ26 are experiments for which PLUDIX measurements were also carried out. TOT and 30 min mass/area are the mass/area determined for the whole collection period and for 30 min (i.e., calculated by multiplying the accumulation rate by 1800 s) respectively. For EJ05 and EJ17 there was not enough material to accurately calculate the deposit density. Acc. Rate is Accumulation Rate. A summary of the sequential sampling carried out at EJ15 is also shown (EJ15 (1) to EJ15 (5)). EJ15 tot was collected on a dedicated container for the total duration of the sequential sampling.

east and southeast sectors with respect to the volcano (Figure 1b and Table 1). Both eruptive and atmospheric conditions were relatively constant during the whole sampling period, which was characterized by a nearly continuous injection of tephra into the atmosphere with a maximum plume height between 5 and 10 km above sea level (as observed by the weather radar of the Icelandic Meteorological Office (IMO)). Wind velocities averaged below these elevations varied between 10 and 16 m s^{-1}, whereas associated wind directions varied between about 280° and 320° from north (Figure 1b) (European Centre for Medium-Range Weather Forecasts (ECMWF) ERA-40 Re-Analysis at 0.25° resolution interpolated above the volcano). Thanks to these nearly constant eruptive and atmospheric conditions, both an isomass map and a total grain-size distribution could be compiled that can be considered representative of 30 min of activity (i.e., average of all sampling times considered; Figure 2).

2.2. Particle Characterization

[5] Collected samples were hand sieved at the University of Geneva down to 0.25 mm and the fine fraction (<0.25 mm) was analyzed using a laser-diffraction instrument (CILAS 1180; http://www.cilas.com/). Mdphi and sorting (σ) were calculated for all samples according to *Inman* [1952]. Particle images were also taken for morphological studies in order to derive morphological parameters (i.e., sphericity and shape factor). For particle sizes smaller than 0.25 mm, images were taken with the 10× microscope of the CILAS 1180; for particles between 0.25 and 2 mm, images were taken using a 10× optical microscope; finally, for particles >2 mm, images were taken directly using a digital scanner. Shape parameters (i.e., the sphericity of *Aschenbrenner* [1956], the shape factor of *Wilson and Huang* [1979], and the equivalent diameter and sphericity of *Riley et al.* [2003]; see Appendix A for more details) were calculated based on the two-dimensional (2-D) analysis of these images, determining for each particle the projected area, perimeter, length, width, and 90 generic diameters measured in different directions (Table 2). In order to determine the sphericity of *Aschenbrenner* [1956] and the shape factor of *Wilson and Huang* [1979], which are based on three-dimensional (3-D) measurements, we have assumed that the projected area of each particle contains the largest axis (*L*, length of the particle) and the smallest axis (*S*, width of the particle), whereas the intermediate axis (*I*) was derived from the average of 90 generic diameters of the projected area. The sphericity and shape factor based on the three perpendicular axes could be determined only for clasts with diameters between about 13 and 30 mm that fell at locality EJ14 (Figure 1b).

[6] Scanning electron microscope (SEM) images were used for grain-size analyses on ash aggregates (samples EJ06, EJ15, EJ18, and EJ22). SEM images were processed with the shareware software for image analysis ImageJ, and particles were measured in the range 0.063–0.006 mm (4–13 ϕ). Areas of particles were reconverted to equivalent diameters (assuming spherical shapes) and then to volumes and ϕ values.

[7] Deposit density was calculated by gently pouring ash samples in a graduated cylinder, and measuring volume and weight (average of five measurements; Table 1), whereas the density of 50 clasts (sizes between about 13 and 30 mm) that fell at location EJ14 (2 km from the vent) was measured by determining weights in air and in water (Archimedes' principle) following the works of *Houghton and Wilson* [1989] and *Polacci et al.* [2003] (i.e., 986 ± 0.2 kg m^{-3}). Clasts were sealed by application of cellulose acetate prior to the determination of the weight in water. The cellulose film is assumed to contribute negligible mass and volume to the clast. Samples were weighted again after cellulose coating in order to control weight variations. The density of glass (i.e., 2738 ± 0.7 kg m^{-3}) was measured with a helium pycnometer at the University of Pisa on powdered scoriae of the EJ14 and EJ15 samples.

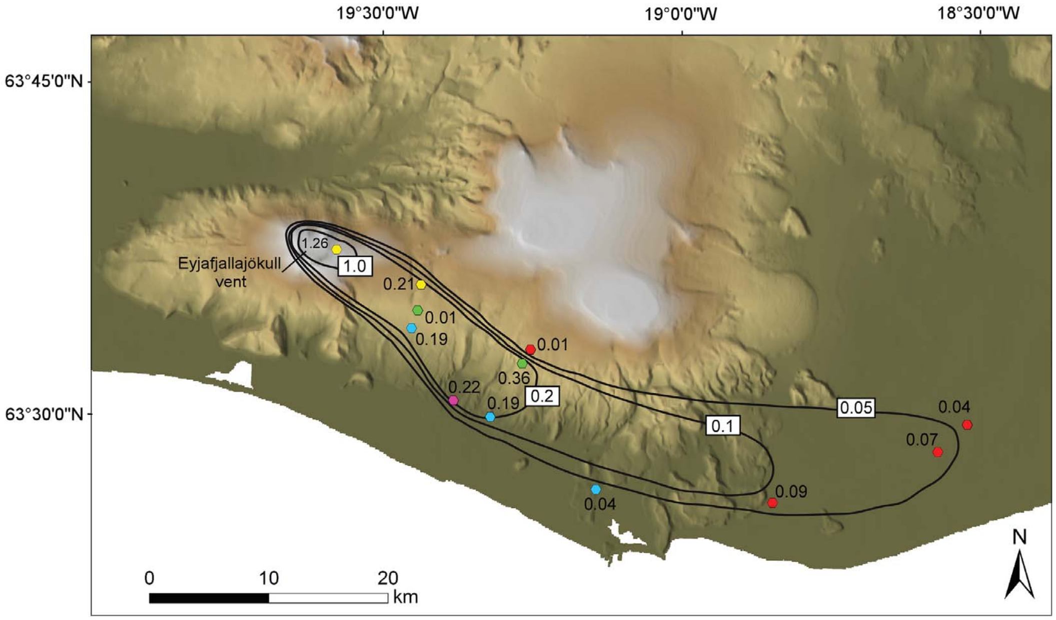

Figure 2. Isomass map (in kg m^{-2}) calculated from the accumulation rate in Table 1 for 30 min of activity (average of sampling time).

2.3. PLUDIX Experiments

[8] PLUDIX experiments were carried out between 5 and 8 May 2010 at locations between 2 and 56 km from the vent (Figure 1 and Table 1). PLUDIX is an X-band, continuous-wavelength, low-power (10 mW) Doppler radar (λ = 9.5 GHz) first dedicated to the characterization of rainfalls within a sampling volume defined as a cylinder of about 3 m high and 1 m wide (http://www.nubila.net/). Falling objects (e.g., water droplets, volcanic ash) crossing the antenna beam generate power echoes backscattered to the radar with a frequency shift related to the object velocity and displayed in real time as Doppler spectra, i.e., power spectral density versus Doppler frequency. The PLUDIX sensitivity to particle size ranges between 500 μm to a few centimeters. Here we have developed an inversion algorithm based on the method of *Gouhier and Donnadieu* [2008] to derive the size and number of particles from each Doppler spectrum (see section 3.3 for details).

2.4. MSG-SEVIRI Retrievals

[9] We began on-reception processing of all Meteosat Second Generation-Spinning Enhanced Visible and Infrared Imager (MSG-SEVIRI) images using the HotVolc Observing System (HVOS) platform starting from the onset of the eruption on 14 April 2010. HVOS has been developed at the Observatoire de Physique du Globe de Clermont-Ferrand (OPGC) and is dedicated to the real-time acquisition and processing of geostationary satellite data, such as Meteosat [*Labazuy et al.*, 2011]. The SEVIRI sensor on board the MSG operates at a very high temporal resolution, up to one image every 5 min, with a spatial resolution up to 1 km^2 and uses 12 channels ranging from the visible to the thermal infrared. Volcanic ash can often be distinguished from nonvolcanic atmospheric clouds using a brightness temperature difference (BTD) method based on the differential extinction features of ash between 11 and 12 μm channels [*Prata*, 1989]. Discrimination and properties characterization of ash within satellite use thermal infrared transmissive features of volcanic ash clouds. The transmission spectrum of volcanic ash is strongly wavelength dependent and has a broad absorption feature between 8 and 12 μm. It was shown that the difference between at-sensor Planck brightness temperatures observed in channels 11 and 12 μm, respectively, is negative in the presence of an ash cloud (BTD < 0), whereas water and ice will have a positive brightness temperature difference (BTD > 0). Then, inversion of the MSG-SEVIRI data based on look-up table (LUT) algorithm techniques [*Wen and R*ose, 1994] was used to provide quantitative parameters such as ash effective radius and ash mass loading in the atmosphere. The effective radius retrieved by this method represents an area-weighted radius and is actually defined as the ratio of the third to the second moment of a particle-size distribution. At a thermal infrared wavelength, the maximum effective radius to be retrieved lies around 15 μm. Note, however, that estimated size distributions may contain particles with actual radii larger than the effective radius.

Table 2. Summary of Samples Analyzed for Morphology Analysis[a]

Locality	Number of Particles	D_V Range (mm)
EJ14	386	0.02–32.00
EJ15	313	0.01–0.17
EJ17	313	0.01–0.36
EJ18	275	0.01–0.20
EJ19	313	0.01–0.20
EJ20	256	0.01–0.20
EJ24	313	0.01–0.43

[a]D_V is the diameter of the equivalent sphere. For the EJ14 sample, the sphericity of *Riley et al.* [2003], which is 2-D based, was determined only for particles between 0.02 and 14.3 mm (i.e., 286 particles) for which we had 2-D images.

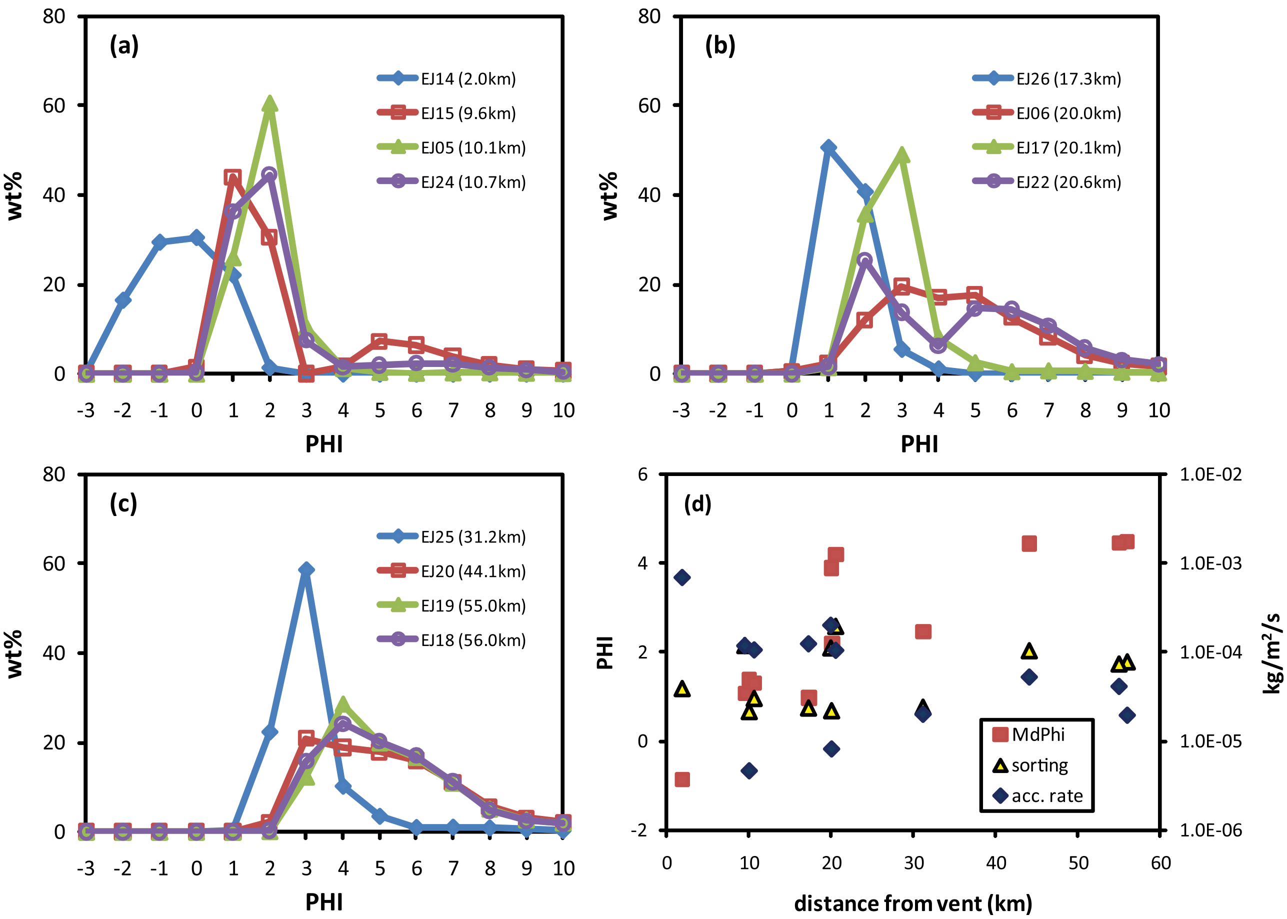

Figure 3. Grain-size distribution for (a) proximal, (b) medial, and (c) distal samples. Sample name and distance from the vent are indicated in the legend. (d) Variation of Mdphi, sorting, and accumulation rate with distance from the vent (the accumulation rate is plotted on a log axis).

[10] In the particular case of this study, the retrieval of ash particles inside each individual pixel has been carried out using a monodisperse distribution. We used the complex refractive index of andesite, 2.0534 + 0.60897*i* and 1.8392 + 0.13786*i* at 11 and 12 μm, respectively [*Pollack et al.*, 1973]. The reverse absorption technique often succeeds in detecting ash particles, especially in clear-sky conditions. However, nonash particles may sometimes have slightly negative BTDs, such as mixed ash-ice particles [e.g., *Pavolonis et al.*, 2006]. Therefore, in an attempt to select only pure-ash particles in our calculation, we set a cutoff BTD at −0.5 instead of 0. This technique ensures better confidence in the pure-ash particle detection, but may lead to a significant underestimation of the total mass of ash particles. Other sources of error potentially leading to incorrect negative BTDs, such as ground-surface temperature inversions or stratospheric cloud top altitude, are not encountered here. Minimum cloud top temperature and surface seawater temperature have been calculated using the 11 μm wave band.

[11] The 6 May 2010, eruption has been recorded as the most powerful episode of the April–May 2010 Eyjafjallajökull eruption in terms of ash amount ejected into the atmosphere [*Labazuy et al.*, 2011]. This corresponds to the day for which we also have detailed deposit and PLUDIX data.

3. Ground Observations

3.1. Tephra Accumulation Rate, Erupted Mass, Mass Eruption Rate, and Grain Size

[12] Tephra accumulation and tephra accumulation rate varied between 0.02 and 0.68 kg m^{-2} and 0.06–7 × 10^{-4} kg m^{-2} s^{-1}, respectively at different locations between 2 and 56 km from the vent and over collection periods between 600 and 8220 s (Table 1). Tephra accumulations at all locations have been normalized over 30 min in order to compile an isomass map for 30 min of activity and to capture transient eruptive behavior of a long-lasting eruption. The resultant map shows an evident dispersal toward south and southeast (Figure 2). Isomass lines on land could be constrained between 1 and 0.05 kg m^{-2}, equivalent to a thickness between 0.08 and 0.004 cm, using an average density of 1226 kg m^{-3} (average of all samples in Table 1, with the exception of the partial EJ15 samples). The associated erupted mass was estimated to 1.1 × 10^8 and 1.8 ± 0.3 × 10^8 kg, as calculated from the integration of one exponential segment and a power law fitting, respectively (according to the methods of *Pyle*

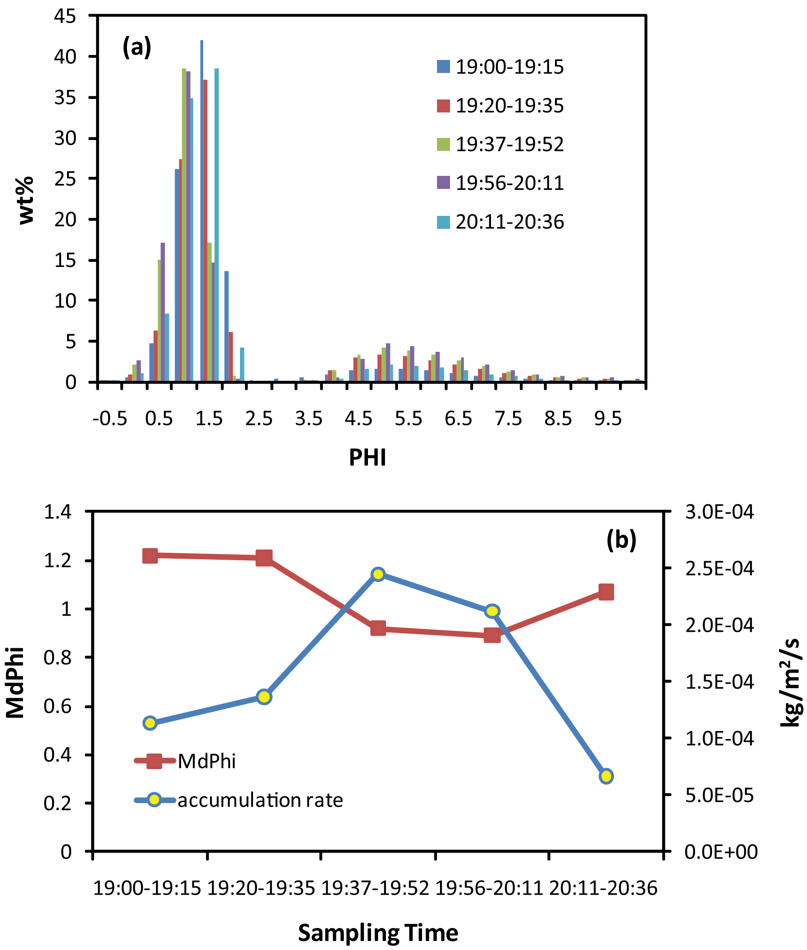

Figure 4. (a) Grain-size distribution sampled at sequential times at EJ15. (b) Variation of Mdphi and accumulation rate with time for the EJ15 sample (9.6 km from the vent).

[1989] and *Bonadonna and Houghton* [2005]). Equivalent volumes are 9.1×10^4 and $1.7 \pm 0.3 \times 10^5$ m^3, respectively. The distal integration limit for the power law integration was chosen between area$^{1/2}$ values of 50–100 km from the vent (considering an area$^{1/2}$ value of 21.4 km for the last isomass line, i.e., 0.05 kg m^{-2}). These values of erupted mass correspond to a mass eruption rate of 6.2×10^4 and $1.0 \pm 0.2 \times 10^5$ kg s^{-1} for 30 min of eruption, respectively. Integration of both the exponential [*Fierstein and Nathenson*, 1992] and the power law fit down to the last isomass line on land (i.e., 0.05 kg m^{-2}) results in about 9.7×10^7 kg, which is about 87% and 53% of the total erupted mass (whether the mass is calculated using the exponential or the power law fit, respectively).

[13] Associated tephra deposits show one or two populations (Figure 3) with Mdphi and sorting varying between −0.9–4.5 ϕ and 0.7–2.6 respectively. Mdphi increases from −0.9 at 2 km from vent to about 4 ϕ at 20 km from the vent, whereas sorting does not show any particular trend and remains pretty constant in the whole sampling area (Figure 3). The amount of fine ash (<63 μm) varies between about 0 and 20 wt % within the first 10 km and is mostly around 50–60 wt % beyond 20 km from the vent (Figure 3). The highest tephra accumulation rates are recorded within the first 20 km, reaching values of about 7×10^{-4} kg m^{-2} s^{-1} at 2 km from the vent (Figure 3). Beyond 20 km, accumulation rates vary between 0.2 and 0.08 × 10^{-4} kg m^{-2} s^{-1} (Table 1). Sequential sampling carried out at EJ15 (9.6 km from the vent) show how grain-size parameters do not vary significantly within 1.5 h of sampling (Mdphi = 0.9–1.2 ϕ; sorting = 0.6–2.4), with an accumulation rate ranging between 2.5 and 0.7×10^{-4} kg m^{-2} s^{-1}. All samples are bimodal, with main modes around 1.0 and 5.5 ϕ (Figure 4). A total grain-size distribution (based on the mass associated with 30 min of activity; Figure 2) was derived using the Voronoi tessellation technique [*Bonadonna and Houghton*, 2005], which is characterized by an Mdphi of 1.7 ϕ and sorting of 3.1 ϕ (Figure 5). The main mode is around 1ϕ with minor modes around −1 ϕ and 5 ϕ.

3.2. Analysis of Volcanic Particles and Aggregates

[14] Particle morphological parameters, as characterized based on the sphericity of *Riley et al.* [2003] and *Aschenbrenner* [1956] and the shape factor of *Wilson and Huang* [1979], all show a similar trend with no significant variation with particle size and distance from the vent (Figure 6). The sphericity of *Aschenbrenner* [1956] (i.e., 0.91 ± 0.02, average and standard deviation of the medians of each sample) is characterized by larger and less variable values than the sphericity of *Riley et al.* [2003] (i.e., 0.83 ± 0.04) and the shape factor of *Wilson and Huang* [1979] (i.e., 0.79 ± 0.01). The morphology of

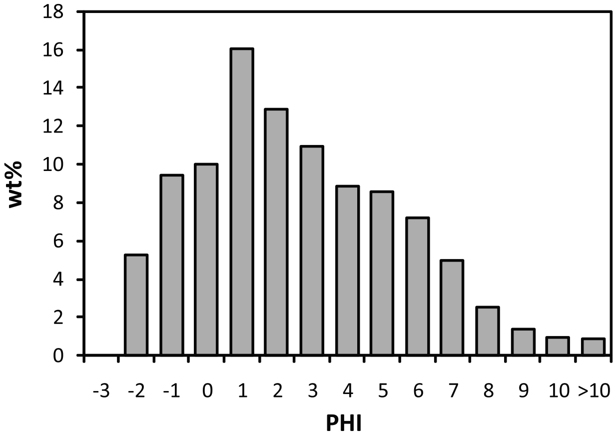

Figure 5. Total grain-size distribution based on the application of the Voronoi tessellation technique to the isomass map of Figure 2.

sedimenting tephra was also investigated on samples collected between 2 and 56 km from the vent on adhesive tape and analyzed using the SEM of the University of Geneva and the University of Pisa. Particles mostly fell as both particle clusters and accretionary pellets according to the nomenclature of *Brown et al.* [2011]. Particle clusters were observed as ash clusters and coated particles (PC1 and PC2), whereas accretionary pellets were observed as poorly structured pellets and liquid pellets (AP1 and AP3) (Figure 7). While the first two types are ubiquitous in the collected samples, poorly structured pellets were observed only at the EJ18 and EJ22 locations and liquid pellets were retrieved only at the EJ06 location, with no direct relation with the occurrence of meteoric rains (Table 3). Nonetheless, collections carried out sequentially on 4, 5, and 6 May showed that aggregate typologies changed spatially. Dedicated SEM grain-size analyses on nine aggregates from samples EJ06, EJ15, EJ18, and EJ22 have shown that they mainly consist of particles <63 μm (>5 ϕ), with liquid pellets (AP3) showing also particles between 125 and 63 μm (4 ϕ) (Figure 8). Associated Mdphi and sorting vary between 4.0 and 6.2 ϕ and 0.5 and 1.2, respectively (Table 3 and Figure 8).

3.3. PLUDIX Measurements

[15] Investigations carried out during the 2010 Eyjafjallajökull eruption using PLUDIX measurements have confirmed that ground-based Doppler radars are valuable tools for real-time retrieval of settling velocities that can be used to derive the particle grain-size distribution of volcanic ash in nearly real time [*Gouhier and Donnadieu*, 2008; *Hort et al.*, 2003; *Scollo et al.*, 2005]. Preliminary results of ash detection using PLUDIX were first carried out by *Scollo et al.* [2005] during the 2002 Etna eruption. Here we performed a complete inversion of PLUDIX data that allowed for a quantitative estimate of the particle-size distribution of volcanic ash (Figure 9). First, particle velocities are converted into sizes using the settling-velocity model of *Kunii and Levenspiel* [1969]. Then, the number of particles is derived from the inversion of the radar power, carried out from the calculation of synthetic Mie backscattering cross-section coefficients [*Gouhier and Donnadieu*, 2008] (Figure 9). In particular, following the work of *Gouhier and Donnadieu* [2008], the strength of backscattered energy detected by the instrument (P_r) is compared with the synthetic value (P_s), computed as

$$P_s = \frac{C_r V_s \eta}{R^4} \tag{1}$$

where C_r is the radar constant, V_s is the volume of measure, R is the mean target distance, and η is the radar reflectivity, expressed as

$$\eta = \sum_{i=1}^{n} \frac{\sigma_{bks(i)}}{V_s} \tag{2}$$

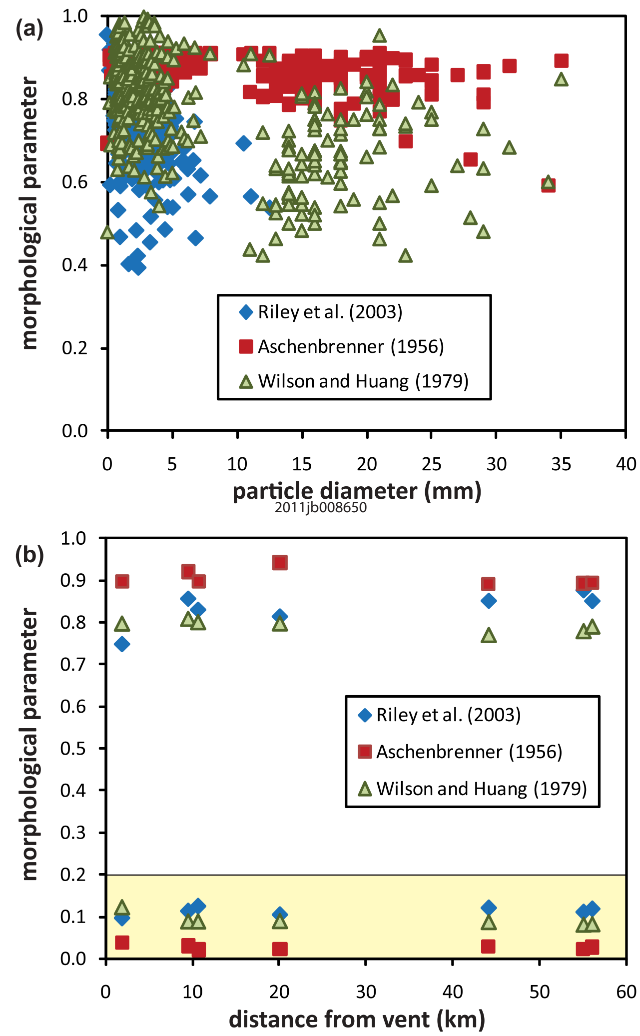

Figure 6. Morphological variation (a) with particle size (for the EJ14 sample; particle diameter refers to the intermediate diameter) and (b) with distance from the vent (for samples EJ14, EJ15, EJ17, EJ18, EJ19, EJ20, EJ24) as characterized according to *Riley et al.* [2003], *Aschenbrenner* [1956], and *Wilson and Huang* [1979]. Values at the top of the plot represent the median of each morphological parameter, whereas values in the shaded area at the bottom of the plot indicate the standard deviation. The 2-D-based sphericity of *Riley et al.* [2003] was calculated only for particles up to about 14 mm, for which 2-D images could be taken (see section 2 for details).

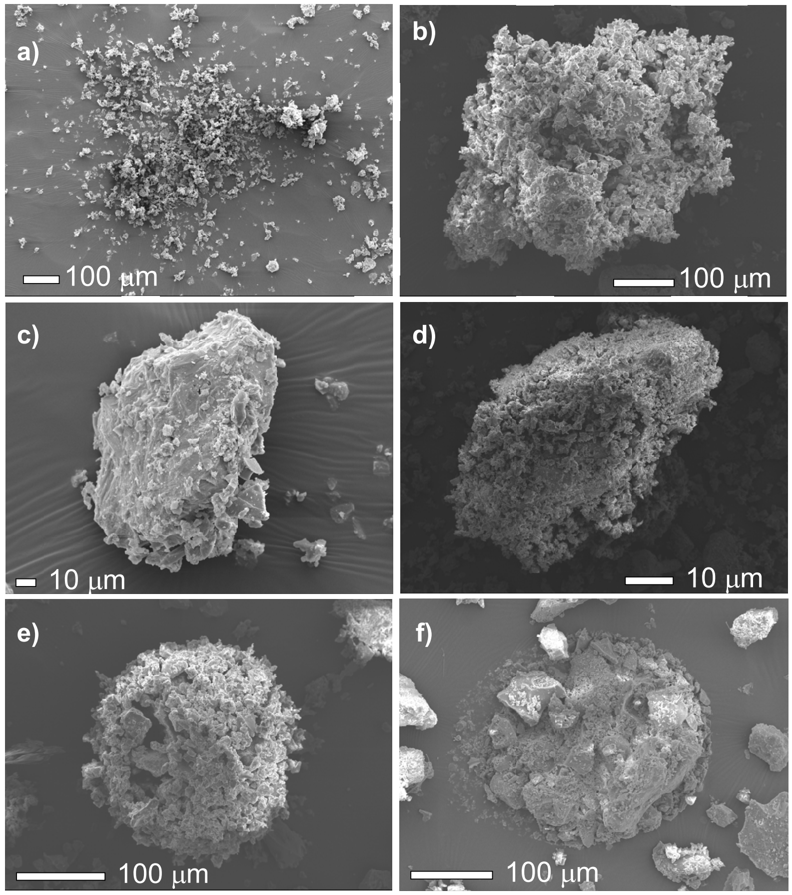

Figure 7. SEM images of ash aggregates: (a) broken ash cluster (EJ15), (b) ash cluster (EJ22), (c) coated particle (EJ15), (d) coated particle (EJ22), (e) poorly structured pellet (EJ18), and (f) liquid pellet (EJ06) (see also Table 3 for more details).

where σ_{bks} is the backscattering cross section of individual particles, calculated based on Mie scattering coefficients. As a result, the particle-size frequency distribution per unit of volume can be obtained. The conversion of concentration (N m^{-3}) into the particle accumulation rate (N m^{-2} s^{-1}) is then achieved by multiplying the number of particles for each size class by the corresponding terminal velocities. The number of particles is then multiplied by the particle mass computed under the assumption of spherical shape and homogeneous particle density, and the groundmass loading (kg m^{-2}) is obtained by integrating over the period of PLUDIX acquisition.

[16] Field experiments on particle sedimentation were carried out during the Eyjafjallajökull eruption on 5–8 May 2010 between 2 and 56 km from the vent under different accumulation rates and grain-size conditions. Collection times varied between about 15 and 100 min in the east and southeast of the volcano according to the prevailing wind direction. For simplicity, here we present only the results associated with the localities EJ14 (2.0 km from the vent; accumulation rate, 7.0×10^{-4} kg m^{-2} s^{-1}; clast size, mostly <8 mm), EJ15 (9.6 km from the vent; accumulation rate, 1.2×10^{-4} kg m^{-2} s^{-1}; clast size, <2 mm), and EJ17 (20.1 km from the vent; accumulation rate, 0.08×10^{-4} kg m^{-2} s^{-1}; clast size, <500 μm) in order to investigate various conditions of sedimentation rate and clast size. For these three samples we calculated the PLUDIX-derived particle-size distribution and compared this with the particle-size distribution of ash collected on the ground during PLUDIX data acquisition (Figures 10 and 11). EJ14 shows a well-defined Gaussian distribution in the range 300–900 Hz, with a main peak around 600 Hz and smaller secondary peaks at 147, 100, and 30 Hz. Sample EJ15 shows a less-pronounced Gaussian distribution between 150 and 350 Hz, with a main peak around 200 Hz and smaller secondary peaks at 25 and 37 Hz. PLUDIX recordings at the EJ17 site do not show any Gaussian distributions but only discrete peaks around 50 Hz. The well-pronounced Gaussian distributions of EJ14 and EJ15 correspond to settling velocities between 5.0 and 14.0 m s^{-1} (with the main peak around 10 m s^{-1}) and 2.5 and 5.5 m s^{-1}, respectively. The maximum velocity recorded at EJ14 is 16 m s^{-1}, which also represents the upper detection limit of PLUDIX. Such a velocity corresponds to a particle diameter of about 10 mm, assuming a density of 986 kg m^{-3}. Measured velocities were converted into grain sizes based on our inversion algorithm resulting in grain sizes ranging between 1 and 6 mm for EJ14 and <1 mm for EJ15 (Figure 11). Most particles of EJ17 are <0.5 mm and grain sizes could not be derived. We can conclude that PLUDIX-derived particle-size distributions agree reasonably well with sieve-derived grain-size distributions only for ϕ classes of ≤ 0.5 ϕ (diameter > 0.75 mm), with an

Table 3. Summary of the Characteristics of Aggregates Collected in Situ on Sticky Collectors[a]

SAMPLE (Collection Date)	Distance From Vent	PC1 (μm)/Aggregating Particles (μm)	PC2 (μm)/ Aggregating Particles (μm)	AP1 (μm)/ Aggregating Particles (μm)	AP3 (μm)/ Aggregating Particles (μm)	Comments
EJ06 (4 May)	20 km	NO	330–700/<50	NO	150–3000/<1000 Mdϕ (3): 4.0–5.3; σ (3): 0.8–1.0	local rain through the cloud; most AP3 show bimodal grain-size distributions; mean AP3 diameter, 1.2 mm (based on 12 measurements)
EJ15 (5 May)	9.6 km	NM/<80 Mdϕ (2): 5.6–5.7; σ (2): 0.5–1.0	<700/<10 Mdϕ (2): 4.9–5.9; σ (2): 0.9–1.2	NO	NO	combination of PC1 and PC2; PC1 are well sorted and do not typically have a big particle as nucleus; most PC1 broke on impact with collector and measurement of original diameter was not possible
EJ17 (6 May)	20.1 km	20–70/<50	<760/<50	NO	NO	mostly consists of PC2; some PC2 have most of their surface coated with small particles, whereas some PC2 are coated only for about 10% of their surface (mainly glass and plagioclase as nuclei)
EJ18 (6 May)	56.0 km	200–380/<70	<350/<40 Mdϕ (1): 6.2; σ (1): 0.8	130–250/<50 Mdϕ (1): 5.6; σ (1): 0.9	NO	characterized by the presence of more aggregates than free particles (mostly PC1); aggregates appear all very compact and homogenous in constitutive particles; this is the sample in which we observed the largest amount of AP1; some AP1 show the presence of a nucleating particle inside
EJ19 (6 May)	55.0 km (3.4 km from EJ18)	120–280/<90	<300/<100	NO	NO	mostly consists of PC2, but more PC1 than in EJ20
EJ20 (6 May)	44.1 km (14.5 km from EJ19)	<260/<50	<430/<70	NO	NO	mostly consists of PC2
EJ22 (7 May)	20.6 km	100–600/<40 Mdϕ (1): 5.5; σ (1): 1.2	400–700/<40 Mdϕ (1): 6.2; σ (1): 0.9	240–350/<30 Mdϕ (1): 5.8; σ (1): 0.8	NO	mostly consists of PC2; smooth transition from PC2 to both PC1 and AP1 characterized by the presence of large particles acting as nuclei

[a]PC1, PC2, AP1, and AP3 are ash clusters, coated particles, poorly structured pellets, and liquid pellets, respectively, according to the nomenclature of *Brown et al.* [2011]. Observed sizes of aggregates and aggregating particles are reported (the smallest aggregating particles that could be detected are around 0.3 μm). Mdphi (Mdϕ) and sorting (σ) of aggregating particles of selected aggregates derived based on 2-D image analysis are also indicated (number of aggregates analyzed is specified in parentheses) (see also Figure 8 for more details). NM, not measurable; NO, not observed.

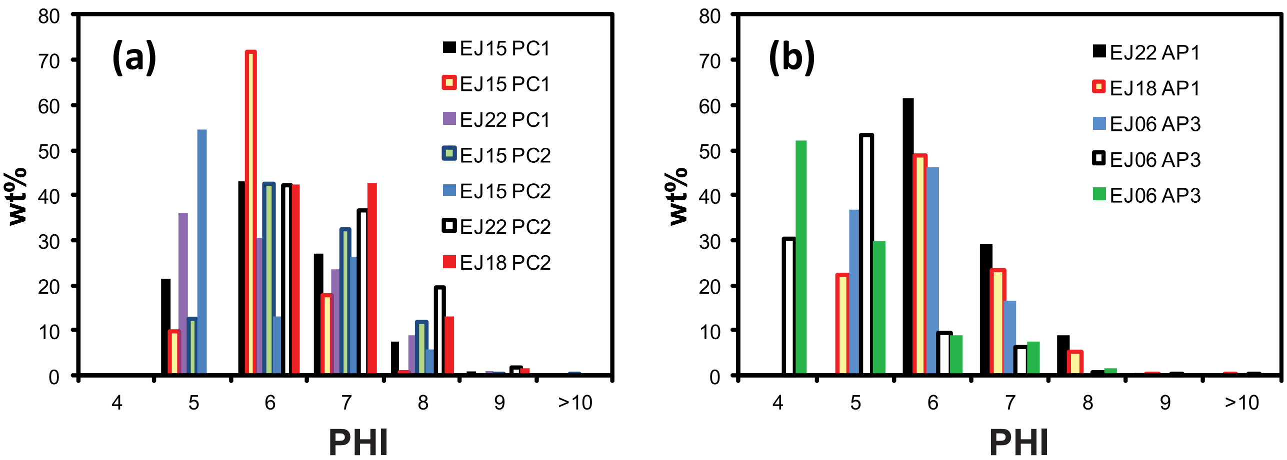

Figure 8. SEM-derived grain-size distributions of (a) particle clusters (ash clusters, PC1 including images in Figures 7a and 7b, and coated particles, PC2, from samples EJ15, EJ18, and EJ22) and (b) accretionary pellets (poorly structured pellets, AP1, including image of Figure 7e, and liquid pellets, AP3, from samples EJ06, EJ18, and EJ22). Mdphi is 5.7, 5.6, 5.5, 4.9, 5.9, 6.2, 6.2 for PC1 and PC2 of Figure 8a and 5.8, 5.6, 4.4, 5.3, 4.0 for AP1 and AP3 of Figure 8b (see also Table 3 for more details).

excellent agreement for classes of ≤1 ϕ (diameter > 0.5 mm) (Figure 11). Nonetheless, the PLUDIX-derived grain size significantly overestimates the weight percents of particles >0.5 ϕ (<0.75 mm). This is interpreted as the effect of the ground echoes developing around the central line of the Doppler spectrum (~0 m s^{-1}), which significantly affects the spectral content below 150 Hz, resulting in a high noise level. Moreover, the observed discrete peaks below 150 Hz,

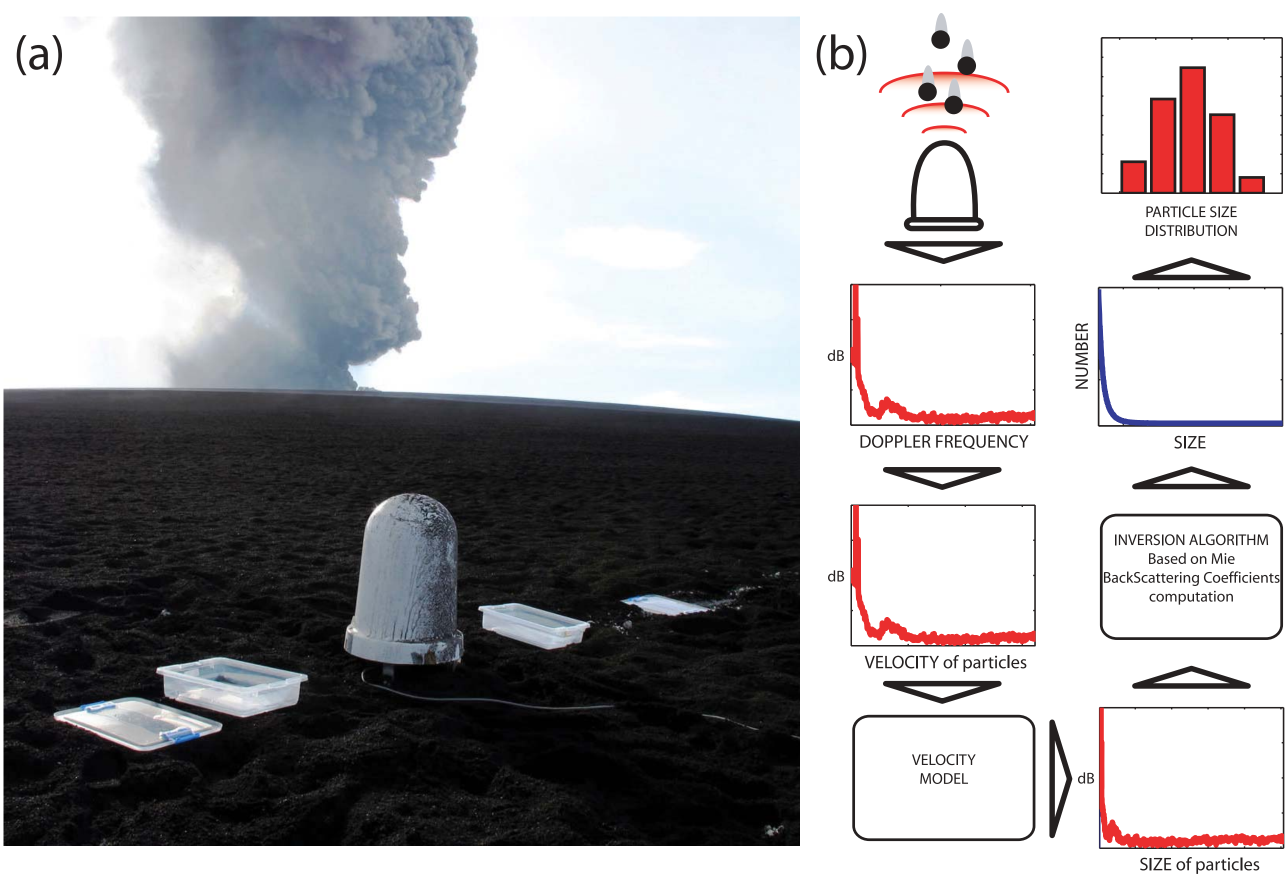

Figure 9. (a) Doppler radar (PLUDIX) during field measurements during May 2010 (EJ14). (b) Conceptual model for the derivation of particle-size distribution from settling velocity data.

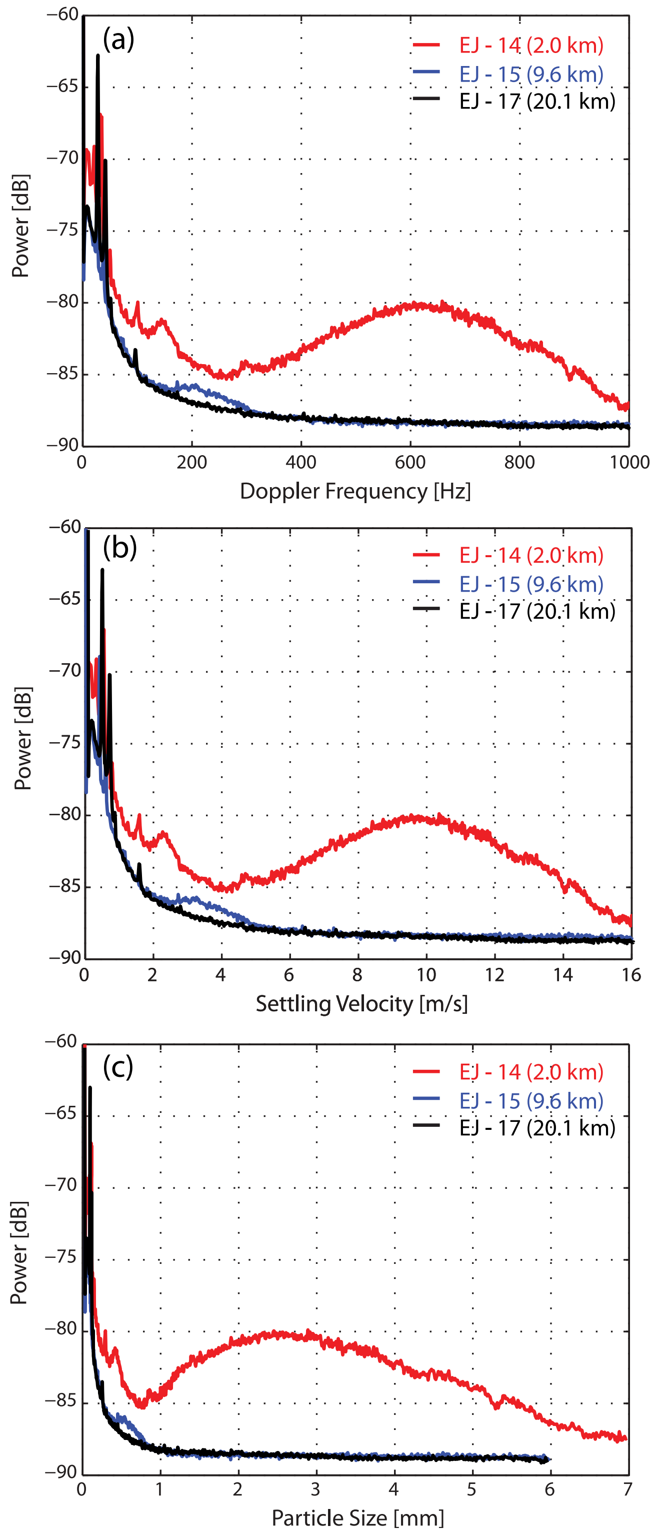

Figure 10. (a) Doppler spectrum averaged over the acquisition time for EJ14, EJ15, and EJ17; (b) associated settling velocities; and (c) grain-size distribution (derived assuming a density of 1443 kg m^{-3} for EJ14, 1683 kg m^{-3} for EJ15, and 1689 kg m^{-3} EJ17, which were weighted for particles ≥500 μm according to the parameterization of *Bonadonna and Phillips* [2003]; see section 3.3 for details).

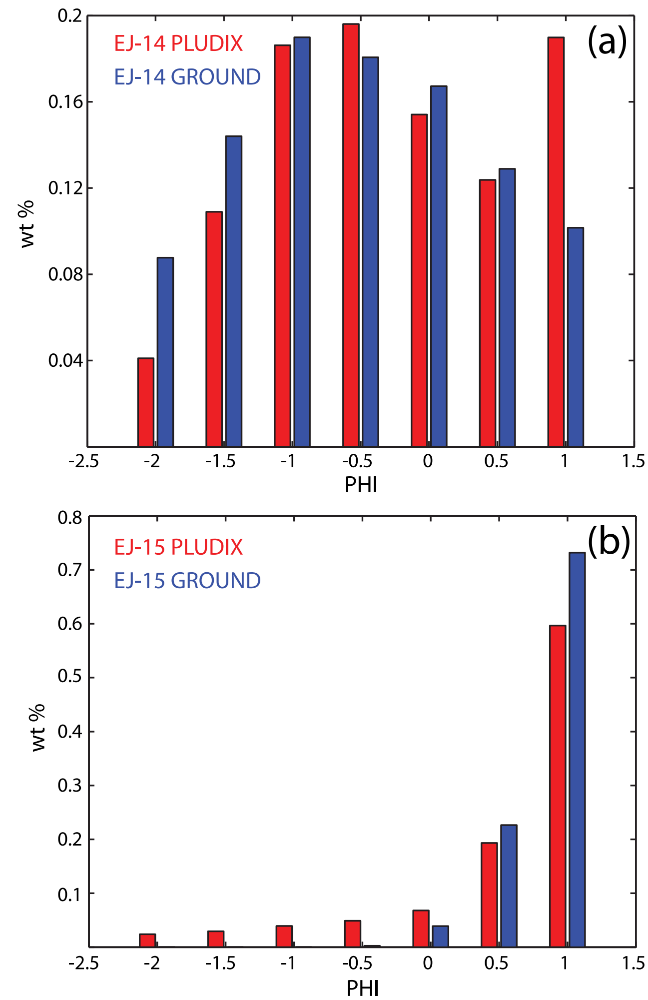

Figure 11. Comparison between PLUDIX-derived grain-size data (gray histograms) and manually sieved data (black histograms) at (a) EJ14 (2 km from the vent) and (b) EJ15 (20 km from the vent). Distributions are normalized with respect to the whole sample weight and the sum of selected size categories if 100% (−2 to 1 ϕ).

once converted into sizes, show no good agreement with the observed grain-size distributions, suggesting no clear relation with the particle terminal velocities.

[17] The application of our inversion algorithm for the conversion of measured velocities into particle size requires a constant particle density. We considered a mean density of the particles >0.5 mm (i.e., particles detected by the PLUDIX), which was calculated based on the parameterization of *Bonadonna and Phillips* [2003] (i.e., linear increase of density between −3 and 7 ϕ), the calculated density of lapilli that fell at EJ14 (i.e., 986 kg m^{-3}), and the density of nonvesicular material derived with the pycnometer (i.e., 2738 kg m^{-3}). Resulting values are 1443 kg m^{-3} for EJ14, 1683 kg m^{-3} for EJ15, and 1689 kg m^{-3} for EJ17. Particle density significantly affects the resulting particle size based on the velocity model considered (Figure 12a). As a consequence, the PLUDIX-derived grain-size distribution strongly depends on the density assumption (Figure 12b). The use of a mean value is justified by Figure 12b, which shows how the two end-members (i.e., density of lapilli and

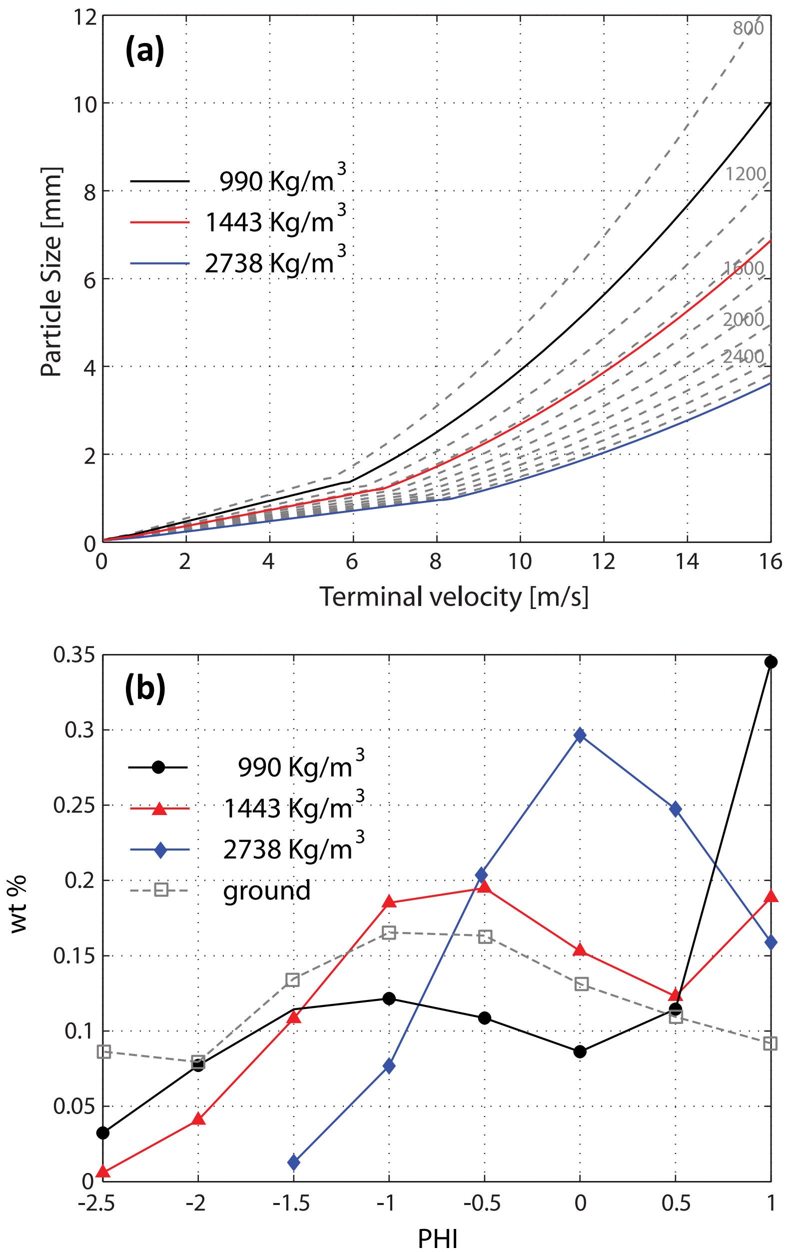

Figure 12. (a) Relationship between velocities and particle sizes according to the model of *Kunii and Levenspiel* [1969] for different density values (gray dashed lines). The two end-member densities, reported in color, as measured for EJ14 samples (blue and black) and the averaged density value (red). (b) Examples of grain-size distribution computation for EJ14 using different density values (blue, red, and black lines) in comparison with the distribution derived from ground sampling (gray).

density of nonvesicular material) show the worst fit with field data. Nonetheless, the use of the mean value also results in an overestimation of the fine-ash fraction and a slight underestimation of the coarse-ash fraction (Figure 12b).

[18] The algorithm used to derive particle size from PLUDIX settling velocities was compared with the settling velocities of samples EJ14, EJ15, and EJ17, theoretically derived according to the models of *Kunii and Levenspiel* [1969], *Wilson and Huang* [1979], and *Ganser* [1993] (Figure 13). The model of *Kunii and Levenspiel* [1969] is based on the assumption of a spherical shape of the particles, and the settling velocity (V) is calculated using specific settling laws in relation to the Reynolds number (Re) of the particles:

$$V = \left(\frac{g\rho Dv^2}{\rho_s}\right); \mathrm{Re} < 0.4, \tag{3}$$

$$V = Dv\sqrt[3]{\frac{4\rho^2 g^2}{255\mu\rho_s}}; \; 0.4 < \mathrm{Re} < 500, \tag{4}$$

$$V = \sqrt{\frac{3.1 g\rho Dv}{\rho_s}}; \; \mathrm{Re} > 500, \tag{5}$$

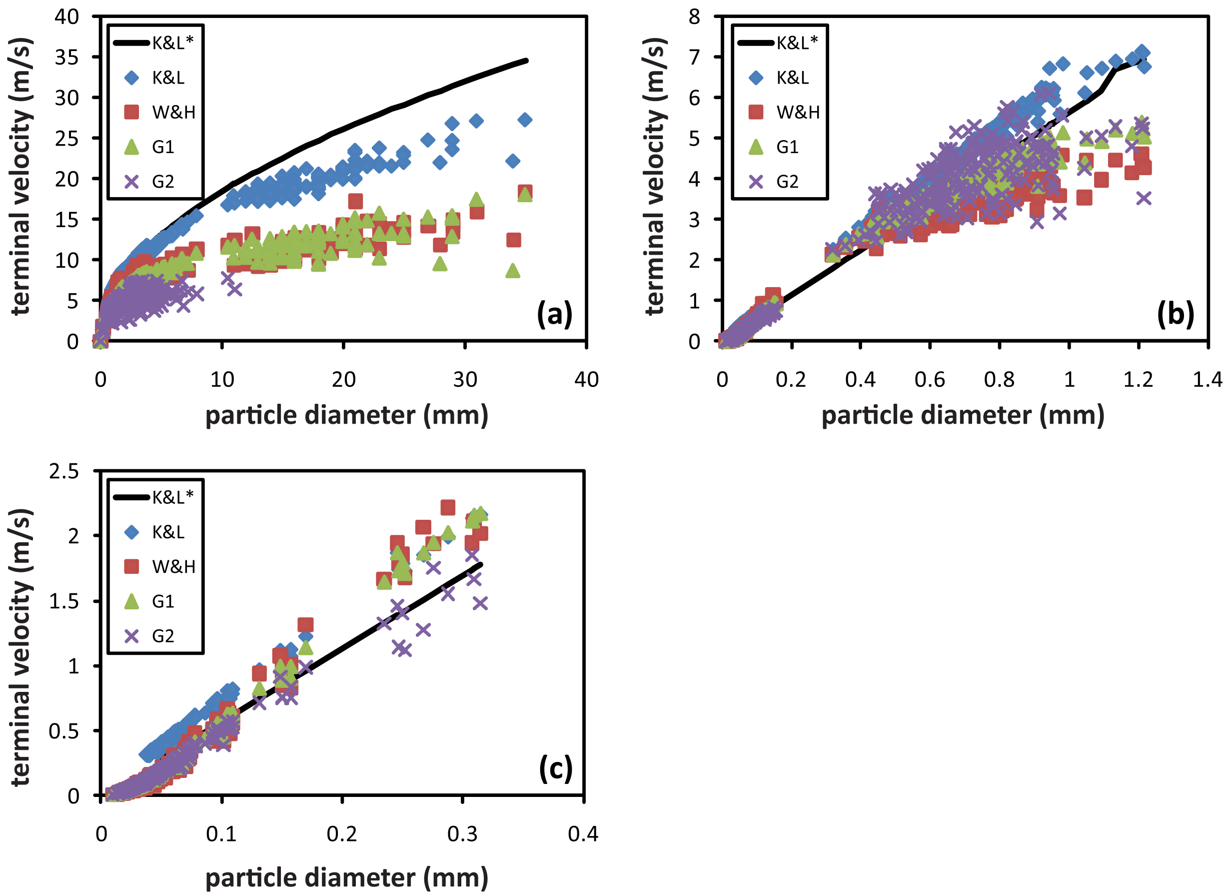

Figure 13. Comparison between the algorithm used to derive particle size from PLUDIX settling velocities (K&L* [*Kunii and Levenspiel*, 1969], with fixed particle density) and settling velocities theoretically derived with variable particle densities [i.e., *Kunii and Levenspiel*, 1969; *Ganser*, 1993; *Wilson and Huang*, 1979] for clasts of (a) EJ14, (b) EJ15, and (c) EJ17. K&L [*Kunii and Levenspiel*, 1969], W&H [*Wilson and Huang*, 1979], and G1 [*Ganser*, 1993], using the 2-D-derived sphericity of *Riley et al.* [2003]; G2 [*Ganser*, 1993], using the geometrical sphericity of *Aschenbrenner* [1956] (see also Figure 6). The settling velocity is calculated based on a particle diameter equivalent to D_v and plotted against the particle intermediate radius for comparison with PLUDIX data. The particle density may vary between 986 and 2738 kg m^{-3} according to the parameterization of *Bonadonna and Phillips* [2003].

where g is the gravity acceleration, ρ is the density of the particle, D_v is the diameter of the equivalent sphere, and ρ_s and μ are the density and the dynamic viscosity, respectively, of the air.

[19] The models of *Wilson and Huang* [1979] and *Ganser* [1993] are based on the calculation of the drag coefficient. In particular, according to the model of *Wilson and Huang* [1979], the drag coefficient is expressed by

$$C_D = \frac{24}{\mathrm{Re}} F^{-0.828} + 2\sqrt{1.07 - F}, \tag{6}$$

where F is the shape factor. *Ganser* [1993] defines the drag coefficient as

$$C_D = \left\{ \frac{24}{\mathrm{Re} K_1 K_2} \left[1 + 0.1118 (\mathrm{Re} K_1 K_2)^{0.6567} \right] + \frac{0.4345}{1 + \frac{3305}{\mathrm{Re} K_1 K_2}} \right\} K_2. \tag{7}$$

The two coefficients K_1 and K_2 express the influence of the morphology on the drag coefficient and are expressed according to

$$K_1 = \left(\frac{1}{3} \frac{I}{Dv} + \frac{2}{3} \Psi^{-1/2} \right)^{-1} - 2.25 \frac{Dv}{3305}, \tag{8}$$

$$K_2 = 10^{1.8148 (-\log \Psi)^{0.5743}}, \tag{9}$$

where Ψ and I are the sphericity and the average diameter, respectively, of the projected area of the particle. The scatter of settling velocity values in Figure 13 is due to the fact that the settling velocity is calculated based on D_v (see Appendix A) but is plotted versus the particle intermediate diameter for simplicity of comparison with the PLUDIX algorithm that is also based on the particle intermediate diameter. Discrepancies of the PLUDIX algorithm (solid line in Figure 13) with the settling velocities of perfect spheres with variable densities according to the model of *Kunii and Levenspiel* [1969] (blue diamonds in Figure 13)

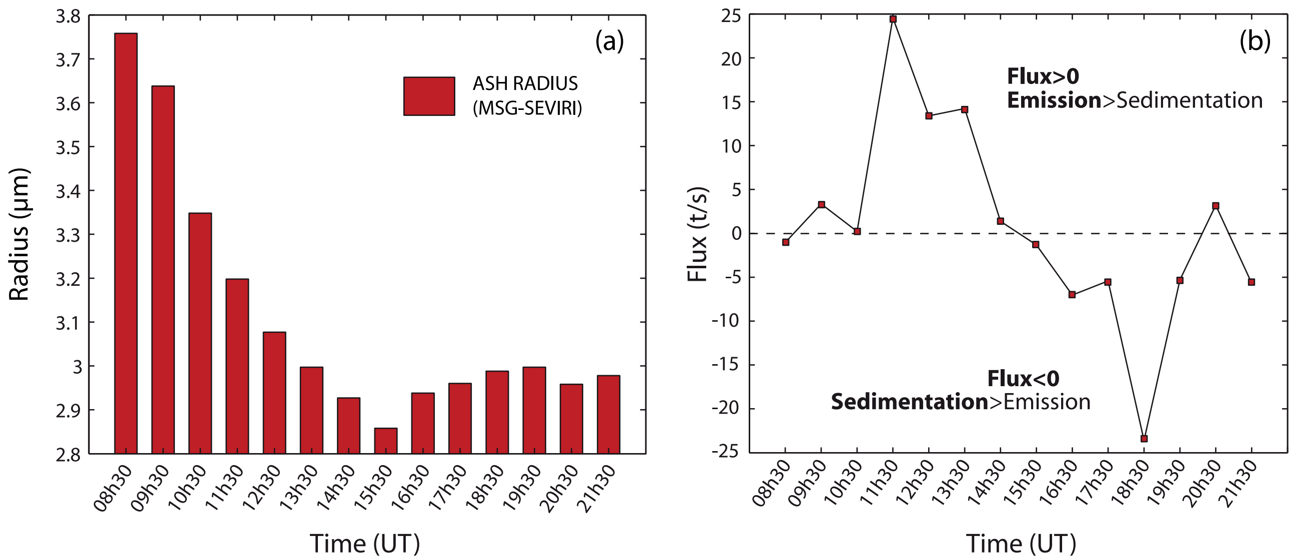

Figure 14. Time series of (a) mean ash radius and (b) ash mass flux inside the Eyjafjallajökull ash plume on 6 May 2010, from 08:30 UT to 22:30 UT using MSG-SEVIRI data.

are of the order of ±50% for EJ14, 3% to −80% for EJ15, and −10% to −80% for EJ17. These discrepancies are related to the different particle densities used. In fact, as mentioned above, because of the necessity of inverting velocity data to derive particle size, the density of particles in the PLUDIX algorithm is kept fixed at a value that represents the density weighted average for particles >0.5 mm (i.e., particles detectable by the PLUDIX). Both the PLUDIX algorithm and the model of *Kunii and Levenspiel* [1969] with variable particle densities result in larger values of settling velocities with respect to the models of *Wilson and Huang* [1979] and *Ganser* [1993] for particles >1 mm. In contrast, the models of *Wilson and Huang* [1979] and *Ganser* [1993], based on the sphericity of *Aschenbrenner* [1956], show similar results for all three samples analyzed, whereas the model of *Ganser* [1993], based on the sphericity of *Riley et al.* [2003], result in slightly lower values.

4. Satellite Observations

4.1. Ash Retrieval for 6 May 2010

[20] The thorough analysis of the 6 May episode using high-sampling-rate satellite data well complements ground-based techniques as resulting data provide insights on the dynamics of an ash cloud far from the vent (>100 km) and better assess transport and sedimentation processes on a large spatial scale. Maps of hourly ash mass concentration and radius from 8:30 to 22:30 UT on 6 May 2010 show that ash mass loading ranged from 0.5 to 5 × 10^{-3} kg m^{-2}, and mean ash radii ranged from 1 to 4 μm. Ash radius and concentration roughly decreased with distance from the vent. The transport of volcanic ash into the atmosphere is directly driven by the wind field direction and velocity, which may widely vary with altitude. From the processing of MSG-SEVIRI images of 6 May, we calculate that the ash cloud drifted southeastward over about 1300 km from 08:30 to 22:30, giving a mean cloud displacement velocity of about 26 m s^{-1}. During the same period, wind velocity was around 13 m s^{-1} at the plume-height level, showing that the cloud must have been also characterized by a diffusion and/or gravitational component in the downwind spreading. The minimum cloud top temperature used as an input to the reverse absorption technique was measured using the 11 μm channel and found to be about 240 K. Both wind field and temperature information yield an ash cloud top altitude of 6700 m (in good agreement with the 6 h based average of IMO plume-height data for the 6 May 2010), i.e., emissions were only tropospheric.

4.2. Ash Radius and Mass Loading

[21] At the onset of the time series (08:30 UT) the emissions were still weak, with a mean radius of 3.76 μm and a mass flux of ash injected into the atmosphere <5 × 10^3 kg s^{-1} (Figure 14). The mean ash radius then continuously decreased down to 2.86 μm at 15:30 UT. On the other hand, the ash emission intensity increased until 11:30 UT, reaching a mass flux of 25 × 10^3 kg s^{-1}. The continuous decrease of the effective radius recorded inside the ash cloud could be interpreted as a steady sedimentation mechanism that made coarse particles fall down close to the vent. However, the simultaneous increase of the mass flux suggests that this sedimentation mechanism could also be associated with an increase of the volcanic explosivity at the source, which could be associated with a more efficient fragmentation and therefore with a larger amount of fine ash. At 16:30 UT a new episode of weak emission occurred, yielding a mean particle radius up to 3.05 μm. At the same time, the mass flux became negative, showing that ash particle sedimentation was higher than ash particle injection into the atmosphere.

[22] The detailed analysis of the single MSG-SEVIRI image occurring at 08:30 has allowed for the retrieval of the particle-size distribution inside the ash cloud located close to the ground sampling area EJ18 (Figure 15a). Note, however, that EJ18 is located at about 56 km from the vent while the main cloud observed by MSG-SEVIRI is located at about 130 km from the vent. The diameters of ash

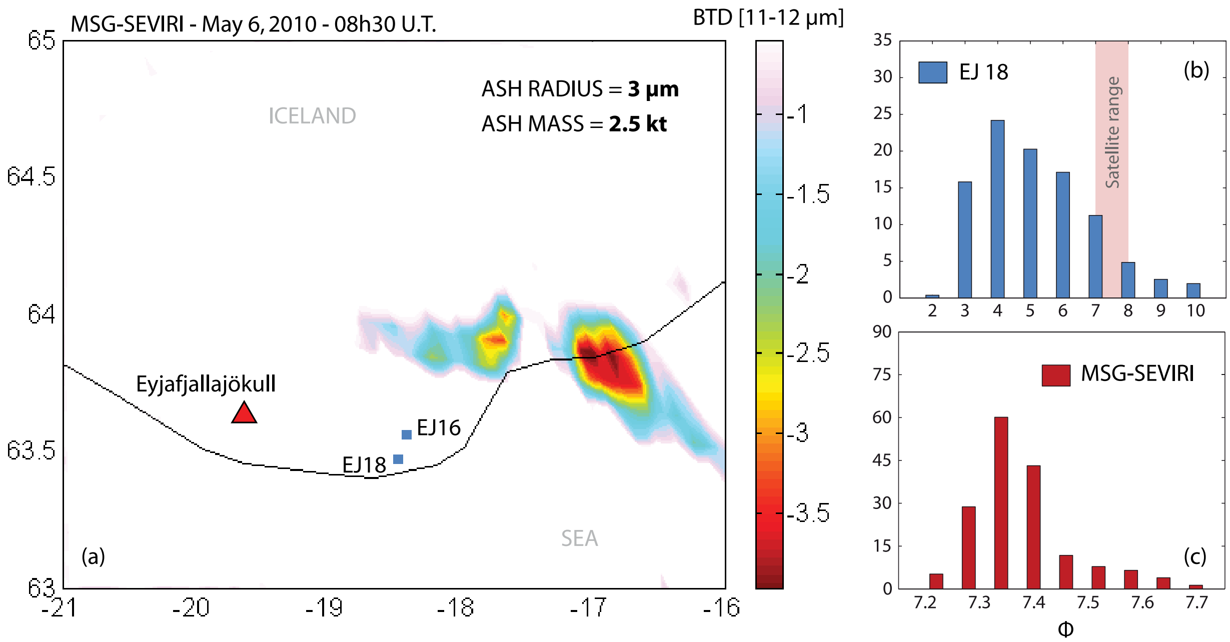

Figure 15. (a) Map of the Eyjafjallajökull ash cloud highlighted by the negative brightness temperature difference (11–12 μm), showing the particle-size distributions derived from both (b) ground sampling measurements (EJ18) and (c) MSG-SEVIRI data. The location of EJ16 is also shown as no ash fall was recorded around 14:00 UT.

particles sampled at EJ18 ranged between 2 and 10 ϕ (Figure 15b) while ash particle diameters estimated from the satellite ranged between 7.2 and 7.7 ϕ (Figure 15c). Using the total area of the ash cloud, we could deduce an average estimate of the sedimentation rate on the whole cloud of 0.2–0.4 × 10^{-6} kg m^{-2} s^{-1}. By comparison with ground sampling measurements carried out much closer to the vent (EJ18 = 56 km from the vent), we obtained an accumulation rate of about 0.2 × 10^{-4} kg m^2 s^{-1}. The lack of continuity between radius sensitivity of ground deposits and satellite retrievals could be responsible for such a discrepancy. In fact, EJ18 sedimentation was associated with a larger size range, including particles larger than the satellite effective radius sensitivity (≈15 μm).

[23] The ash radius and concentration calculated inside the Eyjafjallajökull cloud on 6 May 2010 at 19:30 is shown in Figure 16. The mean ash radius on the whole image was about 3 μm, with minimum and maximum values equivalent to 1 and 4 μm, respectively (Figure 16a). The particle-size distribution shows three distinct modes at 1.2 μm

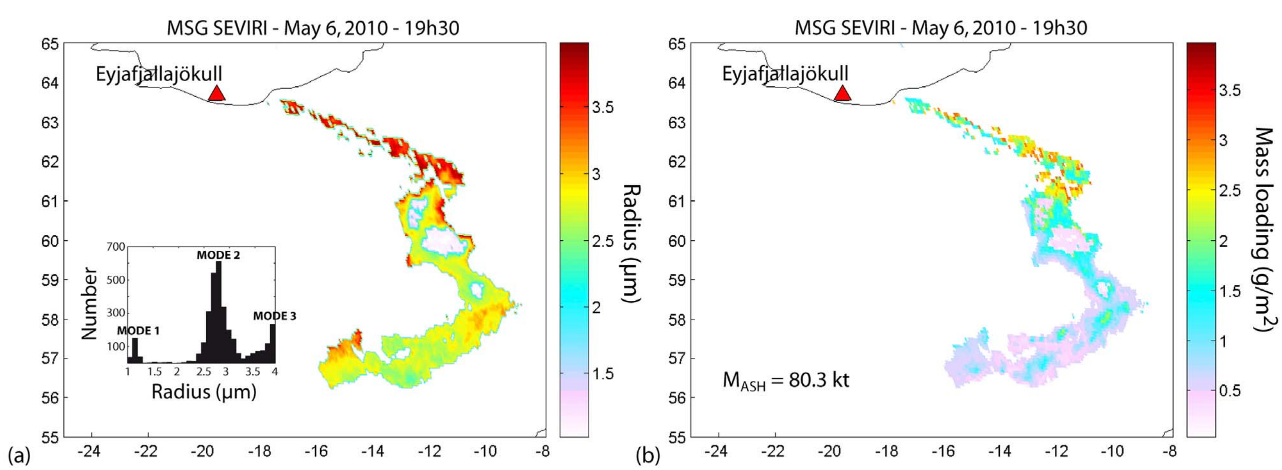

Figure 16. Detailed map of (a) ash effective radius with the corresponding particle-size distribution showing three main modes, (b) ash mass loading inside the Eyjafjallajökull ash plume on 6 May 2010 at 19:30 UT.

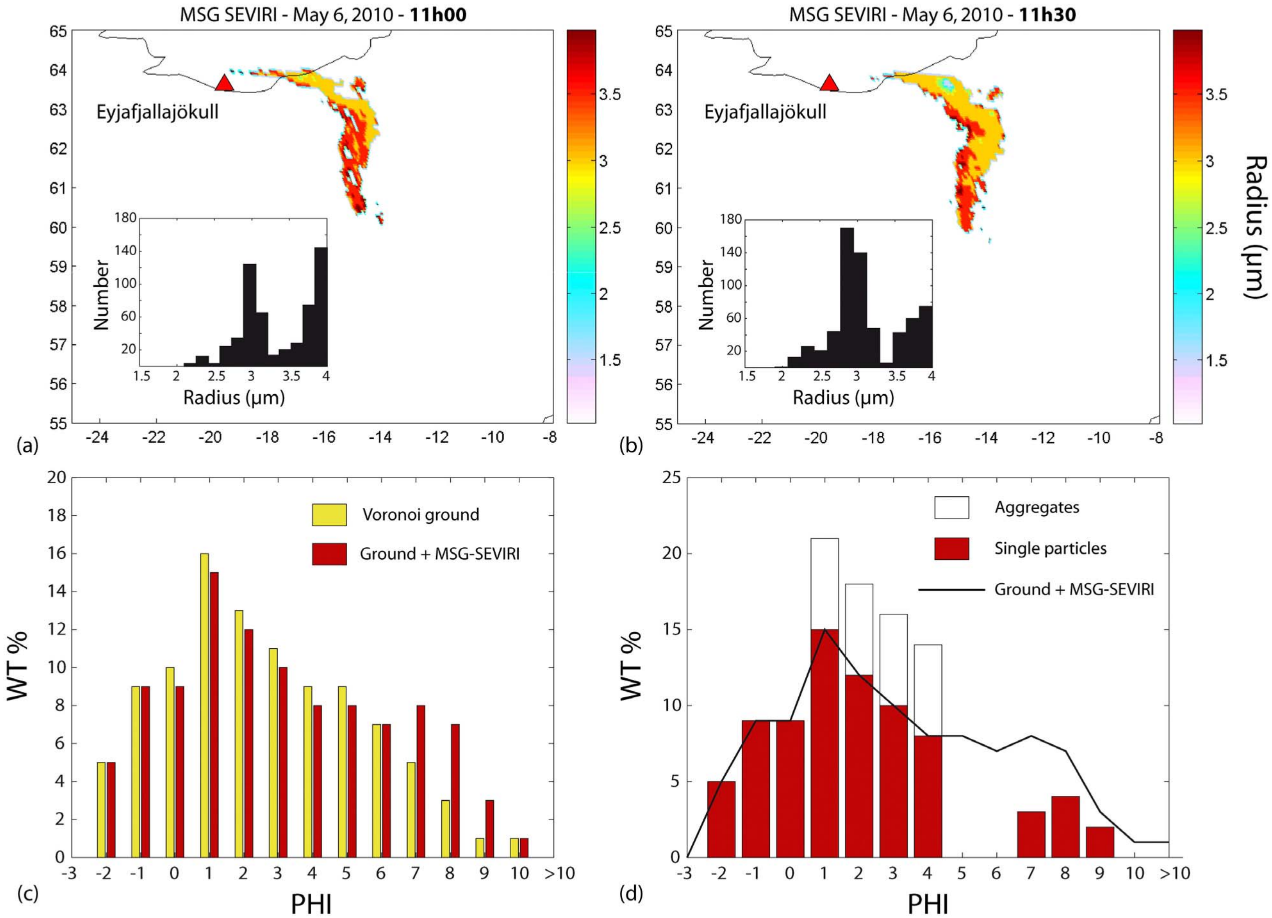

Figure 17. Detailed map of ash effective radius calculated with MSG-SEVIRI with the corresponding particle size distribution occurring at (a) 11:00 and (b) 11:30 UT on 6 May, used for the calculation of the 30 min ash particle emission. (c) Comparison between ground-based total grain-size distribution (yellow histograms) and total grain-size distribution calculated from the combination of the mass deposited on the ground and the mass remaining in the cloud up to 1000 km from the vent (weighted on a 30 min period; red histograms). (d) Combination of the ground-based and satellite-based total grain-size distributions showing particle aggregation. The original grain-size distribution is indicated as a black solid line, whereas aggregates of various sizes and individual particles are indicated as white and red histograms, respectively.

(about 9 ϕ), 2.8 μm (7.5 ϕ), and 4 μm (7 ϕ). The largest particles were observed to be close to the vent, with a mode at 4 μm (mode 3) decreasing with distance. However, some interesting features of the radius spatial distribution may suggest additional transport or sedimentation processes. Indeed, one may observe the abrupt decrease of the mean ash radius around 500 km from 4 μm to less than 3 μm. Besides, the central part of the ash cloud showed the lowest radius values, with a mode centered at 1.2 μm (mode 1). Areas dominated by large radii (mode 3) returned a high mass loading of ash, peaking at 3.5×10^{-3} kg m^{-2} (Figure 16b). The smallest particle areas (mode 1) returned mass loading values lower than 10^{-3} kg m^{-2}. Ash-concentrated areas located at the edge of the ash cloud were also observed. This feature often refers to artifacts that are due to the presence of a thick underlying stratus composed of fine water droplets [*Pavolonis et al.*, 2006]. The total mass of pure-ash particles transiting into the atmosphere at 19:30 was 80.3×10^6 kg.

[24] A total grain-size distribution (weighted average) representative of 30 min of eruption was calculated from the combination of the ground-based grain-size distribution (Figure 5) and the mass of 7–9 ϕ retrieved from the MSG-SEVIRI image occurring at 11:30 between 100 and 1000 km (i.e., 3.3×10^6, 4.5×10^6, and 2.1×10^6 kg for ϕ categories 7, 8, and 9, respectively) (Figures 17a and 17b). These images were chosen because between 11:00 and 11:30 the sedimentation flux was lower than the input flux of ash into the atmosphere. As a result, all the excess mass between 11:00 and 11:30 was associated with ash emitted during this time lapse (i.e., 30 min). Associated size fractions (retrieved between 100 and 1000 km from the vent) were averaged by weight with the size fraction collected on the ground between 2 and 56 km from the vent. The resulting grain-size distribution is comprehensive of the mass that fell up to the coastline (i.e., corresponding to the 0.05 kg m^{-2} isomass line; 9.7×10^7 kg) and the mass that remained in the cloud

up to 1000 km from the vent (i.e., 10^7 kg). Associated Mdphi and sorting are of 2.1 ϕ and 3.6, respectively, and a secondary mode around 7 ϕ is evident. The content of fine ash (<63 μm) is 26 wt % and 33 wt % for the ground-based and the ground combined with MSG-SEVIRI data, respectively. The effect of particle aggregation on the actual grain-size range was investigated by aggregating all particles <63 μm in clusters between 1 mm and 63 μm based on our field and SEM observations (Figure 7). The amount of particles <63 μm in each aggregate-size category and the relative amount of aggregates in each size category could not be characterized in detail from our observations and therefore was equally distributed (white histograms in Figure 17d). The portion observed in the volcanic cloud through the MSG-SEVIRI retrievals was left as individual particles (red histograms associated with the size categories 7, 8, and 9 ϕ in Figure 17d).

5. Discussion

[25] An accurate study of particle transport and deposition from the 4–8 May phase of the 2010 Eyjafjallajökull eruption (Iceland) has highlighted important aspects of sedimentation processes associated with explosive volcanism and long-lasting eruptions. The tephra fall was not uniform even within the first tens of kilometers, but was characterized by variable accumulation rates and grain-size features, possibly related to local phenomena of convective instabilities and particle aggregation. These phenomena could explain the fact that there was no clear correlation of particle morphological parameters with size and distance from the vent (Figure 6). Accumulation rates between 2 and 56 km from the vent varied by 2 orders of magnitude (between 7 × 10^{-4} kg m^{-2} s^{-1} for EJ14 and 8 × 10^{-6} kg m^{-2} s^{-1} for EJ17) with a clear exponential decay away from vent along the dispersal axis. Local deviations from this general trend (as shown, for example, by the accumulation rates at sites EJ05 and EJ17; Figure 3 and Table 1) could be related to oscillations in eruption intensity during the measurement interval and consequent variations in the amount of ash injected into the atmosphere or to local effects of imbalanced accumulation mainly related to the formation of convective instabilities. In fact, sedimentation has been observed to occur through the formation of instabilities a few hundreds of meters wide (e.g., Figure 1) that are recognized as enhancing sedimentation and settling velocities of fine particles [e.g., *Bonadonna et al.*, 2002; *Carey*, 1997; *Schultz et al.*, 2006]. Sedimentation and settling velocities of fine particles were also enhanced by various aggregation processes. During the 4–8 May phase of the 2010 Eyjafjallajökull eruption we observed both dry and wet aggregation that resulted in the generation of various types of aggregates (PC1, PC2, AP1, and AP3) at the same locality and at localities only a few kilometers away (Table 3). For example, PC1 and PC2 were observed in all samples analyzed, whereas poorly structured pellets (AP1) were observed only in the EJ18 and EJ22 samples and liquid pellets (AP3) in the EJ06 sample. Nonetheless, PC1, PC2, and AP1 aggregates all consisted of very similar grain-size distributions with particles <63 μm. The process associated with the formation of liquid pellets (AP3) was the most efficient for scavenging ash particles from the plume, as it involved also particles between 125 and 63 μm. We believe that the formation of poorly structured and liquid pellets was associated with the availability of atmospheric moisture or local effects of condensation in the plume, which favored particle stickiness and resulted in the formation of local rain showers that helped scavenge also coarse-ash particles (e.g., EJ06). The fallout of aggregates started to increase beyond 10 km from the vent because of a combination of factors (e.g., progressive enrichment in fine particles, time of formation, and wind transport; Figure 2). EJ15 (9.6 km from the vent) represents the spatial limit of aggregate fallout in our data set, showing only loosely bounded PC1 and PC2 that broke easily on contact with the collecting paper (Figure 7a). Mdphi showed a clear increase up to about 20 km from the vent, where it reached a plateau around 4 ϕ (Figure 3d). In addition, the compactness of the aggregates could also be a result of the residence time within the cloud that could enhance sticking properties of fine ash. Nonetheless, particle aggregates could also form in the spreading plume within 10 km from the vent but simply fell in more distal areas because of their size and density. Regardless of the presence of the sedimentation of micrometric aggregates at all observed localities, most grain-size distributions are unimodal with relatively good sorting (i.e., 1.4 ± 0.7), reflecting the pretty loose nature of the aggregates (Figure 3). The most pronounced bimodalities are shown by samples EJ15 and EJ22. In fact, EJ15 is characterized by a large amount of coarse-ash particles (main population centered on 1 ϕ) combined with fine-ash particles that made up ash clusters (smaller population centered on 5.5 ϕ). Finally, PC1, PC2, and AP1 of sample EJ22 were particularly efficient at scavenging particles <32 μm, which has resulted in a bimodal grain-size distribution.

[26] The aspect of nonuniform tephra sedimentation was also reflected in the characteristic of the radius and ash-concentration variations with distance from the vent. In fact, Figures 16 and 17 show how particle radius did not uniformly decrease with distance from the vent as would be expected based on classic sedimentation theory [e.g., *Bursik et al.*, 1992; *Sparks et al.*, 1992], with the central part of the ash cloud being characterized by the lowest radius values with a mode centered at 1.2 μm. Ash concentration showed a more evident decrease with distance from the vent but was still characterized by a nonuniform cross-wind distribution and with ash-concentration maxima being sometimes located in the center of the cloud and sometimes at the margins. All these features can be explained by the nonuniform spatial distribution of aggregation processes and the generation of convective instabilities (e.g., Figure 1) [*Bonadonna et al.*, 2002]. The pulsating nature of the Eyjafjallajökull plume characterized by a variable ash injection rate into the atmosphere (Figure 14) might have also played a role in the origin of the patchy distribution of ash concentration. Data of mass flux in and out of the plume suggest, in fact, the occurrence of periods characterized by ash particle sedimentation higher than ash particle injection into the atmosphere (i.e., negative mass flux; e.g., between 15:30 and 19:30 of 6 May 2010; Figure 14).

[27] The variation of particle sphericity between 0.4 and 1 (Figure 6) results in a discrepancy in settling velocity from the model of spheres up to 70% for the coarsest particles of EJ14, EJ15, and EJ17. In particular, velocities calculated

with the method of *Kunii and Levenspiel* [1969] with variable densities are 11.8 ± 5.6, 1.9 ± 2.3, and 0.3 ± 0.4 m s^{-1} for EJ14, EJ15, and EJ17, respectively (blue diamonds in Figure 13). Our application of various models for settling velocity and particle characterization (i.e., diameter, density, and morphology) shows variations up to 70%, highlighting how even the description of particle size, density, and sphericity significantly influences the derivation of settling velocity. Discrepancies among different models increase with particle size.

[28] PLUDIX recordings implemented with our inversion algorithm provide a unique tool for real-time grain-size detection in proximal areas with reasonable agreement with field data. In fact, despite the strong assumptions of spherical shape, size-independent density, and simple velocity model, the results of our inversion well fit the observed grain-size distributions in the $-2 > \phi > 1$ range, proving the reliability of the instrument in real-time particle fall detection. Nevertheless, it is worth noting that the best agreement is given for particles >750 μm and that we were not able to measure ash particles with diameters <500 μm. This is mainly due to the instrumental high noise level in the Doppler frequency spectrum below 150 Hz, which prevents a quantitative interpretation of the backscattered power and is thus likely to be considered a limit of the instrument itself.

[29] The nearly constant wind direction during the period when samples were collected and data recorded (i.e., 4 and 8 May 2010; Figure 1b) allowed an isomass map to be compiled based on the mass accumulation rates observed in the field and normalized to an average collection time of 30 min. Such an isomass map (Figure 2) shows the typical characteristics of a tephra deposit associated with a bent-over plume with no upwind sedimentation, narrow cross-wind deposition, and a rapid increase of Mdphi with distance from the vent [*Bonadonna et al.*, 2005]. In addition, the mass eruption rate derived for a 30 min period varies between 6.2×10^4 and $1.0 \pm 0.2 \times 10^5$ kg s^{-1} (based on the exponential and power law method, respectively). As an example, the 1996 eruption of Ruapehu volcano, New Zealand, which generated a bent-over plume with maximum plume height of 8.5 km, was characterized by an average mass eruption rate of 2.1×10^5 kg s^{-1} calculated over the total eruption period of 6.5 h [*Bonadonna et al.*, 2005].

[30] The lack of usable satellite images over land during the 4–8 May period did not allow for a direct comparison between cloud and deposit width and cloud sedimentation and ground accumulation. Indeed, a large amount of water vapor emission prevented any accurate thermal detection and measurement of ash particles from satellite sensors. Nonetheless, using the total area of the ash cloud between 100 and 1000 km, we deduced an average sedimentation rate of about 2 orders of magnitude lower than ground accumulation rate with a significantly finer-grained particle size. This difference first shows that the sedimentation rate a few hundreds of kilometers away from the vent is still significant, although much lower (~2 orders of magnitude) than that in the first tens of kilometers. However, it is important to bear in mind that the accumulation rate at EJ18 was calculated over 10 min (18:17–18:47, 6 May), while the sedimentation rate on the whole cloud was estimated over the whole period of observation (8:30–21:30, 6 May). For example, the accumulation rate measured at the same site at different steps during more than 1 h shows a 4-time difference between minimum and maximum values (EJ15; Table 1). The image taken at 8:30 on 6 May represents the unique example of ash cloud observed over the land using MSG-SEVIRI data, located at about 130 km from the vent. The overlap of ground and satellite data sets occurs only within the finest range of ground sampled data, suggesting that most of particles with ϕ values smaller than about 7 ϕ (>8 μm) have already settled 130 km away from the vent (location of the cloud image), a clear consequence of ash aggregation and convective instabilities. On a large space scale, the combination of particle-size distribution retrieved from satellite images (100–1000 km from the vent) and ground-based particle-size distribution (2–56 km from the vent) shows how a significant portion of particles between 7 and 9 ϕ did not settle on land. We can conclude that most ground-based grain-size distributions typically lack this size fraction that is also part of the total grain-size distribution generated during volcanic explosions but that stays suspended in the atmosphere for a long time (e.g., several days). Our integrated erupted mass and grain-size calculations over a 30 min period show that the >7 ϕ fraction represents about 20% of the total population erupted during the analyzed period (i.e., ground +satellite = 2.0×10^7 kg) and that about 46% of the total mass of particles in the 7–9 categories (i.e., ground + satellite = 1.9×10^7 kg) fell within the first 56 km from the vent, mostly as aggregates up to 600 μm (i.e., 1 ϕ) (Figure 17). In particular, the mass that remained in the cloud down to 1000 km represents about 9% and 5% of the total deposit based on the one-exponential segment and power law integration, respectively. Previous studies have provided mass ratios between atmospheric fine ash and tephra deposits ranging from 0.7% to 2.1% for the Spurr 1992 eruption, 0.7% for the El Chichón 1982 eruption, 1.4% for the Láscar 1993 eruption, and 0.04% for the Hudson 1991 eruption [*Rose et al.*, 2001; *Schneider et al.*, 1999; *Wen and Rose*, 1994]. However, the overall Mdphi, sorting and fine-ash fraction of the Voronoi ground-based grain-size distribution and the ground + MSG-SEVIRI grain-size distribution do not change significantly (i.e., 1.7 ϕ, 3.1, and 26 wt %, respectively, for Voronoi ground based and 2.1 ϕ, 3.6, and 33 wt % for ground + MSG-SEVIRI). This is probably due to the fact that a large amount of fine ash (about 50% of the 7–9 ϕ fraction) fell on land between 2 and 56 km as a result of particle aggregation and, probably, convective instabilities. The reason for such a large proportion of fine ash (about 20 wt % of the total grain-size distribution is >7 ϕ; Figure 17) during such a low- to mid-intensity eruption remains to be discussed in terms of fragmentation and eruption dynamics.

6. Conclusions

[31] The April–May 2010 eruption of the Eyjafjallajökull volcano provided a wide range of data that could be combined together to bring to light important aspects of both particle sedimentation processes and data acquisition techniques. We also demonstrated how subtle changes in the eruptive style of long-lasting eruptions can be characterized by determining short-duration physical parameters (e.g., erupted mass, mass eruption rate, and total grain-size distribution).

In terms of particle sedimentation, we can draw the following conclusions:

[32] 1. Tephra fall is not uniform but is characterized by spatially nonuniform particle aggregation processes and the generation of convective instabilities that are also affected by local atmospheric conditions (e.g., humidity). The nonuniform aspect of tephra fall was enhanced during the long-lasting Eyjafjallajökull eruption by the pulsating nature of ash injection into the atmosphere that varied significantly during the 4–8 May period. As an example, mass flux varied between ±25 t s^{-1} during 6 May 2010, which was recorded as the most powerful episode of April–May by MSG-SEVIRI.

[33] 2. Our in situ sampling showed how most particles <63 μm fell as aggregates of various types, ranging from ash clusters and coated particles to poorly structured pellets and liquid pellets (average Mdphi and sorting of aggregating particles are around 5.4 ϕ and 0.9, respectively). Liquid pellets could also locally scavenge particles between 125 and 63 μm. The presence of poorly structured pellets and liquid pellets is not related to meteoric rain, but more likely to local variations of atmospheric humidity. The sedimentation of particle aggregates was most efficient beyond 10 km from the vent. Ash clusters and poorly structured pellets reached diameters of up to 600 μm, whereas liquid pellets (observed only at EJ06) reached diameters of 3 mm.

[34] 3. Most individual grain-size distributions are unimodal with Mdphi increasing up to about 20 km from the vent, where it reaches a plateau of about 4 ϕ. Sorting does not vary with distance from the vent (i.e., 1.4 ± 0.7). The amount of fine ash (<63 μm) varies between about 0 and 20 wt % within the first 10 km and is mostly around 50–60 wt % beyond 20 km from vent.

[35] 4. Our short-duration (30 min) isomass map is characterized by typical features of bent-over plume sedimentation, i.e., elongated contours, no upwind sedimentation, rapid cross-wind thinning, and a rapid downwind increase in Mdphi.

[36] 5. Our short-duration (30 min) ground-based total grain-size distribution is characterized by an Mdphi of 1.7 ϕ, a sorting of 3.1, and a content of fine ash of 26 wt % (2–56 km) (derived by applying the Voronoi tessellation technique). The 30 min satellite + ground-based total grain-size distribution is characterized by an Mdphi of 2.1 ϕ, a sorting of 3.6, and a content of fine ash of 33 wt % (2–1000 km). The similarity between Voronoi ground-based and ground + MSG-SEVIRI grain-size distributions is mainly due to the sedimentation of a large amount of fine ash on land as a result of particle aggregation and convective instabilities.

[37] 6. Accumulation rates varied between 0.06 and 7 × 10^{-4} kg m^{-2} s^{-1} between 2 and 56 km with a clear exponential decay away from the vent. The total erupted mass over a period of 30 min was estimated to 1.1 × 10^8 and 1.8 ± 0.3 × 10^8 kg based on the integration of a one-exponential segment and of a power law fit, respectively. Associated mass eruption rates correspond to 6.2 × 10^4 and 1.0 ± 0.2 × 10^5 kg s^{-1}.

[38] 7. About 20 wt % of the total erupted mass was ejected as particles >7 ϕ (<8 μm). About 5 to 9 wt % of the erupted mass remained in the cloud up to 1000 km from the vent (calculated based on the power law and one-exponential-segment integration, respectively), suggesting that about 46% of the total mass of particles in the 7–9 categories fell within the first 56 km from the vent, mostly as aggregates up to 600 μm (1 ϕ).

[39] 8. Particle sphericity and shape factor varied between 0.4 and 1 with no clear correlation to particle size and to distance from the vent. The wide range of particle morphology resulted in a settling velocity that diverged significantly from the assumption of a perfect sphere. Associated discrepancies increase with particle size and are related to both the theoretical model used to derive settling velocities and to the characterization of particles (i.e., diameter, density, and morphology). The absence of a regular variation of shape parameters with distance can be in part related to enhanced sedimentation following ash aggregation in the plume and convective instabilities.

[40] In terms of data acquisition techniques we can draw these conclusions:

[41] 1. Satellite retrievals and Doppler radar grain-size detection represent solid alternatives for the real-time description of the source term that cannot be provided by ground-based traditional observations. This is crucial to the development of optimal forecasting strategies related to aviation safety and global risk mitigation. Satellite retrievals can also complement ground data as they can extend over the ocean and can detect those particles that were injected into the atmosphere but did not fall on the ground. Besides, multidisciplinary approaches also permit the continuity of the object detection as each technique has its own field of application (e.g., concentration threshold, particle sizes, spatial extent, time resolution of acquisition).

[42] 2. Limitations of traditional ground observations for the determination of erupted mass and grain-size distribution mainly include the impossibility (1) of inferring real-time observations and (2) of characterizing the fraction of particles that remains in the volcanic cloud for long distances.

[43] 3. Limitations of thermal satellite retrievals mainly include (1) the difficulty of detecting ash particles under cloudy conditions (e.g., water vapor or droplets, ice crystals) that have prevented almost any measurements close to the vent (over land), (2) size detection limits of thermal infrared techniques that allow only for the retrieval of particles with diameters of <20 μm.

[44] 4. The limitations of PLUDIX detection mainly include (1) the fact that the sizes of particles are limited to the 0.750–10 mm range with the impossibility of resolving for particles <500 μm (with the associated limitation of use in medial and distal areas), (2) use of a defined velocity model and assumption of a single mean density value for the whole range of particle sizes.

Appendix A

[45] Sphericity (Ψ) of *Aschenbrenner* [1956]:

$$\Psi = 12.2\left[\frac{\sqrt[3]{qp^2}}{1+p(1+q)+6\sqrt{1+p^2(1+q^2)}}\right];\ p = S/I \text{ and } q = I/L.$$

[46] Shape factor of *Wilson and Huang* [1979]:

$$F = \frac{I+S}{2L}.$$

[47] Equivalent diameter (Dv) and sphericity (Ψ) of *Riley et al.* [2003]:

$$Dv = 2(1.2247)\sqrt{\frac{\text{projected area}}{\pi}}$$

$$\Psi = 4\pi \frac{\text{projected area}}{(\text{projected perimeter})^2}.$$

[49] **Acknowledgments.** The authors are grateful to Antonella Bertagnini, Mauro Rosi, Martin Hensch, and Þorsteinn Sæmundsson for their contribution and discussion in the field. The Italian Civil Protection is thanked for the use of the PLUDIX. Arnau Folch is thanked for providing the ECMWF ERA-40 reanalysis wind data. C. Bonadonna was supported by a Fond National Suisse project (200020-125024). R. Genco, M. Pistolesi, R. Cioni, and M. Ripepe were supported by Italian Ministero Università e Ricerca funds (PRIN 2008–AshErupt project, responsible R. Cioni). M. Gouhier was funded by the Centre National d'Etudes Spatiales (CNES) and supported by the LabEx ClerVolc (Centre Clermontois de Recherche sur le Volcanisme). MSG-SEVIRI data were provided by the OPGC reception platform (HotVolc) through agreement with EUMETSAT and Météo-France.

References

Aschenbrenner, B. C. (1956), A new method of expressing particle sphericity, *J. Sediment. Petrol.*, *26*(1), 15–31.

Bonadonna, C., and B. F. Houghton (2005), Total grain-size distribution and volume of tephra-fall deposits, *Bull. Volcanol.*, *67*, 441–456, doi:10.1007/s00445-004-0386-2.

Bonadonna, C., and J. C. Phillips (2003), Sedimentation from strong volcanic plumes, *J. Geophys. Res.*, *108*(B7), 2340, doi:10.1029/2002JB002034.

Bonadonna, C., et al. (2002), Tephra fallout in the eruption of Soufrière Hills Volcano, in *The Eruption of Soufrière Hills Volcano, Montserrat, from 1995 to 1999*, edited by T. H. Druitt and B. P. Kokelaar, *Geol. Soc. Lond. Mem. Ser.*, 21, 483–516, doi:10.1144/GSL.MEM.2002.021.01.32.

Bonadonna, C., J. C. Phillips, and B. F. Houghton (2005), Modeling tephra sedimentation from a Ruapehu weak plume eruption, *J. Geophys. Res.*, *110*, B08209, doi:10.1029/2004JB003515.

Brown, R. J., et al. (2011), A review of volcanic ash aggregation, *Phys. Chem. Earth*, in press.

Bursik, M. I., R. S. J. Sparks, J. S. Gilbert, and S. N. Carey (1992), Sedimentation of tephra by volcanic plumes: I. Theory and its comparison with a study of the Fogo A plinian deposit, Sao Miguel (Azores), *Bull. Volcanol.*, *54*, 329–344, doi:10.1007/BF00301486.

Carey, S. N. (1997), Influence of convective sedimentation on the formation of widespread tephra fall layers in the deep sea, *Geology*, *25*(9), 839–842, doi:10.1130/0091-7613(1997)025<0839:IOCSOT>2.3.CO;2.

Costa, A., A. Folch, and G. Macedonio (2010), A model for wet aggregation of ash particles in volcanic plumes and clouds: 1. Theoretical formulation, *J. Geophys. Res.*, *115*, B09201, doi:10.1029/2009JB007175.

Fierstein, J., and M. Nathenson (1992), Another look at the calculation of fallout tephra volumes, *Bull. Volcanol.*, *54*, 156–167, doi:10.1007/BF00278005.

Ganser, G. H. (1993), A rational approach to drag prediction of spherical and nonspherical particles, *Powder Technol.*, *77*(2), 143–152, doi:10.1016/0032-5910(93)80051-B.

Gilbert, J. S., and S. J. Lane (1994), The origin of accretionary lapilli, *Bull. Volcanol.*, *56*(5), 398–411.

Gouhier, M., and F. Donnadieu (2008), Mass estimations of ejecta from Strombolian explosions by inversion of Doppler radar measurements, *J. Geophys. Res.*, *113*, B10202, doi:10.1029/2007JB005383.

Hort, M., R. Seyfried, and M. Vöge (2003), Radar Doppler velocimetry of volcanic eruptions: Theoretical considerations and quantitative documentation of changes in eruptive behavior at Stromboli volcano, Italy, *Geophys. J. Int.*, *154*, 515–532, doi:10.1046/j.1365-246X.2003.01982.x.

Hoskuldsson, A., et al. (2011), Eruption dynamics of the 2010 summit eruption at the Eyjafjallajökull volcano (Iceland): Magma fragmentation, tephra stratigraphy and transport, *Geophys. Res. Abstr.*, *13*, EGU2011-14165.

Houghton, B. F., and C. J. N. Wilson (1989), A vesicularity index for pyroclastic deposits, *Bull. Volcanol.*, *51*(6), 451–462, doi:10.1007/BF01078811.

Inman, D. L. (1952), Measures for describing the size distribution of sediments, *J. Sediment. Petrol.*, *22*(3), 125–145.

Kunii, D., and O. Levenspiel (1969), *Fluidization Engineering*, John Wiley, New York.

Labazuy, P., et al. (2011) Near real-time monitoring of the April–May 2010 Eyjafjallajökull ash cloud: An example of a web-based, satellite-data-driven, reporting system, *Int. J. Environ. Pollut.*, in press.

Pavolonis, M. J., W. F. Feltz, A. K. Heidinger, and G. M. Gallina (2006), A daytime complement to the reverse absorption technique for improved automated detection of volcanic ash, *J. Atmos. Oceanic Technol.*, *23*, 1422–1444.

Polacci, M., L. Pioli, and M. Rosi (2003), The plinian phase of the Campanian Ignimbrite eruption (Phlegrean Field, Italy): Evidence from density measurements and textural characterization of pumice, *Bull. Volcanol.*, *65*, 418–432, doi:10.1007/s00445-002-0268-4.

Pollack, J. B., O. B. Toon, and B. N. Khare (1973), Optical properties of some terrestrial rocks and glasses, *Icarus*, *19*, 372–389.

Prata, A. J. (1989), Infrared radiative-transfer calculations for volcanic ash clouds, *Geophys. Res. Lett.*, *16*(11), 1293–1296, doi:10.1029/GL016i011p01293.

Pyle, D. M. (1989), The thickness, volume and grainsize of tephra fall deposits, *Bull. Volcanol.*, *51*(1), 1–15, doi:10.1007/BF01086757.

Riley, C. M., W. I. Rose, and G. J. S. Bluth (2003), Quantitative shape measurements of distal volcanic ash, *J. Geophys. Res.*, *108*(B10), 2504, doi:10.1029/2001JB000818.

Rose, W. I., G. J. S. Bluth, D. J. Schneider, G. G. J. Ernst, C. M. Riley, L. J. Henderson, and R. G. McGimsey (2001), Observations of volcanic clouds in their first few days of atmospheric residence: The 1992 eruptions of Crater Peak, Mount Spurr volcano, Alaska, *J. Geol.*, *109*(6), 677–694, doi:10.1086/323189.

Schneider, D. J., W. I. Rose, L. R. Coke, G. J. S. Bluth, I. E. Sprod, and A. J. Krueger (1999), Early evolution of a stratospheric volcanic eruption cloud as observed with TOMS and AVHRR, *J. Geophys. Res. 104*(D4), 4037–4050, doi:10.1029/1998JD200073.

Schultz, D. M., et al. (2006), The mysteries of mammatus clouds: Observations and formation mechanisms, *J. Atmos. Sci.*, *63*, 2409–2435, doi:10.1175/JAS3758.1.

Scollo, S., M. Coltelli, F. Prodi, M. Folegani, and S. Natali (2005), Terminal settling velocity measurements of volcanic ash during the 2002–2003 Etna eruption by an X-band microwave rain gauge disdrometer, *Geophys. Res. Lett.*, *32*, L10302 doi:10.1029/2004GL022100.

Sparks, R. S. J., M. I. Bursik, G. J. Ablay, R. M. E. Thomas, and S. N. Carey (1992), Sedimentation of tephra by volcanic plumes: 2. Controls on thickness and grain-size variations of tephra fall deposits, *Bull. Volcanol.*, *54*(8), 685–695, doi:10.1007/BF00430779.

Wen, S., and W. I. Rose (1994), Retrieval of sizes and total masses of particles in volcanic clouds using AVHRR bands 4 and 5, *J. Geophys. Res.*, *99*(D3), 5421–5431, doi:10.1029/93JD03340.

Wilson, L., and T. C. Huang (1979), The influence of shape on the atmospheric settling velocity of volcanic ash particles, *Earth Planet. Sci. Lett.*, *44*, 311–324, doi:10.1016/0012-821X(79)90179-1.

F. Alfano and C. Bonadonna, Section of Earth and Environmental Sciences, University of Geneva, rue des Maraichers, Geneva CH-1205, Switzerland. (costanza.bonadonna@unige.ch)

R. Cioni, Department of Earth Sciences, University of Cagliari, Via Trentino 51, Cagliari I-09127, Italy.

R. Genco and M. Ripepe, Department of Earth Sciences, University of Florence, via La Pira 4, Florence I-50121, Italy.

M. Gouhier, Laboratoire Magmas et Volcans, Université Blaise Pascal, 5, rue Kessler, Clermont-Ferrand F-63038, France.

A. Hoskuldsson, Institute of Earth Sciences, University of Iceland, Sturlugata 7, 101 Reykjavik, Iceland.

M. Pistolesi, Department of Earth Sciences, University of Pisa, via Santa Maria 53, Pisa I-56126, Italy.

Satellite-based evidence for a large hydrothermal system at Piton de la Fournaise volcano (Reunion Island)

Mathieu Gouhier[1] and Diego Coppola[2]

Received 16 November 2010; accepted 30 November 2010; published 21 January 2011.

[1] Hydrothermal systems are active structures present at many volcanoes. Their characterization is essential as they reveal the evolution of the magmatic source and may play a role in the eruptive style. Many studies have already suggested the existence of a shallow hydrothermal system beneath the summit craters at Piton de la Fournaise volcano (La Réunion), although there is still no clear evidence. Here we present new arguments on the basis of satellite-based data acquired during April 2007 eruption suggesting the existence of a large hydrothermal system beneath the Dolomieu crater at Piton de la Fournaise. SO_2 released during the collapse phase of the Dolomieu crater (~April 6–13) has been estimated at 935 ± 244 kilotons whereas erupted SO_2 calculated from lava effusion rates was found to be clearly insufficient (179 ± 89 kilotons). We suggest that the excess of SO_2 originated from a large hydrothermal system suddenly opened by the collapse. **Citation:** Gouhier, M., and D. Coppola (2011), Satellite-based evidence for a large hydrothermal system at Piton de la Fournaise volcano (Reunion Island), *Geophys. Res. Lett.*, *38*, L02302, doi:10.1029/2010GL046183.

1. Introduction

[2] Hydrothermal systems in active volcanic area are fundamental structures although difficult to monitor. They are very permeable medium, often associated with brecciated rocks, capable to stock very large amount of water and dissolved gas species [*Finizola et al.*, 2003; *Revil et al.*, 2008]. Hydrothermal networks are very sensitive systems highly responsive to the changes of source conditions such as magmatic heat flux. Therefore, the study of the exsolved gas content is a valuable tool for early monitoring of volcanic eruption. Since the 1998 eruption at Piton de la Fournaise volcano (La Réunion), many studies have suggested the existence of a hydrothermal system beneath the summit craters from indirect geophysical data. For instance, electric methods have shown positive Self-potential anomalies [*Lénat*, 2007] and resistivity distribution [*Lénat et al.*, 2000] revealing high temperature fluid circulation beneath the summit craters. Gravity field measurements and seismic tomography displayed positive anomalies interpreted as the existence of a low density material beneath the surface [*Gailler et al.*, 2009; *Brenguier et al.*, 2007]. However, there is still no clear evidence for the existence of a large hydrothermal system beneath the summit area. The current central column of Piton de la Fournaise located beneath the Dolomieu crater is the result of successive episodes of construction and destruction of the summit area. The collapse of the Dolomieu crater occurring on April 6, 2007, constitutes the last episode of destruction; however, in 1936, a similar event had already occurred opening the eastern part of the summit area [*Lacroix*, 1936, 1938]. Between each destructive event, the large cavity is progressively filled with products of successive eruptions resulting in a very heterogeneous and fractured column of rocks favourable to the development of a huge hydrothermal system. The collapse of the Dolomieu, associated to the eruption of April 2007, has provided the unprecedented opportunity to study the upper 350 m of the active central column [*Staudacher et al.*, 2009; *Michon et al.*, 2009]. But, almost no gas measurements could have been carried out from ground-based methods during the collapse [*Bhugwant et al.*, 2009]. However, high sensitivity satellite-based sensors can also be used to accurately evaluate the balance between gas and magma emissions [*Steffke et al.*, 2010]. In this study we propose the existence of a large hydrothermal system, as suggested by *Lénat et al.* [2010], but using direct and quantitative SO_2 measurements carried out with satellite-based methods. Key observations are provided by OMI (Ozone Monitoring Instrument) and MODIS (Moderate resolution Imaging Spectroradiometer) sensors, as they can routinely monitor the downwind transport of gases and aerosols, as well as terrestrial lava effusions.

2. April 2007 Eruption

[3] After a progressive increase of seismicity in the last days of March 2007, a short effusive event began on March 30, with the opening of an eruptive fissure at 1900 asl, on the SE flank of the volcano. The effusion of a small lava flow lasted less than 10 hours, but an important summit seismicity persisted until April 2, when a new fissure opened on the lower eastern flank at about 600 m a.s.l. Lava fountains up to 100–150 m high were observed at the new vent, and a large lava flow, covering the south part of Grand Brûlé, reached the sea a few hours after the beginning of the eruption. On April 3, a gradual increase of the effusive activity was recorded together with the intensification of the tremor amplitude and number of VT events below the Dolomieu crater. This phase culminate on April 6 when the collapse of the Dolomieu Crater was first recognized by a camera of the volcanological observatory located at the summit of Piton de la Fournaise. Seismic and geophysical data indicate that the collapse did not occur in a single event but rather from the rapid succession of several collapse events lasting more than 30 hours [*Michon et al.*, 2007]. By April 7, most of the collapse (about 80% in volume) had occurred and was followed by a progressive lowering of the effusive activity down to the initial

[1]Laboratoire Magmas et Volcans, UMR 6524, Clermont Université, Université Blaise Pascal, CNRS, IRD, Clermont-Ferrand, France.
[2]Dipartimento di Scienze Mineralogiche e Petrologiche, Università degli Studi di Torino, Turin, Italy.

0094-8276/11/2010GL046183

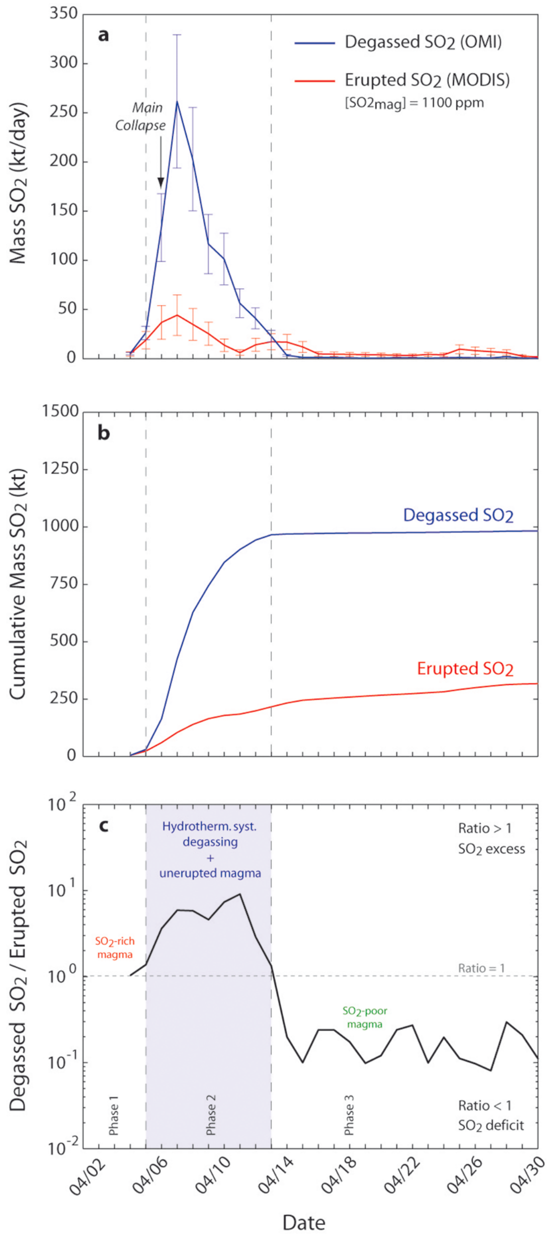

Figure 1. Comparison of erupted and degassed SO_2 using MODIS and OMI sensors respectively. (a) Mass of SO_2 release during the April 2007 eruption. (b) Cumulative sum of the mass released during the same period of time. (c) Degassed over erupted SO_2 ratio highlighting the SO_2 excess released at Piton de la Fournaise volcano.

level. The final geometry of the caldera (~1.2×10^8 m^3) was reached on April 10, when the new collapsed structure measured about the size of the pre-existing Dolomieu structure (800×1100 m), with a depth of about 330 m [*Urai et al.*, 2007]. During the following days the effusive activity continued at moderate to lower level, with minor fluctuation of the tremor amplitude up to the end of the eruption on 1st May. The total volume of the erupted lava was estimated as $1 - 1.4 \times 10^8$ m^3 and it covered an area of 3.6 km^2 [*Michon et al.*, 2007; *Urai et al.*, 2007]. The comparison between the erupted magma volume during the large distal low-elevation eruption and the caldera volume suggests a piston-like mechanism [*Michon et al.*, 2007] initiated by the draining of a shallow magma reservoir (~350 Mm^3) located at sea-level elevation [*Urai et al.*, 2007; *Peltier et al.*, 2009, *Boivin and Bachèlery*, 2009].

3. Results

[4] MODIS sensor data were used here to derive a daily estimate of the SO_2 mass associated to the surface lava effusion only (hereby named "erupted SO_2") using a typical sulphur concentration in the magma of 1100 ppm [*Collins et al.*, 2008] following the method of *Coppola et al.* [2009]. The error margin on erupted SO_2 is estimated at about 50%, taking into account the uncertainty on the mass flux rate, the magma density, and the variation of sulphur concentrations [*Coppola et al.*, 2009]. The total amount of "degassed SO_2" is estimated from the calculation of the mass flux using OMI sensor data, and following the method of *Carn and Bluth* [2003]. The error margin on degassed SO_2 is estimated at about 25% using TRL (low troposphere) and TRM (middle troposphere) SO_2 column algorithms as maximum and minimum values respectively. The day by day comparison between both SO_2 measurements (Figure 1) clearly shows the large excess of total degassed SO_2 during the collapse of the Dolomieu crater. MODIS gives a maximum erupted SO_2 mass flux ranging between 43 ± 21 kt/day on April 7 (Figure 1a), whereas maximum degassed SO_2 mass flux inferred from OMI measurements are estimated at 261 ± 68 kt/day. Conversely, after the high increase of the degassed SO_2 discharge simultaneous to the collapsing phase, the cumulative sum of the degassed SO_2 mass flux is flattening revealing a very low emission of SO_2, while the erupted SO_2 calculated on the basis of lava effusion rates is still increasing (Figure 1b). An illustration of the variable amount of gas and magma emitted is given by the ratio between degassed and erupted SO_2 (Figure 1c) which clearly defines three phases of the eruption. Before the collapse (4–5 April; phase I) the SO_2 degassed (31 ± 8 kt) is almost equal to the SO_2 erupted (23 ± 11 kt). By contrast, during the main collapse and in the following days (6–13 April; phase II) the degassed SO_2 (935 ± 242 kt) strongly exceeds the erupted SO_2 (179 ± 89 kt) giving a total excess of SO_2 equal to 756 ± 331 kt (ratio $\gg 1$). Finally, during the second half of the eruption (14–30 April; phase III), the degassed SO_2 (17 ± 4 kt) was lesser than the erupted SO_2 (94 ± 47 kt) thus producing the ratio $\ll 1$, and hence suggesting that the magma erupted during this period was depleted in SO_2. We believe that estimations of degassed SO_2 given here are most likely minimum values as the linear fit algorithm may underestimate SO_2 loading by about 20% at 100 DU [*Yang et al.*, 2007]. In addition, the rapid transformation of SO_2 into sulphuric acid (H_2SO_4), estimated at about 30% according to *Tulet and Villeneuve* [2010], may also account for the underestimation of SO_2 from satellite-based measurements.

[5] MODIS data, whose spatial resolution is better than that of OMI, has also been used to locate the source of volcanic SO_2 emissions using the 8.6-μm method [e.g., *Realmuto et al.*, 1994; *Watson et al.*, 2004] on the SRTM (90m) digital elevation model (DEM) with a relatively good accuracy. The analysis of the MODIS images acquired before the collapse of the Dolomieu crater, on April 5 (Phase I) reveals a mild volcanic plume of SO_2 (Maximum DU = 50) clearly coming out from the vent (Figure 2a). This observation is in

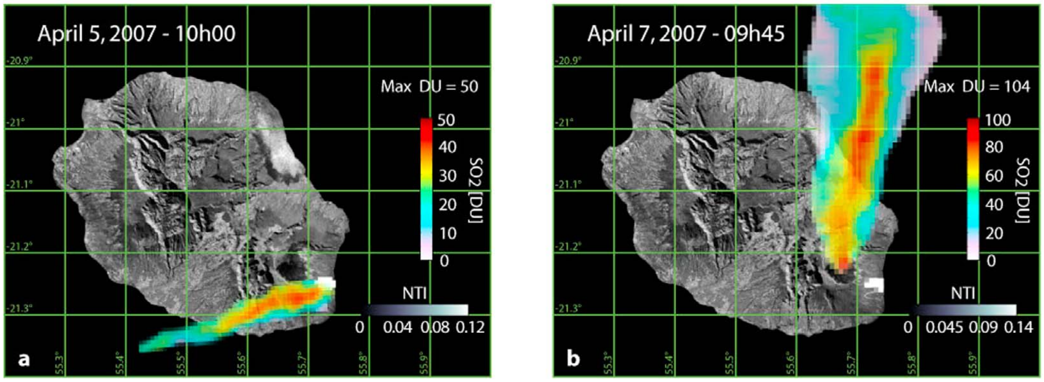

Figure 2. (a) MODIS image of the SO_2 volcanic plume (50 DU) coming out from the vent, taken on April 5, 2007, before the collapse of the Dolomieu crater. The NTI anomaly reveals the location of the distal low-elevation lava flows, which are directly at the origin of the plume. (b) MODIS image taken on April 7, 2007 a few hours after the collapse of the Dolomieu crater, showing a large volcanic plume of SO_2 (104 DU) rising from the summit area.

agreement with a degassed/erupted ratio value of ~1, and confirms that the magma erupted at the vent was at the origin of the measured SO_2. By contrast, a few hours after the main collapse of the Dolomieu crater (April 7) a large volcanic plume of SO_2 (Maximum DU = 104) was coming out from the summit crater area (Figure 2b). At the same time the Normalized Thermal Index (NTI) commonly used to detect thermal anomalies, permits us to locate the distal low-elevation effusion of lava flows, which was not associated to SO_2 emissions despite a high lava discharge rate. This result shows that the whole SO_2 burden observed on April 7, was most likely released from the collapsed summit area and not from the vent.

4. Discussion

[6] The whole SO_2 degassed during the April 2007 eruption cannot be explained by the lava effusion solely, and suggests a second source of SO_2 emission. The fact that on April 7 there was almost no SO_2 degassing from the vent suggests that this second source of SO_2 is likely located above the feeding dike and below the Dolomieu crater (see within the central column of the edifice). In addition the synchronization between the collapse and the net increase of the SO_2 degassed from the summit area clearly indicates that the failure of the central rock column was associated to the excess of SO_2. There are two hypotheses to explain this excess. These involve *(i)* the degassing of unerupted magma (magmatic source) or/and *(ii)* the opening and degassing of the hydrothermal system (hydrothermal source).

[7] The first hypothesis (magmatic source) implies the degassing of a portion of magma, likely stored within the uppermost part of the shallow reservoir, which has not been erupted. Thus if the total amount (983 ± 256 kt) of degassed SO_2 has a magmatic origin (i.e. it derives from erupted plus unerupted magma), the complete degassing of 357 ± 104 Mm^3 of magma would be necessary. In other word, the whole shallow reservoir must have completely degassed during the April 2007 eruption. This huge degassing may occur if the exsolution level suddenly dropped down within the reservoir, in consequence of a depressurization event. However the excess of SO_2 observed during the piston-like development of the collapse, was coeval with a step by step pressurization of the reservoir which, on the contrary, may have raised the exsolution front, thus inhibiting any further SO_2 degassing. We therefore reject the idea of a pure magmatic source at the origin of the SO_2 excess observed in correspondence of the collapse on April 6–7. On the other hand, the excess recorded in the following days (between 8–13 April) might be the consequence of the lithostatic pressure drop associated to the formation of the caldera which in turn promoted the further exsolution of SO_2 coming from the magma stored in the upper part of the reservoir, and escaping through newly opened fractures. The amount of excess SO_2 released from the unerupted magma during the phase 2, and after the collapse, can be assessed from the deficit of SO_2 recorded during the phase 3, which is estimated at 77 kt.

[8] The second hypothesis (hydrothermal origin) implies the opening, exposure and the degassing of a hydrothermal system developed within the central magmatic column of the edifice. Hydrothermal systems are very porous and permeable, which may contain significant amount of gas (H_2O, CO_2 and SO_2). The collapse of the Dolomieu may have partially or completely exposed the hydrothermal system with the consequent release of dissolved gases, without necessarily violent depressurization events. In this view, the SO_2 released by the hydrothermal system is expected to be proportional to the volume of the vaporised fluids. Here we modelled a simple hydrothermal reservoir having the geometry of the caldera (120 Mm^3) in order to derive the possible content of sulphur dioxide dissolved into the water before vaporizing. Giving a minimum water temperature of 70°C, as observed from thermal measurement on rings of steam located on the wall of the caldera [*Staudacher*, 2010], the SO_2 solubility is found to be about 24 ml/l. For a water content taken at about 20–25% of the total volume of the caldera, about 648 ± 72 kt of SO_2 can potentially be stored in the collapsed area. As a comparison, the non-magmatic excess of SO_2 emissions released during phase 2 yields 679 ± 177 kt. This result shows that a large hydrothermal system could be responsible for the sudden release of huge amount of SO_2 in the atmosphere during the collapse of the Dolomieu crater. Note that additional SO_2 may also come out from shallow underlying areas through large fractures opened by the collapse, and probably sealed within a few days (i.e., ~April, 13).

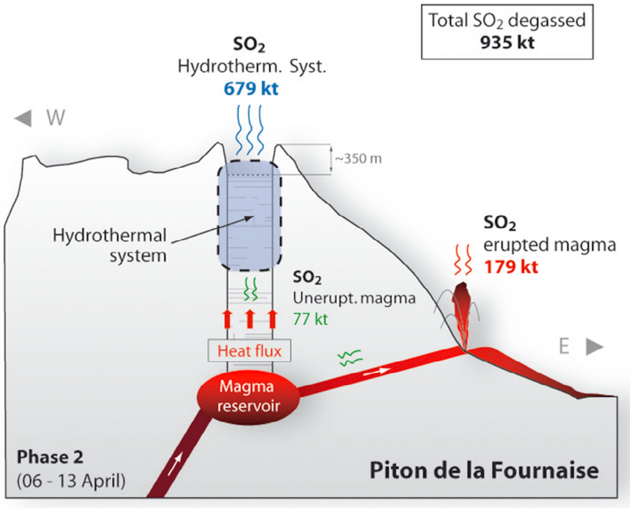

Figure 3. Cross section of the Piton de la Fournaise volcano showing a possible scenario of the SO_2 origin measured during the April 2007 eruption.

[9] The above considerations allowed us to propose a model (Figure 3) in which, the excess of SO_2 recorded during the April 2007 eruption resulted from the coupled effect of the opening of an SO_2-rich hydrothermal system as well as of the degassing of unerupted magma stored within the depressurised reservoir.

5. Conclusion

[10] We have pointed out the existence of a large difference between degassed and erupted SO_2 emissions within the collapse of the Dolomieu Crater and the following days during the April 2007 eruption at Piton de la Fournaise volcano. We interpret the excess of SO_2 degassed as having a double genesis, hydrothermal and magmatic. During the collapse itself the excess was most likely associated to the exposure of a shallow hydrothermal system degassing a large amount of SO_2 whereas during the following days, the SO_2 in excess was associated to the degassing of unerupted magma, stored within the depressurized reservoir. We also consider the possibility of an even larger hydrothermal system extending from the summit area to the shallow magma reservoir at sea-level. Hydrothermal systems are highly responsive structures that could be seen as a low-inertia buffer area that can absorb and release quickly temperature and volatiles, which reveal the evolution of the magmatic source properties. Large hydrothermal systems are frequently observed at more silicic volcanoes. They can have a strong impact on the eruptive style, such as for the Phlegraean Fields (Italy), where the Campanian Ignimbrite emplacement resulted from the combination of magmatic and hydrothermal explosive activity, associated to extensive fracturing and subsidence of the magma-chamber roof [*Rosi et al.*, 1996]. We think that the existence and implication for large hydrothermal systems in the case of large shield basaltic volcanoes have to be further considered as an additional source of volcanic hazards.

[11] **Acknowledgments.** We thank J-F Lénat for helpful discussions on this topic. This research was supported by the Centre National d'Études Spatiales (CNES-France) and by the Italian Ministry for Universities and Research (MIUR). We also thank the NASA/GSFC for the quality and availability of Aura-OMI and Aqua/Terra-MODIS data products.

References

Bhugwant, C., B. Siéja, M. Bessafi, T. Staudacher, and J. Ecormier (2009), Atmospheric sulfur dioxide measurements during the 2005 and 2007 eruptions of the Piton de La Fournaise volcano: Implications for human health and environmental changes, *J. Volcanol. Geotherm. Res.*, *184*, 208–224, doi:10.1016/j.jvolgeores.2009.04.012.

Boivin, P., and P. Bachèlery (2009), Petrology of 1977 to 1998 eruptions of Piton de la Fournaise, La Réunion Island, *J. Volcanol. Geotherm. Res.*, *184*, 109–125, doi:10.1016/j.jvolgeores.2009.01.012.

Brenguier, F., N. M. Shapiro, M. Campillo, A. Nercessian, and V. Ferrazzini (2007), 3-D surface wave tomography of the Piton de la Fournaise volcano using seismic noise correlations, *Geophys. Res. Lett.*, *34*, L02305, doi:10.1029/2006GL028586.

Carn, S. A., and G. J. S. Bluth (2003), Prodigious sulfur dioxide emissions from Nyamuragira volcano, D.R. Congo, *Geophys. Res. Lett.*, *30*(23), 2211, doi:10.1029/2003GL018465.

Collins, S. J., D. Pyle, and J. Maclennan (2008), Degassing of volatiles and transport of semi-volatile trace metals at Piton de la Fournaise—2007, *Eos Trans AGU*, *89*(53), Fall Meet. Suppl., Abstract V21B-2104.

Coppola, D., D. Piscopo, T. Staudacher, and C. Cigolini (2009), Lava discharge rate and effusive pattern at Piton de la Fournaise from MODIS data, *J. Volcanol. Geotherm. Res.*, *184*, 174–192, doi:10.1016/j.jvolgeores.2008.11.031.

Finizola, A., F. Sortino, J. F. Lénat, M. Aubert, M. Ripepe, and M. Valenza (2003), The summit hydrothermal system of Stromboli. New insights from self-potential, temperature, CO_2 and fumarolic fluid measurements, with structural and monitoring implications, *Bull. Volcanol.*, *65*, 486–504, doi:10.1007/s00445-003-0276-z.

Gailler, L., J. F. Lénat, M. Lambert, G. Levieux, N. Villeneuve, and J.-L. Froger (2009), Gravity structure of Piton de la Fournaise volcano and inferred mass transfer during the 2007 crisis, *J. Volcanol. Geotherm. Res.*, *184*, 31–48, doi:10.1016/j.jvolgeores.2009.01.024.

Lacroix, A. (1936), Le volcan actif de l'île de La Réunion et ses produits, 295 pp., Gauthier-Villars, Paris.

Lacroix, A. (1938), Le volcan actif de La Réunion (supplément) et celui de la Grande Comore, 57 pp., Gauthier-Villars, Paris.

Lénat, J.-F. (2007), Retrieving self potential anomalies in a complex volcanic environment: A SP/elevation gradient approach, *Near Surf. Geophys*, *5*, 161–170.

Lénat, J.-F., D. Fitterman, and D. B. Jackson (2000), Geoelectrical structure of the central zone of Piton de la Fournaise volcano (Réunion), *Bull. Volcanol.*, *62*(2), 75–89, doi:10.1007/s004459900058.

Lénat, J.-F., P. Bachèlery, and A. Peltier (2010), The interplay between collapse structures, hydrothermal systems and eruptions: The case of the central area of Piton de la Fournaise volcano, Collapse Caldera Workshop 2010 - La Réunion Island, Oct. 2010.

Michon, L., T. Staudacher, V. Ferrazzini, P. Bachelery, and J. Marti (2007), April 2007 collapse of Piton de la Fournaise: A new example of caldera formation, *Geophys. Res. Lett.*, *34*, L21301, doi:10.1029/2007GL031248.

Michon, L., N. Villeneuve, T. Catry, and O. Merle (2009), How summit calderas collapse on basaltic volcanoes: New insights from the April 2007 caldera collapse of Piton de la Fournaise volcano, *J. Volcanol. Geotherm. Res.*, *184*, 138–151, doi:10.1016/j.jvolgeores.2008.11.003.

Peltier, A., T. Staudacher, P. Bachèlery, and V. Cayol (2009), Formation of the April 2007 caldera collapse at Piton de La Fournaise volcano: Insights from GPS data, *J. Volcanol. Geotherm. Res.*, *184*, 152–163, doi:10.1016/j.jvolgeores.2008.09.009.

Realmuto, V. J., M. J. Abrams, M. F. Buongiorno, and D. C. Pieri (1994), The use of multispectral thermal infrared image data to estimate the sulfur dioxide flux from volcanoes: A case study from Mount Etna, Sicily, July 29, 1986, *J. Geophys. Res.*, *99*(B1), 481–488, doi:10.1029/93JB02062.

Revil, A., et al. (2008), Inner structure of La Fossa di Vulcano (Vulcano Island, southern Tyrrhenian Sea, Italy) revealed by high-resolution electric resistivity tomography coupled with self-potential, temperature, and CO_2 diffuse degassing measurements, *J. Geophys. Res.*, *113*, B07207, doi:10.1029/2007JB005394.

Rosi, M., L. Vezzoli, P. Aleotti, and M. De Censi (1996), Interaction between caldera collapse and eruptive dynamics during the Campanian Ignimbrite eruption, Phlegraean Fields, Italy, *Bull. Volcanol.*, *57*, 541–554, doi:10.1007/BF00304438.

Staudacher, T. (2010), Field observations of the 2008 summit eruption at Piton de la Fournaise (Ile de La Réunion) and implications for the 2007 Dolomieu collapse, *J. Volcanol. Geotherm. Res.*, *191*, 60–68, doi:10.1016/j.jvolgeores.2010.01.012.

Staudacher, T., V. Ferrazzini, A. Peltier, P. Kowalski, P. Boissier, P. Catherine, F. Lauret, and F. Massin (2009), The April 2007 eruption and the Dolomieu crater collapse, two major events at Piton de la Fournaise (La Réunion Island, Indian Ocean), *J. Volcanol. Geotherm. Res.*, *184*, 126–137, doi:10.1016/j.jvolgeores.2008.11.005.

Steffke, A. M., A. J. L. Harris, M. Burton, T. Caltabiano, and G. G. Salerno (2010), Coupled use of COSPEC and satellite measurements to define the volumetric balance during effusive eruptions at Etna, Italy, *J. Volcanol. Geotherm. Res.*, doi:10.1016/j.jvolgeores.2010.06.004, in press.

Tulet, P., and N. Villeneuve (2010), Large scale modeling of the transport, the chemical transformation and the mass budget of the sulfur emitted during the eruption of April 2007 by the Piton de la Fournaise, *Atmos. Chem. Phys. Discuss.*, *10*, 21,357–21,389.

Urai, M., N. Geshi, and T. Staudacher (2007), Size and volume evaluation of the caldera collapse on Piton de la Fournaise volcano during the April 2007 eruption using ASTER stereo imagery, *Geophys. Res. Lett.*, *34*, L22318, doi:10.1029/2007GL031551.

Watson, I. M., V. J. Realmuto, W. I. Rose, A. J. Prata, G. J. S. Bluth, Y. Gu, C. E. Bader, and T. Yu (2004), Thermal infrared remote sensing of volcanic emissions using the moderate resolution imaging spectroradiometer, *J. Volcanol. Geotherm. Res.*, *135*, 75–89, doi:10.1016/j.jvolgeores.2003.12.017.

Yang, K., N. A. Krotkov, A. J. Krueger, S. A. Carn, P. K. Bhartia, and P. F. Levelt (2007), Retrieval of large volcanic SO_2 columns from the Aura Ozone Monitoring Instrument: Comparison and limitations, *J. Geophys. Res.*, *112*, D24S43, doi:10.1029/2007JD008825.

D. Coppola, Dipartimento di Scienze Mineralogiche e Petrologiche, Università degli Studi di Torino, Via Valperga Caluso 35, I-10125 Turin, Italy.

M. Gouhier, Laboratoire Magmas et Volcans, UMR 6524, Clermont Université, Université Blaise Pascal, CNRS, IRD, BP 10448, F-63038 Clermont-Ferrand CEDEX, France. (m.gouhier@opgc.univ-bpclermont.fr)

JOURNAL OF GEOPHYSICAL RESEARCH, VOL. 113, B10202, doi:10.1029/2007JB005383, 2008

Mass estimations of ejecta from Strombolian explosions by inversion of Doppler radar measurements

Mathieu Gouhier[1] and Franck Donnadieu[1]

Received 13 September 2007; revised 25 June 2008; accepted 23 July 2008; published 4 October 2008.

[1] We present a new method for estimating particle loading parameters (mass, number, volume) of eruptive jets by inversion of echo power data measured using a volcano Doppler radar (VOLDORAD) during typical Strombolian activity from the southeast (SE) crater of Mount Etna on 4 July 2001. Derived parameters such as mass flux, particle kinetic and thermal energy, and particle concentration are also estimated. The inversion algorithm uses the complete Mie (1908) formulation of electromagnetic scattering by spherical particles to generate synthetic backscattered power values. In a first data inversion model (termed the polydisperse model), the particle size distribution (PSD) is characterized by a scaled Weibull function. The mode of the distribution is inferred from particle terminal velocities measured by Doppler radar for each explosion. The distribution shape factor is found to be 2.3 from Chouet et al.'s (1974) data for typical Strombolian activity, corresponding to the lognormal PSDs commonly characteristic of other Strombolian deposits. The polydisperse model inversion converges toward the Weibull scale factor producing the best fit between synthetic and measured backscattered power. A cruder, alternative monodisperse model is evaluated on the basis of a single size distribution assumption, the accuracy of which lies within 25% of that of the polydisperse model. Although less accurate, the monodisperse model, being much faster, may be useful for rapid estimation of physical parameters during real-time volcano monitoring. Results are illustrated for two explosions at Mount Etna with contrasted particle loads. Estimates from the polydisperse model give 58,000 and 206,000 kg as maxima for the total mass of pyroclasts, 26,400 and 73,600 kg s^{-1} for mass flux rates, 38 and 135 m^3 (22 and 76 m^3 equivalent magma volume) for the pyroclast volumes, and 0.02–0.4 and 0.06–0.12 kg m^{-3} for particle concentrations, respectively. The time-averaged kinetic energy released is found to be equal to 4.2×10^7 and 3.9×10^8 J, and thermal energy is estimated at 8.4×10^{10} and 3×10^{11} J.

Citation: Gouhier, M., and F. Donnadieu (2008), Mass estimations of ejecta from Strombolian explosions by inversion of Doppler radar measurements, *J. Geophys. Res.*, *113*, B10202, doi:10.1029/2007JB005383.

1. Introduction

[2] Volcanic explosions are important sources of information for understanding eruption mechanisms. The masses and velocities of gas and pyroclasts are particularly important parameters controlling the dynamics of an eruption as they define crucial parameters such as mass fluxes, kinetic and thermal energies released by an explosion. In order to better understand the dynamics of explosive eruptions, satellite imagery, and ground-based weather radars particularly have been used for the sounding of volcanic ash plumes from large eruptions [*Harris et al.*, 1981; *Harris and Rose*, 1983; *Weill et al.*, 1992; *Dean et al.*, 1994; *Dehn et al.*, 2000; *Lacasse et al.*, 2004]. These techniques probe the upper convective parts of high eruption columns and provide information primarily on the small particles that ultimately constitute the distal volcanic products. A major challenge is now to measure physical parameters, such as ejecta velocities and masses, close to the vent in order to retrieve directly the true source parameters. A first approach to measure jet velocities was used at Stromboli with an acoustic Doppler sounder (sodar) [*Weill et al.*, 1992]. Other techniques that potentially provide information on both velocity and mass parameters are ground-based portable Doppler radar, either pulsed such as volcano Doppler radar (VOLDORAD) [*Dubosclard et al.*, 1999; *Dubosclard et al.*, 2004] or frequency-modulated such as VERDEMOS [*Hort and Seyfried*, 1998; *Seyfried and Hort*, 1999]. These techniques allow direct measurement of particle velocities and reflectivities immediately above the vent. In addition to their significant monitoring potential, these radar systems allow us to study, under any weather conditions, explosions

[1]Laboratoire Magmas et Volcans, Clermont-Université, Observatoire de Physique du Globe de Clermont-Ferrand, Clermont-Ferrand, France.

0148-0227/08/2007JB005383$09.00

Table 1. Characteristics of VOLDORAD Version 2

Characteristic	Symbol	VOLDORAD 2
Transmitted frequency (MHz)	f_t	1274
Wavelength (cm)	λ	23.5
Peak power (W)	P_t	60
Pulse repetition period[a] (μs)	t_r	100
Pulse duration[a] (μs)	τ	0.8
Range resolution[a] (m)	L	120
Antenna beam width (deg)	α	9
Antenna beam elevation[a] (deg)	θ	23

[a]Parameters set for the sounding at Etna SE crater on 4 July 2001.

of lesser intensity barely imaged by satellites or weather radars.

[3] VOLDORAD was used to record several eruptive episodes at Etna in July 2001, ranging from mild Strombolian activity to paroxysmal lava fountains [*Donnadieu et al.*, 2005]. A new method based on inversion of echo power data measured using VOLDORAD is now presented for estimating the masses of pyroclasts ejected during individual explosions. The method also provides first-order estimates of mass-related parameters such as mass flux, ejecta volume, particle concentration, thermal and kinetic energy at the vent. The method was applied to two Strombolian explosions with contrasted particle loads that occurred during an eruptive episode of Mount Etna southeast (SE) crater on 4 July 2001. First, an algorithm is developed to simulate radar echoes from pyroclasts of various sizes, using the complete electromagnetic scattering formulation [*Mie*, 1908]. This approach provides synthetic data of power backscattered by particles (P_{synth}) at the particular wavelength employed by VOLDORAD. Second, as an input to the model, a scaled Weibull function [*Weibull*, 1939] is used to characterize the particle size distribution (PSD). The general shape of the Weibull distribution is constrained from published data for typical Strombolian activity [*Chouet et al.*, 1974], and the mode of the PSD is estimated from our own radar velocity measurements for each explosion. All Weibull parameters characterizing a polydisperse (multiple particle size) distribution, such as shape, shift, and scale factors, can then be deduced and used to compute synthetic values of backscattered power. Last, a recursive inversion algorithm is applied in order to obtain a PSD such that the synthetic power (P_{synth}) best fit the measured radar power (P_{mes}). The mass of ejected material and related parameters are then deduced. An alternative model is proposed on the basis of a monodisperse (single particle size) PSD, which turns out to be an acceptable approximation of the polydisperse model. This approach reduces computing time, making it useful for real-time quantitative assessment of ejected mass during volcano monitoring.

2. VOLDORAD: Volcano Doppler Radar

2.1. Radar Description

[4] VOLDORAD is a pulsed volcano Doppler radar developed by the Observatoire de Physique du Globe in Clermont-Ferrand (France) specifically for the active remote sensing of volcanic eruption jets and plumes. The second version of the system is a medium-power (60 W) Doppler radar of limited weight (~70 kg, including PC and antenna), with a 9° beam width (α) and a working wavelength (λ) of 23.5 cm [*Donnadieu et al.*, 2005]. VOLDORAD is designed to monitor all types of explosive volcanic activity of variable magnitude. It operates at a medium distance range (0.4–12 km) under all weather conditions with a high sampling rate ($\geq$10 Hz) that permits detailed analysis of early eruptive processes. The portability and lower electric consumption of this version compared to a first version of VOLDORAD is a valuable technical improvement. The pulse repetition period (t_r) is taken as 100 μs and directly defines the maximum velocity that can be measured by the radar:

$$V_{\max} = \frac{\lambda}{4N_c t_r} \tag{1}$$

where N_c is the number of coherent integrations of radar pulses. Note that the maximum velocity that can be measured in theory by VOLDORAD is very high (1175 m/s). This is valuable in particular for measuring the velocities of small particles traveling with speeds close to that of the gas. The pulse duration (τ) can be varied from 0.4 to 1.5 μs, and a value of 0.8 μs was used during the eruption of Mount Etna SE crater on 4 July 2001. This corresponds to a suitable range resolution of the sampling volume, the so-called range gate, of 120 m (Table 1).

[5] Volcanic ejecta crossing the antenna beam generate radar echoes backscattered to the receiver with an angular frequency Doppler shift ($d\varphi/dt$) between the transmitted and received signal that is related to the particle velocity along the beam axis:

$$\frac{d\varphi}{dt} = \omega = 2\pi f_d \tag{2}$$

where ω is the angular frequency and f_d is the Doppler frequency. Indeed, the Doppler velocity spectrum is related to the frequency spectrum via the relationship

$$f_d = \frac{-2V_r}{\lambda} \tag{3}$$

where V_r is the radial velocity and λ is the radar wavelength. When the target moves away from the radar ($V_r > 0$), the Doppler shift ($d\varphi/dt$) is negative, and vice versa when the target approaches.

2.2. Experimental Conditions

[6] After more than 8 months of minor activity (slow lava flows, degassing, light ash emission, and low-level Strombolian activity), a new episode of vigorous activity began at the SE crater on 9 May. From then until July–August 2001, there were eruptions from the SE crater every 3–5 days, each lasting on average a few hours and involving multiple Strombolian explosions and lava fountaining. Radar soundings reported here were carried out over about 5 h during an eruption on 4 July. The activity began at about 1800 UT and at first involved small explosions repeated every ~10 s. The intensity then increased progressively, culminating in very powerful Strombolian explosions every 2–3 s, with the bursting of very large bubbles between 2100 UT and 2200 UT but without real lava fountains. The eruption intensity then decreased rapidly from 2200 UT and ended at 2300 UT after about 5 h of Strombolian activity.

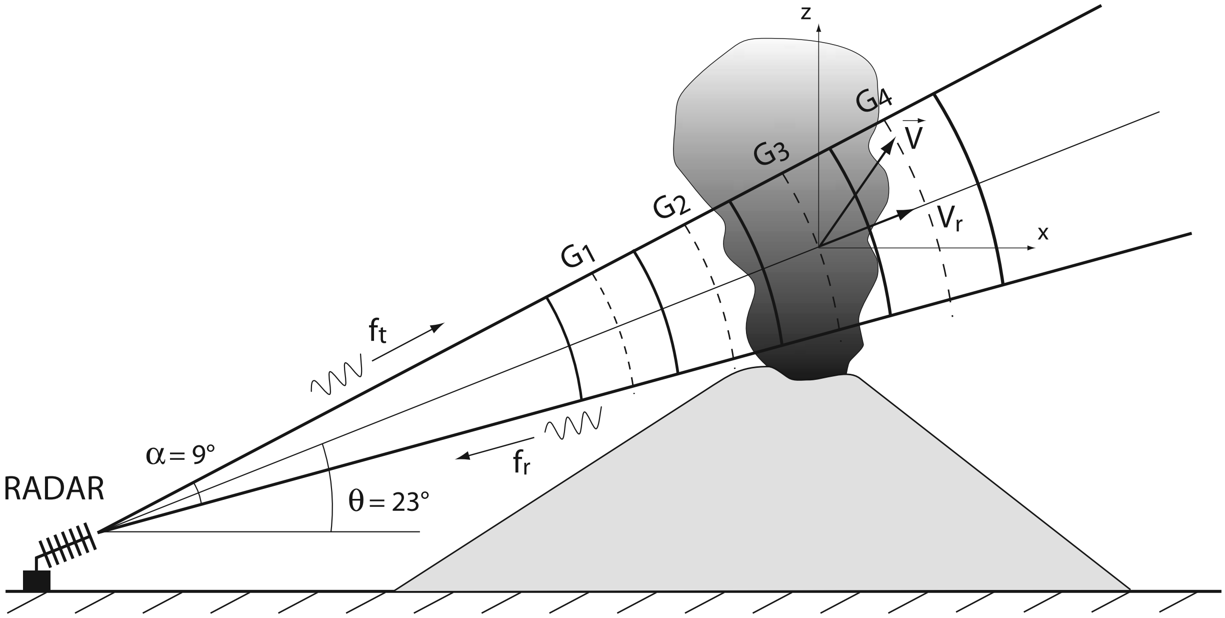

Figure 1. Sketch of the radar sounding geometry used for the acquisition campaign on Mount Etna, on 4 July 2001. VOLDORAD was set up at an altitude of 3000 m, at a slanting distance of 930 m to the crater rim, 280 m below the summit of the SE crater, and with an antenna elevation angle θ of 23°. Note that range gate G_3 is centered above the vent and provides most of the echo power.

VOLDORAD was set up at an altitude of 3000 m, at a slanting distance of 930 m to the crater rim, 280 m below the summit of the SE crater, and with an antenna elevation angle θ of 23° (Figure 1).

[7] Moving particles were detected in successive range gates (G_1 to G_4) corresponding to a slant distance of 807–1167 m (Table 2). In this configuration, particles ascending above the crater in range gate G_3 were recorded mainly with positive radial velocities (away from the antenna) in the Doppler spectra, whereas descending particles were mainly recorded with negative velocities.

2.3. Radar Parameters

[8] Data from successive range gates are displayed in real time as Doppler spectra representing the power spectral density versus radial velocity. From the processing of the series of Doppler spectra, two sets of parameters are directly retrieved for ascending (positive parameters indexed by a plus) and descending (negative parameters indexed by a minus) ejecta crossing the successive range gates above, or on either side of, the eruptive jet axis: (1) velocity information, in particular maximum and mean radial velocity (V^+_{max}, V^-_{max}, V^+_{mean}, V^-_{mean}) and (2) power (P_+, P_-) backscattered by particles contained in the sampling volume at a given instant [*Dubosclard et al.*, 2004].

Table 2. Gate Center Coordinates[a]

	G_1	G_2	G_3	G_4
Gate angle to the vertical (deg)	78	34	−23	−43
Slanting distance to the radar (m)	807	927	1047	1167
Horizontal distance to the crater (m)	−166	−56	54	165
Elevation above crater rim (m)	33	80	127	174
Gate height (m)	127	146	165	184

[a] G_1 to G_4, for an elevation angle of 23° and pulse duration of 0.8 μs.

[9] The received echo power from the particles (spectral moment of order 0) can be defined by the integral of the spectral power density $S(v)$ in a velocity interval between

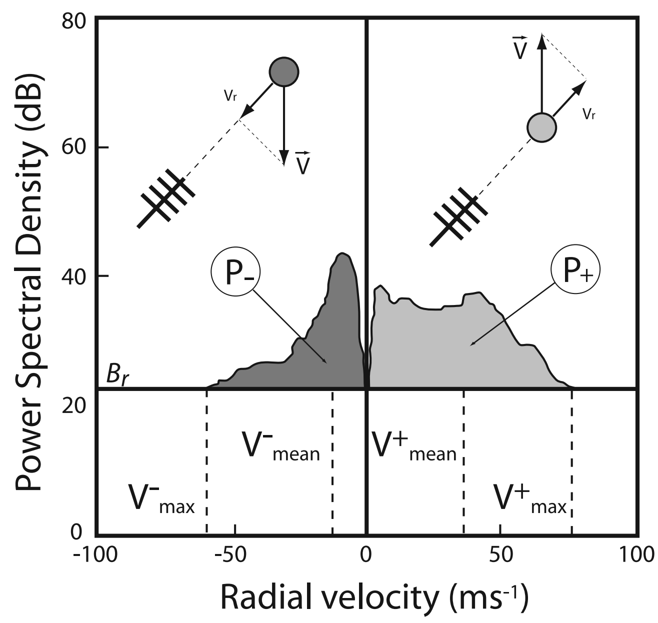

Figure 2. Sketch of a typical Doppler spectrum obtained by VOLDORAD. The power spectral density is displayed as a function of the radial velocity in a given range. The horizontal line (B_r) corresponds to the background noise level. Total echo power and maximum and mean velocities can be deduced from Doppler spectra. They are indexed (plus) and (minus) for ejecta with the radial component of their velocity vector moving away and toward the antenna, respectively.

v and $v + dv$, from 0 to $V^{+}_{\max}$ for ascending particles and from $V^{-}_{\max}$ to 0 for descending particles. The power measured in the Doppler spectra has been calibrated in the laboratory by means of an input signal, the power of which was known, delivered by an external frequency generator:

$$P_{+} = \int_{0}^{V^{+}_{\max}} S(v)dv, \quad P_{-} = \int_{V^{-}_{\max}}^{0} S(v)dv \tag{4}$$

Maximum radial velocities in the directions toward and opposite to the radar, $V^{-}_{\max}$ and $V^{+}_{\max}$, respectively, are defined where $S(v)$ is equal to the background noise level B_r (Figure 2). Likewise, for a given Doppler spectrum, V^{+}_{mean} and V^{-}_{mean} (spectral moment of order 1) of the ejecta are given by

$$V^{+}_{\text{mean}} = \frac{\int_{0}^{V^{+}_{\max}} vS(v)dv}{\int_{0}^{V^{+}_{\max}} S(v)dv}, \quad V^{-}_{\text{mean}} = \frac{\int_{V^{-}_{\max}}^{0} vS(v)dv}{\int_{V^{-}_{\max}}^{0} S(v)dv} \tag{5}$$

3. Electromagnetic Scattering Model

[10] The aim of this study is to estimate masses of volcanic ejecta from two Strombolian explosions with contrasted particle loads by inversion of the Doppler radar measurements. For this purpose, a comparison between the backscattered power measured by the radar (P_{mes}) and the synthetic (i.e., calculated) backscattered power (P_{synth}) is needed (see section 4. for more details on the inversion method). In this section, we first describe how to retrieve P_{mes}, and then we derive P_{synth} using the electromagnetic scattering theory of *Mie* [1908]. As shown by Figure 2, processing of the Doppler spectra yields the total backscattered power ($P_{\text{tot}} = P_{-} + P_{+}$). Raw power values ($P_{\text{mes}}$) can then be deduced directly from the radar conversion constant (C_c) that depends on technical characteristics of the radar acquisition line:

$$P_{\text{mes}} = P_{\text{tot}} C_c \tag{6}$$

On the other hand, P_{synth} can be derived from an electromagnetic scattering model. A good approximation for small particles is the Rayleigh scattering theory, the validity limit of which depends on the radar wavelength [*Sauvageot*, 1992]. This method is commonly used in meteorology, because the typical diameter of water droplets is small compared to the wavelengths of meteorological radars. In our case (λ = 23.5 cm), the Rayleigh theory can only be applied for particles of diameter (D_L) smaller than $\lambda/4$, which corresponds to $\sim$5.9 cm [*Gouhier and Donnadieu*, 2006]. However, considering the wide range of particle diameters characterizing volcanic activity, the complete scattering theory is required to account for the effects of larger particles. A general solution of electromagnetic wave scattering was given by *Mie* [1908]. This approach applies Maxwell's equations for plane waves scattered by compositionally homogeneous particles (Appendix A). For application to volcanic eruptions, we focus on waves scattered at a large distance by spherical particles, which we assume are homogeneously distributed in space. Theoretically, the power backscattered to the radar by a population of such particles in a given range gate is proportional to their radar reflectivity (η). The synthetic power can then be defined as

$$P_{\text{synth}} = \frac{C_r V_s \eta}{R^4} \tag{7}$$

where C_r is the radar constant, V_s, the sampling volume, and R, the slant distance between the radar and the target. The radar constant is defined by a set of technical parameters related to the radar configuration. The radar constant has been calibrated using a classical method comparing the reflectivity of rainfalls probed by the radar and the reflectivity calculated from the drop size distribution and velocity of the falling hydrometeors measured simultaneously with a disdrometer [*Pointin et al.*, 2005]. The radar reflectivity (η) is the sum of the backscattering cross sections (σ_{bks}) of the individual particles per unit volume. The reflectivity factor (Z) is defined by *Sauvageot* [1992] as

$$\eta = \sum_{i=1}^{n} \frac{\sigma_{\text{bks}(i)}}{V_s} \tag{8}$$

and

$$Z = \frac{\eta \lambda^4}{\pi^5 |K|^2} 10^{18} \tag{9}$$

Z (commonly confused with η in the literature) is often expressed in logarithmic units as dBZ and is related to η through the radar wavelength λ, and the particle complex dielectric factor $K = (m^2 - 1)/(m^2 + 2)$. Scattering and attenuation by compositionally homogeneous spheres are significantly influenced by the complex refractive index (m). VOLDORAD transmits power through a square array of four Yagi antennas, such that the incident electromagnetic wave is polarized parallel to the scattering plane. Being a monostatic radar (i.e., the same antenna is used for transmission and reception), we define a backscattering cross section (σ_{bks}) for horizontal linear polarization:

$$\sigma_{\text{bks}} = \frac{\lambda^2}{4\pi} \left| \sum_{n=1}^{\infty} (-1)^2 (2n+1)(a_n - b_n) \right|^2 \tag{10}$$

where a_n and b_n are the complex scattering coefficients (so-called Mie coefficients). Examples of Mie versus Rayleigh scattering patterns of an electromagnetic wave scattered by homogeneous spheres of four different sizes are shown in Figure 3 for a signal at the wavelength used by

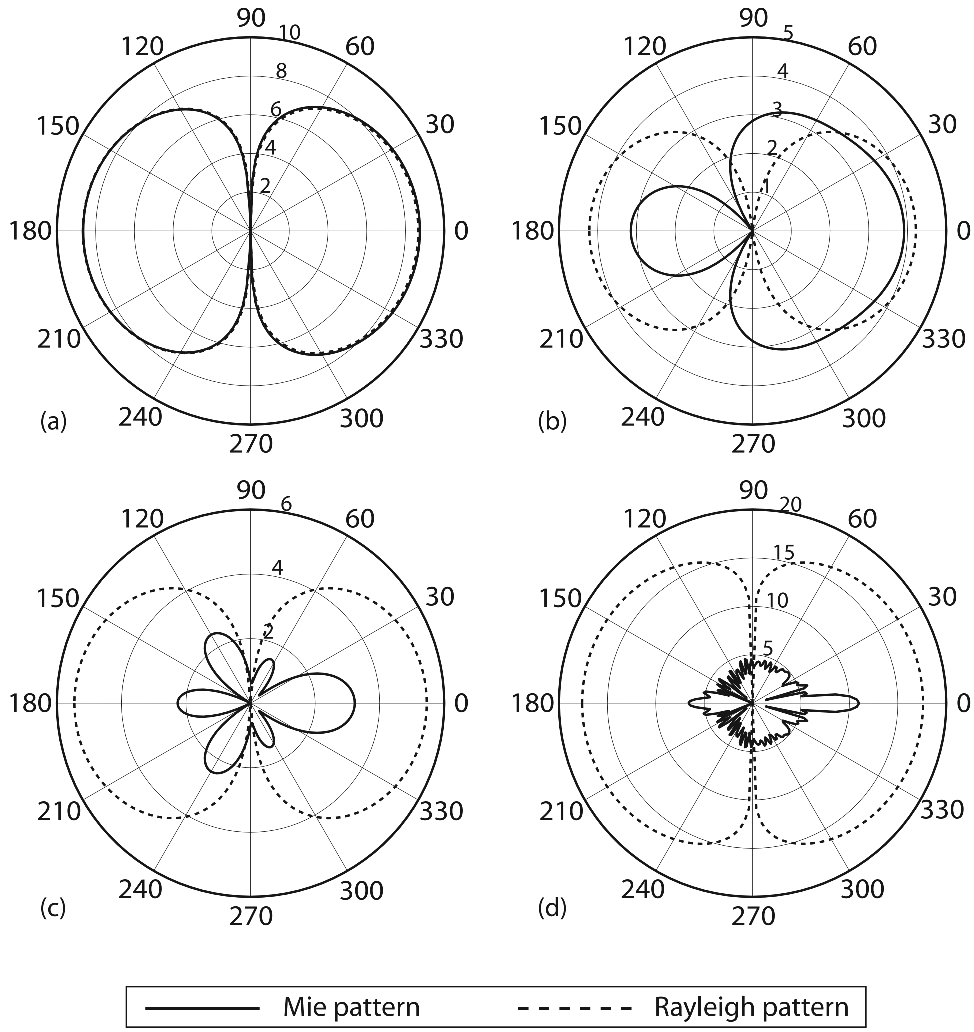

Figure 3. Mie versus Rayleigh scattering patterns of an electromagnetic wave, parallel polarized, scattered by a single homogeneous sphere with the complex dielectric factor of volcanic ash, $|K|^2 = 0.39$ [*Adams et al.*, 1996], and $\lambda = 23.5$ cm. The wave arrives from the left, and the particle is situated at the center of the pattern. Irradiance amplitude is normalized to that of Mie and expressed on a logarithmic scale. (a) Example of a small particle of diameter 2 cm. The Rayleigh and Mie scattering patterns are identical and symmetrical. Irradiance intensity is the same in front of and behind the particle. (b) Particle of diameter 14 cm. The Rayleigh and Mie scattering patterns are now significantly different. The Mie pattern still has two main lobes but is strongly asymmetric, as the backscattered intensity is lower than the forward scattered intensity. (c) Particle of diameter 20 cm. The Rayleigh pattern is still symmetrical, whereas the Mie pattern is divided into several lobes and shows much lower values of irradiance. (d) For a diameter of 2 m, the Mie (true) scattering pattern becomes very complex and shows always much lower values of irradiance than the Rayleigh approximation.

VOLDORAD ($\lambda = 23.5$ cm) and with the complex dielectric factor of volcanic ash ($|K|^2 = 0.39$) [*Adams et al.*, 1996]. These patterns illustrate the large discrepancy between the Rayleigh and Mie formulations for particle diameters larger than a few centimeters at 23.5 cm wavelength. Note that, at smaller radar wavelengths, this discrepancy occurs at even smaller particle diameters, making the complete Mie formulation absolutely necessary for studies of volcanic ejecta from radar measurements.

[11] Figure 4 shows the reflectivity factor (Z) as a function of particle diameter, using both the Mie and Rayleigh formulations for a wavelength of 23.5 cm. Note the overestimation of Z when computed using the Rayleigh approximation for particle diameters greater than ~5.9 cm.

4. Inversion Method

[12] Model inversions are frequently used in geophysics to recover initial parameters and boundary conditions from observed data of natural phenomena. In this case, backscattered power values (P_{mes}) are retrieved from radar measurements, and synthetic power data (P_{synth}) are determined from the forward electromagnetic-scattering model. The inversion algorithm thus seeks the best correlation between P_{mes} and P_{synth}, providing the optimum variable

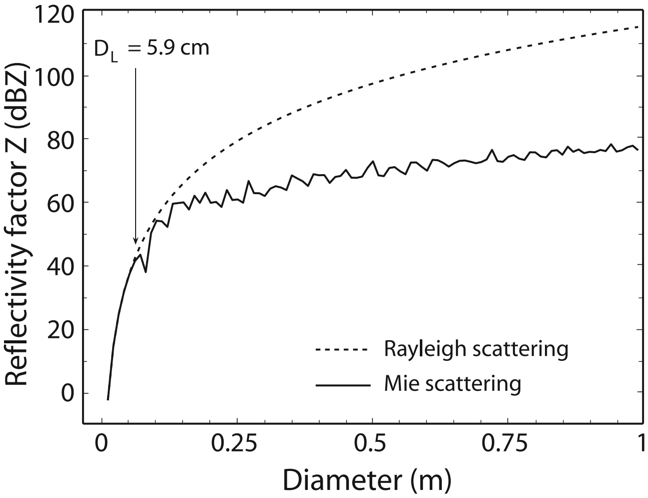

Figure 4. Synthetic reflectivity factor (Z, expressed in dBZ) as a function of particle diameter. Note the large overestimation of Z for large diameters when computed using the Rayleigh approximation. The validity domain depends on the radar wavelength. In the case of VOLDORAD (λ = 23.5 cm), the validity limit (D_L) lies close to 5.9 cm, i.e., $\sim\lambda/4$ [*Gouhier and Donnadieu*, 2006].

input parameters defined by the vector (X) that characterizes the PSD. Physical parameters such as particle mass and volume are then deduced from the PSD. The model takes into account two main classes of parameters: (1) constant parameters describing the geometry of the system, the technical characteristics of the radar or material physical properties; (2) the vector of variable input parameters (X; see below) defining the Weibull function of the PSD. A least squares estimation method is used on the basis of the minimization function $S(X)$ characterized by the squared residual between radar measured data and synthetic data:

$$S(X) = \sum \left[P_{\mathrm{mes}} - P_{\mathrm{synth}}(X)\right]^2 \quad (11)$$

Finally, a comparison criterion between radar-measured (P_{mes}) and synthetic (P_{synth}) power data is used to stop the recursive loop when the fitting criterion is reached. The successive steps of the inversion algorithm are summarized below.

[13] Step 0 is attribution of initial values for estimation of the input parameters:

$$X_j \equiv [X_1, X_2, \ldots, X_n]$$

[14] Step 1 is resolution of the direct model (Mie scattering):

$$X \rightarrow P(X)_{\mathrm{synth}}$$

[15] Step 2 is calculation of the minimization function:

$$S(X) = \sum \left[P_{\mathrm{mes}} - P_{\mathrm{synth}}(X)\right]^2$$

[16] Step 3 is characterization of the iterative comparison criterion:

$$\Delta P\left(X^i\right) = S\left(X^{i-1}\right) - S\left(X^i\right)$$

[17] Step 4 is testing of the fitness criterion:

$$\Delta P(X) < 0$$

where $\Delta P(X)$ is the fitness criterion, and indices i and j refer to the step of the iterative procedure and the number of variable parameters, respectively. When a satisfactory solution is reached, the iterative procedure stops. The computational procedure is summarized in Figure 5.

5. Polydisperse Particle Size Model

5.1. Particle Size Distribution

[18] Solving the inverse problem consists of estimating the shape of the PSD by best fit matching of synthetic and observed data. Various PSDs have been used in, or inferred from, previous studies of volcanic ejecta: exponential [*Ripepe et al.*, 1993], lognormal [*Sheridan*, 1971; *Chouet et al.*, 1974; *McGetchin et al.*, 1974; *Self et al.*, 1974], Rosin

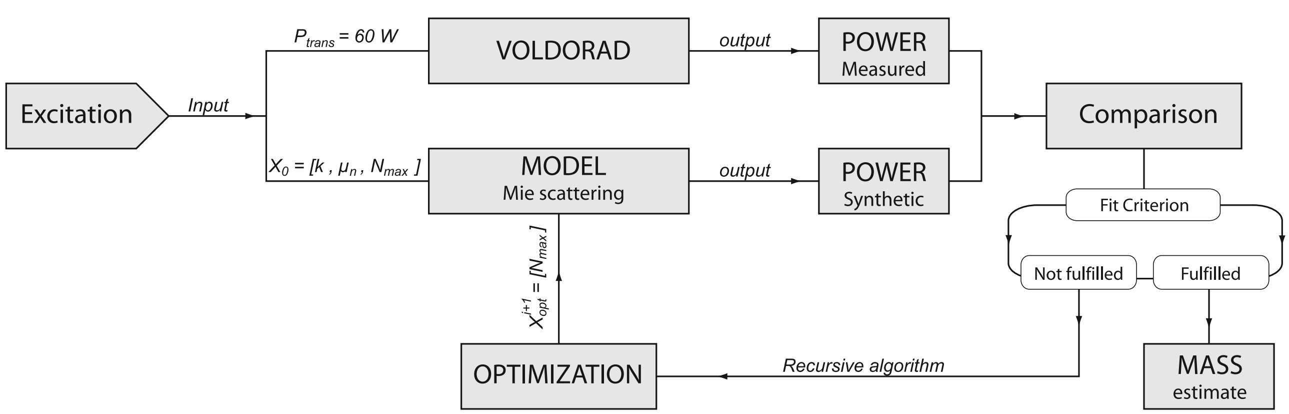

Figure 5. Sketch of the inversion approach. Synthetic radar power data (P_{synth}) are provided from the theoretical model (Mie formulation) and compared to the power data measured (P_{mes}) by VOLDORAD. If the fit criterion is met, the procedure stops and gives the best result. Otherwise, the input parameters (X) are optimized in the recursive loop, and the calculation is repeated.

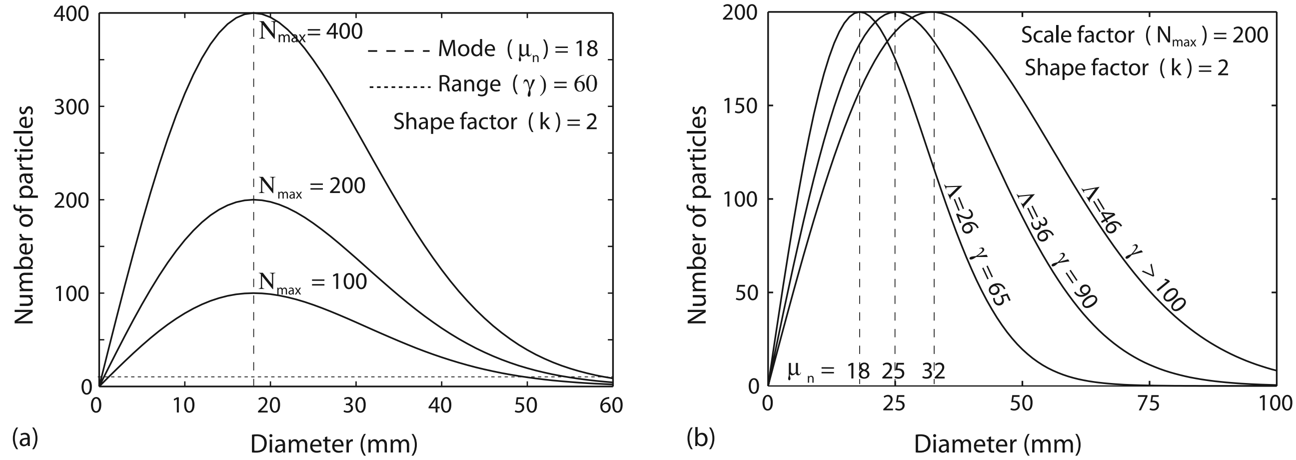

Figure 6. Evolution of the particle size distribution (PSD) for different values of shift (Λ) and scale factors ($N_{\max}$). For both examples, the shape factor is constant at k = 2. (a) The scale factor ($N_{\max}$) represents the maximum number of particles with diameter μ_n and, therefore, directly controls the total number of particles. (b) The mode (μ_n) and range (γ) of the distribution evolve jointly with the shift factor.

Rammler [*Kittleman*, 1964; *Spieler et al.*, 2003], Weibull [*Nakamura*, 1984; *Marzano et al.*, 2006a, 2006b], polymodal [*Sheridan et al.*, 1987; *Riley et al.*, 2003] and sequential fragmentation/transport (SFT) [*Wohletz et al.*, 1989]. However, there is still a lack of consensus on which PSD best characterizes Strombolian activity, particularly for the largest particle diameters. For this reason, a scaled Weibull function is used, because its overall shape may be varied widely from exponential to Gaussian by means of only three factors: shape (k), shift (Λ), and scale ($N_{\max}$). The PSD can then be adjusted easily during the optimization phase of the data inversion procedure. The scaled Weibull distribution S_w is defined through a probability density function f_w of particles with diameter D:

$$S_w(D; k, \Lambda, N_{\max}) = \frac{f_w(D; k, \Lambda)}{\max[f_w(D; k, \Lambda)]} N_{\max} \tag{12}$$

with

$$f_w(D; k, \Lambda) = \left(\frac{k}{\Lambda}\right)\left(\frac{D}{\Lambda}\right)^{(k-1)} \exp\left(\frac{-D}{\Lambda}\right)^k \tag{13}$$

The shape factor (k) allows us to choose from an exponential (k = 1) to Gaussian (k = 3) distribution, along with all intermediate lognormal distributions (1 < k < 3). The shift factor (Λ) directly depends on the mode (μ_n) of the PSD and on the shape factor (k). It can be defined by using

$$\Lambda = \mu_n \left(\frac{k-1}{k}\right)^{-1/k} \tag{14}$$

$N_{\max}$ is the maximum number of particles of diameter μ_n in the scaled Weibull distribution (Figure 6a). It is the dominant term in the computation of the synthetic power because it strongly influences the estimate of particle mass.

[19] The three variable parameters (k, μ_n, $N_{\max}$) controlling the PSD make up the vector X of input parameters to the model. However, in order to obtain a unique solution to the inverse problem, the number of variable parameters is reduced. This also increases the efficiency and speed of the algorithm. Parameters k and μ_n are constrained from the following assumptions argued in subsequent sections: (1) the PSD of Strombolian explosions can be characterized on average by a single shape factor k; (2) the mode of the PSD (μ_n) can be determined from mean particle terminal velocity estimated from the radar measurements. These assumptions then reduce the optimization procedure to a single free parameter ($N_{\max}$).

5.2. Parameter Constraints

5.2.1. Shape Factor, *k*

[20] Data on Strombolian PSDs are scarce in the literature. However, *Chouet et al.* [1974] gave an exhaustive description of two explosions at Stromboli Volcano by photoballistic analysis. They made an estimate of the PSD for inflight ejecta (which is what a radar records), and determined the modes, ranges, numbers and sizes of particles for two explosions. They also deduced eruptive parameters such as number, mass and volume of ejected particles, and found that one explosion contained a number and mass of particles about 17 times greater than the other (Table 3). We use this study, where all output parameters are already known, to determine the input parameter (k) that best describes the two Strombolian explosions observed by *Chouet et al.* [1974]. With this aim, we first calculate the "equivalent" radar power corresponding to the total ejected mass estimated by *Chouet et al.*'s [1974] observations for two Strombolian explosions. Then synthetic radar powers are computed for different values of shape factor k. Finally, the recursive procedure stops when synthetic radar powers match the equivalent radar power and when synthetic particle loading parameters (number, mass, volume) corre-

Table 3. Comparison Between Values Observed by *Chouet et al.* [1974] on Two Explosions at Stromboli and Synthetic Values Calculated by the Inversion Algorithm[a]

	Symbol	Explosion 1: Sep 1971 Observed Data	Explosion 1: Sep 1971 Synthetic Data	Explosion 2: Sep 1971 Observed Data	Explosion 2: Sep 1971 Synthetic Data
Number of particles	N	2588	2588	146	144
Mode (m)	μ_n	0.022	0.022	0.025	0.025
Range (m)	γ	?–0.06	0.004–0.06	?–0.06	0.001–0.06
Volume (m^3)	V	0.033	0.035	0.002	0.0027
Mass (kg)	M	51	53	3	4.1

[a]Note that the best fit for both sets of data is reached for the same shape factor k = 2.3 (lognormal particle size distribution).

spond to those described by *Chouet et al.* [1974]. Note that an alternative method would have been simply to determine k from a best fit function of the *Chouet et al.* [1974] PSD. However, our chosen approach had the advantage of additionally testing our inversion algorithm.

[21] The best fit between the observed and synthetic PSDs is reached in both cases for the same value of k = 2.3, which describes a lognormal distribution. The equivalent synthetic power achieved is about 3.3×10^{-9} and 3.2×10^{-10} mW for explosions 1 and 2 respectively, and corresponds to equivalent reflectivity factors (Z) of 61 and 51 dBZ. The inversion procedure yields three parameters (number, mode and range) characterizing the synthetic PSDs, from which two eruptive parameters (mass and volume) are directly deduced (Table 3). The agreement between observed and synthetic parameters is very good and validates our inversion algorithm. Shape factor estimation can then be used afterward with reasonable confidence. Furthermore lognormal PSDs have also been inferred from deposits of Strombolian activity on other volcanoes, like Etna [*McGetchin et al.*, 1974] and Heimaey [*Self et al.*, 1974]. Although k may vary between individual explosions on Stromboli, as well as between Strombolian eruptions at different volcanoes, we assume in what follows that the value k = 2.3, found for both explosions at Stromboli, represents a suitable average value for Strombolian PSDs and use it as input to the model. Moreover, sensitivity tests reveal a limited dependence of the total ejected mass on k, varying only by a factor of two for values of k ranging from 2.0 to 2.6.

5.2.2. Shift Factor, Λ

[22] The shift factor (Λ) is linked to the mode (μ_n) and range (γ) via the shape factor (k) (Figure 6b). The mode of the distribution is estimated directly from radar measurements using the terminal settling velocities of ejected particles. Indeed, under the assumptions of vertical trajectories, no wind influence, and terminal fall velocity, an average particle diameter D_p can be deduced from the mean negative radial velocity weighted by the power spectral density [*Rogers and Yau*, 1989; *Hort et al.*, 2003]

$$D_p = \frac{C_s}{P_-} \sum_{V^-_{\max}}^{0} S(v) \left(\frac{V_r}{\sin\theta} \right)^2 \tag{15}$$

where $S(v)$ is the spectral power in a velocity interval. P_- refers to the power backscattered mainly by descending particles (left part of the Doppler spectrum), and θ stands for the antenna beam elevation angle. C_s is the shape coefficient, which for a spherical particle is:

$$C_s = \frac{3}{4} C_d \frac{\rho_a}{\rho_p g} \tag{16}$$

with C_d being the drag coefficient, g the gravitational acceleration and ρ_a, ρ_p the densities of air and particles respectively. Importantly, the interpretation of D_p retrieved from Doppler radar spectra differs significantly from μ_n (the mode of the PSD). Indeed, μ_n corresponds to the particle diameter that is most represented in the particle size distribution, i.e., the top of the curve. In radar meteorology, D_p is approximately equal to μ_n because the size distributions of atmospheric water droplets are typically Gaussian and very narrow. In a volcanic jet however, the power spectrum is much wider [e.g., *Dubosclard et al.*, 1999], and the physical interpretation of D_p is therefore more complex. D_p and μ_n are offset by a factor based on the dependence of the reflectivity (calculated at a given radar wavelength) on the number (N) and diameter (D) of particles. Thus μ_n is obtained from D_p using a scattering formulation adequate for the range of particle sizes characterizing explosive volcanic activity [*Woods and Bursik*, 1991; *Gouhier and Donnadieu*, 2006]. Once k and μ_n are obtained, the shift factor Λ can be calculated from equation (14).

5.2.3. Scale Factor, $N_{\max}$

[23] By assuming that k and μ_n are constant throughout the inversion procedure, the parameter vector X then becomes dependent on just a single free parameter, the scale factor, $N_{\max}$. This characterizes the maximum of the scaled Weibull distribution curve (S_w) and evolves during the optimization phase of the algorithm. It describes, along with k and μ_n, the total number of particles ejected during the explosion, and hence controls the erupted mass estimation. The accuracy of the results depends on the step chosen between two successive values of $N_{\max}$ in the recursive loop. However, although a small step leads to a more accurate estimation, it increases considerably the computing time.

6. Monodisperse Particle Size Model

[24] An alternative data inversion model based on a monodisperse PSD approximation is now presented. In this model, the single particle size equals μ_n, as well as D_p.

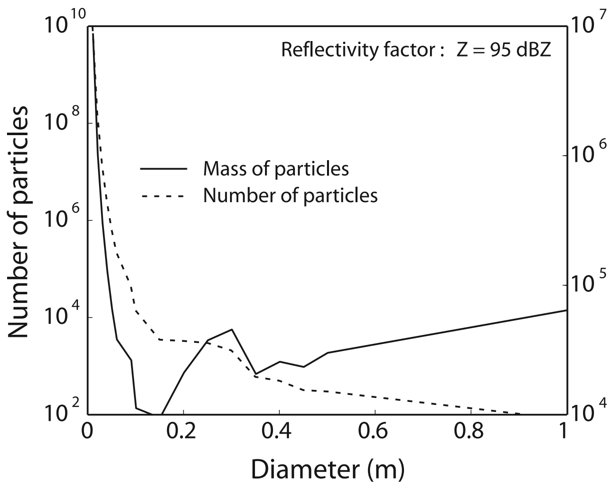

Figure 7. Plot of the total mass and number of particles as a function of their diameter in the monodisperse model for a reflectivity factor $Z = 95$ dBZ. Small particles contribute the most to the total ejected mass, for example, 8.8×10^6 kg for a diameter of 0.01 m, compared to 6.4×10^4 kg for a diameter of 1 m, i.e., a difference of 2 orders of magnitude.

Figure 7 shows that the number of small particles required to generate a given reflectivity can be up to several orders of magnitude larger than the number of corresponding large particles. Because of this huge difference in particle number, the fraction of small ejecta contributes most to the total estimated mass. For example, a reflectivity of 95 dBZ requires 8.8×10^6 kg of 0.01 m particles compared to 6.4×10^4 kg of 1 m particles, a difference of 2 orders of magnitude. This result illustrates that large blocks are not so important in first-order estimations of total ejected mass. This monodisperse PSD model significantly reduces computing time and ensures fast synthetic power calculations. Mass estimations are provided in Figure 8 for a wide range of realistic values of D_p and Z. Since these parameters are derived directly from the Doppler spectra, the corresponding mass can be retrieved instantaneously without any computing phase. This alternative method is valuable because a first-order mass estimate of ejected pyroclasts can be obtained in real time and used for volcano monitoring.

7. Radar Data

[25] Strombolian explosions and lava fountains were monitored with VOLDORAD for several hours during eruptive episodes of the SE crater on 4, 7, and 13 July 2001. We focus on data acquired during two explosions that occurred at 2141:53 and 2141:56 UT during the eruption of 4 July. The two explosions were each short-lived, with durations of about 3 s. Temporal series (Figure 9) of radar power are computed from the power spectral density $S(v)$, and sampled at a high frequency (10 Hz) suitable for such short-lived explosions.

[26] It is important that the power used as input to the inversion model be defined carefully. First, it is essential to ensure that the total power at a given instant is the sum of P_{tot} across the different range gates along the beam axis. Were the jet wider than the width of a single range gate (120 m), it would be necessary to integrate across several range gates in order to obtain the total reflected power. However, in the cases studied here, both jets were sufficiently narrow as to fit within a single range gate (G_3). This is deduced from (1) visual inspection of video snapshots and (2) the lack of echo power signal from neighboring range

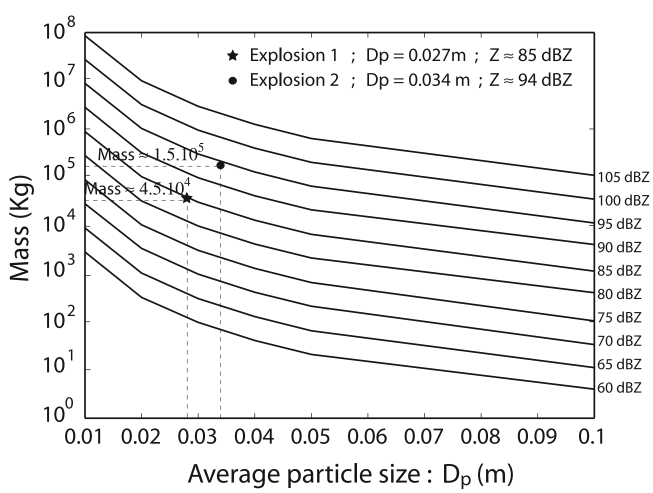

Figure 8. Mass estimate as a function of average particle size (D_p) retrieved from the power spectral density using the monodisperse model for different reflectivity factors (Z) of ejected particles. First-order mass assessments can be given simply from the reflectivity factor (Z) and the average particle size (D_p) determined directly from the Doppler spectra, without any computation phase. Masses of 4.5×10^4 kg and 1.5×10^5 kg are roughly estimated for explosions 1 and 2, respectively.

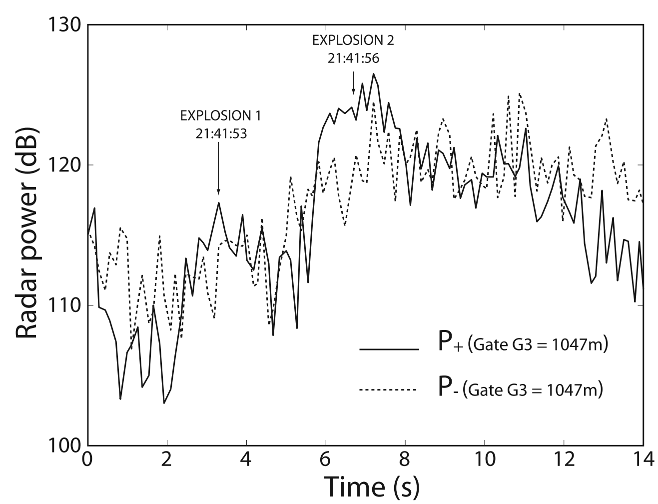

Figure 9. Temporal evolution of radar echo power during the two explosions studied at Mount Etna on 4 July 2001, sampled at 10 Hz. Both echo powers of particles moving away from (P_+) and toward (P_-) the antenna are plotted in order to infer the total power at a given instant in the range gate (G_3) located above the vent. Both explosions are brief, lasting 2.2 and 2.8 s, respectively. The second explosion is much more powerful (125 and 123 dB for P_+ and P_-, respectively) than the first (117 and 115 dB).

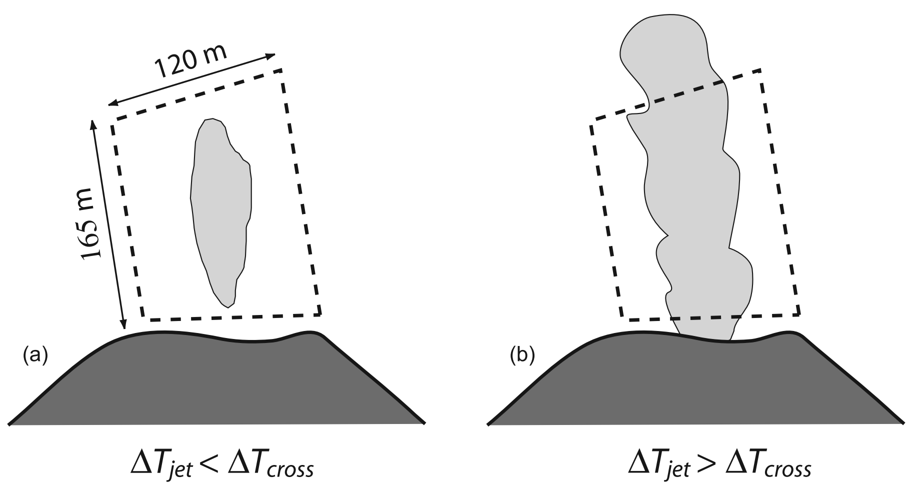

Figure 10. Sketch illustrating the two hypotheses made in the calculation of total power. $\Delta t_{\rm jet}$ is the duration of jet production, and $\Delta t_{\rm cross}$ is the time necessary for the jet to traverse vertically the range gate. (a) Example of a short-lived jet ($\Delta t_{\rm jet} < \Delta t_{\rm cross}$): the jet is short enough to be wholly enclosed in the sampling volume. A single Doppler spectrum can then be used for the calculation of total power. (b) Example of a long-lived jet ($\Delta t_{\rm jet} > \Delta t_{\rm cross}$): the jet is too long to be contained entirely in the sample volume at a given instant. The maximum radar echo power represents only a fraction of the total amount of ejected particles, and several Doppler spectra have to be taken into account for the calculation of the total power. The two explosions jets of 4 July 2001 at Mount Etna studied in this paper were both short-lived.

gates (G_2 and G_4). Integration along the beam axis is therefore unnecessary.

[27] The second requirement is that the reflected power be integrated throughout the entire duration of the explosion as the jet passes vertically across the range gate concerned (G_3). In this case, two situations can be envisaged, as shown schematically in Figure 10. To explain these two cases, we consider two time durations: $\Delta t_{\rm jet}$, the duration of jet production, and $\Delta t_{\rm cross}$, the time necessary for the jet to traverse vertically the given range gate. In the first case (Figure 10a), $\Delta t_{\rm jet} < \Delta t_{\rm cross}$ and the jet is thus short enough for most of the particles to be recorded at the same instant inside a single sampling volume. The peak of radar echo power can therefore be considered as representative of the entire jet and the input parameters to the model can be derived on the basis of a single Doppler spectrum. When $\Delta t_{\rm jet} \geq \Delta t_{\rm cross}$ (Figure 10b), the jet is never entirely contained within a single range gate, and the peak of echo power represents only a fraction of the constituent particles. Integration over the duration of the jet ($\Delta t_{\rm jet}$) is therefore essential. Note that for lava fountaining sustained over longer periods of time at a relatively steady rate, the mean residence time of ejecta inside the range gate would need to be taken into account. This could be inferred from velocities measured by the radar and from the sounding geometry, leading to estimation of the mass flux. The total mass of lava ejected could then be calculated using the duration of the lava fountain.

[28] In the explosions considered here, the average time $\Delta t_{\rm cross}$ taken by the jet to cross the range gate (G_3) is 4.7 s at an average velocity of 38 m s^{-1} for explosion 1, and 2.9 s at 62 m s^{-1} for explosion 2. By comparison, $\Delta t_{\rm jet}$ is estimated from videos and radar time series at 2.2 and 2.8 s for explosions 1 and 2, respectively. In both cases, therefore, $\Delta t_{\rm jet} < \Delta t_{\rm cross}$; no time integration is necessary, and data analysis can be based on a single Doppler spectrum. Moreover, the explosion jets commonly become depleted in blocks, and proportionally richer in gas toward the waning stage of their emission, so that the relevant values for $\Delta t_{\rm jet}$ might actually even be lower.

8. Results

[29] Results of the polydisperse and monodisperse models are shown in Tables 4a–4c and 5a–5c. The fitness between observed and synthetic power data is very good, with 98.7% and 97.8% for explosions 1 and 2, respectively.

8.1. Particle Loading Parameters

[30] Using the more accurate polydisperse model, the total mass of pyroclasts ejected by the first explosion (Tables 4a–4c) is estimated at 58,400 kg, corresponding

Table 4a. Synthetic Results for Explosion 1 (2141:53 UT) at Mount Etna SE Crater[a]

		Synthetic Results	
	Symbol	Monodisperse PSD	Polydisperse PSD
Number of particles	N	2.75×10^6	13.9×10^6
Mode (m)	μ_n	0.027	0.013
Volume (m^3)	V	28.4	38.2
Mass (kg)	M	43.4×10^3	58.4×10^3
Concentration[b] (kg m^{-3})	C	0.01–0.2	0.02–0.4
Reflectivity factor (dBZ)	Z	85.16	85.13
Power (mW)	$P_{\rm synth}$	8.14×10^{-7}	8.08×10^{-7}

[a]Results are from using both the polydisperse particle size distribution model and the monodisperse approximation.

[b]Concentration parameters are poorly constrained and have to be regarded as rough approximations (see text for details).

Table 4b. Model Parameters for Explosion 1 (2141:53 UT) at Mount Etna SE Crater

Parameters	Input/Output
μ_n	0.0129
D_p	0.027
Λ	0.0165
k	2.3
γ	0.01–0.056
$N_{\max}$	8.00×10^5
Fit (%)	98.68

to a volume of 38 m^3 assuming a pyroclast density of 1530 kg m^{-3} [*McGetchin et al.*, 1974] and a reflectivity factor of 85 dB*Z*. The equivalent magma volume (DRE), for a density of 2700 kg m^{-3} [*Williams and McBirney*, 1979] is 22 m^3. The second explosion (Tables 5a–5c) yields higher values of the different parameters, with an ejecta mass of 206,000 kg, a pyroclast volume of 135 m^3, a reflectivity factor of 94 dB*Z*, and a magma volume of 76 m^3. The difference between the reflectivity factors of the two explosions is 9 dB*Z*, meaning that the second explosion jet is about 8 times more reflective than the first, and the ejecta volume and mass are consequently about 3.5 times higher. This agrees with visual observations which show clearly that the first explosion involved a smaller quantity of incandescent lava clots than the second explosion (Figure 11).

[31] Particles numbers, masses and volumes estimated using the monodisperse model lie within ~25% of those of the polydisperse model for both explosions (Tables 4a–4c and 5a–5c). This underestimation is accounted for by small particles that are not considered in the monodisperse model, but that in reality contribute most to the total mass, owing to the great particle number required to match a given reflectivity.

[32] It is instructive to compare the measured reflectivity factors of the two Etna explosions with those theoretically calculated at Stromboli from the *Chouet et al.* [1974] observations. Recall that reflectivity factor (Z) is a positive function of the number (N) and diameters (D) of ejected particles. The two explosions at Stromboli give reflectivity factors of 61 dB*Z* and 51 dB*Z* (Table 3), whereas the two explosions at Etna give 85 and 94 dB*Z* (Tables 4a–4c and 5a–5c). Thus, even a small explosion at Etna is over 250 times more reflective than a large one at Stromboli, and involves a mass of ejecta 3 orders of magnitude higher (Table 3). For comparison, very heavy rainfall induces maximum reflectivity factors of ~60 dB*Z* [*Sauvageot*, 1992].

Table 4c. Characteristics for Explosion 1 (2141:53 UT) at Mount Etna SE Crater

Characteristic	Value
Date	4 July 2001
Time (UT)	2141:53
t_{jet} (s)	2.2
$V^+_{\max}$ (m/s)	60
$\bar{V}^{+\,a}_{\max}$ (m/s)	37.9
Z (dBZ)	85.12
P_{mes} (mW)	8.10×10^{-7}

[a]The parameter $\bar{V}^+_{\max}$ is the time-averaged maximum velocity and differs from the mean velocity calculated by the radar.

Table 5a. Synthetic Results for Explosion 2 (2141:56 UT) at Mount Etna SE Crater[a]

		Synthetic Results	
	Symbol	Monodisperse PSD	Polydisperse PSD
Number of particles	N	5.00×10^6	23.3×10^6
Mode (m)	μ_n	0.034	0.016
Volume (m^3)	V	102.9	134.7
Mass (kg)	M	157×10^3	206×10^3
Concentration[b] (kg m^{-3})	C	0.05–0.1	0.06–0.12
Reflectivity factor (dBZ)	Z	93.78	93.77
Power (mW)	P_{synth}	5.92×10^{-6}	5.87×10^{-6}

[a]Results are from using both the polydisperse particle size distribution model and the monodisperse approximation.

[b]Concentration parameters are poorly constrained and have to be regarded as rough approximations (see text for details).

8.2. Derived Parameters

[33] The mean mass fluxes of ejecta, estimated from the duration of each explosion (Tables 4a–4c and 5a–5c), reach 26,400 and 73,600 kg s^{-1} for explosions 1 and 2, respectively. These represent time-averaged values, and are not expected to be constant over the duration of each explosion.

[34] We have also attempted to estimate particle concentrations in the two explosion jets at Etna. This is difficult since, although the radar data provide estimates of total particle mass, the jet volumes are poorly constrained. One possibility is to make the assumption that each jet filled completely and homogeneously the range gate volume. In this case, concentration estimates have to be regarded as minima. Using the volume of range gate (G_3) above the crater yields values of 0.02 and 0.06 kg m^{-3} for explosions 1 and 2, respectively. However, inspection of video footage (Figure 11) shows that this assumption is probably not realistic. The other option is to make an estimate of the jet volume from video snapshot analysis, but two difficulties are inherent in this approach: first, the jets are spatially heterogeneous, and, second, only large lava clots are visible and the volume occupied by ash and small laplli cannot be estimated. However, taking limiting edges on video snapshots yields that the jets of explosions 1 and 2 represent approximately 5% and 50%, respectively, of the range gate volume. Using these values gives maximum particle concentrations estimates of about 0.4 and 0.12 kg m^{-3} for explosion jets 1 and 2, respectively (Tables 4a–4c and 5a–5c). Note that these concentrations represent spatially averaged values over the estimated jet volume; however, much higher ejecta concentrations can be found locally especially close to the vent.

[35] The high data sampling rate (~10 Hz in the configuration used for this study) allows VOLDORAD to measure rapid signal fluctuations on the timescale of an individual

Table 5b. Model Parameters for Explosion 1 (2141:56 UT) at Mount Etna SE Crater

Parameters	Input/Output
μ_n	0.0164
D_p	0.034
Λ	0.021
k	2.3
γ	0.01–0.072
$N_{\max}$	1.05×10^6
Fit (%)	97.82

Table 5c. Characteristics for Explosion 2 (2141:56 UT) at Mount Etna SE Crater

Characteristic	Value
Date	4 July 2001
Time (UT)	2141:56
t_{jet} (s)	2.8
$\bar{V}^{+}_{max}$ (m/s)	100
$\bar{V}^{+}_{max}$ [a](m/s)	61.6
Z (dBZ)	93.83
P_{mes} (mW)	6.00×10^{-6}

[a]The parameter $\bar{V}^{+}_{max}$ is the time-averaged maximum velocity and differs from the mean velocity calculated by the radar.

explosion. It is therefore possible to calculate an average ejecta velocity, and hence a mean kinetic energy for an explosion, using

$$E_k = \frac{1}{2}M\left(\frac{1}{N_t}\sum_{i=1}^{n} V^{+}_{max}(i)\right)^2 \tag{17}$$

where M is the total ejected mass given in Tables 4a and 5a and $\bar{V}^{+}_{max}$ is the maximum radial velocity, given in Tables 4c and 5c Doppler spectrum (i) recorded in the sampling volume. N_t is the total number of Doppler spectra acquired during a given explosion. A mean kinetic energy of 4.2×10^7 J is obtained for a time-averaged maximum radial velocity ($\bar{V}^{+}_{max}$) of 38 m s^{-1} for explosion 1 and 3.9×10^8 J for 62 m s^{-1} for explosion 2. These values can be compared with the thermal energies of explosions 1 and 2 from equation (18), which are estimated at 8.4×10^{10} J and 3×10^{11} J, respectively, assuming a magma temperature T of 1373 K [*Francalanci et al.*, 1989] and a magma specific heat capacity, C_p, of 1050 J kg^{-1} K^{-1} [*Vosteen and Schellschmidtb*, 2003]:

$$E_T = MTC_p \tag{18}$$

The thermal energies of the two explosions therefore exceed the kinetic energies by approximately 3 orders of magnitude. Note that the kinetic and thermal energies of the gas phase are not taken into account in these calculations.

8.3. Possible Effects of Outsized Particles

[36] The numerical approach to the inverse problem requires us to define a continuous theoretical function for the PSDs characterizing the explosions. In reality, however, explosion-generated PSDs might contain a coarse tail of large, discrete blocks which, although relatively small in number, could have a nonnegligible effect on the mass estimation. For example, the PSDs estimated photoballistically by *Chouet et al.* [1974] at Stromboli contained such coarse tails of blocks. Large blocks ejected during Strombolian explosions at Mount Etna have also been documented by *McGetchin et al.* [1974]. In the present study these have been neglected because they cannot be described by the type of continuous PSD function required by our automatized inversion algorithm. Manual runs have therefore been carried out to assess the sensitivity of mass calculations to an additional fraction of large particles. We define a composite PSD with a continuous part and an additional discrete part that constitute the lower and upper ranges, respectively, of the natural PSD (Figure 12). The coarse tail, consisting of 85 discrete blocks, is represented by an exponential distribution from 0.1 to 1 m in diameter with a median size of 0.23 m, i.e., close to that observed by

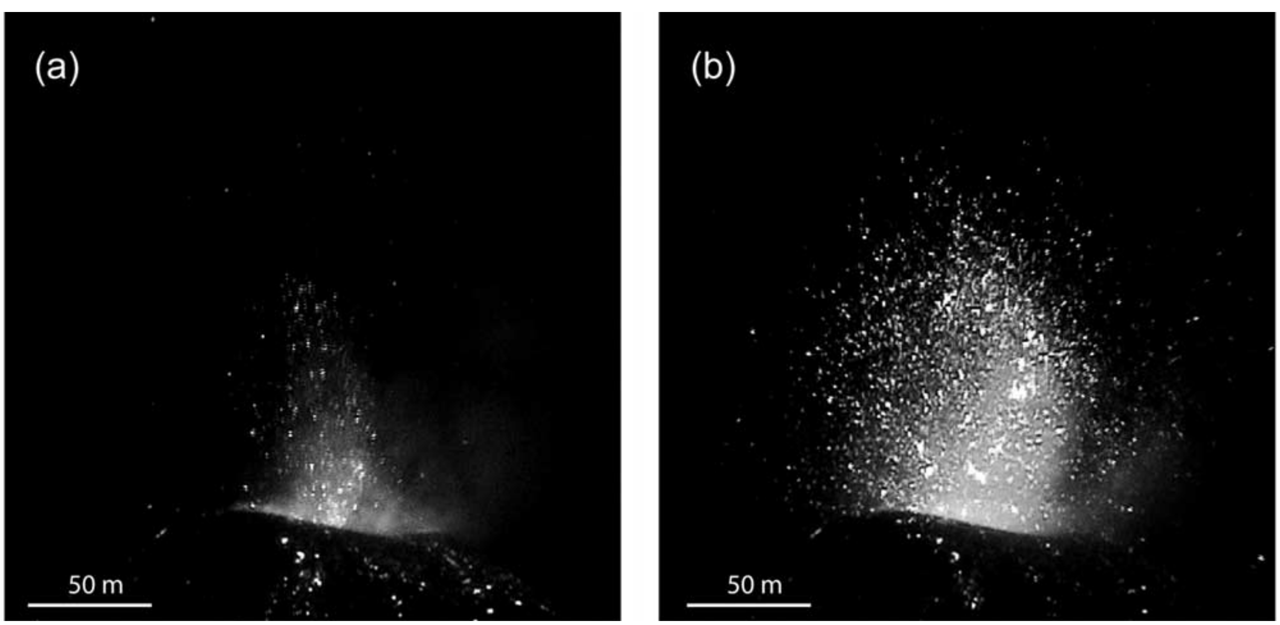

Figure 11. Snapshots of the two explosions from the SE crater of Mount Etna on 4 July 2001. Images are shown at maximum brightness, corresponding to the highest radar reflectivity from lava fragments. (a) The first explosion, occurring at 2141:53 UT, displays a low quantity of lava fragments and lasts 2.2 s, and (b) the second explosion, occurring at 2141:56 UT, displays a much higher number of lava fragments and lasts 2.8 s.

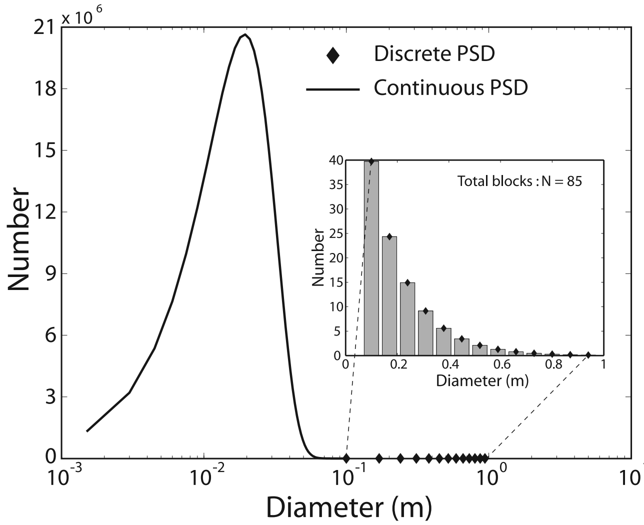

Figure 12. Composite particle size distribution comprising a continuous function to describe the smaller end of the PSD, with an additional coarse tail of large, discrete blocks. The continuous part refers to the PSD of explosion 2 calculated from our algorithm. The coarse tail is constrained from the data of *McGetchin et al.* [1974]; it consists of a total of only 85 blocks with a median size of 0.23 m, but that represents about 10% of the total reflectivity.

McGetchin et al. [1974] at the NE crater of Mount Etna (∼0.2 m). Although numerically less abundant by more than 5 orders of magnitude than the smaller particles constituting the continuous PSD (Figure 12), the blocks of this coarse tail account for ∼10% of the total reflectivity. This composite PSD is probably a more realistic representation of the explosion ejecta, and gives a total mass of 187,000 kg for explosion 2, in comparison to 206,000 kg for the continuous PSD lacking a coarse tail. We conclude that neglecting large blocks results in overestimation of the mass by only 9% for this explosion. This is because the total mass of pyroclasts is mostly controlled by the large number of small particles, as shown in Figure 7. As a result, all the mass-related parameters listed in Tables 4a–4c and 5a–5c can be regarded as maxima.

9. Discussion

[37] A Doppler radar (VOLDORAD) has been used to estimate for the first time a wide range of physical parameters characterizing Strombolian explosions at Mount Etna. In addition to the velocity data routinely provided by Doppler radar [*Donnadieu et al.*, 2005], the results yield estimates of particle loading (number, mass and volume), as well as derived parameters such as mass flux, time-averaged particle kinetic and thermal energies and, more approximately, particle concentration in the eruptive jet.

[38] Our approach in estimating particle loading, and the parameters derived from it, involves certain assumptions. For example, the electromagnetic scattering model assumes that all particles are smooth, spherical and compositionally homogeneous, which is not the case for pyroclasts. However, bearing in mind the statistical effects of a very large number of rough and complexly shaped particles, as well as our objective of first-order estimation, these simplifications seem reasonable. Another assumption concerns the particle size distribution (PSD) used for data inversion. The inversion procedure involves three physical parameters: two constants defining the PSD (mode and shape factor), and the third being the number of particles corresponding to the mode that evolves during the optimization phase of the inversion procedure. In the present study the mode was constrained from the radar measurements at Mount Etna. On the other hand, the shape factor was constrained independently using published photoballistic data of *Chouet et al.* [1974] from explosions at Stromboli, and was assumed to be representative of the explosion ejecta at Mount Etna. Many problems are inherent in this approach. For example, the photoballistically derived PSD of *Chouet et al.* [1974], while not skewed by atmospheric or depositional processes, is inadequate to describe the fine tail of the distribution, particles of which are too small to be detectable on photographs. On the other hand, *McGetchin et al.* [1974] constructed a PSD at Mount Etna from grain size measurements of Strombolian deposits, but this method also failed to take into account the smallest particles, which are dispersed far from source by the wind. Other difficulties involved in determining PSDs from deposits may also arise from bomb agglutination or from block breakage on impact. In addition, such studies probably fail to sample volumes of ejecta large enough to be statistically representative of real amounts of large blocks. Both photoballistic and ground deposits methods therefore fail to take into account small particles, whose contribution to the total mass is important. In contrast, UV satellite methods such as TOMS or more recently OMI [*Carn et al.*, 2008; *Krotkov et al.*, 2008], succeed in imaging gas (particularly SO2), ash and aerosols released by volcanic eruptions. The IR satellite methods such as Meteosat or MODIS [*Watson et al.*, 2004] are further able to provide estimates of the distal ash content of large eruptive clouds far from the emission source that are mainly composed of small particles. But these satellite-based methods fail to image the larger size fractions segregated earlier during plume ascent. These methods might also be biased by atmospheric effects on particles, such as water vapor content and ice formation. Nevertheless, the comparison of near-source estimates of ejecta mass from ground-based Doppler radar with the mass of distal fine ash estimated by satellite-based methods could bring valuable constraints on the particle segregation from ash clouds through space and time and hence on models of ash dispersal. In order to obtain more accurate values of the mass of ejecta, a more thorough knowledge must be acquired of total source granulometries of volcanic explosions, and of their variability for different eruptive regimes. Insights into such source PSDs could be gained for instance by high-resolution imagery and remote sensing methods working at different wavelengths. Such methods should target regions of the eruptive jet close to the vent in order for all ejected particles to be included. Their combination with ground ash collectors would bring even more stringent constraints. Knowledge acquired on PSDs would additionally provide further valuable insights into fragmentation and explosion processes during volcanic eruptions.

[39] By fixing the explosion source PSD shape factor independently, and by determining the PSD mode using the radar measurements, we obtain a way of estimating the particle loading parameters to a first approximation. Neglecting the inevitable coarse tail of large blocks appears justified on the basis of our calculations. The two PSD assumptions used in this paper each have different advantages. The polydisperse model requires an inversion procedure that takes a long time to compute, but which results in mass estimation to a reasonable first-order accuracy. This approach is probably best adapted to studies of eruption dynamics, where the most accurate possible parameter estimates are required. The monodisperse PSD model, on the other hand, does not require any computing phase, so that mass estimation is fast and straightforward. The disadvantage of this method is that it underestimates the particle loading. This monodisperse model is most suitable for volcano monitoring, where the eruptive parameters could be calculated automatically in real time from the Doppler spectra, but where a lower degree of accuracy could probably be tolerated.

[40] This study has shown that Doppler radar is a powerful, as yet underexploited, tool for quantitative studies of eruptive dynamics. The wide range of physical parameters accessible is potentially valuable for testing mathematical models of eruption jets and plumes. VOLDORAD is also well suited to the routine monitoring of active volcanoes. It can be sited at distances of up to 12 km from the vent, making it useful for the monitoring of large, highly explosive edifices. It functions under harsh weather conditions and has a data sampling rate suitable for the study of explosive activity. The relatively low energy consumption allows us either to set up the system quickly in the field with a small power generator for a limited period of time, or to run the radar continuously at a site supplied with electric power. In addition to classical continuous records of temporal series, VOLDORAD has a "trigger" mode, in which sequences of raw data can be recorded at high sampling rate, without basic processing and hence visualization. The system can be activated either on command of the operator [*Dubosclard et al.*, 2004], or by an eruptive seismic signal of some predefined threshold potentially linked to an alarm system. This option is useful when monitoring isolated explosions interspersed with long intervals of quiet activity, as characteristic of many volcanoes. In addition to the immediate benefits for operational surveillance, the long-term deployment of such radar on active volcanoes would enable to document the variability of eruptive behaviors and to build databases potentially useful for future eruptions. Combination with other ground-based methods, such as visual and infrared imagery, broadband seismic, ultrasound detection and gas analysis would shed light on the complex interactions among various eruptive processes. Thermal video such as Forward Looking Infrared Radiometer (FLIR) would be particularly helpful for the study of Strombolian activity. Its capacity to detect both fine ash plumes and large blocks can bring additional constraints on PSDs. This method can also provide further insights on Strombolian source conditions [*Patrick et al.*, 2007]. Besides, our methodology of particle loading estimation could be extended to the study and monitoring of volcanic ash plumes. With this aim, the coupling of multichannel satellite imagery with ground-based radar measurements would be particularly relevant for the mitigation of risks related to ash clouds and for the investigations on ash plume dynamics.

Appendix A: Electromagnetic Scattering Equations

[41] Considering the wide range of particle diameters characterizing volcanic activity, the complete scattering theory is required to account for the effects of large particles. A general solution of electromagnetic wave scattering was given by *Mie* [1908]. The derivation of the electromagnetic scattering model specifically applied to the case of volcanic studies is developed in this section. In this first approach of scattering by volcanic ejecta, we apply Maxwell's equations for plane wave scattered by spherical particles in a homogeneous medium at a large distance [e.g., *Bohren and Huffman*, 1983].

[42] Starting with Maxwell's equation for plane waves:

$$\nabla \cdot E = 0 \tag{A1}$$

$$\nabla \cdot H = 0 \tag{A2}$$

$$\nabla \times E = i\omega\mu H \tag{A3}$$

$$\nabla \times H = -i\omega\varepsilon E \tag{A4}$$

where E and H are the electric and magnetic fields. ε is the dielectric permittivity, μ is the magnetic permeability, and ω is angular frequency. Taking the curl of (A3) and (A4), gives:

$$\begin{aligned} \nabla \times (\nabla \times E) &= i\omega\mu\nabla \times H = \omega^2\varepsilon\mu E \\ \nabla \times (\nabla \times H) &= -i\omega\varepsilon\nabla \times E = \omega^2\varepsilon\mu H \end{aligned} \tag{A5}$$

If we use the vector identity,

$$\nabla \times (\nabla \times A) = \nabla(\nabla \bullet A) - \nabla \bullet (\nabla A) \tag{A6}$$

we obtain

$$\nabla^2 E + \omega^2\varepsilon\mu E = 0 \quad \nabla^2 H + \omega^2\varepsilon\mu H = 0 \tag{A7}$$

where $\nabla^2 A = \nabla \cdot (\nabla A)$. Thus, E and H satisfy the wave equation. The field inside the particle is denoted by (E_1, H_1); the field in the medium surrounding the particle (E_2, H_2) is the superposition of the incident field (E_i, H_i) and the scattered field (E_s, H_s):

$$E_2 = E_i + E_s \quad H_2 = H_i + H_s \tag{A8}$$

The electromagnetic field is required to satisfy the Maxwell equations at points where ε and μ are continuous. However, there is a discontinuity at the boundary of the particle, where the following conditions on the fields are imposed:

$$\begin{aligned} [H_2(x) - H_1(x)] \times n_s &= 0 \\ [E_2(x) - E_1(x)] \times n_s &= 0 \end{aligned} \tag{A9}$$

where n_s is the outward directed normal to the surface of the particle. Under the conditions of our study (far-field region and spherical particle), the scattered field E_s is mainly transverse and can be resolved into components parallel ($E_{//}$) and perpendicular ($E_\perp$) to the scattering plane. The relationship between incident and scattered field amplitudes can be written in matrix form:

$$\begin{pmatrix} E_{//s} \\ E_{\perp s} \end{pmatrix} = \frac{e^{ik_n(R-r_z)}}{-ik_nR} \begin{pmatrix} S_2 & 0 \\ 0 & S_1 \end{pmatrix} \begin{pmatrix} E_{//i} \\ E_{\perp i} \end{pmatrix} \quad \text{(A10)}$$

where $k_n = 2\pi/\lambda$ is the wave number, R, the distance to the particle, and r_z, the component of R on the direction of propagation of the incident wave. The radiation of an electromagnetic wave can be described in terms of intensity from the four Stokes parameters (I, Q, U, V) describing the various states of polarization: not polarized (I), polarized horizontally ($+Q$), polarized vertically ($-Q$), polarized at $+45°$ ($+U$), polarized at $-45°$ ($-U$), right circularly polarized ($+V$) or left circularly polarized ($-V$). The relationship between incident and scattered Stokes parameters (indexed i and s, respectively) follows from the amplitude scattering matrix, also called the Mueller matrix [*Bohren and Huffman*, 1983; *Wolf and Voshchinnikov*, 2004]:

$$\begin{pmatrix} I_s \\ Q_s \\ U_s \\ V_s \end{pmatrix} = \frac{\lambda^2}{4\pi^2R^2} \begin{pmatrix} S_{11}(\Theta) & S_{12}(\Theta) & 0 & 0 \\ S_{12}(\Theta) & S_{11}(\Theta) & 0 & 0 \\ 0 & 0 & S_{33}(\Theta) & S_{34}(\Theta) \\ 0 & 0 & -S_{34}(\Theta) & S_{33}(\Theta) \end{pmatrix} \begin{pmatrix} I_1 \\ Q_i \\ U_i \\ V_i \end{pmatrix} \quad \text{(A11)}$$

The scattering matrix elements ($S_{i,j}$) depend on Θ, which is the angle between the direction of the incident and the scattered radiation of wavelength λ. VOLDORAD transmits power through a square array of four Yagi antennas, such that the incident wave has a horizontal linear polarization (I_i = 1, Q_i = 1, U_i = 0, V_i = 0). Thus, in our case, we denote by $i_{//}$ the corresponding scattered irradiance that only depends on the two first scattering matrix elements (S_{11}, S_{12}):

$$i_{//} = S_{11} + S_{12} = |S_2|^2 \quad \text{(A12)}$$

with

$$S_{11}(\Theta) = \tfrac{1}{2}\left(|S_2(\Theta)|^2 + |S_1(\Theta)|^2\right)$$
$$S_{12}(\Theta) = \tfrac{1}{2}\left(|S_2(\Theta)|^2 - |S_1(\Theta)|^2\right) \quad \text{(A13)}$$

The sum of the two first scattering matrix elements can then be derived from the single complex amplitude function S_2 in the form of a convergent series:

$$S_2(\Theta) = \sum_{n=1}^{\infty} \frac{2n+1}{n(n+1)} (a_n\tau_n(\Theta) + b_n\pi_n(\Theta)) \quad \text{(A14)}$$

where n is a positive integer, a_n and b_n are the complex scattering coefficients (Mie coefficients), and τ_n and π_n are the angular functions. The series can be terminated after n_c sufficiently large terms. The complex scattering coefficients depend particularly on the size parameter x and the refractive index m of the material [*Sauvageot*, 1992] and are defined as

$$a_n = \frac{m\psi_n(mx)\psi_n'(x) - \psi_n(x)\psi_n'(mx)}{m\psi_n(mx)\xi_n'(x) - \xi_n(x)\psi_n'(mx)}$$
$$b_n = \frac{\psi_n(mx)\psi_n'(x) - m\psi_n(x)\psi_n'(mx)}{\psi_n(mx)\xi_n'(x) - m\xi_n(x)\psi_n'(mx)} \quad \text{(A15)}$$

The size parameter $x = k_{nr}$ is a dimensionless variable, r, being the radius of the spherical particle. Ψ and ξ are the Riccati-Bessel functions of first and second kind and can be defined by

$$\psi_n(x) = xj_n(x)$$
$$\xi_n(x) = j_n(x) + iy_n(x) \quad \text{(A16)}$$

where j_n and y_n are the spherical Bessel functions of first and second kind defined as

$$j_n(x) = \sqrt{\tfrac{\pi}{2x}} J_{n+1/2}(x)$$
$$y_n(x) = \sqrt{\tfrac{\pi}{2x}} Y_{n+1/2}(x) \quad \text{(A17)}$$

The spherical Bessel functions satisfy the recurrence relations:

$$z_{n-1}(x) + z_{n+1}(x) = \tfrac{2n+1}{x} z_n(x)$$
$$(2n+1)\tfrac{d}{dp} z_n(x) = nz_{n-1}(x) - (n+1)z_{n+1}(x) \quad \text{(A18)}$$

The angular functions τ_n and π_n depend only on Θ and are defined by the Legendre polynomials,

$$\pi_n(\Theta) = \frac{P_n^1(\Theta)}{\sin\Theta}$$
$$\tau_n(\Theta) = \frac{dP_n^1(\Theta)}{d\Theta} \quad \text{(A19)}$$

and can be found from the recurrence relations:

$$\tau_n(\Theta) = n\cos\Theta\pi_n(\Theta) - (n+1)\pi_{n-1}(\Theta)$$
$$\pi_n(\Theta) = \tfrac{2n-1}{n-1}\cos\Theta\pi_{n-1}(\Theta) - \tfrac{n}{n-1}\pi_{n-2}(\Theta) \quad \text{(A20)}$$

The scattered irradiance can now be calculated for any particle size, under the special conditions of our sounding using VOLDORAD at Mount Etna (Figure 1). Determining the scattering matrix elements enables us to define the scattering cross section of each particle; this then relates irradiance to reflectivity through the Mie coefficients. VOLDORAD is a monostatic radar (i.e., the same antenna is used for transmission and reception), thus we define a backscattering cross section (σ_{bks}) for horizontal linear polarization:

$$\sigma_{bks} = \frac{\lambda^2}{4\pi}\left|\sum_{n=1}^{\infty}(-1)^2(2n+1)(a_n - b_n)\right|^2 \quad \text{(A21)}$$

Note that we often use the backscattering efficiency defined as the cross section coefficient normalized by the particle section such as

$$Q_{bks} = \frac{\sigma_{bks}}{\pi r^2} \quad \text{(A22)}$$

The theoretical radar power for a distributed target in a sampling volume (V_s) at a given distance (R) can then be deduced from the radar reflectivity (η), which is simply the sum of the backscattering cross section (σ_{bks}) of each particle over a unit volume [*Doviak and Zrnic*, 1984; *Sauvageot*, 1992],

$$P_{synth} = \frac{C_r V_s \eta}{R^4} \quad \text{(A23)}$$

$$\eta = \sum_{i=1}^{n} \frac{\sigma_{bks}}{V_s} \quad \text{(A24)}$$

where C_r is the radar constant defined by a set of technical parameters related to the radar configuration.

Notation

α radar beam width (deg).
A_0 amplitude of electromagnetic wave.
a_n, b_n complex scattering coefficients (magnetic and electric mode).
B_r noise of Doppler spectrum (mW).
C mass particle concentration (kg m^{-3}).
C_c constant of conversion.
C_d drag coefficient.
C_p magma specific heat capacity (J kg^{-1} K^{-1}).
C_r radar constant (mW m^2).
C_s shape coefficient of a spherical particle.
D diameter of particle (m).
D_L validity limit diameter (m).
D_p average particle diameter (m).
Δt_{cross} duration for the jet to cross a range gate (s).
Δt_{jet} duration of jet production (s).
E,H electric and magnetic fields (N C^{-1}; A m^{-1}).
ε dielectric permittivity (F m^{-1}).
E_k kinetic energy (J).
E_T thermal energy (J).
f_d Doppler frequency (Hz).
f_t transmitted frequency (Hz).
f_w scaled Weibull probability density function.
γ range of the particle size distribution (m).
G_n range gates (sampling volume).
η radar reflectivity (cm^{-1}).
$i_{//}$ parallel scattered irradiance (W m^{-2}).
j_n, y_n spherical Bessel functions of first and second kind.
K complex dielectric factor.
k shape factor.
k_n wave number (rad m^{-1}).
Λ shift factor.
L length of the range gate (m).
m complex refractive index.
M mass of particles (kg).
μ magnetic permeability (H m^{-1}).
μ_n mode of the particle size distribution (m).
∇ vector differential operator (nabla symbol).
$\nabla \bullet A$ divergence of a vector field A.
$\nabla \times A$ curl of a vector field A.
$\nabla^2 A$ Laplacian of a vector field A.
N number of particles.
N_c number of coherent integrations of radar pulses.
N_{max} scale factor.
N_t characteristic Number of Doppler spectra.
ω angular frequency (rad s^{-1}).
$P_{\pm}$ radar power received (mW).
P_{mes} radar raw power received (mW).
P_{synth} radar synthetic power received (mW).
P_t peak power (W).
P_{tot} total radar power received (mW).
Θ angle between incident and scattered radiation (deg).
θ antenna beam elevation angle (deg).
Q_{bks} backscattering efficiency.
r radius of the particle (m).
R slant distance between radar and target (m).
r_z component of R on the incident wave direction.
ρ_a, ρ_p densities of air and particles (kg m^{-3}).
σ_{bks} backscattering cross section (m^2).
$S(v)$ power spectral density.
S_2 complex amplitude function (parallel component).
S_{11}, S_{12} scattering Mueller matrix elements.
S_w scaled Weibull distribution.
τ pulse duration (μs).
π_n, τ_n angular functions.
T magma temperature (K).
t_r pulse repetition period (μs).
V volume of pyroclasts (m^3).
$\bar{V}^{+}_{max}$ average maximum velocity of ejected pyroclasts (m s^{-1}).
$V^{\pm}_{max}$ maximum velocities of ejected pyroclasts (m s^{-1}).
$V^{\pm}_{mean}$ mean velocities of ejected pyroclasts (m s^{-1}).
V_r radial velocity of ejected pyroclasts (m s^{-1}).
V_s radar sampling volume (m^3).
x size parameter.
X vector of variable input parameters.
ψ, ξ Riccati–Bessel functions of first and second kind.
Z radar reflectivity factor (mm^6 m^{-3}).
λ radar wavelength (cm).
$(I,Q,U,V)_{i,s}$ incident and scattered Stokes parameters (polarization state).

[43] **Acknowledgments.** We acknowledge Geoff Wadge and an anonymous reviewer for their thoughtful reviews that significantly enhanced this

paper, and we thank Richard Arculus and Michael P. Ryan for handling the paper. We also thank T. H. Druitt for his insightful comments that considerably improved the manuscript and S. Vergniolle for discussions on this topic. Georges Dubosclard, Roland Cordesses, and Claude Hervier are especially acknowledged for the precious radar measurements carried out in the field, without which this work could not have been achieved. M. Gouhier's Ph.D. work was supported by a French MESR fellowship. Field work on Etna was possible thanks to the logistical help of the INGV Catania and was funded by the CNRS-INSU PNRN programs 1999–2001.

References

Adams, R. J., W. F. Perger, W. I. Rose, and A. Kostinski (1996), Measurements of the complex dielectric constant of volcanic ash from 4 to 19 GHz, *J. Geophys. Res.*, *101*, 8175–8185, doi:10.1029/96JB00193.

Bohren, C. F., and D. R. Huffman (1983), *Absorption and Scattering of Light by Small Particles*, 489 pp., Wiley-Interscience, New York.

Carn, S. A., A. J. Prata, and S. Karlsdóttir (2008), Circumpolar transport of a volcanic cloud from Hekla (Iceland), *J. Geophys. Res.*, *113*, D14311, doi:10.1029/2008JD009878.

Chouet, B., N. Hamisevicz, and T. R. McGetchin (1974), Photoballistics of Volcanic Jet Activity at Stromboli, Italy, *J. Geophys. Res.*, *79*, 4961–4976, doi:10.1029/JB079i032p04961.

Dean, K., S. A. Bowling, G. Shaw, and H. Tanaka (1994), Satellite analyses of movement and characteristics of the Redoubt Volcano plume, *J. Volcanol. Geotherm. Res.*, *62*, 339–352, doi:10.1016/0377-0273(94)90040-X.

Dehn, J., K. Dean, and K. Engle (2000), Thermal monitoring of North Pacific volcanoes from space, *Geology*, *28*, 755–758, doi:10.1130/0091-7613(2000)28<755:TMONPV>2.0.CO;2.

Donnadieu, F., G. Dubosclard, R. Cordesses, T. Druitt, C. Hervier, J. Kornprobst, J. F. Lénat, P. Allard, and M. Coltelli (2005), Remotely monitoring volcanic activity with ground-based Doppler radar, *Eos Trans. AGU*, *86*, 204, doi:10.1029/2005EO210001.

Doviak, R. J., and D. S. Zrnic (1984), *Doppler Radar and Weather Observations*, 562 pp., Academic, Orlando, Fla.

Dubosclard, G., R. Cordesses, P. Allard, C. Hervier, M. Coltelli, and J. Kornprobst (1999), First testing of a volcano Doppler radar (Voldorad) at Mt. Etna, *Geophys. Res. Lett.*, *26*, 3389–3392, doi:10.1029/1999GL008371.

Dubosclard, G., F. Donnadieu, P. Allard, R. Cordesses, C. Hervier, M. Coltelli, M. Privitera, and J. Kornprobst (2004), Doppler radar sounding of volcanic eruption dynamics at Mount Etna, *Bull. Volcanol.*, *66*, 443–456, doi:10.1007/s00445-003-0324-8.

Francalanci, L., P. Manetti, and A. Pecerillo (1989), Volcanological and magmatological evolution of Stromboli volcano (Aeolian islands): The roles of fractional crystallization, magma mixing, crustal contamination and source heterogeneity, *Bull. Volcanol.*, *51*, 355–378, doi:10.1007/BF01056897.

Gouhier, M., and F. Donnadieu (2006), Numerical modeling of Doppler radar signals of Strombolian eruptions, *Eos Trans. AGU*, *87*(52), Fall Meet. Suppl., Abstract V43B-1794.

Harris, D. M., and W. I. Rose (1983), Estimating particles size, concentrations, and total mass of ash in volcanic clouds using weather radar, *J. Geophys. Res.*, *88*, 10,969–10,983, doi:10.1029/JC088iC15p10969.

Harris, D. M., W. I. Rose, R. Roe, and M. R. Thompson (1981), Radar observations of ash eruptions, *U.S. Geol. Surv. Prof. Pap.*, *1250*, 323–333.

Hort, M., and R. Seyfried (1998), Volcanic eruption velocities measured with a micro radar, *Geophys. Res. Lett.*, *25*, 113–116.

Hort, M., R. Seyfried, and M. Vöge (2003), Radar Doppler velocimetry of volcanic eruptions: Theoritical considerations and quantitative documentation of changes in eruptive behaviour at Stromboli, Italy, *Geophys. J. Int.*, *154*, 515–532, doi:10.1046/j.1365-246X.2003.01982.x.

Kittleman, L. R. J. (1964), Application of Rosin's distribution in size frequency analysis of clastic rocks, *J. Sediment. Petrol.*, *34*, 483–502.

Krotkov, N. A., et al. (2008), Validation of SO_2 retrievals from the Ozone Monitoring Instrument over NE China, *J. Geophys. Res.*, *113*, D16S40, doi:10.1029/2007JD008818.

Lacasse, C., S. Karlsdóttir, G. Larsen, H. Soosalu, W. I. Rose, and G. G. J. Ernst (2004), Weather radar observations of the Hekla 2000 eruption cloud, Iceland, *Bull. Volcanol.*, *66*, 457–473, doi:10.1007/s00445-003-0329-3.

Marzano, F. S., G. Vulpiani, and W. I. Rose (2006a), Microphysical characterization of microwave radar reflectivity due to volcanic ash clouds, *IEEE Trans. Geosci. Remote Sens.*, *44*, 313–327, doi:10.1109/TGRS.2005.861010.

Marzano, F. S., S. Barbieri, G. Vulpiani, and W. I. Rose (2006b), Volcanic ash cloud retreival by ground-based microwave weather radar, *IEEE Trans. Geosci. Remote Sens.*, *44*, 3235–3246, doi:10.1109/TGRS.2006.879116.

McGetchin, T. R., M. Settle, and B. Chouet (1974), Cinder cone growth modeled after northeast crater, Mount Etna, Sicily, *J. Geophys. Res.*, *79*, 3257–3272, doi:10.1029/JB079i023p03257.

Mie, G. (1908), Beiträge zur Optik trüber Medien, speziell kolloidaler Metallösungen, *Ann. Phys.*, *330*(3), 377–445.

Nakamura, Y. (1984), The 1888 eruption of Bandai volcano, Japan: Grain size distribution, paper presented at IAVCEI Meeting, Int. Assoc. of Volcanol. and Chem. of the Earth's Interior, Rome, 13–17 Aug.

Patrick, M. R., A. J. L. Harris, M. Ripepe, J. Dehn, D. A. Rothery, and S. Calvari (2007), Strombolian explosive styles and source conditions: Insights from thermal (FLIR) video, *Bull. Volcanol.*, *69*, 769–784, doi:10.1007/s00445-006-0107-0.

Pointin, Y., J. Fournet-Fayard, and F. Donnadieu (2005), Calibration du radar UHF VOLDORAD 2, par comparaison de ses données avec celles du disdromètre du LaMP/OPGC., *Note OPGC 144*, 61 pp., Obs. de Phys. du Globe, Clermont-Ferrand, France.

Riley, C. M., W. I. Rose, and G. J. S. Bluth (2003), Quantitative shape measurements of distal volcanic ash, *J. Geophys. Res.*, *108*(B10), 2504, doi:10.1029/2001JB000818.

Ripepe, M., M. Rossi, and G. Saccorotti (1993), Image processing of explosive activity at Stromboli, *J. Volcanol. Geotherm. Res.*, *54*, 335–351, doi:10.1016/0377-0273(93)90071-X.

Rogers, R., and M. Yau (1989), *A Short Course on Cloud Physics*, Pergamon, Oxford, U.K.

Sauvageot, H. (1992), *Radar Meteorology*, 366 pp., Artech House, Boston, Mass.

Self, S., R. S. J. Sparks, B. Booth, and G. P. L. Walker (1974), The 1973 Heimaey Strombolian Scoria deposit, Iceland, *Geol. Mag.*, *111*, 539–548.

Seyfried, R., and M. Hort (1999), Continuous monitoring of volcanic eruption: A review of various techniques and new results from a frequency-modulated radar Doppler system, *Bull Volcanol.*, *60*, 627–639.

Sheridan, M. F. (1971), Particle-size characteristics of pyroclastic tuffs, *J. Geophys. Res.*, *76*, 5627–5634, doi:10.1029/JB076i023p05627.

Sheridan, M. F., K. H. Wohletz, and J. Dehn (1987), Discrimination of grain-size subpopulations in pyroclastic deposits, *Geology*, *15*, 367–370, doi:10.1130/0091-7613(1987)15<367:DOGSIP>2.0.CO;2.

Spieler, O., M. Alidibirov, and D. B. Dingwell (2003), Grain-size characteristics of experimental pyroclasts of 1980 Mount St. Helens cryptodome dacite: Effects of pressure drop and temperature, *Bull. Volcanol.*, *65*, 90–104.

Vosteen, H. D., and R. Schellschmidtb (2003), Influence of temperature on thermal conductivity, thermal capacity and thermal diffusivity for different types of rock, *Phys. Chem. Earth*, *28*, 499–509.

Watson, I. M., V. J. Realmuto, W. I. Rose, A. J. Prata, G. J. S. Bluth, Y. Gu, C. E. Bader, and T. Yu (2004), Thermal infrared remote sensing of volcanic emissions using the moderate resolution imaging spectroradiometer, *J. Volcanol. Geotherm. Res.*, *135*, 75–89, doi:10.1016/j.jvolgeores.2003.12.017.

Weibull, W. (1939), A statistical theory of the strength of materials, *R. Swed. Inst. Eng. Res.*, *151*.

Weill, A., G. Brandeis, S. Vergniolle, F. Baudin, J. Bilbille, J. F. Fèvre, B. Piron, and X. Hill (1992), Acoustic sounder measurements of the vertical velocity of volcanic jets at Stromboli volcano, *Geophys. Res. Lett.*, *19*, 2357–2360, doi:10.1029/92GL02502.

Williams, H., and A. R. McBirney (1979), *Volcanology*, 397 pp., Freeman Cooper, San Francisco, Calif.

Wohletz, K. H., M. F. Sheridan, and W. K. Brown (1989), Particle size distributions and the sequential fragmentation/transport theory applied to volcanic ash, *J. Geophys. Res.*, *94*, 15,703–15,715, 721, doi:10.1029/JB094iB11p15703.

Wolf, S., and N. V. Voshchinnikov (2004), Mie scattering by ensembles of particles with very large size parameters, *Comput. Phys. Commun.*, *162*, 113–123, doi:10.1016/j.cpc.2004.06.070.

Woods, A. W., and M. I. Bursik (1991), Particle fallout, thermal disequilibrium and volcanic plumes, *Bull. Volcanol.*, *53*, 559–570, doi:10.1007/BF00298156.

F. Donnadieu and M. Gouhier, Laboratoire Magmas et Volcans (UMR 6524 CNRS-IRD), 5, rue Kessler, F-63038 Clermont-Ferrand, France. (F.Donnadieu@opgc.univ-bpclermont.fr; M.Gouhier@opgc.univ-bpclermont.fr)